Physics of Atomic Nuclei, Vol. 66, No. 2, 2003, pp. 203–205. Translated from Yadernaya Fizika, Vol. 66, No. 2, 2003, pp. 227–229.

NUCLEI
Theory

On the Binding of Atoms with Antiatoms

T. K. Rebane and N. D. Markovski

Institute of Physics, St. Petersburg State University (Petrodvorets Branch), Ul'yanovskaya ul. 1, St. Petersburg, 198904 Russia

Received August 15, 2001; in final form, January 29, 2002

Abstract—The stability of $X^+Y^+X^-Y^-$ Coulomb molecules consisting of X^+Y^- atoms and X^-Y^+ antiatoms to dissociation is studied. On the basis of multiparameter variational calculations, it is found that such molecules are stable to dissociation into X^+X^- atoms and Y^+Y^- antiatoms if the mass ratio of particles X and Y lies in the range $0.4710 < m_X/m_Y < 2.1231$. The $e^+e^+e^-e^-$, $\pi^+\mu^+\pi^-\mu^-$, $t^+d^+t^-d^-$, $p^+K^+p^-K^-$, and $d^+p^+d^-p^-$ molecules satisfy this condition. © *2003 MAIK "Nauka/Interperiodica".*

The stability of four-particle Coulomb systems $A^+B^+C^-D^-$ to dissociation into two-particle atoms was considered in [1–3] versus the masses of particles A, B, C, and D. Among the variety of such system, annihilating symmetric molecules belonging to the $X^+Y^+X^-Y^-$ type and representing a mental combination of an X^+Y^- atom with an X^-Y^+ antiatom stand out for the following reason. While $X^+X^+Y^-Y^-$ symmetric molecules consisting of two identical atoms X^+Y^- are stable to dissociation at any masses m_X and m_Y of particles X and Y, $X^+Y^+X^-Y^-$ molecules are stable to dissociation into X^+X^- and Y^+Y^- atoms only if the mass difference between particles X and Y is not very large. Indeed, let us consider the case of $m_X \gg m_Y$, in which the compact atom X^+X^- undergoes virtually no polarization in the field of the Y^+Y^- atom; therefore, the two atoms do not form a bound molecule. It follows that there exists a critical mass ratio $s_0 = m_X/m_Y$ such that, for $m_X/m_Y \geq s_0$, the atoms in question do not form $X^+Y^+X^-Y^-$ molecules with the corresponding antiatoms. By virtue of the symmetry of energy with respect to the permutation of particles X and Y, the molecules cannot exist for $m_Y/m_X \geq s_0$ either—that is, for $m_X/m_Y \leq 1/s_0$.

Using the variational principle, Richard [1] showed that the stability of the $X^+Y^+X^-Y^-$ molecule to dissociation (hereafter dissociation stability) guarantees the dissociation stability of all four-particle molecules of the general form $A^+B^+C^-D^-$ if the masses of the particles involved satisfy the condition

$$(1/m_A + 1/m_C)/(1/m_B + 1/m_D) = m_Y/m_X. \quad (1)$$

This condition makes it possible to explore the dissociation stability of various four-particle systems $A^+B^+C^-D^-$. In order to apply it, we must determine the mass-ratio ($s = m_X/m_Y$) interval in which there exists a bound state of the $X^+Y^+X^-Y^-$ molecule. The corresponding Monte Carlo calculations were performed in [2] with this aim in view. However, the region of dissociation stability of the molecules being considered could not be determined reliably in this way because the Monte Carlo method does not provide bounds on energy and because two different versions of the method yielded significantly different results.

For this reason, we carried out precise variational calculations of $X^+Y^+X^-Y^-$ molecules consisting of atoms and antiatoms.

In atomic units ($|e| = \hbar = m_e = 1$), the Hamiltonian of such molecules has the form

$$H(m_X, m_Y; \mathbf{r}_1, \mathbf{r}_2, \mathbf{r}_3, \mathbf{r}_4) = -(1/2) \quad (2)$$
$$\times [\Delta_1/m_X + \Delta_2/m_Y + \Delta_3/m_X + \Delta_4/m_Y]$$
$$+ 1/r_{12} - 1/r_{13} - 1/r_{14} - 1/r_{23} - 1/r_{24} + 1/r_{34}.$$

The lower boundary of the energy spectrum of this operator, $E(m_X, m_Y)$, is the ground-state energy of the molecule whose center of mass is immobile. Owing to the symmetry property $E(m_Y, m_X) = E(m_X, m_Y)$, it is sufficient to perform calculations for $m_X \geq m_Y$.

We used Gaussian basis functions, each depending on all six interparticle distances and involving six nonlinear parameters a_j, b_j, c_j, d_j, e_j, and f_j:

$$\phi_j(r_{12}, r_{23}, r_{34}, r_{41}, r_{13}, r_{24}) = \exp(-a_j r_{12}^2 \quad (3)$$
$$- b_j r_{23}^2 - c_j r_{34}^2 - d_j r_{41}^2 - e_j r_{13}^2 - f_j r_{24}^2).$$

Taking into account the symmetry of the Hamiltonian in (2) under charge conjugation—that is, with respect to a simultaneous interchange of particles 1 and 3

1063-7788/03/6602-0203$24.00

Ground-state energy E, dissociation energy D, and expectation values of the kinetic energies of particle pairs for $X^+Y^+X^-Y^-$ molecules at various values of the particle-mass ratio $s = m_X/m_Y$ [all quantities are expressed in $m_Y e^4/\hbar^2$ (modified atomic energy unit)]

$s = m_X/m_Y$	E	D	$\langle -(\Delta_1 + \Delta_3)/2m_X \rangle$	$\langle -(\Delta_2 + \Delta_4)/2m_Y \rangle$
1	−0.5160032	0.0160032	0.2580016	0.2580016
1.3209327	−0.5935444	0.0133112	0.3046277	0.2889167
1.4976017	−0.6338979	0.0094975	0.3401936	0.2937043
1.9004800	−0.7269306	0.0018106	0.4511662	0.2757644
1.9990075	−0.7505212	0.0007693	0.4827830	0.2677382
2	−0.750779	0.000779	0.483214	0.267565
2.02	−0.755600	0.000600	0.489738	0.265862
2.04	−0.760369	0.000369	0.496098	0.264271
2.06	−0.765340	0.000340	0.502006	0.263334
2.08	−0.770221	0.000221	0.508133	0.262088
2.10	−0.775112	0.000112	0.514171	0.260941
2.12	−0.780015	0.000015	0.520120	0.259895

(X^+ and X^-) and of particles 2 and 4 (Y^+ and Y^-)—we constructed the trial variational wave function for the $X^+Y^+X^-Y^-$ molecule in the form

$$\Psi = \sum_{j=1}^{N} C_j \left[\phi_j(r_{12}, r_{23}, r_{34}, r_{41}, r_{13}, r_{24}) \right. \qquad (4)$$
$$\left. + \phi_j(r_{34}, r_{14}, r_{12}, r_{23}, r_{13}, r_{24})\right].$$

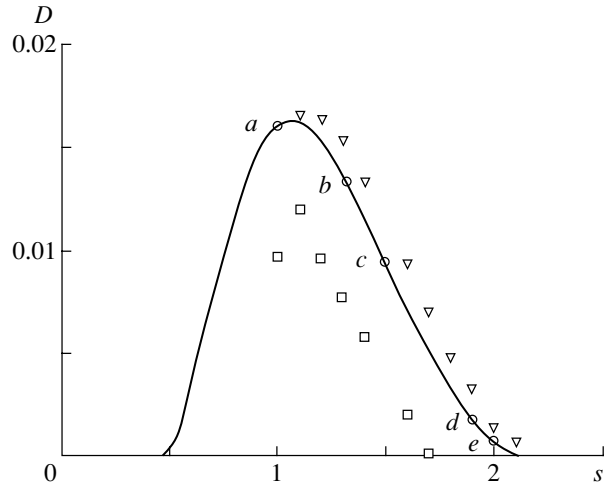

Dissociation energy D [in $m_Y e^4/\hbar^2$ (modified atomic unit)] of $X^+Y^+X^-Y^-$ molecules with respect to decay into X^+X^- and Y^+Y^- atoms versus the particle-mass ratio $s = m_X/m_Y$: (curve) results of the variational calculation performed in this study [open circles represent the dissociation energies calculated for the (*a*) $e^+e^+e^-e^-$, (*b*) $\pi^+\mu^+\pi^-\mu^-$, (*c*) $t^+d^+t^-d^-$, (*d*) $p^+K^+p^-K^-$, and (*e*) $d^+p^+d^-p^-$ molecules] and (open boxes and inverted triangles) results of the calculations based on, respectively, the variational and the diffusion version of the Monte Carlo method [2].

We considered the $e^+e^+e^-e^-$, $\pi^+\mu^+\pi^-\mu^-$, $t^+d^+t^-d^-$, $p^+K^+p^-K^-$, and $d^+p^+d^-p^-$ molecules (for which the particle-mass ratio $s = m_X/m_Y$ takes the values of 1, 1.3209327, 1.4976017, 1.9004800, and 1.9990075, respectively) and hypothetic molecules for the mass ratios of $s = 2.00$, 2.02, 2.04, 2.06, 2.08, 2.10, and 2.12.

The calculation employed a basis of $N = 200$ functions ϕ_j and involved the optimization of all 1200 nonlinear parameters by the method described in [4].

For the $e^+e^+e^-e^-$, $\pi^+\mu^+\pi^-\mu^-$, $t^+d^+t^-d^-$, $p^+K^+p^-K^-$, and $d^+p^+d^-p^-$ molecules, we then extended the original basis to $N = 3200$ functions by adding 3000 functions ϕ_j featuring random values of nonlinear parameters.

The results of our calculations are quoted in the table, which displays the ground-state energies E of the molecules, their dissociation energies D, and the expectation values of the kinetic energies of particle–antiparticle pairs (X^+ and X^-, Y^+ and Y^-). These expectation values satisfy the virial theorem

$$\langle -(\Delta_1 + \Delta_3)/2m_X \rangle \qquad (5)$$
$$+ \langle -(\Delta_2 + \Delta_4)/2m_Y \rangle = -\langle V \rangle/2 = -E,$$

where $\langle V \rangle$ is the expectation value of the potential energy of the molecule.

In the figure, the dissociation energy D computed in the present study for $X^+Y^+X^-Y^-$ molecules is contrasted against the results obtained by the Monte Carlo method [2]. It can be seen that the variational

version of the Monte Carlo method significantly underestimates the dissociation energy, while its diffusion version somewhat overestimates this energy.

It is clear from the table that the dissociation energy D is positive within the mass-ratio interval $1 \le m_X/m_Y \le 2.12$ and that $X^+Y^+X^-Y^-$ Coulomb molecules for $m_X \ge m_Y$ are stable to dissociation.

The stability interval can be slightly extended by means of an additional variational calculation.

We denote by $\Psi(r_{12}, r_{23}, r_{34}, r_{41}, r_{13}, r_{24})$ the variational wave function found for the $X^+Y^+X^-Y^-$ molecule at $m_X = 2.12$ and $m_Y = 1$. Symbols enclosed by angular brackets represent the expectation values calculated with this wave function for the corresponding physical quantities. We further consider the function $\Psi(\alpha r_{12}, \alpha r_{23}, \alpha r_{34}, \alpha r_{41}, \alpha r_{13}, \alpha r_{24})$, where α is a scale factor, and calculate the expectation value of the Hamiltonian in (2) with this function, setting $m_X = M$ and $m_Y = 1$.

Taking into account the variational principle, we obtain an upper bound on the ground-state energy of the molecule formed by particles whose masses are $m_X = M$ and $m_Y = 1$:

$$E(M,1) \le \alpha^2\langle -(\Delta_1+\Delta_3)/2M - (\Delta_2+\Delta_4)/2\rangle + \alpha\langle V\rangle. \quad (6)$$

The optimum value of the scale factor α is determined by minimizing the right-hand side of this inequality. The result is

$$\alpha = -\frac{\langle V\rangle}{\langle -(\Delta_1+\Delta_3)/M - (\Delta_2+\Delta_4)\rangle}. \quad (7)$$

Substituting this value into (6), we obtain

$$E(M,1) \le -\frac{\langle V\rangle^2}{2\langle -(\Delta_1+\Delta_3)/M - (\Delta_2+\Delta_4)\rangle}. \quad (8)$$

Using the expectation values calculated for the kinetic-energy operators of particle pairs at $m_X = 2.12$ and $m_Y = 1$ (see table) and taking into account the virial theorem (5), we obtain an upper bound on the energy of the $X^+Y^+X^-Y^-$ molecule formed by particles whose masses are $m_X = M$ and $m_Y = 1$:

$$E(M,1) \le \frac{-0.6084234}{1.1026544/M + 0.259895}. \quad (9)$$

A molecule is stable to dissociation if its energy is less than the sum of the energies of the X^+X^- and Y^+Y^- atoms. For the case being considered, this condition reads

$$E(M,1) < -(M+1)/4. \quad (10)$$

It follows from (9) that this is so up to $M = 2.1231$.

Since the dissociation energy is invariant under the interchange of particles X and Y, this means that the Coulomb interaction of atoms and antiatoms leads to the formation of $X^+Y^+X^-Y^-$ molecule, which is stable to dissociation if the mass ratio of particles X and Y lies within the range

$$0.4710 \le m_X/m_Y \le 2.1231. \quad (11)$$

Five molecules belonging to the $X^+Y^+X^-Y^-$ type and consisting of atoms and antiatoms satisfy the condition in (11). These are $e^+e^+e^-e^-$, $\pi^+\mu^+\pi^-\mu^-$, $t^+d^+t^-d^-$, $p^+K^+p^-K^-$, and $d^+p^+d^-p^-$. For other combinations of atoms and antiatoms composed of electrons, muons, pions, kaons, and protons and of their antiparticles, the condition in (11) is badly violated, so that the corresponding $X^+Y^+X^-Y^-$ molecules are not formed. For example, the particle-mass ratios for the atom–antiatom pairs t^+p^- and t^-p^+, $K^+\pi^-$ and $K^-\pi^+$, d^+K^- and d^-K^+, and $p^+\pi^-$ and $p^-\pi^+$ are 2.99, 3.51, 3.80, and 6.72, respectively. Since variational calculations yield an upper bound on the energy of the systems under study, an exact value s_0 of the critical particle-mass ratio may slightly exceed the value of 2.1231 obtained here. However, this cannot affect the number of $X^+Y^+X^-Y^-$ molecules stable to dissociation. For this reason, the $p^+e^+p^-e^-$ molecule may be involved, as an intermediate state, in the annihilation of a hydrogen atom p^+e^- and an antihydrogen atom p^-e^+ only through its quasibound (resonance) states [5].

REFERENCES

1. J. M. Richard, Phys. Rev. A **49**, 3573 (1994).
2. D. Bressanini, M. Mella, and G. Morosi, Phys. Rev. A **55**, 200 (1997).
3. T. K. Rebane, Yad. Fiz. **62**, 1749 (1999) [Phys. At. Nucl. **62**, 1630 (1999)].
4. T. K. Rebane and N. D. Markovskiĭ, Opt. Spektrosk. **89**, 725 (2000) [Opt. Spectrosc. **89**, 667 (2000)].
5. B. Zygelman, A. Saenz, P. Froelich, *et al.*, Phys. Rev. A **63**, 052722 (2001).

Translated by M. Kobrinsky

Physics of Atomic Nuclei, Vol. 66, No. 2, 2003, pp. 206–217. From Yadernaya Fizika, Vol. 66, No. 2, 2003, pp. 230–241.

NUCLEI
Theory

Generation of Angular Momentum of Fission Fragments in a Cluster Model*

T. M. Shneidman[1),2)], G. G. Adamian[1),2),3)], N. V. Antonenko[1),2)], S. P. Ivanova[1),2)], R. V. Jolos[1),2)], and W. Scheid[1)]

Joint Institute for Nuclear Research, Dubna, Moscow oblast, 141980 Russia

Received September 5, 2001

Abstract—Based on the dinuclear system concept, the role of bending vibrations in creation of the angular momentum of primary fission fragments is investigated. For ^{252}Cf spontaneous fission, the angular momenta of the fragments are calculated as a function of the neutron multiplicity and compared with available experimental data. Different cluster compositions of the ^{252}Cf fission modes at the scission point are considered. © *2003 MAIK "Nauka/Interperiodica".*

1. INTRODUCTION

The phenomenon of nuclear molecular resonances, which, for their description, require a consideration of the relative motion of two nuclei, has been known for a long time from the study of reactions with certain light nuclei [1, 2]. For heavy nuclei, the experimental facts indicate the formation of a dinuclear system (DNS) with a quite long lifetime (about a few units of 10^{-21} s) which results from the investigation of deep inelastic reactions with heavy ions at energies lower than 15 MeV/nucleon [3, 4]. When the DNS evolves in mass (charge) asymmetry, its decay in relative distance R between the centers of the nuclei determines the charge and mass distribution of the reaction products [3]. The complete fusion process is successfully described as an evolution of the DNS to the compound nucleus by the transfer of nucleons from the light nucleus to the heavy one [5, 6]. This also supports the assumption on the formation of the DNS at the entrance channel of the fusion reaction. The fissioning system just before the scission, when the neck radius is small, can also be treated as a system of two aligned deformed nuclei separated by a constant distance between their tips [7–15]. A thermal equilibrium is usually assumed in the DNS. In order to describe the dependence of the experimental data on the total kinetic energy (TKE) of the fission fragments, we consider the pole–pole configuration of the DNS nuclei. The main observables, like the distributions of mass, charge, and kinetic energy in the fission of a wide range of nuclei from Po to Fm, are reproduced well in scission point fission models [10]. The fragmentation theory [16] treats the fission as a quantum-mechanical process in relative distance and mass asymmetry coordinates and qualitatively explains the general features of the fission mass distributions.

The experimental data show that the difference in the potential energy between the saddle and scission configurations (about several tens of MeV) is not completely transformed into the total kinetic energy of the relative motion of the fission fragments, and other collective or intrinsic degrees of freedom take the rest of the energy. Different types of collective angular oscillations, like wriggling, bending, tilting, and twisting, are possible in the excited pre-scission DNS [4, 8, 9, 17–22]. These collective modes do not contribute to the kinetic energy of the fragments after the decay of the DNS. The angular oscillations can generate rotational energy and angular momenta of the fission fragments. The recent experimental study of spontaneous fission of ^{252}Cf with the Gammasphere detector provides information about the average angular momentum of the fission fragments [23–25]. The primary fission fragments have angular momenta of about $(2–8)\hbar$, whereas the fissioning nucleus initially has zero spin [23]. These data result from the study of the γ transitions between the levels of the ground-state rotational bands of the fragments [25].

The production of angular momentum in the fission fragments and the method of calculating the DNS potential and excitation energies are described

*This article was submitted by the authors in English.

[1)]Institut für Theoretische Physik der Justus-Liebig-Universität, Giessen, Germany.

[2)]Joint Institute for Nuclear Research, Dubna, Moscow oblast, 141980 Russia.

[3)]Institute of Nuclear Physics, Tashkent, Uzbekistan.

in Sections 2 and 3, respectively. The angular momenta of the fission fragments are calculated in Section 4 as a function of the number of postscission neutrons under the assumption of bending angular oscillations at the scission point by which the fragments gain angular momentum. For ^{252}Cf spontaneous fission, the calculated results are compared with the experimental data. The cluster aspects of fission with small TKE are considered. A summary is given in Section 5. The method of calculating the DNS potential is presented in the Appendix.

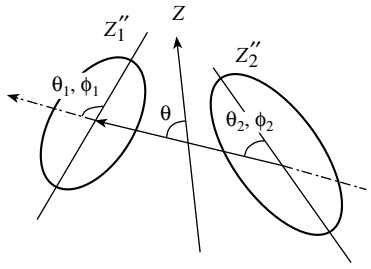

Fig. 1. Schematic picture and definitions of various coordinates of the DNS configuration.

2. GENERATION OF ANGULAR MOMENTUM IN PRIMARY FISSION FRAGMENTS

Bending Vibrations

At the scission point, a fissioning system can be considered approximately as a DNS whose intrinsic degrees of freedom are in thermal equilibrium. However, the shape of the DNS is not equilibrated. In this paper, we assume that the angular momenta of the fission fragments are generated by small bending (butterfly) oscillations of the DNS nuclei around the pole–pole orientation. A similar assumption was made earlier in [8, 9, 24]. In the bending mode, the rolling of nuclear surfaces occurs. The slide of nuclear surfaces in the wriggling mode is assumed to be suppressed by friction and larger stiffness of the potential.

The Hamiltonian describing the collective modes of a DNS (nuclear molecule) was analyzed in [19], where suitable coordinates were introduced and an expression for the kinetic energy operator was derived. The procedure of quantization of the classical Hamiltonian is described in [26]. Below, we consider the case of axially deformed DNS nuclei and exclude from consideration beta and gamma vibrations of the clusters and oscillations of an intercluster distance around the equilibrium value. The frequency of the oscillations in R is at least three times larger than those for the angular oscillations. The equilibrium distance $R = R_{\min} \approx R_1(1 - \beta_1^2/(4\pi) + \sqrt{5/(4\pi)}\beta_1) + R_2(1 - \beta_2^2/(4\pi) + \sqrt{5/(4\pi)}\beta_2) + 0.5$ fm between the centers of nuclei corresponds to the minimum of the nucleus–nucleus potential, which is the sum of nuclear and Coulomb potentials, U_N and U_C [27]:

$$U(R, \beta_i, \Omega_i) = U_C(R, \beta_i, \Omega_i) + U_N(R, \beta_i, \Omega_i). \quad (1)$$

Here, the angles $\Omega_i = (\theta_i, \phi_i)$ $(i = 1, 2)$ specify the orientation of the intrinsic coordinate system of the ith nucleus with respect to the molecular frame whose Z axis goes through centers of the nuclei forming the DNS, and β_i are the deformation parameters.

The coordinates used to describe the motion of clusters forming the DNS are shown in Fig. 1. The center of this coordinate frame lies at the DNS center of mass. The angle θ is the angle of rotation of the DNS as a whole. The angles θ_1 and θ_2 specify the orientation of the cluster with respect to the axis connecting centers of mass of the clusters. The angles ϕ_1 and ϕ_2 specify their azimuthal orientation. The angles θ_1 and θ_2 are related via the condition that clusters touch each other at the poles [19]. If this condition is not fulfilled, potential energy increases considerably. Under this condition,

$$\frac{\tilde{R}_2}{\tilde{R}_1} \approx \frac{\sin|\pi - \theta_1|}{\sin|\theta_2|}, \quad (2)$$

where $\tilde{R}_i = R_i(1 - \beta_i^2/(4\pi) + \sqrt{5/(4\pi)}\beta_i)$ and $R_i = r_0 A_i^{1/3}$ are the radii along the symmetry axis of clusters having prolate deformation and their spherical radii, respectively. If only small values of $(\pi - \theta_1)$ and θ_2 are allowed, then

$$\tilde{R}_1(\pi - \theta_1) = -\tilde{R}_2\theta_2. \quad (3)$$

Thus, the butterfly degree of freedom is given by

$$\epsilon = \pi - \theta_1. \quad (4)$$

Under the assumption formulated above, the model Hamiltonian describing the rotation of the DNS as a whole and small bending angular vibrations can be written as [19]

$$H = T_{\text{rot}} + T_\epsilon + U_\epsilon, \quad (5)$$

where T_{rot} describes rotation of the DNS as a whole, and T_ϵ is the kinetic energy of bending motion:

$$T_\epsilon = -\frac{\hbar^2}{2J_\epsilon}\frac{1}{\epsilon}\frac{d}{d\epsilon}\left(\epsilon\frac{d}{d\epsilon}\right), \quad (6)$$

$$J_\epsilon = J_1 + (\tilde{R}_1/\tilde{R}_2)^2 J_2. \quad (7)$$

Here, $J_{1,2}$ are moments of inertia of clusters forming the DNS. U_ϵ is the potential energy of bending motion. Since the starting Hamiltonian is a two-dimensional one and, therefore, the volume element is $dV = \epsilon d\epsilon$, the kinetic energy term T_ϵ is different from that in the initially one-dimensional problem.

Using the condition that the total angular momentum of the decaying system is zero and constraint (3), one can express the angle θ as a function of ϵ:

$$\theta = \frac{J_1\tilde{R}_2 - J_2\tilde{R}_1}{\tilde{R}_2(\mu R_{\min}^2 + J_1 + J_2)}\epsilon. \quad (8)$$

It is seen from Eq. (8) that, for a nearly symmetrical DNS, $\theta \approx 0$ and the role of $T_{\rm rot}$ in (5) is negligible.

The potential energy was considered in [19] only schematically. The aim of the present paper is to apply to calculations of fission-fragment angular momenta the potential energy calculated by us in previous publications [27] and applied to analysis of the experimental data on fusion and deep inelastic collisions. The potential energy is calculated in the Appendix taking (3) into account. We neglect, as was mentioned above, the oscillations of the intercluster distance. Because of the axial symmetry of the cluster deformation, the potential energy does not depend on the azimuthal vibrations. Then, for small deviations of the ratio of angles θ_1 and θ_2 from (3), the potential energy of bending vibrations takes the form

$$U_\epsilon = \frac{1}{2}C_{11}(\pi - \theta_1)^2 + C_{12}(\pi - \theta_1)\theta_2 + \frac{1}{2}C_{22}\theta_2^2. \quad (9)$$

The stiffness coefficients C_{11}, C_{12}, and C_{22} are given in the Appendix.

Using condition (3) and notation (4), we get from (9)

$$U_\epsilon = \frac{1}{2}C_\epsilon\epsilon^2, \quad (10)$$

where

$$C_\epsilon = C_{11} - 2(\tilde{R}_1/\tilde{R}_2)C_{12} + (\tilde{R}_1/\tilde{R}_2)^2C_{22}. \quad (11)$$

Thus, we get the following Schrödinger equation for the bending vibrations:

$$-\frac{\hbar^2}{2J_\epsilon}\frac{1}{\epsilon}\frac{d}{d\epsilon}\epsilon\frac{d}{d\epsilon}\psi_n + \frac{1}{2}C_\epsilon\epsilon^2\psi_n = E_n\psi_n. \quad (12)$$

Equation (12) describes the harmonic vibrational motion in ϵ.

The solution to Eq. (12) is

$$\psi_n = N_0L_n(J_\epsilon\omega_\epsilon\epsilon^2/\hbar)\exp(-J_\epsilon\omega_\epsilon\epsilon^2/(2\hbar)), \quad (13)$$
$$E_n = \hbar\omega_\epsilon(2n+1), \quad n = 0, 1, 2\ldots,$$

where $\omega_\epsilon = \sqrt{C_\epsilon/J_\epsilon}$, while $N_0 = \sqrt{2J_\epsilon\omega_\epsilon/\hbar}$ and $L_n(x)$ are the normalization coefficient and the Laguerre polynomial [28], respectively.

In order to estimate the angular momentum of the bending mode, we expand $\psi_n = \sqrt{2\pi}\sum_L b_n^L Y_{L0} \times (\theta, \phi = 0)$ into spherical harmonics. With the expansion coefficients b_n^L [8]

$$|b_n^L|^2 = (2L+1)\gamma_0^2[L_n((L+0.5)^2\gamma_0^2)]^2 \times \exp(-(L+0.5)^2\gamma_0^2),$$

we determine the average value of angular momentum $\langle L\rangle_n$ in the state ψ_n as follows:

$$\langle L\rangle_n = \sum_L L|b_n^L|^2. \quad (14)$$

Here, $\gamma_0^2 = \hbar\omega_\epsilon/C_\epsilon$. If the DNS is in thermal equilibrium with an excitation energy E^* (the corresponding temperature is $\Theta = \sqrt{E^*/a}$, $a = A/12$ MeV^{-1}), the average angular momentum $\langle L\rangle$ is calculated as

$$\langle L\rangle = \sum_n \langle L\rangle_n P_n / \sum_n P_n, \quad (15)$$

where $P_n = \exp[-E_n/\Theta]$ is a Boltzmann-like occupation probability of the nth bending state. The applicability of the Boltzmann factor was demonstrated many times for the description of the mass, charge, angular, and kinetic-energy distributions of the fission fragments in the scission-point models. The exact population probability of a given bending state is well approximated by the Boltzmann factor. Since the potential for the bending oscillations has a finite depth, besides smallness of P_n, the maximal value of n in (15) should be restricted by the capacity of this potential to hold a certain number of bound states ψ_n. However, for the temperatures considered, this restriction of n does not affect the results. Note that the maximal value of n is discussed only in connection with the second fission mode of ^{252}Cf.

As was shown in [8, 22], the change in angular momentum due to Coulomb excitation after the DNS decay is negligible. The Coulomb excitation after the DNS decay only increases the width of the distribution of the angular momentum and practically does not change the value of $\langle L\rangle$ for the channels with neutron(s) evaporation.

3. EXCITATION ENERGY OF THE DNS AND TKE OF FISSION FRAGMENTS

In order to calculate the average angular momentum of the fission fragments by Eq. (15), we should determine the excitation energy of the DNS before its decay. The dependence of average angular momentum of the primary fission fragments on the number of evaporated neutrons is extracted from the experiment [23, 24]. For the comparison with the theory, we have to establish a relation between the DNS excitation energy E^* and the number of evaporated neutrons after the DNS decay.

With the assumption that the prescission kinetic energy of the fission fragments is very small [10], the total energy $E_{\rm tot}$ of the DNS is estimated as

$$E_{\rm tot} = E^* + E_n + U_{\rm int} + B_1^{\rm def} + B_2^{\rm def} - B_{12}, \quad (16)$$

where E_n, $U_{\rm int} = U(R_m, \beta_i, \Omega_i)$ [see (1)], and $B_i^{\rm def}$ $(i = 1, 2)$ are the energy of bending oscillations, the energy of interaction of the DNS nuclei, and the binding energies of the DNS deformed nuclei, respectively. Note, that $B_i^{\rm def}$ differs from the experimental binding energy B_i of the separated nuclei in their ground state [29]. Since the energies E_n of low-lying bending states, which give the main contributions to angular momentum, do not exceed a few MeV and are comparable with the accuracy of calculation of $U_{\rm int}$, we can neglect E_n in (16). Indeed, this additional term in (16) does not visibly change the calculated temperature. After the decay, the total energy $E_{\rm tot}$ of the system can be estimated as follows:

$$E_{\rm tot} = E_\nu + {\rm TKE} + B_1 + B_2 - B_{12}, \qquad (17)$$

where E_ν is the energy taken by the ν evaporated neutrons. Assuming that the interaction energy $U_{\rm int}$ of the DNS nuclei is approximately equal to the TKE and using the equality of the two previous expressions, we define the excitation energy E^* as

$$E^* = E_\nu + \Delta B_1 + \Delta B_2 = E_\nu + (B_1 - B_1^{\rm def}) + (B_2 - B_2^{\rm def}). \qquad (18)$$

If the deformation energy $\Delta B_1 + \Delta B_2$ required to deform the DNS nuclei from their ground states is small, we obtain

$$E^* \approx E_\nu = \sum_{m=1}^{\nu} (S_m + 2\Theta_m), \qquad (19)$$

where the average kinetic energy of the mth evaporated neutron is equal to two times the temperature Θ_m of the fragments. The separation energies S_m of the mth neutron of the first or second fragment are taken from [29]. Since the number of evaporated neutrons from each primary fission fragment is available [23–25], the value of E_ν is easily calculated. In the DNS, we deal with two distinct nuclei. Therefore, decay of the DNS is not the same as scission in the traditional description of fission, and no comparison of prescission excitation energy obtained in this description with E^* can be made. In this paper, we assume that the fissioning nucleus after the scission lives for some time as the DNS.

If we consider the decay of ^{252}Cf into the Mo–Ba fragmentation, the value of $(A_{\rm Mo}/A_{\rm Ba})E_\nu^{\rm Ba} - E_\nu^{\rm Mo}$ characterizes the distribution of the excitation energy $E_\nu = E_\nu^{\rm Ba} + E_\nu^{\rm Mo}$ between the primary fission fragments. Using the experimental data [23], we can calculate the dependence of $(A_{\rm Mo}/A_{\rm Ba})E_\nu^{\rm Ba} - E_\nu^{\rm Mo}$ on ν. In Fig. 2, one can see that, up to $\nu = 5$, the excitation energy is distributed approximately proportionally to the masses of the fragments. This indicates the validity of (19) because the excitation energy in the DNS has an equal partition according to the nucleon numbers of the nuclei. For $\nu > 5$, the difference between E^* and E_ν becomes large and we should take the value of $\Delta B_1 + \Delta B_2$ into consideration. From Fig. 2, we can see that the deformation energy is larger in Ba than in Mo.

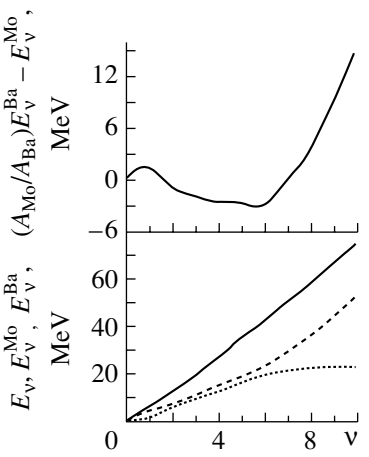

Fig. 2. The values of $(A_{\rm Mo}/A_{\rm Ba})E_\nu^{\rm Ba} - E_\nu^{\rm Mo}$ (upper part) and $E_\nu^{\rm Ba}$, $E_\nu^{\rm Mo}$, and E_ν (lower part; long-dashed, short-dashed, and solid curves, respectively) as a function of the number of evaporated neutrons ν from both nuclei are presented for the primary fission fragments ^{104}Mo+^{148}Ba of ^{252}Cf. The excitation energies of the primary fission fragments $E_\nu^{\rm Ba}$ and $E_\nu^{\rm Mo}$ ($E_\nu = E_\nu^{\rm Ba} + E_\nu^{\rm Mo}$) are taken from experimental data [23].

4. RESULTS OF CALCULATIONS

A. Different Fission Modes

In order to get a correct value of the average total kinetic energy $\langle {\rm TKE} \rangle = 189 \pm 1$ MeV for the first (standard) fission mode of ^{252}Cf leading to the Mo–Ba fragmentation, the quadrupole deformations of ^{104}Mo and ^{148}Ba should be taken as $\beta_1 = 0.50$ and $\beta_2 = 0.40$, respectively. These deformations are larger than the deformations of Mo and Ba in their ground states. They correspond to the local minimum of the potential energy of the DNS configuration calculated with the two-center shell-model scheme [2, 30]. The quadrupole deformations of ^{104}Mo and ^{148}Ba extracted from the reduced $E2$-transition probabilities from the ground state to the first 2^+ state are $\beta_{10} = 0.35$ and $\beta_{20} = 0.22$, respectively [31]. The induced deformations β_i, which are necessary to describe the $\langle {\rm TKE} \rangle$, are caused by the polarization of the DNS nuclei [32]. The deformation energies ΔB_i of each DNS nucleus can be estimated in the harmonic oscillator approximation as

$$\Delta B_i = D_{\beta i}\omega_{\beta i}^2(\beta_i - \beta_{i0})^2, \qquad (20)$$

where $D_{\beta i}$ and $\omega_{\beta i}$ are the mass parameter and the frequency of the beta vibration in the ith nucleus, respectively. Using the experimental data for $D_{\beta i}$ and $\omega_{\beta i}$ [31], one can show that the values of ΔB_i do not exceed 1.0 MeV for the considered fragmentations of ^{252}Cf. These values are rather small and can be neglected in (18). The fact that the deformation energy is small is supported by microscopic calculations giving an energy difference of a few MeV between the superdeformed and ground states even at zero angular momentum [33, 34]. Since the deformation of the DNS nuclei has sufficiently small energies, the difference $Q - \mathrm{TKE}$ mainly corresponds to the excitation energy of the internal degrees of freedom of the DNS for $\nu < 5$ for the case of Mo + Ba splitting. This means that the DNS is heated before the scission and we can use a statistical treatment to find the average angular momentum of each fragment. In the calculations, we consider bending oscillations in the DNS with $\Theta < 1$ MeV that corresponds to excitation energies less than 30 MeV. The coupling between the internal degrees of freedom and the relative motion determines the distribution of the TKE. In order to explain the TKE for fission events with $\nu > 5$, larger deformations of the DNS nuclei should be taken into account for which the values of ΔB_i are not negligible. Note that, for the other splitting, ΔB_i could be sufficient starting with smaller ν.

The second fission mode in the fragmentation of ^{252}Cf into Mo and Ba corresponds to unusually small $\langle \mathrm{TKE} \rangle = 153 \pm 3$ MeV and a large number of emitted neutrons. In this mode, the fragments are highly excited and evaporate more than seven neutrons. A low TKE means enormously elongated nuclei in the decaying DNS. The most likely charge fragmentations are ^{106,107,108}Mo + ^{146,145,144}Ba in the second mode. Since the ground state of Ba has a large octupole deformation [35, 36] that can be described by an α-cluster type configuration of Ba [37], a cluster consideration of the second mode looks reasonable. Thus, we describe large octupole deformations of fragments by cluster-type configurations [37] and assume the formation of a linear chain of two alpha particles between Zr and Xe. The breakup of the system ^{102,103,104}Zr + ^{4}He + ^{4}He + ^{142,141,140}Xe supplies $\langle \mathrm{TKE} \rangle \approx 161$ MeV with the deformations $\beta_i = 0.50$ and 0.25 of Zr and Xe, respectively. In this system, we have $\Delta B_1 + \Delta B_2 = 15$ MeV and one can expect the emission of more than seven neutrons after the decay of the system ($E^* = E_\nu + \Delta B_1 + \Delta B_2$). After decay, the systems ^{102,103,104}Zr + ^{4}He and ^{142,141,140}Xe + ^{4}He remain bound and correspond to the Mo and Ba fragments, respectively. The cluster interpretation is suitable for the second fission mode with $\nu > 7$. In fission events with $5 < \nu < 7$, both fission modes seem to contribute. In [12], the second mode of fission of ^{252}Cf was also described as connected to the formation of the cluster configurations in the Ba fragments.

The large deformations of the fragments in the second fission mode can also be described by the following cluster states of the nuclei: ^{148}Ba $\rightarrow$ ^{74}Ni + ^{74}Ni and ^{104}Mo $\rightarrow$ ^{50}Ca + ^{54}Ti. The deformation energies are equal to 20 and 15 MeV ($\Delta B = 35$ MeV) for such cluster configurations and are close to those for hyperdeformed nuclei [37]. The linear chain (^{74}Ni + ^{74}Ni) + (^{50}Ca + ^{54}Ti) with the deformations of the nuclei taken from [31] reproduces the $\langle \mathrm{TKE} \rangle$ for the second fission mode. The excitation energy E^* of the system near scission is about 30 MeV. After the scission, the systems ^{74}Ni + ^{74}Ni and ^{50}Ca + ^{54}Ti are transformed into ^{148}Ba and ^{104}Mo, respectively, with the transition of deformation energies into intrinsic excitations.

B. Angular Momentum of the Fission Fragments

The potential energy of the DNS as a function of the relative distance R for the fission ^{252}Cf $\rightarrow$ ^{104}Mo + ^{148}Ba is shown in the upper part of Fig. 3. It is seen that the DNS pole–pole configuration has the minimal energy. The minimum of the pocket is located at the distance $R_{\min}$. This minimum moves to smaller values of the relative distance with increasing angles $\tilde{\theta}_i$ ($\tilde{\theta}_1 = \pi - \theta_1, \tilde{\theta}_2 = \theta_2$). In the lower part of Fig. 3, the dependence of the potential energy on the angles $\tilde{\theta}_i$ is shown in two limits: (i) the relative distance corresponds to the minimum of the potential energy at all values of angles (adiabatic limit); (ii) the relative distance does not change ($R = R_{\min}(\tilde{\theta}_i = 0) =$ const) with angles (diabatic limit). For $|\tilde{\theta}_1| < 0.5$, the potentials in these two limits are very similar. It is seen that the oscillator approximation is quite good for describing the angular dependence of the potential energy if the amplitude does not exceed 0.5 rad. In Fig. 4, we present the dependence of the stiffness parameter of the bending mode on the deformation parameters for the ^{100}Zr + ^{100}Zr system. The value of stiffness strongly increases with the deformation parameters $\beta_1 = \beta_2$ from zero and reaches a nearly constant value at $0.12 \leq \beta_i \leq 0.25$. For $\beta_i \geq 0.25$, the stiffness decreases slowly. Thus, for $\beta_i \geq 0.12$, the calculated results seem to be weakly sensitive to the value of the deformation parameters because the stiffness of the potential depends weakly on β_i.

In order to estimate the mean angular momenta of the fission fragments by Eq. (15), we calculated the spectrum of the bending mode for various fragmentations of the ^{252}Cf nucleus. The influence of the fragment deformations β_i and moments of inertia J_i on

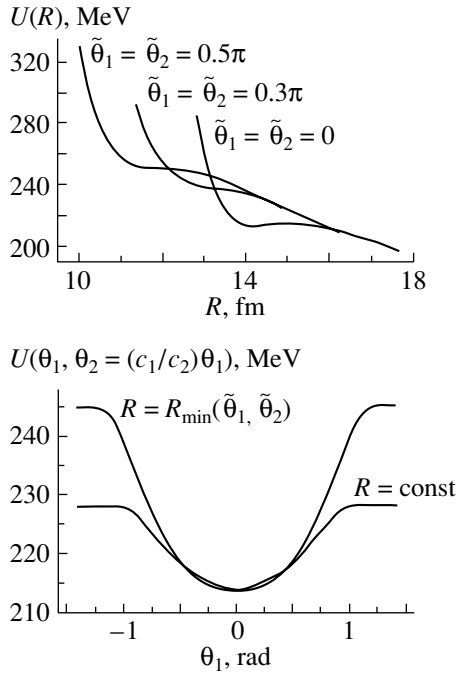

Fig. 3. Upper part: Dependence of the DNS potential energy on the relative distance R between the centers of fragments for the fission of ^{252}Cf $\rightarrow$ ^{104}Mo+^{148}Ba. Calculations are done for different orientations of the DNS nuclei with $\beta_1(^{104}\mathrm{Mo}) = 0.35$ and $\beta_2(^{148}\mathrm{Ba}) = 0.22$. Lower part: Calculated potential energy U of the DNS as a function of the angles $\tilde{\theta}_i$ in two limits: (i) $R = R_{\min}$ (adiabatic limit) and (ii) $R = R_{\min}(\tilde{\theta}_i = 0) = \mathrm{const}$ (diabatic limit). The relation $\tilde{\theta}_2 = (\tilde{R}_1/\tilde{R}_2)\tilde{\theta}_1$ is used in the calculations.

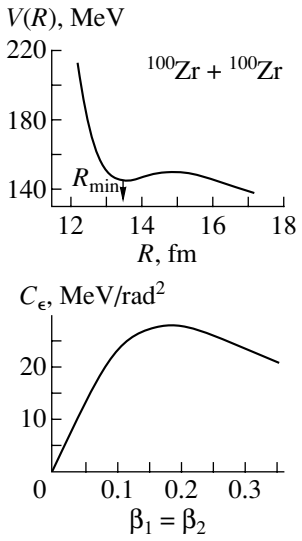

Fig. 4. Upper part: The DNS potential as a function of the relative distance R between the centers of fragments for the symmetric system ^{100}Zr + ^{100}Zr with $\beta_1 = \beta_2 = 0.3$. Lower part: The calculated stiffness parameter C_ϵ of the bending mode in the DNS as a function of the quadrupole deformation parameters $\beta_1 = \beta_2$ for the symmetric system ^{100}Zr + ^{100}Zr.

the excitation of the bending states is demonstrated in the table. In this calculation, we use the experimental moments of inertia J_i of the DNS nuclei that are obtained from the measured values of the energies $E_{2^+\to 0^+}$ of the $2^+ \to 0^+$ rotational transitions: $J_i = 3/E_{2^+\to 0^+}$ ($\hbar^2$/MeV) [31]. When both fragments are well deformed, the energy E_1 of the first excited state ($n = 1$) of the bending mode [see (13)] is about 1.5–2.0 MeV. If one of the fragments is almost spherical, the value of E_1 is about 3.0–6.0 MeV.

The calculated angular momenta of fission fragments as a function of the total number of evaporated neutrons ν are presented in Figs. 5 and 6 for the fragmentations Mo + Ba and Zr + Ce of ^{252}Cf [23–25]. The value of E^* is estimated by formula (19) for the standard fission mode assuming ΔB_i to be small. Since the potential for the bending oscillation in this fission mode is deep enough and contains a quite large number of states, the calculated values of $\langle L \rangle$ practically do not depend on the upper limit of the sums in (15). The calculations of angular momentum for the standard fission mode were performed by using the experimental and rigid-body moments of inertia of the nuclei. The experimental moment of inertia of the nucleus is smaller than the rigid-body one. However, for the system of two interacting nuclei in the field of each other, realistic moments of inertia of nuclei must take values between the two considered limits. For example, the measured moments of inertia for the superdeformed and hyperdeformed states are about 85% of the rigid-body value [33, 34, 37]. A possibility of considering highly deformed states in heavy nuclei as DNS configurations was demonstrated in [37]. Indeed, the corresponding DNS have the same quadrupole moments and moments of inertia as those measured for the superdeformed states and for the hyperdeformed states in actinides [37]. Taking these facts into consideration, we suppose that the correct theoretical values of average angular momenta must lie between two curves presented in Figs. 5 and 6 for the standard fission mode. For the splitting Mo + Ba, the calculated average angular momenta of fragments carried by the bending mode are in satisfactory agreement with the experimental data for $\nu < 5$. The experimental points are located between two theoretical curves. The theoretical curves correctly describe the functional dependence of data on ν up to $\nu = 5$. For Zr + Ce fragmentation, the experimental points are located below both theoretical curves, but the deviations of the theoretical results from the experimental data would not exceed $1.5\hbar$ for $\nu < 5$ if we image the theoretical data between the two curves presented in Fig. 6. Comparing the experimental data

Calculated values of the frequency $\hbar\omega_\epsilon$ and the moment of inertia J_ϵ of the bending mode for even–even fragmentations of ^{252}Cf.

Light fragment	β_1	Heavy fragment	β_2	$\hbar\omega_\epsilon$, keV	J_ϵ, $\hbar^2$/MeV
^{100}Sr	0.372	^{152}Nd	0.274	569	58.1
^{102}Zr	0.421	^{150}Ce	0.274	754	46.1
^{104}Zr	0.42	^{148}Ce	0.246	799	39.7
^{104}Mo	0.325	^{148}Ba	0.22	792	34.39
^{106}Mo	0.353	^{146}Ba	0.218	768	33.13
^{108}Mo	0.354	^{144}Ba	0.193	779	32.49
^{112}Ru	0.302	^{140}Xe	0.11	1030	21.28
^{120}Cd	0.2	^{132}Sn	0.05	1770	6.81

with the results of the calculations, we should note that the angular momenta of primary fragments were not directly measured in the experiment. From the intensities of the γ transitions between different levels of the spontaneous fission fragment (secondary), the experimentalists determine the level populations and calculate the average angular momentum of the secondary fragment. To obtain the angular momentum of the primary fragment, the mean number of evaporated neutrons from the fragments and the spin reduction due to the neutron evaporation are calculated with some statistical model. This model correction of the angular momenta leads to the uncertainties in the experimental results. Taking into consideration these facts and the discussion in [38] on the method of extraction of the data from the set of γ transitions, the agreement of theoretical calculations with the present data is quite satisfactory.

For $\nu > 5$, the calculated values of the angular momenta of the fragments obtained by neglecting a possible formation of an alpha-particle chain in the neck deviate from the experimental ones. However, the higher values of the neutron multiplicity are connected to the second mode of fission, which could have a different cluster composition more complicated than the DNS. Since for $\nu > 5$ the deformation energy ΔB cannot be disregarded in Eq. (18), we overestimate the value of E^* with (19) and the values of $\langle L\rangle$. In order to demonstrate the applicability of our model also for $\nu > 5$, we simulate large deformations of fragments by cluster-type configurations for which the value of ΔB is easily calculated. The system ^{102}Zr + ^{4}He + ^{4}He + ^{142}Xe, which supplies the experimental TKE, is used for the second fission mode. The calculation of the angular momentum of the fragments in Fig. 5 is done for $\nu \geq 8$ by assuming a rigid coupling between the alpha particles and heavy nuclei. This approximation can be applied because the bending frequency of a system consisting of an alpha particle and a heavy nucleus is much larger than that for the whole system. The calculations for this cluster configuration give a better agreement with the experimental data for $\nu \geq 8$ than the calculations with the DNS used for the standard fission mode. We have found that the potential for the bending oscillations in the system ^{102}Zr + ^{4}He + ^{4}He + ^{142}Xe is shallow and contains no more than four states. Therefore, the sum in (15) is taken up to $n = 4$. The analysis of similar cluster configurations allows us to expect the second fission mode with very low $\langle$TKE$\rangle$ for the charge splittings Zr–Ce and Ru–Xe. Further experiments will give the answer to whether our assumption is correct.

A correlation between the maxima of the yields of fission-fragment pairs and of the angular momenta of the fragments is experimentally observed [25]. One can assume that the maximal yields of pairs originating from fission events are associated with the minima of the potential energy at the scission point as a function of β_i and of the N/Z ratios in the fragments. The corresponding DNS has the maximal internal excitation energy in the minimum of potential energy of the fissioning system in comparison with the neighboring configurations. As follows from formula (15), the maximal excitation energy leads to a maximal mean angular momentum of the fragments under the same conditions. The value of angular momentum increases with a decreasing moment of inertia but not so strongly as with temperature. For example, for the charge splittings (secondary) ^{104}Mo + Ba and ^{102}Zr + Ce of ^{252}Cf, the maxima of yields correspond to $4n$ and to $(2–4)n$ evaporation channels, respectively. Thus, for these reactions, the angular distributions of the fragments as functions of ν have maxima corresponding to the evaporation of $4n$ and $(2–4)n$ neutrons. For the neutronless charge splittings ^{104}Mo + ^{148}Ba and ^{102}Zr + ^{150}Ce, the

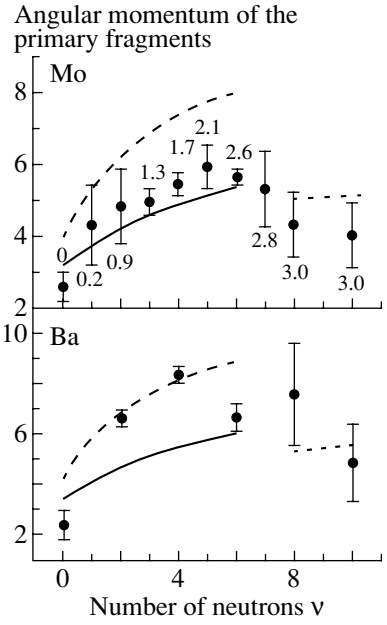

Fig. 5. Calculated and experimental [23, 24] (solid circles) angular momentum (unit $\hbar$) of fission fragments as a function of the total number of evaporated neutrons ν from both nuclei for the Mo + Ba primary fragmentation of ^{252}Cf. The secondary fragment pairs involve ^{104}Mo with different Ba isotopes. The upper part shows the values for the Mo daughter nuclei; the lower part shows those of the corresponding Ba daughter nuclei. The numbers in the upper part are the adjusted numbers of emitted neutrons from the primary Mo fragments. The calculations for the first fission mode performed with experimental and rigid-body moments of inertia are shown by solid and dashed curves, respectively. The calculations for the second fission mode performed with experimental moments of inertia are shown by short-dashed curves.

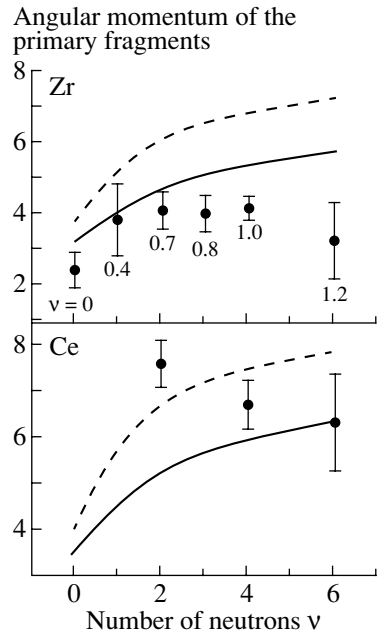

Fig. 6. The same as in Fig. 5, but for the fragmentation of ^{252}Cf into the fragments Zr + Ce. The secondary fragment pairs involve ^{102}Zr with different Ce isotopes.

values of yields and of mean total angular momenta are the smallest compared to the channels with an evaporation of neutrons. In order to describe the yields of fission-fragment pairs and of the angular momenta of the fragments at the same time, one should perform cumbersome calculations of the multidimensional potential energy surface for the DNS. The last point will allow us to define the DNS temperature in a more correct way.

5. SUMMARY

The angular momenta of the fission fragments are calculated under the assumption that the bending angular oscillations of the DNS are responsible for the generation of the angular momenta of the fragments. The calculated results are in qualitative agreement with the experimental data for ^{252}Cf spontaneous fission. No attempt is made to adjust parameters to fit the experimental data. In contrast to some phenomenological calculations, the angular momenta were not normalized to the experimental value obtained for the definite fragments of spontaneous fission. We should stress that the temperature of the system is not a free parameter in our model. It is shown that, for $\nu < 5$, the difference $Q -$ TKE mainly corresponds to the excitation energy of the internal degrees of freedom of the DNS. This means that the considered fissioning system is heated before the scission in the case of postscission evaporation of less than five neutrons. The small $\langle$TKE$\rangle$ of the second fission mode in the fragmentation of ^{252}Cf into Mo and Ba is interpreted as the formation of a chain of two alpha particles between Zr and Xe nuclei ($^{102-104}$Zr + ^{4}He + ^{4}He + $^{142-140}$Xe) at the scission point. The internal excitation energy of this system is sufficient for the emission of more than seven neutrons after the decay of such a cluster state. Taking into account the deformation energy, we are able to describe the angular momenta of the fission fragments in the second fission mode.

APPENDIX

Potential Energy of the DNS and Stiffness of Bending Mode

1. Nuclear part of nucleus–nucleus potential

By following the method proposed in [27], the double-folding procedure is used to calculate the nuclear part of the nucleus–nucleus potential

$$U_N(R, \beta_i, \Omega_i) \qquad \text{(A.1)}$$

$$= \int \rho_1(\mathbf{r}_1)\rho_2(\mathbf{r}_2)F(\mathbf{r}_1-\mathbf{r}_2+\mathbf{R})d\mathbf{r}_1 d\mathbf{r}_2$$

$$= C_0\left[\frac{F_{\text{in}}-F_{\text{ex}}}{\rho_0}\left(\int \rho_1^2(\mathbf{r})\rho_2(\mathbf{R}+\mathbf{r})d\mathbf{r} + \int \rho_1(\mathbf{r})\rho_2^2(\mathbf{R}+\mathbf{r})d\mathbf{r}\right) + F_{\text{ex}}\int \rho_1(\mathbf{r})\rho_2(\mathbf{R}+\mathbf{r})d\mathbf{r}\right]$$

with the effective density-dependent nucleon–nucleon interaction

$$F(\mathbf{r}_1-\mathbf{r}_2+\mathbf{R}) = C_0\left(F_{\text{in}}\frac{\rho_1(\mathbf{r}_1)+\rho_2(\mathbf{r}_2)}{\rho_0} + F_{\text{ex}}\left(1-\frac{\rho_1(\mathbf{r}_1)+\rho_2(\mathbf{r}_2)}{\rho_0}\right)\right)\delta(\mathbf{r}_1-\mathbf{r}_2+\mathbf{R}), \quad \text{(A.2)}$$

$$F_{\text{in,ex}} = f_{\text{in,ex}} + f'_{\text{in,ex}}\frac{N_1-Z_1}{A_1}\frac{N_2-Z_2}{A_2},$$

which is known from the theory of finite Fermi systems [39]. Here, $A = A_1 + A_2$ and N_i (Z_i) are neutron (proton) numbers of nuclei. The values of C_0 and the dimensionless parameters $f_{\text{in,ex}}$ and $f'_{\text{in,ex}}$ are fitted to describe a large number of experimental data [39]. The repulsive core in the double-folding potential is obtained naturally when one uses density-dependent nucleon–nucleon interactions. For the density of deformed nuclei with $A > 16$, one can use the two-parameter symmetrized Woods–Saxon function within the intrinsic frame of the nucleus ($\mathbf{r} = r, \theta', \phi'$)

$$\rho_i(\mathbf{r}, a_i) = \frac{\rho_0 \sinh(R_i(\theta',\phi')/a_i)}{\cosh(R_i(\theta',\phi')/a_i) + \cosh(r/a_i)}, \quad \text{(A.3)}$$

where $\rho_0 = 0.17$ fm^{-3} is the density in the center of nucleus and $a_i = 0.55$ fm denotes the diffuseness parameter of the ith nucleus. The shapes of the DNS nuclei are described as

$$R_i(\theta',\phi') = R_i\left(1-\frac{\beta_i^2}{4\pi}+\beta_i Y_{20}(\theta',\phi')\right). \quad \text{(A.4)}$$

The angles with the prime sign are the angles of $\mathbf{r}$ with respect to the intrinsic coordinate frames of each nucleus. We are interested in the dependence of the DNS potential energy on the orientation angles θ_i with respect to the internuclear axis (molecular frame). Because the functions in (A.1) depend on angles measured in the intrinsic frame of each nucleus, we rewrite them with respect to the molecular frame using D functions. The D functions do not depend on the variables of integration and can be carried outside of the integrals [27].

For the analytical calculation of U_N and the reduction of the number of terms in the expansion, we introduce the following modified expansions in the quadrupole deformation parameters β_i for the nuclear density and for the square of the density in the intrinsic coordinate frames:

$$\rho_i(\mathbf{r}, a_i) = \rho_i(r, a_i) + \xi\left[R_i\frac{d\rho_i(r,b_i)}{dR_i}\beta_i Y_{20}(\theta',\phi') + \frac{R_i^2}{2}\frac{d^2\rho_i(r,b_i)}{dR_i^2}\beta_i^2 Y_{20}^2(\theta',\phi')\right], \quad \text{(A.5)}$$

$$\rho_i^2(\mathbf{r}, a_i) = \rho_i^2(r, a_i) + \xi'\left[R_i\frac{d\rho_i^2(r,b'_i)}{dR_i}\beta_i Y_{20}(\theta',\phi') + \frac{R_i^2}{2}\frac{d^2\rho_i^2(r,b'_i)}{dR_i^2}\beta_i^2 Y_{20}^2(\theta',\phi')\right].$$

The values of ξ, ξ', b_i, and b'_i are fixed by fitting the radial dependences of $\rho_i(\mathbf{r}, a_i)$ and $\rho_i^2(\mathbf{r}, a_i)$ at $\theta' = \alpha_i$ and $\phi' = 0$, where the angle α_i corresponds to the nuclear surface point nearest to the other nucleus. Therefore, expression (A.5) can be used for any values of β_i and should be considered as an approximation to the correct dependences of $\rho_i(\mathbf{r}, a_i)$ and $\rho_i^2(\mathbf{r}, a_i)$ on R at fixed θ_i. Note that the terms proportional to β_i^2 in (A.5) were introduced to increase the accuracy of the calculations. The assumption of a small overlap of nuclei of the DNS allows us to neglect the dependence of ξ, ξ', b_i, and b'_i on θ' and ϕ' in the calculations of U_N at fixed β_i and θ_i.

Since we are interested in the potential energy at condition (3), further calculations are performed assuming a small deviation of the ratio between $\tilde{\theta}_1$ and $\tilde{\theta}_2$ from ratio (3). If the angles $\tilde{\theta}_1 = \pi - \theta_1$ and $\tilde{\theta}_2 = \theta_2$ are small (small bending oscillations) at $R \approx R_{min} = \tilde{R}_1 + \tilde{R}_2 + s$, where $\tilde{R}_i = R_i(1 - \beta_i^2/(4\pi) + \sqrt{5/(4\pi)}\beta_i)$ are the major axes of the prolately deformed nuclei, we can use analytical expressions for α_i:

$$\alpha_1 = c_{11}\tilde{\theta}_1 + c_{12}\tilde{\theta}_2, \quad \alpha_2 = c_{21}\tilde{\theta}_1 + c_{22}\tilde{\theta}_2. \quad \text{(A.6)}$$

Here,

$$c_{11} = 1 - \frac{(\tilde{R}_2 + sg_2^2)(g_1^2-1)}{\tilde{R}_1 g_2^2 + \tilde{R}_2 g_1^2 + s g_1^2 g_2^2},$$

$$c_{12} = \frac{\tilde{R}_2(1-g_2^2)}{\tilde{R}_1 g_2^2 + \tilde{R}_2 g_1^2 + s g_1^2 g_2^2},$$

$$c_{21} = \frac{\tilde{R}_1(1-g_1^2)}{\tilde{R}_1 g_2^2 + \tilde{R}_2 g_1^2 + s g_1^2 g_2^2},$$

$$c_{22} = 1 - \frac{(\tilde{R}_1 + sg_1^2)(g_2^2-1)}{\tilde{R}_1 g_2^2 + \tilde{R}_2 g_1^2 + s g_1^2 g_2^2},$$

and

$$g_i = (1 - \beta_i^2/(4\pi) + \sqrt{5/(4\pi)}\beta_i)/(1 - \beta_i^2/(4\pi)$$

$$- \sqrt{5/(16\pi)}\beta_i)$$

is the major-to-minor axis ratio of the ith nucleus.

Inserting in Eq. (A.1) the expression

$$\rho_i^2(r,a) = -\rho_0 a \sinh\left(\frac{R_i}{a}\right)\frac{d}{dR_i}\frac{\rho_i(r,a)}{\sinh\left(\frac{R_i}{a}\right)} \quad \text{(A.7)}$$

$$= -\rho_0\left(a\frac{d}{dR_i} - \coth\left(\frac{R_i}{a}\right)\right)\rho_i(r,a)$$

$$= \frac{\rho_0}{F_{\text{in}} - F_{\text{ex}}}\Lambda_i(a)\rho_i(r,a),$$

using (A.2) and (A.5), and taking $\phi_1 = \phi_2 = 0$, the nuclear part of the potential energy is written approximately as

$$U_N(R,\beta_i,\theta_i) \approx U_{11} + U_{21}Y_{20}(\theta_2) \quad \text{(A.8)}$$
$$+ U_{22}Y_{20}(\theta_1) + U_{31}Y_{20}^2(\alpha_2) + U_{32}Y_{20}(\alpha_1)Y_{20}(\alpha_2)$$
$$+ U_{33}Y_{20}^2(\alpha_1) + U_{41}Y_{20}(\alpha_1)Y_{20}^2(\alpha_2)$$
$$+ U_{42}Y_{20}^2(\alpha_1)Y_{20}(\alpha_2) + U_{51}Y_{20}^2(\alpha_1)Y_{20}^2(\alpha_2),$$

where the coefficients

$$U_{11} = C_0[\Lambda_1(a_1) + \Lambda_2(a_2) + F_{\text{ex}}]I_0(a_1,a_2), \quad \text{(A.9)}$$

$$U_{21} = C_0\beta_1 R_1\frac{d}{dR_1}[\xi_1\Lambda_2(a_2)I_1(b_1,a_2)$$
$$+ \xi_1'\Lambda_1(b_1')I_1(b_1',a_2) + F_{\text{ex}}\xi_1 I_1(b_1,a_2)],$$

$$U_{22} = C_0\beta_2 R_2\frac{d}{dR_2}[\xi_2\Lambda_1(a_1)I_2(a_1,b_2)$$
$$+ \xi_2'\Lambda_2(b_2')I_2(a_1,b_2') + F_{\text{ex}}\xi_2 I_2(a_1,b_2)],$$

$$U_{31} = C_0\beta_2^2\frac{R_2^2}{2}\frac{d^2}{dR_2^2}[\xi_2\Lambda_1(a_1)I_0(a_1,b_2)$$
$$+ \xi_2'\Lambda_2(b_2')I_0(a_1,b_2') + F_{\text{ex}}\xi_2 I_0(a_1,b_2)],$$

$$U_{33} = C_0\beta_1^2\frac{R_1^2}{2}\frac{d^2}{dR_1^2}[\xi_1'\Lambda_1(b_1')I_0(b_1',a_2)$$
$$+ \xi_1\Lambda_2(a_2)I_0(b_1,a_2) + F_{\text{ex}}\xi_1 I_0(b_1,a_2)],$$

$$U_{32} = C_0\beta_1\beta_2 R_1 R_2\frac{d^2}{dR_1 dR_2}[\xi_1'\xi_2\Lambda_1(b_1')I_0(b_1',b_2)$$
$$+ \xi_1\xi_2'\Lambda_2(b_2)I_0(b_1,b_2') + \xi_1\xi_2 I_0(b_1,b_2)],$$

$$U_{41} = C_0\beta_1\beta_2^2\frac{R_1 R_2^2}{2}\frac{d^3}{dR_1 dR_2^2}[\xi_1'\xi_2\Lambda_1(b_1')I_0(b_1',b_2)$$
$$+ \xi_1\xi_2'\Lambda_2(b_2)I_0(b_1,b_2') + \xi_1\xi_2 I_0(b_1,b_2)],$$

$$U_{42} = C_0\beta_1^2\beta_2\frac{R_1^2 R_2}{2}\frac{d^3}{dR_1^2 dR_2}[\xi_1'\xi_2\Lambda_1(b_1')I_0(b_1',b_2)$$
$$+ \xi_1\xi_2'\Lambda_2(b_2)I_0(b_1,b_2') + \xi_1\xi_2 I_0(b_1,b_2)],$$

$$U_{51} = C_0\beta_1^2\beta_2^2\frac{R_1^2 R_2^2}{4}\frac{d^4}{dR_1^2 dR_2^2}[\xi_1'\xi_2\Lambda_1(b_1')I_0(b_1',b_2)$$
$$+ \xi_1\xi_2'\Lambda_2(b_2)I_0(b_1,b_2') + \xi_1\xi_2 I_0(b_1,b_2)]$$

depend only on the relative distance R and quadrupole deformation parameters β_i. With the Fourier transform of the function $\rho_i(r,a_i)$,

$$\rho_i(p,a_i) = \frac{\sqrt{2\pi}a_i R_i\rho_0}{p\sinh(\pi a_i p)} \quad \text{(A.10)}$$
$$\times\left(\frac{\pi a_i}{R_i}\sin(pR_i)\coth(\pi a_i p) - \cos(pR_i)\right),$$

the following integrals are calculated:

$$I_0(a,b) = -4\pi\int_0^\infty \rho_1(p,a)\rho_2(p,b)j_0(pR)p^2dp, \quad \text{(A.11)}$$

$$I_1(a,b) = -(4\pi)^2\int_0^\infty dpp^2 j_2(pR)\rho_2(p,b)$$
$$\times\int_0^\infty drr^2 j_2(pr)\rho_1(r,a),$$

$$I_2(a,b) = -(4\pi)^2\int_0^\infty dpp^2 j_2(pR)\rho_1(p,a)$$
$$\times\int_0^\infty drr^2 j_2(pr)\rho_2(r,b).$$

Here, $j_2(pR)$ and $j_0(pR)$ are spherical Bessel functions. Due to the small overlap of the DNS nuclei, the spherical functions in some integrands in (A.1) are replaced by their values at $\theta_i' = \alpha_i$ to obtain Eq. (A.8). The direct calculations of the corresponding integrals show that this approximation works well [27]. Thus, using (A.6) and expanding the spherical harmonics in the small angles $\tilde{\theta}_i$ up to the second order, we obtain

$$U_N = U_{N_0} + \frac{1}{2}C_{11}^N\tilde{\theta}_1^2 + C_{12}^N\tilde{\theta}_1\tilde{\theta}_2 + \frac{1}{2}C_{22}^N\tilde{\theta}_2^2, \quad \text{(A.12)}$$

where

$$U_{N_0} = U_{11} + \sqrt{\frac{5}{4\pi}}(U_{21}+U_{22}) + \frac{5}{4\pi} \quad \text{(A.13)}$$
$$\times\left[U_{31}+U_{32}+U_{33} + \sqrt{\frac{5}{4\pi}}(U_{41}+U_{42}) + \frac{5}{4\pi}U_{51}\right],$$

$$C_{11}^N = -3\left(\sqrt{\frac{5}{4\pi}}U_{22} + \frac{5}{4\pi}c_{11}^2\left[2U_{33}+U_{32}\right.\right.$$
$$\left. + \sqrt{\frac{5}{4\pi}}(2U_{42}+U_{41}) + \frac{5}{2\pi}U_{51}\right] + \frac{5}{4\pi}c_{21}^2$$
$$\left.\times\left[2U_{31}+U_{32} + \sqrt{\frac{5}{4\pi}}(2U_{41}+U_{42}) + \frac{5}{2\pi}U_{51}\right]\right),$$

$$C_{12}^N = -\frac{15}{4\pi}\left(c_{12}c_{11}\left[2U_{33}+U_{32}\right.\right.$$
$$\left.+\sqrt{\frac{5}{4\pi}}(2U_{42}+U_{41})+\frac{5}{2\pi}U_{51}\right]+c_{21}c_{22}$$
$$\left.\times\left[2U_{31}+U_{32}+\sqrt{\frac{5}{4\pi}}(2U_{41}+U_{42})+\frac{5}{2\pi}U_{51}\right]\right),$$
$$C_{22}^N = -3\left(\sqrt{\frac{5}{4\pi}}U_{21}+\frac{5}{4\pi}c_{22}^2\left[2U_{31}+U_{32}\right.\right.$$
$$\left.+\sqrt{\frac{5}{4\pi}}(2U_{41}+U_{42})+\frac{5}{2\pi}U_{51}\right]+\frac{5}{4\pi}c_{12}^2$$
$$\left.\times\left[2U_{33}+U_{32}+\sqrt{\frac{5}{4\pi}}(2U_{42}+U_{41})+\frac{5}{2\pi}U_{51}\right]\right).$$

2. Coulomb part of nucleus–nucleus potential

For the Coulomb interaction, we use the formula [40]

$$U_{\rm C} = \frac{Z_1Z_2e^2}{R}+\frac{3}{5}\frac{Z_1Z_2e^2}{R^3}\sum_{i=1}^{2}R_i^2\beta_iY_2(\theta_i) \quad \text{(A.14)}$$
$$+\frac{12}{35}\frac{Z_1Z_2e^2}{R^3}\sum_{i=1}^{2}R_i^2(\beta_iY_2(\theta_i))^2.$$

For a small overlap of the DNS nuclei, the effect of density diffuseness is relatively small and is neglected in this formula. The expansion of (A.14) in $\tilde{\theta}_i$ ($i=1,2$) gives

$$U_{\rm C} = U_{\rm C_0}+\frac{1}{2}C_{11}^C\tilde{\theta}_1^2+\frac{1}{2}C_{22}^C\tilde{\theta}_2^2, \quad \text{(A.15)}$$

where

$$U_{\rm C_0} = \frac{Z_1Z_2e^2}{R} \quad \text{(A.16)}$$
$$\times\left(1+\frac{1}{R^2}\sum_{i=1}^{2}R_{0i}^2\left[\left(\frac{9}{20\pi}\right)^{1/2}\beta_i+\frac{3}{7\pi}\beta_i^2\right]\right),$$
$$C_{ii}^C = -3\frac{Z_1Z_2e^2}{R^3}R_{0i}^2\left[\left(\frac{9}{20\pi}\right)^{1/2}\beta_i+\frac{6}{7\pi}\beta_i^2\right],$$
$$i=1,2.$$

Finally, using Eqs. (A.12) and (A.15), we obtain the expression for the total potential energy U of the DNS in the form of Eq. (1), where $C_{ij}=C_{ij}^N+C_{ij}^C$.

ACKNOWLEDGMENTS

We thank Profs. G.M. Ter-Akopian and V.V. Volkov and Drs. A.V. Daniel, A. Diaz-Torres, A.K. Nasirov, and G.S. Popeko for fruitful discussions and suggestions. G.G.A. and T.M.S. are grateful for support from the Alexander von Humboldt-Stiftung and European Physical Society, respectively.

This work was supported in part by DFG and the Russian Foundation for Basic Research.

REFERENCES

1. K. A. Erb and D. A. Bromley, in *Treatise on Heavy-Ion Science,* Ed. by D. A. Bromley (Plenum, New York, 1985), Vol. 3, p. 201.
2. W. Greiner, J. Y. Park, and W. Scheid, *Nuclear Molecules* (World Sci., Singapore, 1995).
3. V. V. Volkov, *Deep Inelastic Nuclear Reactions* (Énergoizdat, Moscow, 1982).
4. W. U. Schröder and J. R. Huizenga, in *Treatise on Heavy-Ion Science,* Ed. by D. A. Bromley (Plenum, New York, 1984), Vol. 2, p. 115.
5. V. V. Volkov, in *Proceedings of the International School-Seminar on Heavy-Ion Physics, Dubna, 1986* (JINR, Dubna, 1987), p. 528; Izv. Akad. Nauk SSSR, Ser. Fiz. **50**, 1879 (1986); in *Proceedings of the International Conference on Nuclear Reaction Mechanisms, Varenna, 1991,* Ed. by E. Gadioli (Ricerca Scientifica, 1991), p. 39.
6. N. V. Antonenko, E. A. Cherepanov, A. K. Nasirov, *et al.*, Phys. Lett. B **319**, 425 (1993); Phys. Rev. C **51**, 2635 (1995); G. G. Adamian, N. V. Antonenko, and W. Scheid, Nucl. Phys. A **618**, 176 (1997); G. G. Adamian, N. V. Antonenko, W. Scheid, and V. V. Volkov, Nucl. Phys. A **627**, 332 (1997); **633**, 154 (1998); R. V. Jolos, A. K. Nasirov, and A. I. Muminov, Eur. Phys. J. A **4**, 246 (1999); E. A. Cherepanov, Preprint No. E7-99-99, JINR (Dubna, 1999); G. G. Adamian, N. V. Antonenko, and Yu. M. Tchuvil'sky, Phys. Lett. B **451**, 289 (1999).
7. V. A. Shigin, Yad. Fiz. **3**, 756 (1966) [Sov. J. Nucl. Phys. **3**, 555 (1966)]; Yad. Fiz. **14**, 1247 (1971) [Sov. J. Nucl. Phys. **14**, 391 (1972)].
8. J. O. Rasmussen *et al.*, Nucl. Phys. A **136**, 465 (1969).
9. M. Zielinska-Pfabé and K. Dietrich, Phys. Lett. B **49B**, 123 (1974).
10. B. D. Wilkins, E. P. Steinberg, and R. R. Chasman, Phys. Rev. C **14**, 1832 (1976).
11. C. Wagemans, P. Schillebeeck, and A. Deruytter, Nucl. Phys. A **502**, 287c (1989).
12. G. Mouze and C. Ythier, Nuovo Cimento A **103**, 617 (1990); G. Mouze and R. A. Ricci, Nuovo Cimento A **110**, 665 (1997).
13. F. Gönnenwein, in *The Nuclear Fission Process,* Ed. by C. Wagemans (CRC Press, Boca Raton, 1991).
14. Yu. V. Piatkov *et al.*, Nucl. Phys. A **611**, 355 (1996); **624**, 140 (1997).
15. V. V. Volkov, Yad. Fiz. **62**, 1159 (1999) [Phys. At. Nucl. **62**, 1086 (1999)].

16. H. J. Fink *et al.*, in *Proceedings of the International Conference on Reactions between Complex Nuclei, Nashville, USA, 1974* (North-Holland, Amsterdam, 1975).
17. J. R. Nix and W. J. Swiatecki, Nucl. Phys. **71**, 1 (1965).
18. R. Maass and W. Scheid, Phys. Lett. B **202**, 26 (1988); J. Phys. G **16**, 1359 (1990); **18**, 707 (1992).
19. P. O. Hess and W. Greiner, Nuovo Cimento A **83**, 76 (1984); Phys. Rev. Lett. **53**, 1535 (1984).
20. E. Uegaki and Y. Abe, Phys. Lett. B **231**, 28 (1989); **340**, 143 (1994); Prog. Theor. Phys. **90**, 615 (1993); Prog. Theor. Phys., Suppl. **132**, 135 (1998).
21. S. Misicu, A. Sandulescu, and W. Greiner, Mod. Phys. Lett. A **12**, 1343 (1997).
22. S. Misicu, A. Sandulescu, G. M. Ter-Akopian, and W. Greiner, Phys. Rev. C **60**, 034613 (1999).
23. G. M. Ter-Akopian *et al.*, Phys. Rev. C **55**, 1146 (1997).
24. G. S. Popeko *et al.*, in *Proceedings of the International Conference on Fission and Properties of Neutron-Rich Nuclei, 1997,* Ed. by J. H. Hamilton and G. S. Ramayya (World Sci., Singapore, 1998).
25. J. H. Hamilton *et al.*, Prog. Part. Nucl. Phys. **35**, 635 (1995).
26. J. M. Eisenberg and W. Greiner, *Nuclear Theory* (North-Holland, Amsterdam, 1970), Vol. 1.
27. G. G. Adamian *et al.*, Int. J. Mod. Phys. E **5**, 191 (1996).
28. *Handbook of Mathematical Functions,* Ed. by M. Abramowitz and I. A. Stegun (Dover, New York, 1964; Nauka, Moscow, 1979).
29. A. M. Wapstra and G. Audi, Nucl. Phys. A **440**, 327 (1985); S. Liran and N. Zeldes, At. Data Nucl. Data Tables **17**, 431 (1976).
30. G. G. Adamian, N. V. Antonenko, S. P. Ivanova, and W. Scheid, Nucl. Phys. A **646**, 29 (1999).
31. S. Raman *et al.*, At. Data Nucl. Data Tables **36**, 1 (1987).
32. A. Sandulescu *et al.*, Phys. Rev. C **54**, 258 (1996).
33. R. V. Janssens *et al.*, Annu. Rev. Nucl. Part. Sci. **41**, 321 (1991).
34. S. Aberg *et al.*, Annu. Rev. Nucl. Part. Sci. **40**, 439 (1990).
35. S. J. Zhu *et al.*, Phys. Lett. B **357**, 273 (1995); P. A. Butler and W. Nazarewicz, Rev. Mod. Phys. **68**, 349 (1996).
36. A. V. Ramayya *et al.*, Phys. Rev. Lett. **81**, 947 (1998).
37. T. M. Shneidman *et al.*, Nucl. Phys. A **671**, 64 (2000).
38. D. C. Biswas *et al.*, Eur. Phys. J. A **7**, 189 (2000).
39. A. B. Migdal, *Theory of Finite Fermi Systems and Application to Atomic Nuclei* (Nauka, Moscow, 1982).
40. C. Y. Wong, Phys. Rev. Lett. **31**, 766 (1973).

Physics of Atomic Nuclei, Vol. 66, No. 2, 2003, pp. 218–232. Translated from Yadernaya Fizika, Vol. 66, No. 2, 2003, pp. 242–256.

NUCLEI
Theory

Survivability of Excited Superheavy Nuclei

A. S. Zubov[1),2)], G. G. Adamian[1),2),3)], N. V. Antonenko[1),2)], S. P. Ivanova[1),2)], and W. Scheid[1)]

Joint Institute for Nuclear Research, Dubna, Moscow oblast, 141980 Russia

Received September 4, 2001; in final form, February 21, 2002

Abstract—The survivability of even–even and odd superheavy nuclei is analyzed on the basis of a statistical model and various theoretical predictions for nuclear properties. In this analysis, use is made of various methods for computing level densities. For $Z < 114$ nuclei, calculations on the basis of all models predicting nuclear properties lead to close values for the ratio of the width with respect to the neutron channel to the width with respect to the fission channel. For $Z \geq 114$ nuclei, different values are obtained for this ratio. The dependence of the results on model parameters is discussed. The collective-enhancement factor in the level density is taken into account in the calculations. © *2003 MAIK "Nauka/Interperiodica".*

1. INTRODUCTION

The synthesis of new superheavy elements is one of the most interesting branches in contemporary nuclear physics. Since the stability of superheavy nuclei depends predominantly on shell effects, searches for such Z and N at which shell effects are the most pronounced, thereby ensuring long lifetimes of synthesized superheavy nuclei, are of great importance in these investigations. Nuclei of charge number in the range $Z = 106$–112 were obtained in cold-fusion reactions induced by collisions of heavy ions with ^{208}Pb and ^{209}Bi targets. Hot-fusion reactions on ^{232}Th, ^{238}U, ^{242,244}Pu, and ^{248}Cm targets were also used to synthesize $Z = 110$, 112, 114, and 116 elements.

Among all theoretical models, the dinuclear-system model provides the most successful description of the formation of superheavy nuclei. It is assumed within this model that a compound nucleus is formed via the exchange of nucleons or small clusters between the lighter and the heavier nucleus appearing to be in immediate contact. The dynamics of fusion is controlled by diffusion along the mass-asymmetry coordinate $\eta = (A_1 - A_2)/(A_1 + A_2)$, where A_1 and A_2 are the mass numbers of nuclei forming a dinuclear system.

At low angular momenta, the cross section for evaporation-residue formation in the reactions under consideration [1, 2] can be represented in the form [3–7]

$$\sigma_{\rm ER}(E_{\rm c.m.}) \approx P_{\rm CN}(E_{\rm c.m.}, J=0) \times W_{\rm sur}(E_{\rm c.m.}, J=0) \sum_{J=0}^{J_{\max}} \sigma_c(E_{\rm c.m.}, J), \quad (1)$$

where σ_c is the partial capture cross section (it is responsible for the process in which the incident nucleus overcomes the Coulomb barrier), $P_{\rm CN}$ is the probability of compound-nucleus formation upon capture, $W_{\rm sur}$ is the survivability of the compound nucleus formed, and $J_{\max} \approx 10$. At the first step of the reaction, the target captures the projectile nucleus, whereupon the resulting dinuclear system evolves into a compound nucleus. The complete-fusion probability $P_{\rm CN}$ depends on the competition between fusion and quasifission. Since the c.m. projectile energy $E_{\rm c.m.}$ usually exceeds the energy of compound-nucleus formation, the resulting nucleus is formed in an excited state. At the second step of the reaction, the compound nucleus is deexcited predominantly via the emission of particles and γ rays. The compound-nucleus survivability $W_{\rm sur}$, which is determined by the competition between this emission and the fission processes, is therefore a factor of importance in describing the synthesis of heavy and superheavy nuclei.

The survivability of superheavy nuclei synthesized in cold-fusion reactions is calculated in the present study for $Z = 102$–120 even and odd nuclei by using various theoretical predictions for nuclear properties [8–12] and the level density as obtained on the basis of the Fermi gas model and the model allowing for

[1)]Institut für Theoretische Physik, Justus-Liebig-Universität, Ludwigstrasse 23, D-35390 Giessen, Germany.
[2)]Joint Institute for Nuclear Research, Dubna, Moscow oblast, 141980 Russia.
[3)]Institute of Nuclear Physics, Uzbek Academy of Sciences, pos. Ulughbek, Tashkent, 702132 Uzbekistan.

collective enhancement; also examined here are various methods for taking into account the energy dependence of shell effects. In addition, we consider hot-fusion reactions involving the emission of a few neutrons during the formation of the evaporation residue and analyze the survivability of superheavy nuclei in the xn-evaporation channel ($x \geq 2$) as a function of the parameters of the models used.

Experiments aimed at implementing cold- and hot-fusion reactions are complicated by a sharp decrease in the cross section for evaporation-residue formation with increasing Z. By way of example, we indicate that, as Z grows from 104 to 112, this cross section decreases by four orders of magnitude in cold-fusion reactions [1]. It is shown here that this is due primarily to a decrease in the probability of complete fusion rather than to a decrease in the survivability of the compound nucleus.

2. SURVIVABILITY OF A COMPOUND NUCLEUS

In the evaporation of a specific sequence s of x particles, the survivability of a nucleus with respect to fission can be approximately described by the expression

$$W^s_{\rm sur}(E^*_{\rm CN}, J) \approx P_s(E^*_{\rm CN}, J) \prod_{i_s=1}^{x} \frac{\Gamma_i(E^*_{i_s}, J_{i_s})}{\Gamma_t(E^*_{i_s}, J_{i_s})}, \quad (2)$$

where i_s is the index of an evaporation step; P_s is the probability of the s channel at the initial excitation energy $E^*_{\rm CN}$; and $E^*_{i_s}$ and J_{i_s} are the mean values of, respectively, the excitation energy and the angular momentum at the step i_s. For a compound nucleus, the total width Γ_t is defined as the sum of the partial widths Γ_i with respect to all possible particle-evaporation channels, the partial width with respect to γ-ray emission, and the fission width Γ_f. At the first step $i_s = 1_s$, we have $E^*_{1_s} = E^*_{\rm CN}$ and $J_{1_s} = J$. It follows from (1) that, at low angular momenta, the J dependence of the cross section $\sigma_{\rm ER}$ can be approximately taken into account in the effective capture cross section σ_c. Thus, we can calculate the survivability only for the case of $J = 0$.

In the nuclei considered here, γ-ray emission competes with other processes only if the excitation energy is less than (or approximately equal to) the corresponding neutron binding energy; therefore, the contribution of γ-ray emission can be disregarded in the majority of cases. A high Coulomb barrier prevents charged-particle emission from an excited heavy nucleus, so that the partial width with respect to the proton-emission or the alpha-particle-emission channel is much less than the partial neutron-emission width Γ_n. To summarize the foregoing, we can set $\Gamma_t \approx \Gamma_n + \Gamma_f$. According to [13–15], the survival probability in the evaporation of x neutrons can therefore be represented as

$$W_{\rm sur}(E^*_{\rm CN}) \approx P_{xn}(E^*_{\rm CN}) \prod_{i=1}^{x} \frac{\Gamma_n(E^*_i)}{\Gamma_n(E^*_i) + \Gamma_f(E^*_i)}, \quad (3)$$

where P_{xn} is the probability for the xn channel at a specific excitation energy $E^*_{\rm CN}$.

The width with respect to decay through channel i is determined by the probability $R_{{\rm CN}_i}$ of this process [16–18],

$$\Gamma_i = \frac{R_{{\rm CN}_i}}{2\pi\rho(E^*_{\rm CN}, J)}. \quad (4)$$

There exist various methods for calculating the level density $\rho(E^*_{\rm CN}, J)$ in a nucleus, and we will give a detailed account of these in the next section.

We can compute the probability of the evaporation of particle j (a neutron, a proton, or an alpha particle) by the formula

$$R_{{\rm CN}_j} = \sum_{J_d} \int_0^{E^*_{\rm CN} - B_j - \delta} d\varepsilon \quad (5)$$

$$\times \rho_d(E^*_{\rm CN} - B_j - \varepsilon, J_d) \sum_{S=|J_d - s|}^{J_d + s} T_{jS}(\varepsilon)$$

if we know the quantities appearing in it. These are the energy required for separating the spin-s particle j, B_j; the pair correction for nuclei of opposite parities, δ; the level density in the daughter nucleus, $\rho_d(E^*_{\rm CN} - B_j - \varepsilon, J_d)$; and the barrier-penetrability factors, $T_{jS}(\varepsilon)$, which are calculated on the basis of the optical model [16].

The fission probability is calculated in the approximation of a one-humped barrier having a height $B_f(E^*_{\rm CN})$ and a curvature $\hbar\omega$. The result can be represented as

$$R_{{\rm CN}_f} = \int_0^{E^*_{\rm CN} - B_f - \delta} \frac{\rho_f(E^*_{\rm CN} - B_f - \varepsilon, J) d\varepsilon}{1 + \exp[2\pi(\varepsilon + B_f - E^*_{\rm CN})/\hbar\omega]}, \quad (6)$$

where $\rho_f(E^*_{\rm CN} - B_f - \varepsilon, J)$ is the level density at the saddle point. The choice of this approximation is motivated by the fact that it is the one-humped barrier that controls predominantly the stability of excited superheavy nuclei with respect to fission. For all nuclei considered here, we took the value of $\hbar\omega = 2$ MeV, which is slightly above the range of corresponding values for actinides (1.0–1.5 MeV)

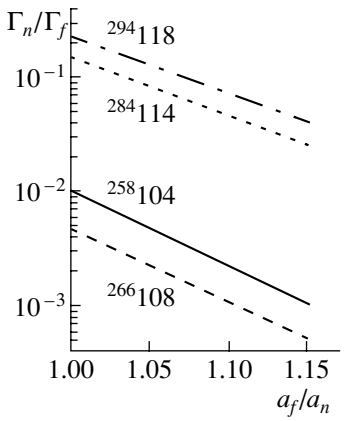

Fig. 1. Ratio Γ_n/Γ_f calculated with the level density obtained on the basis of the Fermi gas model (7) versus the ratio a_f/a_n for the $^{294}118$, $^{284}114$, $^{258}104$, and $^{266}108$ nuclei at the excitation-energy values given below in Fig. 4. The calculations were performed at $a = A/10$ MeV^{-1} and $J = 0$ with the data borrowed from [11].

since, as was shown in the calculations presented in [9, 10], the barrier becomes thinner. The quantity B_f is the sum of the liquid-drop component $B_f^{\rm LD}$ and the microscopic component $B_f^{\rm Mi}$. The latter is given by $B_f^{\rm Mi} = \delta W_{\rm sd}^A - \delta W_{\rm g.s.}^A$, where $\delta W_{\rm sd}^A$ is the shell correction for a nucleus of mass number A at the saddle point and $\delta W_{\rm g.s}^A$ is its ground-state counterpart. For the ^{256}No, ^{258}Rf, and ^{262}Rf nuclei, we took the values of $B_f^{\rm LD} = 1.1$, 0.5, and 0.2 MeV, respectively. For $Z > 106$, we set $B_f^{\rm LD} = 0$. Usually, the shell correction at the saddle point is small, $\delta W_{\rm sd}^A \approx 0$. Thus, we have $B_f^{Mi} = B_f^{\rm Mi}(E^*_{\rm CN} = 0) = |\delta W_{\rm g.s}^A(E^*_{\rm CN} = 0)|$. There exist various theoretical predictions for the properties of superheavy nuclei. We borrowed the fission barriers (shell corrections) and the separation energies from [9–12].

3. CALCULATION OF THE LEVEL DENSITY WITHIN THE FERMI GAS MODEL

The level density can be calculated most straightforwardly on the basis of the Fermi gas model, which yields

$$\rho(E^*_{\rm CN}, J) = \frac{2J+1}{24\sqrt{2}\sigma^3 a^{1/4}(E^*_{\rm CN}-\delta)^{5/4}} \times \exp\left[2\sqrt{a(E^*_{\rm CN}-\delta)} - \frac{(J+1/2)^2}{2\sigma^2}\right], \quad (7)$$

where $\sigma^2 = 6\bar{m}^2\sqrt{a(E^*_{\rm CN}-\delta)}/\pi^2$. For the pair corrections, we use the values of $\delta = 2.4$ and 1.2 MeV for even–even and odd nuclei, respectively. The level-density parameter a is proportional to the density of single-particle states at the Fermi surface. The mean projection of the angular momentum onto these states was estimated as $\bar{m}^2 \approx 0.24A^{2/3}$. We assumed that $a = A/10$ MeV^{-1} for all nuclei considered here. In calculating the level density ρ_f at the fission barrier, we set $a_f = 1.1a_n$ [19], where a_n is the level-density parameter of the daughter nucleus upon neutron emission and a_f is the level-density parameter at the saddle point.

In the calculations with the level density obtained within the Fermi gas model, the ratio Γ_n/Γ_f decreases according to a virtually linear law with increasing a_f/a_n for all nuclei (Fig. 1). In particular, we can see from Fig. 1 that, as a_f/a_n varies from 1.1 to 1.05, the ratio Γ_n/Γ_f increases by a factor of 2. In superheavy nuclei, the fission barriers are rather narrow [9] and the saddle point occurs near the ground state, $\beta_2^{\rm sd} \approx \beta_2^{\rm g.s.} + 0.2$, where $\beta_2^{\rm sd}$ is the quadrupole-deformation parameter at the saddle point and $\beta_2^{\rm g.s.}$ is that in the ground state. The shell correction changes from $\delta W_{\rm g.s.}$ in the ground state to zero at the saddle point. A sharp change in the shell correction within a narrow range of the quadrupole-deformation parameter can be taken into account by choosing the value of $a_f/a_n = 1.1$ for the nuclei considered here. The level density in the ground state (the case of neutron emission) is lower than the single-particle level density, while the level density at the saddle point (fission barrier) is higher than its single-particle counterpart [19].

For modest excitation energies $E^*_{\rm CN}$, the integral in (5) will be unrealistically large if use is made only of formula (7). For $E^*_{\rm CN} < U_x$, we therefore represented the level density in the different form

$$\rho(E^*_{\rm CN}, J) = \frac{1}{T}\exp\left(\frac{E^*_{\rm CN}-U_0}{T}\right) \times \frac{\exp\left[-(J+1/2)^2/(2\sigma^2)\right]}{2\sqrt{2\pi}\sigma^3}, \quad (8)$$

which corresponds to the model assuming a constant temperature T [20]. The parameters T and U_0 can be determined by requiring that the level density and its derivative be continuous at the matching point $E^*_{\rm CN} = U_x$. We took the value of $U_x = 2.2$ MeV for all nuclei considered here. In this case, the results of the calculations do not depend on this parameter for $E^*_{\rm CN} > 11$ MeV.

One of the possible ways to include shell effects in the level density is to introduce an energy dependence in the fission barrier as

$$B_f^i(E^*_{\rm CN}) = B_f^{\rm LD} + B_f^{\rm Mi}(E^*_{\rm CN} = 0)\exp[-E^*_{\rm CN}/E_D] \quad (9)$$

from the value $B_f^i = B_f^i(E^*_{\rm CN} = 0) = B_f^{\rm LD} + B_f^{\rm Mi}(E^*_{\rm CN} = 0)$ at zero excitation energy to the liquid-drop value $B_f^i(E^*_{\rm CN}) = B_f^{\rm LD}$ at high excitation energies, E_D being an effective factor that takes into account the damping of shell effects. Calculations that are based on the level density obtained within the Fermi gas model and on relation (9) are described in [21].

4. CALCULATION OF THE LEVEL DENSITY WITH ALLOWANCE FOR COLLECTIVE EFFECTS

If we take into account pair correlations and vibrational and rotational degrees of freedom, the level density can be represented as

$$\rho(E^*_{\rm CN}, J) = K_{\rm vib}(E^*_{\rm CN})K_{\rm rot}(E^*_{\rm CN}) \times \frac{2J+1}{24\sqrt{2}\sigma_{\rm eff}^3 a^{1/4}(E^*_{\rm CN} - E_c)^{5/4}} \times \exp\left[2\sqrt{a(E^*_{\rm CN} - E_c)} - \frac{(J+1/2)^2}{2\sigma_{\rm eff}^2}\right], \quad (10)$$

where E_c is the condensation energy reducing the ground-state energy of the Fermi gas by 1–3 MeV owing to correlation pair interaction in the nuclei under consideration and

$$\sigma_{\rm eff}^2 = \begin{cases} I_\perp^{2/3} I_{||}^{1/3} \sqrt{(E^*_{\rm CN} - E_c)/a} \\ \text{for axially deformed nuclei} \\ I_{||}\sqrt{(E^*_{\rm CN} - E_c)/a} \\ \text{for spherical nuclei.} \end{cases} \quad (11)$$

The rotational-enhancement factor,

$$K_{\rm rot} = \begin{cases} I_\perp \sqrt{(E^*_{\rm CN} - E_c)/a} \\ \text{for axially deformed nuclei} \\ 1 \\ \text{for spherical nuclei,} \end{cases} \quad (12)$$

and the vibrational-enhancement factor,

$$K_{\rm vib} = \exp[0.0555 A^{2/3}(E^*_{\rm CN} - E_c)^{4/3}/a^{4/3}], \quad (13)$$

take into account the contribution to the level density from collective vibrational and rotational degrees of freedom, respectively. The contribution of collective effects is especially significant for deformed nuclei. The moments of inertia that are orthogonal to the principal axis, $I_\perp$, and parallel to it, $I_{||}$, are defined in [20, 22]. If the temperature of the nucleus is higher than the critical phase-transition temperature, we have $I_{||} = 6\bar{m}^2\sqrt{a(E^* - E_c)}(1 - (2/3)\varepsilon_0)/\pi^2$ and $I_\perp = (2/5)m_0 r_0^2 A^{5/3}(1 + (1/3)\varepsilon_0)$, where $\varepsilon_0 = 1.5\sqrt{5/4\pi}\beta_2/(1 + 0.5\sqrt{5/4\pi}\beta_2)$. The ratio of the level density in a nucleus for $\beta_2 \neq 0$ to that for $\beta_2 = 0$ is about $I_{||}\sqrt{(E^*_{\rm CN} - E_c)/a} \approx 10^2$.

In order to take into account shell effects, we can use a level-density parameter a that depends on the excitation energy $E^*_{\rm CN}$ and on the shell correction δW as [20, 22]

$$a = \tilde{a}(A)\left[1 + \frac{1 - \exp\{-(E^*_{\rm CN} - E_c)/E'_D\}}{E^*_{\rm CN} - E_c}\delta W\right]. \quad (14)$$

Since shell effects are the most pronounced in the ground state, they affect predominantly the level-density parameter for the neutron channel. The function $f(E^*_{\rm CN} - E_c) = (1 - \exp\{-(E^*_{\rm CN} - E_c)/E'_D\})/(E^*_{\rm CN} - E_c)$ determines the energy dependence of a. In [13–15, 20, 22, 23], it was assumed that this energy dependence is universal for all nuclei characterized by a constant value of the parameter E'_D. The values of $E'_D = 18.5$ and 16.5 MeV were chosen in [20] and [14], respectively. In [3, 24], E'_D depends on A as

$$E'_D = \alpha_0 A^{4/3}/\tilde{a}, \quad (15)$$

where $\alpha_0 = 0.4$. In performing calculations on the basis of (14), one can disregard the energy dependence of shell effects in the fission barrier and set $B_f = B_f(E^*_{\rm CN} = 0)$—that is, $E_D = 0$ in (9). Thus, we see that, while, in the Fermi gas model, use can be made of relation (9), here, the energy dependence of the shell correction δW is introduced in the level-density parameter.

There are a few estimates of the asymptotic level-density parameter $\tilde{a}$, but they were obtained for lighter nuclei, whose properties have been well studied experimentally; therefore, they cannot be extrapolated to the region of superheavy nuclei without performing a relevant analysis. The dependence $\tilde{a}(A)$ can be represented in the form

$$\tilde{a}(A) = c_1 A + c_2 A^{2/3}\widetilde{s}, \quad (16)$$

where $\widetilde{s}$ is the nuclear surface expressed in terms of a sphere that is equivalent to it [23, 25, 26]. Since $\beta_2^{\rm sd} \approx \beta_2^{\rm g.s.} + 0.2$ and $\beta_2^{\rm g.s.} \leq 0.3$ for all nuclei considered in the present study, $\widetilde{s}$ is close to unity [27] and $\tilde{a} = \tilde{a}_n \approx \tilde{a}_f$.

Theoretical calculations of c_1 and c_2 on the basis of the shell model or the Thomas–Fermi method are preferable [20] for $K_{\rm rot} \neq 1$ and $K_{\rm vib} \neq 1$ in (10). For levels of the Woods–Saxon potential, Ignatyuk *et al.* [23] propose $c_1 = 0.073$ and $c_2 = 0.095$, which leads to $\tilde{a} \approx A/11.5$ MeV^{-1}. However, the use of the expression with these values of c_1 and c_2 yields results

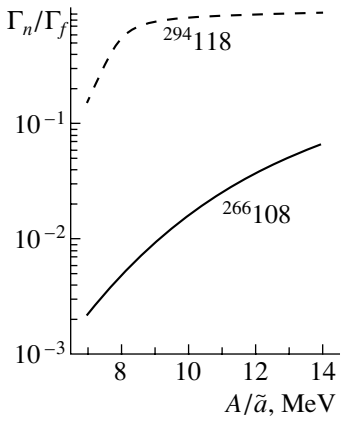

Fig. 2. Ratio Γ_n/Γ_f calculated at $E_D = 0$ by using relations (10) and (14) for $\alpha_0 = 0.4$ in (15) and $\tilde{a} = \tilde{a}_n = \tilde{a}_f$ versus the ratio $A/\tilde{a}$ for the $^{294}118$ and $^{266}108$ nuclei at the excitation-energy values presented below in Fig. 4. The calculations were performed at $J = 0$ with the aid of the data borrowed from [11].

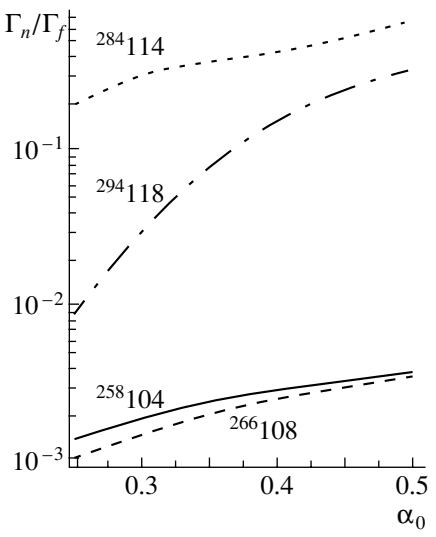

Fig. 3. Ratio Γ_n/Γ_f calculated at $E_D = 0$ by using relations (10) and (14) versus the parameter α_0 in (15) for the $^{294}118$, $^{284}114$, $^{266}108$, and $^{258}104$ nuclei at the excitation-energy values given below in Fig. 4. The calculations were performed at $J = 0$ with the aid of the data borrowed from [11].

that are well corroborated only for $A < 230$ nuclei. The calculations performed in [28] within the superfluid model on the basis of the single-particle spectrum in the Nilsson model result in $\tilde{a} \approx A/9.5$ MeV^{-1} for $A \sim 250$. The values obtained for c_1 and c_2 with the aid of the Thomas–Fermi method on the basis of the Woods–Saxon nuclear-density profile lead to $\tilde{a} \approx A/8$ MeV^{-1} for heavy nuclei (see the Appendix in [25]). For $\tilde{a} < A/10$ MeV^{-1}, the survivability calculated for some superheavy nuclei appears to be unrealistically great.

Among all known parametrizations of the type in (16), the expression

$$\tilde{a}(A) = 0.114A + 0.162A^{2/3}, \qquad (17)$$

which was obtained from an analysis of neutron resonances [20, 23] in light nuclei within the Fermi gas model, is the most appropriate, in our opinion, for describing the properties of superheavy nuclei with the damping parameter (15) and the level density (10). However, a rigorous corroboration of expression (17) requires shell-model calculations, which are not performed in the present study.

Along with (16), there is the parametrization

$$\tilde{a}(A) = 0.134A - 1.21 \times 10^{-4}A^2, \qquad (18)$$

which was proposed in [13–15]. Its parameters were found from an analysis of experimental data for $Z \leq 102$ nuclei on the basis of (10) for $K_{\rm rot} \neq 1$, $K_{\rm vib} \neq 1$, and $E'_D = 16.5$ MeV. Expression (18) leads to $\tilde{a} \approx A/9$ MeV^{-1}, which is rather close to $\tilde{a}$ (17), whence one can conclude that the use of (17) in calculations for superheavy nuclei is admissible. We note that expressions similar to (18) were employed in [20, 29].

As $\tilde{a}(A)$ changes from $A/8$ MeV^{-1} to $A/12$ MeV^{-1}, the ratio Γ_n/Γ_f increases by a factor of up to 3 for $^{294}118$ and by a factor of up to 8 for $^{266}108$ (Fig. 2). Here, the smaller B_f, the greater the relative change in this ratio. The results of the calculations performed at $E_D = 0$ by using relations (10) and (14) and the value of $\alpha_0 = 0.4$ in (15) are presented in Fig. 2. The dependence of the ratio Γ_n/Γ_f on $\tilde{a} = \tilde{a}_n = \tilde{a}_f$ enables us to estimate the uncertainty in the results that is associated with the calculation of the asymptotic level-density parameter.

The α_0 dependence of the ratio Γ_n/Γ_f at $E_D = 0$ according to the calculation employing relations (10) and (14) is displayed in Fig. 3. This dependence becomes stronger with increasing mass number of the nucleus and, hence, with increasing $\tilde{a}$.

The third possibility consists in taking into account the excitation-energy dependence of shell effects both in the expression for the fission barrier and in the level-density parameter. Such calculations, with the damping factor $E''_D = E_D = E'_D$, were performed in [15], where use was made of $B_f(E^*_{\rm CN})$ and $a(A, E^*_{\rm CN} - E_c)$ in calculating the level density. In general, the quantities E'_D and E_D do not coincide.

5. RELATIONSHIP BETWEEN DIFFERENT METHODS FOR TAKING INTO ACCOUNT THE EXCITATION-ENERGY DEPENDENCE OF SHELL EFFECTS

The partial widths with respect to the fission and neutron channels are determined by the correspond-

ing level densities. For a rough estimate, we will replace these level densities by their values at the threshold energies for fission and neutron emission and consider only rather high excitation energies. With the aid of expressions (4)–(6) and (10), we then find that, apart from the preexponential factor,

$$\ln(\Gamma_f) \sim \sqrt{\frac{\tilde{a}}{E^*_{\rm CN} + \delta W^A_{\rm g.s.}(1 - \exp[-U_{\rm g.s.}/E'_D])}} \times [-(B_f + \delta W^A_{\rm g.s.}(1 - \exp[-U_{\rm g.s.}/E'_D]) - \delta W^A_{\rm g.s.}(1 - \exp[-U_f/E'_D]))] \approx -\sqrt{\frac{\tilde{a}}{E^*_{\rm CN}}} B_f \exp[-U_{\rm g.s.}/E'_D] \quad (19)$$

and

$$\ln(\Gamma_n/\Gamma_f) \sim 2\sqrt{a(A-1,U_n)U_n} - 2\sqrt{a(A,U_f)U_f} \approx \sqrt{\frac{\tilde{a}}{E^*_{\rm CN}}}[-B_n + B_f - \delta W^A_{\rm sd}(1 - \exp(-U_f/E'_D)) + \delta W^{A-1}_{\rm g.s.}(1 - \exp(-U_n/E'_D))] \approx \sqrt{\frac{\tilde{a}}{E^*_{\rm CN}}}[-B_n + B_f \exp(-U_n/E'_D)], \quad (20)$$

where $U_{\rm g.s.} = E^*_{\rm CN} - E_c$ and $U_{f,n} = E^*_{\rm CN} - B_{f,n} - E_c$. In deriving the eventual expressions in formulas (19) and (20), we have used the approximations $\delta W^{A-1}_{\rm g.s.} \approx \delta W^A_{\rm g.s.}$, $\delta W^A_{\rm sd} \approx 0$, and $B^i_f = B^{\rm Mi}_f(E^*_{\rm CN} = 0) = |\delta W^A_{\rm g.s.}(E^*_{\rm CN} = 0)|$, which are valid for all $Z > 106$ nuclei.

For the Fermi gas model, the result analogous to that in (20) is obtained from formula (7) and is given by

$$\ln(\Gamma_n/\Gamma_f) \sim 2\sqrt{a(A-1,U_n)U_n} - 2\sqrt{a(A,U_f)U_f} \approx 2\sqrt{a_n E^*_{\rm CN}} - 2\sqrt{a_f E^*_{\rm CN}} - \sqrt{\frac{a_n}{E^*_{\rm CN}}} B_n + \sqrt{\frac{a_f}{E^*_{\rm CN}}} B_f \exp(-E^*_{\rm CN}/E_D). \quad (21)$$

By using the identity $\ln(\Gamma_n/\Gamma_f)_{\rm F} - \ln C_{\rm F} = \ln(\Gamma_n/\Gamma_f) - \ln C$, where C ($C_{\rm F}$) is the preexponential factor for Γ_n/Γ_f [$(\Gamma_n/\Gamma_f)_{\rm F}$] (hereafter, quantities labeled with the subscript F correspond to calculations within the Fermi gas model) and $q = C/C_{\rm F} \approx K_{\rm coll}(U_n)/K_{\rm coll}(U_f) \approx 0.4$–$0.5$ for deformed nuclei ($K_{\rm coll} = K_{\rm vib}K_{\rm rot}$), we can obtain a relation between the damping parameters in the formulas for the fission barrier and the level density (E_D and E'_D, respectively). This relation has the form

$$E_D = -E^*_{\rm CN} \ln^{-1}\left[\frac{E^*_{\rm CN}}{B_f} - \frac{1}{B_f a_f}(\ln q^{-1/2} + \sqrt{a_n(E^*_{\rm CN} - B_n)} - \sqrt{a(A-1,U_n)U_n} + \sqrt{\tilde{a}U_f})^2\right] \approx -E^*_{\rm CN} \ln^{-1}\left[\frac{2E^*_{\rm CN}}{B_f}\left(1 - \sqrt{\frac{a_n}{a_f}}\right) + \sqrt{\frac{a_n}{a_f}}\frac{B_n}{B_f} + \sqrt{\frac{\tilde{a}}{a_f}}\left(\exp(-U_n/E'_D) - \frac{B_n}{B_f}\right) + \frac{\sqrt{E^*_{\rm CN}}\ln q}{\sqrt{a_f}B_f}\right]. \quad (22)$$

If, for example, $a_n = A/10$ MeV^{-1}, $a_f = 1.1a_n$, $E'_D = 18.5$ MeV, and $\tilde{a}(A) = 0.114A + 0.162A^{2/3}$, we obtain $E_D \approx 2E'_D$ for the $^{284}114$ nucleus in the case of the $(1-2)n$ channel. At $E_D = \alpha_0 A^{4/3}/a_n$ and $E'_D = \alpha_0 A^{4/3}/\tilde{a}$, a relation between a_n and $\tilde{a}$, which are basic parameters in calculating the ratio Γ_n/Γ_f within, respectively, the Fermi gas model and the model taking into account collective effects, can be derived from (22), provided that the ratio a_f/a_n is fixed. If we set $C = C_{\rm F}$ and $a_f = a_n = \tilde{a}$ in (22), we have

$$E_D = E'_D \frac{E^*_{\rm CN}}{E^*_{\rm CN} - B_n - E_c}. \quad (23)$$

At an excitation energy of $E^*_{\rm CN} \approx 2(B_n + E_c)$, which corresponds to the $(1-2)n$ channel, we obtain $E_D \approx 2E'_D$ from (23).

In order that the different methods produce identical values for the ratio Γ_n/Γ_f, E'_D and E''_D, the latter being the damping factor for the case where the $E^*_{\rm CN}$ dependence of shell effects is taken into account both in the fission barrier and in the level-density parameter [15], must be related as ($q = 1, a_f = a_n$)

$$E'_D = -U_n \ln^{-1}\left[1 - \frac{U_n}{B_f} + \frac{1}{B_f\tilde{a}}\left(\sqrt{a_c(A-1,U_n)U_n} - \sqrt{\tilde{a}_c\left[U_{\rm g.s.} - B_f \exp\left(-\frac{U_{\rm g.s.}}{E''_D}\right)\right]} + \sqrt{\tilde{a}U_f}\right)^2\right], \quad (24)$$

where the quantities a_c and $\tilde{a}_c$ are used in the calculations allowing for the $E^*_{\rm CN}$ dependence of shell effects both in the fission barrier and in the level-density parameter. By way of example, we indicate that, if $E''_D = 16.5$ MeV, $\tilde{a}(A) = 0.114A + 0.162A^{2/3}$,

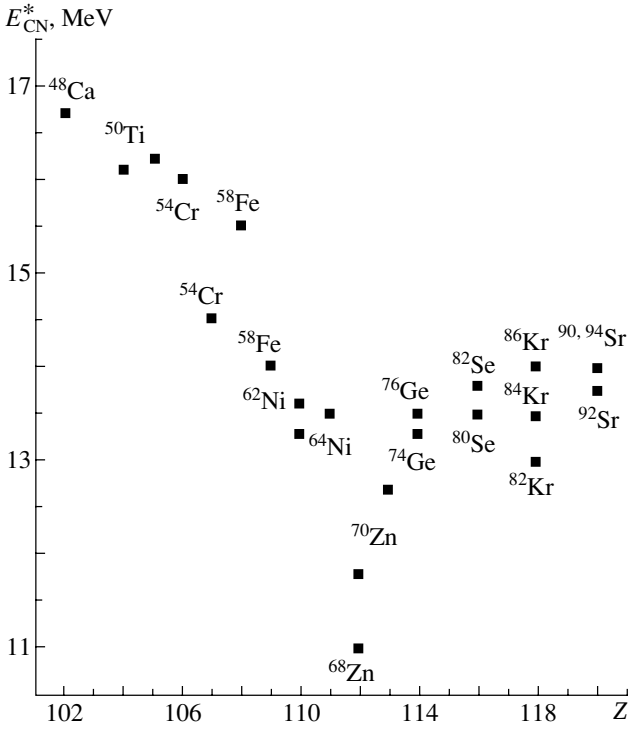

Fig. 4. Excitation energies used in calculating Γ_n/Γ_f and $W_{\rm sur}$ in the $1n$ evaporation channel for nuclei obtained in cold-fusion reactions on ^{208}Pb and ^{209}Bi targets.

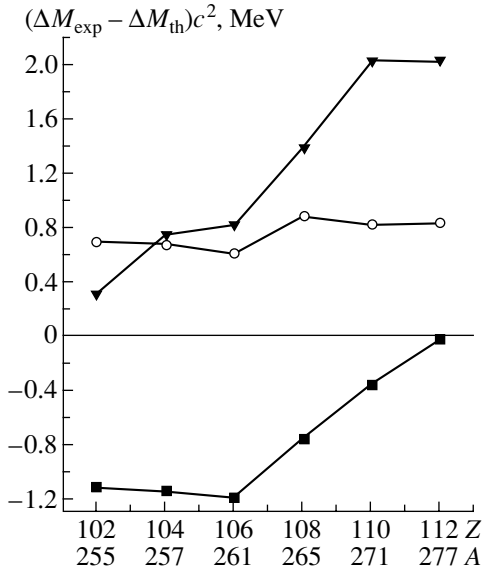

Fig. 5. Theoretically predicted mass defects and their experimental counterparts [1] for nuclei obtained in reactions on a ^{208}Pb target. The displayed experimental data were borrowed from (line connecting circles) [9, 10], (line connecting squares) [11], and (line connecting triangles) [12].

and $\tilde{a}_c(A) = 0.134A - 1.21 \times 10^{-4}A^2$, $E'_D \approx E''_D/2$ for the ^{284}114 nucleus.

In order to obtain identical values of the ratio Γ_n/Γ_f with the different asymptotic expressions for the parameter $\tilde{a}$ in the level density (10), the corresponding damping factors E'_D must be related as in (24), where $\exp(-U_{\rm g.s.}/E''_D)$ is replaced by unity. For example, the calculations with $\tilde{a}$ in (17) and $E'_D = 18.5$ MeV and the calculations with $\tilde{a}(A) = 0.073A + 0.095A^{2/3}$ and $E'_D = 16.3$ MeV lead to the same value of the ratio Γ_n/Γ_f for the ^{284}114 nucleus at the excitation energy of $E^*_{\rm CN} = 13.5$ MeV.

6. DISCUSSION OF THE RESULTS

In the GROGIF statistical code [16–18], which was used here, the sequence of evaporated particles is specified as input information. The initial distribution of the compound nucleus with respect to the excitation energy $E^*_{\rm CN}$ and the angular momentum J is determined on the basis of the optical model (see [21]). In this code, the probabilities for all types of decays of the initial nucleus are calculated at each point ($E^*_{\rm CN}$, J). After that, the sum is taken over all these points. The resulting distribution of the daughter nucleus with respect to the energy and the angular momentum is taken to be new input information for the next step of the evaporation cascade.

6.1. 1n Evaporation Channel

We have calculated the ratio Γ_n/Γ_f for $102 \le Z \le 120$ nuclei produced in cold-fusion reactions on ^{208}Pb and ^{209}Bi targets. The calculations were performed at the excitation energies shown in Fig. 4. We are interested in precisely these energies since they correspond to the maximal values of the cross sections for evaporation-residue formation in the $1n$ channel [1, 7]. For $Z < 108$ nuclei, the energies $E^*_{\rm CN}$ fall between the optimum energies for the $1n$ and $2n$ channels; therefore, the quantity $W_{\rm sur}$ for these nuclei will be less than the ratio Γ_n/Γ_f because of the effect of the factor P_{1n} [see (2)]. The excitation energies of $Z > 108$ nuclei nearly coincide with the optimum energies for the $1n$ channel—for them, P_{1n} is close to unity. We assume that all nuclei are axisymmetric and mirror-symmetric both in the ground state and at the saddle point.

We have calculated the ratio Γ_n/Γ_f using nuclear properties as predicted by the theoretical models from [9–12]. The energies of α-particle separation and the ground-state nuclear masses are the only experimental quantities with which one can compare their theoretical predictions. In relation to what was found in [11], a trend was revealed in [12] toward

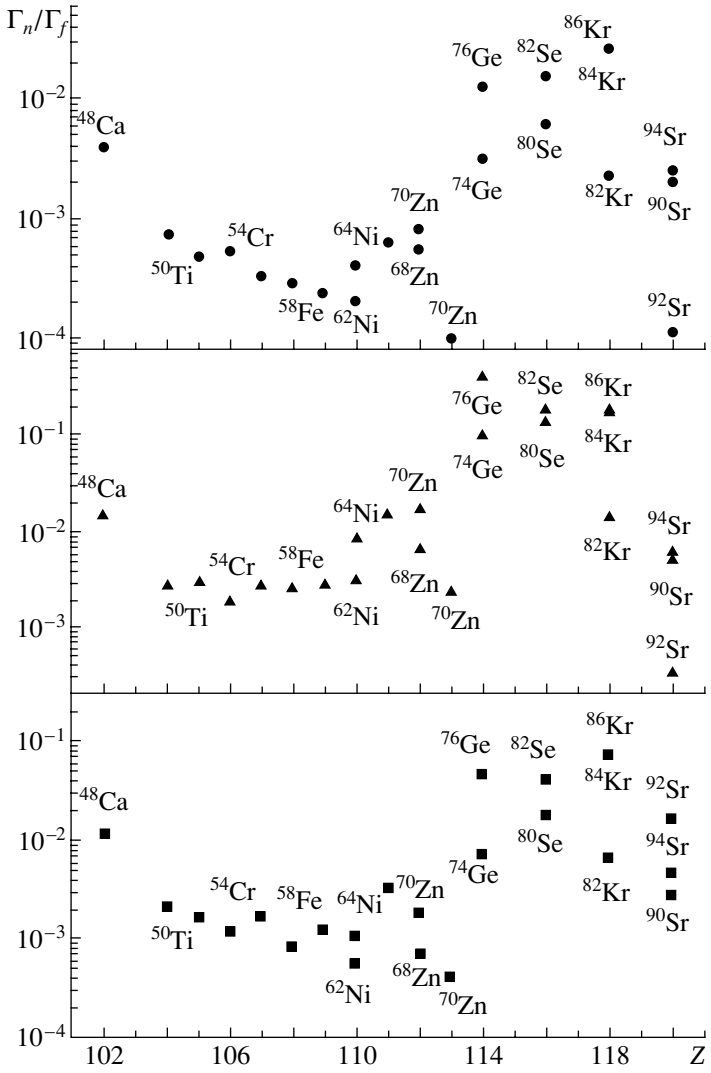

Fig. 6. Ratios Γ_n/Γ_f calculated for nuclei obtained in reactions between ^{208}Pb and ^{209}Bi targets and the displayed projectile nuclei at the excitation-energy values given in Fig. 4 (data borrowed from [11] were used in the calculations, and the angular momentum was taken to be $J = 0$): (upper and middle panels) Γ_n/Γ_f values calculated on the basis of the model taking into account collective enhancement, respectively, with $\tilde{a}$ given by (17), $E'_D = \alpha_0 A^{4/3}/\tilde{a}$, and $E_D = 0$ and with $\tilde{a}$ given by (18) and $E_D = E'_D = \alpha_0 A^{4/3}/\tilde{a}$; (lower panel) results obtained on the basis of the Fermi gas model with $a = A/10$ MeV^{-1}, $a_f/a_n = 1.1$, and $E_D = \alpha_0 A^{4/3}/a$.

a systematic increase in the distinction between the masses predicted on the basis of a model obtained by slightly modifying the finite-range-droplet-model (FRDM) version involving microscopic corrections that was used in [11] and the experimental values deduced from an analysis of the α-decay energies (Fig. 5). For $102 \leq Z \leq 106$ nuclei, the data from [9, 10] should be preferred to the data from [11]. In our opinion, the data from [9–11] are appropriate for $Z > 106$. For all $Z > 102$ elements, the results of the calculations based on the macroscopic–microscopic model [9, 10] differ from the experimental values of the nuclear masses by 0.6–0.8 MeV.

Figure 6 displays the ratio Γ_n/Γ_f calculated for the $1n$ channel by using the theoretical predictions made in [11]. It is assumed that, with the exception of ^{300}120, all nuclei are deformed in such a way that $\beta_2^{\text{g.s.}} > 0.04$. The calculations were performed with the level density obtained on the basis of the Fermi gas model (7); the level density (10), where the parameter a was determined from (14) and (17); and the level density for which the parameter a was determined from (14) and (18), with the damping of the fission barrier being taken into account with the aid of (9). Thus, we have taken into consideration all methods for including the energy dependence of shell effects in the level density. The damping factors E_D

Table 1. Ratio Γ_n/Γ_f calculated for a number of nuclei with (rows 1–9) the level density (10) by using various asymptotic expressions for $\tilde{a}$ and various values for the factor allowing for the damping of shell effects and (row 10) the level density obtained on the basis of the Fermi gas model {the energy dependence of shell effects in rows 1–9 was taken into account by formula (14); the asymptotic expression $\tilde{a} = 0.073A + 0.095A^{2/3}$ was obtained for the Woods–Saxon potential [23]; the data borrowed from [11] were used in the calculations; and the excitation-energy values are given in Fig. 4}

No.	Method	$^{258}104$	$^{266}108$	$^{284}114$	$^{294}118$
1	$\tilde{a} = 0.114A + 0.162A^{2/3}$, $E_D = 0$, $E'_D = 0.4A^{4/3}/\tilde{a}$	2.9×10^{-3}	2.6×10^{-3}	4.2×10^{-1}	1.8×10^{-1}
2	$\tilde{a} = 0.073A + 0.095A^{2/3}$, $E_D = 0$, $E'_D = 0.4A^{4/3}/\tilde{a}$	3.1×10^{-2}	2.9×10^{-2}	8.2×10^{-1}	8.7×10^{-1}
3	$\tilde{a} = 0.073A + 0.095A^{2/3}$, $E_D = 0$, $E'_D = 18.5$ MeV	1.9×10^{-2}	1.5×10^{-2}	7.2×10^{-1}	7.9×10^{-1}
4	$\tilde{a} = 0.134A - 1.21 \times 10^{-4}A^2$, $E_D = 0$, $E'_D = 0.4A^{4/3}/\tilde{a}$	1.5×10^{-2}	1.4×10^{-2}	7.4×10^{-1}	8.3×10^{-1}
5	$\tilde{a} = 0.134A - 1.21 \times 10^{-4}A^2$, $E_D = 0$, $E'_D = 18.5$ MeV	5.5×10^{-3}	9.0×10^{-3}	6.9×10^{-1}	7.8×10^{-1}
6	$\tilde{a} = A/10$, $E_D = 0$, $E'_D = 0.4A^{4/3}/\tilde{a}$	1.8×10^{-2}	1.5×10^{-2}	7.4×10^{-1}	8.2×10^{-1}
7	$\tilde{a} = A/10$, $E_D = 0$, $E'_D = 18.5$ MeV	6.3×10^{-3}	9.7×10^{-3}	6.9×10^{-1}	7.7×10^{-1}
8	$\tilde{a}_n = A/10$, $\tilde{a}_f = 1.1\tilde{a}_n$, $E_D = 0$, $E'_D = 0.4A^{4/3}/\tilde{a}_n$	5.2×10^{-3}	5.0×10^{-3}	6.8×10^{-1}	7.6×10^{-1}
9	$\tilde{a}_n = A/10$, $\tilde{a}_f = 1.1\tilde{a}_n$, $E_D = 0$, $E'_D = 18.5$ MeV	3.5×10^{-3}	3.1×10^{-3}	5.7×10^{-1}	6.6×10^{-1}
10	$a_n = A/10$, $a_f = 1.1a_n$, $E_D = 0.4A^{4/3}/a_n$, $E'_D = 0$	2.2×10^{-3}	8.7×10^{-4}	4.8×10^{-2}	7.6×10^{-2}

and E'_D (15) were used in the calculations with $\alpha_0 = 0.4$. For all nuclei considered here, these quantities proved to be in the region around 18.5 MeV.

In the majority of the cases, the Γ_n/Γ_f values computed with the level density obtained on the basis of the Fermi gas model fall between the results that the level density (10) gives in the case where use is made of relations (14) and (17) at $E_D = 0$ and in the case where use is made of relations (14) and (18) at $E_D = E'_D$. From Fig. 6, it can easily be seen that, for deformed nuclei, the dependence of the results on the method for calculating the level density is rather moderate. The ratio Γ_n/Γ_f changes quite modestly as the charge number Z increases from 104 to 112 (in just the same way as in [30]); it increases approximately by an order of magnitude as we go over from the $^{272}110$ nucleus, where the neutron shell is filled at $N = 162$, to the $Z = 114$ nucleus and reaches a maximum in the region $Z = 114$–118. This indicates that nuclei with these values of Z are highly stable with respect to fission. That the survivability takes large values for the $^{284}114$, $^{290}116$, and $^{294}118$ nuclei is explained by the proximity of the numbers of neutrons in them to the theoretically predicted magic number of $N = 178$ [11, 12]. While, in the lower and the upper panel of Fig. 6, the ratio Γ_n/Γ_f has a maximum for the $^{294}118$ nucleus, in the middle panel, the maximum corresponds to $^{284}114$. This distinction is due to the use of the different methods for taking into account the energy dependence of shell effects.

Table 2. Factors of the collective enhancement of the level density in the neutron and fission channels for the displayed nuclei (the results correspond to the excitation-energy values given in Fig. 4; the data from [11] and the data from [12] for the $^{302}120$ nucleus, which is assumed to be spherical in that article, were used in the calculations)

Nucleus	K^n_{vib}	K^n_{rot}	K^f_{vib}	K^f_{rot}
$^{258}104$	2.3	107.0	3.7	158.2
$^{266}108$	2.3	106.9	3.5	159.8
$^{272}110$	2.0	91.2	3.1	150.9
$^{284}114$	2.3	99.9	3.2	153.3
$^{290}116$	2.4	108.1	3.2	158.1
$^{294}118$	2.2	102.5	3.3	160.9
$^{300}120$	2.3	1.0	2.5	134.3
$^{302}120$	2.4	137.7	2.7	160.1
$^{302}120$ [12]	2.4	1.0	2.7	134.5

It should be emphasized that the neutron-separation energy and the height of the fission barrier are of greatest importance in determining the ratio Γ_n/Γ_f for each specific compound nucleus. If the quantity $(B_n - B_f)$ takes close values in neighboring nuclei, the values of Γ_n/Γ_f for these nuclei will also be close.

Table 1 gives the values of the ratio Γ_n/Γ_f that were calculated with the level density (10), where the energy dependence of shell effects in a was taken into account according to (14), and with different damping

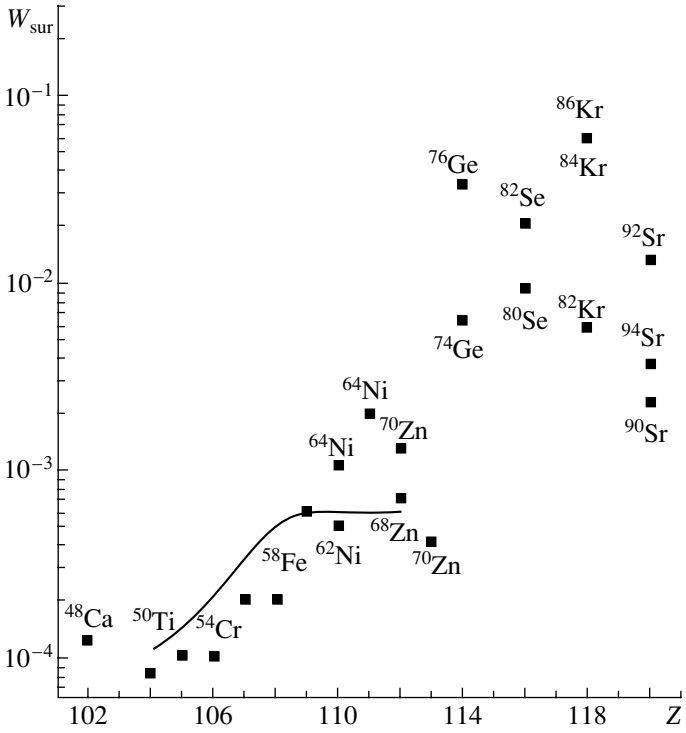

Fig. 7. Survivability $W_{\rm sur}$ calculated with the Γ_n/Γ_f values given in the lower panel of Fig. 6. The solid curve represents the $W_{\rm sur}$ values obtained in [5].

factors and different asymptotic expressions for the level-density parameter. In the calculations with the asymptotic form of $\tilde{a}$ for the Woods–Saxon potential, the values of Γ_n/Γ_f are approximately one order of magnitude greater than those obtained by using expression (17) for $\tilde{a}$. In order to obtain close values of Γ_n/Γ_f, smaller values of E_D must be taken in the case of the Woods–Saxon potential. By comparing the tenth and the eighth row in Table 1, one can arrive at the conclusion that the ratio Γ_n/Γ_f is more sensitive to the damping of shell effects in the fission barrier than to the damping of shell effects in the level density.

The factors that take into account the collective enhancement of the level density in the neutron and fission channels are given in Table 2 for some nuclei at energies making a dominant contribution to the integrals in (5) and (6). In deformed nuclei, the collective-enhancement contribution is characterized by the factor $K^n_{\rm coll}/K^f_{\rm coll} \approx 0.4$–$0.5$. At the saddle point, collective enhancement is of importance for all nuclei, while, in the ground state, it is of importance only for spherical ones, $K_{\rm rot} = 1$; therefore, we have $K^n_{\rm coll}/K^f_{\rm coll} \approx 0.006$ in the latter case. For spherical (magic) superheavy nuclei, this circumstance severely reduces the cross section for evaporation-residue formation [31], and stabilizing shell effects in the ground state cannot compensate for this. As can be seen from Fig. 6, the calculation within the Fermi gas model ($K_{\rm coll} = 1$) leads to a much greater value of Γ_n/Γ_f for the spherical nucleus $^{300}120$. The production of spherical superheavy nuclei cannot be reliably predicted without properly taking into account the contribution of collective effects to the level density. However, there arises the question of whether an excited nucleus having a nonzero angular momentum can be considered as a spherical one.

Since the distinction between the survivability $W_{\rm sur}$ and the ratio Γ_n/Γ_f reduces exclusively to the factor P_{1n}, which is independent of the parametrization of the level density, we have calculated $W_{\rm sur}$ only for the values of Γ_n/Γ_f that were obtained by using the level density within the Fermi gas model (Fig. 7). We have employed the P_{1n} values identical to those in [21]. In the $1n$ channel, the majority of odd nuclei have a higher survivability than the neighboring even–even nuclei. For $106 \le Z \le 112$ nuclei, the values of $W_{\rm sur}$ that were calculated here are close to the estimates obtained in [5, 7], the latter faithfully reproducing the experimental values of $\sigma_{\rm ER}$ [5, 7]. For ^{256}No, our result for Γ_n/Γ_f is close to that which is given in the first article cited in [1]. It should be emphasized that, from our calculations, it follows that survivability is not the reason for the experimentally observed sharp decrease in the cross section $\sigma_{\rm ER}$ with increasing charge number Z of superheavy nuclei since $W_{\rm sur}$

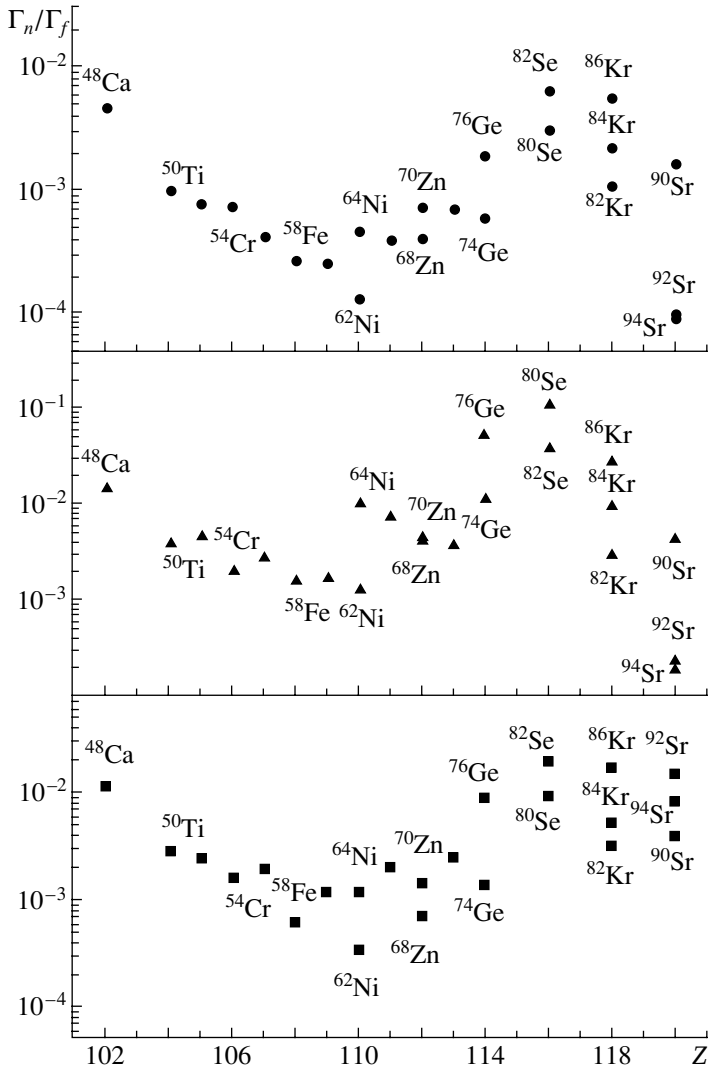

Fig. 8. As in Fig. 6 according to the calculations employing the data borrowed from [12].

changes only within one order of magnitude, while the cross section σ_{ER} decreases by four orders of magnitude as the charge number changes from $Z = 104$ to $Z = 112$ [1, 2].

If the level density is taken in the simplified form $\rho(E^*_{\mathrm{CN}}) = \mathrm{const} \cdot \exp[2\sqrt{aE^*_{\mathrm{CN}}}]$, it can be found from (4)–(6) that [19]

$$\frac{\Gamma_n(E^*_{\mathrm{CN}})}{\Gamma_f(E^*_{\mathrm{CN}})} = \frac{4A^{2/3}(E^*_{\mathrm{CN}} - B_n)}{k(2[a(E^*_{\mathrm{CN}} - B_f(E^*_{\mathrm{CN}}))]^{1/2} - 1)} \times \exp[2a^{1/2}((E^*_{\mathrm{CN}} - B_n)^{1/2} - (E^*_{\mathrm{CN}} - B_f(E^*_{\mathrm{CN}}))^{1/2})], \quad (25)$$

where $k = 9.8$ MeV. In [7], the survivability W_{sur} was calculated by using this formula and the value of $a = A/12$ MeV^{-1}. The results obtained in this way are close to our results displayed in Fig. 7. Since we have dealt with modest values of J and E^*_{CN}, $\rho(E^*_{\mathrm{CN}}, J)$ values calculated by different methods are approximated in (25) by appropriately choosing the parameter a.

Figure 8 shows Γ_n/Γ_f values computed in the same way as those in Fig. 6 but with the aid of the theoretical predictions from [12]. By comparing the data in Fig. 6 and Fig. 8, one can easily see that the predictions made in [11] and [12] lead to close results for all deformed nuclei, with the exception of $^{300}120$ and $^{302}120$. Distinctions within a factor of two to three that are observed for some nuclei are within the errors in determining the parameters involved. For even $Z \geq 108$ nuclei, the use of the predictions from [12] leads to Γ_n/Γ_f values smaller than those obtained with the predictions from [11], while, for $Z \leq 106$ nuclei, the values of Γ_n/Γ_f are somewhat larger in the former than in the latter case. Since our consideration here

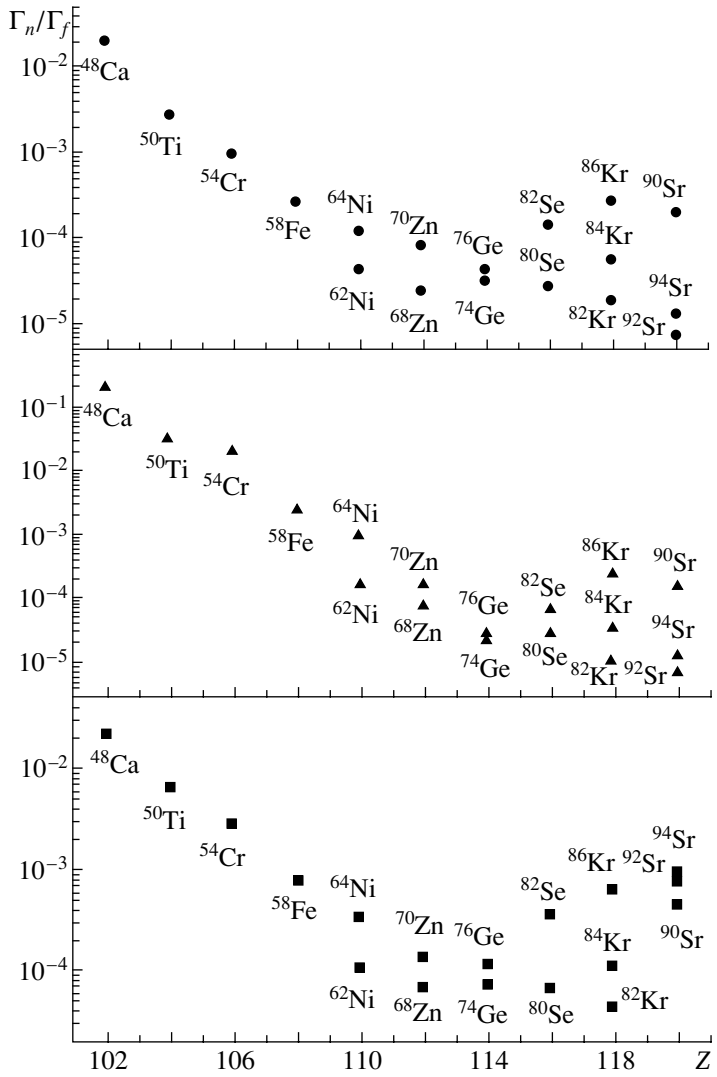

Fig. 9. As in Fig. 6 according to the calculations employing the data borrowed from [9, 10].

was more accurate for small E^*_{CN}, the results that we obtained for the $Z = 110$ and 112 nuclei differ slightly from those in [21]. In the calculation with the predictions from [12], the distinction between the values of Γ_n/Γ_f for ^{270}110 and ^{272}110 is greater than in the calculation employing the data from [11]. The $N = 162$ neutron shell at $Z = 110$ stands out distinctly if use is made of the data from [12] and the level density (10). But if we employ the data from [11], the ratio Γ_n/Γ_f becomes greater at $Z = 111$ than at $Z = 110$ in all versions of the calculation. Irrespective of the computational method, the predictions in [12] lead to a maximum in the ratio Γ_n/Γ_f at ^{290}116 for all nuclei considered here.

The calculations employing the theoretical predictions from [9, 10] lead to greater values of the ratio Γ_n/Γ_f for the $Z = 102$, 104, and 106 nuclei and a close result for the $Z = 108$ nucleus, but they yield much smaller values of Γ_n/Γ_f for the $Z \geq 110$ nuclei (see Fig. 9). The ratio Γ_n/Γ_f begins to grow from $Z = 116$, but, at $Z = 118$, it is approximately two orders of magnitude smaller than the values in Figs. 6 and 8. This result is independent of the method for calculating the level density. For the $Z = 112$ and $Z = 114$ nuclei, the values of Γ_n/Γ_f are considerably smaller in Fig. 9 than in Figs. 6 and 8. The $N = 162$ neutron shell at $Z = 110$ does not stand out among the nuclei being considered.

The analyses performed in [9–12] predict nearly the same neutron binding energies but different fission barriers. The distinction between the results obtained with the data from [9, 10] and with the data from [11, 12] for $Z \geq 114$ can be explained by the distinction between the predictions for the behavior of the fission barrier with increasing charge number of the compound nucleus. In [9, 10], $(B_n - B_f)$ re-

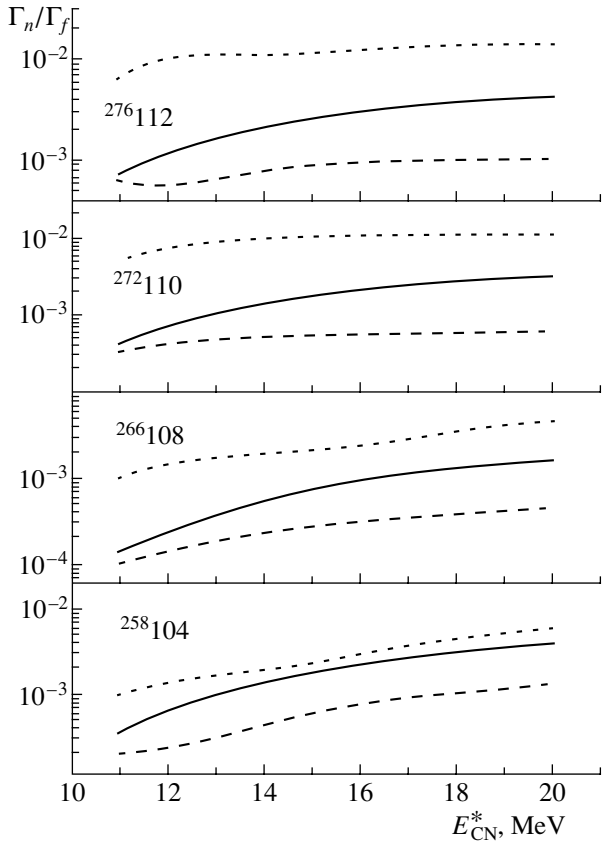

Fig. 10. Ratio Γ_n/Γ_f as a function of E^*_{CN} for the $^{258}104$, $^{266}108$, $^{272}110$, and $^{276}112$ nuclei obtained in the reactions on a ^{208}Pb target. The calculations employed the data borrowed from [11] and relied either (solid curve) on the Fermi gas model with $a = A/10$ MeV^{-1}, $a_f/a_n = 1.1$, and $E_D = \alpha_0 A^{4/3}/a$ or on the model including collective enhancement in two versions, that with (dotted curve) $\tilde{a}$ determined by (17), $E'_D = \alpha_0 A^{4/3}/\tilde{a}$, and $E_D = 0$ and that with (dashed curve) $\tilde{a}$ determined by (18) and $E_D = E'_D = \alpha_0 A^{4/3}/\tilde{a}$. In the calculations, the angular momentum was everywhere set to $J = 0$.

mains rather large for $Z \geq 114$, while, in [11, 12], it is very small. Because of high excitation energies, shell corrections allowing for damping become close for $Z \leq 108$ in all predictions. This explains a relatively small distinction between the values of Γ_n/Γ_f that were obtained by using the different predictions for nuclear properties.

Figure 10 displays the ratio Γ_n/Γ_f as a function of E^*_{CN}. This dependence was obtained with the data from [11] by using various methods for computing the level density and for taking into account the energy dependence of shell effects. We can see that, for fixed E^*_{CN}, the values of Γ_n/Γ_f vary within one order of magnitude as one goes over from one method for calculating the level density to another. By choosing different values of E_D, we can reduce or increase this factor. The results obtained on the basis of the Fermi gas model with $a_n = A/10$ MeV^{-1} and $a_f = 1.1a_n$ fall between the results of the two calculations employing the level density given by (10). The values of Γ_n/Γ_f that were calculated with the aid of (10) depend on E^*_{CN} more weakly than those computed on the basis of the Fermi gas model, this trend becoming more pronounced with increasing mass number of nuclei.

6.2. xn Evaporation Channel, $x \geq 2$

Despite a relatively small difference of the values of W_{sur} that were obtained by the different methods for calculating the level density in the $1n$ channel, one can expect that, for the xn channel, $x \geq 2$, the corresponding difference of the values of W_{sur} will be greater. In Table 3, we present the values of W_{sur} that were calculated with the data from [11] by using the level density according to the Fermi gas model with $a_n = A/10$ MeV^{-1}, $a_f = 1.1a_n$, and $E_D = \alpha_0 A^{4/3}/a_n$ and according to the model including collective enhancement on the basis of (17) at $E'_D = \alpha_0 A^{4/3}/\tilde{a}$ and $E_D = 0$. The values of W_{sur} that were obtained in [7] with the aid of (25) are the closest to those corresponding to the use of the model including the collective enhancement of the level density. For the $2n$ channel, the distinction between the results calculated by the different methods is within one order of magnitude. It grows with increasing x. In the case of the $3n$ and $4n$ channels, this distinction becomes as great as two orders of magnitude. It follows that, in the case of the xn channel ($x \geq 2$), W_{sur} becomes sensitive to the method for calculating the level density and to the choice of parameter values. For the sake of comparison, we also quote the results obtained with the data from [12] at $Z = 105$. With a smaller value of the parameter a in the Fermi gas model, one can arrive at the values of W_{sur} that were obtained by using the model taking into account the collective enhancement of the level density. If we set $E'_D = 16.5$ MeV for the $^{292}114$ nucleus in the $4n$ channel, the survivability W_{sur} calculated on the basis of formulas (10) and (17) becomes two orders of magnitude less than that at $E'_D = \alpha_0 A^{4/3}/\tilde{a}$, approaching the W_{sur} value obtained in [7]. While the damping factor in the form (15) with $\alpha_0 = 0.4$ was deduced from an analysis of data at small E^*_{CN}, the damping factor $E'_D = 16.5$ MeV [13, 15] was obtained from an analysis of the $(4–5)n$ channels in hot-fusion reactions on actinide targets. In these reactions, the number of neutrons in a compound nucleus is usually greater than in reactions involving ^{208}Pb and ^{209}Bi nuclei.

Table 3. Survivabilities calculated for specific compound nuclei at the displayed values of the excitation energy E^*_{CN} {the calculations were performed on the basis of the Fermi gas model by using the values of $a_n = A/10\ \mathrm{MeV}^{-1}$, $a_f/a_n = 1.1$, and $E_D = 0.4A^{4/3}/a_n$ (W^{I}_{sur}) and on the basis of the model taking into account the collective enhancement of the level density with $\tilde{a}$ given by formula (17) at $E'_D = 0.4A^{4/3}/\tilde{a}$ and $E_D = 0$ (W^{II}_{sur}) (in these calculations, we used the predictions borrowed from [11]); the results obtained by using the predictions presented in [12] are specifically highlighted; for $^{292}114$ (W^{II}_{sur}), the calculation of the $4n$ channel at $E'_D = 16.5$ MeV was also performed; the results calculated in [7] by formula (25) with the predictions given in [11] are denoted by W^{III}_{sur}}

Reaction	E^*_{CN}, MeV	W^{I}_{sur}	W^{II}_{sur}	W^{III}_{sur}
$^{50}\mathrm{Ti} + {}^{208}\mathrm{Pb} \to {}^{257}104 + 1n$	16.1	8.0×10^{-5}	1.3×10^{-4}	9×10^{-5}
$^{50}\mathrm{Ti} + {}^{208}\mathrm{Pb} \to {}^{256}104 + 2n$	21.5	2.1×10^{-5}	1.0×10^{-5}	4×10^{-5}
$^{50}\mathrm{Ti} + {}^{208}\mathrm{Pb} \to {}^{255}104 + 3n$	29.5	1.5×10^{-8}	3.1×10^{-8}	3×10^{-7}
$^{50}\mathrm{Ti} + {}^{209}\mathrm{Bi} \to {}^{258}105 + 1n$	16.2	1.0×10^{-4}	1.5×10^{-4}	3×10^{-4}
		1.3×10^{-4} [12]	2.3×10^{-4} [12]	
$^{50}\mathrm{Ti} + {}^{209}\mathrm{Bi} \to {}^{257}105 + 2n$	21.9	1.0×10^{-6}	6.8×10^{-6}	4×10^{-5}
		1.2×10^{-5} [12]	3.6×10^{-5} [12]	
$^{50}\mathrm{Ti} + {}^{209}\mathrm{Bi} \to {}^{256}105 + 3n$	30.0	2.0×10^{-9}	2.9×10^{-8}	3×10^{-7}
		3.0×10^{-8} [12]	2.4×10^{-7} [12]	
$^{54}\mathrm{Cr} + {}^{208}\mathrm{Pb} \to {}^{261}106 + 1n$	16.0	7.3×10^{-5}	1.8×10^{-4}	1×10^{-4}
$^{54}\mathrm{Cr} + {}^{208}\mathrm{Pb} \to {}^{260}106 + 2n$	22.0	7.0×10^{-6}	3.7×10^{-6}	3×10^{-5}
$^{58}\mathrm{Fe} + {}^{208}\mathrm{Pb} \to {}^{265}108 + 1n$	15.5	2.0×10^{-4}	5.8×10^{-4}	4×10^{-4}
$^{58}\mathrm{Fe} + {}^{208}\mathrm{Pb} \to {}^{264}108 + 2n$	19.5	2.6×10^{-6}	5.4×10^{-6}	1×10^{-5}
$^{84}\mathrm{Ge} + {}^{208}\mathrm{Pb} \to {}^{290}114 + 2n$	18.5	6.0×10^{-2}	9.1×10^{-2}	2×10^{-1}
$^{48}\mathrm{Ca} + {}^{244}\mathrm{Pu} \to {}^{288}114 + 4n$	37.0	7.0×10^{-6}	1.2×10^{-4}	8.6×10^{-7}
			4.9×10^{-6} [$E'_D = 16.5$ MeV]	

While, in cold-fusion reactions, the survivabilities calculated within the different approaches are nearly identical, in hot-fusion reactions ($x \geq 2$), they greatly depend on the computational method and on the parameters used. In all probability, the E^*_{CN} dependence of the damping factor E'_D becomes more pronounced with increasing number of neutrons. We can assume that, for the $3n$ channel, the factor that takes into account the damping of shell effects is less than that in (15), approaching the value of 16.5 MeV quoted in [13, 15].

7. CONCLUSION

The survivability of even–even and odd superheavy nuclei has been analyzed on the basis of various methods for calculating the level density, the neutron- and fission-channel parameters obtained within various theoretical models being used in this analysis. The calculations for the $1n$ channel with the data from [11, 12] have revealed that the ratio Γ_n/Γ_f decreases as Z increases up to $Z = 112$, whereupon it strongly increases at $Z = 114$, which suggests the existence of a nuclear-stability region. The calculations employing the data from [9–12] give close results for $Z < 114$. For $Z \geq 114$, the calculations with the data from [9, 10] lead to considerably lower values of Γ_n/Γ_f than the calculations with the data from [11, 12] and, accordingly, smaller cross sections for evaporation-residue formation. As the charge Z changes from $Z = 102$ to $Z = 120$, W_{sur} varies within two orders of magnitude. For $104 < Z < 112$ nuclei, the survivability takes nearly the same value. Since the experimental values of the cross section for evaporation-residue formation [1, 2] strongly decrease with increasing Z (approximately by four orders of magnitude as the charge number grows from $Z = 104$ to $Z = 112$), we can therefore conclude that, in cold-fusion reactions, which are considered here, a decrease in the complete-fusion probability with increasing Z is the main reason for the occurrence of this phenomenon.

Since the results for xn channels ($x \geq 2$) are highly sensitive to the choice of model used in the

calculations, only those calculations of Γ_n/Γ_f are of interest that employ a common set of parameters and assumptions for a great number of reactions. By comparing the results of such calculations with experimental data, one can answer the question of whether the choice of statistical-model parameters was correct.

ACKNOWLEDGMENTS

This work was supported in part by the Russian Foundation for Basic Research (project no. 01-02-16033), DAAD, Volkswagen-Stiftung (Germany), and STCU (Uzb-45).

REFERENCES

1. G. Münzenberg, Rep. Prog. Phys. **51**, 57 (1988); S. Hofmann and G. Münzenberg, Rev. Mod. Phys. **72**, 733 (2000); G. Münzenberg, Philos. Trans. R. Soc. London, Ser. A **356**, 2083 (1998); S. Hofmann, Rep. Prog. Phys. **61**, 636 (1998).
2. Yu. Ts. Oganessian *et al.*, Eur. Phys. J. A **5**, 63 (1999); Phys. Rev. Lett. **83**, 3154 (1999); A. V. Yeremin, V. K. Utyonkov, and Yu. Ts. Oganessian, AIP Conf. Proc. **425**, 16 (1998).
3. K.-H. Schmidt and W. Morawek, Rep. Prog. Phys. **54**, 949 (1991); K.-H. Schmidt *et al.*, in *Proceedings of Symposium on Physics and Chemistry of Fission, Julich* (IAEA, Vienna, 1980), p. 409.
4. N. V. Antonenko, E. A. Cherepanov, A. K. Nasirov, *et al.*, Phys. Lett. B **319**, 425 (1993); Phys. Rev. C **51**, 2635 (1995).
5. G. G. Adamian, N. V. Antonenko, W. Scheid, and V. V. Volkov, Nucl. Phys. A **633**, 409 (1998); Nuovo Cimento A **110**, 1143 (1997).
6. G. G. Adamian, N. V. Antonenko, S. P. Ivanova, and W. Scheid, Nucl. Phys. A **646**, 29 (1999).
7. G. G. Adamian, N. V. Antonenko, and W. Scheid, Nucl. Phys. A **678**, 24 (2000).
8. A. Sobiczewski, Z. Patyk, and S. Cwiok, Phys. Lett. B **186**, 6 (1987).
9. R. Smolanczuk, J. Skalski, and A. Sobiczewski, Phys. Rev. C **52**, 1871 (1995).
10. R. Smolanczuk, Phys. Rev. C **59**, 2634 (1999).
11. P. Möller and R. Nix, At. Data Nucl. Data Tables **39**, 213 (1988).
12. P. Möller *et al.*, At. Data Nucl. Data Tables **59**, 185 (1995).
13. E. A. Cherepanov, A. S. Iljinov, and M. V. Mebel, J. Phys. G **9**, 931 (1983).
14. E. A. Cherepanov, in *Proceedings of the International Symposium on In-Beam Nuclear Spectroscopy, Debrecen, 1984,* p. 499; E. A. Cherepanov and A. S. Iljinov, Nukleonika **25**, 611 (1980).
15. E. A. Cherepanov, Preprint No. E7-99-27, OIYaI (Dubna, 1999).
16. J. Gilat, Phys. Rev. C **1**, 1432 (1970).
17. O. V. Grusha *et al.*, Nucl. Phys. A **429**, 313 (1984).
18. O. V. Grusha, S. P. Ivanova, and Yu. N. Shubin, Vopr. At. Nauki Tekh., Ser.: Yad. Konstanty, No. 1, 36 (1987).
19. R. Vandenbosch and J. R. Huizenga, *Nuclei Fission* (Academic, New York, 1973).
20. A. V. Ignatyuk, *Statistical Properties of Excited Atomic Nuclei* (Énergoatomizdat, Moscow, 1983).
21. G. G. Adamian, N. V. Antonenko, S. P. Ivanova, and W. Scheid, Phys. Rev. C **62**, 064303 (2000).
22. A. V. Ignatyuk, K. K. Istekov, and G. N. Smirenkin, Yad. Fiz. **29**, 875 (1979) [Sov. J. Nucl. Phys. **29**, 450 (1979)].
23. A. V. Ignatyuk, M. G. Itkis, V. N. Okolovich, *et al.*, Yad. Fiz. **21**, 1185 (1975) [Sov. J. Nucl. Phys. **21**, 612 (1975)].
24. K.-H. Schmidt, H. Delagrange, J. P. Dufour, *et al.*, Z. Phys. A **308**, 215 (1982); J.-J. Gaimard and K.-H. Schmidt, Nucl. Phys. A **531**, 709 (1991); A. S. Iljinov *et al.*, Nucl. Phys. A **543**, 517 (1992).
25. J. Toke and W. J. Swiatecki, Nucl. Phys. A **372**, 141 (1981).
26. W. Reisdorf and J. Toke, Z. Phys. A **302**, 183 (1981).
27. W. D. Myers and W. J. Swiatecki, Ann. Phys. (N.Y.) **84**, 186 (1974).
28. G. D. Adeev and G. A. Cherdantsev, Yad. Fiz. **21**, 491 (1975) [Sov. J. Nucl. Phys. **21**, 258 (1975)].
29. A. V. Ignatyuk, G. N. Smirenkin, and A. S. Tishin, Yad. Fiz. **21**, 485 (1975) [Sov. J. Nucl. Phys. **21**, 255 (1975)].
30. B. I. Pustylnik, in *Proceedings of the International Conference on Dynamical Aspects of Nuclear Fission, Casta-Papiernicka, Slovak Republic, 1996,* p. 121.
31. A. R. Junghans, M. de Jong, H.-G. Clerc, *et al.*, Nucl. Phys. A **629**, 635 (1998).

Translated by A. Isaakyan

Physics of Atomic Nuclei, Vol. 66, No. 2, 2003, pp. 233–246. Translated from Yadernaya Fizika, Vol. 66, No. 2, 2003, pp. 257–270.

NUCLEI
Theory

Energy Dependence of Effective Nucleon–Nucleon Interaction and Position of the Nucleon Drip Line

M. Baldo[1)], U. Lombardo[1),2)], E. E. Saperstein, and M. V. Zverev

Russian Research Centre Kurchatov Institute, pl. Kurchatova 1, Moscow, 123182 Russia

Received March 15, 2002

Abstract—A semimicroscopic version of the self-consistent theory of finite Fermi systems is proposed. In this approach, the standard theory of finite Fermi systems is supplemented with relations that involve the external values of the invariant components of the Landau–Migdal amplitude and which follow from microscopic theory. The Landau–Migdal amplitude at the nuclear surface is expressed in terms of the off-shell T matrix for free nucleon–nucleon scattering at the energy E equal to the doubled chemical potential of the nucleus being considered. The strong energy dependence of the free T matrix at low E changes the properties of nuclei in the vicinity of the nucleon drip line. It is shown that, upon taking into account the energy dependence of the effective interaction, the neutron drip line is shifted considerably toward greater neutron-excess values. This effect is illustrated by considering the example of the tin-isotope chain.

1. INTRODUCTION

Until the present time, analyses of the properties of nuclei in the vicinity of the nucleon drip line, as well the calculations of the position of the drip line itself, have been performed on the basis of phenomenological approaches exclusively. These approaches employ parameters whose values are fitted to the properties of stable nuclei. This is the weakest point in applying phenomenological approaches to nuclei occurring far off the beta-stability valley.

It is well known that nucleon pairing is of importance for nuclei in the vicinity of the nucleon drip line, where the chemical potential μ of the neutron or the proton subsystem vanishes. Nuclear pairing ensures additional stability of even–even nuclei, with the result that there arises a region where even nuclei are stable, but where odd ones are unstable. In the majority of studies aimed at calculating drip lines, attention is therefore given primarily to exploring special features of nucleon pairing at small values of the chemical potential μ [1–3]. This involves considering problems such as those of correctly taking into account continuum states, comparing exact Bogolyubov solutions with solutions found within the Bardeen–Cooper–Schrieffer (BCS) approximation, and contrasting surface against volume pairing. At the same time, the possibility that the parameters of the effective pairing interaction themselves may change in the vicinity of the nucleon drip line is disregarded, to say nothing about the possibility of changes in the interaction components responsible for the mean nuclear field.

In the present study, we consider precisely the last possibility and focus on exploring the features of the neutron mean field in the vicinity of the neutron drip line that are associated with this possibility. We will analyze the scalar components of the effective nucleon–nucleon interaction that generate the central mean field. Our consideration will be based on the theory of finite Fermi systems [4, 5], which is supplemented with relations that involve external values of the amplitude for the interaction of Landau–Migdal quasiparticles and which follow from microscopic theory [6]. In order to distinguish the present version from the standard theory of finite Fermi systems, which employs a purely phenomenological Landau–Migdal amplitude, we refer to this version as a semimicroscopic one.

As we will see below, the neutron–neutron component of the interaction does indeed undergo considerable changes in the surface region of nuclei at small values of the chemical potential μ_n, with the result that the mean neutron potential becomes deeper. This in turn may lead to a noticeable shift of the nucleon drip line. Qualitatively, this effect can be analyzed on the basis of the self-consistent version of the theory of finite Fermi systems, where it is required, as in the theory of many-body systems, that the single-particle mass operator be consistent with the effective interaction [7]. Such an analysis is performed in

[1)]Istituto Nazionale di Fisica Nucleare, Sezione di Catania, 57 Corso Italia, I-95129 Catania, Italy.
[2)]Universita di Catania, Dipartimento di Fisica, 57 Corso Italia, I-95129 Catania, Italy.

Section 2 by using the self-consistency condition in the simplified form where the self-consistent mean nuclear field is expressed in terms of the Landau–Migdal amplitude. For the scalar components of this amplitude, which determine the central part (dominant one) of the mean-field potential, an interpolation formula that is controlled by two parameters (the external and the internal value of this amplitude) is used in the theory of finite Fermi systems [4]. It was shown in [6] that, for stable nuclei, in which case one can set $\mu_n = \mu_p = \mu$, the external values of Landau–Migdal amplitudes can be expressed in terms of the off-shell T matrix for free nucleon–nucleon scattering at the negative energy value of $E = 2\mu$. For nuclei in the vicinity of the nucleon drip line, where the neutron chemical potential differs significantly from the proton chemical potential, different isotopic components of the Landau–Migdal amplitude appear at different values of energy. In particular, the neutron–neutron component is taken at the energy of $E = 2\mu_n$. The neutron chemical potential μ_n tends to zero as one approaches the neutron drip line. Since the free two-neutron T matrix has a pole near the origin in the complex plane of the variable E, the external constant of interaction of two neutrons must change in this region from one nucleus to another, increasing in magnitude as we move toward the drip line. As a result, the neutron mean field for nuclei in the vicinity of the drip line becomes deeper, which shifts the position of the drip line itself toward greater neutron-excess values.

For our specific calculations, we made use of a somewhat modified quasiparticle Lagrangian method [8, 9]. By this, we mean that version of the self-consistent theory of finite Fermi systems in which the effects of the energy dependence of quasiparticle interaction are taken into account by means of a quasiparticle Lagrangian rather than by means of the Hartree–Fock method employing effective forces [10] and relying on the Hamiltonian formalism. The modification that must be introduced in the quasiparticle Lagrangian method for nuclei in the vicinity of the nucleon drip line consists, first, in that isotopic invariance is violated here, whence it follows that the isotopic structure of the effective Lagrangian must be more complicated than for stable nuclei, and, second, in that it is necessary to take into account the dependence on the chemical potentials μ_n and μ_p in those Lagrangian parameters that are related to the external values of the invariant Landau–Migdal interaction amplitudes. An account of this modification of the quasiparticle Lagrangian method is given in Section 3. Specific calculations are performed for the chains of tin isotopes. The results are presented in Section 4. Section 5 contains a discussion of the results and a brief summary.

2. CONDITION OF SELF-CONSISTENCY OF THE THEORY OF FINITE FERMI SYSTEMS FOR NUCLEI IN THE VICINITY OF THE NUCLEON DRIP LINE

The exact form of the many-body consistency condition [7] between the mass operator $\Sigma(\mathbf{r}, \mathbf{r}'; \varepsilon)$, which is nonlocal and which depends on the energy ε; the effective interaction, and the single-particle Green's function $\mathcal{G}$ for a bounded finite Fermi system can be represented as

$$\frac{\partial\Sigma(\mathbf{r}, \mathbf{r}'; \varepsilon)}{\partial\mathbf{R}} = \int \frac{d\varepsilon'}{2\pi i} d\mathbf{r}_1 d\mathbf{r}'_1 \mathcal{U}(\mathbf{r}, \mathbf{r}', \mathbf{r}_1, \mathbf{r}'_1; \varepsilon, \varepsilon') \times \frac{\partial\mathcal{G}(\mathbf{r}_1, \mathbf{r}'_1; \varepsilon')}{\partial\mathbf{R}_1}, \quad (1)$$

where we have introduced the center-of-mass coordinates $\mathbf{R} = (\mathbf{r}+\mathbf{r}')/2$ and $\mathbf{R}_1 = (\mathbf{r}_1+\mathbf{r}'_1)/2$ and where $\mathcal{U}$ is the NN-interaction block irreducible in the particle–hole channel. The obvious spin and isospin indices are omitted in (1).

In Hartree–Fock theory involving effective forces [10], one disregards the energy dependence of the effective nucleon–nucleon interaction. In this case, the mass operator Σ coincides with the Hartree–Fock mean field U_{HF} (which is nonlocal, in general) and integration with respect to energy in (1) is performed explicitly, which leads to the Hartree–Fock relation

$$\frac{\partial U_{\mathrm{HF}}(\mathbf{r}, \mathbf{r}')}{\partial\mathbf{R}} = \int d\mathbf{r}_1 d\mathbf{r}'_1 \mathcal{U}_{\mathrm{HF}}(\mathbf{r}, \mathbf{r}', \mathbf{r}_1, \mathbf{r}'_1) \frac{\partial\hat{\rho}(\mathbf{r}_1, \mathbf{r}'_1)}{\partial\mathbf{R}_1}, \quad (2)$$

where $\hat{\rho}(\mathbf{r}, \mathbf{r}')$ is the density matrix.

A renormalization of the consistency condition (1) in accordance with ideas of Fermi liquid theory due to Landau [11, 12]—that is, its formulation in terms of quasiparticles, along with the substitution of the Landau amplitude Γ^{ω} for the interaction block $\mathcal{U}$—was performed in [9]. Here, we only present the idea of this renormalization and its result. By using the identity

$$\frac{\partial\mathcal{G}}{\partial\mathbf{R}} = \mathcal{G}\mathcal{G}\frac{\partial\Sigma}{\partial\mathbf{R}}, \quad (3)$$

we recast the consistency condition (1) into the form

$$\frac{\partial\Sigma}{\partial\mathbf{R}} = \mathcal{U}\mathcal{G}\mathcal{G}\frac{\partial\Sigma}{\partial\mathbf{R}}, \quad (4)$$

which is convenient for performing the Landau renormalization.

As usual, the symbolic multiplication in Eqs. (3) and (4) implies integration with respect to intermediate coordinates and energies and summation over the spin and isospin indices. Following further the same line of reasoning as in Landau Fermi liquid theory, we represent the Green's function as the sum of a

quasiparticle (pole) and a regular component: $\mathcal{G} = \mathcal{G}_q + \mathcal{G}_R$. The quasiparticle Green's function obeys the Dyson equation

$$(\varepsilon - \varepsilon_p^0 - \Sigma_q)\mathcal{G}_q = 1, \tag{5}$$

which involves the quasiparticle mass operator

$$\Sigma_q(\mathbf{r}, \mathbf{k}; \varepsilon) = \Sigma_0(\mathbf{r}) + \frac{1}{(k_\mathrm{F}^0)^2}\mathbf{k}\Sigma_1(\mathbf{r})\mathbf{k} + \frac{\varepsilon}{\varepsilon_\mathrm{F}^0}\Sigma_2(\mathbf{r}). \tag{6}$$

Here, we have used the notation adopted in [9], where the normalization parameters in (6) were expressed in terms of the inverse density of states at the Fermi surface, $C_0 = (dn/d\varepsilon_\mathrm{F})^{-1}$; that is, $k_\mathrm{F}^0 = \pi/(mC_0)$ and $\varepsilon_\mathrm{F}^0 = (k_\mathrm{F}^0)^2/(2m)$. We will employ the value of $C_0 = 300$ MeV fm^3, which was recommended in [5].

The first two terms in Σ_q are familiar in Hartree–Fock theory involving velocity-dependent effective forces (for example, Skyrme forces). The third term, $\Sigma_2(\mathbf{r})$, reflects the energy dependence that is taken into account in the theory of finite Fermi systems, but which is disregarded in the Hartree–Fock approach. It determines the coordinate-dependent Z factor

$$Z(\mathbf{r}) = \left(1 - \Sigma_2(\mathbf{r})/\varepsilon_\mathrm{F}^0\right)^{-1}. \tag{7}$$

Following the Landau recipe, we represent the particle–hole propagator (the product of two Green's functions) in (4) as the sum

$$\mathcal{G}\mathcal{G} = A + B, \tag{8}$$

where A is a singular part of the particle–hole propagator (it corresponds to the product of two quasiparticle Green's functions), while B does not involve singularities that are close to the Fermi surface. The standard Landau renormalization of Eq. (4) reduces it to a form that includes only quasiparticle characteristics; that is,

$$\frac{\partial\Sigma_q}{\partial\mathbf{R}} = \Gamma^\omega A\frac{\partial\Sigma_q}{\partial\mathbf{R}}, \tag{9}$$

where the quasiparticle-interaction amplitude Γ^ω satisfies the equation

$$\Gamma^\omega = \mathcal{U} + \mathcal{U}B\Gamma^\omega. \tag{10}$$

In [9], Eq. (9) was recast into a form that is analogous to the Hartree–Fock relation (2); that is,

$$\frac{\partial U_q(\mathbf{r}, \mathbf{r}'; \varepsilon)}{\partial\mathbf{R}} = \int d\mathbf{r}_1 d\mathbf{r}_1' F(\mathbf{r}, \mathbf{r}', \mathbf{r}_1, \mathbf{r}_1'; \varepsilon, \mu) \times \frac{\partial\hat{\rho}_q(\mathbf{r}_1, \mathbf{r}_1')}{\partial\mathbf{R}_1}, \tag{11}$$

where

$$U_q(\mathbf{r}, \mathbf{r}'; \varepsilon) = Z^{1/2}(\mathbf{r})\Sigma_q(\mathbf{r}, \mathbf{r}'; \varepsilon)Z^{1/2}(\mathbf{r}') \tag{12}$$

is the energy-dependent quasiparticle mean field and $\hat{\rho}_q$ is the quasiparticle density matrix. The Landau–Migdal interaction amplitude

$$F(\mathbf{r}_1, \mathbf{r}_2, \mathbf{r}_3, \mathbf{r}_4; \varepsilon, \varepsilon') = \sqrt{Z(\mathbf{r}_1)Z(\mathbf{r}_2)Z(\mathbf{r}_3)Z(\mathbf{r}_4)}\Gamma^\omega(\mathbf{r}_1, \mathbf{r}_2, \mathbf{r}_3, \mathbf{r}_4; \varepsilon, \varepsilon') \tag{13}$$

also depends on the energies of incoming and outgoing particles.

As was shown in [9], the quasiparticle density matrix is related to the particle density matrix via the nonlocal quasiparticle form factor $\hat{e}_q$ as

$$\hat{\rho}_q = \hat{e}_q\hat{\rho}. \tag{14}$$

In just the same way as above, symbolic multiplication in Eq. (14) includes integration with respect to intermediate coordinates. By virtue of the Landau–Luttinger theorem, which states that the number of particles is equal to the number of quasiparticles, the integral of $\hat{e}_q$ with respect to all coordinates must be equal to unity. It should be noted that the self-consistency condition (11) includes, in addition to relation (2) of the Hartree–Fock type for the mean field, the consistency condition for the Z factor, the latter being obtained by differentiating relation (1) with respect to energy [13].

With the aim of performing a qualitative analysis of energy-dependence effects for nuclei in the vicinity of the nucleon drip line, we will simplify the self-consistency condition (11) to the maximum possible degree, disregarding the nonlocality of the effective interaction and replacing the quasiparticle form factor by unity. Explicitly introducing isotopic indices and energy variables, we represent the self-consistency condition simplified in this way as follows:

$$\frac{\partial U_n(\mathbf{r}; \mu_n)}{\partial\mathbf{r}} = \int F_{nn}(\mathbf{r}, \mathbf{r}'; \mu_n, \mu_n)\frac{\partial\rho_n}{\partial\mathbf{r}'}d\mathbf{r}' + \int F_{np}(\mathbf{r}, \mathbf{r}'; \mu_n, \mu_p)\frac{\partial\rho_p}{\partial\mathbf{r}'}d\mathbf{r}', \tag{15}$$

$$\frac{\partial U_p(\mathbf{r}; \mu_p)}{\partial\mathbf{r}} = \int F_{pn}(\mathbf{r}, \mathbf{r}'; \mu_p, \mu_n)\frac{\partial\rho_n}{\partial\mathbf{r}'}d\mathbf{r}' + \int F_{pp}(\mathbf{r}, \mathbf{r}'; \mu_p, \mu_p)\frac{\partial\rho_p}{\partial\mathbf{r}'}d\mathbf{r}'. \tag{16}$$

For nuclei in the beta-stability valley, one can approximately set $\mu_n = \mu_p = \mu$ and make use of the isotopically invariant Landau–Migdal amplitude whose central part has the form

$$F(\mathbf{r}, \mathbf{r}') = C_0[f_0(\mathbf{r}) + f_0'(\mathbf{r})\boldsymbol{\tau}_1\cdot\boldsymbol{\tau}_2 + (g_0(\mathbf{r}) + g_0'(\mathbf{r})\boldsymbol{\tau}_1\cdot\boldsymbol{\tau}_2)\boldsymbol{\sigma}_1\cdot\boldsymbol{\sigma}_2]\delta(\mathbf{r} - \mathbf{r}'), \tag{17}$$

where we have used the notation adopted in the theory of finite Fermi systems and where $\boldsymbol{\sigma}$ and $\boldsymbol{\tau}$ are, respectively, the spin and isospin Pauli matrices.

The central (main) components of the potentials $U_{n,p}(\mathbf{r})$ are determined by the scalar components f and f' of the Landau–Migdal amplitude (17) as

$$F_{nn}(\mathbf{r},\mathbf{r}') = F_{pp}(\mathbf{r},\mathbf{r}') = C_0[f_0(\mathbf{r}) + f'_0(\mathbf{r})]\delta(\mathbf{r}-\mathbf{r}'), \quad (18)$$

$$F_{np}(\mathbf{r},\mathbf{r}') = F_{pn}(\mathbf{r},\mathbf{r}') = C_0[f_0(\mathbf{r}) - f'_0(\mathbf{r})]\delta(\mathbf{r}-\mathbf{r}'). \quad (19)$$

The scalar–isoscalar amplitude $f_0(\mathbf{r})$ plays a dominant role in nuclei featuring a moderately small neutron excess $N-Z$. Within the theory of finite Fermi systems, it was found that this amplitude greatly depends on the observation point $\mathbf{r}$. In the monograph of Migdal [4], it was proposed to describe this dependence by the simple interpolation formula

$$f_0(\mathbf{r}) = f^{\mathrm{ex}} + (f^{\mathrm{in}} - f^{\mathrm{ex}})\frac{\rho_+(\mathbf{r})}{\rho_0}, \quad (20)$$

where $\rho_+(\mathbf{r}) = \rho_n(\mathbf{r}) + \rho_p(\mathbf{r})$ is the isoscalar density and $\rho_0 = \rho_+(r=0)$. The subscript "0," which labels the zeroth Landau harmonic, is suppressed on the right-hand side of Eq. (20) and in what follows in order to avoid encumbering the presentation. It should be emphasized that the density dependence of phenomenological Skyrme forces [10] is consistent with the ansatz in (20). There also exist alternative versions of the interpolation formula for $f_0(\mathbf{r})$ where the ratio ρ/ρ_0 on the right-hand side of Eq. (20) is replaced by the function $(\rho/\rho_0)^\alpha$ with $\alpha \neq 1$. The value of $\alpha = 1/3$ or $\alpha = 2/3$ is considered most often because it is the Fermi momentum $k_{\mathrm{F}} \propto \rho^{1/3}$ rather than the density that is a characteristic parameter in the theory of many-body systems. Use is also made of more complicated forms of the density dependence of the amplitude f_0 [3, 9, 14, 15]; however, a feature that is common to all of these versions of the density dependence of the scalar–isoscalar amplitude is that the dimensionless parameters f^{ex} and f^{in} differ dramatically: $f^{\mathrm{ex}} \simeq -3$, whereas the internal constant f^{in} is close to zero. Such parameter values were first found in [16] from a global analysis of the quadrupole moments of nuclei and isotopic shifts of atomic levels and levels of mesic atoms that was performed on the basis of the theory of finite Fermi systems. These values have a simple qualitative explanation: on one hand, a strong attraction between low-energy nucleons in a vacuum leads to a large negative value of the external constant f^{ex}; on the other hand, the condition $f^{\mathrm{in}} > -0.5$ must be satisfied within a nucleus for the emergence of the Pomeranchuk instability to be avoided [4].

It should be noted that, in [3, 15, 17, 18], the density dependence of the scalar–isovector amplitude $f'_0(\mathbf{r})$ was investigated in detail by using a new version of the density-functional method. Although such a dependence was taken there in a form that is more complicated than that in (20), the amplitude $f'_0(\mathbf{r})$ can be roughly approximated by the expression

$$f'_0(\mathbf{r}) = f'^{\mathrm{ex}} + (f'^{\mathrm{in}} - f'^{\mathrm{ex}})\frac{\rho_+(\mathbf{r})}{\rho_0}, \quad (21)$$

which is similar to (20).

The analysis of binding energies and radii in long isotopic chains that was performed in [3, 17, 18] led to the conclusion that the distinction between the parameters f'^{in} and f'^{ex} is also significant, but that it is not as dramatic as in the isoscalar case.

In principle, relations of the type in (20) can also be written for the spin-dependent terms in (17), but no indications of a considerable distinction between the external and internal values of these amplitudes have been revealed so far. In view of this, it is assumed, within the theory of finite Fermi systems, that $g^{\mathrm{in}} = g^{\mathrm{ex}} = g$ and $g'^{\mathrm{in}} = g'^{\mathrm{ex}} = g'$.

It was mentioned in the Introduction that the external values of the Landau–Migdal amplitudes can be calculated in terms of the off-shell T matrix for free nucleon–nucleon scattering at the negative energy of $E = 2\mu$ [6]. Reasonable agreement with known phenomenological results was obtained at a chemical-potential value of $\mu \simeq -8$ MeV, which is peculiar to stable nuclei. We note that the phenomenological results in question depend somewhat on the type of interpolation formula for $f_0(\mathbf{r})$. The best agreement was achieved for the parameters of spin-independent amplitudes corresponding to the energy functional in [3] and for the spin-dependent amplitudes from [19]. The latter were found from a detailed analysis of a vast body of data on the magnetic properties of nuclei neighboring ^{208}Pb, pion and rho-meson exchange being explicitly taken into account in this analysis. This agreement with the aforementioned phenomenological values revealed that the relation $F \to T(2\mu)$, which is asymptotically correct at long distances from a nucleus for stable nuclei, can be applied even in the immediate vicinity of the nuclear surface.

The explicit expressions for the external values of the scalar amplitudes being considered are

$$f_0^{\mathrm{ex}} = \frac{3}{16}[t_0(E=2\mu) + t_1(E=2\mu)], \quad (22)$$

$$f_0'^{\mathrm{ex}} = \frac{1}{16}[t_0(E=2\mu) - 3t_1(E=2\mu)], \quad (23)$$

where t_0 and t_1 are dimensionless values of the off-shell T matrix for the total spin of two nucleons that is equal to $S=0$ and $S=1$, respectively, at zero value

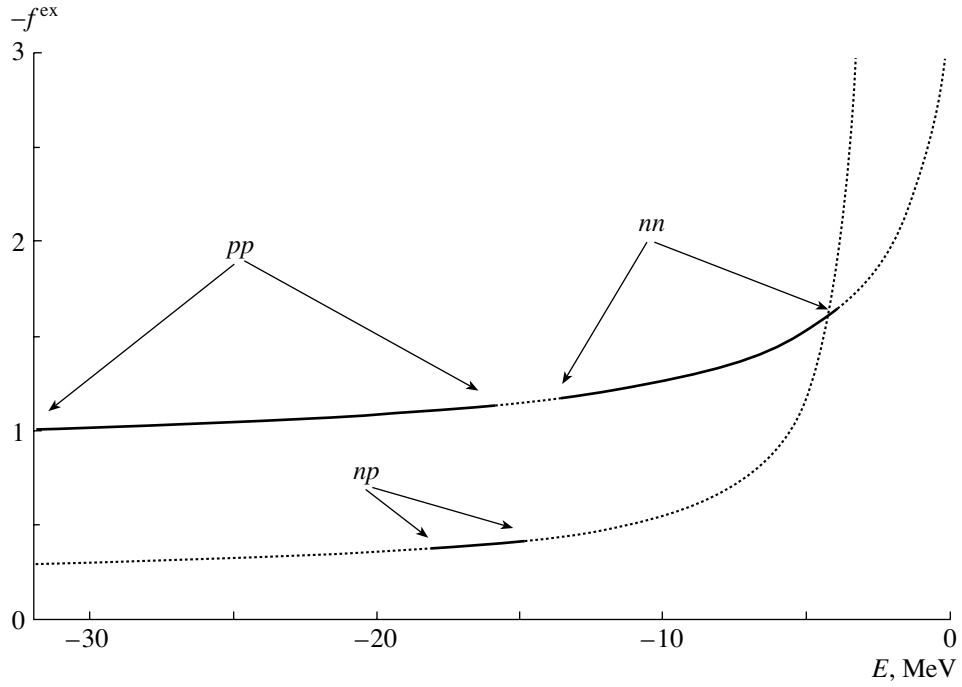

Fig. 1. Sign-reversed external values $f^{\mathrm{ex}}_{nn}(E)$, $f^{\mathrm{ex}}_{pp}(E)$, and $f^{\mathrm{ex}}_{np}(E)$ of the Landau–Migdal amplitude (the last one was divided by 10). The solid segments of the curves represent these amplitudes in those energy intervals that are peculiar to tin isotopes.

of the momenta of all nucleons.[3)] For stable nuclei, isospin symmetry holds to a fairly high precision, and one can set

$$f^{\mathrm{ex}}_{nn} = f^{\mathrm{ex}}_{pp} = f^{\mathrm{ex}}_0 + f'^{\mathrm{ex}}_0 = \frac{1}{4}t_0(E = 2\mu), \qquad (24)$$

$$f^{\mathrm{ex}}_{np} = f^{\mathrm{ex}}_0 - f'^{\mathrm{ex}}_0 = \frac{1}{8}[t_0(E = 2\mu) + 3t_1(E = 2\mu)]. \qquad (25)$$

For nuclei in the vicinity of the nucleon drip line, the neutron and proton chemical potentials differ significantly: one of these approaches zero, while the other, on the contrary, grows in magnitude. Since both free amplitudes $t_0(E)$ and $t_1(E)$ depend sharply on the energy E at low E, isospin symmetry is violated, with the result that there arises a situation where $f^{\mathrm{ex}}_{nn} \neq f^{\mathrm{ex}}_{pp}$. As before, either of these amplitudes can be found from relation (24), but this is done at $E = 2\mu_n$ for the interaction of two neutrons and at $E = 2\mu_p$ for the interaction of two protons. The neutron–proton amplitude f^{ex}_{np} is found from (25) at $E = \mu_n + \mu_p$. For the sake of definiteness, we will consider the neutron drip line. It is then precisely the neutron chemical potential that tends to zero, and, of the three amplitudes being considered, only f^{ex}_{nn} undergoes sizable changes. This can be seen in Fig. 1, which displays various isotopic components of the external Landau–Migdal amplitude. The quantities t_0 and t_1, which appear in Eqs. (24) and (25), were found by solving the Lippmann–Schwinger equation for the free T matrix with the Paris nucleon–nucleon potential [20]. In order to obtain a convenient graphical representation, we took sign-reversed dimensionless amplitudes and reduced the component f^{ex}_{np} by a factor of 10. The amplitudes f^{ex}_{nn} and f^{ex}_{pp} lie on the same curve, but they correspond to its different segments. The arrows indicate intervals within which the energy E appearing in the definition of a given component changes as we move along the isotopic chain of tin. As can be seen, the amplitudes f^{ex}_{np} and f^{ex}_{pp} change by not more than 5 to 10%, whereas the amplitude f^{ex}_{nn} undergoes changes as great as 30%.

The simplified self-consistency conditions (15) and (16), taken together with the Landau–Migdal amplitude F in the form specified by Eqs. (17), (20), and (21), can easily be integrated in an explicit form for a spherical nucleus. By way of example, we indicate that the result for the neutron potential is

$$U_n(r) = C_0\Bigg[f^{\mathrm{ex}}_{nn}\rho_n(r) \qquad (26)$$

$$+ (f^{\mathrm{in}}_{nn} - f^{\mathrm{ex}}_{nn})\frac{\rho_n(r)}{2\rho_0}(\rho_+(r) + \rho_p(r)) + f^{\mathrm{ex}}_{np}\rho_p(r)$$

[3)] A transition to these dimensionless values is accomplished with the aid of the same constant C_0 as in the case of the amplitude F.

$$+ (f_{np}^{\rm in} - f_{np}^{\rm ex})\frac{\rho_p(r)}{2\rho_0}(\rho_+(r) + \rho_p(r))\Big].$$

The analogous expression for the proton potential $U_p(r)$ can be obtained from (26) by interchanging the subscripts "n" and "p." Needless to say, the resulting quantity must be supplemented with the Coulomb potential.

In order to assess the scale of the energy (more precisely, chemical-potential) dependence of the external interaction amplitude $f_{nn}^{\rm ex}$, we will find the neutron potential at the center of the nucleus being considered, $U_n(0)$. For the sake of simplicity, we make use of the approximate relations $\rho_n(0) = (N/A)\rho_0$ and $\rho_p(0) = (Z/A)\rho_0$. We then obtain

$$U_n(0) = \frac{1}{2}C_0\rho_0\left[f_{nn}^{\rm ex}\frac{N^2}{A^2} + f_{nn}^{\rm in}\left(1 - \frac{Z^2}{A^2}\right)\right. \quad (27)$$
$$\left. + f_{np}^{\rm ex}\frac{Z^2}{A^2} + f_{np}^{\rm in}\left(1 - \frac{N^2}{A^2}\right)\right].$$

Let us evaluate the change in μ_n in response to the addition of one or two neutrons to a heavy nucleus. For the sake of simplicity, we will disregard, for the time being, pairing effects and also assume that neutrons are added to an unfilled j level. The variation in μ_n is then equal to the change in the energy of the last level whose quantum numbers are λ_0:

$$\delta\mu_n = \delta\varepsilon_{\lambda_0}. \quad (28)$$

In a sufficiently heavy nucleus, one can approximately set

$$\delta\varepsilon_{\lambda_0} = \delta U_n(0). \quad (29)$$

Upon varying expression (27), we arrive at the sum of terms,

$$\delta U_n(0) = \delta U_1 + \delta U_2, \quad (30)$$

which are of different origins. The first stems from a variation of the quantities N and A, while the second arises owing to the chemical-potential (μ) dependence of the amplitude $f_{nn}^{\rm ex}$:

$$\delta U_2 = \frac{1}{2}C_0\rho_0\frac{N^2}{A^2}\delta f_{nn}^{\rm ex}. \quad (31)$$

If this μ dependence is disregarded, then the standard expression for the variation of the chemical potential is restored:

$$\delta\mu_n^0 = \delta U_1. \quad (32)$$

In can easily be verified that, in considering nuclei in the vicinity of the nucleon drip line, the inclusion of the second term in (30) leads to a considerable deviation from a conventional result. Indeed, the amplitude $f_{nn}^{\rm ex}$ given by Eq. (24) at $E = 2\mu_n$ is singular at small μ_n; that is,

$$f_{nn}^{\rm ex} = \frac{a}{\sqrt{|E|}} = \frac{a}{\sqrt{2|\mu_n|}}, \quad (33)$$

where a is a constant. In the denominator on the right-hand side of (33), we have disregarded, against μ_n, the energy of a virtual level that determines the position of the T-matrix pole in the singlet channel. By varying relation (33), we arrive at

$$\delta f_{nn}^{\rm ex} = -f_{nn}^{\rm ex}\frac{\delta\mu_n}{2\mu_n}. \quad (34)$$

Substituting expressions (30), (31), (32), and (34) into (29) and (28), we obtain

$$\delta\mu_n = \frac{\delta\mu_n^0}{1 + V_0/(2\mu_n)}, \quad (35)$$

where, for the first term in expression (27), we have introduced the condensed notation

$$V_0 = \frac{1}{2}C_0\rho_0\frac{N^2}{A^2}f_{nn}^{\rm ex}. \quad (36)$$

In the case where the added neutrons fill a new j level, relation (28) is inapplicable, but it can straightforwardly be generalized to this case. It can easily be proven that this only leads to a modification of the method for computing the quantity $\delta\mu_n^0$, but that relation (35) remains valid.

We will see below that, for nuclei characterized by a small value of μ_n, the denominator of the expression on the right-hand side of (35) is considerably greater than unity. By way of example, we will compute this quantity for two tin isotopes lying in the vicinity of the "old" neutron drip line ($A_{\rm max} \simeq 176$), which can approximately be considered to be common to all of the calculations that we know. We make use of the values of μ_n that are determined below. The corresponding values of the amplitude $f_{nn}^{\rm ex}$ can be found on the basis of Eq. (24) and are precisely those that are depicted in Fig. 1. We employ the standard normalization-parameter values of $C_0 = 300$ MeV fm^3 and $\rho_0 = 0.16$ fm^{-3}. We begin by considering the ^{150}Sn nucleus. In this case, we have $\mu_n = -3.4$ MeV, $f_{nn}^{\rm ex} = -1.4$, and $V_0 = -15$ MeV. The substitution of these values into relation (35) yields $\delta\mu_n = \delta\mu_n^0/3.2$. A similar calculation for ^{200}Sn ($\mu_n = -2.0$ MeV, $f_{nn}^{\rm ex} = -1.66$, $V_0 = -22.4$ MeV) leads to $\delta\mu_n = \delta\mu_n^0/6.5$. It can be seen that deviations from the traditional scheme are indeed large and grow with decreasing $|\mu_n|$. This explains qualitatively why there exist nuclei in the present approach (for example, ^{200}Sn) that are strongly unbound in the traditional approach.

3. MODIFICATION OF THE QUASIPARTICLE LAGRANGIAN METHOD FOR NUCLEI IN THE VICINITY OF THE NUCLEON DRIP LINE

In order to perform specific calculations, we make use of the quasiparticle Lagrangian method somewhat modified with allowance for the energy dependence of the external values of the amplitude of effective nucleon–nucleon interaction. The quasiparticle Lagrangian method was developed in [8, 9] for magic nuclei, in which there is no superfluidity, and was extended in [21, 22] to the case featuring superfluidity. All of the required modifications to the quasiparticle Lagrangian method can be demonstrated more straightforwardly for the simpler case where there is no superfluidity. Here, we will give a very concise account of the quasiparticle Lagrangian method, referring the interested reader to [9, 21, 22] for details. In this approach, use is made of the Lagrangian formalism, which is more convenient in the situation where energy-dependence effects are taken into account explicitly. The effective quasiparticle Lagrangian is constructed in such a way that its variation would lead to the Dyson Eq. (5) for the quasiparticle Green's function. A solution to this equation can be expressed in terms of the eigenfunctions Ψ_λ for the corresponding homogeneous equation; that is,

$$\mathcal{G}_q(\mathbf{r_1}, \mathbf{r_2}; \varepsilon) = \sum_\lambda \frac{\Psi^*_\lambda(\mathbf{r}_1)\Psi_\lambda(\mathbf{r}_2)}{\varepsilon - \varepsilon_\lambda + i\delta \mathrm{sgn}(\varepsilon_\lambda - \mu)}, \quad (37)$$

where δ is an infinitely small positive value. The eigenfunctions in question are orthonormalized with a weight:

$$\int d\mathbf{r}\Psi^*_\lambda(\mathbf{r})Z^{-1}(\mathbf{r})\Psi_{\lambda'}(\mathbf{r}) = \delta_{\lambda\lambda'}. \quad (38)$$

The quasiparticle density $\nu_0(\mathbf{r})$ associated with the functions Ψ_λ has the form

$$\nu_0(\mathbf{r}) = \sum_\lambda n_\lambda |\Psi_\lambda(\mathbf{r})|^2, \quad (39)$$

where $n_\lambda = (0, 1)$ are quasiparticle occupation numbers.

Along with the functions Ψ_λ, the functions

$$\phi_\lambda(\mathbf{r}) = Z^{-1/2}(\mathbf{r})\Psi_\lambda(\mathbf{r}), \quad (40)$$

which obey the standard normalization condition, were also introduced in [9]. The corresponding quasiparticle density

$$\rho(\mathbf{r}) = \sum_\lambda n_\lambda |\phi_\lambda(\mathbf{r})|^2 \quad (41)$$

is normalized to the total number of particles and is perfectly analogous to the density considered in Hartree–Fock theory. Obviously, the two densities introduced in the quasiparticle Lagrangian method differ by the Z factor:

$$\nu_0(\mathbf{r}) = Z(\mathbf{r})\rho(\mathbf{r}). \quad (42)$$

Two more quantities that have the meaning of densities were introduced in [8, 9]. These are the single-particle kinetic-energy density

$$\nu_1(\mathbf{r}) = \frac{1}{(k^0_\mathrm{F})^2}\sum_\lambda n_\lambda |\nabla\Psi_\lambda(\mathbf{r})|^2 \quad (43)$$

and the total-quasiparticle-energy density

$$\nu_2(\mathbf{r}) = \frac{1}{\varepsilon^0_\mathrm{F}}\sum_\lambda n_\lambda \varepsilon_\lambda |\Psi_\lambda(\mathbf{r})|^2 \quad (44)$$

The density $\nu_1(\mathbf{r})$ is an analog of the density $\tau(\mathbf{r})$ introduced in Hartree–Fock theory involving effective forces [10], whereas the density $\nu_2(\mathbf{r})$ has no Hartree–Fock analogs, its emergence being peculiar precisely to the quasiparticle Lagrangian method.

The main objective pursued in [8, 9] was to reveal effects of the linear energy dependence of the quasiparticle mass operator (6). Therefore, the form chosen there for the quasiparticle Lagrangian was maximally close to that which corresponds to the Hamiltonian of the Hartree–Fock method involving effective Skyrme forces [10]. Retaining the notation adopted in [9], we express the density L'_q of the quasiparticle interaction Lagrangian in terms of the above densities $\nu_i(\mathbf{r})$ as

$$\begin{aligned}\mathcal{L}'(\mathbf{r}) = -C_0\Bigg[&\frac{\lambda_{00}}{2}\nu^2_{0+}(\mathbf{r}) + \frac{\lambda'_{00}}{2}\nu^2_{0-}(\mathbf{r}) \\ &+ \frac{2\gamma}{3\rho^0_0}\nu_{0+}(\mathbf{r})\nu_{0n}(\mathbf{r})\nu_{0p}(\mathbf{r}) + \lambda_{01}\nu_{0+}(\mathbf{r})\nu_{1+}(\mathbf{r}) \\ &+ \lambda'_{01}\nu_{0-}(\mathbf{r})\nu_{1-}(\mathbf{r}) + \lambda_{02}\nu_{0+}(\mathbf{r})\nu_{2+}(\mathbf{r}) \\ &- \frac{\lambda_{00}r^2_0}{2}(\nabla\nu_{0+}(\mathbf{r}))^2\Bigg] + \mathcal{L}_1,\end{aligned} \quad (45)$$

where

$$\nu_{i+,-} = \nu_{in} \pm \nu_{ip} \quad (46)$$

and λ_{ik} and γ are dimensionless coupling constants. The normalization density is $\rho^0_0 = 2(k^0_\mathrm{F})^3/(3\pi^2)$, while the term $\mathcal{L}_1$ includes the Coulomb energy and spin-dependent terms (of these, the spin–orbit term is a dominant one). We note that the isotopic structure of that term in (45) which is proportional to the constant γ and which involves the product of three densities was taken in [9] to be similar to the isotopic structure present in the Hamiltonian for Skyrme forces [10].

According to the recipe of Landau, the amplitude F of effective quasiparticle interaction must be determined as the second variational derivative of the ground-state-energy functional with respect to the density. In order to extract it from the Lagrangian

L'_q, one must first find the corresponding Hamiltonian H_q (the terms that contain the density ν_2 drop out in doing this [14]) and express it in terms of the densities $\rho(\mathbf{r})$ and $\tau(\mathbf{r})$ normalized in a conventional way. After that, it is necessary to find the second variational derivative of H_q with respect to the density ρ. This leads to rather cumbersome expressions, which can be found in [23]. However, the relations between the constants λ_{00} and λ'_{00}, on one hand, and the external Landau–Migdal amplitudes $f^{\rm ex}$ and $f'^{\rm ex}$ appearing in Eqs. (20) and (21), on the other hand, can be found without resort to explicit formulas for F. Indeed, the Z factor tends to unity in the asymptotic region beyond the nuclear surface, with the result that the densities $\nu_0(\mathbf{r})$ and $\rho(\mathbf{r})$ coincide there. Therefore, the variation of L'_q with respect to ρ can be replaced by its variation with respect to ν_0. The amplitudes being considered stem from the first three terms in (45). Obviously, the variation of the term proportional to γ with respect to the density dies out at large r, so that we arrive at the identities

$$\lambda_{00} = f^{\rm ex}, \quad \lambda'_{00} = f'^{\rm ex}. \tag{47}$$

It goes without saying that they also follow from the explicit expression presented in [23] for the Landau–Migdal amplitude F.

The objective of this study is to single out effects associated with the energy dependence of effective quasiparticle interaction beyond the linear dependence, which is taken into account within the standard quasiparticle Lagrangian method. The dependence beyond the linear one is due primarily to the strong energy dependence of the external values of the invariant Landau–Migdal amplitudes, which was considered in Section 2. For the sake of convenience, we write separately the first three terms in (45), which are associated with these external values and which correspond to zero-range forces, replacing there the parameters λ_{00} and λ'_{00} by $f^{\rm ex}$ and $f'^{\rm ex}$. Specifically, we have

$$\mathcal{L}_0(\mathbf{r}) = -C_0\left[\frac{f^{\rm ex}}{2}\nu_{0+}^2(\mathbf{r}) + \frac{f'^{\rm ex}}{2}\nu_{0-}^2(\mathbf{r}) + \frac{2\gamma}{3\rho_0^0}\nu_{0+}(\mathbf{r})\nu_{0n}(\mathbf{r})\nu_{0p}(\mathbf{r})\right]. \tag{48}$$

If the quantities $f^{\rm ex}$ and $f'^{\rm ex}$ are treated as phenomenological parameters, there is no difference between this expression and the original one—only the physical meaning of the constants λ_{00} and λ'_{00} becomes clearer. The next step consists in replacing these parameters by the values following from a microscopic theory—that is, by expressions (22) and (23). At the chemical-potential value of $\mu = -8$ MeV, which is characteristic of stable nuclei, they are $f^{\rm ex} = -2.62$ and $f'^{\rm ex} = 1.56$ [6], instead of the empirical values of $\lambda_{00} = -3.25$ and $\lambda'_{00} = 2.4$, which were found in [9]. It should be noted that these values of $f^{\rm ex}$ and $f'^{\rm ex}$ are closer to the empirical constants corresponding to the energy functional constructed by Fayans *et al.* [3]. The semimicroscopic expression (48) now involves only one adjustable parameter γ instead of three in the corresponding part of the Lagrangian given by (45).

Proceeding now to consider nuclei characterized by a large neutron excess and, accordingly, by a small value of the neutron chemical potential, we run into the situation where isotopic symmetry is violated (see the preceding section), so that $f_{nn}^{\rm ex} \neq f_{pp}^{\rm ex}$. The generalization of expression (48) to this case obviously has the form

$$\tilde{\mathcal{L}}_0(\mathbf{r}) = -C_0\left[\frac{1}{2}f_{nn}^{\rm ex}(E=2\mu_n)\nu_{0n}^2(\mathbf{r}) + \frac{1}{2}f_{pp}^{\rm ex}(E=2\mu_p)\nu_{0p}^2(\mathbf{r}) + f_{np}^{\rm ex}(E=\mu_n+\mu_p)\nu_{0n}(\mathbf{r})\nu_{0p}(\mathbf{r}) + \frac{2\gamma}{3\rho_0^0}\nu_{0+}(\mathbf{r})\nu_{0n}(\mathbf{r})\nu_{0p}(\mathbf{r})\right], \tag{49}$$

where the external values $f_{nn}^{\rm ex}$, $f_{pp}^{\rm ex}$, and $f_{np}^{\rm ex}$ of the Landau–Migdal amplitudes are dependent on the neutron and proton chemical potentials and must be calculated for a given nucleus according to the formulas of the preceding section in just the same way as this was done in deriving expression (26). In considering the neutron drip line, only the energy dependence of the first of these amplitudes is of importance. In the remaining components, this dependence is retained for the sake of generality, in order that expression (49) be appropriate, say, for nuclei in the vicinity of the proton drip line, in which case it is the amplitude $f_{pp}^{\rm ex}$ that depends strongly on energy.

For superfluid nuclei, we make use of that modification to the quasiparticle Lagrangian method which was developed for this case in [21, 22]. In principle, this method is quite general and involves solving the Bogolyubov equations for the functions u_i and v_i forming a bispinor. However, a simplified BCS scheme that assumes diagonal pairing and which proved to be fairly accurate for stable nuclei was employed in the systematic calculations performed in those studies. We will now briefly describe the simplified version of the quasiparticle Lagrangian method for superfluid nuclei, referring the reader to [21, 22] for details and for a more general formulation.

Instead of one Dyson Eq. (5) for the quasiparticle Green's function $\mathcal{G}_q$, there arises the set of Gor'kov equations for superfluid nuclei, which involves the

anomalous Green's function $\mathcal{F}_q$, along with the normal one, $\mathcal{G}_q$, and the order parameter $\Delta(\mathbf{r})$ (superfluid gap),[4] along with the mass operator Σ_q. The quasiparticle Lagrangian must now be constructed in such a way that its variation would lead to Gor'kov equations. Further, the set of Bogolyubov equations for the functions u_i and v_i appears instead of the Schrödinger equation for quasiparticle wave functions Ψ_λ. The interaction Lagrangian (45) is taken in the same form, but the densities ν_0, ν_1, and ν_2 are now defined as

$$\nu_0(\mathbf{r}) = \sum_i |v_i(\mathbf{r})|^2, \tag{50}$$

$$\nu_1(\mathbf{r}) = \frac{1}{(k_\mathrm{F}^0)^2}\sum_i |\nabla v_i(\mathbf{r})|^2, \tag{51}$$

$$\nu_2(\mathbf{r}) = \frac{1}{\varepsilon_\mathrm{F}^0}\sum_i (-E_i+\mu)|v_i(\mathbf{r})|^2, \tag{52}$$

where E_i stands for the eigenenergies of the set of Bogolyubov equations; these energies are reckoned from the chemical potential μ, which, for systems that involve pairing, is equal to half the energy required for the detachment of two nucleons from the system. In just the same way as in [21, 22], we employ here the so-called scheme of fully developed pairing, where there is no distinction between the chemical potentials μ^- and μ^+ that are associated with nucleon detachment and attachment, respectively. As is well known, this approximation entails violation of the law of particle-number conservation; therefore, the chemical potential $\mu = \mu^- = \mu^+$ is determined from the condition requiring that the number of nucleons be conserved on average.

In superfluid nuclei, there appears, in addition to the aforementioned three densities, the anomalous density

$$\chi_0(\mathbf{r}) = \sum_i v_i(\mathbf{r})u_i(\mathbf{r}). \tag{53}$$

The superfluid component of the quasiparticle Lagrangian contains the anomalous density χ_0 and effective pairing forces, which we choose here in the simplest delta-function form, but with allowance for the possible density dependence. The term that must be added to Lagrangian (45) in the case of superfluid pairing then has the form

$$\mathcal{L}_s(\mathbf{r}) = -C_0\left[\frac{\eta}{2}(\chi_0^n(\mathbf{r})\chi_0^{*n}(\mathbf{r})+\chi_0^p(\mathbf{r})\chi_0^{*p}(\mathbf{r})) + \frac{\theta}{2}(\nu_0^p\chi_0^n(\mathbf{r})\chi_0^{*n}(\mathbf{r}) + \nu_0^n\chi_0^p(\mathbf{r})\chi_0^{*p}(\mathbf{r}))\right]. \tag{54}$$

[4] For the sake of simplicity, we consider the case where the gap is local.

The equation for the gap is found from expression (54) by doubly varying it with respect to the anomalous density and is given by

$$\Delta^\tau(\mathbf{r}) = \mathcal{V}^\tau(\mathbf{r})\chi_0^\tau(\mathbf{r}), \tag{55}$$

where $\tau = \pm 1/2$, with the upper and the lower sign corresponding to neutrons and protons, respectively. The effective pairing interaction $\mathcal{V}^\tau$ is expressed in terms of the parameters of the superfluid part of the Lagrangian as

$$\mathcal{V}^\tau(\mathbf{r}) = \eta + \theta\nu_0^{-\tau}(\mathbf{r}). \tag{56}$$

Further, the quasiparticle mass operator in the presence of the superfluid Lagrangian given by (54) develops the additional term

$$\delta\Sigma_q^\tau(\mathbf{r}) = \theta|\chi_0^{-\tau}(\mathbf{r})|^2. \tag{57}$$

The density dependence of the effective pairing interaction in the form (56) admits the existence of both purely volume pairing ($\theta = 0$) and surface pairing [a combination of η and θ such that $\mathcal{V}^\tau(\mathbf{r})$ is close to zero in the interior of the nucleus being considered]. An intermediate case is also possible. In [22], it was shown that a version close to the surface limit is preferable, but that, for practical purposes, one can also make use of the volume-pairing model, introducing a weak dependence of the parameter η on the mass number A.

Following [21, 22], we will employ the λ representation

$$v_i(\mathbf{r}) = \sum_\lambda v_i^\lambda\phi_\lambda(\mathbf{r}), \tag{58}$$

$$u_i(\mathbf{r}) = \sum_\lambda u_i^\lambda\phi_\lambda(\mathbf{r}), \tag{59}$$

where the functions ϕ_λ are assumed to obey the standard normalization conditions.

In the λ representation, the equation for the order parameter Δ has the form

$$\Delta_{\lambda,\lambda'}^\tau = \sum_{\lambda_1,\lambda_2,i} (\mathcal{V}^\tau)_{\lambda,\lambda'}^{\lambda_1,\lambda_2} v_i^{\lambda_1}u_i^{\lambda_2}, \tag{60}$$

where

$$(\mathcal{V}^\tau)_{\lambda,\lambda'}^{\lambda_1,\lambda_2} = \int d\mathbf{r}\phi_\lambda^*(\mathbf{r})\phi_{\lambda'}^*(\mathbf{r})\mathcal{V}^\tau(\mathbf{r})\phi_{\lambda_1}(\mathbf{r})\phi_{\lambda_2}(\mathbf{r}). \tag{61}$$

It is worth noting that Eq. (60) is formally exact if one implies a more general definition of the matrix element of the effective pairing interaction than that in (61). Further, the locality of the interaction, as implied in Eq. (61), does not exhaust the approximations adopted in this study, which follows the same line of reasoning as the analyses in [21, 22]. The

Single-particle spectrum of the ^{124}Sn nucleus

λ	ε_λ, MeV		E_λ, MeV		
	[21]	our study	[21]	our study	experiment
$2p_{1/2}$	−16.86	−17.94	−16.96	−18.05	
$1g_{9/2}$	−15.15	−15.93	−15.29	−16.11	
$2d_{5/2}$	−10.19	−10.82	−10.42	−11.05	
$3s_{1/2}$	−9.53	−8.82	−9.97	−9.18	−8.64
$1g_{7/2}$	−8.34	−8.32	−8.81	−9.19	−9.63
$2d_{3/2}$	−8.08	−8.05	−8.68	−8.66	−8.52
$1h_{11/2}$	−7.19	−6.87	−5.83	−5.08	−5.73
$2f_{7/2}$	−2.34	−2.29	−2.24	−2.14	
$3p_{3/2}$	−0.97	−0.96	−0.94	−0.91	
$3p_{1/2}$	−0.42	−0.26	−0.39	−0.23	

main among these approximations are the application of a truncated λ basis [$\varepsilon_{\min} < \varepsilon_\lambda < \varepsilon_{\max}$, where $\varepsilon_{\min} = -(20\text{–}25)$ MeV and $\varepsilon_{\max} = 5$ MeV], and a discretization of the continuum. In addition, we rely on the volume-pairing model [$\theta = 0$ in (56)], with the constant η being dependent on the dimension of the model subspace in accordance with the recipe formulated in [4]; that is,

$$\eta = \Gamma_\xi = \frac{C_0}{\ln(C_p/\xi)}, \tag{62}$$

where $\xi = \sqrt{(\mu - \varepsilon_{\min})(\varepsilon_{\max} - \mu)}$ and C_p is a phenomenological parameter. Finally, we employ the diagonal approximation

$$v_i^\lambda = v_\lambda \delta_{i,\lambda}, \tag{63}$$

$$u_i^\lambda = u_\lambda \delta_{i,\lambda}, \tag{64}$$

whence it follows that

$$\Delta_{\lambda\lambda'} = \Delta_\lambda \delta_{\lambda\lambda'}. \tag{65}$$

Upon introducing these approximations, the originally general method for analysis of pairing actually reduces to the BCS model. As applied to nuclei in the vicinity of the nucleon drip line, this model possesses well-known drawbacks (see, for example, [2, 3]), but we preserved all the details of the computational scheme used in [21, 22] (including the value of the parameter C_p, which is responsible for pairing) in order to single out more clearly the discussed effect of the energy dependence of the Landau–Migdal amplitude through a comparison with the results of those studies.

4. NEUTRON DRIP LINE FOR THE CHAIN OF TIN ISOTOPES

The chain of tin isotopes is one of the most popular objects of both experimental and theoretical investigations. A few calculations of the position of the neutron drip line are known for this chain—in particular, a calculation within the standard quasiparticle Lagrangian method [22]. This is the reason why we have chosen precisely this chain for investigating the effect being discussed. All of the parameters, with the exception of those entering into the Lagrangian component (49), which corresponds to zero-range forces, were set to the values used in [22]. After that, the amplitudes $f_{nn}^{\text{ex}}(E = 2\mu_n)$, $f_{pp}^{\text{ex}}(E = 2\mu_p)$, and $f_{np}^{\text{ex}}(E = \mu_n + \mu_p)$ appearing in Eq. (49) were calculated microscopically for each nucleus by using formulas (24) and (25), whereupon γ remains the only adjustable parameter in (49). It was determined on the basis of a fit to the single-particle spectrum of the ^{124}Sn nucleus, which occurs in the middle of the tin-isotope region studied experimentally. It should be emphasized that it was precisely the properties of this nucleus that were used in [21] to fix the value of the pairing constant C_p. In the present study, we do not pursue the aim of analyzing the total binding energies and density distributions, focusing our attention on calculating single-particle spectra, since it is these spectra that determine the chemical potentials of nuclei and, hence, the position of the drip line. We decided on the value of $\gamma = 1.6$ (instead of $\gamma = 3.2$ in [9, 21, 22]). So pronounced a change in the parameter γ is due to the fact that the ab initio values of f^{ex} and f'^{ex} are anyway sharply different from the phenomenological constants [9, 21, 22] (see also

Section 2). The results of our calculations are quoted in the table, which displays both the single-particle energies ε_λ obtained without allowance for pairing, which are the most direct characteristic of the mean field, and the energies $E_\lambda = \mu \pm \sqrt{(\varepsilon_\lambda - \mu)^2 + \Delta_\lambda^2}$, which include pairing. As can be seen, the single-particle spectrum is in fairly good agreement both with that which was computed in [21] and with that which was measured experimentally. We note that the characteristic value of the order parameter is $\Delta = \overline{\Delta_\lambda} \simeq 1$ MeV.

Further, we performed self-consistent calculations of the properties of a long chain of even–even tin isotopes from $A = 100$ to $A = 208$ with a step of $\delta A = 4$. The chemical potentials found in this way are depicted in Fig. 2, along with the results based on the standard quasiparticle Lagrangian approach [22] and the predictions presented by Dobaczewski *et al.* [2] and by Fayans *et al.* [3]. As was indicated above, the chemical potentials μ_n must be contrasted against half the energy required for the detachment of two neutrons (S_{2n}). The last two calculations employed phenomenological energy-independent forces. As is known from [9, 14], the linear energy dependence, which was taken into account in [22] by adding a term involving the density $\nu_2(\mathbf{r})$ to the Lagrangian in (45), reduces predominantly to renormalizations and also disregards the effect being discussed. Therefore, it comes as no surprise that all of the three calculations quoted here lead to close results, which, in Fig. 2, are represented by symbols virtually lying on the common "phenomenological" curve, this curve being in good agreement with available experimental data. In particular, all three calculations predict approximately the same neutron-drip-line position corresponding to a value of $A_{\max} \simeq 176$. The reason for this is quite simple: the value of $A = 176$ is associated with the magic number of neutrons that is equal to $N = 126$. In all three calculations, the neutron chemical potential for the ^{172}Sn nucleus, which is close to the neutron drip line, is negative and is comparatively small in magnitude: $\mu_n \simeq -0.1$ MeV in [2, 22] and $\mu_n \simeq -0.3$ MeV in [3]. Further calculations were terminated in [3] (obviously, because the preceding even–even isotope ^{170}Sn already had a positive chemical potential in those calculations). This nonmonotonic behavior of $\mu_n(A)$ in the calculations reported in [3] is an indirect manifestation of the fact that the number $N = 126$ is magic. The calculations in [2] do not reveal the shell effect at $A = 176$—there, the value of $A_{\max} = 174$ corresponds to the position of the neutron drip line. Finally, we would like to mention the results presented in [22]. There, the ^{176}Sn nucleus is bounded more strongly than all of the preceding isotopes ($\mu_n \simeq -1$ MeV) owing to the magicity effect, but, since the magicity gap exceeds 2 MeV, the attached 127th neutron occurs in the continuum. We note that $A_{\max} = 176$ corresponds to the asymmetry-parameter value of $y = (N - Z)/A = 0.43$, which exceeds considerably the critical value of $y_0 = 0.37$ predicted by the calculations for asymmetric nuclear matter in [24].

The results of our semimicroscopic calculation at comparatively small values of the asymmetry parameter y deviate from the phenomenological curve and, hence, from experimental data, but these deviations are insignificant. As we approach the neutron drip line—that is, as $|\mu_n|$ becomes smaller—the distinctions become more pronounced, the semiempirical curve lying much higher than the phenomenological one. As can be seen, the present calculation predicts the existence of stable nuclei for isotopes lying beyond the previous drip line inclusive (that is, $A > 176$), the stability margin being rather wide. Indeed, the ^{176}Sn isotope is strongly bound in our calculations ($\mu_n \simeq -3.5$ MeV), so that the next magicity gap is readily overcome—for example, the ^{180}Sn isotope is also bound quite strongly ($\mu_n \simeq -2.4$ MeV). As the neutron excess increases further, $|\mu_n|$ decreases, but this occurs very slowly. This is a qualitative manifestation of the effect of relation (35), which indicates that the system being considered hinders the emergence of small values of $|\mu_n|$ via the deepening of the neutron potential. We terminated our calculations at $A = 208$, since it is clear that, with decreasing $|\mu_n|$, the errors of the present calculation become greater. Among the factors responsible for these errors, there is, first of all, an oversimplified description of pairing. Moreover, the very application of the theory of finite Fermi systems is questionable at small $|\mu_n|$, in which case the energy dependence of the Landau–Migdal amplitude becomes rather sharp. In addition, there arise pairing corrections to expression (24) at $|\mu_n| \simeq \Delta \simeq 1$ MeV. Of course, this expression remains valid at large distances from the surface, but, in the vicinity of the surface, the free T matrix must be replaced by the quantity $\tilde{T}$ calculated with the single-particle spectrum of our superfluid system. This is expected to result in a shift of the pole in (33) by a value of about Δ. It follows that, for $|\mu_n| \leq 1$ MeV, the present calculation would strongly exaggerate the effect of the energy dependence of the Landau–Migdal amplitude.

Let us dwell at some length on the aforementioned discrepancy between the results of the present calculation and those reported in [2, 3, 22] for isotopes featuring a small neutron excess, which were explored experimentally. Since the results obtained in [2, 3, 22] reproduce experimental data quite satisfactorily, our results are at odds with these data as well, the discrepancy being sometimes as great as 1 MeV. This

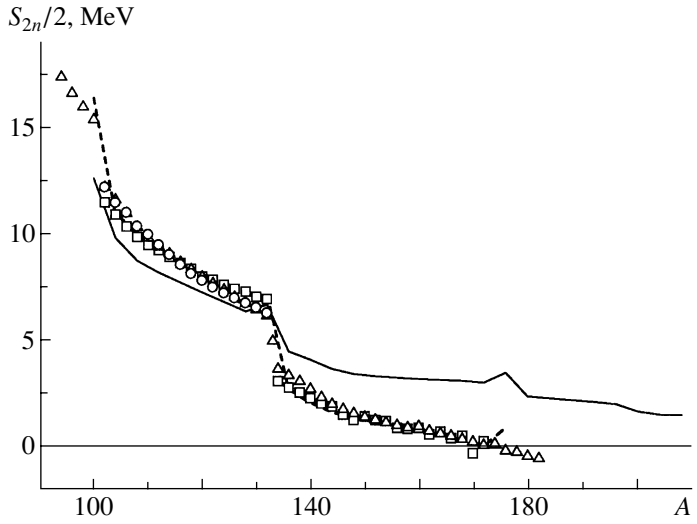

Fig. 2. Half the energy required for the detachment of two neutrons, $S_{2n}/2$, from even–even tin isotopes. The results of the present semimicroscopic calculation (solid curve) are given along with the predictions made in (dashed curve) [22], (open triangles) [2], and (open boxes) [3]. Open circles represent the experimental values of $S_{2n}/2$.

glaring flaw is obviously due to the use of a specific (Skyrme) isotopic structure taken for the triple forces in the Lagrangian specified by Eqs. (45) and (49) for historical reasons. Since, in the original expression for that part of the Lagrangian in (49) which corresponds to zero-range forces, there were three free parameters in [9, 22], it could be chosen in such a way as to reproduce reasonably well the internal values $f^{\rm in}$ and $f'^{\rm in}$ of both scalar amplitudes simultaneously in relations (20) and (21). As is well known from [4], the first of these internal values is related by a simple equation to the coefficient K_0 of nuclear-matter compressibility,[5)]

$$K_0 = \frac{2}{3}\varepsilon_{\rm F}(1+2f^{\rm in}), \qquad (66)$$

while the second is related to the coefficient β in the symmetry term of the Weizsäcker mass formula,

$$\beta = \frac{1}{3}\varepsilon_{\rm F}(1+2f'^{\rm in}). \qquad (67)$$

As is well known, both these quantities are of paramount importance for correctly describing the ground-state properties of nuclei. The semimicroscopic expression (49), which is employed in the present study, involves only one free parameter γ, and this gives no way to obtain the required values of K_0 and β simultaneously. The value of $\gamma = 1.6$ chosen here is compromising in this respect. While enabling one to reproduce faithfully the chemical potentials for the nearest neighbors of the reference chain of ^{124}Sn, it leads to an insufficiently accurate description of data in the vicinity of $A = 110$. Yet, the scale of this inaccuracy is much less than the magnitude of the effect under study in the region $A > 132$.

By no means, however, is the Skyrme form of the isotopic structure of triple forces mandatory for effective Lagrangians (and for effective Hamiltonians as well). The simplest generalization of expression (48) such that it involves two adjustable parameters has the form

$$\mathcal{L}_0(\mathbf{r}) = -C_0\left[\frac{f^{\rm ex}}{2}\nu_{0+}^2(\mathbf{r}) + \frac{f'^{\rm ex}}{2}\nu_{0-}^2(\mathbf{r}) + \frac{1}{6\rho_0^0}(\gamma\nu_{0+}^3(\mathbf{r}) + \gamma'\nu_{0+}(\mathbf{r})\nu_{0-}^2(\mathbf{r}))\right]. \qquad (68)$$

At $\gamma' = -\gamma$, this relation reduces to (48). Expression (49) can be generalized in a similar way. In all probability, the use of this, more general, structure of the quasiparticle Lagrangian would make it possible to obtain a better description of available experimental data. We postpone such calculations until the future, deliberately restricting ourselves to a computational scheme that is maximally close to that which was employed in [22], the only modification being that the parameters $f^{\rm ex}$ and $f'^{\rm ex}$ were set to the values dictated by the microscopic theory. It is the energy dependence of these parameters that leads to the effect being discussed.

5. CONCLUSION

A semimicroscopic version of the self-consistent theory of finite Fermi systems has been proposed in this study. Within this version, the standard theory of

[5)] The normalization of K_0 in [4] differs from the standard one adopted in nuclear physics [25] by a factor of 9.

finite Fermi systems, which employs a phenomenological Landau–Migdal amplitude, is supplemented with relations following from microscopic theory for the external values $f^{\rm ex}$ and $f'^{\rm ex}$ of the scalar–isoscalar and scalar–isovector components of this amplitude. As was shown in [6], these values are determined by the off-shell T matrix for free nucleon–nucleon scattering at the negative energy E that is equal to the doubled chemical potential of the nucleus being considered. Since the free T matrix depends greatly on E at low energies, there arise pronounced changes for nuclei in the vicinity of the nucleon drip line in relation to purely phenomenological approaches, which disregard the energy dependence of the effective interaction. In particular, a decrease in the absolute value of the neutron chemical potential, $|\mu_n|$, in considering the neutron drip line leads to the growth of neutron attraction at the surface, with the result that the mean neutron potential becomes deeper. This in turn results in a shift of the neutron drip line toward greater values of $N - Z$.

In order to demonstrate the effect of the energy dependence of the Landau–Migdal amplitude, we have chosen the chain of tin isotopes, for which a few calculations were performed within phenomenological approaches in order to determine the position of the neutron drip line. Two alternative methods for taking this effect into account have been considered. The first is based on using, within the theory of finite Fermi systems, the condition of consistency between the mass operator, effective interaction, and single-particle Green's function [7] in a simplified form where the consistency condition involves the mean field, the Landau–Migdal amplitude, and the density. The second employs the quasiparticle Lagrangian method [9], which is a version of the self-consistent theory of finite Fermi systems. In the standard form, this version was previously used to calculate the neutron drip line for tin isotopes [22]. It should be emphasized that these two methods for taking into account the energy dependence of the interaction do not lead to fully identical results. By way of example, we indicate that, within the first method, the internal amplitudes $f^{\rm in}$ and $f'^{\rm in}$ feature absolutely no dependence on energy. But within the second method, it is the parameter γ that is independent of energy, whereas the internal amplitudes $f^{\rm in}$ and $f'^{\rm in}$ calculated in terms of this parameter and in terms of the external amplitude values change somewhat with energy. Within a pure phenomenology, it is difficult to decide on either of the two ansätze. For our systematic calculations, we choose the second version merely because of the fact that a well-developed and tested computational scheme exists for it.

In order to predict more reliably the properties of nuclei in the vicinity of the nucleon drip line, it is desirable to have a more consistent microscopic approach at our disposal. Such an approach is being presently developed [23, 26] on the basis of the Brueckner method for finite nuclei, but the work is far from completion. It should be noted that, in [23], a semimicroscopic model for the scalar–isoscalar Landau–Migdal amplitude $f(\mathbf{r})$ was developed on the basis of approximately computing the Brueckner G matrix for a planar slab of nuclear matter [26]. This model leads to an insignificant dependence of the parameter $f^{\rm in}$ on energy. In all probability, the truth is somewhere in between the aforementioned two versions of the semimicroscopic theory of finite Fermi systems. What is of importance, however, is that both lead to qualitatively the same result—namely, a decrease in $|\mu_n|$ as one approaches the neutron drip line leads to an increase in the absolute value of the external potential $f^{\rm ex}_{nn}$, whence it follows that the neutron potential becomes deeper. This effect hinders the emergence of small values of $|\mu_n|$, giving rise to nuclei featuring an enormous neutron excess. Known calculations fix the position of the neutron drip line for tin isotopes somewhere at $A_{\max} = 176$, which corresponds to the magic number of neutrons that is equal to $N = 126$. The present calculation has shifted considerably the drip line toward greater values of N. For example, we have obtained $\mu_n \simeq -2$ MeV for ^{196}Sn. We have terminated the calculations at the ^{208}Sn isotope, for which $\mu_n \simeq -1.5$ MeV, since the errors of this calculation increase with decreasing $|\mu_n|$. In all probability, the most significant error stems from the fact that, at $|\mu_n| \simeq \Delta \simeq 1$ MeV, it is necessary to take into account pairing corrections to formula (24), which expresses the external value of the scalar Landau–Migdal amplitude in terms of the free T matrix. Estimations revealed that these corrections reduce the effect being considered. Nonetheless, one can hope that, in the region of isotopes where $|\mu_n| > \Delta$ (and the previous drip line lies precisely in this region), the calculations are valid, at least qualitatively. Moreover, we believe that, upon all necessary refinements, the effect in question will survive, at least at a qualitative level, since it has a clear physical origin.

ACKNOWLEDGMENTS

We are grateful to S.V. Tolokonnikov for stimulating discussions and for placing data used in [3] at our disposal.

This work was supported in part by the Russian Foundation for Basic Research (project nos. 00-02-17319 and 00-15-96590).

REFERENCES

1. J. Dobaczewski, H. Flocard, and J. Treiner, Nucl. Phys. A **422**, 103 (1984).
2. J. Dobaczewski *et al.*, Phys. Rev. C **53**, 2809 (1996).
3. S. A. Fayans, S. V. Tolokonnikov, E. L. Trykov, and D. Zawischa, Nucl. Phys. A **676**, 49 (2000) .
4. A. B. Migdal, *Theory of Finite Fermi Systems and Applications to Atomic Nuclei* (Nauka, Moscow, 1965; Interscience, New York, 1967).
5. A. B. Migdal, *Theory of Finite Fermi Systems and Properties of Atomic Nuclei* (Nauka, Moscow, 1983).
6. M. Baldo, U. Lombardo, E. E. Saperstein, and M. V. Zverev, Phys. Lett. B **421**, 8 (1998).
7. S. A. Fayans and V. A. Khodel', Pis'ma Zh. Éksp. Teor. Fiz. **17**, 633 (1973) [JETP Lett. **17**, 444 (1973)].
8. E. E. Saperstein and V. A. Khodel', Zh. Éksp. Teor. Fiz. **81**, 22 (1981) [Sov. Phys. JETP **54**, 12 (1981)].
9. V. A. Khodel and E. E. Saperstein, Phys. Rep. **92**, 183 (1982).
10. D. Vautherin and D. Brink, Phys. Rev. C **5**, 626 (1972).
11. L. D. Landau, Zh. Éksp. Teor. Fiz. **35**, 97 (1958) [Sov. Phys. JETP **8**, 70 (1959)].
12. A. A. Abrikosov, L. P. Gor'kov, and I. E. Dzyaloshinskii, *Methods of Quantum Field Theory in Statistical Physics* (Fizmatgiz, Moscow, 1962; Prentice-Hall, Englewood Cliffs, 1963).
13. M. V. Zverev and E. E. Saperstein, Pis'ma Zh. Éksp. Teor. Fiz. **73**, 425 (2001) [JETP Lett. **73**, 381 (2001)].
14. V. A. Khodel, E. E. Saperstein, and M. V. Zverev, Nucl. Phys. A **465**, 397 (1987).
15. S. A. Fayans, Pis'ma Zh. Éksp. Teor. Fiz. **68**, 161 (1998) [JETP Lett. **68**, 169 (1998)].
16. G. G. Bunatyan and M. A. Mikulinskiĭ, Yad. Fiz. **1**, 38 (1965) [Sov. J. Nucl. Phys. **1**, 26 (1965)].
17. S. A. Fayans and D. Zawischa, Phys. Lett. B **363**, 12 (1995).
18. S. A. Fayans and D. Zawischa, Phys. Lett. B **383**, 19 (1996).
19. I. N. Borzov, S. V. Tolokonnikov, and S. A. Fayans, Yad. Fiz. **40**, 1151 (1984) [Sov. J. Nucl. Phys. **40**, 732 (1984)].
20. M. Lacombe *et al.*, Phys. Rev. C **21**, 861 (1980).
21. M. V. Zverev and E. E. Saperstein, Yad. Fiz. **39**, 1390 (1984) [Sov. J. Nucl. Phys. **39**, 878 (1984)].
22. M. V. Zverev and E. E. Saperstein, Yad. Fiz. **42**, 1082 (1985) [Sov. J. Nucl. Phys. **42**, 683 (1985)].
23. M. Baldo, U. Lombardo, E. E. Saperstein, and M. V. Zverev, Yad. Fiz. **64**, 509 (2001) [Phys. At. Nucl. **64**, 454 (2001)].
24. W. Zuo, I. Bombaci, and U. Lombardo, Phys. Rev. C **60**, 024605 (1999).
25. A. Bohr and B. R. Mottelson, *Nuclear Structure* (Benjamin, New York, 1974; Mir, Moscow, 1977), Vol. 2.
26. M. Baldo, U. Lombardo, E. E. Saperstein, and M. V. Zverev, Yad. Fiz. **64**, 247 (2001) [Phys. At. Nucl. **64**, 203 (2001)].

Translated by A. Isaakyan

Physics of Atomic Nuclei, Vol. 66, No. 2, 2003, pp. 247–252. Translated from Yadernaya Fizika, Vol. 66, No. 2, 2003, pp. 271–278.

NUCLEI
Theory

On a Microscopic Mechanism of Collisions between Extremely Light Nuclei

J. V. Mebonia, P. J. Saralidze, K. I. Sulakadze, and G. E. Skhirtladze

Tbilisi State University, pr. Chavchavadze 1, GE-380077 Tbilisi, Republic of Georgia

Received June 5, 2001; in final form, April 1, 2002

Abstract—The method previously proposed by one of the present authors for studying three-body problems is generalized with the aim of exploring more complicated nuclear processes. The idea underlying the method consists in preserving the unitarity property for the scattering amplitude determined approximately. A specific analysis is performed for elastic collisions of ^{3}He nuclei and for quasielastic deuteron–triton collisions. The theoretical results obtained by our method are compared with experimental data, and the agreement is found to be quite satisfactory. © *2003 MAIK "Nauka/Interperiodica".*

Investigation of collisions between extremely light nuclei in the nonrelativistic-scattering region and analysis of corresponding elastic and inelastic channels may provide important information about the character of nuclear forces and special features of multinucleon problems. However, interpretation of experimental data requires specifying the mechanism of the processes being studied, but this is a very involved mathematical problem, which does not have an unambiguous solution. Difficulties of fundamental character that are inherent in many-body problems appear even in three-body problems; therefore, the formulation of the set of Faddeev integral equations [1] has given impetus not only to a vigorous development of three-body theory proper but also to advances in constructing more consistent approaches to complicated processes. However, an immediate extension to the many-body case leads to formidable technical problems. It seems more natural to begin by developing physically reasonable approximate methods for solving Faddeev equations and, then, to perform an extension in question.

Previously, two apparently different approaches to three-body processes—the cutoff three-body impulse approximation (CTBIA) and the unitarized three-body impulse approximation (UTBIA)—were proposed in [2] and [3], respectively. Either approach claims to provide a consistent description of the single-collision mechanism, but the second seems more consistent theoretically, involving the use of the K-matrix formalism to solve Faddeev equations approximately. The CTBIA approach is based on the statement that, in solving Faddeev equations within the T-matrix formalism, only in the case where the projectile particle does not hit simultaneously both particles of the bound state do the first-order terms in the resulting solution correspond to a true single collision. This is achieved by cutting off the Fourier transform of the bound-state wave function $\varphi(r)$—that is, by making the substitution $G(p) \to G(p, R)$, where

$$G(p, R) = \sqrt{2/\pi} \int_R^\infty r^2 dr \varphi(r) \frac{\sin(pr)}{pr}. \qquad (1)$$

The cutoff radius R must be longer than the de Broglie wavelength λ of the relative motion of colliding particles and is related to the corresponding momentum $\boldsymbol{\omega}$ as

$$R = \frac{C}{|\boldsymbol{\omega}|}, \qquad (2)$$

where C is a constant that ensures fulfillment of the condition $\lambda < R$.

Although the CTBIA approach has no reliable theoretical grounds, it appeared to be rather efficient in analyzing various three-body processes [4–7]. In view of the simplicity of this approach, it is therefore advisable to make an attempt at generalizing the CTBIA in such a way as to render it applicable to processes more complicated than three-particle ones. In the present study, this is done for collisions of extremely light nuclei. Specifically, we analyze elastic ^{3}He^{3}He scattering and quasielastic triton–deuteron scattering in the reaction $d(t, tp)n$.

Let us first consider elastic ^{3}He^{3}He scattering in the laboratory frame. We label projectile nucleons with the indices α, β, and γ ($\alpha\beta\gamma = 123, 231, 312$) and target nucleons with the indices δ, μ, and ν ($\delta\mu\nu = 456, 564, 645$). We will also use the following notation: $\mathbf{k}$ is the projectile-nucleus momentum, $\mathbf{k}_{\beta\gamma}$ is the momentum of the relative motion of particles β

1063-7788/03/6602-0247$24.00

and γ, $\mathbf{K}_{\beta\gamma}$ is the momentum of the center of mass of particles β and γ, $\mathbf{p}_\alpha$ is the momentum corresponding to the motion of particle α with respect to the center of mass of particles β and γ, $\varepsilon_{\alpha\delta}$ is the energy of the relative motion of particles α and δ, $t_{\alpha\delta}$ is the two-nucleon-scattering operator, $\psi(\mathbf{k}_{\beta\gamma}\mathbf{p}_\alpha)$ is the ^{3}He wave function, m is the nucleon mass, E is the total energy of the system, and $\hat{A}$ is the operator of antisymmetrization with respect to identical nucleons. The primed momenta correspond to the final state. We use the system of units where $\hbar = c = 1$.

If more than three particles are involved in a reaction, there is no recipe for unambiguously defining two-particle amplitudes in the iteration multiparticle-scattering series (Watson series). In view of this, the mechanism of ^{3}He^{3}He scattering is represented here as follows: the projectile nucleus $(\alpha\beta\gamma)$ as a discrete unit collides with the target nucleus formed by two fragments, $\delta + \mu\nu$, with the matrix element being written as the sum of all possible $(\alpha\beta\gamma)\delta$ (that is, ^{3}HeN) amplitudes; further, the projectile nucleus is represented as a two-fragment system, $\alpha + \beta\gamma$, with the $(\alpha\beta\gamma)\delta$ amplitude being written as the sum of all possible $\alpha\delta$ (NN) amplitudes. At either step, we will therefore have a three-body problem, to which we will apply the CTBIA approach. This will enable us to determine unambiguously two-nucleon amplitudes and to implement consistently the cutoff procedure.

Under the assumption that the aforesaid is correct, the differential cross section for elastic 3He^{3}He scattering can be represented in the form

$$\frac{d\sigma}{d\Omega} = (2\pi)^4 \frac{3m^2k'^2}{2k} \frac{\sum\limits_{\text{spins}} |M|^2}{k\cos\theta - 2k'}, \tag{3}$$

where

$$M = \hat{A} \sum_{\substack{\alpha\beta\gamma = 123,\,231,\,312 \\ \delta\mu\nu = 456,\,564,\,645}} \int \psi^*(\mathbf{k}'_{\beta\gamma}, \mathbf{p}'_\alpha) \tag{4}$$
$$\times\, \psi^*(\mathbf{k}'_{\mu\nu}, \mathbf{p}'_\delta) t_{\alpha\delta}(\mathbf{k}'_{\alpha\delta}, \mathbf{k}_{\alpha\delta}; \varepsilon_{\alpha\delta}) \psi(\mathbf{k}_{\beta\gamma}, \mathbf{p}_\alpha; R_\alpha)$$
$$\times\, \psi(\mathbf{k}_{\mu\nu}, \mathbf{p}_\delta; R_\delta) d\mathbf{k}_{\beta\gamma} d\mathbf{K}_{\beta\gamma} d\mathbf{k}_{\mu\nu}, d\mathbf{K}_{\mu\nu}$$

$$\left.\begin{aligned} \mathbf{p}_\alpha &= \frac{2}{3}\mathbf{k} - \mathbf{K}_{\beta\gamma}, \\ \mathbf{p}_\delta &= -\mathbf{K}_{\mu\nu}, \\ \mathbf{k}_{\alpha\delta} &= \frac{1}{2}\mathbf{k} - \frac{1}{2}(\mathbf{K}_{\beta\gamma} + \mathbf{K}_{\mu\nu}), \end{aligned}\right\} \qquad \left.\begin{aligned} \mathbf{p}'_\alpha &= \frac{2}{3}\mathbf{k}' - \mathbf{K}_{\beta\gamma}, \\ \mathbf{p}'_\delta &= \frac{2}{3}(\mathbf{k} - \mathbf{k}') - \mathbf{K}_{\mu\nu}, \\ \mathbf{k}'_{\alpha\delta} &= \frac{1}{2}(\mathbf{k}' - \mathbf{k}) - \frac{1}{2}(\mathbf{K}_{\beta\gamma} + \mathbf{K}_{\mu\nu}), \end{aligned}\right\} \tag{5}$$

$$\varepsilon_{\alpha\delta} = \frac{1}{2m}\left\{2mE - \frac{1}{2}k^2 - 2k_{\beta\gamma}^2 - K_{\beta\gamma}^2 - 2k_{\mu\nu}^2 \right. \tag{6}$$
$$\left. - K_{\mu\nu}^2 + \mathbf{k}(\mathbf{K}_{\beta\gamma} + \mathbf{K}_{\mu\nu}) - \mathbf{K}_{\beta\gamma}\cdot\mathbf{K}_{\mu\nu}\right\}.$$

Summation in (3) is performed over the spin projections of colliding nuclei prior to and after scattering. These spin projections, as well as the function $G(p, R)$, appear explicitly upon expanding ψ and $t_{\alpha\delta}$ in partial waves.

If the cutoff procedure is not applied, the matrix element (4) corresponds to the first-order terms in the iteration Watson series involving, however, unambiguously defined nucleon–nucleon amplitudes.

For specific calculations, the off-shell two-nucleon T matrix was constructed for the nonlocal separable Mongan potential [8]. For the wave function ψ, we took the ^{3}He variational function; in the coordinate representation, it has the form (see [9])

$$\psi(r_1, r_2, r_3) = \sum_{\alpha=1}^{2} B_\alpha \exp\left(-\frac{1}{2}a_\alpha \sum_{\beta=1}^{3} r_\beta^2\right), \tag{7}$$

where r_β is the radius vector of the motion of nucleon β with respect to the center of mass of the ^{3}He nucleus, and B_α and a_α are variational parameters.

The differential cross section for four scattering-angle values of $\theta = 30.6^\circ$, 54.8°, 70.1°, and 90° was analyzed here as a function of the energy of relative motion in the system of two ^{3}He nuclei in the c.m. frame. The results obtained under these conditions (see Figs. 1–4) could be compared with experimental data.

In each case, the solid curve corresponds to the CTBIA calculation, while the dashed curve represents the results of the analogous cutoff-free calculation ($R_\alpha = R_\delta = 0$). The displayed experimental data were borrowed from [10]. It can be seen that the application of the cutoff procedure leads to nearly an order of magnitude change in the differential cross section, also deforming its shape. As a result, fairly good agreement between the theoretical and experimental data is achieved in all four cases.

Let us now consider the reaction $d(t, tp)n$ in the laboratory frame. The projectile triton collides with the deuteron at rest, splitting it into two nucleons.

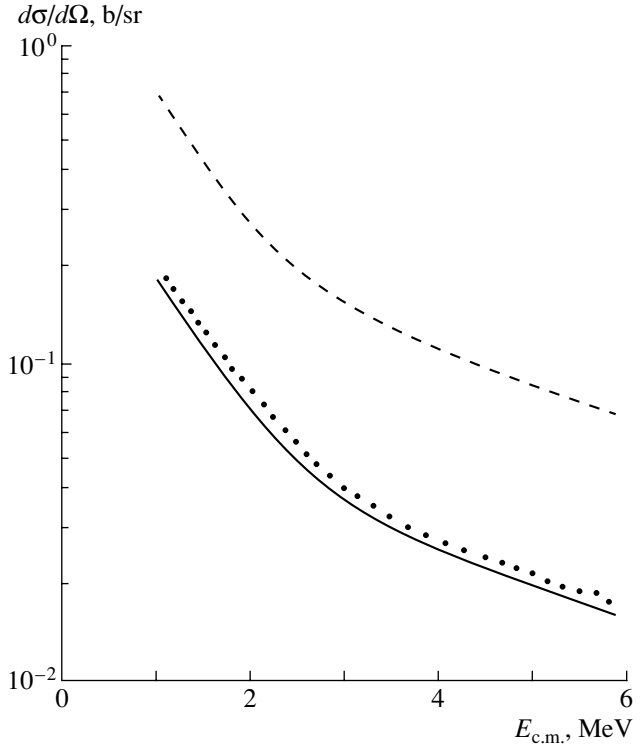

Fig. 1. Differential cross section for elastic ^{3}He^{3}He scattering as a function of the energy of relative motion in the system of colliding nuclei in the c.m. frame at scattering a angle of $\theta = 30.6°$: (solid curve) results of the CTBIA calculation, (dashed curve) results of the analogous cutoff-free calculation, and (points) experimental data from [10].

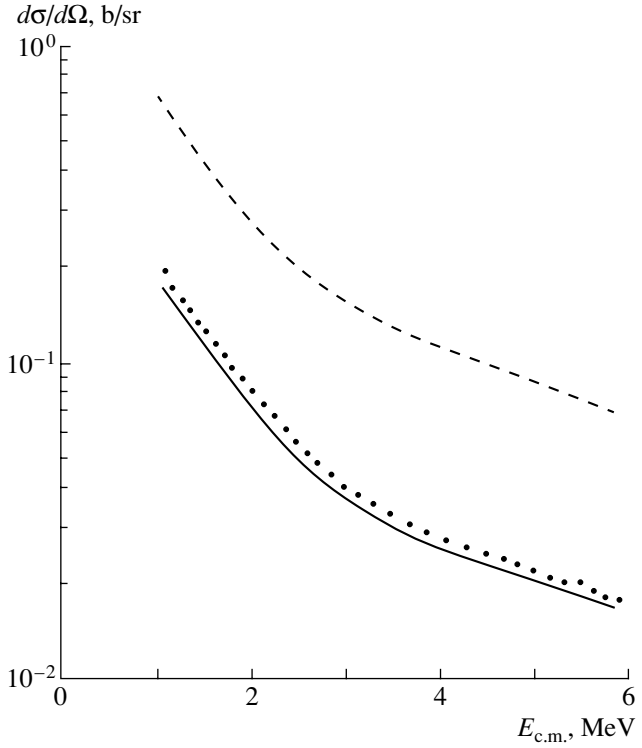

Fig. 2. As in Fig. 1, but for $\theta = 54.8°$.

We label the triton nucleons with the indices α, β, and γ ($\alpha\beta\gamma = 123,\ 231,\ 312$) and the deuteron nucleons with the indices δ and μ ($\delta\mu = 45,\ 54$). We also introduce the following notation: E and $\mathbf{k}$ are, respectively, the energy and the momentum of projectile triton; $\mathbf{k}_t$ is the momentum of the scattered triton; $\mathbf{k}_4$ ($\mathbf{k}_5$) is the momentum of the scattered proton (neutron) originating from deuteron breakup; θ_t and θ_4 are, respectively, the triton and the proton scattering angle; m_t is the triton mass; and ψ_t (ψ_d) is the triton (deuteron) wave function. The rest of the notation ($\mathbf{k}_{\beta\gamma}$, $\mathbf{K}_{\beta\gamma}$, $\mathbf{p}_\alpha$, $\varepsilon_{\alpha\delta}$, $t_{\alpha\delta}$) is identical to that which was used in the preceding problem.

Experimental studies of quasielastic-scattering reactions of the $d(t, tp)n$ type are usually performed in coplanar geometry. The differential cross section is measured as a function of the scattering angles of two final particles (the triton and the proton in our case) and of the energy of one of them (the proton in our case).

We represent the mechanism of the reaction $d(t, tp)n$ in just the same way as above: the triton $(\alpha\beta\gamma)$ as a discrete unit collides with a deuteron consisting of two nucleons, $\delta + \mu$, with the matrix element being written as the sum of all possible $(\alpha\beta\gamma)\delta$ (that is, tN) amplitudes; now, the projectile nucleus is treated as a two-fragment system, $\alpha + \beta\gamma$, with the $(\alpha\beta\gamma)\delta$ amplitude being written as the sum of all possible $\alpha\delta$ (that is, NN) amplitudes. As before, we are to solve a three-body problem at each step and can again apply the CTBIA approach.

Taking the aforesaid into account, we can represent the differential cross section for the reaction $d(t, tp)n$ within the CTBIA approach as

$$\frac{d^3\sigma}{d\Omega_t d\Omega_4 dE_4} = (2\pi)^4 \frac{2m_t m^2 k_t k_4}{k} \times \frac{\sum\limits_{\text{spins}} |M|^2}{|3k\cos\theta_t - 4k_t - 3k_4\cos(\theta_t - \theta_4)|}, \tag{8}$$

where

$$M = \hat{A} \sum_{\substack{\alpha\beta\gamma = 123,\,231,\,312 \\ \delta\mu = 45,\,54,}} \psi_d(-\mathbf{k}_\mu; R_\mu) \times \int \psi_t^*(\mathbf{k}'_{\beta\gamma}, \mathbf{p}'_\alpha) t_{\alpha\delta}(\mathbf{k}'_{\alpha\delta}, \mathbf{k}_{\alpha\delta}; \varepsilon_{\alpha\delta}) \tag{9}$$

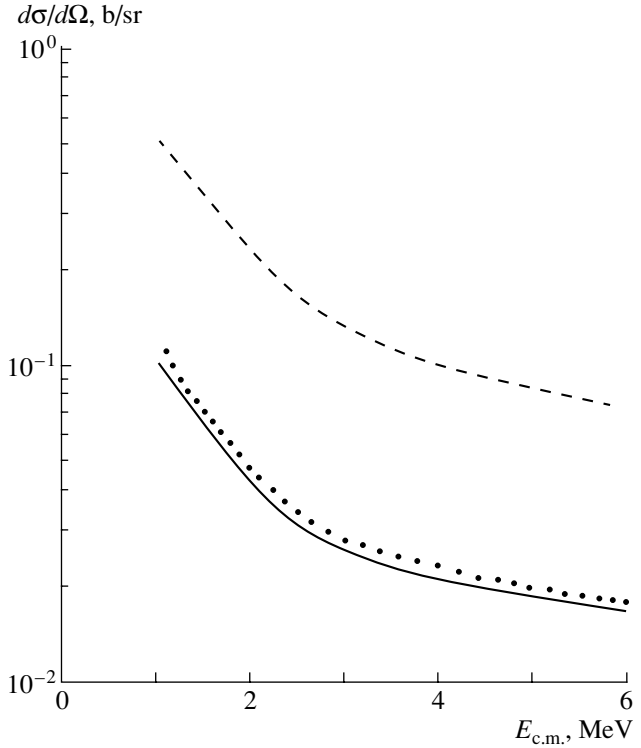

Fig. 3. As in Fig. 1, but for $\theta = 70.1°$.

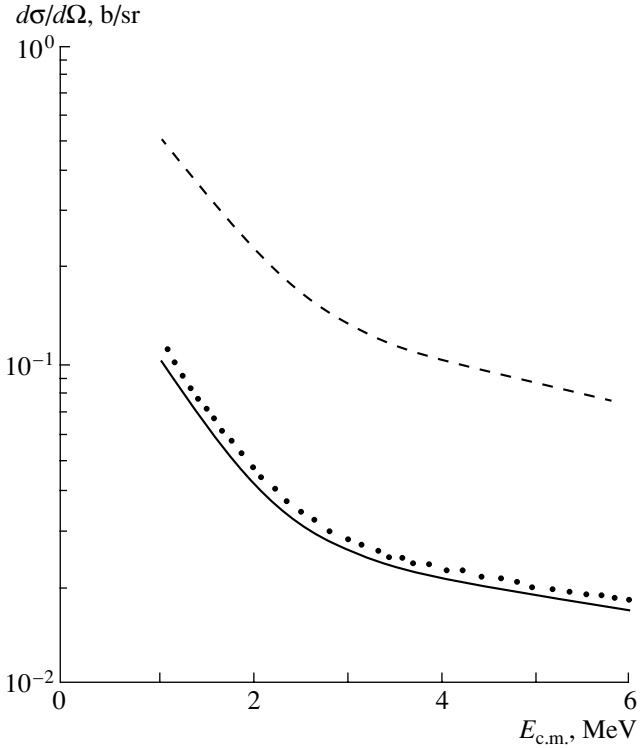

Fig. 4. As in Fig. 1, but for $\theta = 90°$.

$$\times \psi_t(\mathbf{k}_{\beta\gamma}, \mathbf{p}_\alpha, R_\alpha) d\mathbf{k}_{\beta\gamma} d\mathbf{K}_{\beta\gamma},$$

$$\left.\begin{aligned} \mathbf{p}_\alpha &= \frac{2}{3}\mathbf{k} - \mathbf{K}_{\beta\gamma}, \quad \mathbf{p}'_\alpha = \frac{2}{3}\mathbf{k}_t - \mathbf{K}_{\beta\gamma}, \\ \mathbf{k}_{\alpha\delta} &= \frac{1}{2}(\mathbf{k} + \mathbf{k}_\delta) - \frac{1}{2}\mathbf{K}_{\beta\gamma}, \\ \mathbf{k}'_{\alpha\delta} &= \frac{1}{2}(\mathbf{k}_t - \mathbf{k}_\delta) - \frac{1}{2}\mathbf{K}_{\beta\gamma}, \end{aligned}\right\} \quad (10)$$

$$\varepsilon_{\alpha\delta} = \frac{1}{2m}\left\{2mE - \frac{1}{2}k^2 - K^2_{\beta\gamma} - 2k^2_{\beta\gamma} \right. \quad (11)$$
$$\left. - \frac{1}{2}k^2_\delta + \mathbf{k}(\mathbf{K}_{\beta\gamma} - \mathbf{k}_\delta) + \mathbf{K}_{\beta\gamma} \cdot \mathbf{k}_\delta \right\}.$$

Summation in (8) is carried out over the triton- and deuteron-spin projections in the initial state and over the triton- and nucleon-spin projections in the final state. These spin projections, as well as the function $G(p, R)$, appear explicitly upon expanding ψ_d, ψ_t, and $t_{\alpha\delta}$ in partial waves.

For specific calculations, the off-shell two-nucleon T matrix and the radial part of the deuteron wave function were constructed for the Mongan potential. In order to describe the internal state of the triton, we again use the variational function having a correct asymptotic behavior [9]; in the coordinate representation, it has the same form as the function in (7), but the variational parameters take different values.

The differential cross section for the reaction $d(t, tp)n$ as a function of the final-proton energy in the laboratory frame is studied here for two sets of fixed kinematical parameters: $E = 35.5$ MeV, $\theta_t = 25°$, and $\theta_4 = -20°$ (Fig. 5) and $E = 35.5$ MeV, $\theta_t = 20°$, and $\theta_4 = -50°$ (Fig. 6). As before, the choice of parameter values was dictated by the desire to perform a comparison with experimental data. In the calculations, we took into account the $^1S_0$, $^1P_1$, $^1D_2$, $^3S_1 + ^3D_1$, $^3P_0$, $^3P_1$, $^3P_2 + ^3F_2$, and $^3D_2$ two-nucleon states. In contrast to the problem considered first, where zero partial-wave amplitudes make a dominant contribution to the final result, all of the above amplitudes must be taken into account here.

A comparison of the theoretical and experimental results shows that the cutoff procedure affects substantially both the magnitude and the shape of the cross section, improving the agreement with the experimental data.

A few comments are in order here.

(i) A more consistent way would be to construct the ^{3}He and triton wave functions by using the Mongan potential. However, this would complicate the

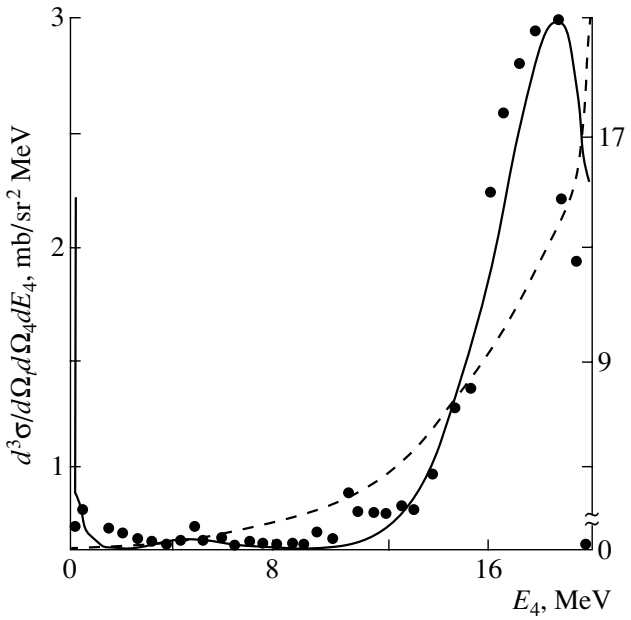

Fig. 5. Differential cross section for the reaction $d(t, tp)n$ as a function of the final-proton energy in the laboratory frame at $E = 35.5$ MeV, $\theta_t = 25°$, and $\theta_4 = -20°$: (solid curve, left-hand scale) results of the CTBIA calculation, (dashed curve, right-hand scale) results of the analogous cutoff-free calculation, and (points, left-hand scale) experimental data from [11].

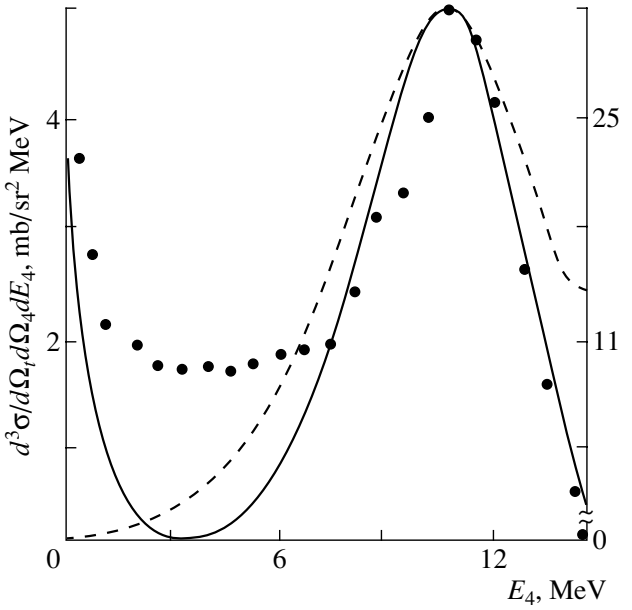

Fig. 6. As in Fig. 5, but for $E = 35.5$ MeV, $\theta_t = 20°$, and $\theta_4 = -50°$.

calculations considerably. Since the internal states of the ^{3}He nuclei and triton do not change in the problems under study, our choice cannot have a pronounced effect on the final results.

(ii) The dependence of the relative-motion energy $\varepsilon_{\alpha\delta}$ appearing in the element $t_{\alpha\delta}(\mathbf{k}'_{\alpha\delta}, \mathbf{k}_{\alpha\delta}; \varepsilon_{\alpha\delta})$ of the off-shell two-nucleon T matrix on all of the integration variables complicates substantially the calculation of the reaction amplitudes (4) and (9). However, our estimates showed that the replacement of the matrix element $t_{\alpha\delta}(\mathbf{k}'_{\alpha\delta}, \mathbf{k}_{\alpha\delta}; \varepsilon_{\alpha\delta})$ by the half-off-shell matrix element $t_{\alpha\delta}(\mathbf{k}'_{\alpha\delta}, \mathbf{k}_{\alpha\delta}; k_{\alpha\delta})^2/m$ or by $t_{\alpha\delta}(\mathbf{k}'_{\alpha\delta}, \mathbf{k}_{\alpha\delta}; k'_{\alpha\delta})^2/m$ is quite a reasonable approximation. This means that the off-shell effects are somehow smoothed out by integration over the entire space. In all probability, the problem of taking such effects into account in constructing the amplitude of nucleon–nucleon scattering is less acute here than in the case of $\alpha\alpha$ scattering [12].

(iii) There was some degree of arbitrariness in choosing the cutoff parameter ($C > 1$), and we used this arbitrariness to fit the theoretical curve to the experimental data. In all four cases considered here, elastic ^{3}He^{3}He scattering is best described with a value of $C \approx 1.5$, which is within the range of values of the cutoff parameter that were found earlier for the problems of nucleon–deuteron scattering [7]. However, this is not so for the reaction $d(t, tp)n$, where we had to use values of $C \approx 2$ and 3 (see Fig. 5 and Fig. 6, respectively). Possibly, the situation here is not exhausted by the mechanism of a direct single collision, and it is necessary to take into account some other mechanisms—for example that which involves final-state interaction [11]. This especially concerns Fig. 6.

Despite the above reservations, the results of this study give reasons to state that a consistent use of the single-collision mechanism may open some hidden possibilities for describing complex nuclear processes. If we consider that the cutoff procedure can be qualitatively associated with the unitarization of the approximate scattering amplitude taking into account only single collisions [7], we can say that the success of the CTBIA approach highlights once again the importance of respecting fundamental physical principles in specific theoretical studies.

REFERENCES

1. L. D. Faddeev, Zh. Éksp. Teor. Fiz. **39**, 1459 (1960) [Sov. Phys. JETP **12**, 1014 (1960)].
2. J. V. Mebonia, Phys. Lett. A **48A**, 196 (1974).
3. J. V. Mebonia and T. I. Kvaratskhelia, Phys. Lett. B **90B**, 17 (1980).
4. J. V. Mebonia and T. I. Kvaratskhelia, J. Phys. G **10**, R1677 (1984).

5. O. L. Bartaya and Dzh. V. Meboniya, Yad. Fiz. **33**, 987 (1981) [Sov. J. Nucl. Phys. **33**, 521 (1981)].
6. V. Sh. Jikia, T. I. Kvaratskhelia, and J. V. Mebonia, Yad. Fiz. **58**, 30 (1995) [Phys. At. Nucl. **58**, 27 (1995)].
7. J. V. Mebonia, M. A. Abusini, P. J. Saralidze, *et al.*, Yad. Fiz. **63**, 2181 (2000) [Phys. At. Nucl. **63**, 2085 (2000)].
8. Th. Mongan, Phys. Rev. **178**, 1597 (1969).
9. K. Wildermuth and Y. C. Tang, *A Unified Theory of the Nucleus* (Vieweg, Braunschweig, 1977; Mir, Moscow, 1980).
10. P. Descouvemont, Phys. Rev. C **50**, 2635 (1994).
11. S. Blagus *et al.*, Phys. Rev. C **44**, 325 (1991).
12. V. V. Balashov and J. V. Mebonia, Nucl. Phys. A **107**, 369 (1968).

Translated by O. Chernavskaya

Physics of Atomic Nuclei, Vol. 66, No. 2, 2003, pp. 253–258. Translated from Yadernaya Fizika, Vol. 66, No. 2, 2003, pp. 278–283.

NUCLEI
Theory

Diffractive Dissociation of Deuterons and Exotic Nuclei ^{6}He and ^{19}C

M. V. Evlanov, A. M. Sokolov, and V. K. Tartakovsky

Institute for Nuclear Research, National Academy of Sciences of Ukraine, pr. Nauki 47, Kiev, 252028 Ukraine

Received February 19, 2001; in final form, July 10, 2001

Abstract—A theory is developed for describing the diffractive dissociation of loosely bound two-cluster nuclei in the nuclear and Coulomb fields of nuclei having a diffuse boundary. The energy spectra of charged products of the breakup of ^{2}H, ^{6}He, and ^{19}C nuclei are calculated on the basis of the proposed approach, and the results are found to be rather sensitive to nuclear structure. For some angles of neutron and proton emission from the reaction ^{12}C$(d, np)^{12}$C, the calculated cross sections are in satisfactory agreement with the results of kinematically complete experiments performed recently to study the breakup of intermediate-energy deuterons. © *2003 MAIK "Nauka/Interperiodica".*

1. INTRODUCTION

To a considerable extent, the present theoretical study devoted to the diffractive dissociation of loosely bound two-cluster nuclei was motivated by the article of Okamura *et al.* [1], who reported on unique kinematically complete experiments that studied the breakup of intermediate-energy deuterons in the field of various nuclei ranging from those of carbon (^{12}C) to those of lead (^{208}Pb). The experiments in question measured the differential cross section $d^3\sigma/d\Omega_n d\Omega_p dE_p$ for $A(d, np)A$ reactions (where A is the mass number of the target nucleus) versus the product-proton energy E_p at small neutron and proton emission angles denoted by θ_n and θ_p, respectively. It follows that, under the conditions of the experiments being discussed, their results can be described on the basis of the diffraction approximation.

In our previous study [2], a general formalism was developed within which the diffractive elastic scattering and the diffractive dissociation of loosely bound two-cluster nuclei containing one charged cluster were treated with allowance for Coulomb interaction with target nuclei and for the diffuseness of their boundary; also, the differential cross section was calculated there for the process where an exotic nucleus ^{11}Li assumed to consist of $(2n)$ and ^{9}Li clusters is elastically scattered by a ^{28}Si nucleus, a Gaussian function being used for the internal wave function describing the relative motion of the clusters. The calculated cross section proved to be in satisfactory agreement with its experimental counterpart as a function of ^{11}Li scattering angle, this being due largely to correctly eliminating the divergence in that part of the amplitude allowing for Coulomb interaction which is associated with double scattering.

In the present study, we develop further the mathematical formalism proposed in [2], but we concentrate here exclusively on the amplitude and the cross section for the diffractive dissociation of a two-cluster nucleus featuring one charged cluster, taking no account of particle spins. In the amplitude for the dissociation process, we include a term that is analogous to the term discarded in [2] and which is small in the case of elastic scattering (see below) and introduce a more general profile function that takes simultaneously into account absorption, Coulomb interaction, and the diffuseness of the target-nucleus edge.

We begin by calculating the differential cross section for the process ^{12}C$(d, np)^{12}$C and show that, in order to describe relevant experimental data (see [1]), it is necessary to take simultaneously into account the following factors: (i) Coulomb interaction, for which use must be made of the method developed in [2] for eliminating logarithmic divergences; (ii) the diffuseness of the target-nucleus edge; and (iii) the correct asymptotic behavior of the wave function for the relative motion of the clusters both at short and at long distances between them (here, we took the Hulthén wave function for this purpose).

Our calculation of the cross section for the process ^{12}C$(d, np)^{12}$C was some kind of test for the theoretical approach developed here and, partly, in [2] within the diffraction approximation, and this test yielded results that are in fairly good agreement with experimental data reported in [1]. This approach is further used to compute the cross sections for the two-body diffractive dissociation of unstable exotic nuclei, such as ^{6}He (into $2n$ and ^{4}He clusters) and ^{19}C (into

1063-7788/03/6602-0253$24.00

n and ^{18}C clusters), that is induced by their collisions with nuclei. That the energies required for the separation of two peripheral neutrons from the ^{6}He nucleus and for the separations of the loosely bound neutron from the ^{19}C nucleus are rather small ($\varepsilon_{2n} = 0.975 \pm 0.040$ MeV [3] and $\varepsilon_n = 0.530 \pm 0.130$ MeV [4], respectively) suggests the two-cluster structure of these exotic nuclei.

As we indicated in [5, 6], the use of relevant experimental data in exploring the diffractive interaction of ^{6}He with nuclei may aid in refining the separation energy of two loosely bound neutrons in the ^{6}He nucleus and in deriving an independent estimate of the probability of a dineutron configuration in this exotic nucleus.

The ^{19}C nucleus, which features a large neutron excess and which is highly unstable, was discovered quite recently [7, 8], and available information about it [9–13] is still incomplete. In particular, experimental data suggest that the energy ε_n required for the separation of the peripheral neutron from the ^{19}C nucleus is rather low, but the value of ε_n has so far been found with a large uncertainty. As will be seen below, the differential cross section for the diffractive dissociation of a ^{19}C nucleus into a neutron and a ^{18}C nucleus is rather sensitive to variations in ε_n, and this circumstance may be of use in refining the value of ε_n and in clarifying other details of the structure of ^{19}C.

Since there are presently no experiments that would study the interaction of ^{6}He and ^{19}C beams with nuclei, our calculations of cross sections for processes involving these exotic nuclei are of a predictive character. We hope that the results of these calculations will be of use in analyzing future experiments.

2. DESCRIPTION OF THE FORMALISM

For the amplitude of the diffrative dissociation of a two-cluster nucleus such that only its second cluster is charged, it is convenient to use, as in [2], the general expression

$$iG^Z_{\mathbf{u}}(\mathbf{q}) = e^{2i\eta_2(R_2)}\{iG_{\mathbf{u}}(\mathbf{q}) + g^{(1)}_{\mathbf{u}}(\mathbf{q}) + g^{(2)}_{\mathbf{u}}(\mathbf{q})\}, \tag{1}$$

where $iG_{\mathbf{u}}(\mathbf{q})$ is the amplitude in which Coulomb interaction is disregarded, but the diffuseness of the target-nucleus edge is taken into account, while $g^{(1)}_{\mathbf{u}}(\mathbf{q})$ and $g^{(2)}_{\mathbf{u}}(\mathbf{q})$ are contributions to the amplitude in (1) that are associated with the Coulomb interaction of the second (charged) cluster with the target nucleus, the former and the latter stemming from, respectively, the single and the double scattering of the clusters. Hereafter, the notation is identical to that in [2].

The profile function for the second (charged) cluster will be taken in the form

$$\omega^{(\Delta)Z}_2(\rho_2) = 1 - e^{2i\eta_2(\rho_2)} + e^{2i\eta_2(\rho_2)}\left(1 + \exp\frac{\rho_2 - R_2}{\Delta}\right)^{-1}, \tag{2}$$

where Δ is the parameter of diffuseness of the target-nucleus edge and $\eta_2(\rho_2)$ is the Coulomb phase shift. The profile function $\omega^{(\Delta)}_1(\rho_1)$ for the first cluster, which is not charged, is obtained from (2) upon replacing the index 2 by 1 and going over to the limit $\eta_1(\rho_1) \to 0$.

By using the properties of Bessel functions and the fact that the minimum momentum transfer q in the disintegration of projectile nuclei does not vanish, one can recast the contributions to the amplitude in (1) that stem from the Coulomb interaction into the form

$$g^{(1)}_{\mathbf{u}}(\mathbf{q}) = ik\Phi_{\mathbf{u}}(-\beta_2\mathbf{q})[e^{-2i\eta_2(R_2)} - 1] \times \int_0^\infty d\rho_1\rho_1\frac{J_0(q\rho_1)}{1 + \exp\frac{\rho_1 - R_1}{\Delta}} - \frac{2kn_2}{q^2}\Phi_{\mathbf{u}}(\beta_1\mathbf{q}) \times \left[J_0(qR_2) + 2in_2\int_{R_2}^\infty d\rho_2\frac{J_0(q\rho_2)}{\rho_2} \times \exp\left(2in_2\ln\frac{\rho_2}{R_2}\right)\right] + ik\Phi_{\mathbf{u}}(\beta_1\mathbf{q}) \times \left[\int_0^{R_2} d\rho_2\rho_2 J_0(q\rho_2)\left(1 - \exp\left(2in_2\ln\frac{\rho_2}{R_2}\right)\right) - \int_0^\infty d\rho_2\rho_2 J_0(q\rho_2)\frac{1 - \exp\left(2in_2\ln\frac{\rho_2}{R_2}\right)}{1 + \exp\frac{\rho_2 - R_2}{\Delta}}\right], \tag{3}$$

$$g^{(2)}_{\mathbf{u}}(\mathbf{q}) = \int d^{(2)}\mathbf{g}F_{\mathbf{u}}(\mathbf{g}), \tag{4}$$

$$F_{\mathbf{u}}(\mathbf{g}) = \frac{k}{2\pi i}\Phi_{\mathbf{u}}(\mathbf{g})\int_0^\infty d\rho_1\rho_1\frac{J_0(|\beta_1\mathbf{q} - \mathbf{g}|\rho_1)}{1 + \exp\frac{\rho_1 - R_1}{\Delta}} \times \left\{\frac{2in_2}{|\beta_2\mathbf{q} + \mathbf{g}|^2}\left[J_0(|\beta_2\mathbf{q} + \mathbf{g}|R_2) + 2in_2\int_{R_2}^\infty d\rho_2\frac{J_0(|\beta_2\mathbf{q} + \mathbf{g}|\rho_2)}{\rho_2}\exp\left(2in_2\ln\frac{\rho_2}{R_2}\right)\right]\right.$$

$$+\int_0^{R_2} d\rho_2\rho_2 J_0(|\beta_2\mathbf{q}+\mathbf{g}|\rho_2)$$
$$\times\left(1-\exp\left(2in_2\ln\frac{\rho_2}{R_2}\right)\right)$$
$$-\int_0^{\infty} d\rho_2\rho_2 J_0(|\beta_2\mathbf{q}+\mathbf{g}|\rho_2)\frac{1-\exp\left(2in_2\ln\dfrac{\rho_2}{R_2}\right)}{1+\exp\dfrac{\rho_2-R_2}{\Delta}}\Bigg\}.$$

In (3), we have retained the first term involving the inelastic form factor $\Phi_{\mathbf{u}}(-\beta_2\mathbf{q})$, while, in [2], we disregarded the analogous term involving the elastic form factor $\Phi_0(-\beta_2\mathbf{q})$ since its contribution to the cross section for elastic scattering was quite small. The integrals in (3) and (4) with respect to ρ_1 and ρ_2 are transformed in such a way that they already converge quite fast both at the lower and at the upper limits of integration. We have kept the cluster indices on the variables ρ_1 and ρ_2 in order to indicate explicitly which contributions refer to each of the clusters. Logarithmic divergences associated with Coulomb interaction that arise in the integration in (4) with respect to the variable $\mathbf{g}$ at $\mathbf{g}=-\beta_2\mathbf{q}$ were eliminated by the method proposed in [2]. This method is based on a procedure within which, upon the inclusion of Coulomb interaction, the momentum-conservation law is taken into account more correctly than in the earlier version of the diffraction nuclear model [14, 15].

For the wave functions describing the relative motion of the two clusters in a bound state, $\varphi_0(\mathbf{r})$ (where $\mathbf{r}$ is the radius vector connecting the two clusters), and in a continuum state, $\varphi_{\mathbf{u}}(\mathbf{r})$ (where $\mathbf{u}$ is the relative momentum of the clusters that fly apart), we took the Hulthén wave function and a function that is orthogonal to it; that is,

$$\varphi_0(\mathbf{r})=\sqrt{\frac{\alpha\beta(\alpha+\beta)}{2\pi(\beta-\alpha)^2}}\frac{e^{-\alpha r}-e^{-\beta r}}{r}, \qquad (5)$$
$$\alpha=\sqrt{\frac{2m_1m_2\varepsilon}{\hbar^2(m_1+m_2)}},$$

$$\varphi_{\mathbf{u}}(\mathbf{r})=e^{i\mathbf{u}\cdot\mathbf{r}}+f(u)\frac{e^{-iur}-e^{-\beta r}}{r}, \qquad (6)$$
$$f(u)=-\left[\beta-\frac{\beta^2+u^2}{2\beta}-\frac{(\beta^2+u^2)^2}{2(\alpha+\beta)^2\beta}-iu\right]^{-1},$$

where m_1 and m_2 are the cluster masses and ε is the binding energy of the projectile nucleus with respect to its breakup into the two clusters.

The differential cross section for the diffractive dissociation of the projectile nucleus into two clusters in the nonrelativistic approximation is related to the amplitude in (1) by the equation [16]

$$\frac{d^3\sigma}{d\Omega_1 d\Omega_2 dE_2} \qquad (7)$$
$$=\frac{m_1m_2E_1E_2}{2^{2/3}\pi^3k^2}\left(\frac{m_1+m_2}{E}\right)^{1/2}\left|G^Z_{\mathbf{u}}(\mathbf{q})\right|^2,$$

where k and E are the projectile momentum and energy, respectively; E_1 and E_2 are the energies of the emitted clusters (the first and the second, charged, one, respectively); and $d\Omega_1$ and $d\Omega_2$ are the solid-angle elements in which their momenta occur.

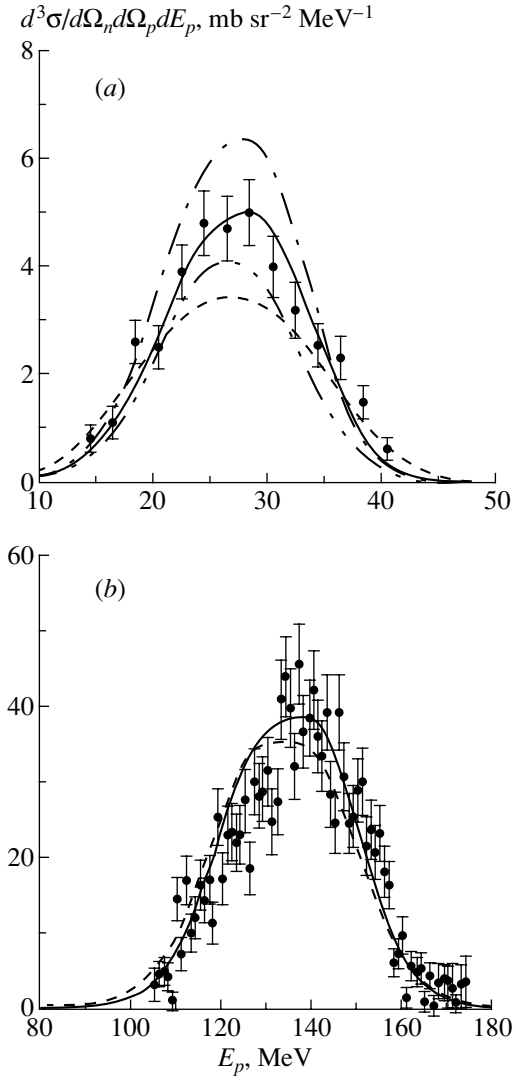

Fig. 1. Cross section for the process $^{12}\mathrm{C}(d, np)^{12}\mathrm{C}$ versus the product-proton energy at (*a*) the incident-deuteron energy of $E_d=56$ MeV and the nucleon-emission angles of $\theta_n=\theta_p=15^\circ$ and (*b*) $E_d=270$ MeV and $\theta_n=\theta_p=4^\circ$. The notation for the curves is explained in the main body of the text. The displayed experimental values were borrowed from [1].

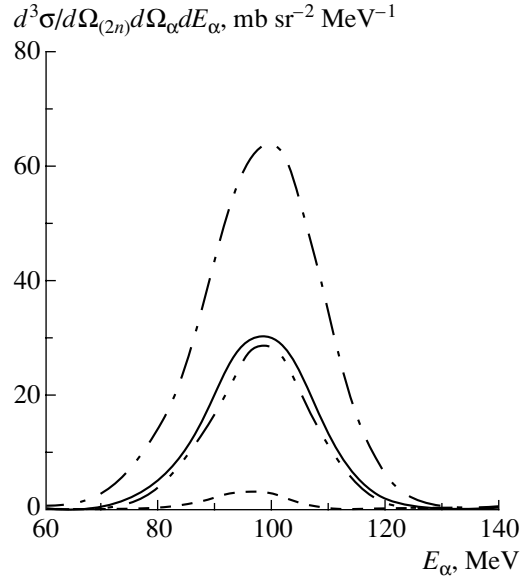

Fig. 2. Cross section for the process ^{12}C(^{6}He, $(2n)\alpha$)^{12}C versus the alpha-particle energy at the ^{6}He energy of $E = 150$ MeV and the cluster-emission angle of $\theta_{(2n)} = \theta_\alpha = 7^\circ$.

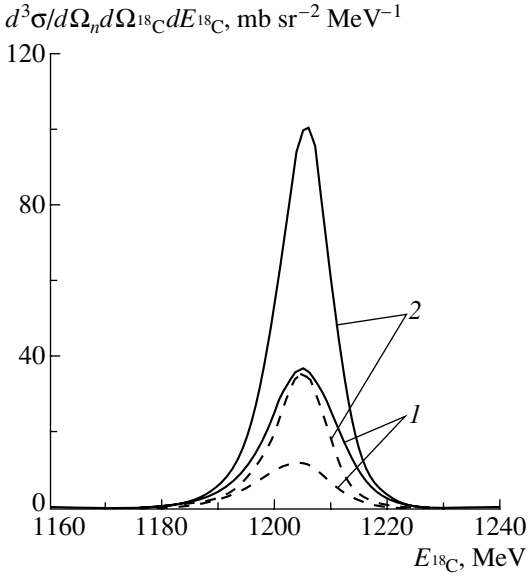

Fig. 3. Cross section for the dissociation of 1273-MeV projectile nuclei ^{19}C in the field of a ^{12}C nucleus into a neutron and a ^{18}C nucleus versus the energy of the product nucleus ^{18}C for the neutron and ^{18}C emission angles of $\theta_n = 3^\circ$ and $\theta_{^{18}C} = -3^\circ$, respectively, the neutron separation energy being set to $\varepsilon_n = 0.53$ MeV (curves *1*) or $\varepsilon_n = 0.24$ MeV (curves *2*). The solid curves correspond to taking into account both the nuclear and the Coulomb interaction, while the dashed curves represent the results obtained with allowance for only the nuclear interaction.

3. NUMERICAL CALCULATIONS AND DESCRIPTION OF EXPERIMENTAL DATA

Results obtained by calculating the cross sections by formula (7) with the aid of expressions (1)–(6) are displayed in Figs. 1–3. In all of the figures, the solid curves correspond to taking into account both the nuclear and the Coulomb interaction of incident particles with target nuclei, whereas the dashed curves represent the results obtained with allowance for only the nuclear interaction. The diffuseness parameter of the target was set to $\Delta = 0.75$ fm, while the parameter β appearing in the wave functions in (5) and (6) was assumed to be equal to 7α.

The calculated cross section $d^3\sigma/d\Omega_n d\Omega_p dE_p$ for diffractive deuteron dissociation in the field of a ^{12}C nucleus versus the product-proton energy E_p are shown in Fig. 1 for the projectile-deuteron energies of $E_d = 56$ MeV (Fig. 1*a*) and $E_d = 270$ MeV (Fig. 1*b*), along with experimental data (points with error bars) from [1]. The ranges $R_1(=R_n)$ and $R_2(=R_p)$ of nucleon-cluster interaction with a target nucleus of mass number A were taken to be equal to $R = r_0 A^{1/3}$, the dependences in Figs. 1*a* and 1*b* being computed for $r_0 = 1.3$ and 1.1 fm, respectively. This distinction between the values of r_0 for different projectile-deuteron energies E_d is associated with the well-known general regularity of a decrease in the ranges of interaction of colliding strongly interacting particles (nuclei) with increasing energy [17] (this was also confirmed by the optical-model calculations performed in [18]). The use of somewhat different values of r_0 for different projectile-deuteron energies per nucleon, $(1/2)E_d \geq 130$ MeV and $E_d \leq 30$ MeV, leads to better agreement with experimental data from [1] than the use of the averaged value of $r_0 = 1.2$ fm. The deuteron-binding energy was set to $\varepsilon_d = 2.225$ MeV.

The calculations, as well as the kinematically complete experiments reported in [1], were performed for the case where the momentum of the product neutron was parallel to the momentum of the product proton—that is, the nucleon emission angles θ_n and θ_p (with respect to the deuteron-momentum vector) were equal to each other. These angles were 15° in the case corresponding to Fig. 1*a* and 4° in the case corresponding to Fig. 1*b*.

From Fig. 1, it can be seen that, if the Coulomb interaction of the second, charged, cluster (proton) with the target nucleus ^{12}C is taken into account along with nuclear interaction, the dissociation cross section at maxima grows, while the distribution itself in the region of these maxima becomes narrower. As a result, the agreement with the experimental data being considered is significantly improved, especially

at the deuteron energy of $E_d = 56$ MeV in Fig. 1*a*, where the uncertainties in the cross-section values are much less than in Fig. 1*b* at $E_d = 270$ MeV. The cross sections calculated here for the angles of $\theta_n = \theta_p = 7^\circ$ and 10° and $E_d = 270$ MeV are also in fairly good agreement with their experimental counterparts from [1].

Figure 1*a* also displays the cross sections computed with allowance for both the nuclear and the Coulomb interaction at $\Delta = 0$ and $\beta = 7\alpha$ (dash-and-dot curve) and at $\Delta = 0.75$ fm and $\beta = \infty$ (dash-and-double-dot curve). It can be seen that, as the region of target-nucleus-edge diffuseness is widened, the cross-section value at the maximum decreases and that, upon including (increasing) the range of nuclear forces between the clusters (that is, upon reducing the parameter β), the cross section at the maximum becomes larger; therefore, the agreement with experimental data is improved in either case. As soon as the uncertainties in preliminary data reported by Okamura *et al.* [1] (especially in those given in Fig. 1*b*) are reduced, the pattern of the dependence of the observed dissociation cross sections on the properties of projectile nuclei (deuterons) and target nuclei will become clearer. Even at present, however, one can deduce from the data in Fig. 1 that the deuteron-breakup cross section is rather sensitive to these properties; moreover, these data indicate that a comparison of the theoretical and experimental results may provide the possibility of determining the parameters of the structure of nuclei. Our analysis of the cross section for the process $^{12}\mathrm{C}(d, np)^{12}\mathrm{C}$ and good agreement with available experimental data give every reason to state that the cross sections presented below that were calculated on the basis of our approach in the diffraction approximation for the dissociation of nuclei more complex than the deuteron—namely, those of ^{6}He and ^{19}C—may be optimistically viewed as reliable predictions.

The calculated differential cross section $d^3\sigma/(d\Omega_{(2n)} \times d\Omega_\alpha dE_\alpha)$ for the diffractive dissociation of 150-MeV projectile exotic nuclei ^{6}He in the field of a ^{12}C nucleus into a two-neutron cluster $(2n)$ and a ^{4}He cluster is presented in Fig. 2 versus the product-alpha-particle energy E_α for the case where the two-neutron system $(2n)$ as a discrete unit (presumed dineutron) and the alpha particle are both emitted at an angle of $\theta_{(2n)} = \theta_\alpha = 7^\circ$ with respect to the momentum of the projectile nucleus ^{6}He. The ranges of the interaction of the two clusters (presumed dineutron and alpha particle) with the target nucleus of mass number A were determined here (and for the data in Fig. 3 as well) by the formula $R_i = r_0(A^{1/3} + A_i^{1/3})$, $i = 1, 2$, where A_i are the mass numbers of the clusters ($A_1 = A_{(2n)} = 2$ and $A_2 = A_\alpha = 4$ for the data in Fig. 2), at $r_0 = 1.2$ fm. We note that the results reported in [19–22] suggest the presence of a dineutron configuration in the ^{6}He nucleus, the values obtained in [22] for the linear dimensions of the dineutron in the ^{6}He nucleus corresponding to the parameter value of $r_0 = 1.2$ fm.

The notation for the curves in Fig. 2 is identical to that in Fig. 1: the dash-and-dot curve in Fig. 2 corresponds to $\Delta = 0$ and $\beta = 7\alpha$, while the dash-and-double-dot curve represents the relevant cross section for $\Delta = 0.75$ fm and $\beta = \infty$ [the energy required for separating the $(2n)$ system from the ^{6}He nucleus was set to $\varepsilon_{(2n)} = 0.975$ MeV]. As can be seen, the sensitivity to the range of the forces between the $(2n)$ system and the alpha particle is comparatively low here; however, allowance for the diffuseness of the target-nucleus edge may reduce the cross section by nearly a factor of 2 (as this occurs upon the transition from $\Delta = 0$ to $\Delta = 0.75$ fm), while the inclusion of Coulomb interaction increases the cross-section values in the region of the maximum by about one order of magnitude.

A comparatively high sensitivity of the theoretical cross section for the process $^{12}\mathrm{C}(^6\mathrm{He}, (2n)\alpha)^{12}\mathrm{C}$ to a number of various factors may aid, upon performing relevant experiments, in refining the energy ε_{2n} of two-neutron separation from the ^{6}He nucleus and clarify, without recourse to other investigations, such as those reported in [19–22], the question of whether a dineutron exists in the ^{6}He nucleus.

The calculated cross section for the diffractive dissociation of an exotic nucleus ^{19}C (as was mentioned above, this nuclear species was discovered in [7, 8]) in the field of a ^{12}C nucleus into a loosely bound neutron (the separation energy is $\varepsilon_n = 0.53$ MeV) and a ^{18}C nucleus is displayed in Fig. 3 versus the energy of the second cluster (^{18}C nucleus) at the projectile energy of 67 MeV per nucleon—that is, $E = 67(A_1 + A_2)$ MeV ($A_1 = A_n = 1$ and $A_2 = A_{^{18}\mathrm{C}} = 18$ for the data in Fig. 3). The emission angles were set to $\theta_n = 3^\circ$ and $\theta_{^{18}\mathrm{C}} = -3^\circ$ for the neutron and the ^{18}C nucleus, respectively. This means that the calculations were performed for coplanar geometry—that is, for the case where the the neutron momentum lies in the plane spanned by the momenta of the ^{18}C and ^{19}C nuclei and where, in contrast to the cases considered above, the product particles travel on different sides of the projectile-momentum direction.

Curves *1* in Fig. 3 were computed for the optimum (most probable) value of the neutron-separation energy in the ^{19}C nucleus ($\varepsilon_n = 0.53$ MeV), while curves *2* correspond to $\varepsilon_n = 0.24$ MeV. It can be seen from Fig. 3 that, if the Coulomb interaction is switched off, the cross-section maximum is reduced

by nearly a factor of 3. At the same time, the cross-section maximum becomes almost threefold higher upon the transition from the larger value of ε_n to the smaller one. So high a sensitivity of the cross section to variations in ε_n can be used to shrink the region of experimental uncertainties in the energy ε_n of neutron separation from the ^{19}C nucleus.

The calculations reveal that, upon going over from light to extremely heavy target nuclei, the cross section for the diffractive dissociation of a projectile nucleus ^{19}C into a neutron and a ^{18}C nucleus may increase by a few orders of magnitude, which is due primarily to a strong effect of Coulomb interaction. Therefore, it is advisable to perform relevant experiments, first of all, with heavy nuclear targets.

4. CONCLUSIONS

(i) Within the diffraction approximation, a theory has been developed for describing the diffractive dissociation of loosely bound two-cluster nuclei, Coulomb interaction and the diffuseness of the target-nucleus edge being taken into account in this theory; as a result, the amplitude of the process has been represented as the sum of a few integrals characterized by a low multiplicity and a fast convergence at both limits.

(ii) The efficiency of the proposed approach in calculating the differential cross section for the diffractive dissociation of deuterons has been demonstrated, the results of these calculations, where the use of projectile wave functions having a correct asymptotic behavior both at short and at long distances between the clusters involved is of importance, being in fairly good agreement with data of kinematically complete experiments.

(iii) It has been shown that the cross sections computed within the proposed approach for the diffractive dissociation of exotic nuclei ^{6}He and ^{19}C are highly sensitive to some of their features, which have so far been determined with a large uncertainty; the results obtained here for the dissociation of ^{6}He and ^{19}C nuclei can justifiably be considered as predictive ones—they can be of use in planning and performing relevant experiments.

ACKNOWLEDGMENTS

We are grateful to H. Okamura for kindly placing at our disposal detailed tables of data from the experiment reported in [1].

REFERENCES

1. H. Okamura, S. Ishida, N. Sakamoto, *et al.*, Phys. Rev. C **58**, 2180 (1998).
2. M. V. Evlanov, A. M. Sokolov, and V. K. Tartakovskiĭ, Yad. Fiz. **59**, 679 (1996) [Phys. At. Nucl. **59**, 647 (1996)].
3. F. Ajzenberg-Selove, Nucl. Phys. A **490**, 1 (1988).
4. T. Nakamura, N. Fukuda, T. Kobayashi, *et al.*, Phys. Rev. Lett. **83**, 1112 (1999).
5. M. V. Evlanov, A. M. Sokolov, and V. K. Tartakovskiĭ, Izv. Akad. Nauk, Ser. Fiz. **64**, 894 (2000).
6. M. V. Evlanov, A. M. Sokolov, and V. K. Tartakovsky, Yad. Fiz. **63**, 1813 (2000) [Phys. At. Nucl. **63**, 1724 (2000)].
7. D. Bazin, B. A. Brown, J. Brown, *et al.*, Phys. Rev. Lett. **74**, 3569 (1995).
8. D. Bazin, W. Benenson, B. A. Brown, *et al.*, Phys. Rev. C **57**, 2156 (1998).
9. F. M. Marques, E. Liegard, N. A. Orr, *et al.*, Phys. Lett. B **381**, 407 (1996).
10. T. Baumann, M. J. G. Borge, H. Geissel, *et al.*, Phys. Lett. B **439**, 256 (1998).
11. I. Tanihata, Nucl. Phys. A **654**, 235 (1999).
12. A. Bonaccorco, Phys. Rev. C **60**, 054604 (1999).
13. R. Kanungo, I. Tanihata, Y. Ogawa, *et al.*, Nucl. Phys. A **677**, 171 (2000).
14. A. I. Akhiezer and A. G. Sitenko, Phys. Rev. **106**, 1236 (1957).
15. A. I. Akhiezer and A. G. Sitenko, Zh. Éksp. Teor. Fiz. **32**, 794 (1957) [Sov. Phys. JETP **5**, 652 (1957)].
16. M. V. Evlanov, A. M. Sokolov, and V. K. Tartakovskiĭ, Yad. Fiz. **53**, 1559 (1991) [Sov. J. Nucl. Phys. **53**, 957 (1991)].
17. Yu. A. Berezhnoĭ and N. A. Shlyakhov, Ukr. Fiz. Zh. **21**, 192 (1976).
18. K. Seth, Nucl. Phys. A **138**, 61 (1969).
19. M. V. Zhukov, B. V. Danilin, D. V. Fedorov, *et al.*, Phys. Rep. **231**, 151 (1993).
20. Yu. Ts. Oganesyan *et al.*, in *Proceedings of the 49th International Conference on Nuclear Spectroscopy and Nuclear Structure, St. Petersburg, 1999,* p. 275.
21. Yu. Ts. Oganessian, V. I. Zagrebaev, and J. S. Vaagen, Phys. Rev. C **60**, 044605 (1999).
22. G. D. Alkhazov, Yad. Fiz. **63**, 285 (2000) [Phys. At. Nucl. **63**, 229 (2000)].

Translated by A. Isaakyan

Physics of Atomic Nuclei, Vol. 66, No. 2, 2003, pp. 259–267. Translated from Yadernaya Fizika, Vol. 66, No. 2, 2003, pp. 284–292.

NUCLEI
Theory

Scattering of $\pi^{\pm}$ Mesons on a ^{9}Be Nucleus in the Δ_{33}-Resonance Region

E. T. Ibraeva*

Institute of Nuclear Physics, National Nuclear Center of the Republic of Kazakhstan, Almaty, 480082 Republic of Kazakhstan

Received September 3, 2001; in final form, January 23, 2002

Abstract—Within the Glauber diffraction theory of multiple scattering, the differential cross sections for the elastic and inelastic scattering of $\pi^{\pm}$ mesons are calculated for energies in the range between 130 and 260 MeV. This is the region where the broad Δ_{33} resonance in the $\pi^{\pm}N$ system occurs, the maximum corresponding to this resonance being at approximately 165 MeV. The wave function for the ^{9}Be nucleus was chosen on the basis of the $2\alpha N$ multicluster model. The sensitivity of the resulting differential cross sections to the target-nucleus wave functions computed with various intercluster-interaction potentials, to the contributions of wave-function components, and to various scattering multiplicities in the Glauber operator Ω is analyzed. A comparison with experimental data and with the results of other calculations is performed, and conclusions concerning the quality of the wave functions used and advantages of the present approach are drawn. © *2003 MAIK "Nauka/Interperiodica".*

INTRODUCTION

Information of importance for obtaining deeper insights into pion-induced nuclear reactions and for assessing the potential of investigations into nuclear structure with the aid of such reactions is deduced predominantly from data on the elastic and inelastic scattering of $\pi^{\pm}$ mesons on nuclei. The properties of the π mesons—specifically, their low mass, zero spin, and three charge states—make it possible to study charge-exchange reactions and render them a link between the short- and the long-range region of nuclear forces. At $\pi^{\pm}$-meson energies below 250 MeV, the Δ_{33} ($J^{\pi} = 3/2^{-}$, $T = 3/2$) resonance plays a dominant role in $\pi^{\pm}N$ interaction, and its presence affects pion–nucleus interaction.

Although pion scattering on nuclei has received quite an adequate study in recent decades [this became possible upon commissioning the meson factories at the Los Alamos National Laboratory (LAMPF) and at the Paul Scherrer Institute in Switzerland], measurements and theoretical calculations have been most often performed for spinless nuclei, like ^{4}He, ^{12}C, and ^{16}O. However, the advent of new technologies for manufacturing polarized targets made it possible to perform experiments with polarized target nuclei, and this quickened interest in pion scattering on nuclei of nonzero spin [1–3]. For spin-1/2 nuclei, there arises asymmetry because of the interference between ordinary and spin-flip $\pi^{\pm}N$ amplitudes. Such effects are especially pronounced for deformed nuclei—in particular, spin-flip quadrupole scattering must have a strong effect not only on differential cross sections but also on polarization observables, as was demonstrated in pion scattering on ^{6}Li [1] and ^{7}Li nuclei [2, 3].

An experiment that studied $\pi^{\pm}$-meson scattering on ^{9}Be, ^{28}Si, ^{58}Ni, and ^{208}Pb at an energy of 162 MeV was performed at LAMPF [4]. For all even–even nuclei, the angular distributions possess a pronounced diffraction structure characteristic of strong pion absorption. Only for ^{9}Be is the angular distribution different from the others, changing much more smoothly and exhibiting but small inflections in the cross section at scattering angles in the regions around $\theta \sim 60^{\circ}$ and 100°. An optical-model calculation fails to describe experimental data for ^{9}Be, but it ensures good agreement with data for the other nuclei studied in that experiment. As was hypothesized in [4], the discrepancy may be due to a nonzero spin or an unusual structure of the loosely bound nucleus ^{9}Be. The simple Woods–Saxon potential, which is usually used in the optical model, does not take into account these features. In their next study [5], the same group of authors explained the unusual behavior of the differential cross section by the additional contribution of quadrupole scattering: if the target spin is nonzero (it is $J^{\pi} = 3/2^{-}$ for ^{9}Be), all multipoles of order $2J$ must be taken into account in elastic scattering.

As a continuation of the investigation devoted to hadron scattering on a ^{9}Be nucleus and begun in [6, 7], the differential cross sections for elastic and

*e-mail: ibr@inp.kz

1063-7788/03/6602-0259$24.00

inelastic scattering of $\pi^{\pm}$ mesons were computed here and compared with experimental data from [4] and with the theoretical differential cross sections obtained in [4, 5]. The present calculation was based on the Glauber diffraction theory of multiple scattering. If the target-nucleus wave function and the elementary $\pi^{\pm}N$ amplitude are known, this theory enables one to calculate the scattering matrix element, which is related to the observed differential cross section by a simple equation. One of the first detailed calculations with $\pi^{\pm}$ mesons that was performed within Glauber theory was that of Oset and Strottman [8], who considered the case of elastic scattering on ^{12}C, ^{16}O, and ^{24}Mg nuclei and the case of inelastic scattering on ^{7}Li, ^{12}C, ^{15}N, etc., nuclei. Those authors arrived at the important conclusion that, for angles in the region $\theta < 50^{\circ}$, the description of pion scattering on the basis of Glauber theory is not inferior to that within the distorted-wave impulse approximation (DWIA). It was shown that the model is appropriate for analyzing elastic and inelastic scattering in the Δ_{33}-resonance region with a renormalized $\pi N^{\pm}$ amplitude; however, the wave functions were chosen there in the form of simple shell-model functions (which may include particle–hole components), and this was a weak point of those calculations.

In order to make a further step, one can take full advantage of Glauber theory, where it is possible to perform calculations with complicated wave functions and to allow for multiple-scattering effects. This is done in the present study by employing three-body wave functions for the ^{9}Be nucleus that were computed in [9] and by taking into account, in the calculation of differential cross sections, all multiplicities of scattering on the clusters and the nucleon in the Glauber operator Ω.

Previously, these wave functions were used in calculating the differential cross sections for elastic and inelastic proton scattering [6, 7], and the results of these calculations were in agreement with experimental data.

DESCRIPTION OF THE FORMALISM

The ^{9}Be nucleus possesses a nonzero spin, a large quadrupole moment ($Q = 53$ mb), and an anomalously low binding energy in the $(\alpha + \alpha + N)$ channel ($E_{\text{bind}} = 1.57$ MeV). The $2\alpha N$ model is the most natural for this nucleus, and it is precisely the model within which its wave functions were calculated in [9] for realistic intercluster-interaction potentials. For the ^{9}Be nucleus of total angular momentum J and its projection M_J, the wave function can be represented in the form

$$\Psi_{i,f}^{JM_J} = \varphi_{J_\alpha = T_\alpha = 0}(1,2,3,4) \times \varphi_{J_\alpha = T_\alpha = 0}(5,6,7,8)\Psi^{JM_J}(\mathbf{r},\mathbf{R}), \quad (1)$$

where $\varphi_{J_\alpha = T_\alpha = 0}$ is the alpha-particle wave function depending on the internal coordinates of the four-nucleon system. For the ground state of ^{9}Be, three components make commensurate contributions; that is,

$$\Psi^{JM_J}(\mathbf{r},\mathbf{R}) = \Psi_{\lambda=0,l=1,L=1}(\mathbf{r},\mathbf{R}) + \Psi_{\lambda=2,l=1,L=1}(\mathbf{r},\mathbf{R}) + \Psi_{\lambda=2,l=1,L=2}(\mathbf{r},\mathbf{R}), \quad (2)$$

where $\mathbf{r}$ is the coordinate of the relative motion of two alpha particles in the ^{9}Be nucleus; $\mathbf{R}$ is the coordinate of the relative motion of the neutron and the center of mass of two alpha particles there; λ and l are the orbital angular momenta conjugate to them; and L is the total orbital angular momentum of the nucleus, $\boldsymbol{\lambda} + \mathbf{l} = \mathbf{L}$. The individual components of the wave function (2) are given by

$$\Psi_{011}(\mathbf{r},\mathbf{R}) = \frac{1}{\sqrt{4\pi}} \sum_{M_L M_S} \left\langle 1M_L \frac{1}{2} M_S \,\middle|\, \frac{3}{2} M_J \right\rangle \times \delta_{mM_L} R Y_{1m}(\mathbf{R}) \chi_{\frac{1}{2}M_S} \sum_{ij} C_{ij}^{01} \exp(-\alpha_i r^2 - \beta_j R^2), \quad (3)$$

$$\Psi_{211}(\mathbf{r},\mathbf{R}) = \sum_{M_L M_S,\mu,m} \left\langle 1M_L \frac{1}{2} M_S \,\middle|\, \frac{3}{2} M_J \right\rangle \times \langle 2\mu 1m \,|1M_L\rangle r^2 Y_{2\mu}(\mathbf{r}) R Y_{1m}(\mathbf{R}) \chi_{\frac{1}{2}M_S} \times \sum_{kp} C_{kp}^{21} \exp(-\alpha_k r^2 - \beta_p R^2), \quad (4)$$

$$\Psi_{212}(\mathbf{r},\mathbf{R}) = \sum_{M_L M_S,\mu,m} \left\langle 2M_L \frac{1}{2} M_S \,\middle|\, \frac{3}{2} M_J \right\rangle \times \langle 2\mu 1m \,|2M_L\, 2M_L\rangle\, r^2 Y_{2\mu}(\mathbf{r}) R Y_{1m}(\mathbf{R}) \chi_{\frac{1}{2}M_S} \times \sum_{qt} C_{qt}^{21} \exp(-\alpha_q r^2 - \beta_t R^2), \quad (5)$$

where C_{ij}^{01}, C_{kp}^{21}, C_{qt}^{21}, α_i, β_j, α_k, β_p, α_q, and β_t are coefficients that are determined by means of a special procedure of expanding the wave functions (which are obtained in a numerical form by solving the Schrödinger equation) in multidimensional Gaussian functions and which are tabulated in [9]; μ and m are the projections of the orbital angular momenta $\lambda = 2$ and $l = 1$, respectively; and the rest of the notation is standard. The relative weights of the configurations and some static features of the ^{9}Be nucleus are quoted in the table.

The $\lambda = 2$, $l = 1$, $L = 2$ component saturates 97% of the wave function for the $J^{\pi} = 5/2^{-}$ excited state and has the same form as the component (5)

Included configurations, their relative weights in the ground-state wave function for ^{9}Be, root-mean-square charge radius $r_{\rm ch}$, quadrupole moment Q, and magnetic moment μ for the ^{9}Be nucleus from [9]

Configuration			Model 1	Model 2	Model 3
λ	l	L			
0	1	1	0.4078	0.4295	0.3876
2	1	1	0.3471	0.3554	0.3496
2	1	2	0.2131	0.1957	0.2590
				$r_{\rm ch}$, fm	
$r_{\rm ch}^{\rm exp} = 2.519(12)$ fm			2.526	2.352	2.401
				Q, mb	
$Q_{\rm exp} = 53 \pm 3$ mb			49.5	37.5	41.55
				μ, μ_0	
$\mu_{\rm exp} = -1.1778(9)\mu_0$			−0.8662	−0.9325	−0.9912

Note: Experimental data were taken from [10].

of the ground-state wave function; here, it is used in calculating the cross section for inelastic scattering.

The following intercluster-interaction potentials were used in [9] to calculate the ground-state wave function: $V_{\alpha\alpha}$, the Ali–Bodmer potential featuring repulsion at short distances; $V_{\alpha n}$, a potential involving an even–odd splitting of phase shifts (model 1); $V_{\alpha\alpha}$, a deep potential involving forbidden states that is taken in the Buck form; $V_{\alpha n}$, a potential that is analogous to that in model 1 (model 2); $V_{\alpha\alpha}$, a potential that is identical to that in model 2; $V_{\alpha n}$, the Sach–Biedenharn–Breit potential (model 3).

For the excited state, the wave function was calculated only within model 1.

Assuming that the scattering of incident protons occurs on the neutron and two alpha particles forming the ^{9}Be nucleus, one can represent the multiple-scattering operator within Glauber theory in the form

$$\Omega = \sum_{\nu=1}^{3}\omega_\nu - \sum_{\nu<\mu}^{3}\omega_\nu\omega_\mu + \omega_{\alpha_1}\omega_{\alpha_2}\omega_n, \qquad (6)$$

where $\nu = 1, 2, 3$; here, $\nu = 1$ and 2 correspond to α_1 and α_2, while $\nu = 3$ corresponds to n. The individual profile functions ω_ν are expressed in terms of the elementary $\pi^{\pm}N$ and $\pi^{\pm}\alpha$ amplitudes $f_{\pi\nu}(q)$ as

$$\omega_\nu(\boldsymbol{\rho} - \boldsymbol{\rho}_\nu) \qquad (7)$$
$$= \frac{1}{2\pi ik}\int d^2\mathbf{q}\exp(-i\mathbf{q}\cdot(\boldsymbol{\rho} - \boldsymbol{\rho}_\nu))f_{\pi\nu}(q).$$

where $\boldsymbol{\rho}$ is the impact parameter; $\boldsymbol{\rho}_\nu$ stands for the coordinates of the nucleon (or alpha particles); and

$$f_{\pi N}(q) = \frac{k\sigma_{\pi N}}{4\pi}(i + \varepsilon_{\pi N})\exp\left(-\frac{\beta_{\pi N}q^2}{2}\right), \qquad (8)$$

$$f_{\pi\alpha}(q) = \frac{k\sigma_{\pi\alpha}}{4\pi}(i + \varepsilon_{\pi\alpha}) \qquad (9)$$
$$\times\left(1 - \frac{q^2}{t_1}\right)\left(1 - \frac{q^2}{t_2}\right)\exp\left(-\frac{\beta_{\pi\alpha}q^2}{2}\right),$$

The notation for the quantities involved is identical to that in [6, 7]. The parameters of the amplitudes are given in [11].

In the above form, the elementary $\pi^{\pm}\alpha$ amplitude $f_{\pi\alpha}(q)$ was proposed in [12]. This parametrization makes it possible to describe correctly the diffraction pattern (involving three maxima and two minima in the differential cross section) of $\pi^{\pm}\alpha$ scattering over a broad region of momentum transfers that extends up to $q^2 = 0.8$ (GeV/c)^2. This is achieved by introducing the complex-valued constants t, whose real parts determine the position of the minima of the function in (9), while the imaginary parts control their depth. That use is made not only of the $\pi^{\pm}N$ but also of the $\pi^{\pm}\alpha$ amplitude enables us to take phenomenologically into account effects associated with nucleon correlations, the Fermi motion of intranuclear nucleons, and the Pauli exclusion principle, as well as spin effects, but it is of course hardly possible to include these effects in the independent-nucleon model. Moreover, the introduction of the $\pi^{\pm}\alpha$ amplitude makes it possible to calculate analytically, without restricting oneself to the approximation of single scattering on target nucleons, scattering processes of all multiplicities, whereby the accuracy of the calculation is improved. This approach was first applied to the alpha-particle nuclei ^{12}C and ^{16}O [13] and then extended to other nuclei containing an alpha particle, such as ^{6}Li and ^{7}Li [6, 7, 14].

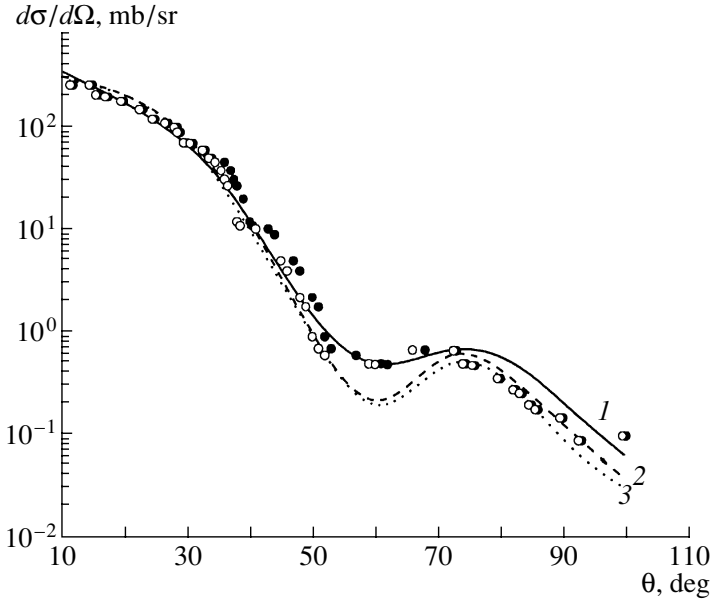

Fig. 1. Differential cross sections for elastic $\pi^{\pm}$-meson scattering on a ^{9}Be nucleus at $E_\pi = 162$ MeV for various model ^{9}Be wave functions. Curves *1*, *2*, and *3* represent the results of our calculations with the wave functions obtained on the basis of models 1, 2, and 3. Closed and open circles correspond to the scattering of π^+ and π^- mesons, respectively. The experimental data displayed in this figure and in those that follow were borrowed from [4].

Within diffraction theory, the scattering matrix element is represented in the form

$$M_{if}(\mathbf{q}) = \sum_{M_J M'_J} \frac{ik}{2\pi} \int d^2\boldsymbol{\rho} \tag{10}$$

$$\times \prod_{\nu=1}^{3} d\mathbf{r}_\nu \exp(i\mathbf{q}\cdot\boldsymbol{\rho})\delta(\mathbf{R}_9)\langle\Psi_i^{JM_J}|\Omega|\Psi_f^{JM'_J}\rangle,$$

where r_ν stands for the single-particle coordinates of the nucleon and two alpha particles in the target nucleus and $\mathbf{q}$ is the momentum transfer in the reaction being considered. By definition, we have $\mathbf{q} = \mathbf{k} - \mathbf{k}'$, where $\mathbf{k}$ and $\mathbf{k}'$ are the momenta of, respectively, the incident and the scattered $\pi^{\pm}$ meson. In the case of elastic scattering, $\mathbf{k} = \mathbf{k}'$ and $|q| = 2k\sin(\theta/2)$, with θ being the scattering angle.

Substituting the wave function in the form (2) into (10), we find that nonzero matrix elements are the following:

$$M_{if}(\mathbf{q}) = \sum_{M_J M'_J} \frac{ik}{2\pi} \int d^2\boldsymbol{\rho} d\mathbf{R} d\mathbf{r} d\mathbf{R}_9 \tag{11}$$

$$\times \exp(i\mathbf{q}\cdot\boldsymbol{\rho})\delta(\mathbf{R}_9)[\langle\Psi_{011}|\Omega|\Psi_{011}\rangle + \langle\Psi_{211}|\Omega|\Psi_{211}\rangle$$
$$+ \langle\Psi_{212}|\Omega|\Psi_{212}\rangle + \langle\Psi_{212}|\Omega|\Psi_{211}\rangle + \langle\Psi_{211}|\Omega|\Psi_{212}\rangle].$$

But if one substitutes the operator Ω in (6) into (10), the matrix element will assume the form

$$M_{if}(\mathbf{q}) = \sum_{M_J M'_J} \frac{ik}{2\pi} \int d^2\boldsymbol{\rho} \prod_{\nu=1}^{3} d\mathbf{r}_\nu \exp(i\mathbf{q}\cdot\boldsymbol{\rho}) \tag{12}$$

$$\times \delta(\mathbf{R}_9)\left\{\left\langle\Psi_i^{JM_J}\middle|\sum_\nu \omega_\nu\middle|\Psi_f^{JM'_J}\right\rangle\right.$$
$$- \left\langle\Psi_i^{JM_J}\middle|\sum_{\nu<\mu} \omega_\nu\omega_\mu\middle|\Psi_f^{JM'_J}\right\rangle$$
$$\left. + \left\langle\Psi_i^{JM_J}\middle|\,\omega_{\alpha_1}\omega_{\alpha_2}\omega_n\middle|\Psi_f^{JM'_J}\right\rangle\right\}.$$

Thus, it is necessary to calculate 15 matrix elements for different scattering multiplicities with different wave-function components. A detailed description of the technique for calculating Glauber amplitudes with multicluster-model wave functions is given in [6, 7].

The differential scattering cross section measured experimentally is proportional to the squared modulus of the matrix element:

$$\frac{d\sigma}{d\Omega} = \frac{1}{2J+1}|M_{if}(\mathbf{q})|^2. \tag{13}$$

DISCUSSION OF THE RESULTS

Here, the differential cross sections computed within diffraction theory are contrasted against experimental data obtained at LAMPF [4].

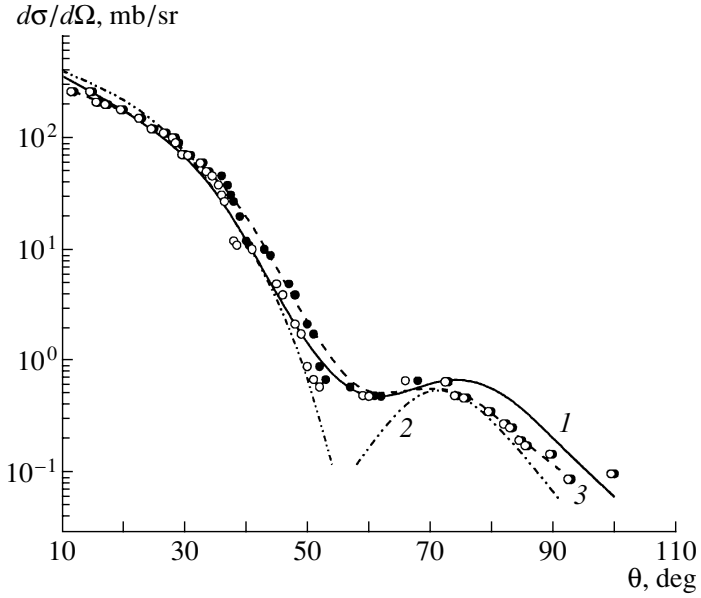

Fig. 2. Differential cross sections computed within diffraction theory along with those obtained on the basis of the optical model: (curve *1*) results identical to those represented by curve *1* in Fig. 1, (curve *2*) results of the first-order optical-model calculation allowing for only monopole scattering [4], and (curve *3*) results of the optical-model calculation allowing for quadrupole scattering [5].

The objective of this study was to assess the degree to which diffraction theory is able to describe $\pi^{\pm}$-meson scattering on a ^{9}Be nucleus and the degree to which this scattering process is sensitive to the structure of this nucleus, which is represented here by the three-body $2\alpha n$-model wave function computed with various intercluster-interaction potentials, and to the dynamics of pion–nucleus interaction—that is, to the contribution of various scattering multiplicities in the Glauber operator [expression (6)] and to the dependence of the differential cross sections on the energy of scattered $\pi^{\pm}$ mesons.

Let us consider the question of how the differential cross sections depend on the form of model wave functions. The results of a calculation that is aimed at clarifying this question for the elastic scattering of 162-MeV $\pi^{\pm}$ mesons are displayed in Fig. 1, where curves *1*, *2*, and *3* represent our results obtained with the wave functions constructed on the basis of models 1, 2, and 3. The results for all of the wave functions used faithfully reproduce the behavior of the cross section, but, in the region of the cross-section minimum, curve *1*, which was computed with the $\alpha\alpha$ potential proposed by Ali and Bodmer, lies closer to experimental data than curves *2* and *3*. The last two are close to each other, since the wave functions in models 2 and 3 differ only by the form of the αn potential (a potential featuring an even–odd splitting of phase shifts in model 2 versus the Sach–Biedenharn–Breit potential in model 3), but this potential does not have a significant effect on the wave functions and, hence, on the cross sections.

Comparing the cross sections calculated with the wave functions for the ^{9}Be nucleus that were obtained for the different $\alpha\alpha$-interaction potentials, one can conclude that that the cross section is best described with the wave function for the Ali–Bodmer potential (curve *1*). The distinctions between the wave functions computed for the different potentials are the following. The wave function for the relative motion of the two alpha particles in the Ali–Bodmer potential is more superficial because of the repulsive-core effect at short distances; it reaches a maximum value at 3 fm. The wave function in the Buck potential involving forbidden states extends deeper into the interior of the nucleus, having a node and two maxima there. Therefore, the former is expected to describe better peripheral processes (for example, elastic and inelastic scattering in the Δ_{33}-resonance region), while the latter is more appropriate for analyzing processes occurring over the entire volume of the nucleus. Here, it is worthwhile to compare the results in the table for the quadrupole moment that were obtained with the different model wave functions. The quadrupole moment is the largest in model 1, and this result is the closest to the experimental value.

In all the ensuing calculations, use will be made of the wave function based on model 1.

In Fig. 2, the results of our calculations for the differential cross sections with the wave function corresponding to model 1 (curve *1* was taken from Fig. 1)

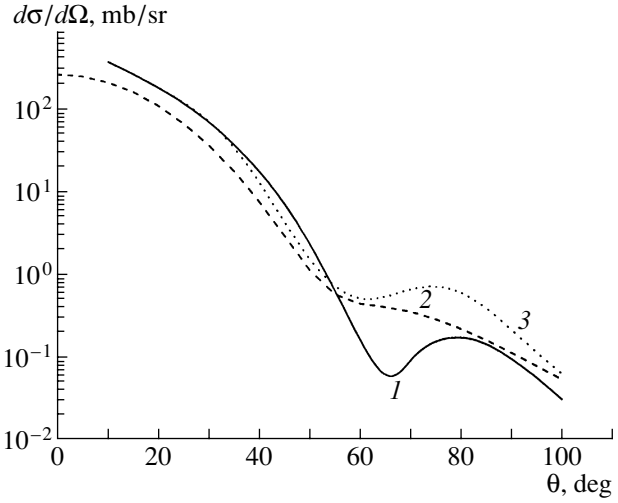

Fig. 3. Differential cross sections for the elastic scattering of $\pi^{\pm}$ mesons on (curve *1*) ^{6}Li, (curve *2*) ^{7}Li, and (curve *3*) ^{9}Be nuclei at $E_{\pi} = 180$, 164, and 162 MeV, respectively.

are contrasted against the results of optical-model calculations (curve *2* from [4] and curve *3* from [5]). In addition to measuring the differential cross sections over a wide range of angles from 10° to 100°, Zeidman *et al.* [4] calculated this quantity for the ^{9}Be, ^{28}Si, ^{58}Ni, and ^{208}Pb nuclei. While, for all even–even nuclei, the optical model, which is based on the convolution of the pion–nucleon t matrix with the nuclear density as determined from an analysis of electron scattering, yields a fairly good description of experimental data, for the ^{9}Be nucleus, the first-order optical-model calculation allowing only for monopole scattering leads to a large discrepancy with experimental data in the region $50° < \theta < 60°$, where curve *2* has a deep minimum, but there is no such minimum in experimental data. The next study of the same group of authors (see [5]) was devoted to taking into account the quadrupole-scattering contribution. The results of their calculation (curve *3*) are in excellent agreement with experimental data. Comparing curve *3* with our curve *1*, one can see that the optical model is more universal—in contrast to diffraction theory, which, in view of limitations inherent in it, is applicable only in the region of forward scattering angles, it faithfully reproduces the differential cross sections over the entire range of angles. That the strong absorption of $\pi^{\pm}$ mesons in the Δ_{33}-resonance region somewhat extends the applicability region of diffraction theory does not provide a perfect explanation of a close proximity of the theoretical and experimental results in the region $\theta > 60°$—this may be a fact of mere coincidence rather than an indication of the correctness of the method. On the other hand, the conceptual value of the optical model is plagued by the presence of a large number of adjustable parameters whose physical meaning can hardly be recognized. But in diffraction theory, there are no free parameters—all input parameters (of the elementary amplitudes and of the $\alpha\alpha$ and αn potentials) were extracted from data of independent experiments and cannot be arbitrarily varied. From Fig. 2, it can be seen that the description of experimental data in the region of forward scattering angles is of the same quality in the optical model and in diffraction theory. The distinction between curves *2* and *3* and the large quadrupole moment of the ^{9}Be nucleus clearly indicate that this nucleus is deformed.

Yet another example that demonstrates how the deformation of the target nucleus affects the differential cross sections in question is presented in Fig. 3, which displays angular distributions that are computed within diffraction theory for target nuclei ^{6}Li ($Q \sim 0$) [7], ^{7}Li ($Q = 42$ mb) [7], and ^{9}Be ($Q = 53$ mb). For the nuclei having a large quadrupole deformation, the diffraction minimum is smoothed, in contrast to what we have for the ^{6}Li nucleus, whose quadrupole deformation is negligible. Only theoretical curves are given here, but they are quite close to experimental data (for a comparison with those, the interested reader is referred to [7]).

Let us now consider in greater detail the result presented in Fig. 1. Figure 4 shows the contribution to the cross section from each of the wave-function components [see expression (2)]. Curves *1*, *2*, and *3* represent the differential cross sections computed with the components Ψ_{011}, Ψ_{211}, and Ψ_{212}, respectively, while the solid curve corresponds to their total contribution. From Fig. 4, it can be seen that, none of these partial cross sections dominates the total differential cross section, so that it is necessary to take into account all three components in order to describe relevant experimental data. In contrast to what we have for the case of the ^{6}Li nucleus, where the S wave dominates the wave function and where a modest contribution of the D wave partly fills the diffraction minimum in the cross section [7], all cross-section curves for ^{9}Be are similar to one another, the absolute values of the cross sections being proportional to the wave-function weights given in the table. Similar results were obtained in [6] for the case of proton scattering.

We now proceed to consider the case of inelastic scattering. The differential cross section for inelastic scattering accompanied by the transition of the target nucleus ^{9}Be to the $E^{*} = 2.43$ MeV, $J^{\pi} = 5/2^{-}$ state of a rotational series is shown in Fig. 5 according to the present calculations within Glauber theory (solid curve) and according to optical-model calculations (dashed curve, which was borrowed from [5]). At

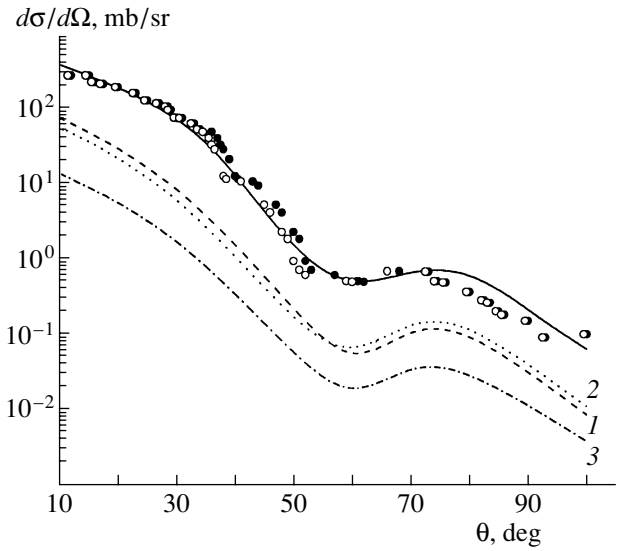

Fig. 4. Contributions to the differential cross sections from individual wave-function components. Curves *1*, *2*, and *3* represent the results of the calculations performed with the components Ψ_{011}, Ψ_{211}, and Ψ_{212}, respectively, while the solid curve corresponds to the total contribution of these components.

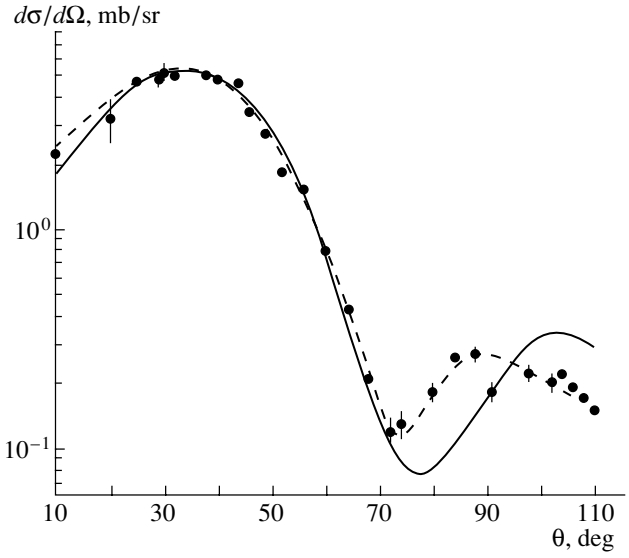

Fig. 5. Differential cross section for the inelastic scattering of 162-MeV $\pi^{\pm}$ mesons that is accompanied by the transition of the ^{9}Be to the $J^{\pi} = 5/2^{-}$ state at $E^* = 2.43$ MeV: (solid curve) results of the calculation in Glauber theory and (dashed curve) results of the optical-model calculation from [5].

small scattering angles, the two methods in question reproduce experimental data equally well; however, the minimum and the second maximum as given by the diffraction method are shifted by 5° to 10° toward larger angles with respect to their experimental positions. As has already been indicated, Glauber theory is inapplicable in this angular region, and the optical model, which is free from the limitations of diffraction theory, provides a better description here. Because of strong absorption in the Δ_{33}-resonance region, inelastic scattering is localized in the surface region of the nucleus involved, so that the application of the wave function in model 1 featuring the Ali–Bodmer potential for $\alpha\alpha$ interaction is most justified here.

The contributions to the differential cross section from various multiplicities of scattering in the Glauber operator Ω were calculated here in order to find out how the dynamics of the process affects the form of the cross section; the results are shown in Fig. 6. Curve *1* was computed upon the substitution of the first term in expression (12) into (13). This is so-called single scattering. It is worth noting here that, in the present approach, the alpha particle is assumed to be structureless, so that the incident $\pi^{\pm}$ meson interacts with it as with a discrete unit (rather than with four nucleons forming this alpha particle). The use of this approximation is compensated by taking the $\pi^{\pm}\alpha$ amplitude in a form [see expression (9)] that describes elastic $\pi^{\pm}\alpha$ scattering over a broad range of momentum transfers. From Fig. 6, it can be seen that single scattering is dominant in the region of small angles ($\theta < 50°$). Curve *2* results from substituting the second term in expression (12) into (13). These is so-called double rescattering—that is, collisions of two alpha particles with each other and of each alpha particle with a valence nucleon. In the region of small angles, the contribution of such collisions is an order of magnitude less than the contribution of single collisions, but, with increasing scattering angle, higher multiplicities decrease more slowly than the contribution of single scattering; as a result, double scattering makes a dominant contribution to the total differential cross section (curve *4*, which was computed with allowance for all scattering multiplicities) for $\theta > 60°$. This is because, with increasing θ, the momentum transfer q also increases—that is, a particle can penetrate deeper into the interior of the nucleus, where the density of nucleons is higher, which increases the probability of multiple collisions. For example, the momentum-transfer values at $\theta = 10°$ and 70° for $E_{\pi} = 162$ MeV are $q =$ 44 and 291 MeV/c, respectively. The region where the values represented by the curves in question are commensurate is the region of inflection in the total differential cross section, as is demonstrated by curve *4*, which corresponds to taking into account all terms of (12) in (13). A deep minimum does not arise there, since, in ^{9}Be, strong quadrupole scattering smooths the minimum that is associated with

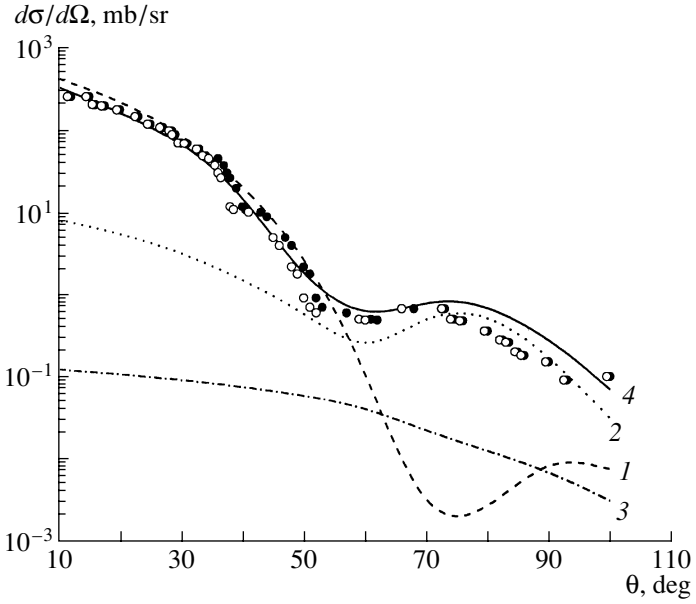

Fig. 6. Contributions to the differential cross section from various multiplicities of scattering in the Glauber operator Ω. Curves *1*, *2*, and *3* represent the results of the calculations taking into account single, double, and triple collisions, respectively, while curve *4* corresponds to the sum of their contributions.

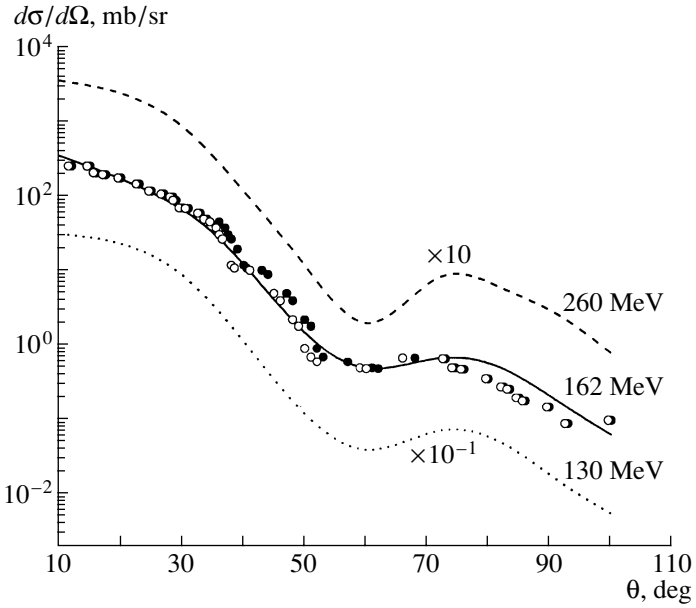

Fig. 7. Differential cross section for various energies of scattered $\pi^{\pm}$ mesons in the resonance region (the energy values are indicated on the curves).

the interference between the amplitudes for single and double scattering.

Curve *3*, which represents triple rescattering, is obtained upon substituting the third term of (12) into (13). Its contribution at $\theta = 0^\circ$ is three orders of magnitude less that the contribution of single collisions, and it has virtually no effect on the behavior of the differential cross sections over the entire angular range.

At a few values of the energy of scattered $\pi^{\pm}$ mesons, Fig. 7 illustrates the behavior of differential cross sections in the resonance region. In order to avoid the overlap of the curves in Fig. 7, the values corresponding to the dashed ($E_\pi = 260$ MeV) and dotted ($E_\pi = 130$ MeV) curves were multiplied by

10 and 10^{-1}, respectively. From this figure, it can be seen, that the minimum occurs at $\theta \approx 60^{\circ}$, not undergoing a shift toward smaller angles with increasing energy, in contrast to what was found for proton scattering [7]. But in the case of $\pi^{\pm}$-meson scattering in the Δ_{33}-resonance region, the minimum is stably localized at 85° for ^{3}He [15], 75° for ^{4}He [16], and 60° for ^{6}Li [14]. This is because the Δ_{33} resonance is dominant here, other effects being insignificant in this region.

CONCLUSIONS

It has been shown that Glauber diffraction multiple-scattering theory, used together with the wave function in the $2\alpha N$ three-body model, describes adequately the behavior of the differential cross sections for elastic and inelastic scattering in the region of forward scattering angles. The use of both the $\pi^{\pm}N$ and the $\pi^{\pm}\alpha$ elementary amplitude makes its possible to calculate analytically the scattering-matrix element, whereby one avoids spoiling the accuracy, which is what occurs in truncating the multiple-scattering series and in numerically calculating the multidimentional integrals involved. From the results of calculations performed by other authors, it follows that the description of experimental data within Glauber theory is not inferior to the description on the basis of the optical model.

The present investigation of nuclear-structure and dynamical effects has led to the following conclusions:

(i) The differential cross section computed with the wave function in the Ali–Bodmer potential for $\alpha\alpha$ interaction describes correctly the angular distribution over a wider angular range than that obtained with the wave function in the Buck potential. Since $\pi^{\pm}$-meson scattering occurs predominantly in the surface region of the target nucleus, it is better described by a wave function that is localized in the surface region and which has a more extended asymptotic tail.

(ii) The calculation of the contributions to the differential cross section from various wave-function components has revealed that, if the weights of these components are commensurate, none of these can be disregarded. All of them contribute to the differential cross section, and only their sum faithfully reproduces the absolute cross-section value.

(iii) In order to describe satisfactorily differential cross sections over a wide range of angles, it is necessary to take into account all multiplicities of scattering on target nucleons or to employ a realistic $\pi^{\pm}\alpha$ amplitude if the cluster being considered is assumed to be structureless, as is done here for alpha-particle clusters.

(iv) As the energy of $\pi^{\pm}$ mesons scattered in the Δ_{33}-resonance region is increased, the minimum in the differential cross section is not shifted toward the region of smaller scattering angles, in contrast to what occurs in the case of proton scattering; instead, it is localized at $\theta \approx 60^{\circ}$, which is explained by the presence of a broad resonance and by the absence of other open channels below the threshold for $\pi^{\pm}$-meson production.

REFERENCES

1. R. Meier *et al.*, Phys. Rev. C **42**, 2222 (1990); S. Ritt, E.T. Boschitz, R. Meier, *et al.*, Phys. Rev. C **43**, 745 (1991); P. B. Siegel and W. R. Gibbs, Phys. Rev. C **48**, 1939 (1993).
2. R. Tacik *et al.*, Phys. Rev. Lett. **63**, 1784 (1989); R. Meier, E.T. Boschitz, B. Brinkmoller, *et al.*, Phys. Rev. C **49**, 320 (1994).
3. Naoko Nose, Kenji Kume, and Shinichiro Yamaguchi, Phys. Rev. C **50**, 321 (1994).
4. B. Zeidman, C. Olmer, D. F. Geesaman, *et al.*, Phys. Rev. Lett. **40**, 1539 (1978).
5. D. F. Geesaman, C. Olmer, B. Zeidman, *et al.*, Phys. Rev. C **18**, 2223 (1978).
6. M. A. Zhusupov and E. T. Ibraeva, Izv. Akad. Nauk, Ser. Fiz. **61**, 2182 (1997); Yad. Fiz. **61**, 51 (1998) [Phys. At. Nucl. **61**, 46 (1998)].
7. M. A. Zhusupov and E. T. Ibraeva, Fiz. Élem. Chastits At. Yadra **31**, 1427 (2000) [Phys. Part. Nucl. **31**, 723 (2000)].
8. E. Oset and D. Strottman, Nucl. Phys. A **377**, 297 (1982).
9. V. I. Kukulin, V. N. Pomerantsev, G. G. Ryzhikh, *et al.*, Izv. Akad. Nauk, Ser. Fiz. **57** (1), 170 (1993); V. T. Voronchev, V. I. Kukulin, V. N. Pomerantsev, *et al.*, Yad. Fiz. **57**, 1964 (1994) [Phys. At. Nucl. **57**, 1890 (1994)]; V. T. Voronchev, V. I. Kukulin, and V. N. Pomerantsev, Few-Body Syst. **18**, 191 (1995).
10. F. Ajzenberg-Selove, Nucl. Phys. A **490**, 1 (1988).
11. E. T. Ibraeva, B. A. Prmantaeva, and A. V. Sanfirova, Available from KazGosINTI, No. 8599-Ka99 (1999).
12. F. Binon, P. Duteil, M. Gouanere, *et al.*, Nucl. Phys. A **298**, 499 (1978).
13. K. A. Kabir, M. Silver, and N. Austern, Phys. Rev. C **27**, 2104 (1983); Li Qing-Run, Nucl. Phys. A **415**, 445 (1984).
14. M. A. Zhusupov, E. T. Ibraeva, and A. Yu. Zaĭkin, Izv. Akad. Nauk, Ser. Fiz. **65**, 50 (2001); M. A. Zhusupov, E. T. Ibraeva, and B. A. Prmantayeva, in *Proceedings of the I Eurasia Conference on Nuclear Science and Its Application, Poster Presentation Buildilier, Ankara, Turkey, 2001,* Vol. 2, p. 866.
15. N. Nagaoka and K. Ohta, Phys. Rev. C **33**, 1393 (1986).
16. B. Brinkmoller, C. L. Blilie, D. Dehnhard, *et al.*, Phys. Rev. C **44**, 2031 (1991).

Translated by A. Isaakyan

Physics of Atomic Nuclei, Vol. 66, No. 2, 2003, pp. 268–273. Translated from Yadernaya Fizika, Vol. 66, No. 2, 2003, pp. 293–298.

ELEMENTARY PARTICLES AND FIELDS
Experiment

Background of External γ Radiation in the Proportional Counters of the SAGE Experiment

V. N. Gavrin and V. V. Gorbachev

Institute for Nuclear Research, Russian Academy of Sciences, pr. Shestidesyatiletiya Oktyabrya 7a, Moscow, 117312 Russia

Received February 7, 2002

Abstract—The effect of external γ radiation on the process of counting ^{71}Ge decays in the proportional counters of the SAGE experiment measuring the solar-neutrino flux is considered. The systematic uncertainty in the SAGE result due to radon decays inside the air volume surrounding the counters is estimated. The background counting rate in the proportional counters that is caused by γ radiation from the enclosing shield is also determined. © *2003 MAIK "Nauka/Interperiodica".*

1. INTRODUCTION

Proportional counters are among the basic elements of radiochemical detectors used in solar-neutrino experiments [Davis chloride detector, SAGE and GNO (GALLEX) gallium detectors]. These counters make it possible to determine the number of atoms produced owing to neutrino interaction with target matter [1]. The number of background pulses in the counters affects the statistical and systematic uncertainties in the results of such measurements. The decays of radon (^{222}Rn) and of its daughter elements in the counting gas [2] and in the ambient-air volume, as well as decays of elements belonging to the natural radioactive sequences in counter materials [3] and in the enclosing passive (and active) shields from external radiation, make the main contribution to the background in proportional counters. In this article, we describe the response of the proportional counters used in the SAGE experiment to γ radiation produced in shield materials and in the air volume surrounding the counters.

Since 1990, the Russian–American SAGE experiment has been measuring the solar-neutrino-capture rate in a target containing about 60 tons of metallic gallium. Neutrino interaction with the ^{71}Ga isotope induces the reaction $^{71}\mathrm{Ga}(\nu_e, e^-)^{71}\mathrm{Ge}$. At the end of each exposure run (1–1.5 months), the product ^{71}Ge atoms are extracted from the target by means of a special chemical procedure; are converted into the gaseous state of GeH_4 (germane); and are placed into a proportional counter, where the decays of these atoms are observed for 5 to 6 months. A detailed account of the experiment, including the description of the chemical procedures for extracting germanium from the gallium target, the process of counting ^{71}Ge decays, and data analysis, is given in [4].

Prior to determining the effect of external γ radiation on the process of counting ^{71}Ge decays in the proportional counters, we will briefly consider the design of the counters and of the system for counting ^{71}Ge decays.

2. PROPORTIONAL COUNTERS AND SYSTEM FOR COUNTING ^{71}Ge DECAYS

To record ^{71}Ge decays, the SAGE experiment employs cylindrical proportional counters from quartz. The counter cathode is fabricated from iron. It has an inner diameter of 0.4 cm, a length of 5 cm, and a wall thickness of 0.1 cm. The anode is a tungsten wire 10–12 μm in diameter. The counting gas is a mixture of xenon and germane (GeH_4) at a pressure of about 1 atm. Germane makes up to 30% of the gas volume and operates as a quenching admixture. The decay of ^{71}Ge ($T_{1/2} = 11.4$ d) proceeds via electron capture followed by the emission of 10.4-, 1.2-, and 0.1-keV Auger electrons (K, L, and M modes, respectively). Short tracks of these electrons in the counting gas generate pulses of short rise time at the proportional-counter output (so-called pointlike events differing from extended ones—that is, those that are characterized by long tracks).

The system counting ^{71}Ge decays indicates the time of pulse arrival; a digital oscilloscope records the shape of each pulse, and this information is then used to assess the energy and the pulse rise time. An active shield based on a NaI crystal selects pulses accompanied by γ radiation. The dynamical range of energy measurements between 0.3 and 16 keV allows

1063-7788/03/6602-0268$24.00

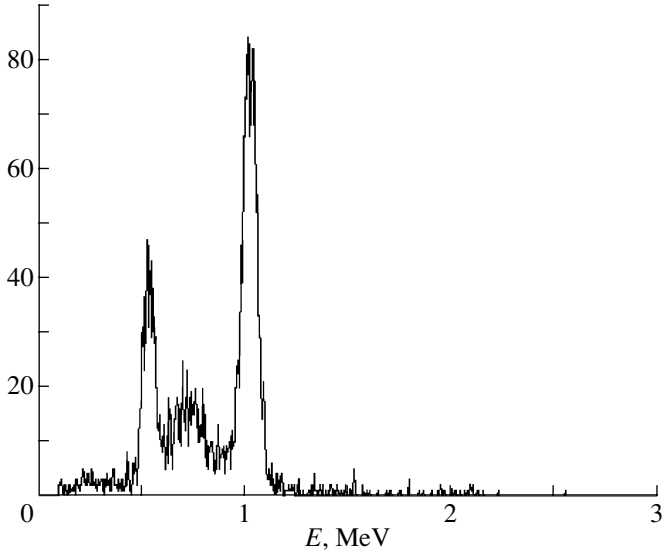

Fig. 1. Spectrum of pulses in the NaI detector that coincide with events in the proportional counter where ^{68}Ge decays in the counting gas.

one to record the K and L modes of ^{71}Ge decay. Thus, events appearing as candidates for ^{71}Ge decay are selected in accordance with three signatures: (i) the pulse height falls within the intervals (windows) of the K or the L peak; (ii) the pulse rise time is short (pointlike event); and (iii) there is no accompanying γ radiation.

A time analysis of events selected in this way is performed upon the completion of counting ^{71}Ge decays in the proportional counter. In this analysis, the sequence of pulses is represented as a superposition of the number of ^{71}Ge decays, which decreases exponentially with time, and an invariable background [5].

A NaI detector records photons of energy up to 3 MeV. The spectra of NaI pulses that do not coincide with pulses of the proportional counter are recorded every 30 min (1024 analog-to-digital-converter channels). The NaI crystal is taken in the form of a cylinder 22.9 cm in diameter and 22.9 cm in height. It has a well of diameter 8.9 cm and height 14.5 cm, where the proportional counters (eight channels) are arranged in a vertical position symmetrically along a circle of radius about 2.5 cm. The upper edge of the counter cathodes is at a distance of 2 to 3 cm from the upper edge of the well.

3. MEASUREMENTS

In order to determine the effect of the external γ background on the process of counting ^{71}Ge decays, we measured the efficiency with which photons of different energies were detected in the proportional counter. In the measurements, which were performed under conditions identical to those of counting the decays of ^{71}Ge produced in the course of solar exposures, use was made of ^{68}Ge and ^{40}K monochromatic γ sources ($E_\gamma = 511$ keV and 1460 keV, respectively).

The radiation sources were placed within the shield near the counters. As one of the radiation sources, we took a proportional counter filled with a gaseous mixture containing the ^{68}Ge isotope (GeH_4) used for calibration in the recording system [6]. The second (^{40}K) radiation source in the form of the KCl salt ($m = 1.00 \pm 0.01$ g) was uniformly distributed in a flask reproducing the dimensions of the proportional-counter cathode. This flask was placed at the site of one of the counters within the shield. Thus, geometric efficiencies for the two sources were identical.

3.1. Intensity of the Sources

In the measurements reported here, it was important to know the absolute values of the intensity of the γ-radiation sources used. The intensity of the $E_\gamma = 1460$ keV source was obtained from reference data on the average content of the ^{40}K isotope in natural potassium, $p_\gamma(1460\ \text{keV}) = 1.71\ \text{s}^{-1}$, and was then confirmed by measurements with the NaI detector. For ^{68}Ge γ radiation (511 keV), the counting rate measured by the NaI detector appeared to be $p_1 = 0.29 \pm 0.01\ \text{s}^{-1}$. The decay of ^{68}Ge via electron capture results in the formation of ^{68}Ga ($T_{1/2} = 271$ d), which in turn is converted into stable ^{68}Zn ($T_{1/2} = 68.3$ min) via electron capture (10% of cases) and via β^+ decay (90% of cases). In the sequence of

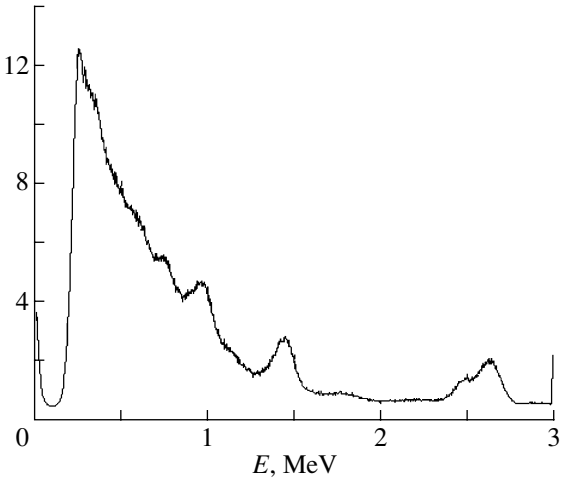

Fig. 2. Spectrum of pulses in the NaI detector according to solar-run measurements (actually, the spectrum is recorded into a separate file every 30 min, but we displayed the result obtained by averaging the measured spectra over a few days of the measurements).

^{68}Ge decay, photons are emitted almost exclusively in the β^+ decay of ^{68}Ga (pairs of annihilation quanta), but about 3.3% of them are due to nuclear radiation of different energies. The efficiency with which the NaI detector detects 511-keV photons emitted from the region of the proportional counter located at a distance of 2.0–2.8 cm from the central axis of the NaI crystal is $\varepsilon_1 = 0.81$. This value, obtained by the Monte Carlo method, is confirmed by the intensity ratio in the observed spectra of NaI both in the spectra of coincidences with pulses from the counter containing ^{68}Ge (during the calibration tests) and in the NaI spectrum recorded upon switching off this counter. If the probabilities of recording annihilation photons (one of the pair, ε_{12}, and both of them, ε_2) are expressed in terms of the efficiency of recording single 511-keV photons (ε_1) as $\varepsilon_{12} = 2\varepsilon_1(1-\varepsilon_1)$ and $\varepsilon_2 = \varepsilon_1^2$, the ratio of the intensities at the 511- and 1022-keV peaks (Fig. 1) will be

$$A \equiv \frac{I_{1022}}{I_{511}} = \frac{\varepsilon_2}{\varepsilon_{12}} = \frac{\varepsilon_1}{2(1-\varepsilon_1)},$$
$$\varepsilon_1 = 2A/(1+2A).$$

A value in the range $A = 2.10$–2.46 was obtained in the measurements, and this corresponds to $\varepsilon_1 =$ 81–83%. When a photon pair is emitted, the NaI efficiency increases up to $\varepsilon_{2\gamma} = 96.4\%$.

The measurements with ^{68}Ge took about three months. The source intensity changed by 20% over this period. Thus, the γ activity of the source in the middle of the measurement period was $p_\gamma(511\ \text{keV}) = p_1\dfrac{1.10}{\varepsilon_{2\gamma}} = 0.33 \pm 0.01\ \text{s}^{-1}$ (p_1 was determined at the end of the measurements). The number of photons coming from the source to the counter region (geometric efficiency ε_g) varied between 1.8×10^{-3} and 8.6×10^{-3} for different channels, depending on the relative positions of the counter and the source.

3.2. Results

The rate at which the counting of pulses from the γ source of intensity p_γ occurs in a proportional counter is $p = p_\gamma \varepsilon_g \varepsilon_0$, where ε_g is the geometric efficiency and ε_0 is the sought probability of recording a photon that reached the proportional-counter region. In the measurements, use was made of five to seven counters, some of these being periodically switched off for technical reasons. For different counters, the values of p were determined by the difference of the counting rates in the presence of the source and in the ordinary (background) mode. Each time after closing the shield (see Subsection 4.1), a period of 2.6 h was eliminated from our analysis; the first 35 days after installing the counters (a period within which ^{71}Ge extracted from the gallium target after the solar exposure decays) was also eliminated. For each counter, the time of background measurements was more than 60 days.

As a result, the probability of photon detection by the counter appeared to be $\varepsilon_0(1460) = (3.3 \pm 0.4)\%$ for the $E = 1460$ keV source. The probability that a photon is recorded as that which is associated with the L or the K peak, with the pulse being selected for a ^{71}Ge-decay analysis, is $\varepsilon_L(1460) = (5.4 \pm 5.2) \times 10^{-4}$ or $\varepsilon_K(1460) = (4.1 \pm 3.7) \times 10^{-4}$, respectively.

The value of $\varepsilon_0(511) = (1.2 \pm 0.3)\%$ was obtained for the $E = 511$ keV source. However, ε_L and ε_K could not be calculated directly in this case, since pair photons emitted by the source prevented a determination of the selection efficiency by using the coincidence with NaI pulses. In view of this, the probabilities were estimated under the assumption that the selection by NaI for $E_\gamma = 511$ keV is identical to that for $E_\gamma = 1460$ keV. Without allowance for the selection by NaI, the efficiencies of detection at the L and K peaks for $E_\gamma = 511$ keV are $\varepsilon_{L1}(511) = (13.1 \pm 8.5) \times 10^{-4}$ and $\varepsilon_{K1}(511) = (5.4 \pm 4.6) \times 10^{-4}$, respectively. It follows that, if the selection by NaI for $E = 511$ keV is identical to that for 1460 keV, the probabilities that a photon is recorded, with the pulse passing all selections for the L and K peaks, are $\varepsilon_L(511) = (2.6 \pm 1.7) \times 10^{-4}$ and $\varepsilon_K(511) = (2.1 \pm 1.8) \times 10^{-4}$.

Results of a Monte Carlo calculation for the probability that photons emitted in NaI come into the counter

E, keV	50	100	200	300	400	500	600	800	1000	1500	2000	3000
ε_g, 10^{-4}	0	0.4	1.5	3.5	4.1	4.6	5.7	6.6	7.2	8.2	9.6	10.0

4. SOURCES OF γ RADIATION

In the course of solar runs, the materials of the shield (the NaI crystal first of all) and radon coming into the volume within the shield from ambient air are sources of γ radiation inside the shield. Let us estimate the contribution of these sources to the proportional-counter counting rate.

4.1. External Radon

In the course of counting, evaporating liquid nitrogen is blown through the internal cavity of the shield, where the counters are installed, and radon is displaced from the cavity by nitrogen. But during periodic calibrations (which are usually performed every two weeks), radon penetrates into the cavity volume, and its decay products precipitate onto the inner surface of the shield. After the shield is closed, the NaI counting rate in the region of the ^{214}Pb and ^{214}Bi γ peaks decreases, following approximately an exponential law (with $T_{1/2} = 43.7$ min for ^{214}Bi, this half-life period being in good agreement with its calculated value). According to the procedure adopted in the SAGE experiment for selecting events treated as candidates for ^{71}Ge decay, all events that come within a period of 2.6 h after closing the shield are rejected. Over this period, the radiation intensity decreases to 8.4% of the initial level and the number of ^{214}Bi decays, which cause additional counting in the counter, does not exceed 100. Assuming that, within the photon-energy range observed in NaI (up to 3 MeV), there is no abrupt variations in the probability of photon detection in the counter, we will use for further estimates, the value of $\varepsilon_0 = 1.2\%$ for $E_\gamma < 1000$ keV and the value of $\varepsilon_0 = 3.3\%$ for $E_\gamma > 1000$ keV, which were obtained for $E_\gamma = 511$ and 1460 keV, respectively. It follows that, every time after closing the shield, the additional counting rate in the counter from ^{214}Pb and ^{214}Bi decays[1)] is $N_g \sim 100\varepsilon_s \sum_i (\varepsilon_0(E_i)\varepsilon_{\gamma i}) = 0.018$ pulses, where $\varepsilon_{\gamma i}$ is the yield of the γ line at energy E_i in the ^{214}Pb and ^{214}Bi spectra and $\varepsilon_s = 0.59\%$ is the geometric efficiency with which a photon emitted from the inner surface of the shield finds its way into the counter (its value was obtained by the Monte Carlo method). The total number of additional counts at the L and K peaks will be about 6.6×10^{-4} pulses.

An analysis performed with the ^{71}Ge decay constant over the times of closing the shield revealed that, in each solar run, pulses selected after closing the shield 3.2 ± 0.9 times are associated with ^{71}Ge decays. Considering that the mean number of pulses at the L and K peaks of ^{71}Ge is about 5 and that the measured rate of neutrino capture in the gallium target is 77 SNU[2)] [7], we can therefore estimate the systematic uncertainty due to the external-radon effect in the SAGE measurements at $6.6 \times 10^{-4} \times 3.2 = 2 \times 10^{-3}$ pulses per run of solar-neutrino measurements or $(2 \times 10^{-3}/5) \times 77$ SNU $= 0.03$ SNU.

4.2. Radiation of Shield Materials

The activity of shield materials—first of all, of the NaI crystal—is yet another source of the γ background within the shield. If the radiation of the copper shield around NaI is neglected, upper limits on the content of radioactive elements in the NaI crystal can be determined by measuring the intensity of the peaks in the spectrum of NaI pulses. With allowance for the probability that photons produced uniformly over the NaI volume will be absorbed in the crystal, upper limits on the content of decaying elements in the NaI material can be estimated by using the spectrum of events in the NaI detector. The results are 6.8×10^{-11} g^{40}K/g for ^{40}K (or 5.8×10^{-7} gK/g), 2.2×10^{-9} gTh/g for ^{232}Th, and 9.6×10^{-11} gU/g for ^{238}U (or 3.9×10^{-17} gRa/g for ^{226}Ra).

The geometric dimensions of the crystal and the arrangement of the counters determine the probability that photons produced within NaI enter the counter (see table).

Thus, we find that the counting rate in the proportional counter due to NaI γ radiation is $p_1 = \sum_i p_i \varepsilon_0(E_i)\varepsilon_{gi}$, where summation is performed over all channels of the NaI spectrum (p_i is the counting rate in the ith channel—see Fig. 2). Here, we disregard the distinction between the spectrum recorded

[1)] The amount of ^{214}Pb is less than the amount of ^{214}Bi, but we added the former in order to obtain a more reliable estimate of the upper limit on the sought uncertainty.

[2)] SNU corresponds to one neutrino capture per 10^{36} target atoms per second.

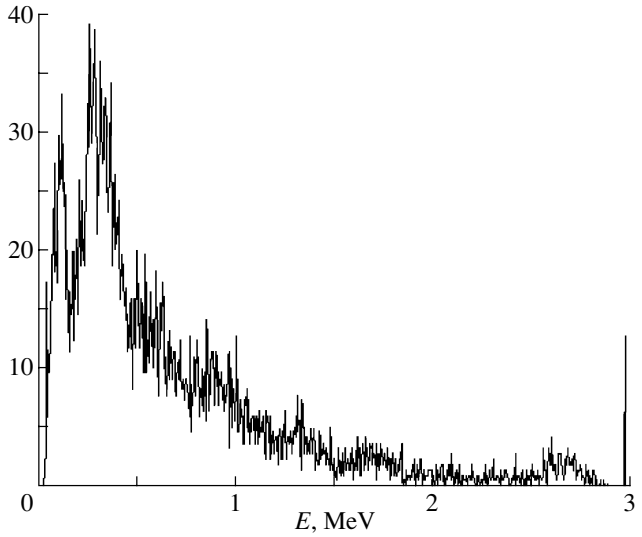

Fig. 3. Spectrum of pulses in the NaI detector that coincide with events in the proportional counters during solar-run measurements.

by the NaI detector and the photon spectrum near the counters. We take the efficiencies ε_g from the table and, in just the same way as for external radon (see Subsection 4.1), use the ε_0 values of 1.2% for $E_\gamma < 1000$ keV and 3.3% for $E_\gamma > 1000$ keV. The resulting counting rate in the proportional counter from NaI γ radiation is $p_1 = 1.3 \pm 0.5$ d^{-1}, which is more than half of the mean background counting rate (about 2.3 ± 0.5 d^{-1}).

The spectrum of NaI pulses coinciding with counter pulses that was obtained in the conventional operation mode of the recording system (without additional γ sources; see Fig. 3) exhibits the only peak at 2614 keV, which is due to nonscattered photons from the decay of ^{208}Tl belonging to the ^{232}Th sequence in counter materials [3]. The energy of these photons is higher than the energies of all other photons occurring in natural radioactive sequences. Other peaks, which are associated with nonscattered photons from the β decays of elements in source materials, are masked by a heavy background of the Compton scattering of photons produced outside the counters. This confirms qualitatively a large value obtained for the pulse counting rate in the counter due to γ radiation external to the counters.

The frequency at which events associated with NaI γ radiation that are selected according to the ^{71}Ge criteria appear is 0.02 ± 0.01 d^{-1} at the L and K peaks—that is, 2 to 3 events at each peak per run (within the actual observation time of 120–130 days). This affects the statistical uncertainty in the measurements of the number of ^{71}Ge decays, not causing, however, a systematic bias of the result.

Thus, we see that, although the majority of background events in the counter are due to external γ radiation, the criteria used to select ^{71}Ge pulses discriminate these events fairly well. At a mean counting rate of about 0.07 d^{-1} for background events at the L and K peaks in solar runs, the bulk of the background seems to be determined by the α radiation of elements that decay in counter materials [3]. Therefore, the background conditions can be somewhat improved upon replacing the NaI detector by a purer and more secure copper shield, but this will inevitably lead to losing important information about the nature of background processes.

5. CONCLUSION

The present study, performed to clarify the γ-radiation effect on the counting of ^{71}Ge decays in the proportional counters of the SAGE experiment, has made it possible to assess the systematic uncertainty in the measurement of the solar-neutrino flux due to radon decay in the air volume around the counters. The result is 0.03 SNU (0.04%).

In addition, we have determined the contribution to the constant background counting rate from photons produced in the decay of elements belonging to natural radioactive sequences in shield materials (NaI crystal). Although photons generate the majority of background pulses, the event-selection procedure adopted in the SAGE experiment reduces considerably the corresponding background counting rate.

ACKNOWLEDGMENTS

We are grateful to our colleagues involved in the SAGE experiment for their stimulating interest in this study and enlightening discussions.

REFERENCES

1. J. N. Bahcall, *Neutrino Astrophysics* (Cambridge Univ. Press, Cambridge, 1989; Mir, Moscow, 1993).
2. V. N. Gavrin, V. V. Gorbachev, and I. N. Mirmov, Yad. Fiz. **65**, 875 (2002) [Phys. At. Nucl. **65**, 843 (2002)].
3. V. V. Gorbachev, T. V. Ibragimova, and A. V. Kalikhov, in *Proceedings of the X International School: Particles and Cosmology, Baksan, Russia, 1999,* p. 81.
4. J. N. Abdurashitov *et al.*, Phys. Rev. C **60**, 055801 (1999).
5. B. T. Cleveland, Nucl. Instrum. Methods **214**, 451 (1983).
6. V. N. Gavrin, V. V. Gorbachev, T. V. Ibragimova, and B. T. Cleveland, Yad. Fiz. **65**, 1309 (2002) [Phys. At. Nucl. **65**, 1276 (2002)].
7. V. N. Gavrin, Nucl. Phys. B (Proc. Suppl.) **91**, 36 (2001).

Translated by E. Kozlovskiĭ

Physics of Atomic Nuclei, Vol. 66, No. 2, 2003, pp. 274–280. Translated from Yadernaya Fizika, Vol. 66, No. 2, 2003, pp. 299–305.

ELEMENTARY PARTICLES AND FIELDS
Theory

Deuteron Photodisintegration within the Bethe–Salpeter Formalism: Effects of Negative-Energy Components

K. Yu. Kazakov* **and D. V. Shulga****

Far East State University, ul. Sukhanova 8, Vladivostok, 690600 Russia

Received August 6, 2001; in final form, December 21, 2001

Abstract—Relativistic covariance requires that an analysis of the reaction $\gamma d \to pn$ within a field-theoretical model of the nucleon–nucleon interaction involve negative-energy states. Relativistic effects and the contributions of negative-energy states in the Bethe–Salpeter amplitude to the differential cross section, the asymmetry of linearly polarized photons, and tensor asymmetries of the target deuteron are estimated on the basis of the Bethe–Salpeter formalism as applied to describing the interaction of an electromagnetic field with a two-nucleon system. It is found that the contribution of such states becomes sizable with increasing photon energy, but that it does not change the general qualitative behavior of observables as functions of angles. © *2003 MAIK "Nauka/Interperiodica".*

1. INTRODUCTION

At present, investigation of deuteron-photodisintegration observables that are associated with beam or target polarization is of interest in two respects. At photon energies in the region around the threshold for the production of a pion or a $\Delta(1232)$ resonance, investigation of the reaction in question makes it possible to explore the role of the short-range component of the tensor force of the nucleon–nucleon (NN) interaction. For example, the effect that the tensor force as calculated on the basis of various models exerts on the asymmetry Σ^l of linearly polarized photons was considered in [1]. Here, an important aspect is that of taking into account $N\Delta$ interaction, since the interference between meson-exchange and delta-isobar currents affects the angular and energy distributions of the beam asymmetry [2, 3]. On the other hand, experiments at the Yerevan Physics Institute [4] and at TJNAL [5] (see also [6]) were devoted to measuring the differential cross section and beam asymmetry in the region of energies that are commensurate with the nucleon rest energy. In that case, phenomena were sought that are due to the quark structure of the nucleus—these may include the scaling property of the cross section and the law of hadron-helicity conservation. Approaches underlying inquiries into the question of the possible origin of the scaling property and its violation were presented in [7–9]. A key problem in these investigations is that of whether the scaling property is a phenomenon peculiar precisely to perturbative QCD or whether alternative mechanisms are possible—for example, those that arise within a nonperturbative approach based on the model of quark–gluon strings [7, 8] or within a Lorentz- and gauge-invariant approach allowing for the internal structure of the deuteron in a theory involving nucleons and mesons [9]. As to observables measured in experiments with a target that has a tensor polarization, they have received the least extensive study among all polarization observables of deuteron photodisintegration. There are no precision experimental data on the asymmetry T_{20} at present, and the relevant theoretical analysis was performed within an approach that is essentially nonrelativistic [10].

In the recent studies reported in [11, 12], the contributions of relativistic effects to the differential cross section for deuteron photodisintegration in the photon-energy region $E_\gamma < 1$ GeV were investigated on the basis of the Bethe–Salpeter formalism. These effects stem from taking into account Lorentz boosts for ${}^3S_1^{++}$–${}^3D_1^{++}$ positive-energy states in the deuteron Bethe–Salpeter amplitude. However, relativistic covariance requires that the partial-wave expansion of the amplitude be performed with allowance for negative-energy spinor states satisfying the Dirac equation. Although the integrated contribution from such states of $L = 0$ and 2, as well as of $L = 1$ (P waves), to the absolute normalization exceeds 0.1% only slightly, their interference with positive-energy S- and D-wave components leads to a noticeable effect. For example, negative-energy states must be taken into consideration even in analyzing the deuteron quadrupole and magnetic moments [13]. By numerically calculating the deuteron magnetic moment, it was shown in [14] that the interference

*e-mail: kazakovk@ifit.phys.dvgu.ru
**e-mail: denis@ifit.phys.dvgu.ru

between the S- and P-wave components contributes up to 50% to the total relativistic effect. By applying the procedure of a relativistic reduction of the matrix elements of the electromagnetic-current operator in the deuteron-photodisintegration reaction at the threshold, it was additionally found that, within the Bethe–Salpeter approach, terms corresponding to the so-called pair current are formed by the contributions of the P-wave components of the deuteron Bethe–Salpeter amplitude [15].

The objective of the present study is to analyze the role that relativistic effects and negative-energy spinor states in the Bethe–Salpeter amplitude play in deuteron photodisintegration at photon energies in the region $E_\gamma < 1$ GeV. We consider polarization observables, which are highly sensitive, as a rule, to various ingredients of the theory used. A relativistic description of the deuteron bound state is implemented on the basis of the Bethe–Salpeter equation for a two-nucleon system with a realistic one-boson-exchange kernel, this equation generating negative-energy components of the deuteron Bethe–Salpeter amplitude. In view of limitations of a purely computational character, our analysis is performed without taking into account final-state interaction and two-body electromagnetic-current operators. In a future publication, we will consider these important effects within a Lorentz-invariant Bethe–Salpeter approach.

2. BRIEF SURVEY OF THE THEORY

In the c.m. frame of the proton–neutron (pn) pair, the kinematical variables of the deuteron-photodisintegration process

$$\gamma(q) + D(K) \to P(k_p) + N(k_n) \qquad (1)$$

are defined as follows: $q = (\omega, \boldsymbol{\omega})$ is the 4-momentum of the real photon; $K = (\sqrt{M_d^2 + \boldsymbol{\omega}^2}, -\boldsymbol{\omega})$ is the 4-momentum of the deuteron; and k_p and k_n are the 4-momenta of the proton and the neutron, respectively, their masses being taken to be identical ($k_{p,n}^2 = m^2$). It is convenient to introduce the total 4-momentum $P = k_p + k_n = (\sqrt{s}, \mathbf{0})$ of the proton–neutron pair and the relative 4-momentum $p = \frac{1}{2}(k_p - k_n)$ in it if these 4-momenta satisfy the condition $P \cdot p = 0$.

Here, we are interested primarily in the reaction amplitude, which, in the c.m. frame, can be represented in the form [16]

$$T_{Sm_s\lambda m_d}(\Phi_p, \theta_p) = e^{\mathbf{i}(\lambda + m_d)\Phi_p} t_{Sm_s\lambda m_d}(\theta_p), \qquad (2)$$

where the indices stand for the photon helicity ($\lambda = \pm 1$) and the projection of the total angular momentum of the deuteron ($m_d = 0, \pm 1$) onto the quantization axis z. It is convenient to align the quantization axis with the photon 3-momentum vector $\boldsymbol{\omega}$. The x axis coincides with the direction of the maximum linear polarization of the photon. The final state of the pn pair in the c.m. frame is determined by the energy $\sqrt{s}$, the 3-momentum $\mathbf{p}$ of relative motion (it should be noted here that $\mathbf{p} = \mathbf{k}_p$), the total spin $S = 0, 1$, and its projection m_s onto the quantization axis. In the coordinate frame chosen here, the direction of the pair momentum $\mathbf{k}_p$ is specified by the polar angles Φ_p and θ_p.

According to formulas presented in the Appendix, the observables in which we are interested are expressed in terms of the products of the relevant reduced amplitudes $t_{Sm_s\lambda m_d}$. The definitions of the beam and target asymmetries correspond to the formulas obtained in [16]. Accordingly, the reaction amplitude in the Bethe–Salpeter formalism is expressed in terms of the matrix element of the irreducible electromagnetic-current 4-operator J for the two-nucleon system (Mandelstam vertex) between the initial and the final state (deuteron and pn pair, respectively). Specifically, we have

$$T_{Sm_s\lambda m_d}(\Phi_p, \theta_p) = \frac{1}{4\pi^3} \qquad (3)$$
$$\times \int d^4k d^4k' \overline{\chi}_{\sqrt{s}\mathbf{k}_p Sm_s}(k') \epsilon_\lambda \cdot J(k', k; P, K) \chi_{Km_d}(k),$$

where $\overline{\chi}_{\sqrt{s}\mathbf{k}_p Sm_s}$ and χ_{Km_d} are the Bethe–Salpeter amplitudes for, respectively, the proton–neutron pair and the deuteron, these amplitudes being solutions to a homogeneous and a nonhomogeneous Bethe–Salpeter equation involving the same kernel, and where ϵ_λ is the photon polarization 4-vector ($q \cdot \epsilon = 0$). In expression (3), the Bethe–Salpeter amplitudes and the electromagnetic-current operator can be represented as 4×4 matrices formed by Dirac spinors. Since electromagnetic interaction with an NN system does not conserve its total isospin, the amplitudes given by (3) that correspond to $\Delta I = 1$ isovector transitions interfere with the amplitudes of $\Delta I = 0$ isoscalar transitions. A detailed account of the approach used here can be found in [11, 12].

The law of electromagnetic-current conservation requires that the Mandelstam vertex involve both the single- and the two-particle contribution. In calculating the amplitudes given by (3), we, however, had to use the plane-wave and the single-particle approximation—that is, in the electromagnetic-current operator, we disregarded the two-particle contribution ($J^{[2]} = 0$), which ensures the necessary condition of gauge invariance for transition amplitudes. The inclusion of final-state interaction and of the two-particle contribution in the Mandelstam vertex would require a dedicated investigation. In view of this, the

radiation field was fixed by choosing the Coulomb gauge, $\epsilon^0 = 0$ and $\boldsymbol{\epsilon} \cdot \boldsymbol{\omega} = 0$.

For the deuteron Bethe–Salpeter amplitude, we have used a solution to the homogeneous Bethe–Salpeter equation whose NN-interaction kernel involves a superposition of the exchanges of pions (their coupling being assumed to be of an axial-vector character) and of sigma, omega, rho, and other mesons [17]. The static parameters of the deuteron that were obtained with this function are the following: the asymptotic D/S ratio is $\rho_{D/S} = 0.02497$, the quadrupole moment is $Q_d = 0.2678$ fm^2, the magnetic moment is $\mu_d = 0.856140$ $(e/2m)$, the tensor component is $P_D = 5.1\%$, and the pseudoprobability of negative-energy states is $P_- = -0.12\%$ [14]. For states characterized by the deuteron quantum numbers, the number α of partial-wave channels in the Bethe–Salpeter equation is equal to eight:

$$\chi_{Km_d} = \sum_{\alpha=1}^{8} g_\alpha \chi_{Km_d}(\alpha).$$

This number is determined by the set of quantum numbers $^{2S+1}L_J^{\rho_1\rho_2}$, where S is the total spin; L is the orbital angular momentum; ρ_i is the energy spin, which singles out nucleon and antinucleon states in a given positive-parity two-particle state antisymmetric under particle permutations; and $J = 1$. All these channels must be taken into account because the bound-state vertex function depends on the relative energy k_0 of the nucleons, and the property of covariance requires that the expansion of the amplitude involve both positive- and negative-energy states of the Dirac equation. It follows that, in addition to the components $\chi_{Km_d}(\alpha_{1,2})$, featuring only the positive-energy states $\alpha_1 = {}^3S_1^{++}$ and $\alpha_2 = {}^3D_1^{++}$ and having nonrelativistic analogs, one has to deal with six additional components $\chi_{Km_d}(\alpha_{3-8})$, which are denoted by

$$^3S_1^{--},\ ^3D_1^{--},\ ^3P_1^{+-},\ ^3P_1^{-+},\ ^1P_1^{+-},\ ^1P_1^{-+}. \quad (4)$$

For the P-wave components represented in this form, the radial functions do not possess symmetry under the substitution $k_0 \to -k_0$. For the ensuing analysis, it is convenient to go over from the P-wave components ($\alpha = 5$–8) to the linear combinations

$$^3P_1^o, \quad ^1P_1^e, \quad ^3P_1^e, \quad ^1P_1^o, \quad (5)$$

where $^3P_1^{o/e} = \dfrac{1}{\sqrt{2}}(^3P_1^{+-} \mp {}^3P_1^{-+})$ and $^1P_1^{e/o} = \dfrac{1}{\sqrt{2}}(^1P_1^{+-} \pm {}^1P_1^{-+})$. The superscripts e and o in (5) indicate that the corresponding partial-wave states are symmetric (even) and antisymmetric (odd) under the interchange of the energy spins between the two nucleons. From the Pauli exclusion principle, it then follows that the radial functions g_α for these partial-wave channels are even ($\alpha = 5, 6$, their pseudoprobability being -0.092%) or odd ($\alpha = 7, 8$, their pseudoprobability being -0.023%) functions of the relative energy k_0. In the case of $k_0 = 0$, the radial functions for the last two channels vanish identically.

3. DISCUSSION OF THE RESULTS

One of the methods for taking into account relativistic effects is based on the quasipotential approximation of the Bethe–Salpeter equation and on the corresponding reduction of relevant matrix elements [18]. In [19], $\mathcal{O}(1/m)$ corrections to the current-density operator that arise in this case and the effect of these corrections on observables were studied within the potential approach. There are two classes of relativistic corrections to the current-density operator. The first includes terms that are obtained upon the reduction of the small components of Dirac spinors (spin–orbit contribution), while the second comprises terms that are generated by the Lorentz boost of the initial-state amplitude from the rest frame to the c.m. frame, where the deuteron moves at the velocity ω/M_d; that is,

$$\chi_{Km_d}(k) = \Lambda(\mathcal{L})\chi_{K_{(0)}m_d}(\mathcal{L}^{-1}k), \quad (6)$$

where $\Lambda(\mathcal{L})$ is the matrix of the Lorentz boost of spinors and $\mathcal{L}$ is the matrix of the corresponding transformation of the total deuteron 4-momentum $K_{(0)} = (M_d, \mathbf{0})$. In the low-energy region, first-class corrections are dominant. With increasing photon energy, however, effects like changes in nucleon-spin projections, $\Lambda(\mathcal{L}) \neq 1$ (spin precession), and changes in the relative nucleon 4-momentum, $\mathcal{L} \neq 1$ (Lorentz contraction), become important. Within the Bethe–Salpeter formalism, all these effects are calculable exactly.

In addition, it is necessary to take into account dynamical relativistic effects associated with the nonstatic character of NN interaction. In the approach used here, this is manifested in the dependence of the Bethe–Salpeter amplitude on the relative nucleon energy and in the emergence of six partial waves of negative energy. Only if the relevant solution to the Bethe–Salpeter equation is available can one obtain quantitative estimates of these effects. For the amplitude in question, we will take a parametrization of a numerical solution to the Bethe–Salpeter equation in terms of the one-boson-exchange kernel, which was repeatedly employed to describe the static properties of the nucleon [14] and reactions involving a deuteron [20].

The procedure for calculating the matrix elements (3) for various values of particle polarizations

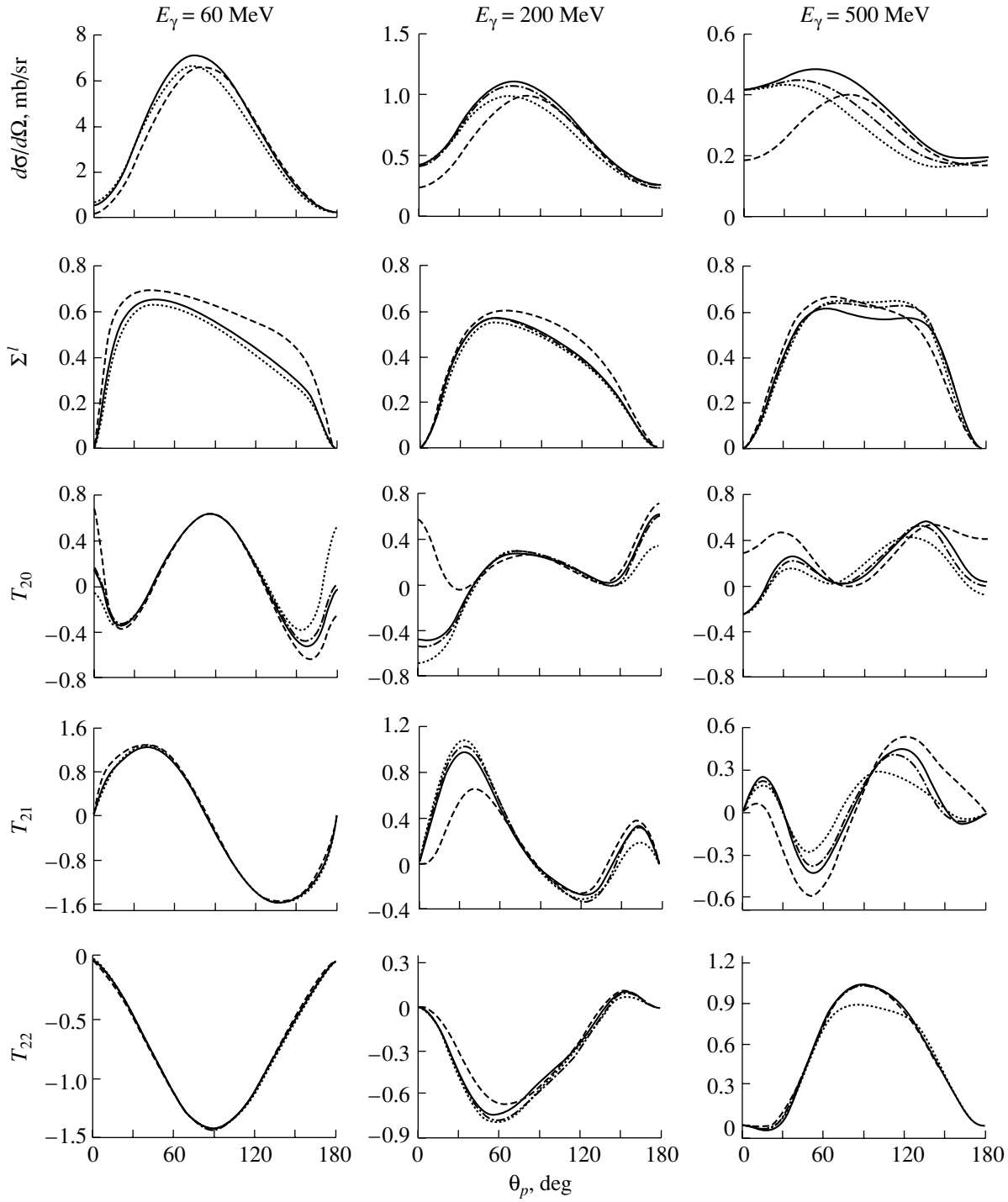

Differential cross section $d\sigma/d\Omega$, asymmetry Σ^l of linearly polarized photons, and three tensor asymmetries T_{2M} ($M = 0, 1, 2$) for the deuteron versus the proton emission angle θ_p in the c.m. frame for various values of the photon energy E_γ. Our calculation was performed within the Bethe–Salpeter formalism, where the deuteron Bethe–Salpeter amplitude was obtained as a solution to the Bethe–Salpeter equation for a one-boson-exchange kernel (exchange of pions and of omega, rho, and sigma mesons). In calculating all the displayed curves, the following approximations were made: (i) the two-particle electromagnetic-current operators and final-state interactions were disregarded, and (ii) the radial functions for the partial waves of the Bethe–Salpeter amplitude were taken at the relative nucleon energy of $k_0 = 0$. The solid curves correspond to the calculation that is exact within these approximations (the ${}^3S_1^{++} - {}^3D_1^{++}$, ${}^3S_1^{--} - {}^3D_1^{--}$, ${}^3P_1^o$, and ${}^1P_1^e$ partial waves are included); the dashed curves represent the results of the calculation disregarding the Lorentz boost of the Bethe–Salpeter amplitude; the dotted curves were calculated with allowance for only the positive-energy components of the Bethe–Salpeter amplitude; and the dash-dotted curves correspond to the contribution of the ${}^3P_1^{-+}$ partial wave to the observables in question.

(in all, there are 12 independent amplitudes) was somewhat changed in relation to that in [11, 12]. The REDUCE system for analytic calculations was used here to find the relevant transition amplitudes for given values of the polarizations of the particles involved in the reaction. By using Eqs. (A.1)–(A.3) from the Appendix, we then perform numerically their multiplication and summation over particle polarizations. The code is composed in such a way that, within the approximations used, it is possible to compute all polarization observables, which are expressed in terms of the real part of the transition amplitudes $t_{Sm_s\lambda m_d}$.

For the differential cross section $d\sigma/d\Omega$; the asymmetry Σ^l of linearly polarized photons; and three tensor asymmetries T_{20}, T_{21}, and T_{22} for the deuteron, the figure shows the angular dependences in the c.m. frame. All the calculations were performed for the following three values of the laboratory photon energy: $E_\gamma = 60$, 200, and 500 MeV. The solid curves correspond to the calculation within the single-particle plane-wave approximation with allowance for all relativistic effects mentioned above. In the calculations, we disregarded the dependence of the Bethe–Salpeter wave function on the relative nucleon energy (so-called zero approximation for the vertex function). The analysis performed in [11] revealed that this retardation effect is not very important. We had to use this approximation because the problem of constructing an analytic continuation of the solution to the homogeneous Bethe–Salpeter equation to the physical axis of relative energy (such a solution can be found only at imaginary energies ik_4) has not yet been solved. Setting $k_0 = 0$, we eliminate the states $\chi_{Km_d}({}^3P_1^e)$ and $\chi_{Km_d}({}^1P_1^o)$, which are odd in relative energy. In computing the angular distributions that are shown in the figure by the dashed curves, we excluded completely the contribution of effects that are associated with the Lorentz transformation of the deuteron Bethe–Salpeter amplitude. The behavior of observables that is determined by the positive-energy components of the deuteron Bethe–Salpeter amplitude is represented by the dotted curves. The dash-dotted curves illustrate the behavior of the triplet component $\chi_{Km_d}({}^3P_1^{-+})$.

From the results displayed in the figure, we can draw the following conclusion: the inclusion of partial waves in the deuteron Bethe–Salpeter amplitude that are generated by negative-energy states leads to a general increase in the differential cross section for deuteron photodisintegration. At the maximum, (compare the solid and the dotted curve), this effect amounts to 10% at $E_\gamma = 200$ MeV and is as large as 30% at $E_\gamma = 500$ MeV. However, the general character of the angular dependences remains by and large unchanged. At the same time, the inclusion of relativistic effects associated with the Lorentz boost also changes the angular dependence, sizably increasing the differential cross section in the region of small angles. The asymmetry Σ^l of a linearly polarized photon beam is less affected by these phenomena. As to the tensor asymmetries of the target, their behavior changes substantially with increasing photon energy. The general trend is such that, for the proton emission angles around $\theta_p = 90°$, the tensor asymmetries T_{20} and T_{21} are weakly sensitive to the contribution of relativistic effects. However, the role of these effects is decisive for small and large values of θ_p, their contribution to the asymmetry T_{22} being significant even at the photon energy of $E_\gamma = 60$ MeV.

4. CONCLUSION

Within the relativistic-covariant Bethe–Salpeter formalism, we have calculated the differential cross section for deuteron photodisintegration and polarization observables of this reaction. In these calculations, we have considered only those observables that are related to beam and target polarizations and which are expressed in terms of the real part of the reaction amplitude (3). In employing the Bethe–Salpeter formalism to describe the deuteron, we have taken into account the fact that, in this approach, the spinor component of the amplitude for the bound state involves symmetrically positive- and negative-energy single-particle Dirac states.

At present, the set of solutions to the Bethe–Salpeter equation whose NN-interaction kernel is such that it ensures the coupling of positive- and negative-energy states, on one hand, and enables one to describe satisfactorily elastic NN scattering at moderate energies, along with static properties of the deuteron, on the other hand, is rather limited. A solution to the equation with the one-boson-exchange kernel, whose parameters (meson masses, interaction parameters, and form factors) are tightly fixed on the basis of a fit to phase shifts for elastic NN scattering at energies in the region $T_{\text{lab}} \leq 350$ MeV and to the static features of the deuteron, is an extensively explored solution of this type. For this solution, the relative contribution of negative-energy partial waves is approximately one-thousandth of the contribution of the positive-energy components of the Bethe–Salpeter amplitude.

Both kinematical and dynamical relativistic effects are considered in studying relevant observables. An analysis of dynamical effects reveals that, in the zero approximation for the vertex function ($k_0 = 0$), the even P-wave components ${}^3P_1^o$ and ${}^1P_1^e$ of the deuteron vertex function play a dominant role. This is because they are even in the relative energy of

the nucleons and have the highest probability among negative-energy states. The contribution of the even partial waves ${}^3S_1^{--}-{}^3D_1^{--}$ is insignificant since their pseudoprobability is low, -0.005%. Therefore, one may hope that, because of the smallness of the contribution to the absolute normalization from the ${}^3P_1^e$ and ${}^1P_1^o$ states, which are odd in the relative energy of the nucleons and which were disregarded here, the contribution of these states to the polarization observables of deuteron photodisintegration would also be insignificant. We have had to invoke here the zero approximation for the vertex function since it is impossible at present to establish the dependence of the Bethe–Salpeter amplitude on the relative energy k_0 of the nucleons in the physical region. The problem is that this requires performing an inverse analytic continuation of the solution to the Bethe–Salpeter equation from Euclidean space to the physical axis, but this is a mathematically ill-posed problem, which requires much additional work.

The emerging pattern shows that, if kinematical relativistic effects are taken into consideration, negative-energy spinor states have a pronounced effect on the differential cross section, but they do not cause qualitative changes in its behavior. These states must be taken into account in further developing a full theory of deuteron photodisintegration within the Lorentz-invariant approach with allowance for the internal structure of the deuteron. The respective contributions to the polarization observables T_{20} and T_{21} are significant at large and small values of the proton emission angle. The observable T_{22} is the least sensitive to relativistic effects, since the Clebsch–Gordan coefficient in Eq. (A.3) leaves only one product of the amplitudes, $t_{Sm_s\lambda m_d=-1}t_{Sm_s\lambda m_d=+1}$. In the case of T_{20} and T_{21}, the products of the amplitudes for, respectively, three and two projections m_d contribute, which leads to a greater effect in the case of forward and backward proton emission.

It is of paramount importance to perform a gauge-invariant calculation of transition amplitudes and to choose the electromagnetic-current operator in a form that is consistent with Siegert's long-wave limit [21], but these problems, which are closely related, have yet to be solved. A possible way to do this is to introduce the two-particle electromagnetic-current operator in the nucleon sector [22]. We deem it important to resolve these issues since this would make it possible to perform a comparison with experimental data. In this respect, our calculations are still of a methodological value. However, the effects of negative-energy spinor states in the deuteron amplitude must be taken into account in developing a full theory of deuteron photodisintegration within the relativistic Bethe–Salpeter approach.

ACKNOWLEDGMENTS

We are grateful to A.A. Goy and S.E. Shirmovsky for stimulating discussions and to S.M. Dorkin and L.P. Kaptari for consultations in performing numerical calculations.

This work was funded in part by the Program for Support of Fundamental Investigations within Higher Educational Centers: Universities of Russia (project no. 015.02.01.022).

APPENDIX

The polarization observables Σ^l and T_{2M} and the differential cross section $d\sigma/d\Omega$ can be expressed in terms of the invariant amplitude $t_{Sm_s\lambda m_d}(\theta_p)$ as

$$\frac{d\sigma}{d\Omega_p} = \frac{\alpha}{16\pi s}\frac{|\mathbf{k}_p|}{\omega}f(\theta_p), \tag{A.1}$$

$$f(\theta_p) = \frac{1}{3}\sum_{Sm_Sm_d}|t_{Sm_s1m_d}(\theta_p)|^2,$$

$$-\Sigma^l = \frac{1}{3}\sum_{Sm_Sm_d} t^*_{Sm_s1m_d}t_{Sm_s-1m_d}\Big/ f(\theta_p), \tag{A.2}$$

$$T_{2M} = (2-\delta_{M0})\frac{\sqrt{5}}{3}\sum_{Sm_Sm_d} \mathrm{C}^{1M+m_d}_{1m_d2M}\mathrm{Re}\{t^*_{Sm_s1m_d}t_{Sm_s1M+m_d}\}/f(\theta_p), \quad M \geq 0, \tag{A.3}$$

where $\alpha = e^2/(4\pi)$. The observables in question are functions of the photon energy E_γ in the laboratory frame and the proton emission angle θ_p; we also have

$$s = M_d(M_d + 2E_\gamma), \quad |\mathbf{k}_p| = \sqrt{\frac{s}{4} - m^2}, \quad \omega = \frac{M_d}{\sqrt{s}}E_\gamma. \tag{A.4}$$

REFERENCES

1. LEGS Collab. (G. S. Blanpied *et al.*), Phys. Rev. Lett. **67**, 1206 (1991).
2. LEGS Collab. (G. S. Blanpied *et al.*), Phys. Rev. C **61**, 024604 (2000).
3. S. Wartenberg *et al.*, Few-Body Syst. **25**, 213 (1999).

4. F. Adamian *et al.*, Eur. Phys. J. A **8**, 423 (2000).
5. C. Bochna *et al.*, Phys. Rev. Lett. **81**, 4576 (1998).
6. Jefferson Lab. Hall A Collab. (K. Wijesooriya *et al.*), Phys. Rev. Lett. **86**, 2975 (2001).
7. L. A. Kondratyuk *et al.*, Phys. Rev. C **48**, 2491 (1993).
8. V. Yu. Grishina *et al.*, Eur. Phys. J. A **10**, 355 (2001).
9. A. E. L. Dieperink and S. I. Nagorny, Phys. Lett. B **456**, 9 (1999).
10. M. Schwamb, H. Arenhövel, P. Wilhelm, and Th. Wilbois, Nucl. Phys. A **631**, 583c (1998).
11. K. Yu. Kazakov and S. Eh. Shirmovsky, Phys. Rev. C **63**, 014002 (2001).
12. K. Yu. Kazakov and S. É. Sus'kov, Yad. Fiz. **64**, 935 (2001) [Phys. At. Nucl. **64**, 870 (2001)].
13. N. Honzawa and S. Ishida, Phys. Rev. C **45**, 47 (1992).
14. L. P. Kaptari, A. Yu. Umnikov, S. G. Bondarenko, *et al.*, Phys. Rev. C **54**, 986 (1996).
15. S. G. Bondarenko, V. V. Burov, M. Beyer, and S. M. Dorkin, Phys. Rev. C **58**, 3143 (1998).
16. H. Arenhövel, Few-Body Syst. **4**, 55 (1988).
17. A. Yu. Umnikov, Z. Phys. A **357**, 333 (1997).
18. W. Jaus and W. S. Woolcock, Helv. Phys. Acta **57**, 644 (1984).
19. S. Ying, E. M. Henley, and G. A. Miller, Phys. Rev. C **38**, 1584 (1988).
20. A. Yu. Umnikov, F. C. Khanna, and L. P. Kaptari, Phys. Rev. C **56**, 1700 (1997).
21. A. F. Siegert, Phys. Rev. **52**, 787 (1937).
22. W. Benz, Nucl. Phys. A **446**, 678 (1985).

Translated by A. Isaakyan

Physics of Atomic Nuclei, Vol. 66, No. 2, 2003, pp. 281–293. Translated from Yadernaya Fizika, Vol. 66, No. 2, 2003, pp. 306–318.

ELEMENTARY PARTICLES AND FIELDS
Theory

Anomalous Magnetic Moment of the Muon in the Left–Right Model

G. G. Boyarkina, O. M. Boyarkin*, and V. V. Makhnach

Belarussian State Pedagogical University, Sovetskaya ul. 18, Minsk, 220050 Belarus

Received August 13, 2001; in final form, January 31, 2002

Abstract—The effect of Higgs bosons on the anomalous magnetic moment of the muon is considered within the model that is based on the $SU(2)_L \times SU(2)_R \times U(1)_{B-L}$ gauge group and which involves a bidoublet and two triplets of Higgs fields (left–right model). For the Yukawa coupling constants and the masses of Higgs bosons, the regions are found where the model leads to agreement with experimental results obtained at the Brookhaven National Laboratory (BNL) for the anomalous magnetic moment of the muon. In order to explore corollaries from the constraints obtained for the parameters of the Higgs sector, the processes $e^+e^- \to \mu^+\mu^-$, $\tau^+\tau^-$ and $\mu^+\mu^- \to \mu^+\mu^-$, $\tau^+\tau^-$ are considered both within the left–right model and within the model involving two Higgs doublets (two-Higgs-doublet model). It is shown that, if the mass of the lightest neutral Higgs boson does indeed lie in the range 3.1–10 GeV, as is inferred from the condition requiring the consistency of the two-Higgs-doublet model with the data of the BNL experiment, this Higgs boson may be observed as a resonance peak at currently operating e^+e^- colliders (VEPP-4M, CESR, KEKB, PEP-II, and SLC). In order to implement this program, however, it is necessary to reduce considerably the scatter of energy in the e^+ and e^- beams used, since the decay width of the lightest neutral Higgs boson is extremely small at such mass values. It is demonstrated that, in the case of the left–right model, for which the mass of the lightest neutral Higgs boson is not less than 115 GeV, the resonance peak associated with it may be detected at a muon collider. © *2003 MAIK "Nauka/Interperiodica".*

1. INTRODUCTION

Experiments that measured the magnetic moments of particles have played time and again a crucial role in microscopic physics. For example, the detection of anomalous values of the nucleon magnetic moments was a compelling argument in favor of the π-meson theory of nuclear forces that was proposed by Yukawa. Agreement of the theoretical and experimental values of the electron magnetic moment to within 10^{-12} leads one to recognize that QED is one of the most precise physical theories. It was natural to expect that the E821 experiment, which was aimed at measuring the anomalous magnetic moment of the muon and which has been performed at the Brookhaven National Laboratory (BNL), would be a good test for the Standard Model of electroweak interactions. As early as the end of 1999, the precision achieved in the E821 experiment was more than five times higher than the precision of the preceding experiment devoted to this subject and performed at CERN [1]. By averaging the CERN data [1] and those obtained at BNL over a period spanning 1998 and 1999 [2], one obtains

$$\frac{a_\mu^{\rm expt}}{\mu_0} = 116592023(151) \times 10^{-11}, \qquad (1)$$

where $\mu_0 = e\hbar/m_\mu c$ is the muon magnetic moment predicted by Dirac theory. The final objective of the E821 experiment is to achieve a precision of $\pm 40 \times 10^{-11}$.

An anomalous value of the magnetic moment of a particle can be considered either as an indication of its complicated structure or as the result of taking into account radiative corrections. Since all experiments performed so far give every reason to believe that leptons, in just the same way as quarks, are structureless objects, the inclusion of muon interaction with the physical vacuum, whose structure is controlled by the theory, is expected to provide a natural explanation of the result in (1). Within the Standard Model, the theoretical value of the muon anomalous magnetic moment can be represented as the sum

$$a_\mu^{\rm SM} = a_\mu^{\rm QED} + a_\mu^{\rm had} + a_\mu^{\rm ew}. \qquad (2)$$

The main contribution to (2) comes from the QED corrections, μ^{QED}, which were determined in [3] to the fifth order of perturbation theory. The result was

$$\frac{a_\mu^{\rm QED}}{\mu_0} = 116584705.7(2.9) \times 10^{-11}. \qquad (3)$$

Effects of vacuum polarization by hadrons contribute a much smaller value to the anomalous magnetic moment of the muon, and this contribution, $a_\mu^{\rm had}$, was

*e-mail: boyarkin@bspu.unibel.by

determined with a poorer precision [4],

$$\frac{a_\mu^{\rm had}}{\mu_0} = 6739(67) \times 10^{-11}. \quad (4)$$

The electroweak corrections ($a_\mu^{\rm ew}$) are the smallest, but their precision is high [5],

$$\frac{a_\mu^{\rm ew}}{\mu_0} = 152(4) \times 10^{-11}. \quad (5)$$

The substitution of the estimates in (3)–(5) into expression (2) and a comparison with the result in (1) yields

$$\frac{\delta a_\mu}{\mu_0} = \frac{a_\mu^{\rm expt} - a_\mu^{\rm SM}}{\mu_0} = 426(165) \times 10^{-11}; \quad (6)$$

that is, the disagreement of the theoretical and experimental values is at the level of 2.6σ. The existence of so great a discrepancy, along with such phenomena as oscillations of cosmic and laboratory neutrinos, suggests that the Standard Model must be extended. We note, however, that, for the estimate in (6) to be treated with confidence as a signal of new physics, it is necessary, first of all, to reduce the uncertainty in the calculation of $a_\mu^{\rm had}$ down to the level of experimental errors. It follows from (6) that, at a 90% C.L., the quantity $\delta a_\mu/\mu_0$ must lie in the range

$$215 \times 10^{-11} \le \frac{\delta a_\mu}{\mu_0} \le 637 \times 10^{-11}. \quad (7)$$

The model that is based on the same gauge group as the Standard Model and which involves two doublets of Higgs fields (two-Higgs-doublet model or THDM),

$$\Phi_j\left(\frac{1}{2}, 1\right) = \begin{pmatrix} \Phi_j^+ \\ \Phi_j^0 \end{pmatrix}, \quad j = 1, 2,$$

provides one of the most economical extensions of the Standard Model. Within this framework, the fermion flavor can be either violated or conserved at the tree level, and extensions of the type in question can be classified in accordance with these two options. In the THDM1 and THDM2, the Yukawa Lagrangian and the Higgs potential possess additional discrete symmetry that ensures fermion-flavor conservation. In the former case (THDM1), fermions corresponding to up and down components of the weak-isospin doublet develop masses owing to the vacuum expectation values of one of the doublets of Higgs fields. In the latter case (THDM2), the generation of masses of up and down fermions is associated with the vacuum expectation values of Φ_1 and Φ_2, respectively. A model that does not possess a discrete symmetry is referred to as the THDM3 or the general THDM.

Within the THDM1 and THDM2, the observed value of the muon anomalous magnetic moment can be explained, at the one-loop level, by the contribution of the neutral CP-even Higgs boson h, an analog of the Higgs boson in the Standard Model. For the THDM1 and THDM2, the use of existing constraints on $\tan\beta$ ($\tan\beta = v_1/v_2$, with v_1 and v_2 being the vacuum expectation values of the neutral components of Higgs fields) and on m_h from searches for the decay [6]

$$J/\Psi \to h\gamma \quad (8)$$

and for the reaction [7]

$$e^+e^- \to hf\bar{f}, \qquad f = b, \tau, \quad (9)$$

means that, for the constraints in (7) to be valid, these parameters must satisfy the conditions [8]

$$m_{J/\Psi} \le m_h \le 2m_B, \quad \sin(\beta - \alpha) \approx 0, \quad (10)$$
$$30 \le \tan\beta \le 35,$$

where m_B is the mass of the lightest B meson (5.279 GeV) and α is the mixing angle in the sector of the CP-even Higgs bosons h and H. Since $\tan\beta$ specifies the coupling of the h boson to the down terms of the fermion doublets both in the THDM1 and in the THDM2,

$$g_{\bar{f}fh} = \frac{m_{f_a^d}}{\sqrt{v_1^2 + v_2^2}} [\sin(\beta - \alpha) - \tan\beta\cos(\beta - \alpha)],$$

where $m_{f_a^d}$ is the mass of the down fermion of flavor a, the constraints in (10) would inevitably entail the presence of a resonance peak associated with the Higgs boson h in the reaction

$$\mu^-\mu^+ \to \mu^-\mu^+.$$

This reaction can be studied in detail at a muon collider, which is known to be an perfect means for exploring particles manifesting themselves in s channels as resonances. Muon colliders possess the following advantages that are necessary for this. They are characterized by a low momentum spread, and the root-mean-square deviation from a Gaussian energy distribution for them in the beam, R, takes values in the range 0.04–0.08%. By cooling a muon beam, R can be reduced down to 0.01%, which is much lower than the corresponding value in e^-e^+ colliders. Muon colliders are also advantageous in that they can quickly be readjusted to operate either in the $\mu^-\mu^-$ or in the $\mu^+\mu^+$ mode. The design of muon colliders admits the existence of a special storage ring that makes it possible to optimize the luminosity in the vicinity of a resonance. Here, the quantity $\sigma_{\sqrt{s}}$ ($\sqrt{s}$ is the c.m. energy) determining the energy spread in

a beam is a characteristic of fundamental importance. For a muon collider, this quantity is given by

$$\sigma_{\sqrt{s}} = (7\ \text{MeV})\left(\frac{R}{0.01\%}\right)\left(\frac{\sqrt{s}}{100\ \text{GeV}}\right). \quad (11)$$

We emphasize that the detection and investigation of a Higgs boson via a resonance peak will be successful only if the quantity $\sigma_{\sqrt{s}}$ is on the same order of magnitude as the total decay width of the Higgs boson. Presently, two projects of muon colliders are being intensively studied [9]: the First Muon Collider, which would operate at $\sqrt{s} \sim 0.5$ TeV and a luminosity of $L \sim 10^{33}$ cm^{-2} s^{-1}, and the Next Muon Collider, which would operate at $\sqrt{s} = 4$ TeV and a luminosity of $L \sim 10^{35}$ cm^{-2} s^{-1}.

The results of the E821 experiment can also be explained within supersymmetric theories (SUSY), where the anomalous magnetic moment of the muon receives contributions from smuon–neutralino and sneutrino–chargino loops. For a wide class of SUSY models, agreement between theoretical and experimental results is ensured if the model parameters obey the conditions [10]

$$4 \le \tan\beta \le 40, \quad m_{\text{SUSY}} \simeq 100\text{–}450\ \text{GeV}, \quad (12)$$

where m_{SUSY} is a typical mass of SUSY particles. The conditions in (12) have two very far reaching consequences. First, SUSY particles can be observed at the 2-TeV FERMILAB $p\bar{p}$ collider. Second, it appears that partial-fermion-flavor-violation processes associated with higher order diagrams of perturbation theory,

$$\mu^\pm \to e^\pm\gamma, \quad \tau^\pm \to e^\pm\gamma, \quad \mu^\pm \to e^\pm e^\mp e^\pm, \quad (13)$$
$$\tau^\pm \to e^\pm e^\mp e^\pm, \quad \mu^+ e^- \to \mu^- e^+, \quad \mu^- N_1 \to e^- N_2,$$
$$\text{etc.},$$

are characterized by cross-section values that make it possible to detect them even with currently available experimental equipment.

One could expect that, in models based on an extended gauge group, such as $SU(2)_L \times U(1) \times U(1)'$, $SU(2)_L \times SU(2)_R \times U(1)_{B-L}$, or $SU(3)_L \times U(1)_N$, the quantity δa_μ will be induced by loops involving extra gauge bosons (those that are not contained in the Standard Model). For the condition in (7) to be satisfied, however, the masses of these bosons must be about 100 GeV (see, for example, [11]), which is much less than their experimental lower limits. Within nonsupersymmetric extensions of the Standard Model, Higgs bosons may also appear to be candidates for particles generating significant contributions to the anomalous magnetic moment of the muon. The objective of the present study is to analyze, from precisely this point of view, the model that is based on the $SU(2)_L \times SU(2)_R \times U(1)_{B-L}$ gauge group and which involves two triplets and one bidoublet in the Higgs sector—that is, the left–right model (LRM). This choice of model is motivated by the fact that it includes Higgs bosons that also appear in other popular extensions of the Standard Model—for example, in the THDM and in the model based on the $SU(3)_L \times U(1)_N$ gauge group.

The ensuing exposition is organized as follows. In Section 2, we calculate corrections to the muon magnetic moment in the one-loop approximation that are induced by Higgs bosons. The parameters of the Higgs sector that ensure agreement with the data of the E821 experiment are used in Section 3, where prospects for observing, at e^+e^-- and $\mu^+\mu^-$ colliders, a resonance peak that is associated with the lightest neutral Higgs boson are analyzed for the THDM and LRM. In the Conclusion, we discuss our results.

2. CONTRIBUTIONS TO $(g-2)_\mu/2$ FROM THE HIGGS SECTOR

The LRM belongs to the class of models where the choice of Yukawa potential affects the form of Lagrangian describing the interactions of Higgs bosons both with fermions and with gauge bosons. The most general form of the Yukawa potential $\mathcal{L}_{\text{Y}}^g$ was proposed in [12]. Although $\mathcal{L}_{\text{Y}}^g$ has a rather complicated form, it is not difficult to diagonalize the mass matrix of charged Higgs bosons. For the mass matrix of neutral Higgs bosons, M_n, this procedure can be implemented, however, only upon introducing some simplifications in $\mathcal{L}_{\text{Y}}^g$ [13]. For example, the matrix M_n can be diagonalized if the parameters of the Yukawa potential satisfy the conditions (we retain the notation introduced in [12])

$$\alpha_1 = \frac{2\alpha_2 k_2}{k_1}, \quad \alpha_3 = \frac{2\alpha_2 k_-^2}{k_1 k_2}, \quad (14)$$
$$\beta_1 = \frac{2\beta_3 k_2}{k_1},$$

where k_1 and k_2 are the vacuum expectation values of the neutral components of the bidoublet of Higgs fields and $k_\pm = \sqrt{k_1^2 \pm k_2^2}$. Assuming fulfillment of the conditions in (14), we present the Lagrangians that are necessary for the ensuing calculations.

For doubly charged Higgs bosons $\Delta_{1,2}^{(\pm\pm)}$, they have the form

$$\mathcal{L}_{\gamma\Delta\Delta} = 2ie[(\partial_\mu \Delta_1^{(--)*}(x))\Delta_1^{(--)}(x) \quad (15)$$
$$- \Delta_1^{(--)*}(x)(\partial_\mu \Delta_1^{(--)}(x))] + (1 \to 2),$$

$$\mathcal{L}_l^{dc} = -\sum_{a,b} \frac{f_{ab}}{2}[\bar{l}_a^c(x)(1+\gamma_5) l_b(x) \mathrm{c}_{\theta_d} \quad (16)$$

$$- \bar{l}_a^c(x)(1-\gamma_5)l_b(x)\mathrm{s}_{\theta_d}]\Delta_1^{(--)*}(x)$$
$$+ (1 \to 2, \theta_d \to \theta_d - \pi/2) + \text{conj.},$$

where the superscript c denotes the charge-conjugation operation; $\mathrm{c}_{\theta_d} \equiv \cos\theta_d$ and $\mathrm{s}_{\theta_d} \equiv \sin\theta_d$,[1] θ_d being the mixing angle in the sector of doubly charged Higgs bosons [$\tan\theta_d \sim k_+^2/v_R^2$; here, v_R is the vacuum expectation value of the neutral component of the right-handed triplet, $v_R \gg \max(k_1, k_2)$]; and f_{ab} is the triplet Yukawa coupling constant.

For the singly charged Higgs bosons $h^{(\pm)}$ and $\tilde{\delta}^{(\pm)}$, the corresponding Lagrangians are given by

$$\mathcal{L}_{W_1\gamma h} = g_R e g_L^{-1} m_{W_1} \cos 2\beta(\alpha - \rho_3/2 + \rho_1 + 1) \times \mathrm{s}_\xi h^{(-)*}(x) W_{1\mu}(x) A_\mu(x), \quad (17)$$

$$\mathcal{L}_{W_2\gamma h} = \mathcal{L}_{W_1\gamma h}(\mathrm{s}_\xi \to \mathrm{c}_\xi), \quad (18)$$

$$\mathcal{L}_{W_1\gamma\tilde{\delta}} = g_R e g_L^{-1} \beta_1 m_{W_1} \mathrm{s}_\xi \tilde{\delta}^{(-)*}(x) W_{1\mu}(x) A_\mu(x), \quad (19)$$

$$\mathcal{L}_{W_2\gamma\tilde{\delta}} = \mathcal{L}_{W_1\gamma\tilde{\delta}}(\mathrm{s}_\xi \to \mathrm{c}_\xi), \quad (20)$$

$$\mathcal{L}_l^{sc} = \sum_{a,b}\Bigg\{\Bigg[\frac{h'_{ab}k_2 - h_{ab}k_1}{2k_+}\bar{\nu}_a(x)(1-\gamma_5)l_b(x) - \frac{h_{ab}k_2 - h'_{ab}k_1}{2k_+}\bar{N}_a(x)(1+\gamma_5)l_b(x)\Bigg] h^{(-)*}(x) + \frac{f_{ab}}{\sqrt{2}}[\bar{l}_a^c(x)(1+\gamma_5)\nu_b(x) \times \left(\frac{\beta_0 k_0^2}{(\alpha+\rho_1-\rho_3/2)v_R^2}h^{(-)*}(x) - \tilde{\delta}^{(-)*}(x)\right) + \bar{l}_a^c(x)(1-\gamma_5)N_b(x)\left(\frac{k_0}{v_R}h^{(-)*}(x) + \frac{\beta_0 k_0}{(\alpha+\rho_1-\rho_3/2)v_R}\tilde{\delta}^{(-)*}(x)\right)\Bigg] + \text{conj.}\Bigg\}, \quad (21)$$

where

$$\alpha = \frac{\alpha_3 k_+^2}{2k_-^2}, \quad \beta_0 = \frac{\beta_1 k_+^2}{k_-^2}, \quad k_0 = \frac{k_-^2}{\sqrt{2}k_+};$$

ρ_1, ρ_3, α_3, and β_1 are the parameters of the Yukawa potential (see [12]); g_R is the gauge constant of the $SU(2)_R$ group (in the following, we assume that $g_L = g_R$); $A_\mu(x)$ describes an electromagnetic field; $N_a(x)$ is the field function for the heavy neutrino of flavor a; $\tan\beta = k_1/k_2$; and the angle ξ controls mixing in the sector of charged gauge bosons.

The Lagrangian describing the interaction of neutral Higgs bosons with charged leptons has the form

$$\mathcal{L}_l^n = -\frac{1}{\sqrt{2}k_+}\Bigg\{\sum_{a,b}\bar{l}_a(x)l_b(x) \times \left[(h_{ab}k_1 + h'_{ab}k_2)(S_1(x)\mathrm{s}_{\theta_0} + S_2(x)\mathrm{c}_{\theta_0}) + (h'_{ab}k_1 - h_{ab}k_2)(S_1(x)\mathrm{c}_{\theta_0} - S_2(x)\mathrm{s}_{\theta_0})\right] + i\bar{l}_a(x)\gamma_5 l_b(x)(h_{ab}k_1 - h'_{ab}k_2)P_1(x)\Bigg\}, \quad (22)$$

where $S_{1,2}$ and P_1 are, respectively, the scalar and pseudoscalar Higgs bosons (S_1 is an analog of the Higgs boson in the Standard Model) and the angle θ_0 is defined in terms of the parameters of the Yukawa potential and the vacuum expectation values of the neutral components of Higgs fields through the relation

$$\tan 2\theta_0 = \frac{4k_1k_2k_-^2[-2(2\lambda_2+\lambda_3)k_1k_2 + \lambda_4 k_+^2]}{k_1k_2[(4\lambda_2+2\lambda_3)(k_-^4 - 4k_1^2k_2^2) - k_+^2(2\lambda_1 k_+^2 - 8\lambda_4 k_1k_2)] + \alpha_2 v_R^2 k_+^4}. \quad (23)$$

The Lagrangian in (22) provides a very clear example of the effect that the choice of Yukawa potential may have in the LRM. If we make the substitution $k_2 \to -k_2$ in (14), the following expression will appear instead of (22):

$$\mathcal{L}_l^n = -\frac{1}{\sqrt{2}k_+}\Bigg\{\sum_a m_a\bar{l}_a(x)l_a(x)(S_1(x)\mathrm{c}_{\theta_0} - S_2(x)\mathrm{s}_{\theta_0}) + \sum_{a,b}\Big[\bar{l}_a(x)l_b(x)(h_{ab}k_1 - h'_{ab}k_2) \times (S_1(x)\mathrm{s}_{\theta_0} + S_2(x)\mathrm{c}_{\theta_0}) + i\bar{l}_a(x)\gamma_5 l_b(x) \times (h_{ab}k_1 + h'_{ab}k_2)P_1(x)\Big]\Bigg\}. \quad (24)$$

The Yukawa constants h_{ab} can be expressed in terms of the lepton mass, the mixing angles in the neutrino sector, and $\tan\beta$ [13]. By using the regions allowed for the neutrino-oscillation parameters and varying $\tan\beta$, we can draw conclusions on the values of the cross sections for processes involving neutral Higgs bosons. If, for example, we use the Lagrangian in (24) to obtain the cross section for the electron–muon

[1] A similar notation is introduced below for other trigonometric functions.

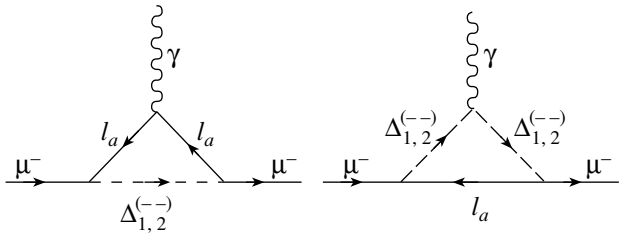

Fig. 1. Contributions to the anomalous magnetic moment of the muon from doubly charged Higgs bosons $\Delta^{(--)}_{1,2}$.

charge-exchange reaction

$$e^-\mu^+ \to e^+\mu^-, \tag{25}$$

a resonance peak that is associated with the S_1 boson will not appear at any values of the neutrino-oscillation parameters and $\tan\beta$; at the same time, the existence of such a peak is quite possible if use is made of the Lagrangian in (22).

The diagrams in Fig. 1 involve doubly charged Higgs bosons. In the anomalous magnetic moment of the muon, they induce the contribution

$$\frac{\delta a_\mu^\Delta}{\mu_0} = \frac{1}{8\pi^2} \tag{26}$$
$$\times \left(4f_{\mu e}^2 \sum_{i=1}^{2} I_e^{\Delta_i} + f_{\mu\mu}^2 \sum_{i=1}^{2} I_\mu^{\Delta_i} + 4f_{\mu\tau}^2 \sum_{i=1}^{2} I_\tau^{\Delta_i}\right),$$

where

$$I_{l_a}^{\Delta_i} = \int_0^1 \left(\frac{2m_\mu^2(z^2-z^3)}{m_\mu^2(z^2-z)+m_{\Delta_i}^2 z + m_{l_a}^2(1-z)}\right.$$
$$\left. + \frac{m_\mu^2(z^2-z^3)}{m_\mu^2(z^2-z)+m_{\Delta_i}^2(1-z)+m_{l_a}^2 z}\right) dz.$$

Singly charged Higgs bosons also affect the anomalous magnetic moment of the muon. The corresponding diagrams are shown in Fig. 2. For the diagrams containing $W_1^\pm$ and $h^{(\pm)}$ bosons in the loops, we have the relation

$$\frac{M_{W_1 N_\mu h}}{M_{W_1 \nu_\mu h}} = \mathrm{s}_\xi,$$

where $M_{W_1\nu_\mu h}$ ($M_{W_1 N_\mu h}$) are the matrix elements corresponding to diagrams featuring the exchange of light (heavy) neutrinos. Since the mixing angle in the sector of charged gauge bosons is small ($|\xi| \approx 10^{-2}$–10^{-5} [1]), we can disregard the corrections from diagrams involving a virtual heavy neutrino. Taking into account the analogous relations

$$\frac{M_{W_2\nu_\mu h}}{M_{W_2 N_\mu h}} = \mathrm{s}_\xi, \qquad \frac{M_{W_1 N_\mu \tilde\delta}}{M_{W_1 \nu_\mu \tilde\delta}} = \mathrm{s}_\xi, \tag{27}$$

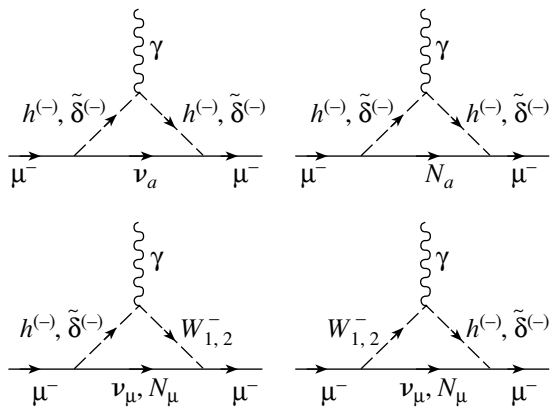

Fig. 2. Contributions to the anomalous magnetic moment of the muon from the singly charged Higgs bosons $h^{(-)}$ and $\tilde\delta^{(-)}$.

$$\frac{M_{W_2\nu_\mu\tilde\delta}}{M_{W_2 N_\mu\tilde\delta}} = \mathrm{s}_\xi,$$

we find that the dominant contributions to the muon anomalous magnetic moment from the diagrams in Fig. 2 are

$$\frac{\delta a_\mu^{(hh)}}{\mu_0} = \frac{1}{8\pi^2}\sum_{a=e,\mu,\tau}\left(\alpha^2_{\bar\mu N_a h} I^{hh}_{N_a} + \alpha^2_{\bar\mu\nu_a h} I^{hh}_{\nu_a}\right), \tag{28}$$

$$\frac{\delta a_\mu^{(\tilde\delta\tilde\delta)}}{\mu_0} = \frac{1}{8\pi^2}\sum_{a=e,\mu,\tau}\left(\alpha^2_{\bar\mu N_a\tilde\delta} I^{\tilde\delta\tilde\delta}_{N_a} + \alpha^2_{\bar\mu\nu_a\tilde\delta} I^{\tilde\delta\tilde\delta}_{\nu_a}\right), \tag{29}$$

$$\frac{\delta a_\mu^{(W_1 h)}}{\mu_0} = \frac{(\alpha-\rho_3/2+\rho_1+1)\mathrm{c}_{2\beta}\mathrm{s}_\xi m_{W_1}}{16\sqrt{2}\pi^2}\alpha_{\bar\mu\nu_\mu h} I^{W_1 h}, \tag{30}$$

$$\frac{\delta a_\mu^{(W_2 h)}}{\mu_0} \tag{31}$$
$$= \frac{(\alpha-\rho_3/2+\rho_1+1)\mathrm{c}_{2\beta}\mathrm{c}_\xi m_{W_1}}{16\sqrt{2}\pi^2}\alpha_{\bar\mu N_\mu h} I^{W_2 h},$$

$$\frac{\delta a_\mu^{(W_1\tilde\delta)}}{\mu_0} = \frac{\beta_1\mathrm{c}_{2\beta}\mathrm{s}_\xi m_{W_1}\alpha_{\bar\mu\nu_\mu\tilde\delta}}{16\sqrt{2}\pi^2} I^{W_1\tilde\delta}, \tag{32}$$

$$\frac{\delta a_\mu^{(W_2\tilde\delta)}}{\mu_0} = \frac{\beta_1\mathrm{c}_{2\beta}\mathrm{c}_\xi m_{W_1}\alpha_{\bar\mu N_\mu\tilde\delta}}{16\sqrt{2}\pi^2} I^{W_2\tilde\delta}, \tag{33}$$

where

$$\alpha_{\bar l_a\nu_b h} = \frac{h'_{ab}k_2 - h_{ab}k_1}{2k_+}, \quad \alpha_{\bar l_a N_b h} = \frac{h'_{ab}k_1 - h_{ab}k_2}{2k_+},$$
$$\alpha_{\bar l_a\nu_b\tilde\delta} = \frac{f_{ab}}{\sqrt{2}},$$

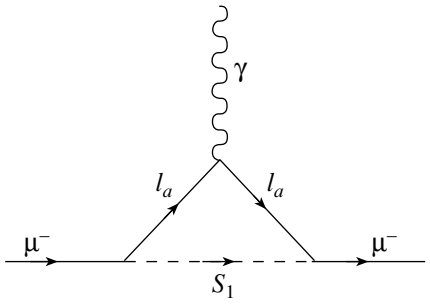

Fig. 3. Contribution to the anomalous magnetic moment of the muon from the neutral Higgs boson S_1.

$$\alpha_{\bar{l}_a N_b \tilde{\delta}} = \frac{f_{ab}}{\sqrt{2}} \frac{\beta_0 k_0}{(\alpha + \rho_1 - \rho_3/2) v_R},$$

$$I_i^{hh} = \int_0^1 \frac{m_\mu^2 (z^3 - z^2) dz}{m_\mu^2 z^2 + (m_h^2 - m_i^2 - m_\mu^2) z + m_i^2},$$

$$I_i^{\tilde{\delta}\tilde{\delta}} = I_i^{hh}(m_h \to m_{\tilde{\delta}}), \quad i = \nu_a, N_a,$$

$$I^{W_1 h} = \frac{m_\mu}{m_{W_1}^2 - m_h^2} \left\{ \ln\left(\frac{m_{W_1}^2}{m_h^2}\right) - \left[\int_0^1 \frac{z^2 [m_\mu^2 (2z-1) + m_{W_1}^2 - m_{\nu_\mu}^2] dz}{m_\mu^2 z^2 + (m_{W_1}^2 - m_{\nu_\mu}^2 - m_\mu^2) z + m_{\nu_\mu}^2} - (m_{W_1} \to m_h) \right] \right\},$$

$$I^{W_2 h} = I^{W_1 h}(m_{W_1} \to m_{W_2}, m_{\nu_\mu} \to m_{N_\mu}),$$

$$I^{W_k \tilde{\delta}} = I^{W_k h}(m_h \to m_{\tilde{\delta}}).$$

The contribution of the neutral Higgs boson S_1 to the anomalous magnetic moment of the muon is caused by the diagram in Fig. 3 and is given by

$$\frac{\delta a_\mu^{S_1}}{\mu_0} = \frac{1}{8\pi^2} \sum_{l_a = e,\mu,\tau} \alpha_{\bar{\mu} l_a S_1}^2 I_{l_a}^{S_1}, \qquad (34)$$

where

$$\alpha_{\bar{l}_a l_b S_1} = -\frac{1}{\sqrt{2} k_+} \left[(h_{ab} k_1 + h'_{ab} k_2) \mathrm{s}_{\theta_0} + (h'_{ab} k_1 - h_{ab} k_2) \mathrm{c}_{\theta_0} \right],$$

$$I_{l_a}^{S_1} = \int_0^1 \frac{[m_\mu^2 (z^2 - z^3) + m_{l_a}^2 z^2] dz}{m_\mu^2 (z^2 - z) + m_{S_1}^2 (1 - z) + m_{l_a}^2 z}.$$

The total correction to the muon anomalous magnetic moment from Higgs bosons, $\delta a_\mu / \mu_0$, is determined by the sum of expressions (26) and (28)–(34). In order to analyze the resulting expression, it is necessary to know the leptonic coupling constants of Higgs bosons, $\alpha_{\bar{L}_a L_b H_i}$ ($L_a = l_a, \nu_a, N_a$), and the Higgs boson masses m_{H_i}. Up to the present time, information about these quantities has been deduced from the results of searches for deviations from Standard Model predictions and can be represented as upper bounds on the ratio $\alpha_{\bar{L}_a L_b H_i}/m_{H_i}$ or, what is done much more often, on the quantity

$$\sum_i C_i \epsilon_i^{aba'b'} = \sum_i C_i \frac{(\alpha_{\bar{L}_a L_b H_i} \alpha_{\bar{L}_{a'} L_{b'} H_i})^2}{m_{H_i}^4},$$

where C_i are constant coefficients. As a rule, the problem of determining upper bounds on only one quantity $\alpha_{\bar{L}_a L_b H_i}/m_{H_i}$ is rather complicated. By way of example, we consider the decay process

$$\mu^- \to e^- \gamma. \qquad (35)$$

The corresponding diagrams in the third order of perturbation theory are obtained from the diagrams in Figs. 1–3 upon replacing the final-state muon by an electron. The decay width corresponding to (35) includes a set of the quantities $\epsilon_i^{aba'b'}$. Moreover, the presence of diagrams involving singly charged Higgs bosons leads to a destructive interference between the amplitudes for reaction (35), and this complicates still further the problem of extracting information about each of the quantities $\epsilon_i^{aba'b'}$ individually.

We can try to express the leptonic coupling constants $\alpha_{\bar{L}_a L_b H_i}$ of Higgs bosons in terms of the parameters determining the structure of the lepton sector. This problem can be solved analytically only in the two-flavor approximation. By way of example, we indicate that, in the basis

$$\Psi = \begin{pmatrix} \nu_{aL} \\ N_{aR} \\ \nu_{bL} \\ N_{bR}, \end{pmatrix},$$

the neutrino mass matrix has the form

$$\mathcal{M} = \begin{pmatrix} f_{aa} v_L & m_D^a & f_{ab} v_L & M_D \\ m_D^a & f_{aa} v_R & M'_D & f_{ab} v_R \\ f_{ab} v_L & M'_D & f_{bb} v_L & m_D^b \\ M_D & f_{ab} v_R & m_D^b & f_{bb} v_R \end{pmatrix}, \qquad (36)$$

where $m_D^a = h_{aa} k_1 + h'_{aa} k_2$, $M_D = h_{ab} k_1 + h'_{ab} k_2$, $M'_D = h_{ba} k_1 + h'_{ba} k_2$, and v_L are the vacuum expectation values of the neutral component of the left-handed triplet of Higgs fields. Taking into account the

definition of m_D^a and formulas for the charged-lepton masses,

$$m_{l_a} = h_{aa}k_2 + h'_{aa}k_1, \tag{37}$$

and for the W_1 boson mass, we can easily obtain

$$\alpha_{\bar{l}_a\nu_a h} = \frac{h'_{aa}k_2 - h_{aa}k_1}{2k_+} = \frac{g_L}{2\sqrt{2}m_{W_1}\mathrm{c}_{2\beta}} \times (m_{l_a}\mathrm{s}_{2\beta} + m_D^a). \tag{38}$$

We cannot be optimistic about the form of expression (38), since the constants $\alpha_{\bar{L}_a L_b H_i}$ involve quantities about which there are virtually no data (for example, m_D^a).

The coupling constants and masses of Higgs bosons will be conclusively determined either from data on the processes of their direct production or from their manifestation in the form of resonance enhancements in cross sections for specific reactions. For example, the quantities $\alpha_{\bar{e}N_a h}$, $\alpha_{\bar{\mu}N_a h}$, and m_h can be measured by detecting the processes

$$e^-\gamma \to h^{(-)}N_a, \quad \mu^-\gamma \to h^{(-)}N_a \tag{39}$$

in the $e^-\gamma$ and $\mu^-\gamma$ modes of future e^-e^+ and $\mu^-\mu^+$ colliders. The muonic coupling constant of $\Delta^{(--)}$ bosons, $f_{\mu\mu}$, and the mass m_Δ will be determined by studying a $\Delta^{(--)}$-resonance peak in the reaction

$$\mu^-\mu^- \to \mu^-\mu^-. \tag{40}$$

However, investigation of such reactions is a problem for future experiments. At the same time, currently available information about the quantities $\epsilon_i^{aba'b'}$ is not sufficient (for details, see [14]) for making unambiguous predictions for the quantity $\delta a_\mu/\mu_0$. In this situation, we can only assume that the coupling constants and masses of Higgs bosons obey some hierarchy that is not in conflict with existing experimental data. Specifically, our assumption is the following:

$$\left.\begin{aligned} f_{e\mu} &= 0.01 f_{\mu\mu}, & f_{\mu\tau} &= 0.1 f_{\mu\mu}, & \alpha_{\bar{\mu}N_e h} &= 0.1 f_{\mu\mu},\\ \alpha_{\bar{\mu}N_\mu h} &= 0.9 f_{\mu\mu}, & \alpha_{\bar{\mu}N_\tau h} &= 0.2 f_{\mu\mu}, & \alpha_{\bar{\mu}N_e\tilde{\delta}} &= 0.01 f_{\mu\mu},\\ \alpha_{\bar{\mu}N_\mu\tilde{\delta}} &= 0.1 f_{\mu\mu}, & \alpha_{\bar{\mu}N_\tau\tilde{\delta}} &= 0.01 f_{\mu\mu}, & \alpha_{\bar{\mu}eS_1} &= 0.01 f_{\mu\mu},\\ \alpha_{\bar{\mu}\mu S_1} &= 0.9 f_{\mu\mu}, & \alpha_{\bar{\mu}\tau S_1} &= 0.1 f_{\mu\mu}, \end{aligned}\right\} \tag{41}$$

$$\left.\begin{aligned} m_{\Delta_1} &= 1.8 m_{S_1}, & m_{\Delta_2} &= 2 m_{S_1},\\ m_h &= 1.5 m_{S_1}, & m_{\tilde{\delta}} &= 0.6 m_{S_1}. \end{aligned}\right\} \tag{42}$$

In order to simplify the analysis, we also assume that the negative contributions from the diagrams involving the $h^{(-)}h^{(-)}\nu_a$- and $\tilde{\delta}^{(-)}\tilde{\delta}^{(-)}\nu_a$ loops are equal in magnitude to the positive contributions from the diagrams involving W_1-boson exchange and that the following relations hold:

$$(\alpha - \rho_3/2 + \rho_1 + 1)\mathrm{c}_{2\beta}\mathrm{c}_\xi \sim 1, \qquad \beta_1\mathrm{c}_\xi \sim 1. \tag{43}$$

Before proceeding to perform our numerical analysis, we must assess a lower limit on the mass of the lightest neutral Higgs boson in the LRM. In other words, we must discuss the question of how and to what extent the lower limit obtained at LEP II for the mass of the Higgs boson in the Standard Model [15] by investigating the reaction

$$e^+e^- \to Z^* \to Zh \tag{44}$$

can be used to evaluate the mass of the lightest neutral Higgs boson in the extensions of the Standard Model. The quantity

$$\sigma_{e^+e^-\to Zh}\Gamma_Z\Gamma_h \tag{45}$$

for four Zh-decay channels

$$Zh \to q\bar{q}q'\bar{q}',\ q\bar{q}\nu\bar{\nu},\ q\bar{q}l_a\bar{l}_a \quad (l_a = e,\mu),\ \tau^+\tau^- q\bar{q}, \tag{46}$$

where the $h \to q\bar{q}$ final state involves both a quark–antiquark and a gluon–gluon pair, was analyzed in that case.

For the THDM, there are considerable deviations from the Standard Model both in the cross section $\sigma_{e^+e^-\to Zh}$ and in the decay widths Γ_h. Since, in these models, the coupling constant specifying the interaction of the neutral CP-even Higgs boson h with Z bosons has the form

$$g_{ZZh} = \frac{g_L m_Z \sin(\beta-\alpha)}{\mathrm{c}_{\theta_\mathrm{W}}}, \tag{47}$$

where $\sin(\beta-\alpha) \sim 0$ and θ_W is the Weinberg angle, the cross section $(\sigma_{e^+e^-\to Zh})_\mathrm{THDM}$ in the THDM proves to be considerably smaller than the corresponding cross section in the Standard Model. At the same time, the widths of the h boson with respect to decay into quarks and leptons are greater in the THDM than in the Standard Model, since the following relation holds:

$$\frac{(g_{\bar{f}fh})_\mathrm{THDM}}{(g_{\bar{f}fh})_\mathrm{SM}} \approx \tan\beta, \quad f = b,\tau. \tag{48}$$

Obviously, an analysis of the quantity in (45) would lead to different values for the mass of the Higgs boson in the Standard Model and the mass of the h boson in the THDM. Indeed, the LEP data at $|\sin(\beta-\alpha)| \le 0.06$ yields a value of $m_h \sim 10$ GeV at a 98% C.L. [8].

Within the LRM, the reason for the deviation of the cross section $\sigma_{e^+e^-\to ZS_1}$ from the corresponding cross section in the Standard Model may be only the constant of S_1-boson coupling to Z_1 bosons (the Z_1 boson is an analog of the Z boson in the Standard Model),

$$g_{Z_1Z_1S_1} = \frac{g_L \mathrm{s}^2_{\theta_\mathrm{W}} m_{Z_1}[\mathrm{c}_{\theta_0}(1-\tan^2\beta) - 2\mathrm{s}_{\theta_0}\tan\beta]}{2\mathrm{c}_{\theta_\mathrm{W}}(\tan^2\beta+1)} \times (2g_R g'^{-1}\mathrm{c}_\varphi \mathrm{s}_\varphi \mathrm{s}^{-1}_{\theta_\mathrm{W}} - \mathrm{c}^2_\varphi \mathrm{s}^{-2}_{\theta_\mathrm{W}} - g^2_R g'^{-2}\mathrm{s}^2_\varphi), \tag{49}$$

where φ is the angle of mixing of the Z_1 and Z_2 bosons ($\varphi \approx 10^{-2}$–10^{-3}) and g' is the gauge constant of the subgroup $U(1)_{B-L}$. At

$$\varphi = k_2 = 0,$$

$g_{Z_1Z_1S_1}$ reduces to the constant of the Higgs boson coupling to the Z boson in the Standard Model. Since the symmetric LRM reproduces the Standard Model for g_R and g' taking the values

$$g_L = g_R = e\mathrm{s}^{-1}_{\theta_\mathrm{W}}, \quad g' = e\sqrt{\mathrm{c}^2_{\theta_\mathrm{W}} - \mathrm{s}^2_{\theta_\mathrm{W}}}, \tag{50}$$

the quantity $g_R g'^{-1}$ may only slightly differ from unity. Therefore, the factor

$$\Delta g = \frac{\mathrm{c}_{\theta_0}(1-\tan^2\beta) - 2\mathrm{s}_{\theta_0}\tan\beta}{\tan^2\beta+1} \tag{51}$$

is the main source of the deviation of the quantity $g_{Z_1Z_1S_1}$ from the value in the Standard Model. As follows from (23), the angle θ_0 is determined primarily by the parameter α_2, which appears in the Yukawa potential. At $\alpha_2 \sim 10^{-2}$, the angle θ_0 can take values of about $\pi/4$. Concurrently, the S_1 boson can remain light, as before, since its mass is determined by the expression

$$m^2_{S_1} = 2\lambda_1 k^2_+ + 8k^2_1 k^2_2(2\lambda_2+\lambda_3)/k^2_+ - 8\lambda_4 k_1 k_2 + \frac{4k_1k_2k^4_-[2(2\lambda_2+\lambda_3)k_1k_2/k^2_+ - \lambda_4]^2}{\alpha_2 v^2_R k^2_+}, \tag{52}$$

but the S_2 boson ceases to be superheavy,

$$m^2_{S_2} = \frac{\alpha_2 v^2_R k^2_+}{k_1k_2} - \frac{4k_1k_2k^4_-[2(2\lambda_2+\lambda_3)k_1k_2/k^2_+ - \lambda_4]^2}{\alpha_2 v^2_R k^2_+}. \tag{53}$$

We recall that the requirement

$$m_{S_2} \ge 10 \ \text{TeV} \tag{54}$$

is dictated by the need for suppressing fermion-flavor-violating neutral currents in the Lagrangian

$$\mathcal{L}^n_q = -\frac{1}{\sqrt{2}k_+}\sum_{a,b}\bar{u}_a \times \left\{\left[m_{u_a}\left(\mathrm{c}_{\theta_0} + \frac{2k_1k_2}{k^2_-}\mathrm{s}_{\theta_0}\right)S_1 - m_{u_a}\left(\mathrm{s}_{\theta_0} - \frac{2k_1k_2}{k^2_-}\mathrm{c}_{\theta_0}\right)S_2 - im_{d_a}\gamma_5 P_1\right]\delta_{ab} + \frac{k^2_+}{k^2_-}(\mathcal{K}\mathcal{M}_d\mathcal{K}^*)_{ab}(S_1\mathrm{s}_{\theta_0} + S_2\mathrm{c}_{\theta_0})\right\}u_b + (u_a \to d_a, m_{u_a} \leftrightarrow m_{d_a}, \gamma_5 \to -\gamma_5), \tag{55}$$

where u_a (d_a) is the field function for the up (down) quark of flavor a, $\mathcal{M}_d = \mathrm{diag}(m_d, m_s, m_b)$, and $\mathcal{K}$ is the Cabibbo–Kobayashi–Maskawa matrix. This in turn makes it possible to describe correctly $\bar{K}^0 \leftrightarrow K^0$ transitions. However, it was shown in [13] that a consistent scheme for constructing the LRM requires redefining the traditional Yukawa Lagrangian for quarks, with the result that, instead of (55), there arises the expression

$$\mathcal{L}^n_q = -\frac{1}{\sqrt{2}k_+}\sum_a \bar{u}_a\left\{m_{u_a}\left[\left(\mathrm{c}_{\theta_0} - \frac{k_1}{k_2}\mathrm{s}_{\theta_0}\right)S_1 - \left(\mathrm{s}_{\theta_0} + \frac{k_1}{k_2}\mathrm{c}_{\theta_0}\right)S_2\right] + \frac{im_{u_a}k_1}{k_2}\gamma_5 P_1\right\}u_a + (u_a \to d_a, \theta_0 \to -\theta_0). \tag{56}$$

Since the Lagrangian in (56) does not induce any fermion-flavor-violating currents, the inequality in (54) ceases to be valid. It follows from (56) that, with increasing angle θ_0, the deviations of Δg from unity can become fairly large.

By using the Lagrangian in (56), it can be deduced that the S_1-boson widths with respect to decays into quarks and gluons can differ considerably from their counrterparts in the Standard Model. The quantity $\Gamma_{S_1\to\tau^+\tau^-}$ may also differ from the corresponding value in the Standard Model since the constant of S_1-boson coupling to τ leptons has the form

$$g_{\bar{\tau}\tau S_1} = \frac{h'_{aa}k_1 - h_{aa}k_2}{\sqrt{2}k_+} = \frac{g_L}{\sqrt{2}m_Z c_{\theta_\mathrm{W}}}\left(m^\tau_D \tan 2\beta - \frac{m_\tau}{\mathrm{c}_{2\beta}}\right). \tag{57}$$

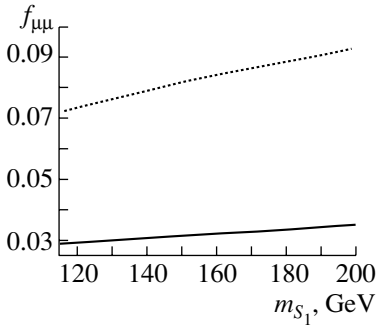

Fig. 4. Curves bounding the region allowed for the parameters $f_{\mu\mu}$ and m_{S_1}. The solid (dotted) curve corresponds to the value of $\delta a_\mu/\mu_0 = 215 \times 10^{-11}$ ($\delta a_\mu/\mu_0 = 637 \times 10^{-11}$.) For both curves, we choose the values of $m_{N_e} = 0.9$ TeV, $m_{N_\mu} = 1$ TeV, $m_{N_\tau} = 1.1$ TeV, and $m_{W_2} = 0.8$ TeV.

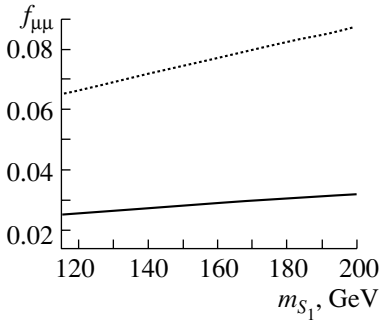

Fig. 5. As in Fig. 4, but for $m_{N_e} = 110$ GeV, $m_{N_\mu} = 140$ GeV, $m_{N_\tau} = 180$ GeV, and $m_{W_2} = 1400$ GeV.

It is therefore obvious that lower limits on the mass of the lightest neutral Higgs boson in the LRM must not be identical to those in the Standard Model. Since, however, no studies analyzing reaction (44) from the point of view of the LRM have thus far been performed, we will also use the value of 115 GeV for the lower limit on the S_1-boson mass.

In Fig. 4, the solid and dotted curves corresponding to $\delta a_\mu/\mu_0$ values equal to 215×10^{-11} and 637×10^{-11}, respectively, are plotted in the plane spanned by the variables $f_{\mu\mu}$ and m_{S_1}. For the heavy-neutrino and W_2-boson masses, we took here the values (in TeV)

$$m_{N_e} = 0.9, \quad m_{N_\mu} = 1, \quad m_{N_\tau} = 1.1, \quad m_{W_2} = 0.8. \tag{58}$$

We recall that the masses of the heavy electron neutrino and of the W_2 boson satisfy the inequality

$$m_{N_e} > 63 \text{ GeV} \cdot \left(\frac{1.6 \text{ TeV}}{m_{W_2}}\right)^4,$$

which was obtained from searches of neutrinoless double-β^- decay.

The region of m_{S_1} and $f_{\mu\mu}$ values allowed from the point of view of the BNL experiment is bounded by the two curves in Fig. 4. As the masses of the N_l neutrino decreases, the Higgs boson coupling constants occurring in the allowed region also decrease. At the masses (in GeV)

$$m_{N_e} = 110, \quad m_{N_\mu} = 140, \quad m_{N_\tau} = 180, \quad m_{W_2} = 1400 \tag{59}$$

and at the same values of the remaining parameters as in Fig. 4, Fig. 5 displays two curves bounding the allowed region of m_{S_1} and $f_{\mu\mu}$ (the solid and the dotted curve correspond to the $\delta a_\mu/\mu_0$ values of 215×10^{-11} and 637×10^{-11}, respectively).

We must now verify whether the values of the coupling constants and masses of Higgs bosons lying within the allowed regions in Figs. 4 and 5 are consistent with the available upper bounds on the parameters $\epsilon_i^{aba'b'}$. Results obtained by studying the direct and inverse muon decays

$$\mu^- \to e^- \bar{\nu}_e \nu_\mu, \tag{60}$$

$$\nu_\mu e^- \to \mu^- \nu_e \tag{61}$$

lead to the inequality [14]

$$\frac{f_{e\mu}^2}{m_{\tilde{\delta}}^2} < 0.109 \times 10^{-5} \text{ GeV}^{-2}, \tag{62}$$

which is compatible with our conclusions. An investigation of the decay process

$$\mu^- \to e^- e^+ e^- \tag{63}$$

yielded the constraint [14]

$$f_{ee} f_{e\mu} \sqrt{\frac{1}{m_{\Delta_1}^4} + \frac{1}{m_{\Delta_2}^4}} < 2.33 \times 10^{-11} \text{ GeV}^{-2}. \tag{64}$$

Under the assumption that $f_{ee} \sim f_{e\mu}$, the inequality in (64) does not contradict the results presented in Figs. 4 and 5, provided that relations (41) and (42) hold. So far, no constraints have been obtained either for the constant $f_{\mu\tau}$ or for the quantity $\alpha_{\bar{l}_a l_b h}$. Since there exists, however, the relation

$$\alpha_{\bar{N}_l l' h} \approx \frac{\alpha_{\bar{l} l' S_1}}{\sqrt{2}},$$

required information could be deduced from the results of searches for the Higgs boson in the Standard Model or for its analog if the relevant experiment is analyzed from the point of view of some extension of the Standard Model. At present, the LEP experiments investigating the processes in (9) and (44) can

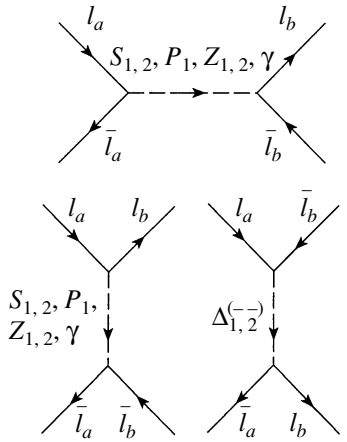

Fig. 6. Feynman diagrams for $l_a\bar{l}_a \to l_b\bar{l}_b$ process ($l_a = e^-, \mu^-$, $l_b = \mu^-, \tau^-$).

serve as a source of information about the parameters of the S_1 boson. An analysis of the processes in (9) can yield constraints only on the constants of S_1-boson coupling to the τ lepton ($\alpha_{\bar{\tau}\tau S_1}$) and to the b quark ($\alpha_{\bar{b}bS_1}$), but, within the LRM, there is no relation between them and $\alpha_{\bar{\mu}\mu S_1}$. It is also obvious that no reliable constraints on $\alpha_{\bar{\mu}\mu S_1}$ can be obtained from an analysis of reaction (44). Analogously, the results of the CUSB collaboration on searches for the decay process (8) [6] would lead to constraints only on $\alpha_{\bar{b}bS_1}$.

3. ROLE OF $l_a\bar{l}_a \to l_b\bar{l}_b$ PROCESSES IN DETERMINING THE PARAMETERS OF THE HIGGS SECTOR

There exists yet another possibility of deriving information about the coupling constants of an analog of the Higgs boson in the Standard Model in analyzing experiments at lepton colliders.

Let us consider the reactions

$$l_a\bar{l}_a \to l_b\bar{l}_b, \quad l_a = e, \mu, l_b = \mu, \tau. \tag{65}$$

The diagrams in the second order of perturbation theory for the Feynman process (65) in the LRM are shown in Fig. 6. Owing to the presence of the s-channel diagram involving S_1-boson exchange, this reaction provides a useful means for obtaining upper bounds on $\alpha_{\bar{\mu}\mu S_1}$. We will assume that, in the initial and final state, the particles involved are unpolarized. The differential cross section for the process in (65) is then given by

$$d\sigma = \frac{d\Omega}{16(2\pi)^2 s}\sum_{\rho,\kappa}\mathcal{M}_{\rho\kappa}, \tag{66}$$

where $\rho, \kappa = Z_1, Z_2, \gamma, \Delta_1, \Delta_2, S_1, S_2, P_1$;

$$\mathcal{M}_{kr} = \frac{1}{8}\{[(G_{kr}^2 - P_{kr}^2)t^2 + (G_{kr}^2 + P_{kr}^2)u^2]$$
$$\times D_k(s)D_r^*(s) + \delta_{l_al_b}[(G_{kr}^2 - P_{kr}^2)s^2$$
$$+ (G_{kr}^2 + P_{kr}^2)u^2]D_k(t)D_r^*(t)\},$$
$$k, r = Z_1, Z_2, \gamma;$$

$$G_{kr} = g_{Vk}g_{Vr} + g_{Ak}g_{Ar},\ P_{kr} = g_{Vk}g_{Ar} + g_{Vr}g_{Ak},$$

$$g_{A\gamma} = 0, \quad g_{V\gamma} = 2e,$$

$$g_{VZ_1} = \frac{e\mathrm{c}_\varphi}{\mathrm{c}_{\theta_\mathrm{W}}\mathrm{s}_{\theta_\mathrm{W}}}\left(2\mathrm{s}_{\theta_\mathrm{W}}^2 - \frac{1}{2}\right)$$
$$+ \frac{e\mathrm{s}_\varphi}{\mathrm{c}_{\theta_\mathrm{W}}\sqrt{\mathrm{c}_{\theta_\mathrm{W}}^2 g_R^2 e^{-2} - 1}}\left(\frac{3}{2} - \frac{\mathrm{c}_{\theta_\mathrm{W}}^2 g_R^2}{2e^2}\right),$$

$$g_{AZ_1} = \frac{e\mathrm{s}_\varphi\sqrt{\mathrm{c}_{\theta_\mathrm{W}}^2 g_R^2 e^{-2} - 1}}{2\mathrm{c}_{\theta_\mathrm{W}}} - \frac{e\mathrm{c}_\varphi}{2\mathrm{s}_{\theta_\mathrm{W}}\mathrm{c}_{\theta_\mathrm{W}}},$$
$$g_{VZ_2} = g_{VZ_1}(\varphi \to \varphi + \pi/2),$$
$$g_{AZ_2} = g_{AZ_1}(\varphi \to \varphi + \pi/2),$$

$$D_\rho(q^2) = [q^2 - m_\rho^2 + i\Gamma_\rho m_\rho]^{-1}, \quad q^2 = s, u, t;$$

$$\sum_{i=1}^{2}\mathcal{M}_{\Delta_i\Delta_i} = 16f_{l_al_b}^4 u^2(2 - \delta_{ab})^2|D_{\Delta_1}(u)|^2$$
$$+(1 \to 2),$$

$$\sum_{jn}\mathcal{M}_{jn} = 4t^2(2 - \delta_{ab})^2[|\alpha_{\bar{l}_al_bS_1}^2 D_{S_1}(t)$$
$$+ \alpha_{\bar{l}_al_bS_2}^2 D_{S_2}(t)|^2 + \alpha_{\bar{l}_al_bP_1}^4|D_{P_1}(t)|^2] + 4s^2$$
$$\times [|\alpha_{\bar{l}_al_aS_1}\alpha_{\bar{l}_bl_bS_1}D_{S_1}(s) + \alpha_{\bar{l}_al_aS_2}\alpha_{\bar{l}_bl_bS_2}D_{S_2}(s)|^2$$
$$+ \alpha_{\bar{l}_al_aP_1}^2\alpha_{\bar{l}_bl_bP_1}^2|D_{P_1}(s)|^2] + 2st(2 - \delta_{l_al_b})\sum_{j,n}I_{jn},$$
$$j, n = S_1, S_2, P_1;$$

$$\sum_j\mathcal{M}_{kj} = 2(g_{Ak}^2 - g_{Vk}^2)t^2(2 - \delta_{l_al_b})$$
$$\times \{\alpha_{\bar{l}_al_bS_1}^2[(t - m_{S_1}^2)(s - m_k^2) + \Gamma_{S_1}\Gamma_k m_{S_1}m_k]$$
$$\times |D_{S_1}(t)D_k(s)|^2 + (\alpha_{\bar{l}_al_bS_1} \to \alpha_{\bar{l}_al_bS_2}, m_{S_1} \to m_{S_2})$$
$$+ (\alpha_{\bar{l}_al_bS_1} \to \alpha_{\bar{l}_al_bP_1}, m_{S_1} \to m_{P_1})\}$$
$$+ 2\delta_{l_al_b}(g_{Ak}^2 - g_{Vk}^2)s^2\{\alpha_{\bar{l}_al_aS_1}^2[(s - m_{S_1}^2)(t - m_k^2)$$
$$+ \Gamma_{S_1}\Gamma_k m_{S_1}m_k]|D_{S_1}(s)D_k(t)|^2$$
$$+ (\alpha_{\bar{l}_al_aS_1} \to \alpha_{\bar{l}_al_aS_2}, m_{S_1} \to m_{S_2})$$
$$+ (\alpha_{\bar{l}_al_aS_1} \to \alpha_{\bar{l}_al_aP_1}, m_{S_1} \to m_{P_1})\},$$

$$\sum_{i=1}^{2}\mathcal{M}_{k\Delta_i} = -2f_{l_al_b}^2(g_{Vk} - g_{Ak})^2u^2$$

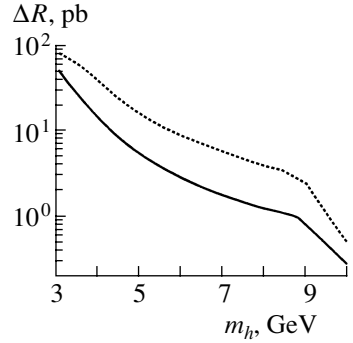

Fig. 7. ΔR as a function of m_h for the process $e^+e^- \to \tau^+\tau^-$: (solid curve) results obtained within the THDM1 and (dotted curve) results obtained within the THDM2.

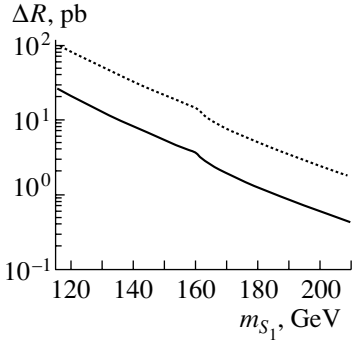

Fig. 8. ΔR as a function of m_{S_1} for the processes (solid curve) $\mu^+\mu^- \to \mu^+\mu^-$ and (dotted curve) $\mu^+\mu^- \to \tau^+\tau^-$ within the LRM at $f_{\mu\mu} = 2 \times 10^{-2}$.

$$\times \sum_{i=1}^{2}\{(2-\delta_{ab})[(u-m_{\Delta_i}^2)(s-m_k^2) + \Gamma_{\Delta_i}\Gamma_k m_{\Delta_i} m_k]|D_{\Delta_i}(u)D_k(s)|^2 + \delta_{l_a l_b}[(t-m_k^2)(u-m_{\Delta_i}^2) + \Gamma_k\Gamma_{\Delta_i} m_k m_{\Delta_i}] \times |D_k(t)D_{\Delta_i}(u)|^2\},$$

$$I_{jn} = a_{jn}[(t-m_j^2)(s-m_n^2) + m_j\Gamma_j m_n\Gamma_n] \times |D_j(t)D_n(s)|^2,$$

$$a_{S_iS_j} = \alpha_{\bar{l}_a l_a S_i}\alpha_{\bar{l}_b l_b S_i}\alpha^2_{\bar{l}_a l_b S_j},$$
$$\alpha_{S_iP_1} = -\alpha_{\bar{l}_a l_a S_i}\alpha_{\bar{l}_b l_b S_i}\alpha^2_{\bar{l}_a l_b P_1},$$
$$\alpha_{P_1S_i} = -\alpha_{\bar{l}_a l_a P_1}\alpha_{\bar{l}_b l_b P_1}\alpha^2_{\bar{l}_a l_b S_i};$$

s, u, and t are the Mandelstam variables; and the expressions for the decay widths of Higgs bosons can be found in [13].

Let us investigate physical colloraries of the constraints obtained for the parameters of the Higgs sector for reactions (65). By way of example, we will consider not only the LRM, but also the THDM1 and THDM2. The LRM is advantageous in that cross sections within a number of nonsupersymmetric extensions of the Standard Model can be derived under specific assumptions from the LRM cross section. For example, the THDM1 and THDM2 expressions for the differential cross section for reaction (65) are obtained from (66) upon the substitutions

$$\left.\begin{aligned} g_{VZ_2} = g_{AZ_2} = \varphi = f_{l_a l_b} = 0, & \\ \alpha_{\bar{l}_a l_b S_1} = \alpha_{\bar{l}_a l_b S_2} = \alpha_{\bar{l}_a l_b P_1} = 0, & \quad a \neq b, \\ \alpha_{\bar{l}_a l_a S_1} = \alpha_{\bar{l}_a l_a P_1} = m_{l_a}\tan\beta/v, & \quad \alpha_{\bar{l}_a l_a S_2} \approx 0, \end{aligned}\right\} \quad (67)$$

where the S_1, S_2, and P_1 bosons are, respectively, the THDM h, H, and A bosons and $v = 246$ GeV. We recall that the Higgs boson couplings to the down members of the fermion doublets are identical in the THDM1 and in the THDM2, but that, for the up members of the fermion doublets, they are given, respectively, by $m_{f_a^u}\tan\beta/v$ and by $m_{f_a^u}\cot\beta/v$ ($m_{f_a^u}$ is the mass of the up fermion of flavor a). It follows that, in these two models, the only difference between the cross sections for reactions (65) stems from the fact that the decay widths of Higgs bosons are different there. If the mass of the Higgs boson h does indeed lie in the range from 3.1 to 10 GeV, resonance peaks associated with the h boson will be present in the cross sections for the processes

$$e^+e^- \to \mu^+\mu^-, \quad (68)$$

$$e^+e^- \to \tau^+\tau^-. \quad (69)$$

In order to characterize the height of this peak with respect to the cross section within the Standard Model, we introduce the quantity (the contribution of the Higgs boson to the cross section within the Standard Model is not included!)

$$\Delta R = \left(\frac{d\sigma}{d\Omega}\right)^{\mathrm{THDM}}_{\sqrt{s}=m_h} - \left(\frac{d\sigma}{d\Omega}\right)^{\mathrm{SM}}_{\sqrt{s}=m_h}.$$

In the THDM1 term at $\sqrt{s} = m_h$, $\tan\beta$ appearing in all fermion modes of h decay is canceled by $\tan\beta$, which specifies the strength of h-boson coupling to leptons, so that ΔR proves to be independent of $\tan\beta$. This in turn means that, if the contribution of the Higgs boson is taken into account in the Standard Model, the height of the corresponding resonance peak will be identical to that in the THDM1. Only the decay widths will then be different:

$$\Gamma^{\mathrm{THDM1}}_{h\to\bar{f}_i f_i} = \tan\beta \cdot \Gamma^{\mathrm{SM}}_{h\to\bar{f}_i f_i}.$$

The height of the h-resonance peak is weakly dependent on the scattering angle θ and is determined primarily by the Higgs boson mass m_h. For example,

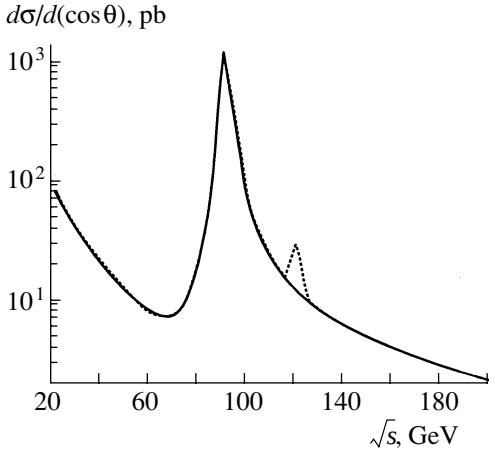

Fig. 9. Differential cross section for the process $\mu^+\mu^- \to \mu^+\mu^-$ as a function of $\sqrt{s}$ at $\theta = \pi/2$: (solid curve) results within the Standard Model and (dotted curve) LRM results at $f_{\mu\mu} = 2 \times 10^{-2}$.

ΔR reaches a value of 4 pb at $m_h = 3.1$ GeV for reaction (68). So great a height of the peak is due to an extreme smallness of the decay width ($\Gamma_h \approx 8$ keV). With increasing h-boson mass, Γ_h grows, which is accompanied by a decrease in the peak height; at $m_h = 10$ GeV, ΔR becomes as small as 1.5 fb. For the THDM1, the conditions for detecting the Higgs boson appear to be more favorable in the case of reaction (69).

For the THDM2, some of the partial decay widths of the h boson into fermions are not proportional to $\tan\beta$. By virtue of this circumstance, ΔR depends on the values chosen for $\tan\beta$. By way of example, we indicate that, at $\tan\beta = 30$ and $m_h = 3.1$ GeV, the height of the h peak in reaction (68), $\Delta R_{\mu\mu}$, is as great as 2.3×10^4 pb, while, in reaction (69), $\Delta R_{\tau\tau}$ is only 81.5 pb. With increasing mass, however, $\Delta R_{\mu\mu}$ decreases much faster than $\Delta R_{\tau\tau}$: at $m_h \approx 3.865$ GeV, $\Delta R_{\mu\mu} \approx \Delta R_{\tau\tau}$, while, at $m_h = 5$ GeV, $\Delta R_{\tau\tau}$ is approximately 20 times as great as $\Delta R_{\mu\mu}$. Figure 7 shows ΔR as a function of m_h for reaction (69) at $\tan\beta = 30$. The solid and dotted curves were calculated within the THDM1 and the THDM2, respectively.

In the process

$$\mu^+\mu^- \to \mu^+\mu^-, \tag{70}$$

the probability of observing a Higgs boson of mass predicted by the THDM is even higher. By way of example, we indicate that, in the THDM1, ΔR reaches the value of 66 pb at $m_h = 10$ GeV, while, in the THDM2, ΔR is equal to 153 pb at $\tan\beta = 30$.

Let us now proceed to discuss reactions (65) within the LRM. As before, we assume that the coupling constants and masses of the Higgs bosons obey relations (41) and (42), respectively. Since there is no information about the constants of Higgs boson coupling to τ leptons, we have to make some assumption on their magnitude. Specifically, we set:

$$f_{\tau\tau} = 2f_{\mu\mu}, \qquad \alpha_{\bar\tau\tau S_1} = 2\alpha_{\bar\mu\mu S_1}. \tag{71}$$

For reaction (68), the relative height of the S_1-resonance peak,

$$\Delta R = \left(\frac{d\sigma}{d\Omega}\right)^{\mathrm{LRM}}_{\sqrt{s}=m_{S_1}} - \left(\frac{d\sigma}{d\Omega}\right)^{\mathrm{SM}}_{\sqrt{s}=m_{S_1}},$$

appears to be small. For example, the ΔR value at $m_{S_1} = 115$ GeV is as small as a few femtobarns. However, prospects for observing the lightest neutral Higgs boson of the LRM in reactions (65) are quite good at a muon collider. In Fig. 8, we present ΔR as a function of m_{S_1} for reaction (70) (solid curve) and for the reaction

$$\mu^+\mu^- \to \tau^+\tau^- \tag{72}$$

(dotted curve) at $f_{\mu\mu} = 2 \times 10^{-2}$. The quantity ΔR is independent of $\tan\beta = k_1/k_2$ and exhibits an extremely weak dependence on the scattering angle θ. The differential cross section for reaction (70) within (dotted curve) the LRM and (solid curve) the Standard Model are shown in Fig. 9 at $\theta = \pi/2$, $m_{S_1} = 120$ GeV, and $f_{\mu\mu} = 2 \times 10^{-2}$. The two curves nearly coincide, and only in the energy range between $m_{S_1} - \Gamma_{S_1}/2$ and $m_{S_1} + \Gamma_{S_1}/2$ do they become distinguishable.

4. CONCLUSION

We have investigated the effect of the Higgs sector on the the anomalous magnetic moment of the muon within the LRM. In doing this, we have taken into account the contributions from the interactions of the doubly charged ($\Delta^{(--)}_{1,2}$), singly charged ($h^{(-)}$, $\tilde\delta^{(-)}$), and neutral (S_1) Higgs bosons with leptons and gauge bosons. The resulting anomalous magnetic moment of the muon is a function of the parameters of the Higgs sector. Available experimental data are insufficient for making unambiguous predictions for the structure of the Higgs sector in the LRM. For this reason, we have assumed a specific hierarchy both for the Yukawa constants and for the Higgs boson masses. For independent parameters, we have chosen the triplet diagonal Yukawa constant $f_{\mu\mu}$ and the mass of the neutral Higgs boson S_1. Our analysis has revealed that, if $f_{\mu\mu}$ lies in the interval from 0.025 to 0.09, the expression obtained here for the muon anomalous magnetic moment falls within the interval of E821 results at a 90% C.L. for m_{S_1} ranging between 115 and 210 GeV.

The values of the Yukawa constants determine the strength of the interaction of physical Higgs bosons with fermions. It is therefore reasonable to use their estimates obtained in calculating the anomalous magnetic moment of the muon in studying other processes. For this purpose, we have considered the production of lepton pairs at e^+e^- and $\mu^+\mu^-$ colliders. We have obtained analytic expressions for differential cross sections with allowance for Higgs boson contributions. Since the LRM includes the THDM, we have first performed our analysis of cross sections within the THDM. It has appeared that, if the mass of the lightest neutral Higgs boson does indeed fall within the range 3.1–10 GeV, as is inferred from the condition requiring that the THDM1 and THDM2 be consistent with the data of the E821 experiment [8], the resonance peak associated with this Higgs boson may be detected at currently operating e^+e^- colliders (VEPP-4M, CESR, KEKB, PEP-II, SLC). However, this will call for a considerable amount of effort aimed at reducing the energy spread in e^+ and e^- beams since the decay width of the h boson is extremely small.

In performing the analogous analysis within the LRM, we have assumed that the mass of the lightest neutral Higgs boson (S_1 boson) is greater than 115 GeV. For the reaction $e^+e^- \to \mu^+\mu^-$, the height of the corresponding resonance peak is a few femtobarns at $m_{S_1} = 115$ GeV. It has been shown that the detection of the lightest neutral Higgs boson of the LRM can be implemented at a muon collider.

REFERENCES

1. Review of Particle Physics, Eur. Phys. J. C **15**, 1 (2000).
2. Muon g-2 Collab. (H. N. Brown *et al.*), Phys. Rev. D **62**, 091101 (2000); Phys. Rev. Lett. **86**, 2227 (2001).
3. A. Czarnecki and W. J. Marciano, Nucl. Phys. B (Proc. Suppl.) **76**, 245 (1999).
4. M. Davier and A. Hoker, Phys. Lett. B **435**, 427 (1998); M. Hayakawa and T. Kinoshita, Phys. Rev. D **57**, 465 (1998).
5. G. Altarelli, N. Cabibbo, and L. Maiani, Phys. Lett. B **40B**, 415 (1972); A. Czarnecki, B. Krause, and W. J. Marciano, Phys. Rev. Lett. **76**, 3267 (1996).
6. CUSB Collab. (P. Franzini *et al.*), Phys. Rev. D **35**, 2883 (1987).
7. DELPHI Collab. (J. Kurowska, O. Grajek, and P. Zalewski), CERN-OPEN-99-385.
8. A. Dedes and H. E. Haber, hep-ph/0102297.
9. V. Barger *et al.*, in *Proceedings of the First Workshop on the Physics Potential and Development of $\mu^+\mu^-$ Colliders, Napa, California, 1992,* Nucl. Instrum. Methods Phys. Res. A **350**, 24 (1994); in *Proceedings of the 5th International Conference on Physics Potential and Development of Muon Colliders (MUMU 99), San Francisco, California, 1999*, AIP Conf. Proc. **542**, 77 (2000).
10. A. Czarnecki and W. J. Marciano, Alberta Thy 03-01, BNL-HET-01/4; hep-ph/0102122.
11. T. Kinoshita and W. J. Marciano, in *Quantum Electrodynamics,* Ed. by T. Kinoshita (World Sci., Singapore, 1990), p. 419.
12. J. F. Gunion *et al.*, Phys. Rev. D **40**, 1546 (1989).
13. G. G. Boyarkina and O. M. Boyarkin, Eur. Phys. J. C **13**, 99 (2000).
14. O. M. Boyarkin and T. I. Bakanova, Phys. Rev. D **62**, 075008 (2000).
15. DELPHI Collab. (P. Abren *et al.*), Phys. Lett. B **499**, 23 (2001).

Translated by A. Isaakyan

Physics of Atomic Nuclei, Vol. 66, No. 2, 2003, pp. 294–301. Translated from Yadernaya Fizika, Vol. 66, No. 2, 2003, pp. 319–326.

ELEMENTARY PARTICLES AND FIELDS
Theory

Process $\gamma\gamma \to \nu\bar{\nu}$ in a Strong Magnetic Field

A. V. Kuznetsov*, N. V. Mikheev, and D. A. Rumyantsev*****

Yaroslavl State University, Sovetskaya ul. 14, Yaroslavl, 150000 Russia

Received September 14, 2001

Abstract—The three-vertex loop amplitude in a strong magnetic field are analyzed in a general form by using the asymptotic behavior of the electron propagator in an external field. The process $\gamma\gamma \to \nu\bar{\nu}$ is studied in terms of the scalar–vector–vector (SVV), pseudoscalar–vector–vector (PVV), vector–vector–vector (VVV), and axial-vector–vector–vector (AVV) combinations of couplings. It is shown that only in the case of the SVV combination does the amplitude grow linearly with increasing magnetic-field strength, the amplitudes evaluated with the other combinations of couplings (PVV, VVV, and AVV) featuring no linearly increasing terms. The process $\gamma\gamma \to \nu\bar{\nu}$ is also studied within the left–right model, which is an extension of the Standard Model of electroweak interactions and which may involve an effective scalar $\nu\nu ee$ coupling. Possible astrophysical manifestations of this process are discussed.

1. INTRODUCTION

There are interesting quantum processes that are kinematically forbidden or strongly suppressed in a vacuum, but which are possible in a sufficiently strong magnetic field. Magnetic fields of required strength can be generated in astrophysical cataclysms such as a supernova explosion or the merger of neutron stars. A natural scale of the strength of a magnetic field is determined by the critical (or Schwinger) value of $B_e = m_e^2/e \simeq 4.41 \times 10^{13}$ G.[1)] There are reasons to believe that such fields may exist in astrophysical objects. For example, so-called magnetars, which are neutron stars featuring a magnetic field of strength about 4×10^{14} G, were observed [1, 2]. Models of astrophysical processes and objects where magnetic fields may be as strong as 10^{17} to 10^{18} G were discussed in the literature [3–6]. Thus, the physics of quantum processes in strong external fields forms an interesting and important realm of research.

Of particular interest are loop quantum processes involving only electrically neutral particles (such as the photon or the neutrino) in the initial and final states. The effect of an external field on such processes is associated with two factors. First, charged virtual fermions are sensitive to a magnetic field, a major part being played here by the electron, since this particle has the maximum specific charge e/m_e. Second, a strong magnetic field has a pronounced effect on the dispersion properties of photons and, hence, on their kinematics.

Two-vertex loop processes of the $\gamma \to \gamma$ type (photon polarization operator in an external field) or the decays $\gamma \to \nu\bar{\nu}$, $\nu \to \nu\gamma$, etc., have been studied for a long time. Without going into details, we only mention that the most general expression for the two-vertex loop amplitude for $j \to f\bar{f} \to j'$ transitions in a uniform external magnetic field and in a crossed field was obtained in [7], where the analysis was performed by using various combinations of the scalar, pseudoscalar, vector, and pseudovector couplings of the generalized currents j and j' to fermions.

In this study, we consider the general case of a three-vertex loop process in a strong magnetic field (see the corresponding Feynman diagram in Fig. 1).

The transformation of a photon pair into a neutrino–antineutrino pair, $\gamma\gamma \to \nu\bar{\nu}$—this reaction is strongly suppressed in a vacuum—is among processes of the above type that are being discussed most extensively. In the diagram for this reaction, two vertices may be only of the vector type ($\Gamma_1 = \Gamma_2 = V$). Within the Standard Model (SM), the third vertex may be either of the vector or of the axial-vector type ($\Gamma_3 = V, A$), while, beyond the SM, it may also involve a scalar or a pseudoscalar coupling ($\Gamma_3 = S, P$).

The splitting of a photon into two photons into a magnetic field, $\gamma \to \gamma\gamma$ (this reaction is kinematically forbidden in a vacuum), is yet another three-vertex loop process that has attracted the attention of theorists for many years. A review devoted to this

*e-mail: avkuzn@uniyar.ac.ru
**e-mail: mikheev@uniyar.ac.ru
***e-mail: rda@uniyar.ac.ru

[1)]Here, we use the system of units where $c = \hbar = 1$. Throughout the article, $e > 0$ is an elementary charge.

1063-7788/03/6602-0294$24.00

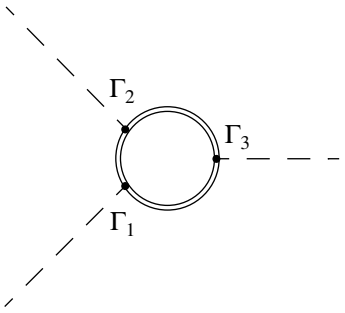

Fig. 1. Feynman diagram for a three-vertex process in a strong magnetic field. Double lines represent the electron propagators obtained on the basis of exact solutions to the Dirac equation in an external field.

process is given in [8], where the interested reader can also find references to earlier studies devoted to the subject; among more recent articles, mention can be made of [9–14]. All three vertices in this process involve only a vector coupling, $\Gamma_1 = \Gamma_2 = \Gamma_3 = V$.

In what follows, we therefore consider the case where two vertices—for example, Γ_1 and Γ_2—are of a vector type and are associated with coupling to a photon and where the third vertex Γ_3 is arbitrary and is assumed to involve coupling to the respective current. The ensuing exposition is organized as follows. A survey of the literature devoted to studying the amplitude for the electroweak process of photon-pair transformation into a neutrino–antineutrino pair, $\gamma\gamma \to \nu\bar{\nu}$, in a vacuum and in a weak field is given in Section 2. A general analysis of a three-vertex process in a strong magnetic field is performed in Section 3. In Section 4, the amplitude and the cross section for the process $\gamma\gamma \to \nu\bar{\nu}$ in a strong magnetic field are calculated within the model where left–right symmetry is broken. Possible astrophysical manifestations of the process in question are discussed in Section 5, where its contribution to the rate of the energy loss of a star per unit volume is estimated numerically for various mechanisms of the process. We also estimate the neutrino emissivity of a magnetized star.

2. PROCESS $\gamma\gamma \to \nu\bar{\nu}$ IN A VACUUM AND IN A WEAK FIELD

2.1. Standard Electroweak Interaction

In all probability, it was Pontecorvo who initiated investigations into the transition of two photons into a neutrino–antineutrino pair and who indicated, for the first time, that neutrino processes may have important implications for astrophysics [15]. This transition is described by two Feynman diagrams of the type in Fig. 2, where a virtual fermion propagates along the loop and where one implies the interchange of the photons involved, the large circle denoting the effective weak fermion–neutrino interaction.

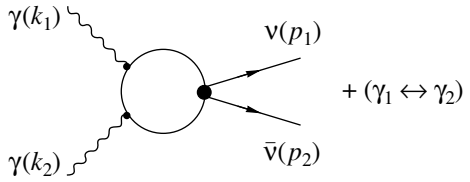

Fig. 2. Feynman diagram for the process $\gamma\gamma \to \nu\bar{\nu}$.

With allowance for the gauge invariance of electromagnetic interaction, the general expression for the reaction amplitude can be represented in the form

$$\mathcal{M} = \frac{\alpha}{\pi}\frac{G_F}{\sqrt{2}}[\bar{\nu}_i(p_1)T_{\alpha\beta\mu\nu}\nu_i(-p_2)]f_1^{\alpha\beta}f_2^{\mu\nu}, \qquad (1)$$

where the subscript i specifies the neutrino flavor ($i = e, \mu, \tau$)[2)] and $f^{\alpha\beta} = k^\alpha\varepsilon^\beta - k^\beta\varepsilon^\alpha$ is the photon-electromagnetic-field tensor in the momentum representation. The tensor $T_{\alpha\beta\mu\nu}$ is a Dirac matrix and must be constructed from available covariant quantities, its dimension being that of inverse mass.

It was found in [16] that, in the case of massless neutrinos and real photons, this amplitude is strictly equal to zero in the local limit of standard weak interaction (Gell-Mann theorem). A qualitative explanation of this statement is as follows: in the c.m. frame, the angular momentum taken away by the left-handed neutrino and the right-handed antineutrino is equal to unity; however, a two-photon system cannot have the angular momentum of unity, as was first indicated by Landau [17] (Yang theorem [18]). In terms of tensor calculus, this means that there are no covariant quantities for constructing the tensor $T_{\alpha\beta\mu\nu}$ such that it would adequately describe the chiral properties of massless neutrinos and satisfy Bose symmetry.

If at least one of the conditions of the Gell-Mann theorem is violated, the amplitude in (1) does not vanish. In the case of massive neutrinos, the reaction under consideration is allowed [19, 20] because the chiral properties of massive neutrinos differ from those in the massless case, the amplitude being proportional to the neutrino mass. The Lorentz structure of the amplitude can be illustrated by the expression for the tensor $T_{\alpha\beta\mu\nu}$ at low photon energies ($\omega \ll m_e$), in which case the electron loop makes a dominant contribution to the amplitude:

$$T_{\alpha\beta\mu\nu} = -\frac{i}{24}(2\delta_{ie} - 1)\frac{m_{\nu_i}}{m_e^2}\gamma_5\varepsilon_{\alpha\beta\mu\nu}. \qquad (2)$$

[2)]Expression (1) is readily extended to the case of lepton mixing.

If weak interaction is described in terms of W-boson exchange, the nonlocality of the interaction results in that the amplitude depends on the momenta of the neutrino and the antineutrino individually rather than on their sum. By virtue of this, the expression for the amplitude develops the structure [21–23]

$$T_{\alpha\beta\mu\nu} = \frac{8i}{3}\left(\ln\frac{m_W^2}{m_e^2} + \frac{3}{4}\right)\frac{1}{m_W^2} \times [\gamma_\alpha g_{\beta\mu}(p_1 - p_2)_\nu + \gamma_\mu g_{\nu\alpha}(p_1 - p_2)_\beta](1+\gamma_5). \quad (3)$$

It can be seen that the amplitude is strongly suppressed in both cases, either by a small neutrino mass in the numerator or by a large W-boson mass in the denominator.

Yet another case of a nonzero amplitude is realized if one photon [24] or both of them [25–27] are off the mass shell. This being so, $k_\mu f^{\mu\nu} \neq 0$, so that the photon momenta can be used to construct the tensor $T_{\alpha\beta\mu\nu}$. In the case of $\omega \ll m_e$, we arrive at

$$T_{\alpha\beta\mu\nu} = -\frac{i}{24}(2\delta_{ie} - 1)\frac{1}{m_e^2}\gamma^\rho(1+\gamma_5) \times (\varepsilon_{\rho\alpha\mu\nu}k_{1\beta} + \varepsilon_{\rho\mu\alpha\beta}k_{2\nu}), \quad (4)$$

where $k_{1,2}$ are the photon momenta. Note that, since the neutrino mass is zero, one can make the substitution $k_1 \leftrightarrow -k_2$ in (4).

2.2. Extension of the Standard Model with Broken Left–Right Symmetry

If the effective Lagrangian of neutrino–lepton interaction does not conserve neutrino helicity, the conditions of the Gell-Mann theorem are violated, with the result that the transition $\gamma\gamma \to \nu\bar{\nu}$ becomes possible. This situation is realized in the presence of coupling between scalar and pseudoscalar neutral currents in the effective Lagrangian written in terms of neutral currents. As was shown in [28], this is so in the model where left–right symmetry is broken and where vector bosons interacting with left- and right-handed weak currents are mixed [29]. Recall that, in this model, the Lagrangian of νeW interaction has the form

$$\mathcal{L} = \frac{g}{2\sqrt{2}}\{[\bar{e}\gamma_\alpha(1+\gamma_5)\nu_e](W_1^\alpha\cos\zeta + W_2^\alpha\sin\zeta) + [\bar{e}\gamma_\alpha(1-\gamma_5)\nu_e](-W_1^\alpha\sin\zeta + W_2^\alpha\cos\zeta) + \text{h.c.}\}, \quad (5)$$

where $W_{1,2}$ are the mass-matrix eigenstates and ζ is the mixing angle. The existing constraints on the parameters of this model come from low-energy accelerator experiments and have the form [30]

$$M_{W_2} > 715\ \text{GeV}, \quad \zeta < 0.013. \quad (6)$$

Owing to the smallness of the mixing angle, the W_2 state differs only slightly from the right-handed boson W_R.

The constraint on the parameters of the model from astrophysical data—specifically, from an analysis of neutrino events from the supernova SN1987A—is more stringent. Combining it with the accelerator data, one obtains [31]

$$M_{W_R} > 23\ \text{TeV}, \quad \zeta < 10^{-5}. \quad (7)$$

The terms in the effective Lagrangian of $\nu\nu ee$ interaction that are responsible for the reaction $\gamma\gamma \to \nu\bar{\nu}$ are those owing to which the product neutrino or antineutrino has a "nonstandard" helicity. Such terms are due to boson mixing, which is associated with the product of the left- and right-handed currents in the effective Lagrangian (5). Taking into account the smallness of the mixing angle and of the mass ratio M_{W_1}/M_{W_2}, we can recast the Lagrangian of $\nu\nu ee$ interaction into the form

$$\mathcal{L}_{\text{eff}} \simeq -4\zeta\frac{G_\text{F}}{\sqrt{2}}\left[(\bar{e}e)(\bar{\nu}_e\nu_e) - (\bar{e}\gamma_5 e)(\bar{\nu}_e\gamma_5\nu_e)\right]. \quad (8)$$

Here, there are two channels through which two photons are transformed into a neutrino–antineutrino pair and which are forbidden in the SM. These are

$$\gamma\gamma \to (\nu_e)_L(\bar{\nu}_e)_L, \quad \gamma\gamma \to (\nu_e)_R(\bar{\nu}_e)_R, \quad (9)$$

where $(\nu_e)_R$ and $(\bar{\nu}_e)_L$ are sterile neutrinos (that is, neutrinos that are not involved in standard weak interactions). In the c.m. frame, the total spin of the neutrino–antineutrino pairs in (9) is zero, whence it follows that the transition $\gamma\gamma \to \nu\bar{\nu}$ becomes allowed.

For the tensor $T_{\alpha\beta\mu\nu}$, a straightforward calculation of the relevant amplitude with the effective Lagrangian (8) leads to the expression

$$T_{\alpha\beta\mu\nu} = \frac{4\zeta m_e}{k_1k_2}\left\{\left[1 + \frac{1}{2}(1-4\tau)I(\tau)\right]g_{\alpha\nu}g_{\beta\mu} - \frac{i}{4}I(\tau)\gamma_5\varepsilon_{\alpha\beta\mu\nu}\right\}, \quad (10)$$

where

$$\tau = \frac{m_e^2}{2(k_1k_2)}, \quad (11)$$

$$I(\tau) = \int_0^1 dx\int_0^{1-x} dy\frac{1}{\tau - xy - i0}.$$

It should be noted that the general structure of the tensor in (10) is identical to that of the tensor that can be extracted from the results presented in [28]; however, the numerical coefficients are different in the two expressions under comparison.

In the model being considered, the amplitude of the process $\gamma\gamma \to \nu\bar{\nu}$ is suppressed by the mixing angle ζ, which is a small parameter.

2.3. Effect of an External Field

As was mentioned above, an external magnetic field can enhance the rate of the reaction under study. In this case, the presence of the electromagnetic-field tensor $F_{\mu\nu}$ associated with an external field offers a new possibility for constructing the tensor $T_{\alpha\beta\mu\nu}$, which enters into expression (1) for the amplitude. As a matter of fact, the field appears in the amplitude in the form of the dimensionless tensor $\mathcal{F}_{\mu\nu} = eF_{\mu\nu}/m_e^2$, and this can lead to an additional enhancement if the strength of the field is greater than the Schwinger value $B_e = m_e^2/e$.

In [32], the reaction $\gamma\gamma \to \nu\bar{\nu}$ was studied on the basis of the SM in the leading order of the expansion in a relatively weak magnetic field ($B \ll B_e$, the expansion parameter being B/B_e) and at low photon energies ($\omega \ll m_e$). It is precisely in this approximation that the use of the effective Lagrangian obtained in [33] from an analysis of the amplitude for the reaction $\gamma\gamma \to \gamma\nu\bar{\nu}$ is appropriate. It should be noted that the expression obtained in [32] for the amplitude [formulas (4) and (5) in that article] is rather cumbersome. Recasting this amplitude into the form (1), we find that the tensor $T_{\alpha\beta\mu\nu}$ can be represented as

$$T_{\alpha\beta\mu\nu} = \frac{g_V}{90m_e^2}\gamma^\rho(1+\gamma_5) \tag{12}$$
$$\times \{3g_{\alpha\nu}g_{\beta\mu}\mathcal{F}_{\rho\sigma}(k_1+k_2)^\sigma - 3\mathcal{F}_{\alpha\beta}g_{\mu\rho}k_{1\nu}$$
$$- 3\mathcal{F}_{\mu\nu}g_{\alpha\rho}k_{2\beta} - 14g_{\alpha\rho}k_1^\sigma(g_{\beta\mu}\mathcal{F}_{\nu\sigma} + \mathcal{F}_{\beta\mu}g_{\nu\sigma})$$
$$- 14g_{\mu\rho}k_2^\sigma(g_{\nu\alpha}\mathcal{F}_{\beta\sigma} + \mathcal{F}_{\nu\alpha}g_{\beta\sigma})\},$$

where $g_V = \pm 1/2 + 2\sin^2\theta_W$, the upper (lower) sign corresponding to the electron neutrino (muon and tau neutrinos). It can be seen that the amplitude of the process grows linearly with increasing field. Below, we will show that, within the standard theory of weak interactions, this is so only in the weak-field limit ($B \ll B_e$), the amplitude in the strong-field limit ($B \gg B_e$) approaching a constant value.

In [34–36], the process $\gamma\gamma \to \nu\bar{\nu}$ and the respective processes in the crossing channels were studied in the weak-field approximation, but the photon energy was allowed there to vary over the region $\omega < m_W$. In the limit of $\omega \ll m_e$, the amplitude obtained in [35] is consistent with that from [32]. Unfortunately, the expression for the amplitude in [35] is so cumbersome that even the simplest test for gauge invariance presents a problem.

In the earlier study reported in [37], the process $\gamma\gamma \to \nu\bar{\nu}$ was analyzed in the strong-field limit ($B \gg B_e$) at low photon energies ($\omega \ll m_e$) without taking into account the Z-boson contribution.

However, an analysis of the three-vertex loop process $\gamma\gamma \to \nu\bar{\nu}$ in a strong magnetic field under arbitrary kinematical conditions has not yet been performed.

3. GENERAL ANALYSIS OF A THREE-VERTEX LOOP PROCESS IN A STRONG MAGNETIC FIELD

The electron propagator in a magnetic field can be represented in the form

$$S(x,y) = e^{i\Phi(x,y)}\hat{S}(x-y), \tag{13}$$

$$\Phi(x,y) = -e\int_x^y d\xi_\mu\left[A_\mu(\xi) + \frac{1}{2}F_{\mu\nu}(\xi-y)_\nu\right], \tag{14}$$

where A_μ is the 4-potential of a constant uniform external magnetic field. In this propagator, the factor that is invariant under translations, $\hat{S}(x-y)$, admits different representations. For our purposes, it is convenient to write it as a partial decomposition in the Fourier integral; that is,

$$\hat{S}(X) = -\frac{i}{4\pi}\int_0^\infty \frac{d\tau}{\tanh\tau}\int\frac{d^2p}{(2\pi)^2} \tag{15}$$
$$\times\left\{[(p\gamma)_{||} + m_e]\Pi_-(1+\tanh\tau)\right.$$
$$+ [(p\gamma)_{||} + m_e]\Pi_+(1-\tanh\tau)$$
$$\left. - (X\gamma)_\perp\frac{ieB}{2\tanh\tau}(1-\tanh^2\tau)\right\}$$
$$\times\exp\left(-\frac{eBX_\perp^2}{4\tanh\tau} - \frac{\tau(m_e^2 - p_{||}^2)}{eB} - i(pX)_{||}\right),$$
$$d^2p = dp_0dp_3, \qquad \Pi_\pm = \frac{1}{2}(1 \pm i\gamma_1\gamma_2),$$
$$\Pi_\pm^2 = \Pi_\pm, \qquad [\Pi_\pm, (a\gamma)_{||}] = 0,$$

where γ_α are the Dirac matrices in the standard representation and 4-vectors labeled with the $\perp$ and $||$ symbols in the subscripts are defined in the {1, 2} Euclidean subspace and in the {0, 3} Minkowski subspace, respectively, the field **B** being directed here along the third axis. For arbitrary vectors a_μ and b_μ, we have

$$a_\perp = (0, a_1, a_2, 0), \quad a_{||} = (a_0, 0, 0, a_3), \tag{16}$$
$$(ab)_\perp = (a\Lambda b) = a_1b_1 + a_2b_2,$$
$$(ab)_{||} = (a\widetilde{\Lambda}b) = a_0b_0 - a_3b_3,$$

where we have introduced the matrices $\Lambda_{\alpha\beta} = (\varphi\varphi)_{\alpha\beta}$ and $\widetilde{\Lambda}_{\alpha\beta} = (\tilde{\varphi}\tilde{\varphi})_{\alpha\beta}$ involving the dimensionless external-electromagnetic-field tensor $\varphi_{\alpha\beta} = F_{\alpha\beta}/B$ and its dual counterpart $\tilde{\varphi}_{\alpha\beta} = \frac{1}{2}\varepsilon_{\alpha\beta\mu\nu}\varphi_{\mu\nu}$ and satisfying the equation $\widetilde{\Lambda}_{\alpha\beta} - \Lambda_{\alpha\beta} = g_{\alpha\beta} = \mathrm{diag}(1,-1,-1,-1)$, the 4-vector and tensor indices being contracted consecutively in the parenthetical expressions according to the rule specified, by way of example, as $(a\Lambda b) = a_\alpha\Lambda_{\alpha\beta}b_\beta$.

Although the propagator in (13) involves the phase $\Phi(x,y)$, which is not invariant either under translations or under gauge transformations, the resulting phase that is associated with all three propagators in the loop is invariant:

$$\Phi(x,y) + \Phi(y,z) + \Phi(z,x) = -\frac{e}{2}(z-x)_\mu \times F_{\mu\nu}(x-y)_\nu.$$

The invariant amplitude of the process described by the diagram in Fig. 1 has the form

$$\mathcal{M} = e^2 g_3 \int d^4X d^4Y \mathrm{tr}\{(j_3\Gamma_3)\hat{S}(Y)(\varepsilon_2\gamma) \times \hat{S}(-X-Y)(\varepsilon_1\gamma)\hat{S}(X)\}e^{-ie(XFY)/2} \times e^{i(k_1X-k_2Y)} + (\gamma_1 \leftrightarrow \gamma_2), \quad (17)$$

where $X = z - x$; $Y = x - y$; Γ_3 is the matrix associated with the S, the P, the V, or the A vertex; g_3 is a coupling constant; j_3 is the neutrino current or the photon polarization vector in momentum space; ε_1 and ε_2 are the polarization vectors of the photons in the initial state; and k_1 and k_2 are their 4-momenta.

In general, the use of the propagators given by (13)–(15) in three-vertex loop diagrams leads to very cumbersome expressions. Relatively simple results were obtained only for photon splitting in two cases: in the weak-field limit [38] and in the approximation of collinear kinematics for a strong field [10, 11].

In order to analyze the reaction amplitude (17) in a strong field, it is reasonable to replace the electron propagator by its asymptotic expression that is readily obtained by approximately calculating the relevant integral with respect to τ in the limit $eB/|m_e^2 - p_{||}^2| \gg 1$. The translation-invariant factor in the propagator then takes the simple form

$$\hat{S}(X) \simeq \frac{ieB}{2\pi}\exp\left(-\frac{eBX_\perp^2}{4}\right)\int\frac{d^2p}{(2\pi)^2} \times \frac{(p\gamma)_{||} + m_e}{p_{||}^2 - m_e^2}\Pi_- e^{-i(pX)_{||}}. \quad (18)$$

This expression was first obtained in [39, 40].

The amplitude can be divided in two parts such that each part is obtained from the other by interchanging the photons. Substituting the propagator given by (13), (14), and (18) into the amplitude, we find that each of the two parts of this amplitude that differ from each other by the interchange of photons is proportional to the field strength B; that is,

$$\mathcal{M} \simeq -\frac{i\alpha g_3 eB}{(4\pi)^2}\exp\left\{-\frac{k_{1\perp}^2 + k_{2\perp}^2 + (k_1k_2)_\perp}{2eB}\right\} \times \exp\left\{-i\frac{(k_1\varphi k_2)}{2eB}\right\} \times \int d^2p \mathrm{tr}\{(j_3\Gamma_3)S_{||}(p+k_2)(\varepsilon_2\gamma)S_{||}(p)(\varepsilon_1\gamma) \times S_{||}(p-k_1)\} + (\gamma_1 \leftrightarrow \gamma_2), \quad (19)$$

where $S_{||}(p) = 2\Pi_-((p\gamma)_{||} + m_e)/(p_{||}^2 - m_e^2)$. Note that, in the amplitude in (19), the projection operator Π_- singles out photons of one specific polarization ($\perp$) of the two possible ones (we use the Adler notation [38]):

$$\varepsilon_\alpha^{(||)} = \frac{F_{\alpha\beta}k_\beta}{\sqrt{(kFFk)}}, \qquad \varepsilon_\alpha^{(\perp)} = \frac{\widetilde{F}_{\alpha\beta}k_\beta}{\sqrt{(k\widetilde{F}\widetilde{F}k)}}. \quad (20)$$

Using a conventional procedure, we can recast the trace in the second term of expression (19) (that featuring interchanged photons) into the form of the trace in the first term, whereupon the sign of this term is reversed for $\Gamma_3 = P, V, A$ and is conserved for $\Gamma_3 = S$, the total amplitude acquiring the factor $\sin[(k_1\varphi k_2)/2eB]$ in the former and the factor $\cos[(k_1\varphi k_2)/2eB]$ in the latter case.

It follows that, if the field strength is the greatest physical parameter in the theory, $eB \gg k_\perp^2, k_{||}^2$, only the amplitude associated with the scalar vertex grows linearly with increasing field.

4. AMPLITUDE AND CROSS SECTION FOR THE PROCESS $\gamma\gamma \to \nu\bar{\nu}$ IN THE MODEL WITH BROKEN LEFT–RIGHT SYMMETRY

Upon making, according to (8), the substitutions $\Gamma_3 = 1$, $g_3 = -4\zeta G_\mathrm{F}/\sqrt{2}$, and $j_3 = [\bar{\nu}_e(p_1)\nu_e(-p_2)]$ in the amplitude given by (19) and performing integration there with respect to the virtual momentum in the strong-field limit, we arrive at

$$\mathcal{M} = \frac{8\alpha}{\pi}\frac{G_\mathrm{F}}{\sqrt{2}}\frac{\zeta}{m_e}\frac{B}{B_e}[\bar{\nu}_e(p_1)\nu_e(-p_2)]\varepsilon_{1\alpha}^{(\perp)}\varepsilon_{2\beta}^{(\perp)} \times \int_0^1 dx \int_0^{1-x}\frac{dy}{a^2}\Big\{[k_{1||}^2 x(1-2x) + k_{2||}^2 y(1-2y) \quad (21)$$

$$- (k_1k_2)_{||}(1-4xy)]\widetilde{\Lambda}^{\alpha\beta} - (1-2x) \times (1-2y)k_{1||}^{\alpha}k_{2||}^{\beta} + (1-4xy)k_{2||}^{\alpha}k_{1||}^{\beta} - 2x(1-2x)k_{1||}^{\alpha}k_{1||}^{\beta} - 2y(1-2y)k_{2||}^{\alpha}k_{2||}^{\beta}\Big\},$$

$$a = 1 - \frac{q_{||}^2}{m_e^2}xy - (1-x-y)\left(\frac{k_{1||}^2}{m_e^2}x + \frac{k_{2||}^2}{m_e^2}y\right), \quad (22)$$

where $q_{||} = k_{1||} + k_{2||}$. We now recast the amplitude in (21) into the gauge-invariant form (1):

$$\mathcal{M} = \frac{\alpha}{\pi}\frac{G_\mathrm{F}}{\sqrt{2}}\left[\bar{\nu}_e(p_1)T_{\alpha\beta\mu\nu}\nu_e(-p_2)\right] f_1^{(\perp)\alpha\beta} f_2^{(\perp)\mu\nu}. \quad (23)$$

This formula involves the tensors of the field generated by photons of only one polarization,

$$f_{\alpha\beta}^{(\perp)} = k_{\alpha||}\varepsilon_\beta^{(\perp)} - k_{\beta||}\varepsilon_\alpha^{(\perp)}.$$

In this case, the expression for the tensor $T_{\alpha\beta\mu\nu}$ takes the form

$$T_{\alpha\beta\mu\nu} = \frac{4\zeta}{m_e}\frac{B}{B_e}\int_0^1 dx\int_0^{1-x}\frac{dy}{a^2} \times \Big\{(1-4xy)\widetilde{\Lambda}_{\alpha\nu}\widetilde{\Lambda}_{\beta\mu} + 4(1-x-y) \times (1-2x-2y)\frac{1}{q_{||}^2}k_{1||\alpha}\widetilde{\Lambda}_{\beta\mu}k_{2||\nu}\Big\}. \quad (24)$$

In order to reduce the amplitude to the form (23), we have used the nontrivial integral identities

$$\int_0^1 dx\int_0^{1-x} dy\frac{Sx(1-2x) - Ty(1-2y)}{A^N} \equiv 0, \quad (25)$$

$$\int_0^1 dx\int_0^{1-x} dy \times \frac{Zy(1-2y) + S(1-x-y)(1-2x-2y)}{A^N} \equiv 0, \quad (26)$$

$$A = 1 - Zxy - (1-x-y)(Sx+Ty), \quad (27)$$

where Z, S, and T are arbitrary parameters and N is an arbitrary integer (in the case under study, $N = 2$).

The expression for the amplitude is simplified in two limiting cases [expressions (20) for the polarization vectors $\varepsilon_{1,2}^{(\perp)}$ have already been substituted into the formulas that are given immediately below]:

(i) At low photon energies ($\omega \lesssim m_e$), we have

$$\mathcal{M} \simeq \frac{8\alpha}{3\pi}\frac{G_\mathrm{F}}{\sqrt{2}}\frac{\zeta}{m_e}\frac{B}{B_e}\left[\bar{\nu}_e(p_1)\nu_e(-p_2)\right]\sqrt{k_{1||}^2k_{2||}^2}. \quad (28)$$

(ii) At high photon energies ($\omega \gg m_e$), the result obtained in the leading-logarithm approximation is

$$\mathcal{M} \simeq \frac{16\alpha}{\pi}\frac{G_\mathrm{F}}{\sqrt{2}}\zeta\frac{B}{B_e}m_e^3\left[\bar{\nu}_e(p_1)\nu_e(-p_2)\right] \times \frac{1}{\sqrt{k_{1||}^2k_{2||}^2}}\ln\frac{\sqrt{k_{1||}^2k_{2||}^2}}{m_e^2}. \quad (29)$$

Computing the cross sections for the processes $\gamma\gamma \to (\nu_e)_L(\bar{\nu}_e)_L$ and $\gamma\gamma \to (\nu_e)_R(\bar{\nu}_e)_R$ by a conventional method, we find that they are equal, $\sigma_{LL} = \sigma_{RR} \equiv \sigma$. In the above two limiting cases, the expressions for the cross sections are

$$\sigma(\omega \lesssim m_e) \simeq \frac{2\alpha^2G_\mathrm{F}^2\zeta^2}{9\pi^3}\left(\frac{B}{B_e}\right)^2\frac{k_{1||}^2k_{2||}^2}{m_e^2}, \quad (30)$$

$$\sigma(\omega \gg m_e) \simeq \frac{2\alpha^2G_\mathrm{F}^2\zeta^2}{\pi^3}\left(\frac{B}{B_e}\right)^2\frac{m_e^6}{k_{1||}^2k_{2||}^2}\ln^2\frac{k_{1||}^2k_{2||}^2}{m_e^4}. \quad (31)$$

5. ASTROPHYSICAL MANIFESTATIONS OF THE PROCESS $\gamma\gamma \to \nu\bar{\nu}$

The energy loss of a star per unit volume per unit time by neutrino emission (neutrino emissivity) is an important observable in astrophysics. For the process $\gamma\gamma \to \nu\bar{\nu}$, its general form is

$$Q = \frac{1}{2}\int\frac{d^3k_1}{(2\pi)^3}\frac{2}{e^{\omega_1/T}-1}\int\frac{d^3k_2}{(2\pi)^3}\frac{2}{e^{\omega_2/T}-1} \times (\omega_1+\omega_2)\frac{(k_1k_2)}{\omega_1\omega_2}\sigma(\gamma\gamma \to \nu\bar{\nu}), \quad (32)$$

where T is the photon-gas temperature. In the case under consideration, expression (32) must be multiplied by a factor of 1/4 since photons of only one polarization are involved in the process. Considering that only a sterile (anti)neutrino in the pair [see formula (9)] can leave freely hot and dense star matter (a neutrino involved in standard interactions is easily absorbed, the respective range being rather short), we take the expression $(\sigma_{LL} + \sigma_{RR})/2 = \sigma$ for the relevant cross section.

(a) Low-temperature limit, $T \lesssim m_e$. In this case, we substitute (30) into (32) and obtain

$$Q_{(B)} \simeq 2.5\times10^{13}\frac{\mathrm{erg}}{\mathrm{cm}^3\,\mathrm{s}}\left(\frac{\zeta}{0.013}\right)^2 \times \left(\frac{B}{B_e}\right)^2\left(\frac{T}{m_e}\right)^{11}. \quad (33)$$

This result must be compared with the contributions to the neutrino emissivity from the other mechanisms of the transition $\gamma\gamma \to \nu\bar{\nu}$ that were mentioned in Section 2. In [20], it was found that

$$Q_{(m_\nu)} \simeq 0.4 \times 10^5 \frac{\mathrm{erg}}{\mathrm{cm}^3\ \mathrm{s}} \left(\frac{m_\nu}{1\ \mathrm{eV}}\right)^2 \left(\frac{T}{m_e}\right)^{11}. \quad (34)$$

On the other hand, the cross section derived with allowance for the nonlocal character of four-fermion weak interaction [23] can also be substituted into (32). This yields

$$Q_{(\mathrm{NL})} \simeq 10 \frac{\mathrm{erg}}{\mathrm{cm}^3\ \mathrm{s}} \left(\frac{T}{m_e}\right)^{13}. \quad (35)$$

It can be seen that, for $B \gtrsim B_e$, the field-induced mechanism makes a dominant contribution to the transition $\gamma\gamma \to \nu\bar{\nu}$ even if the mixing angle is as small as $\zeta \sim 10^{-5}$.

(b) High-temperature limit, $T \gg m_e$. In this case, the substitution of (31) into (32) leads to

$$Q_{(B)} \simeq 0.4 \times 10^{12} \frac{\mathrm{erg}}{\mathrm{cm}^3\mathrm{s}} \left(\frac{\zeta}{0.013}\right)^2 \left(\frac{B}{B_e}\right)^2 \times \left(\frac{T}{m_e}\right)^3 \ln^5 \frac{T}{m_e}. \quad (36)$$

For standard weak interaction, the contribution of the process $\gamma\gamma \to \nu\bar{\nu}$ to Q was calculated in [34] for a relatively weak magnetic field and high temperatures.

For a numerical estimate, we consider the case where the explosion of a supernova of volume $V \sim 10^{19}$ cm^3 and temperature $T \sim 35$ MeV [41], which is typical of the supernova core, is accompanied by the generation of a very strong magnetic field ($B \sim 10^3 B_e$) [3–6]. For the contribution to the neutrino luminosity of such a star from the field-induced process $\gamma\gamma \to \nu\bar{\nu}$, we then obtain

$$L \sim 10^{45} \frac{\mathrm{erg}}{\mathrm{s}} \left(\frac{\zeta}{0.013}\right)^2. \quad (37)$$

This value is much smaller than a typical neutrino luminosity of a supernova (10^{52} erg/s).

As was mentioned above, the amplitude in (19) for the case of a vector or an axial-vector vertex, $\Gamma_3 = V, A$, features no contribution that grows linearly with increasing field in the strong-field limit $eB \gg k_\perp^2, k_{||}^2$. This means that the amplitude for the process $\gamma\gamma \to \nu\bar{\nu}$ governed by the standard $\nu\nu ee$ interaction and the amplitude for the photon-splitting process $\gamma \to \gamma\gamma$ are both independent of the field in this limit. This case was considered in [13, 14, 42].

6. CONCLUSION

We have performed a general analysis of a three-vertex loop diagram in a strong external field and have analyzed the reaction $\gamma\gamma \to \nu\bar{\nu}$. We have shown that different types of effective electron–neutrino interaction lead to different field-strength dependences of the reaction amplitude. In particular, an external magnetic field enhances the amplitude of the process $\gamma\gamma \to \nu\bar{\nu}$ if effective $\nu\nu ee$ interaction involves a scalar coupling, which emerges in the SM extension where left–right symmetry is broken. A general expression for the amplitude has been derived [Eqs. (23), (24)]; it is valid at all photon energies and has been represented in a gauge-invariant form. The cross section for the process under study has been calculated both at low ($\omega \lesssim m_e$) and at high ($\omega \gg m_e$) photon energies. A quantitative analysis has revealed that the contribution of this process to changes in the supernova energy is rather small. For $B \gtrsim B_e$, however, the contribution to the neutrino emissivity of a magnetized star from the transition $\gamma\gamma \to \nu\bar{\nu}$ proceeding via the mechanism in question may exceed considerably the contribution of other mechanisms discussed in the literature.

ACKNOWLEDGMENTS

This work was supported in part by the Russian Foundation for Basic Research (project no. 01-02-17334) and by the Ministry for Higher Education of the Russian Federation (grant no. E00-11.0-5).

REFERENCES

1. C. Kouveliotou *et al.*, Astrophys. J. **510**, L115 (1999).
2. K. Hurley *et al.*, Nature **397**, 41 (1999).
3. G. S. Bisnovatyĭ-Kogan, Astron. Zh. **47**, 813 (1970) [Sov. Astron. **14**, 652 (1970)].
4. R. C. Duncan and C. Thompson, Astrophys. J. **392**, L9 (1992).
5. P. Bocquet *et al.*, Astron. Astrophys. **301**, 757 (1995).
6. C. Y. Cardall, M. Prakash, and J. M. Lattimer, Astrophys. J. **554**, 322 (2001).
7. M. Yu. Borovkov, A. V. Kuznetsov, and N. V. Mikheev, Yad. Fiz. **62**, 1714 (1999) [Phys. At. Nucl. **62**, 1601 (1999)].
8. V. O. Papanyan and V. I. Ritus, Tr. Fiz. Inst. Akad. Nauk SSSR **168**, 120 (1986).
9. S. L. Adler and C. Schubert, Phys. Rev. Lett. **77**, 1695 (1996).
10. V. N. Baier, A. I. Milstein, and R. Zh. Shaisultanov, Phys. Rev. Lett. **77**, 1691 (1996).
11. V. N. Baĭer, A. I. Mil'shteĭn, and R. Zh. Shaĭsultanov, Zh. Éksp. Teor. Fiz. **111**, 52 (1997) [JETP **84**, 29 (1997)].
12. C. Wilke and G. Wunner, Phys. Rev. D **55**, 997 (1997).

13. M. V. Chistyakov, A. V. Kuznetsov, and N. V. Mikheev, Phys. Lett. B **434**, 67 (1998).
14. A. V. Kuznetsov, N. V. Mikheev, and M. V. Chistyakov, Yad. Fiz. **62**, 1638 (1999) [Phys. At. Nucl. **62**, 1535 (1999)].
15. B. M. Pontekorvo, Zh. Éksp. Teor. Fiz. **36**, 1615 (1959) [Sov. Phys. JETP **9**, 1148 (1959)].
16. M. Gell-Mann, Phys. Rev. Lett. **6**, 70 (1961).
17. L. D. Landau, Dokl. Akad. Nauk SSSR **60**, 207 (1948).
18. C. N. Yang, Phys. Rev. **77**, 242 (1950).
19. R. J. Crewther, J. Finjord, and P. Minkowski, Nucl. Phys. B **207**, 269 (1982).
20. S. Dodelson and G. Feinberg, Phys. Rev. D **43**, 913 (1991).
21. M. J. Levine, Nuovo Cimento A **48**, 67 (1967).
22. D. A. Dicus, Phys. Rev. D **6**, 941 (1972).
23. D. A. Dicus and W. W. Repko, Phys. Rev. D **48**, 5106 (1993).
24. L. Rosenberg, Phys. Rev. **129**, 2786 (1963).
25. V. K. Cung and M. Yoshimura, Nuovo Cimento A **29**, 557 (1975).
26. A. V. Kuznetsov and N. V. Mikheev, Phys. Lett. B **299**, 367 (1993).
27. A. V. Kuznetsov and N. V. Mikheev, Yad. Fiz. **56** (6), 108 (1993) [Phys. At. Nucl. **56**, 773 (1993)].
28. J. Liu, Phys. Rev. D **44**, 2879 (1991).
29. M. A. B. Bég, R. Budny, R. N. Mohapatra, and A. Sirlin, Phys. Rev. Lett. **38**, 1252 (1977).
30. Particle Data Group (D. E. Groom *et al.*), Eur. Phys. J. C **15**, 1 (2000).
31. R. Barbieri and R. N. Mohapatra, Phys. Rev. D **39**, 1229 (1989).
32. R. Shaisultanov, Phys. Rev. Lett. **80**, 1586 (1998).
33. D. A. Dicus and W. W. Repko, Phys. Rev. Lett. **79**, 569 (1997).
34. T. K. Chyi *et al.*, Phys. Lett. B **466**, 274 (1999).
35. T. K. Chyi *et al.*, Phys. Rev. D **62**, 105014 (2000).
36. D. A. Dicus and W. W. Repko, Phys. Lett. B **482**, 141 (2000).
37. Yu. M. Loskutov and V. V. Skobelev, Vestn. Mosk. Univ., Ser. 3: Fiz., Astron., No. 22, 10 (1981).
38. S. L. Adler, Ann. Phys. (N.Y.) **67**, 599 (1971).
39. V. V. Skobelev, Izv. Vyssh. Uchebn. Zaved., Fiz., No. 10, 142 (1975).
40. Yu. M. Loskutov and V. V. Skobelev, Phys. Lett. A **56A**, 151 (1976).
41. G. G. Raffelt, *Stars as Laboratories for Fundamental Physics* (Univ. Chicago Press, Chicago, 1996).
42. M. V. Chistyakov *et al.*, in *Proceedings of Ringberg Euroconference "New Trends in Neutrino Physics," Tegernsee, Germany, 1998,* Ed. by B. Kniehl *et al.* (World Sci., Singapore, 1999), p. 245, hep-ph/9808246.

Translated by R. Rogalyov

Physics of Atomic Nuclei, Vol. 66, No. 2, 2003, pp. 302–306. Translated from Yadernaya Fizika, Vol. 66, No. 2, 2003, pp. 327–331.

ELEMENTARY PARTICLES AND FIELDS
Theory

Investigation of the Nucleon Spin in Neutrino Processes

S. I. Timoshin

Gomel State Technical University, Gomel, Belarus
Received August 7, 2001; in final form, December 25, 2001

Abstract—The possibility of obtaining new information about the spin properties of the nucleon from observables of the deep-inelastic scattering of neutrinos and antineutrinos on polarized nucleons that is caused by a weak neutral current is discussed. © *2003 MAIK "Nauka/Interperiodica".*

1. INTRODUCTION

The deep-inelastic scattering of neutrinos and antineutrinos on polarized nucleons may serve as a source of new information about the spin structure of the nucleon. This is due to the ability of neutrinos to distinguish, in deep-inelastic-scattering processes, between quark flavors and between quarks and antiquarks, as well as to a greater number of polarization structure functions involved in such processes than in deep-inelastic electron–nucleon and muon–nucleon scattering [1–3].

The procedure that is based on a QCD analysis of polarization data and which is of paramount importance for solving the nucleon-spin problem was vigorously brought into use in recent years [4–6]. At present, a set of data on the polarization structure function g_1 measured for a proton, a neutron, and a deuteron in experiments with beams of polarized electrons and muons (see [5, 7–10] and references therein) is employed in such an analysis. However, the fact that there are no results of neutrino experiments with polarized targets imposes limitations on conclusions that could be drawn from a QCD analysis. Indeed, a QCD analysis of deep-inelastic lepton scattering on unpolarized nucleons yields a decomposition of the structure function into the contributions of valence quarks, sea quarks of each flavor, and gluons. For this, use is made of experimental data on the scattering of charged leptons, neutrinos, and antineutrinos by various targets over a wide region of the kinematical variables x and Q^2. Therefore, the presence of neutrino data is highly desirable for performing a full QCD analysis of deep-inelastic scattering with allowance for the polarizations of the particles involved.

In the case where polarizations are involved, the luminosity of existing neutrino beams requires targets whose dimensions are about a few meters; therefore, they cannot be polarized. As a new method for achieving high energies and luminosities, muon colliders were proposed in [11, 12] a few years ago. The possibility of obtaining highly focused beams of neutrinos originating from muon decays is associated precisely with such colliders. In order to accumulate required statistics with such neutrino beams, one needs polarized targets, and it becomes feasible to manufacture them by means of modern technologies [13]. It was indicated in [14] that muon colliders have a high potential for neutrino physics. In particular, this concerns high-precision measurements of unpolarized and polarized structure functions. Such results would make it possible to obtain an adequate decomposition of structure functions, including spin-dependent ones, into the contributions of individual quark flavors and gluons, and this is precisely a final result of a QCD data analysis.

In view of future neutrino experiments with polarized targets, it is highly desirable even at present to study theoretically deep-inelastic (anti)neutrino–nucleon scattering for the case of polarized particles and, above all, to reveal the potential of such processes for obtaining new data on the spin structure of the nucleon. In recent years, the deep-inelastic scattering of neutrinos in the polarized case was studied on the basis of the parton model [15–17] or on the basis of QCD [1, 3, 18, 19].

A few schemes were proposed in [16] for determining the quark contributions to the nucleon spin with the aid of observables (asymmetries and cross sections) of deep-inelastic (anti)neutrino scattering on polarized targets. For deep-inelastic-scattering processes induced by a charged weak current, a different method was employed in [17] to derive such contributions. This method was based on the use of polarization boson–nucleon asymmetries and, eventually, of a different set of observables.

In the present study, this approach is generalized to deep-inelastic (anti)neutrino scattering on polarized nucleons that is caused by a weak neutral current; that is,

$$\nu(\bar{\nu}) + N \xrightarrow{Z} \nu(\bar{\nu}) + X. \qquad (1)$$

1063-7788/03/6602-0302$24.00

The ensuing exposition is organized as follows. In Section 2, the virtual boson–nucleon asymmetries $A_{1,6}$ and the polarized structure functions $g_{1,6}$ are determined from observables of processes belonging to the type in (1). For the case of (anti)neutrino–deuteron scattering, expressions for the contributions of quark flavors and valence quarks to the nucleon spin are obtained in Section 3. Section 4 is devoted to discussing the results of numerical calculations of the asymmetries $A_{1,6}$ and of the structure functions $g_{1,6}$ and to formulating conclusions.

2. POLARIZATION ASYMMETRIES AND STRUCTURE FUNCTIONS

The total cross section for the absorption of a virtual Z boson by a polarized nucleon is given by

$$\sigma = k\varepsilon_\mu^*(q)\varepsilon_\nu(q)W_{\mu\nu}, \tag{2}$$

where $k = \sqrt{2}\pi G m_Z^2/\sqrt{v^2-q^2}$. The following notation is also used here: $\varepsilon_\mu(q)$ is the polarization vector of a virtual Z boson with a momentum $q = k - k'$; $\nu = Pq/M$; k (k') and P are the momenta of, respectively, the initial (final) neutrino and the nucleon involved; m_Z is the Z-boson mass; M is the nucleon mass; and G is the Fermi constant. The hadronic tensor $W_{\mu v}$ has the same structure as that for reactions induced by a charged current (see [17]), the only difference being that, now, the nucleon structure function for neutrino scattering is identical to that for antineutrino scattering because of identity of the initial and the final lepton in reactions (1).

In the scaling limit ($q^2, v \to \infty$, with $x = -q^2/2M\nu$ being fixed), in which case the total angular momenta of the boson–nucleon system are $\pm 1/2$ and $\pm 3/2$, the cross sections given by (2) become

$$\sigma_{\substack{1/2\\3/2}} = \frac{k}{M}\left(\frac{F_2(x)}{2x} - \frac{F_3(x)}{2} \pm g_1(x) \mp g_6(x)\right), \tag{3}$$

$$\sigma_{\substack{-1/2\\-3/2}} = \frac{k}{M}\left(\frac{F_2(x)}{2x} + \frac{F_3(x)}{2} \pm g_1(x) \pm g_6(x)\right),$$

where $F_{2,3}(x)$ and $g_{1,6}(x)$ are, respectively, the spin-averaged structure functions and the polarized nucleon structure functions for processes (1). The virtual polarization asymmetries defined as

$$A_{1,6}(x) = \frac{(\sigma_{1/2} \pm \sigma_{-1/2}) - (\sigma_{3/2} \pm \sigma_{-3/2})}{(\sigma_{1/2} \pm \sigma_{-1/2}) + (\sigma_{3/2} \pm \sigma_{-3/2})}$$

then assume the form

$$A_1(x) = \frac{2xg_1(x)}{F_2(x)}, \tag{4}$$

$$A_6(x) = \frac{2xg_6(x)}{xF_3(x)}. \tag{5}$$

Asymmetries directly measured in polarization experiments represent various combinations of differential cross sections for specific orientations of beam-particle and target-particle spins. For deep-inelastic $\nu(\bar\nu)N$ scattering, we consider the asymmetries [16]

$$A_{\nu,\bar\nu}(x,y) = \frac{\sigma_{\nu,\bar\nu}^{\downarrow\uparrow,\uparrow\uparrow} - \sigma_{\nu,\bar\nu}^{\downarrow\downarrow,\uparrow\downarrow}}{\sigma_{\nu,\bar\nu}^{\downarrow\uparrow,\uparrow\uparrow} + \sigma_{\nu,\bar\nu}^{\downarrow\downarrow,\uparrow\downarrow}},$$

where $\sigma \equiv d^2\sigma/dxdy$ stands for the differential cross sections for processes (1), $y = \nu/E$ is a scaling variable, and E is the energy of the primary neutrino or the primary antineutrino.

These asymmetries can be measured by using, for example, the method applied in the SMC experiment at CERN in the case of a longitudinal asymmetry [20]. There, the target consisted of two oppositely polarized blocks arranged in such a way that one could distinguish between events occurring within either block. In order to implement a single measurement of asymmetry, two successive measurements are performed prior to and after a change in polarization in both blocks. The measured asymmetry is then expressed in terms of the number of events in each block prior to and after a change in polarization in them. For neutrino experiments employing processes of the type in (1), events that will be recorded in either target block are naturally associated with the final hadron system.

In just the same way as for a charged current [17], the observed polarization asymmetries $A_{\nu,\bar\nu}(x,y)$ for processes (1) can be expressed in terms of $A_{1,6}(x)$ as

$$A_{\nu,\bar\nu}(x,y) = \frac{xy_+A_6(x)F_3(x) \pm y_-A_1(x)F_2(x)}{y_+F_2(x) \pm y_-xF_3(x)}, \tag{6}$$

where $y_\pm = 1 \pm y_1^2$, $y_1 = 1 - y$.

If the structure functions $F_{2,3}(x)$ are assumed to be known, the quantities $A_1(x)$ and $A_6(x)$ can be expressed, with the aid of Eq. (6), in terms of the measurable asymmetries A_ν and $A_{\bar\nu}$ in deep-inelastic $\nu(\bar\nu)N$ scattering that involves Z-boson exchange; that is,

$$A_1(x) = \frac{1}{2}\left[\frac{xF_3}{F_2(x)}(A_\nu + A_{\bar\nu}) + \frac{y_+}{y_-}(A_\nu - A_{\bar\nu})\right], \tag{7}$$

$$A_6(x) = \frac{1}{2}\left[\frac{F_2(x)}{xF_3(x)}(A_\nu + A_{\bar\nu}) + \frac{y_-}{y_+}(A_\nu - A_{\bar\nu})\right].$$

With the aid of Eqs. (4) and (5), we can further obtain polarized nucleon structure functions

$$g_1(x) = \frac{F_2(x)A_1(x)}{2x}, \qquad (8)$$
$$g_6(x) = \frac{xF_3(x)A_6(x)}{2x}.$$

It should be emphasized that data of neutrino experiments employing reactions of the type in (1) alone are sufficient for extracting polarized nucleon structure functions from observables. Moreover, the proposed scheme can be implemented for arbitrary nucleon-containing targets. Owing to these two features, processes of the type in (1) compare favorably with reactions induced by a charged current [17]. For the latter, g_1 and g_6 can be determined only for the deuteron and only in the presence of data on the asymmetry A_1^d, which is measured in experiments with beams of polarized electrons and muons.

3. DETERMINATION OF QUARK CONTRIBUTIONS TO THE NUCLEON SPIN

For observables characterizing processes of the type in (1) and carrying information about the spin properties of the nucleon, we will take here the first moments of the structure functions $g_1(x)$ and $g_6(x)$; that is,

$$\Gamma_{1,6} = \int_0^1 g_{1,6}(x)dx. \qquad (9)$$

The expressions obtained for the structure functions $g_{1,6}(x)$ on the basis of the quark-parton model are

$$g_1(x) = \frac{1}{2}\sum_q (g_V^2 + g_A^2)_q[\Delta q(x) + \Delta\bar{q}(x)], \qquad (10)$$
$$g_6(x) = \sum_q (g_V g_A)_q[\Delta q(x) - \Delta\bar{q}(x)],$$

where $(\Delta\bar{q}(x))\Delta q(x)$ is the distribution of polarized (anti)quarks $q = u, d, s$; $(g_V)_u = 1/2 - (4/3)\sin^2\theta_W$; $(g_A)_u = 1/2$; $(g_V)_{d,s} = -1/2 + (2/3)\sin^2\theta_W$; and $(g_A)_{d,s} = -1/2$.

Further, we consider deep-inelastic neutrino scattering on polarized deuterons. Such processes are of particular interest because neutrino experiments with unpolarized targets are performed for the case of isoscalar targets—that is, targets containing equal numbers of protons and neutrons. Data on the structure functions $F_{2,3}(x)$ measured in experiments employing unpolarized deuteron targets are required for determining the virtual asymmetries $A_{1,6}(x)$ and, accordingly, the polarized structure functions $g_{1,6}(x)$ [see Eqs. (7), (8)].

The polarized deuteron structure functions can be represented as [5]

$$g_{1,6}^d(x) = \frac{g_{1,6}^p(x) + g_{1,6}^n(x)}{2}\left(1 - \frac{3}{2}\omega_D\right), \qquad (11)$$

where $\omega_D \cong 0.05$ is the probability of the D-wave state in the deuteron wave function. With the aid of Eqs. (9)–(11), the deuteron moments $\Gamma_{1,6}$ can then be represented in the form

$$\Gamma_1^d = \frac{1}{4}[(g_V^2 + g_A^2)_u(\Delta u + \Delta\bar{u} + \Delta d + \Delta\bar{d}) \qquad (12)$$
$$+ (g_V^2 + g_A^2)_d(\Delta u + \Delta\bar{u} + \Delta d$$
$$+ \Delta\bar{d} + 2(\Delta s + \Delta\bar{s}))]\left(1 - \frac{3}{2}\omega_D\right),$$

$$\Gamma_6^d = \frac{b}{2}(\Delta u_V + \Delta d_V)\left(1 - \frac{3}{2}\omega_D\right). \qquad (13)$$

In expressions (12) and (13),

$$\Delta q(\Delta\bar{q}) = \int_0^1 \Delta q(x)(\Delta\bar{q}(x))dx$$

is the contribution of the quark (antiquark) q ($\bar{q}$) to the nucleon spin, $b = \sum_{q=u,d}(g_V g_A)_q$, and $\Delta q_V = \Delta q - \Delta\bar{q}$ is the contribution of valence quarks to the nucleon spin.

In order to isolate, in (12), the contribution of each quark flavor, we must have at least two more measurable quantities at our disposal. For these, it is convenient to take the quantities a_3 and a_8 [2], which are defined in terms of the hyperon-beta-decay constants F and D as

$$a_3 = F + D = (\Delta u + \Delta\bar{u}) - (\Delta d + \Delta\bar{d}),$$
$$a_8 = \frac{1}{\sqrt{3}}(3F - D) \qquad (14)$$
$$= \frac{1}{\sqrt{3}}[\Delta u + \Delta\bar{u} + \Delta d + \Delta\bar{d} - 2(\Delta s + \Delta\bar{s})],$$
$$F = 0.477 \pm 0.012, \quad D = 0.756 \pm 0.011.$$

By simultaneously solving Eqs. (12) and (14), we obtain the contributions of individual quark flavors to the nucleon spin in the form

$$\Delta u + \Delta\bar{u}(\Delta d + \Delta\bar{d}) \qquad (15)$$
$$= \frac{1}{2}\left[\sqrt{3}a_8 \pm a_3 + \frac{1}{a}\left(\frac{4\Gamma_1^d}{1 - \frac{3}{2}\omega_D} - \sqrt{3}a_8 c\right)\right],$$

$$\Delta s + \Delta\bar{s} = \frac{1}{a}\left(\frac{2\Gamma_1^d}{1 - \frac{3}{2}\omega_D} - \frac{\sqrt{3}}{2}a_8 c\right),$$

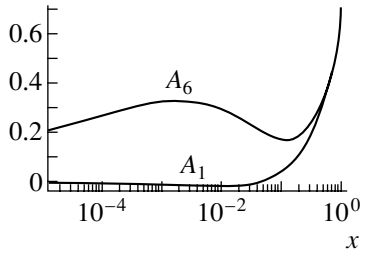

Fig. 1. Asymmetries $A_1(x)$ and $A_6(x)$ versus the variable x ($Q_0^2 = 4$ GeV^2; the parton distributions were borrowed from [21]).

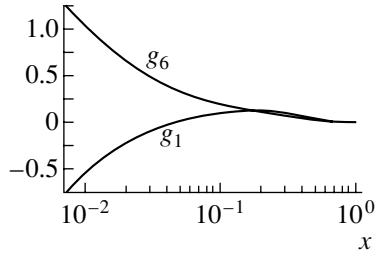

Fig. 2. Polarization structure functions $g_1(x)$ and $g_6(x)$ versus the variable x ($Q_0^2 = 4$ GeV^2; the parton distributions were borrowed from [21]).

where the plus (minus) sign in the parenthetical expression refers to u (d),

$$a = c + (g_V^2 + g_A^2)_d, \quad c = \sum_{q=u,d} (g_V^2 + g_A^2)_q.$$

From relation (13), we immediately obtain the total valence-quark contribution $\Delta q_V \equiv \Delta u_V + \Delta d_V$,

$$\Delta q_V = 2\Gamma_6^d/b \left(1 - \frac{3}{2}\omega_D\right). \qquad (16)$$

It follows that, knowing the moments Γ_1^d and Γ_6^d measured in neutrino processes of the type in (1), one can determine the quark contributions (15) and (16) to the nucleon spin.

4. NUMERICAL CALCULATIONS OF POLARIZATION OBSERVABLES AND STRUCTURE FUNCTIONS; CONCLUSIONS

In order to get an idea of the scale of the asymmetries $A_{1,6}(x)$ and the polarized structure functions $g_{1,6}(x)$ and of their behavior, these quantities were calculated numerically for deep-inelastic (anti)neutrino scattering on a deuteron target.

From Figs. 1 and 2, it can be seen that the asymmetries $A_1(x)$ and $A_6(x)$, as well as the polarized structure functions $g_1(x)$ and $g_6(x)$, show substantially different types of behavior in the region $x \leq 0.1$. A considerable polarization of the quark sea in the low-x region may be a reason behind these distinctions, since g_6 and, hence, A_6 depend only on the distributions of valence quarks. The contribution of quark-sea polarization cancels almost completely the polarization of valence quarks in $A_1(x)$ (Fig. 1) for $x \leq 0.01$; therefore, this asymmetry is close to zero. It follows that measurement of the asymmetries $A_{1,6}$ and the structure functions $g_{1,6}$ in experiments employing deep-inelastic scattering on polarized nucleons in processes of the type in (1), which are induced by a weak neutral current, may also be of use in solving the fundamental problem of strange-quark polarization.

Thus, a method has been proposed in the present study for extracting, with the aid of the virtual asymmetries $A_{1,6}(x)$, the polarization structure functions $g_1(x)$ and $g_6(x)$ from experimental data on processes of the type in (1) on arbitrary polarized targets. For the example of deep-inelastic neutrino scattering on a deuteron, a scheme has been developed for determining, with the aid of the first moments $\Gamma_{1,6}$ of the polarized structure functions, the contributions of individual quark flavors and valence quarks to the nucleon spin. Numerical estimates have been obtained for $A_{1,6}(x)$ and $g_{1,6}(x)$. An analysis of these estimates has revealed that the polarization of the quark sea has a pronounced effect on the behavior of $A_1(x)$ and $g_1(x)$ in the region $x \leq 0.1$.

Thus, an experimental investigation of the asymmetries $A_{1,6}$ and of the polarized structure functions $g_{1,6}$ in reactions belonging to the type in (1) may furnish new information about the polarization of strange quarks and of the quark sea, and this is of importance for establishing the nature of the nucleon spin.

REFERENCES

1. V. Ravishankar, Nucl. Phys. B **374**, 309 (1992).
2. M. Anselmino, A. Efremov, and E. Leader, Phys. Rep. **261**, 1 (1995).
3. S. Forte, M. L. Mangano, and G. Ridolfi, hep-ph/0101192 (v2).
4. K. Abe, T. Akagi, B. D. Anderson, *et al.*, Preprint SLAC-PUB-7461 (1997).
5. D. Adams, B. Adeva, E. Arik, *et al.*, Preprint CERN-PPE97-22 (1997).
6. G. Altarelli, R. D. Ball, S. Forte, and G. Ridolfi, Preprint CERN-TH/96-345 (1996).
7. J. Ashmann, B. Badelek, G. Baum, *et al.*, Nucl. Phys. B **328**, 1 (1989).
8. K. Abe, T. Akagi, P. L. Anthony, *et al.*, Preprint SLAC-PUB-7753 (1998).

9. K. Abe, T. Akagi, B. D. Anderson, *et al.*, Preprint SLAC-PUB-7459 (1997).
10. K. Ackestaff, A. Airapetian, I. Arushevich, *et al.*, Preprint DESY 97-085 (1997).
11. D. M. Kaplan, physics/0001037.
12. B. J. King, hep-ex/9911008; hep-ex/0001043.
13. P. S. Isaev and V. A. Tsarev, Fiz. Élem. Chastits At. Yadra **20**, 997 (1989) [Sov. J. Part. Nucl. **20**, 419 (1989)].
14. I. Bigi *et al.*, Preprint BNL-67404.
15. M. Anselmino, P. Gambino, and J. Kalinowski, Z. Phys. C **64**, 267 (1994).
16. P. P. Kuzhir, S. I. Timoshin, and N. M. Shumeĭko, Yad. Fiz. **58**, 507 (1995) [Phys. At. Nucl. **58**, 456 (1995)].
17. S. I. Timoshin, Yad. Fiz. **61**, 119 (1998) [Phys. At. Nucl. **61**, 110 (1998)].
18. R. Mertig and W. L. van Neerven, Z. Phys. C **70**, 637 (1996).
19. W. Vogelsang, Phys. Rev. D **54**, 2023 (1996); Nucl. Phys. B **475**, 47 (1996).
20. D. Adams, B. Adeva, E. Arik, *et al.*, Preprint CERN-EP/99-31 (1999).
21. J. Bartelski and S. Tatur, Acta Phys. Pol. B **27**, 4 (1996).

Translated by A. Isaakyan

Physics of Atomic Nuclei, Vol. 66, No. 2, 2003, pp. 307–312. From Yadernaya Fizika, Vol. 66, No. 2, 2003, pp. 332–337.

ELEMENTARY PARTICLES AND FIELDS
Theory

Leading-Particle Effects in the Spectra of Λ_c and $\bar{\Lambda}_c$ Produced in $\Sigma^- p$, pp, and $\pi^- p$ Interactions*

O. I. Piskounova**

Lebedev Institute of Physics, Russian Academy of Sciences, Leninskiĭ pr. 53, Moscow, 117924 Russia

Received August 22, 2001; in final form, March 1, 2002

Abstract—The spectra of leading and nonleading charmed baryons (Λ_c and $\bar{\Lambda}_c$) and the asymmetries between these spectra measured in $\Sigma^- A$, $\pi^- A$, and pA collisions at $p_L = 600$ GeV/c in the E781 experiment are simultaneously described within the framework of the Quark–Gluon String Model (QGSM). It is shown that the charmed baryon spectra can be fitted by QGSM curves calculated with the parameter of diquark fragmentation, $a_f^{\Lambda_c} = 0.006$. It was found in this experiment that the asymmetry between the spectra of Λ_c and $\bar{\Lambda}_c$ in $\pi^- A$ collisions is of nonzero value. It might be described in our model only assuming that the string junction is transferred from target proton into the kinematical region of pion projectile fragmentation. © *2003 MAIK "Nauka/Interperiodica"*.

1. INTRODUCTION

The data of the E781 experiment [1] (FNAL) on the spectra of charmed baryons and the asymmetries between Λ_c and $\bar{\Lambda}_c$ in $\Sigma^- A$, $\pi^- A$, and pA interactions at $p_L = 600$ GeV/c have recently amplified the results of the WA89 experiment [2] (CERN) at $p_L = 340$ GeV/c and the E791 experiment [3] (FNAL) at $p_L = 500$ GeV/c. The data of these experiments on charmed meson spectra and asymmetries have been already considered in the recent paper [4] from the point of view of the Quark–Gluon String Model (QGSM) in order to understand the influence of the quark composition of beam particles on the shape of the production spectra of heavy flavored particles.

The difference in x spectra ($x = x_F = 2p_\parallel/\sqrt{s}$) of leading and nonleading particles has been explained successfully by several theoretical models as an effect of interplay between the quark content of the projectile and of the produced hadron.

Most advanced QCD models [5, 6] have to take into account the so-called intrinsic charm (IC) in order to describe the high value of asymmetry between the x spectra of charmed particles and antiparticles in the fragmentation region, $x \to 1$. In QGSM [7] and other models [8] with elaborated concepts of fragmentation functions (FFs), there is no need to make such an assumption, because the specifically written FFs give the asymmetries rising with x. Some amount of IC can only suppress the asymmetry, as was shown in previous calculations [4, 9].

It should be noted that there is a large difference between leading effects in charmed meson spectra and those effects in charmed baryon spectra. Leading Λ_c baryons in pp interaction might be produced by the leading fragmentation of proton ud diquarks bringing a large fraction of proton momentum that gives an important enhancement of Λ_c spectra over the spectra of $\bar{\Lambda}_c$. We suggest here considering the spectra in the full x region, $-1 < x < 1$, so that the left side of plots always corresponds to target proton fragmentation. For example, in the case of hyperon–proton interactions, the Λ_c spectra will have two different wings: the left one at negative x shows the high asymmetry towards $\bar{\Lambda}_c$ spectra due to the leading fragmentation of target protons, and the other one in the positive-x region should have a slightly lower asymmetry because the fragmentation of hyperon diquarks is supposed to have a less strongly leading character [10] than proton ud-diquark fragmentation.

The asymmetry between Λ_c and $\bar{\Lambda}_c$ spectra in pion–proton interaction should be equal to zero in the region of pion fragmentation because pions can have the valent quark (antiquark) in common with Λ_c as well as with $\bar{\Lambda}_c$, so both spectra will provide a leading character and be equal.

2. VALENCE QUARK DISTRIBUTIONS IN QGSM

The inclusive production cross section of hadrons of type H is written as a sum over n-Pomeron cylinder

*This article was submitted by the author in English.

** e-mail: piskoun@sci.lebedev.ru

diagrams:

$$f_1 = x\frac{d\sigma^H}{dx}(s,x) = \int E\frac{d^3\sigma^H}{d^3p}d^2p_\perp \qquad (1)$$
$$= \sum_{n=0}^{\infty}\sigma_n(s)\varphi_n^H(s,x).$$

Here, the function $\varphi_n^H(s,x)$ is a particle distribution in the configuration of n-cut cylinders and σ_n is the probability of this process. The cross sections σ_n depend on the parameter of the supercritical Pomeron Δ_P, which is equal to 0.12 in our model [7].

The distribution functions of Λ_c in case of $\pi^- p$ collisions are given by

$$\varphi_n^{\Lambda_c}(s,x) \qquad (2)$$
$$= a_0^{\bar\Lambda_c}[F_q^{(n)}(x_+)F_{qq}^{(n)}(x_-) + F_{qq}^{(n)}(x_+)F_q^{(n)}(x_-)$$
$$+ 2(n-1)F_{q_{\rm sea}}^{(n)}(x_+)F_{\bar q_{\rm sea}}^{(n)}(x_-)] + a_f^{\Lambda_c}F_{1qq}^{(n)}(x_-),$$

where $a_0^{\bar\Lambda_c}$ is the central (vacuum) density parameter of charmed baryon production and $a_f^{\Lambda_c}$ is the fragmentation parameter of proton target diquark. In the case of Λ_c production in proton fragmentation, the diquark fragmentation plays an important role; this diquark part of the distribution should be written separately. Thus, the distribution for pp collisions will include two diquark parts, for positive x as well as for negative x:

$$\varphi_n^{\Lambda_c}(s,x) = a_f^{\Lambda_c}F_{1qq}^{(n)}(x_+) + a_f^{\Lambda_c}F_{1qq}^{(n)}(x_-) \qquad (3)$$
$$+ a_0^{\bar\Lambda_c}[F_q^{(n)}(x_+)F_{0qq}^{(n)}(x_-) + F_{0qq}^{(n)}(x_+)F_q^{(n)}(x_-)$$
$$+ 2(n-1)F_{q_{\rm sea}}^{(n)}(x_+)F_{\bar q_{\rm sea}}^{(n)}(x_-)],$$

where $F_{1qq}^{(n)}(x_+)$ is the distribution at the leading fragmentation of diquarks, while $F_{0qq}^{(n)}(x_+)$ is the ordinary part of fragmentation written with the central density parameter $a_0^{\bar\Lambda_c}$.

The Λ_c distribution functions for $\Sigma^- p$ collisions also include additional diquark parts:

$$\varphi_n^{\Lambda_c}(s,x) = a_f^{\Lambda_c}F_{1qq}^{(n)}(x_+) + a_f^{\Lambda_c}F_{1qq}^{(n)}(x_-) \qquad (4)$$
$$+ a_0^{\bar\Lambda_c}[F_q^{(n)}(x_+)F_{qq}^{(n)}(x_-) + F_{qq}^{(n)}(x_+)F_q^{(n)}(x_-)$$
$$+ 2(n-1)F_{q_{\rm sea}}^{(n)}(x_+)F_{\bar q_{\rm sea}}^{(n)}(x_-)],$$

where $a_0^{\bar\Lambda_c}$ and $a_f^{\Lambda_c}$ are the same density parameters as in Eqs. (2) and (3).

The particle distribution on each side of the chain can be built on account of the quark content of beam particles ($x_+ = (x + \sqrt{x^2+x_\perp^2})/2$, $x_\perp = 2\sqrt{m_{\Lambda_c}^2 + \overline{p_\perp^2}}/\sqrt{s}$) and of target particles ($x_- = (x - \sqrt{x^2+x_\perp^2})/2$). In the case of $\Sigma^- p$ collisions, they are

$$F_q^{(n)}(x_+) = \frac{1}{3}F_s^{(n)}(x_+) + \frac{2}{3}F_d^{(n)}(x_+), \qquad (5)$$
$$F_{qq}^{(n)}(x_+) = \frac{1}{3}F_{dd}^{(n)}(x_+) + \frac{2}{3}F_{ds}^{(n)}(x_+),$$
$$F_q^{(n)}(x_-) = \frac{1}{3}F_d^{(n)}(x_-) + \frac{2}{3}F_u^{(n)}(x_-),$$
$$F_{qq}^{(n)}(x_-) = \frac{1}{3}F_{uu}^{(n)}(x_-) + \frac{2}{3}F_{ud}^{(n)}(x_-).$$

Each $F_i(x_\pm)$ ($i = s, u, d, ud, dd, ds, \ldots$) is constructed as the convolution

$$F_i(x_\pm) = \int_{x_\pm}^1 f_{\Sigma^-}^i(x_1)\frac{x_\pm}{x_1}\mathcal{D}_i^H\left(\frac{x_\pm}{x_1}\right)dx_1, \qquad (6)$$

where $f^i(x_1)$ is a structure function of the ith quark (diquark or antiquark) which has a fraction of energy x_1 in the interacting hadron and $\mathcal{D}_i^H(z)$ is a FF of this quark into the considered type of produced hadrons H.

The structure functions of quarks in interacting proton, hyperon, or pion beams have already been described in previous papers [11–13]. In the case of a hyperon beam, they depend on the parameter of the Regge trajectory of φ mesons ($s\bar s$) because of an s quark contained in Σ^- ($\alpha_\varphi(0) = 0$).

3. DIQUARK FRAGMENTATION FUNCTION AND STRING JUNCTION TRANSFER

The FFs of diquark and quark chains into charmed baryons or antibaryons are based on the rules formulated in [14].

The ud- and dd-diquark FF includes the constant $a_f^{\Lambda_c}$, which could be interpreted as a "leading" parameter, but the value of $a_f^{\Lambda_c}$ is fixed due to the baryon number sum rule and should be approximately equal to the value taken for Λ_c spectra in our previous calculations [11]:

$$\mathcal{D}_{dd}^{\Lambda_c}(z) = \frac{a_f^{\Lambda_c}}{a_0^{\bar\Lambda_c}z}z^{2\alpha_R(0)-2\alpha_N(0)} \qquad (7)$$
$$\times (1-z)^{-\alpha_\psi(0)+\lambda+2(1-\alpha_R(0))},$$

where the term $z^{2\alpha_R(0)-2\alpha_N(0)}$ means the probability for an initial diquark to have z close to 0, and the intercepts of Regge trajectories, $\alpha_R(0)$, $\alpha_N(0)$, and $\alpha_\psi(0)$, are taken to be the same values as in [11], 0.5, −0.5, and −2.0, respectively. The λ parameter is a remnant of the transverse momentum dependence;

it is equal to 0.5 here (for more information, see the early publications [7, 11]).

It is important here to keep in mind the possibility of creating the Λ_c baryon only on the basis of the string junction taken from the interacting proton or Σ^-. The string junction brings the positive baryon number in baryons and the negative one in antibaryons. In the proton and hyperon reactions, we have diquarks, so only the positive baryon number should be transferred. The FF of the string junction that can be transferred to region $z > 0$ has a similar form as the diquark FF written above [Eq. (7)]:

$$\mathcal{D}^{\Lambda_c}_{SJ}(z) = \frac{a_f^{\Lambda_c}}{a_0^{\bar{\Lambda}_c} z} z^{1-\alpha_{SJ}(0)} \times (1-z)^{-\alpha_\psi(0)+\lambda+2(1-\alpha_R(0))}, \quad (8)$$

where $\alpha_{SJ}(0)$ is the intercept of the string-junction Regge trajectory. We do not discuss here the two possible values of the string junction intercept, 0.5 [15] and 1.0 [16], just taking it equal to 0.5. This choice of the intercept is a reason for the target proton string junction going with a higher probability into the region of opposite z than the diquark, as is seen from the comparison of the $z \to 0$ asymptotic behavior in the last formulas. It will become significant when we study the baryon spectra in pion interactions. The full list of the FFs of diquarks and of the string junction into charmed baryons is presented in the Appendix.

The main difference between the concepts of asymmetry for D-meson production [4] and for Λ_c production is the difference between the forms of leading FFs. The parameter a_1, which was taken for the leading fragmentation of valence quark into D mesons (see [4]), is the ratio of the leading-D-meson density in the fragmentation region, $z \to 1$, to the density in the central region, $z \to 0$. The $a_f^{\Lambda_c}$ parameter is an absolute fraction of the diquark energy that is brought by the produced Λ_c. But both parameters actually reflect the same idea of the high density of leading hadrons near the fragmentation region ($z \to 1$) of those quarks (diquarks) of beam particles which can contribute to this leading hadron. This phenomenon was also named a "beam-drag" effect in some publications.

4. SEA-QUARK FRAGMENTATION FUNCTIONS

The main feature of the QGSM is the multiple-Pomeron exchanges [7] that are taken into account in the calculations of the spectra of multiparticle production [Eq. (1)]. In this case, the $2(n-1)$ quark–antiquark chains are connected to paired sea quark–antiquarks of the beam and target particles.

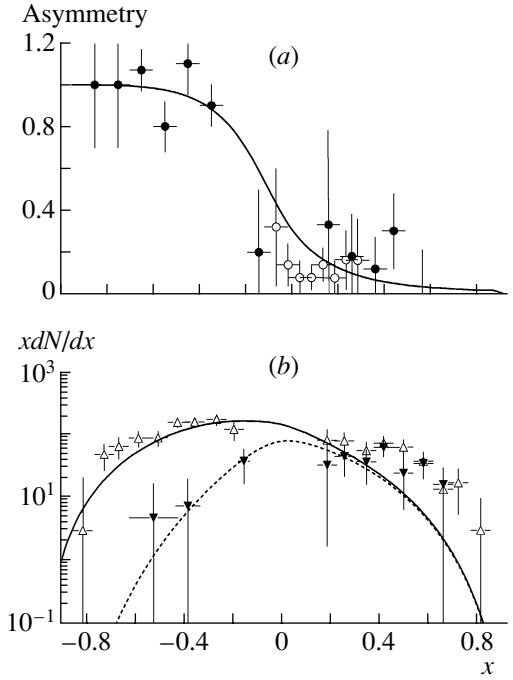

Fig. 1. (a) Asymmetry between Λ_c and $\bar{\Lambda}_c$ spectra obtained for πA ($x > 0$) and for pA ($x < 0$) collisions in the E781 experiment (black circles) [1] and in the E791 experiment (empty circles) [3]; the QGSM calculation with the string junction transfer (solid curve); (b) The distributions of Λ_c (empty triangles and solid curve) and $\bar{\Lambda}_c$ (black triangles and dashed curve) in E781 for these reactions and QGSM calculations.

The structure functions of sea-quark pairs can be written in the same way as the valence quark distributions. The structure function of d quark in hyperon, for example, is the following:

$$f^d_{\Sigma^-}(x_1) = C^{(n)}_{d,\bar{d}} x_1^{-\alpha_R(0)} \times (1-x_1)^{\alpha_R(0)-2\alpha_N(0)+(\alpha_R(0)-\alpha_\varphi(0))+n-1+2(1-\alpha_R(0))}. \quad (9)$$

Here, sea quarks and antiquarks have an additional power term $2(1-\alpha_R(0))$ corresponding to the quark distribution of the two-Pomeron diagram that includes one sea quark pair.

The FFs of light u, d sea quark fragmentation into Λ_c as well as $\bar{u}, \bar{d}$ quark into $\bar{\Lambda}_c$ are easily built from valence quark FFs. They are also written in the Appendix.

5. SPECTRA AND ASYMMETRY OF $\Lambda_c/\bar{\Lambda}_c$ IN $\pi^- p$ COLLISIONS

The asymmetry between the spectra of Λ_c and $\bar{\Lambda}_c$ measured in $\pi^- A$ and pA collisions at $p_L = 600$ GeV/c [1] is shown in Fig. 1a. The nonzero asymmetry in the region of pion fragmentation is

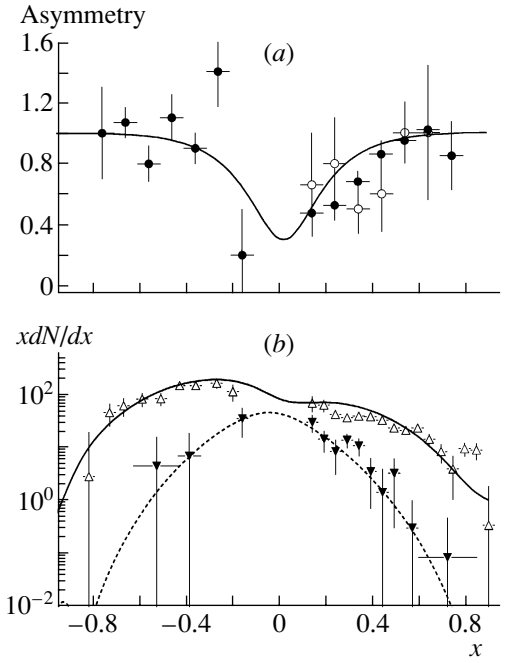

Fig. 2. (a) Asymmetry between Λ_c and $\bar{\Lambda}_c$ spectra obtained for $\Sigma^- A$ ($x > 0$) and for pA ($x < 0$) collisions in the E781 experiment (black circles) [1] and in the WA89 experiment (empty circles) [2]; the QGSM calculations (solid curve); (b) The spectra of Λ_c (empty triangles and solid curve) and $\bar{\Lambda}_c$ (black triangles and dashed curve) in E781 for these interactions and corresponding QGSM calculations.

described on the basis of baryon string junction transfer from the proton fragmentation region (see Section 3).

The asymmetry is defined as

$$A(x) = \frac{dN^{\Lambda_c}/dx - dN^{\bar{\Lambda}_c}/dx}{dN^{\Lambda_c}/dx + dN^{\bar{\Lambda}_c}/dx}. \qquad (10)$$

Here, dN^{Λ_c}/dx and $dN^{\bar{\Lambda}_c}/dx$ are the event distributions measured in the experiment [1].

The invariant distributions xdN/dx of charmed baryons and antibaryons obtained in pion interactions in the E781 experiment are shown in Fig. 1b with the QGSM curves calculated for pion fragmentation (the side of positive x) and for proton fragmentation (the side of negative x). The ratio of the values of $xdN/dx(p \to \Lambda_c, \bar{\Lambda}_c)$ and $xdN/dx(\pi^- \to \Lambda_c, \bar{\Lambda}_c)$ depends on the ratio of the cross sections of these two reactions. The absolute values of the cross sections are not measured in the present experiment, so the left side of the experimental plot in Fig. 1b can be shifted toward the right side by an arbitrary factor, and we did it here in order to make a better description.

6. THE SPECTRA AND ASYMMETRY OF $\Lambda_c/\bar{\Lambda}_c$ IN $\Sigma^- p$ COLLISIONS

The asymmetry between the spectra of Λ_c and $\bar{\Lambda}_c$ measured in $\Sigma^- A$ and pA collisions at $p_L = 600$ GeV/c is shown in Fig. 2a. Asymmetry is high on both sides of the graph because diquark fragmentation takes place for the beam and target particles.

The invariant distributions xdN/dx of charmed baryons and antibaryons obtained in hyperon interactions in the E781 experiment are shown in Fig. 2b with the QGSM curves calculated as hyperon fragmentation (the side of positive x) as well as for proton fragmentation (the side of negative x). The ratio between the values of $xdN/dx(p \to \Lambda_c, \bar{\Lambda}_c)$ and $xdN/dx(\Sigma^- \to \Lambda_c, \bar{\Lambda}_c)$ depends on the ratio of the cross sections of these two reactions. The left side of the experimental plot is shifted toward the right side by an arbitrary factor to produce a better description, as we did in the case of pion reaction.

The complete calculations carried out with the FFs written for Λ_c and $\bar{\Lambda}_c$ production give a good description of data with the value of parameter $a_f^{\Lambda_c} = 0.006$.

7. CONCLUSIONS

In this paper, we have examined the data on charmed baryon production in proton, pion, and hyperon beam interactions with a fixed target at $p_L = 600$ GeV/c in the E781 experiment. The following new ideas about Λ_c and $\bar{\Lambda}_c$ spectra and asymmetries should be mentioned here as the outcome of the QGSM study:

(i) The features of baryon charge transfer by the string junction of the target proton are disclosed in the nonzero baryon/antibaryon asymmetry in the pion beam fragmentation region, although we did not intend here to distinguish between two values of $\alpha_{\rm SJ}(0)$.

(ii) Λ_c and $\bar{\Lambda}_c$ spectra in the proton and hyperon beam interactions can be described with the same leading fragmentation parameter, $a_f^{\Lambda_c} = 0.006$.

(iii) The asymmetry is not a proper quantity to study the behavior of baryon spectra in the region of x close to 1; although the baryon/antibaryon asymmetry for the πp reaction shows good agreement with QGSM curves, the spectra of charmed baryons require a more detailed description in the pion fragmentation region.

(iv) There is no need to involve the intrinsic charm in the calculations of charmed baryon spectra at the up-to-date level of experimental data.

ACKNOWLEDGMENTS

I am grateful to Prof. A.B. Kaidalov, Dr. M. Iori, Dr. F. Garcia, and Dr. S. Baranov for numerous discussions.

This work was supported by NATO, grant no. PST.CLG. 977021.

APPENDIX

The concept of quark chain FFs is described in [7, 14]. The production of Λ_c as well as $\bar{\Lambda}_c$ ($\mathcal{D}_{0ud}^{\bar{\Lambda}_c}(z)$, etc.) takes place in the central region ($z = 0$) of the quark–antiquark chain with constant density parameter $a_0^{\bar{\Lambda}_c} = 4.0 \times 10^{-4}$. The FFs of projectile diquarks into Λ_c ($\mathcal{D}_{1ud}^{\Lambda_c}(z)$ and the similar) require the specific parameter $a_f^{\Lambda_c} = 0.006$. In departure from these statements, the full set of FFs that is necessary for calculating the spectra of Λ_c and $\bar{\Lambda}_c$ is written as follows:

$$\mathcal{D}_u^{\Lambda_c}(z) = \mathcal{D}_d^{\Lambda_c}(z) \tag{A.1}$$
$$= \frac{a_0^{\bar{\Lambda}_c}}{z}(1-z)^{\alpha_R(0)-2\alpha_N(0)+\lambda+\alpha_R(0)-\alpha_\psi(0)},$$
$$\mathcal{D}_{\bar{u}}^{\Lambda_c}(z) = \mathcal{D}_u^{\bar{\Lambda}_c}(z)$$
$$= \frac{a_0^{\bar{\Lambda}_c}}{z}(1-z)^{\alpha_R(0)-2\alpha_N(0)+\lambda+\alpha_R(0)-\alpha_\psi(0)+2(1-\alpha_R(0))},$$

$$\mathcal{D}_s^{\Lambda_c}(z) = \frac{a_0^{\bar{\Lambda}_c}}{z}(1-z)^{\alpha_R(0)-2\alpha_N(0)+\lambda+\alpha_R(0)-\alpha_\psi(0)+2(1-\alpha_R(0))+\alpha_R(0)-\alpha_\phi(0)},$$

$$\mathcal{D}_{1ud}^{\Lambda_c}(z) = \frac{a_f^{\Lambda_c}}{a_0^{\bar{\Lambda}_c} z} z^{1+\alpha_R(0)-2\alpha_N(0)} \times (1-z)^{-\alpha_\psi(0)+\lambda},$$

$$\mathcal{D}_{1dd}^{\Lambda_c}(z) = \frac{a_f^{\Lambda_c}}{a_0^{\bar{\Lambda}_c} z} z^{2\alpha_R(0)-2\alpha_N(0)} \times (1-z)^{-\alpha_\psi(0)+\lambda+2(1-\alpha_R(0))},$$

$$\mathcal{D}_{1ds}^{\Lambda_c}(z) = \frac{a_f^{\Lambda_c}}{2a_0^{\bar{\Lambda}_c} z} z^{-2\alpha_N(0)+3\alpha_R(0)-\alpha_\phi(0)} \times (1-z)^{-\alpha_\psi(0)+\lambda+2(1-\alpha_R(0))+\alpha_R(0)-\alpha_\phi(0)},$$

$$\mathcal{D}_{\mathrm{SJ}}^{\Lambda_c}(z) = \frac{a_f^{\Lambda_c}}{a_0^{\bar{\Lambda}_c} z} z^{1-\alpha_{\mathrm{SJ}}(0)} \times (1-z)^{-\alpha_\psi(0)+\lambda+2(1-\alpha_R(0))},$$

$$\mathcal{D}_{0uu}^{\Lambda_c}(z) = \mathcal{D}_{0dd}^{\Lambda_c}(z)$$
$$= \frac{a_0^{\bar{\Lambda}_c}}{z}(1-z)^{-\alpha_\psi(0)+\lambda+4(1-\alpha_N(0))},$$
$$\mathcal{D}_{0ds}^{\Lambda_c}(z) = \frac{a_0^{\bar{\Lambda}_c}}{z} \times (1-z)^{-\alpha_\psi(0)+\lambda+4(1-\alpha_N(0))+\alpha_R(0)-\alpha_\phi(0)};$$

$$\mathcal{D}_d^{\bar{\Lambda}_c}(z) = \mathcal{D}_u^{\bar{\Lambda}_c}(z) = \frac{a_0^{\bar{\Lambda}_c}}{z} \tag{A.2}$$
$$\times (1-z)^{\alpha_R(0)-2\alpha_N(0)+\alpha_R(0)-\alpha_\psi(0)+\lambda+2(1-\alpha_N(0))},$$
$$\mathcal{D}_{\bar{u}}^{\bar{\Lambda}_c}(z) = \mathcal{D}_u^{\Lambda_c}(z),$$
$$\mathcal{D}_s^{\bar{\Lambda}_c}(z) = \mathcal{D}_s^{\Lambda_c}(z),$$

$$\mathcal{D}_{0ud}^{\bar{\Lambda}_c}(z) = \mathcal{D}_{0dd}^{\bar{\Lambda}_c}(z) = \frac{a_0^{\bar{\Lambda}_c}}{z}(1-z)^{\alpha_R(0)-2\alpha_N(0)+\lambda+2(1-\alpha_N(0))+\alpha_R(0)-\alpha_\psi(0)},$$

$$\mathcal{D}_{0ds}^{\bar{\Lambda}_c}(z) = \frac{a_0^{\bar{\Lambda}_c}}{z}(1-z)^{\alpha_R(0)-2\alpha_N(0)+\lambda+2(1-\alpha_N(0))+\alpha_R(0)-\alpha_\psi(0)+\alpha_R(0)-\alpha_\phi(0)}.$$

REFERENCES

1. SELEX Collab. (F. Garcia *et al.*), Fermilab-Pub-01/258-E; Phys. Lett. B **528**, 49 (2002); SELEX Collab. (J. Russ *et al.*), in *Proceedings of ICHEP 2000, Osaka, 2000*, Fermilab-Conf-00/252, hep-ex/0010011.
2. WA89 Collab. (M. I. Adamovich *et al.*), Eur. Phys. J. C **8**, 593 (1999).
3. E791 Collab. (E. M. Aitala *et al.*), Phys. Lett. B **411**, 230 (1997); Nucl. Phys. B **478**, 311 (1996).
4. O. I. Piskounova, Yad. Fiz. **64**, 101 (2001) [Phys. At. Nucl. **64**, 98 (2001)].
5. R. Vogt and R. Brodsky, Nucl. Phys. B **438**, 261 (1995).
6. G. Herrera and J. Magnin, Eur. Phys. J. C **2**, 477 (1998).

7. A. B. Kaidalov and K. A. Ter-Martirosyan, Yad. Fiz. **39**, 1545 (1984) [Sov. J. Nucl. Phys. **39**, 979 (1984)]; Yad. Fiz. **40**, 211 (1984) [Sov. J. Nucl. Phys. **40**, 135 (1984)]; A. B. Kaidalov, Phys. Lett. B **116B**, 459 (1982).
8. A. K. Likhoded and S. R. Slabospitsky, Yad. Fiz. **60**, 1097 (1997) [Phys. At. Nucl. **60**, 981 (1997)].
9. G. H. Arakelyan, Yad. Fiz. **61**, 1682 (1998) [Phys. At. Nucl. **61**, 1570 (1998)].
10. O. I. Piskounova, in *Proceedings of BEACH 2000, Valencia, 2000*; hep-ph/0010263.
11. A. B. Kaidalov and O. I. Piskounova, Yad. Fiz. **43**, 1545 (1986) [Sov. J. Nucl. Phys. **43**, 994 (1986)]; O. I. Piskounova, Yad. Fiz. **56** (8), 176 (1993) [Phys. At. Nucl. **56**, 1094 (1993)].
12. O. I. Piskounova, Preprint FIAN-140 (Moscow, 1987).
13. O. I. Piskounova, Nucl. Phys. B (Proc. Suppl.) **50**, 508 (1996); Yad. Fiz. **60**, 513 (1997) [Phys. At. Nucl. **60**, 439 (1997)]; hep-ph/9904208.
14. A. B. Kaidalov, Yad. Fiz. **45**, 1452 (1987) [Sov. J. Nucl. Phys. **45**, 902 (1987)].
15. G. C. Rossi and G. Veneziano, Nucl. Phys. B **123**, 507 (1977); A. Capella *et al.*, hep-ph/0103337.
16. B. Z. Kopeliovich and B. G. Zakharov, Phys. Lett. B **211**, 221 (1988).

Physics of Atomic Nuclei, Vol. 66, No. 2, 2003, pp. 313–322. Translated from Yadernaya Fizika, Vol. 66, No. 2, 2003, pp. 338–347.

ELEMENTARY PARTICLES AND FIELDS
Theory

What New Information about the Microscopic Quark Structure of Meson–Baryon Degrees of Freedom in Nucleons Can Be Deduced from Data on Quasielastic Pion Knockout?

I. T. Obukhovsky, V. G. Neudatchin, L. L. Sviridova, and N. P. Yudin

Institute of Nuclear Physics, Moscow State University, Vorob'evy gory, Moscow, 119899 Russia

Received August 15, 2001; in final form, February 14, 2002

Abstract—The emergence of $B+\pi$ virtual subsystems, which manifest themselves in quasielastic-knockout processes of the $N(e,e'\pi)B$ type, where B is the final-state baryon in various excited states, is considered within the microscopic quark model of a $^3P_0$ localized scalar fluctuation of the QCD vacuum. The relevant technique for taking into account the rearrangement of quark degrees of freedom is demonstrated. The model provides a good description of known momentum distributions for $B=N$ channels. The momentum distributions are predicted for $N\to\pi+B$ channels, where $B=\Delta$, $N^*(1535)$, or $N^{**}(1440)$. It would be of interest to study these channels in exclusive coincidence experiments at accelerators producing electron beams of energy ranging between 5 and 10 GeV. © *2003 MAIK "Nauka/Interperiodica".*

1. INTRODUCTION

Presently, questions concerning hadronic degrees of freedom in nucleons are being vigorously discussed in the literature (in this connection, attention is given primarily to the properties of various nucleon-decay channels of the type $N\to B+м$, where B is a baryon and $м$ is a meson). These degrees of freedom play an important role in the formation of the nucleon size [1] and the nucleon magnetic moment [2]; in addition, they take an active part in deep-inelastic lepton scattering on nucleons [3], pion-photoproduction reactions [4], and processes involving quasielastic pion knockout from a nucleon [5–7]. According to the theoretical estimates presented in [8], which are based on experimental data of the types indicated above, the contribution of nonnucleon components in the nucleon may be as great as 40%. Naturally, much attention is given to a microscopic quark description of the hadronic degrees of freedom being discussed [8–10].

In the present study, the model of a localized $^3P_0$ scalar quark–antiquark fluctuation [9] is used to describe the meson cloud arising around the nucleon owing to the polarization of the QCD vacuum by color quark charges. In principle, this model can form a basis for a unified description of a wide variety of meson–baryon components in the nucleon. The process of quasielastic meson knockout provides a highly efficient means for studying the microscopic quark structure of the nucleon and of its meson cloud [5–7]. By quasielastic meson knockout, we imply exclusive reactions of the type $p+e\to B+\pi+e'$ that proceed via a binary collision of the electron e with the meson $м$ in the virtual-proton-decay channel $p\to B+м$, the meson $м$ being rearranged into a pion upon an electron impact accompanied by a high momentum transfer to this meson. This process, recorded with the aid of a coincidence scheme, manifests itself under kinematical conditions close to those of the free-scattering process $м+e\to\pi+e'$ in the case where the momentum of the spectator baryon B is much less than the momenta of the fast final particles π and e and where, in addition, the final-pion energy is much greater than the binding energy of the meson $м$ in the channel $p\to B+м$. Such kinematical conditions are realized if the square of the virtual-photon mass, Q^2, satisfies the condition $Q^2\geq 2\,(\mathrm{GeV}/c)^2$ [5–7], in which case a description in the laboratory frame is essentially dominated by two simple pole diagrams in Figs. 1*a* and 1*b*. This simple mechanism makes it possible to single out the cross section for free electron scattering on a meson as an individual factor and to extract, from experimental data in the most direct way, the momentum distributions $\overline{\left|\Psi_p^{Bм}(k^2)\right|^2}$ of mesons $м$ in the channel $p\to B+м$, including the corresponding spectroscopic factor (probability) $S_p^{Bм}$ as a normalization of the momentum distributions [6]. It should be noted, however, that the square of the virtual-photon mass, Q^2, cannot be overly large in our theory: for $Q^2>5$–$10\ (\mathrm{GeV}/c)^2$, the knockout process must be considered on the basis of perturbative QCD and the relevant diagram technique without recourse to concepts of intermediate-energy physics, such as quasielastic meson knockout and the

1063-7788/03/6602-0313$24.00

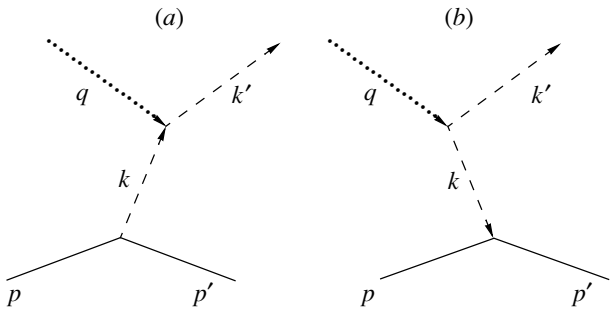

Fig. 1. Pole diagrams representing pion production on a nucleon.

momentum distribution of mesons in various channels [11].

Owing to the fact that, under specific kinematical conditions, the cross section for longitudinal (transverse) polarization receives a dominant contribution from virtual-photon absorption by a virtual pion (virtual rho meson), $\gamma_L^* + \pi \to \pi$ ($\gamma_T^* + \rho \to \pi$), the momentum distributions of a pion and a rho meson in the nucleon could be reconstructed on the basis of the experimental cross sections for, respectively, longitudinal and transverse polarization [for rho mesons, this was done only for soft momenta ($\mathbf{k}^2 < m_\rho^2$)] [5, 6]. Unfortunately, there are only a few relevant experiments that studied pion electroproduction [12] and which produced data under the kinematical conditions of quasielastic knockout. However, such investigations can be developed further, for example, at the Thomas Jefferson Laboratory. Namely, the aforementioned problem of thoroughly testing theoretical models of QCD-vacuum polarization, which is responsible for the emergence of the meson cloud of the nucleon, can be solved by combining experimental results on quasielastic meson knockout at electron-beam energies in the range 5–10 GeV for a few different channels of the $B + м$ type (processes like $p + e \to \Lambda + K + e'$ and $\Sigma + K + e'$ being included).

In the present article, devoted to developing, at the microscopic quark level, the investigations presented in [6, 7], we consider the question of what predictions for the momentum distributions of pions in the channels $p \to N + \pi$, $p \to \Delta + \pi$, $p \to N^*(3/2^-, 1/2^-) + \pi$, and $p \to N^{**}(1/2^+, \text{Roper}) + \pi$ one can make on the basis of the model of a $^3P_0$ scalar quark–antiquark fluctuation [9]. In a similar way, one can calculate the family of momentum distributions in rho-meson knockout with the nondiagonal $\gamma_T^* + \rho \to \pi$ amplitude, the momentum distributions of kaons in channels involving final Λ and Σ, and other similar quantities.

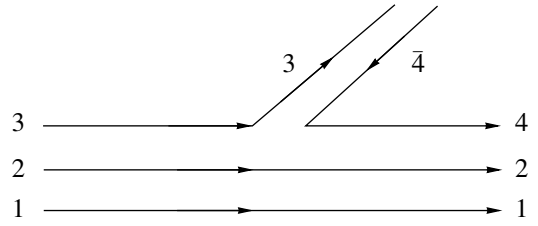

Fig. 2. Quark pattern of pion production.

2. DESCRIPTION OF THE FORMALISM

In the theory of the nucleus, methods for studying few-particle subsystems in multiparticle systems have been well developed for cases where, for example, in discussing the problem of quasielastic alpha-particle knockout from a nucleus [13], one has to deal with virtual-decay channels of the type $A_i \to (A-4)_f + \alpha_n$, where α_n is an internally excited alpha-particle cluster (the impact of a fast projectile induces the $\alpha_n \to \alpha_0$ transition). Apart from a constant factor, the wave function describing the relative motion of the alpha-particle cluster α_n and the final nucleus $(A-4)_f$ can be defined as [13]

$$\Psi_i^{f\alpha_n}(\mathbf{R}) = c\,\langle (A-4)_f \alpha_n | A_i \rangle \qquad (1)$$

(where the numbers of nucleons in the alpha particles are fixed, integration is performed with respect to the intrinsic variables of the subsystems involved, and $\mathbf{R}$ is the relative coordinate) and can be calculated on the basis of the shell model by combining the technique of multiparticle shell fractional-parentage coefficients with the technique that employs coefficients corresponding to the Talmi–Moshinsky–Smirnov transformation from single-particle to cluster Jacobi coordinates for oscillator wave functions [14]. The observed momentum distribution of knock-on alpha particles (of high energy) in the real channel $A_i \to (A-4)_f + \alpha_0$ is the square of the sum of the Fourier transforms $\Psi_i^{f\alpha_n}(\mathbf{q})$ of the wave functions taken with the corresponding weights for different n [13]. These momentum distributions are sharply different for different final states f.

By and large, the physical content of the problem being considered corresponds to the same scheme: the $(1\,2\,3\,4\,\bar{4})$ quark system fragments into the $(1\,2\,4)$ and the $(3\,\bar{4})$ subsystem (Fig. 2), which can be formed in various final states, this information being of great value. Of course, the formalism used here is different from that in the theory of the nucleus, although there are some common ingredients—these include the shell structure of $3q$ nucleon wave functions (nonrelativistic model), fractional-parentage coefficients, and the transformation from one set of Jacobi coordinates to another. The redistribution of quarks between the $(1\,2\,3)$ and the $(4\,\bar{4})$ subsystem is necessary

for the spin-1 scalar $^3P_0$ quark–antiquark fluctuation (which is considered below) of the QCD vacuum to be compatible with the formation of a spinless pion in the field of a baryon B.

In the momentum representation, the above fluctuation is described by the creation operator T [9], which has the obvious form

$$T = -v\sum_{\alpha,\bar\beta} d\mathbf{p}_q d\mathbf{p}_{\bar q}\delta(\mathbf{p}_q+\mathbf{p}_{\bar q}) \times C_{\alpha\bar\beta}F_{\alpha\bar\beta}Z(\mathbf{p}_q,\mathbf{p}_{\bar q})\sum_m (1m1-m|00)X^m_{\alpha\bar\beta} \times Y_1^{-m}(\mathbf{p}_q-\mathbf{p}_{\bar q})b^+_\alpha(\mathbf{p}_q)d^+_{\bar\beta}(\mathbf{p}_q), \quad (2)$$

where $\alpha=\{s_\alpha,f_\alpha,c_\alpha\}$, $(\bar\beta=\{s_{\bar\beta},f_{\bar\beta},c_{\bar\beta}\})$ are the projections of the quark spin, flavor, and color; $C_{\alpha\bar\beta}$ and $F_{\alpha\bar\beta}$ are the singlet wave functions for color and flavor, respectively; $X^m_{\alpha\bar\beta}$ is the spin function for the triplet state; $Y_1^{-m}(\mathbf{p}_q-\mathbf{p}_{\bar q})$ is a spherical harmonic; and b^+_α and $d^+_{\bar\beta}$ are, respectively, the quark and the antiquark creation operator. The phenomenological constant v specifies the degree of polarizability of the QCD vacuum, its value being fixed according to the well-known pion–nucleon coupling constant $g_{\pi NN}$. The function $Z(\mathbf{p}_q,\mathbf{p}_{\bar q})$, which characterizes the dimension and shape of the fluctuation being considered, is usually set to unity since it is assumed that the phenomenological nucleon-radius parameter b (see below) also effectively takes into account the degree of localization of the fluctuation. Here, we do not go beyond this simplification either, but we hope that the appearance of experimental data on quasielastic meson knockout in various channels of the $N\to B+\pi$ type would make it possible to determine this function in the future.

By analogy with expression (1), the amplitude for the transition $N\to B+\pi^\lambda$ $(\lambda=0,\pm1)$ is defined as

$$J(N\to B+\pi^\lambda)=\langle B\pi^\lambda|T|N\rangle, \quad (3)$$

where the quantities $T|N\rangle$, B, and π^λ characterize, respectively, the (1 2 3 4 $\bar4$) quark system, the (1 2 $\bar4$) subsystem, and the (3 $\bar4$) subsystem (see Fig. 2).

In the Appendix, it is shown that expression (3) can be represented as

$$J(N\to B+\pi^\lambda)=\langle B|3H_\lambda|N\rangle, \quad (4)$$

where the factor of 3 reflects the identity of quarks and the operator H_λ has the form

$$H_\lambda(\boldsymbol{\rho}_2',\boldsymbol{\rho}_2)=ve^{i\frac{2}{3}\mathbf{k}\cdot\boldsymbol{\rho}_2'}\boldsymbol{\tau}^{(3)}_{-\lambda}\hat O(\boldsymbol{\rho}_2',\boldsymbol{\rho}_2)\boldsymbol{\sigma}^{(3)} \times\left[\frac{\varepsilon_\pi}{2m_q}\left(\frac{2}{i}\nabla_{\rho_2}+\frac{2}{3}\mathbf{k}\right)+\left(1+\frac{\varepsilon_\pi}{6m_q}\right)\mathbf{k}\right], \quad (5)$$

the nonlocal kernel $\hat O(\boldsymbol{\rho}_2',\boldsymbol{\rho}_2)$ of this operator being proportional to the wave function for the pion as a quark–antiquark state. For the pion wave function chosen in the Gaussian form $\Psi_\pi(\rho^2)\sim\exp(-\rho^2/4b_\pi^2)$, the kernel is given by

$$\hat O(\boldsymbol{\rho}_2',\boldsymbol{\rho}_2)=\exp\left(i\frac{1}{2}\mathbf{k}\cdot(\boldsymbol{\rho}_2'-\boldsymbol{\rho}_2)\right) \times\frac{1}{(4\pi b_\pi^2)^{3/2}}\exp\left(-\frac{1}{4b_\pi^2}(\boldsymbol{\rho}_2'-\boldsymbol{\rho}_2)^2\right), \quad (6)$$

where $\boldsymbol{\rho}_2=(\mathbf{r}_1+\mathbf{r}_2)/2-\mathbf{r}_3$; $\boldsymbol{\rho}_2'=(\mathbf{r}_1+\mathbf{r}_2)/2-\mathbf{r}_4$; $\mathbf{r}_i$ are the coordinates of the ith quark; $\mathbf{k}$ is the momentum of a virtual meson; $\varepsilon_\pi=\sqrt{\mathbf{k}^2+m_\pi^2}$ is its relativistic energy; $\boldsymbol{\sigma}^{(3)}$ and $\boldsymbol{\tau}^{(3)}$ are, respectively, the spin and the isospin Pauli matrix for the third quark; $\lambda=0,\pm1$ are the spherical components of the vector $\boldsymbol{\tau}^{(3)}$ that correspond to the production of the pion π^λ; $m_q=313$ MeV is the constituent quark mass; and b_π is the pion radius.

In the ket and bra vectors, there appear the baryon wave functions, which have the form [15]

$$|N\rangle=\left|s^3[3]_xL=0\right\rangle_{\rm TISM}\left|[1^3]_C([21]_S\circ[21]_T)[3]_{ST}:[1^3]_{CST}\right\rangle, \quad (7)$$
$$|N^*(1535)\rangle=\left|s^2p[21]_xL=1\right\rangle_{\rm TISM}\left|[1^3]_C([21]_S\circ[21]_T)[21]_{ST}:[21]_{CST}\right\rangle^{J=1}_{[1^3]_{xCST}},$$
$$|N^{**}(1440)\rangle=\left|sp^2[3]_xL=0\right\rangle_{\rm TISM}\left|[1^3]_C([21]_S\circ[21]_T)[3]_{ST}:[1^3]_{CST}\right\rangle,$$
$$|\Delta\rangle=\left|s^3[3]_xL=0\right\rangle_{\rm TISM}\left|[1^3]_C([3]_S\circ[3]_T)[3]_{ST}:[1^3]_{CST}\right\rangle,$$

where Young diagrams in corresponding subspaces are used everywhere; the subscript TISM means the translation-invariant shell model; the values of S and T are not indicated since they are in a bijective relation with $[f]_S$ and $[f]_T$, respectively; and the obvious relationship $\mathbf{S}+\mathbf{L}=\mathbf{J}$ is omitted for the sake of brevity.

The calculation is performed on the basis of the fractional-parentage expansion of the three-quark states (7) in a sum of the products of a two- and a

one-quark cluster, $3q \to 2q \times q$, summation being performed over all possible states of the third quark and the "12" two-quark cluster.

Basis vectors that correspond to a specific permutation symmetry in the clusters are expressed in terms of harmonic-oscillator wave functions as

$$\left|s^3[3]_x L=0\right\rangle_{\rm TISM} = |0s\left(\boldsymbol{\rho}_1/2\alpha_1\right)\rangle\,|0s\left(\boldsymbol{\rho}_2/2\alpha_2\right)\rangle\,, \tag{8}$$
$$\left|s^2p[21]_x L=1\right\rangle_{\rm TISM} = |0s\left(\boldsymbol{\rho}_1/2\alpha_1\right)\rangle\,|1p\left(\boldsymbol{\rho}_2/2\alpha_2\right),m\rangle\,,|1p\left(\boldsymbol{\rho}_1/2\alpha_1\right),m\rangle\,|0s\left(\boldsymbol{\rho}_2/2\alpha_2\right)\rangle\,,$$
$$\left|sp^2[3]_x L=0\right\rangle_{\rm TISM} = \left(|2s\left(\boldsymbol{\rho}_1/2\alpha_1\right)\rangle\,|0s\left(\boldsymbol{\rho}_2/2\alpha_2\right)\rangle + |0s\left(\boldsymbol{\rho}_1/2\alpha_1\right)\rangle\,|2s\left(\boldsymbol{\rho}_2/2\alpha_2\right)\rangle\right)/\sqrt{2},$$

where $\alpha_1 = b/\sqrt{2}$, $\alpha_2 = \sqrt{3/8}b$, $b \approx 0.5$–0.6 fm is the nucleon radius, and $\boldsymbol{\rho}_1 = \mathbf{r}_1 - \mathbf{r}_2$.

In the CST sector, use is made of basis vectors that possess a similar permutation symmetry in the clusters. The baryon wave functions are represented in the form of fractional-parentage expansions that correspond to the separation of the third quark; that is,

$$|N\rangle = \left|s^3[3]_x\left([2]_x\times[1]_x\right)L=0\right\rangle_{\rm TISM}\left|[1^3]_C([21]_S\circ[21]_T)[3]_{ST}:[1^3]_{CST}\left([1^2]_{CST}\times[1]_{CST}\right)\right\rangle, \tag{9}$$
$$|N^*(1535)\rangle$$
$$= \frac{1}{\sqrt{2}}\left\{\left|s^2p[21]_x\left([2]_x\times[1]_x\right)L=1\right\rangle_{\rm TISM}\left|[1^3]_C([21]_S\circ[21]_T)[21]_{ST}:[21]_{CST}\left([1^2]_{CST}\times[1]_{CST}\right)\right\rangle_{J=1}\right.$$
$$\left. - \frac{1}{\sqrt{2}}\left|s^2p[21]_x\left([1^2]_x\times[1]_x\right)L=1\right\rangle_{\rm TISM}\left|[1^3]_C([21]_S\circ[21]_T)[21]_{ST}:[21]_{CST}\left([2]_{CST}\times[1]_{CST}\right)\right\rangle_{J=1}\right\},$$
$$|N^{**}(1440)\rangle = \left|sp^2[3]_x\left([2]_x\times[1]_x\right)L=0\right\rangle_{\rm TISM}\left|[1^3]_C([21]_S\circ[21]_T)[3]_{ST}:[1^3]_{CST}\left([1^2]_{CST}\times[1]_{CST}\right)\right\rangle,$$
$$|\Delta\rangle = \left|s^3[3]_x\left([2]_x\times[1]_x\right)L=0\right\rangle_{\rm TISM}\left|[1^3]_C([3]_S\circ[3]_T)[3]_{ST}:[1^3]_{CST}\left([1^2]_{CST}\times[1]_{CST}\right)\right\rangle.$$

All the aforesaid refers to the microscopic pattern that is displayed in Fig. 2 and which is associated with the diagram for quasielastic knockout proper (Fig. 1*a*). For the diagram in Fig. 1*b*, the physical situation is generally different (here, one is dealing with the virtual-capture process $N + \pi \to B$ rather than with the virtual-decay process $N \to B + \pi$). However, the corresponding matrix element, which is similar to the amplitude in (4) with the interchanged left- and right-hand sides and with the necessary replacement of the coordinates $\boldsymbol{\rho}_2$ and $\boldsymbol{\rho}'_2$ in the operator given by (5), will coincide with (4), since there occurs the same orbital transition of a valence quark from N to B, only the substitution $3 \to 4$ being made for the number of this quark. Of course, the pole denominators are different for the diagram in Fig. 1*a* and the diagram in Fig. 1*b*, and this is taken into account in going over to momentum distributions (see below).

It is interesting to note that the $^3P_0$ scalar fluctuation as it is can be knocked out without quark exchange with the nucleon involved, provided that one records the quasielastic knockout of, say, the f_0 meson of mass 980 MeV, which is the lowest scalar meson and which has quantum numbers ($L = 1$, $S = 1$, $J = 0$, $T = 0$) that are identical to those of the fluctuation in question. It seems that the process $p(\pi, \pi f_0)p$ at a pion-beam energy of a few GeV and the detection of triple coincidences, since the knock-on f_0 meson decays, would be appropriate here. In the momentum distribution extracted from such experimental data, the existence of the fluctuation would correspond to a peak at zero momentum against the

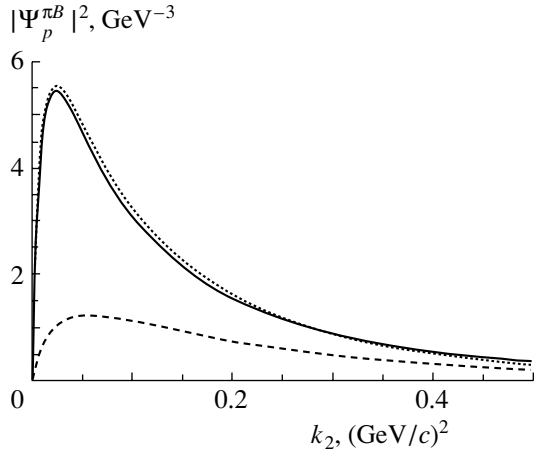

Fig. 3. Momentum distribution of pions in the $N \to N + \pi$ and $N \to \Delta + \pi$ channels: (solid curve) results of the calculation from [6] for $N + \pi$, (dotted curve) results of the calculation for $N + \pi$ on the basis of the present microscopic model, and (dashed curve) results of the calculation for $\Delta + \pi$ on the basis of the present microscopic model.

background of the component that is associated with the $3 \to 4$ change in the number of the valence quark involved and which is discussed here.

Upon averaging over the projections of the initial-state spin and summation over the projections of the final-state spin, the square of the amplitude for the $N \to B + \pi$ transition within the quark model assumes the form

$$\overline{|J^{qm}(p \to n\pi)|^2} = g^2_{\pi NN} \cdot 2\mathbf{k}^2 F^2_{\pi NN}(\mathbf{k}^2), \quad (10)$$

$$\overline{|J^{qm}(p \to \Delta\pi)|^2} = g^2_{\pi \Delta N} \cdot 2\mathbf{k}^2 F^2_{\pi \Delta N}(\mathbf{k}^2), \quad (11)$$

$$\overline{|J^{qm}(p \to N^*\pi)|^2} = g^2_{\pi NN^*} \cdot 2\varepsilon^2_\pi F^2_{\pi NN^*}(\mathbf{k}^2), \quad (12)$$

$$\overline{|J^{qm}(p \to N^{**}\pi)|^2} = g^2_{\pi NN^{**}} \cdot 2\mathbf{k}^2 F^2_{\pi NN^{**}}(\mathbf{k}^2), \quad (13)$$

where

$$g_{\pi NN} \equiv \frac{2M}{m_\pi} f_{\pi NN} = \frac{2M}{m_\pi}\frac{5}{3}\frac{1}{N}\left(1 + \frac{m_\pi}{6m_q}\right) f_{\pi qq}, \quad (14)$$

$$g_{\pi \Delta N} = \frac{2\sqrt{MM_\Delta}}{m^2_\pi}\frac{4\sqrt{2}}{5} f_{\pi NN}, \quad (15)$$

$$g_{\pi NN^*} = \frac{2\sqrt{MM_{N^*}}}{m^2_\pi}\frac{2\sqrt{2}}{5\sqrt{3}}\frac{1 - 2a/3}{m_q b\left(1 + \dfrac{m_\pi}{6m_q}\right)} f_{\pi NN}, \quad (16)$$

$$g_{\pi NN^{**}} = \frac{2\sqrt{MM_{N^{**}}}}{m_\pi}\frac{1}{3\sqrt{3}} \quad (17)$$

$$\times \left[3a + \frac{m_\pi}{m_q}\frac{1}{1 + \dfrac{m_\pi}{6m_q}}\left(1 - \frac{1}{3}a + \frac{5}{9}a^2\right)\right] f_{\pi NN}.$$

Here, $a = x^2(1 + 2x^2/3)^{-1}$, $x = b_\pi/b$, $N = (1 + 2x^2/3)^{3/2}$, $f^2_{\pi NN}/4\pi = 0.088$, and M is the nucleon mass. The form factors appearing in Eqs. (11)–(13) are given by

$$F_{\pi NN}(\mathbf{k}^2) = F_{\pi \Delta N}(\mathbf{k}^2) = \exp\left\{-\frac{1}{6}\mathbf{k}^2 b^2\left(1 + \frac{a}{6}\right)\right\}, \quad (18)$$

$$F_{\pi NN_*}(\mathbf{k}^2) \quad (19)$$

$$= \left[1 - \frac{\mathbf{k}^2 b^2}{6}\frac{(3 + a)}{(3 - 2a)}\left(1 + \frac{\varepsilon_\pi}{6m_q} - \frac{4a}{9}\right)\right] F_{\pi NN}(\mathbf{k}^2),$$

$$F_{\pi NN^{**}}(\mathbf{k}^2) = \left[\frac{m_\pi}{m_q}\frac{1}{1 + \dfrac{m_\pi}{6m_q}}\left(1 - \frac{a}{3} + \frac{5a^2}{9}\right) + 3a\right]^{-1}\frac{1 + \dfrac{\varepsilon_\pi}{6m_q}}{1 + \dfrac{m_\pi}{m_q}} \quad (20)$$

$$\times \left[\frac{\varepsilon_\pi}{m_q}\frac{1}{1 + \dfrac{\varepsilon_\pi}{6m_q}}\left\{1 - \frac{a}{3} + \frac{5a^2}{9} - \frac{\mathbf{k}^2 b^2}{18}a\left(1 + \frac{a}{3}\right)^2\right\} + 3a - \frac{\mathbf{k}^2 b^2}{2}\left(1 + \frac{a}{3}\right)^2\right] F_{\pi NN}(\mathbf{k}^2).$$

Upon going over to momentum distributions, the wave function corresponding to the diagram for the quasielastic-knockout process proper (Fig. 1*a*) [7] can be represented as

$$\Psi^{B\pi}_p(\mathbf{k}) = \frac{J(p \to B\pi)}{k_0 - \varepsilon_\pi(\mathbf{k})}, \quad (21)$$

where $k_0 = M - M_B - \mathbf{k}^2/2M_B$. The total contribution of the diagrams in Figs. 1*a* and 1*b* is given by

$$\frac{J(p \to B\pi)}{k_0 - \varepsilon_\pi(\mathbf{k})} - \frac{J(p \to B\pi)}{k_0 + \varepsilon_\pi(\mathbf{k})} \quad (22)$$

$$= J(p \to B\pi)\frac{2\varepsilon_\pi(\mathbf{k})}{k^2_0 - \varepsilon^2_\pi(\mathbf{k})} = \Psi^{B\pi}_p(\mathbf{k})\frac{2\varepsilon_\pi(\mathbf{k})}{k_0 + \varepsilon_\pi(\mathbf{k})}.$$

With allowance for (22), the cross section for quasielastic pion knockout from nucleons by high-energy electrons has the form

$$\frac{d^5\sigma}{dE_{e'}d\Omega_{e'}d\Omega_\pi} = |\mathbf{p}_\pi|\, E_\pi \overline{\left|\Psi^{B\pi}_p(\mathbf{k})\right|^2} \quad (23)$$

$$\times \left(\frac{\varepsilon_\pi(\mathbf{k})}{k_0 + \varepsilon_\pi(\mathbf{k})}\right)^2\left(1 - \frac{|\mathbf{p}_\pi|}{E_\pi}\cos\theta_\pi\right)\left(\frac{d^2\sigma_{\rm el}}{d\Omega_\pi}\right)_{\rm free},$$

where $\mathbf{p}_\pi$ and E_π are, respectively, the 3-momentum and the energy of the knock-on pion; $E_{e'}$ is the energy of the scattered electron; $d\Omega_{e'}$ is an element of the solid angle in which it is scattered; $d\Omega_\pi$ is an element of the solid angle in which the knock-on pion is emitted; θ_π is the angle between the electron and the pion 3-momentum; and $\left(d^2\sigma_{el}/d\Omega_\pi\right)_{\rm free}$ is the cross section for elastic $e\pi$ scattering.

3. RESULTS AND DISCUSSION

A. $N \to \pi + N$ channel. The momentum distribution of pions in this channel and the form factor

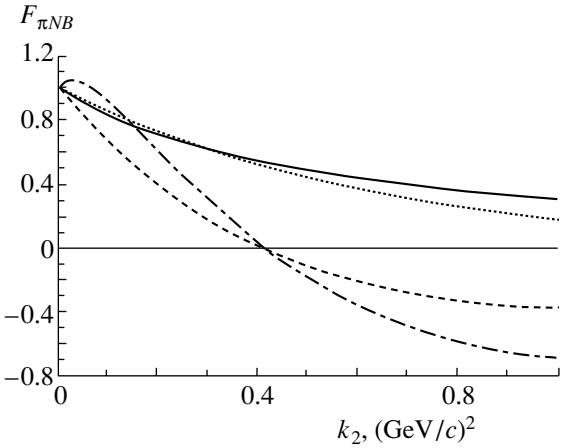

Fig. 4. Form factors for the πNN and πNB vertices: (solid curve) form factor $F_{\pi NN}(k^2)$ computed by formula (24); (dotted curve) same form factor computed by formula (18); and (dashed and dash-dotted curves) form factors for the $N \to \pi + N^*$ and $N \to \pi + N^{**}$ channels, respectively, according to the calculations on the basis of the present microscopic model at $x = 0.5$.

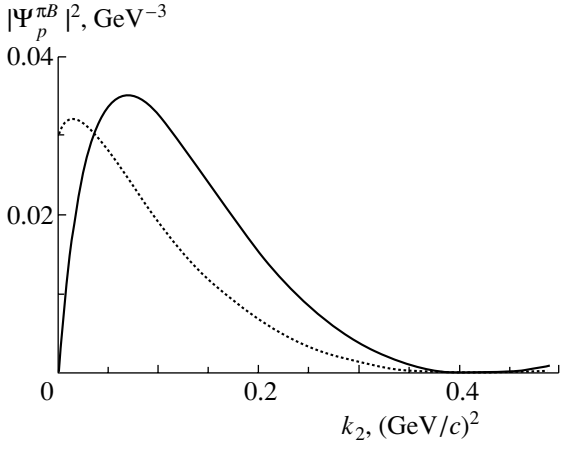

Fig. 5. Momentum distributions in the (solid curve) $N \to N^{**}(1440) + \pi$ and (dotted curve) $N \to N^*(1535) + \pi$ channels according to the calculations on the basis of the present microscopic model.

$F_{\pi NN}(k^2)$ associated with this distribution and computed according to the above scheme are represented by the dotted curves in Figs. 3 and 4, respectively. These results (they were obtained at the value of $b = 0.6$ fm, which is typical for the quark model) agree fairly well with the momentum distributions (at various values of Q^2) that were extracted in [6] from experimental data of Brauel *et al.* [12] by using the form factor parametrized in the standard form

$$F_{\pi NN}\left(k^2\right) = F_{\pi\Delta N}\left(k^2\right) = \frac{\Lambda_\pi^2 - m_\pi^2}{\Lambda_\pi^2 - k^2} \qquad (24)$$

(the solid curves in Figs. 3 and 4 correspond to the value of $\Lambda_\pi = 0.7$ GeV/c, which was determined previously in [6] on the basis of data from [12]; k^2 is the square of the pion 4-momentum, $k^2 \approx -\mathbf{k}^2$).

Of course, this is an argument in favor of the microscopic model being considered, the more so as it does not involve, at a fixed value of b, free parameters, apart from the parameter $x = b_\pi/b$, to which the observables of the $\pi + N$ channel are insensitive. (Only in the $\pi + N^*$ and $\pi + N^{**}$ channels is there a noticeable sensitivity to x, whose optimum value obtained for that case previously in [10] from a fit to baryon-resonance widths with respect to pionic decays is $x = 0.5$.)

In Fig. 4, the form factor $F_{\pi NN}(k^2)$ is displayed over a momentum interval that is wider than that which is required for explaining currently available data on quasielastic pion knockout. We can see that, in the region $|k^2| > 0.5$ (GeV/c)^2, the microscopic model yields a form factor that decreases much faster than expression (24), which corresponds to a $1/|k^2|$ behavior at large $|k^2|$. However, it is necessary to consider that the nonrelativistic constituent-quark model, which was used here to describe data for $|k^2| < 0.25$ (GeV/c)^2, must be modified at relativistic momenta in the region $|k^2| > 0.5$ (GeV/c)^2, where it is mandatory not only to include relativistic effects in it but also to take effectively into account hard processes predicted by QCD.

B. $N \to \pi + B$ channels. Going over to $N \to \pi + B$ channels, we note that, for the $N \to \pi + \Delta$ channel, the form factor $F_{\pi N\Delta}(k^2)$ is predicted to be identical to that in the preceding case; however, the momentum distribution will be different (see Fig. 3), since the pole factor on the right-hand side of formula (21) for $B = \Delta$, N^*, N^{**} is smaller in absolute value and, in the k^2 region being considered, is close to a constant. Of particular interest, however, are the predictions for the momentum distributions (Fig. 5) and for the form factors (Fig. 4) in the $N \to \pi + N^*$ and $N \to \pi + N^{**}$ channels. A comparison with the $N \to \pi + N$ channel (Figs. 3, 5) reveals that they are totally different. Indeed, the πNN form factor decreases monotonically with increasing $|k^2|$, remaining positive, while the πNN^* and πNN^{**} form factors (that is, $F_{\pi NN^*}(k^2)$, etc.) vanish at $|k^2| \cong 0.4$ (GeV/c)^2, changing sign. The square of either of the last two—and it is the square of a form factor that enters into the relevant cross section—unexpectedly appears to be a U-shaped quantity, in contrast to the monotonically decreasing πNN form factor. We also note a peculiar behavior of the πNN^{**} form factor in the region of small $|k^2|$: it first increases, attains a maximum, and then decreases. This specific type of behavior is due to the interplay of the gradient and the

nongradient component of the transition operator and is eventually associated with the structure of the N^* and N^{**} resonances (s^2p and sp^2, respectively). The localization of the above anomaly in the region of low momenta naturally suggests that more fundamental chiral properties of hadrons have some bearing on this phenomenon. In this context, we are going to address this issue in our subsequent studies.

Concluding our discussion, we emphasize that the structure (2) of the fluctuation being considered can be tested (and such experiments are highly desirable) at a totally new level, that of quasielastic knockout. Conceptually analogous results for the quasielastic knockout of vector mesons (with a subsequent rearrangement into a real pion via the process $\gamma + \rho \to \pi$) and for processes involving kaon knockout and leading to the production of spectator strange baryons like Λ and Σ must also be taken into account is such tests. We plan to consider all these processes in the future, relying on a modern relativistic model of the scalar fluctuation (at present, such a model is only being developed [16]).

Further, it is advisable to refine the simplest quark shell wave functions for baryons on the basis of the Glozman three-body model [17] involving a pseudoscalar exchange between quarks, with the quark–antiquark fluctuation considered here being retained. Finally, it would be necessary to go over from the plane-wave approximation used here for the final meson to the distorted-wave approximation.

The present study, which is based on a naive nonrelativistic model of the $^3P_0$ scalar fluctuation, has been aimed at preliminarily outlining a new horizon in experimental and theoretical investigations of nonperturbative QCD at intermediate energies (with electron beams of energy in the range 5–10 GeV) and of its potential in providing a unified basis for explaining in detail and for predicting the properties of various meson–baryon degrees of freedom.

ACKNOWLEDGMENTS

We are grateful to L.D. Blokhintsev and N.P. Zotov for valuable advice and stimulating discussions.

This work was supported by the Russian Foundation for Basic Research (project no. 00-02-16117).

APPENDIX

Within the $^3P_0$ model of pair production [9, 18], it is assumed that the pair-creation operator P^+ has the simplest form that is compatible with vacuum quantum numbers ($J^P I^G = 0^+0^+$, zero total momentum, color, flavor). For the numbering of quarks that was chosen here (see Fig. 2), the production of a $\bar{4}$ 4 $\bar{q}q$ pair is described by the following combination of the quark and antiquark creation operators [$b_\mu^{a+}(\mathbf{p}_4)$ and $d_\mu^{a+}(\mathbf{p}_{\bar{4}})$ ($\mu, \mu' = \pm 1/2; a, a' = u, d, s$), respectively]:

$$P_{4\bar{4}}^+ = v \int d^3\mathbf{p}_4 \int d^3\mathbf{p}_{\bar{4}} \delta(\mathbf{p}_4 + \mathbf{p}_{\bar{4}}) \times \sum_m (-1)^m \{\mathbf{p}_4 - \mathbf{p}_{\bar{4}}\}^m \times \sum_{\mu\mu'} \frac{\sigma_m^{\mu\mu'}}{\sqrt{2}} \sum_{aa'} \delta_{aa'} d_\mu^{a+}(\mathbf{p}_{\bar{4}}) b_{\mu'}^{a'+}(\mathbf{p}_4). \quad \text{(A.1)}$$

Here, v is a phenomenological constant that determines the probability amplitude for the process in question (eventually, v is normalized to the known value of the πNN coupling constant, $f_{\pi NN} \approx 1$), while $m = \pm 1, 0$ are the spherical indices of three-dimensional vectors.

In expression (A.1), the form $\sum_{\mu\mu'} \frac{\sigma_m^{\mu\mu'}}{\sqrt{2}} \times d_\mu^+(\mathbf{p}_{\bar{4}}) b_{\mu'}^+(\mathbf{p}_4)$ corresponds to the $\bar{q}q$ state of total spin $S = 1$ and spin projection m (here, the elements of the Pauli matrices $\sigma_m^{\mu\mu'}$ play the role of Clebsch–Gordan coefficients in the spin space of the $\bar{q}q$ system). Similarly, the form $\sum_{aa'} \delta_{aa'} d_a^+(\mathbf{p}_{\bar{4}}) b_{a'}^+(\mathbf{p}_4)$, where $a = t = \pm 1/2$ ($a' = t' = \pm 1/2$) are the projections of the quark (antiquark) isospin, generates a state of total isospin $T = 0$. Thus, the production of a $\bar{q}q$ pair in the $^3P_0$ state is described by the operator

$$\delta(\mathbf{p}_4 + \mathbf{p}_{\bar{4}}) \times \sum_m (-1)^m \{\mathbf{p}_4 - \mathbf{p}_{\bar{4}}\}^m \sigma_m^{\mu\mu'} d_\mu^{a+}(\mathbf{p}_{\bar{4}}) b_{\mu'}^{a'+}(\mathbf{p}_4), \quad \text{(A.2)}$$

the delta function in expression (A.1) and the delta function in expression (A.2) fixing at zero the total momentum of the $\bar{q}q$ pair in the primary-baryon rest frame. [In accordance with the Zweig rule [19], it is postulated that pair production is a purely vacuum process not involving momentum transfer (or the transfer of some virtual quantum—for example, a gluon) from the initial (bare) quark state to a virtual $\bar{q}q$ pair. We note that this mechanism of pion emission leads to a momentum distribution of pions that is essentially the momentum distribution of quarks in the relevant baryon.]

The process depicted in Fig. 2 can be considered as a manifestation of effective quark–pion coupling. The corresponding matrix element for the $q^{(3)} \to q^{(4)} + \pi^\lambda$ transition,

$$T_{\pi qq}^\lambda = \left\langle q^{(4)}, \mathbf{p}_4'; \pi^\lambda, \mathbf{k} | P_{4\bar{4}}^+ | q^{(3)}, \mathbf{p}_3 \right\rangle, \quad \text{(A.3)}$$

can be calculated by using the operator in (A.1), along with the pion wave function $\pi^\lambda(\mathbf{k})$ and the quark wave

functions $|q^{(3)}(\mathbf{p}_3)\rangle$ and $|q^{(4)}(\mathbf{p}'_4)\rangle$ expressed in terms of the corresponding creation operators acting on a vacuum; that is,

$$|\pi^\lambda, \mathbf{k}\rangle = \int d^3\mathbf{p}'_3 \tag{A.4}$$
$$\times \int d^3\mathbf{p}'_4 \delta(\mathbf{k} - \mathbf{p}'_3 - \mathbf{p}'_4)\Phi_\pi(\mathbf{p}'_3 - \mathbf{p}'_4)$$
$$\times \sum_{\nu'_3\nu'_4}\sum_{t'_3t'_4} \tau^{t'_3t'_4}_{-\lambda}\delta_{\nu'_3\nu'_4} d^{t'_4}_{\nu'_4+}(\mathbf{p}'_4) b^{t'_3}_{\nu'_3+}(\mathbf{p}'_3)\,|0\rangle\,,$$

$$\left|q^{(i)}, \mathbf{p}_i\right\rangle = \sum_{\nu_i}\sum_{t_i} \chi^{(i)}_{\nu_i}\varphi^{(i)}_{t_i} b^{t_i}_{\nu_i+}(\mathbf{p}_i)\,|0\rangle\,, \quad i = 3, 4, \tag{A.5}$$

where $\chi^{(i)}_{\nu_i}(\varphi^{(i)}_{t_i})$ are the Pauli spinors (isospinors) describing the spin (isospin) state of the ith quark in the primary or the secondary baryon and $\Phi_\pi(\mathbf{p})$ is the quark–antiquark wave function for the pion.

The matrix element (A.3) is calculated on the basis of a standard technique that employs relations between the operators d and b. These include the following:

$$\{d_\nu(\mathbf{p}), d^+_{\nu'}(\mathbf{p}')\} \tag{A.6}$$
$$= \{b_\nu(\mathbf{p}), b^+_{\nu'}(\mathbf{p}')\} = \delta_{\nu\nu'}\delta(\mathbf{p} - \mathbf{p}'),$$

$$\langle 0|\int d^3\mathbf{p}' d^+_\nu(\mathbf{p}')d_{\nu'}(\mathbf{p}')\,|0\rangle = \delta_{\nu\nu'}. \tag{A.7}$$

As a result, the amplitude for effective πqq coupling can be represented in the form

$$T^\lambda_{\pi qq} = v\sum_{\nu'_4\nu_3}\sum_{t'_4t_3}\int d^3\mathbf{p}'_5 \tag{A.8}$$
$$\times \delta(\mathbf{k} - \mathbf{p}_3 - \mathbf{p}'_5)\delta(\mathbf{p}'_4 + \mathbf{p}'_5)\Phi_\pi\left(\frac{\mathbf{p}_3 - \mathbf{p}'_5}{2}\right)$$
$$\times \sum_m (-1)^m\{\mathbf{p}'_4 - \mathbf{p}'_5\}^m_1$$
$$\times \left(\chi^{(4)+}_{\nu'_4}\varphi^{(4)+}_{t'_4}\tau^{t'_4t_3}_{-\lambda}\sigma^{\nu'_4\nu_3}_m\chi^{(3)}_{\nu_3}\varphi^{(3)}_{t_3}\right).$$

The parenthetical expression in the last line of (A.8) can be considered as the matrix element of the isospin and spin Pauli matrices between the initial and the final state of the third quark. This makes it possible to recast expression (A.8) into the form of a matrix element of the nonlocal single-particle operator acting on the variables of the third quark; that is,

$$T^{(3)\lambda}_{\pi qq}(\mathbf{p}_3, \mathbf{p}'_4) = v\int d^3\mathbf{p}'_5\delta(\mathbf{k} - \mathbf{p}_3 - \mathbf{p}'_5) \tag{A.9}$$
$$\times \delta(\mathbf{p}'_4 + \mathbf{p}'_5)\Phi^*_\pi\left(\frac{\mathbf{p}_3 - \mathbf{p}'_5}{2}\right)\tau^{(3)}_{-\lambda}\boldsymbol{\sigma}^{(3)}$$
$$\cdot (\mathbf{k} - (\mathbf{p}_3 + \mathbf{p}'_4)).$$

In deriving expression (A.8), we have taken into account the identity

$$\delta(\mathbf{k} - \mathbf{p}_3 - \mathbf{p}'_5)\delta(\mathbf{p}'_4 + \mathbf{p}'_5)(\mathbf{p}'_4 - \mathbf{p}'_5) \tag{A.10}$$
$$= \delta(\mathbf{k} - \mathbf{p}_3 - \mathbf{p}'_5)\delta(\mathbf{p}_4 + \mathbf{p}'_5)(\mathbf{p}'_4 + \mathbf{p}_3 - \mathbf{k}).$$

We note that the matrix elements of the operator

$$\boldsymbol{\sigma}^{(3)}\cdot(\mathbf{k} - (\mathbf{p}_3 + \mathbf{p}'_4)) \tag{A.11}$$

between physical baryons (that is, those on the mass shell) will disturb the Galilean invariance of physical amplitudes. Recall that the simplest scalar expression (A.2), which was proposed above for the pair creation operator, is invariant only under translations and rotations, but it is not invariant under transitions to a moving coordinate frame. In order to restore Galilean invariance, it is necessary to modify the delta function in expression (A.2) in such a way that operator (A.11) in the final expression (A.9) for the single-particle amplitude would transform into the Galilean-invariant expression

$$\boldsymbol{\sigma}^{(3)}\cdot\left(\mathbf{k} - \frac{\varepsilon_\pi(\mathbf{k})}{2m_q}(\mathbf{p}_3 + \mathbf{p}'_4)\right). \tag{A.12}$$

It goes without saying that, for an individual quark, which is always off the mass shell (since it is unobservable in a free state), the concept of Galilean invariance is meaningless; for physical baryons (on-shell ones), however, the matrix element of the operator in (A.12) leads to an amplitude that is invariant under Galilean transformations, the quantity $\left(-\frac{\varepsilon_\pi(\mathbf{k})}{2m_q}(\mathbf{p}_3 + \mathbf{p}'_4)\right)$ in this operator generating a term that takes into account baryon recoil in pion emission (see, for example, the discussion of this problem in [10]). By way of example, we indicate that, even in the first study devoted to the pair-production model [20], it was noticed that the operator $\boldsymbol{\sigma}^{(3)}\cdot\mathbf{k}$ poorly describes threshold decays—$N(1535) \to \eta(540) + N(940)$, for instance; to remedy the situation, it was proposed there to include a correction that takes into account baryon recoil and which leads to expression (A.12). Even in the vicinity of the threshold ($\mathbf{k} \to 0$), the matrix element does not then vanish, and we arrive at a gradient coupling (see below), which is of importance for threshold processes.

Prior to going over to the coordinate representation of the operator in (A.9) [with allowance for the modification in (A.12)], we express it in terms of the relative momenta $\boldsymbol{\pi}^{(3)}$ and $\boldsymbol{\pi}^{(3)\prime}$ of the third quark in, respectively, the primary (B) and the secondary (B') baryon; that is,

$$\boldsymbol{\pi}^{(3)} = (\mathbf{p}_1 + \mathbf{p}_2)/3 - (2/3)\mathbf{p}_3 = \mathbf{P}_B/3 - \mathbf{p}_3, \tag{A.13}$$

$$\mathbf{P}_B = \mathbf{p}_1 + \mathbf{p}_2 + \mathbf{p}_3.$$
$$\boldsymbol{\pi}^{(3)\prime} = (\mathbf{p}_1 + \mathbf{p}_2)/3 - (2/3)\mathbf{p}'_4 = \mathbf{P}_{B'}/3 - \mathbf{p}'_4,$$
$$\mathbf{P}_{B'} = \mathbf{p}_1 + \mathbf{p}_2 + \mathbf{p}'_4.$$

As a result, the modified operator (A.9) assumes the form

$$\tilde{T}^{(3)\lambda}_{\pi qq}(\mathbf{p}_3, \mathbf{p}'_4) = -v\tau^{(3)}_{-\lambda}\boldsymbol{\sigma}^{(3)} \quad \text{(A.14)}$$
$$\times \left[\mathbf{k} + \frac{\varepsilon_\pi}{2m_q}\left(\boldsymbol{\pi}^{(3)} + \boldsymbol{\pi}^{(3)\prime}\right) - \frac{\varepsilon_\pi}{6m_q}\left(\mathbf{P}_B + \mathbf{P}_{B'}\right)\right]$$
$$\times \delta\left(\frac{2}{3}\mathbf{k} + \boldsymbol{\pi}^{(3)} - \boldsymbol{\pi}^{(3)\prime}\right)\Phi^*_\pi\left(\frac{1}{3}\mathbf{P}_B - \boldsymbol{\pi}^{(3)} - \frac{1}{2}\mathbf{k}\right).$$

In view of the Galilean invariance of final results for baryons, expression (A.14) can further be used in a fixed reference frame. The simplest choice of it is that of the primary-baryon rest frame:

$$\mathbf{P}_B = 0, \quad \mathbf{P}_{B'} = -\mathbf{k}. \quad \text{(A.15)}$$

Upon the Fourier transformation to the relative coordinates of the quarks,

$$\boldsymbol{\rho}_1 = \mathbf{r}_1 - \mathbf{r}_2, \quad \boldsymbol{\rho}_2 = (\mathbf{r}_1 + \mathbf{r}_2)/2 - \mathbf{r}_3, \quad \text{(A.16)}$$
$$\boldsymbol{\rho}'_2 = (\mathbf{r}_1 + \mathbf{r}_2)/2 - \mathbf{r}'_4,$$

we obtain the nonlocal operator

$$\tilde{T}^{(3)\lambda}_{\pi qq}(\boldsymbol{\rho}_2, \boldsymbol{\rho}'_2; \mathbf{k}) \quad \text{(A.17)}$$
$$= -v\frac{e^{i\frac{2}{3}\mathbf{k}\cdot\boldsymbol{\rho}'_2}}{(2\pi)^{3/2}}\tau^{(3)}_{-\lambda}\hat{O}^{(3)}_\pi(\boldsymbol{\rho}_2 - \boldsymbol{\rho}'_2)\boldsymbol{\sigma}^{(3)}$$
$$\times \left[\frac{\varepsilon_\pi}{2m_q}\left(\frac{2}{i}\nabla_{\rho_2} + \frac{2}{3}\mathbf{k}\right) + \left(1 + \frac{\varepsilon_\pi}{6m_q}\right)\mathbf{k}\right],$$

which acts on the variables $\boldsymbol{\rho}_2$ and $\boldsymbol{\rho}'_2$. In (A.17), the nonlocal part is the Fourier transform of the pion wave function

$$\hat{O}^{(3)}_\pi(\boldsymbol{\rho}_2 - \boldsymbol{\rho}'_2) = \exp\left(i\frac{1}{2}\mathbf{k}\cdot(\boldsymbol{\rho}_2 - \boldsymbol{\rho}'_2)\right)\Phi^*_\pi(\boldsymbol{\rho}_2 - \boldsymbol{\rho}'_2). \quad \text{(A.18)}$$

Thus, the interaction term that takes into account baryon recoil generates a gradient coupling [the first term of the bracketed expression in (A.17)].

In the pointlike-pion limit—that is, for $\Phi^*_\pi(\boldsymbol{\rho}_2 - \boldsymbol{\rho}'_2) \to \delta(\boldsymbol{\rho}_2 - \boldsymbol{\rho}'_2)$—the effective quark–gluon coupling becomes local; that is,

$$\tilde{T}^{(3)\lambda}_{\pi qq}(\boldsymbol{\rho}'_2, \boldsymbol{\rho}_2; \mathbf{k})\Big|_{\Phi_\pi(\boldsymbol{\rho}'_2 - \boldsymbol{\rho}_2)\to\delta(\boldsymbol{\rho}'_2 - \boldsymbol{\rho}_2)} \quad \text{(A.19)}$$
$$= T^{(3)\lambda}_{\pi qq}(\boldsymbol{\rho}_2; \mathbf{k}) = -v\frac{e^{i\frac{2}{3}\mathbf{k}\cdot\boldsymbol{\rho}_2}}{(2\pi)^{3/2}}\tau^{(3)}_{-\lambda}\boldsymbol{\sigma}^{(3)}$$
$$\times \left[\frac{\varepsilon_\pi}{2m_q}\left(\frac{2}{i}\nabla_{\rho_2} + \frac{2}{3}\mathbf{k}\right) + \left(1 + \frac{\varepsilon_\pi}{6m_q}\right)\mathbf{k}\right].$$

It is coincident in form with the operator representing pseudovector πqq coupling in the first order in v/c. Therefore, the phenomenological constant v, which specifies the amplitude for the production of a vacuum $\bar{q}q$ pair, can be normalized to the well-known value of the pseudovector πNN coupling constant,

$$v = -i\frac{f_{\pi qq}}{m_\pi\,(2\varepsilon_\pi)^{1/2}}, \quad f_{\pi qq} = (3/5)f_{\pi NN}, \quad \text{(A.20)}$$

and can further be used in calculating the amplitudes for transitions into each of the $B = N$, Δ , N^*, N^{**} baryon channels.

REFERENCES

1. T. E. O. Ericson and W. Weise, *Pions and Nuclei* (Clarendon, Oxford, 1988); W. Weise, *Quarks and Nuclei,* Ed. by W. Weise (World Sci., Singapore, 1984), p. 59.
2. N. N. Nicolaev, A. Szczurek, J. Speth, and V. Zoller, Z. Phys. A **349**, 59 (1994).
3. W. Y. P. Hwang, J. Speth, and G. E. Brown, Z. Phys. A **339**, 383 (1991); A. Szczurek and J. Speth, Nucl. Phys. A **555**, 249 (1993); A. Szczurek, J. Speth, and G. T. Garvey, Nucl. Phys. A **570**, 765 (1994); A. Mair and M. Traini, Nucl. Phys. A **628**, 296 (1998).
4. M. Guidal, J.-M. Laget, and M. Vanderhaeghen, Nucl. Phys. A **627**, 645 (1998).
5. Güttner, G. Chanfray, H. J. Pirner, and B. Povh, Nucl. Phys. A **429**, 389 (1984); J. Speth and V. R. Zoller, Phys. Lett. B **351**, 533 (1995).
6. V. G. Neudachin, N. P. Yudin, and L. L. Sviridova, Yad. Fiz. **60**, 2020 (1997) [Phys. At. Nucl. **60**, 1848 (1997)]; N. P. Yudin, L. L. Sviridova, and V. G. Neudachin, Yad. Fiz. **61**, 1689 (1998) [Phys. At. Nucl. **61**, 1577 (1998)]; Yad. Fiz. **62**, 694 (1999) [Phys. At. Nucl. **62**, 645 (1999)].
7. V. G. Neudachin, L. L. Sviridova, and N. P. Yudin, Yad. Fiz. **64**, 1680 (2001) [Phys. At. Nucl. **64**, 1600 (2001)]; V. G. Neudachin, N. P. Yudin, and L. L. Sviridova, Yad. Fiz. **65**, 1598 (2002) [Phys. At. Nucl. **65**, 1560 (2002)].
8. H. Holtmann, A. Szczurek, and J. Speth, Nucl. Phys. A **596**, 631 (1996); S. Theberge, A. W. Thomas, and G. A. Miller, Phys. Rev. D **22**, 2838 (1980); L. R. Dodd, A. W. Thomas, and R. F. Alvarez-Estrada, Phys. Rev. D **24**, 1961 (1981); A. W. Thomas, Phys. Lett. B **126B**, 97 (1983).
9. A. Le. Yaounc, L. Oliver, O. Pene, and J. C. Raynal, Phys. Rev. D **9**, 1415 (1974); **11**, 1272, 2247 (1975); B. Desplanques, C. Gignoux, B. Silvestre-Brac, *et al.*, Z. Phys. A **343**, 331 (1992); F. Cano, P. Gonzalez, S. Noguera, and B. Desplanques, Nucl. Phys. A **603**, 257 (1996); P. J. A. Bicudo, L. S. Ferreira, C. M. Placido, and J. Ribeiro, Phys. Rev. C **56**, 670 (1997).
10. S. Captick and W. Roberts, Phys. Rev. D **47**, 1994 (1993); I. T. Obukhovsky, A. Faessler, G. Wagner, and A. J. Buchmann, Phys. Rev. C **60**, 035207 (1999).

11. M. Strikman, Nucl. Phys. A **663–664**, 64c (2000); M. Vanderhaeghen, P. A. Guichon, and M. Guidal, Nucl. Phys. A **663–664**, 324c (2000).
12. P. Brauel, T. Canzler, D. Cords, *et al.*, Z. Phys. C **3**, 101 (1979); C. J. Bebek, C. N. Brown, S. D. Holmes, *et al.*, Phys. Rev. D **17**, 1693 (1978).
13. V. G. Neudatchin, A. A. Sakharuk, V. V. Kurovsky, and Yu. M. Tchuvil'sky, Phys. Rev. C **50**, 148 (1994); **51**, 784 (1995); V. G. Neudachin, A. A. Sakharuk, V. V. Kurowsky, and Yu. M. Tchuvil'sky, Yad. Fiz. **58**, 1234 (1995) [Phys. At. Nucl. **58**, 1155 (1995)].
14. V. G. Neudachin and Yu. F. Smirnov, *Nucleon Clusters in Light Nuclei* (Nauka, Moscow, 1969); O. F. Nemets, V. G. Neudachin, A. T. Rudchik, *et al.*, *Nucleon Clustering in Nuclei and Multinucleon-Transfer Reactions* (Naukova Dumka, Kiev, 1988).
15. I. T. Obukhovsky, Yu. F. Smirnov, and Yu. M. Tchuvil'sky, J. Phys. A **15**, 7 (1982); I. T. Obukhovsky, Z. Phys. A **308**, 253 (1982); Prog. Part. Nucl. Phys. **36**, 359 (1996); I. T. Obukhovsky, K. Itonaga, G. Wagner, *et al.*, Phys. Rev. C **56**, 3295 (1997).
16. L. Theussl, R. F. Wagenbrunn, B. Desplanques, and W. Plessas, nucl-th/0010099; F. Cano, B. Desplanques, P. Gonzalez, and S. Noguera, nucl-th/0102013.
17. L. Ya. Glozman, Phys. Lett. B **459**, 589 (1999); L. Ya. Glozman, Z. Papp, W. Plessas, *et al.*, Phys. Rev. C **61**, 019804 (2000); R. F. Wagenbrunn, W. Plessas, L. Ya. Glozman, and K. Varga, Nucl. Phys. A **663–664**, 703 (2000); **666–667**, 29 (2000).
18. L. Micu, Nucl. Phys. B **10**, 521 (1969); A. Le. Yaounc, L. Olivier, O. Pene, and J. C. Raynal, Phys. Rev. D **8**, 2223 (1973).
19. G. Zweig, CERN Report No. 8419/TH 412 (1964); S. Okubo, Phys. Lett. **5**, 163 (1963); J. Iizuka, Prog. Theor. Phys. Suppl., Nos. **37–38**, 21 (1966).
20. A. Mitra and M. Ross, Phys. Rev. **158**, 1630 (1967).

Translated by A. Isaakyan

Physics of Atomic Nuclei, Vol. 66, No. 2, 2003, pp. 323–333. Translated from Yadernaya Fizika, Vol. 66, No. 2, 2003, pp. 348–358.

ELEMENTARY PARTICLES AND FIELDS
Theory

Contribution of the Hadronic Component of a Virtual Photon to the Structure Function for Charm Leptoproduction at High x and Q^2

D. Yu. Golubkov[1)] and Yu. A. Golubkov[*]

Institute of Nuclear Physics, Moscow State University, Vorob'evy gory, Moscow, 119899 Russia

Received January 28, 2002

Abstract—The contribution of the hadronic component of a virtual photon to the structure function for charm leptoproduction is calculated. This contribution comes from the scattering of c quarks of a virtual photon on proton quarks and gluons. A comparison of the results of our calculations for this structure function with relevant data obtained by the European Muon Collaboration (EMC) for μ^+p scattering gives reasons to believe that the contribution of the resolved photon may be responsible for the excess in these EMC data over the predictions of the model of photon–gluon fusion at high momentum transfers. Therefore, it may become possible to describe the EMC data without resort to the hypothesis of a nonperturbative charmed-quark admixture in the proton wave function (intrinsic-charm hypothesis).

1. INTRODUCTION

Investigation of heavy-flavor formation at high energies is still a very important tool for qualitatively and quantitatively testing QCD and for studying the internal structure of hadrons. Although impressive results, both theoretical and experimental, have been obtained over the past decade, owing predominantly to experiments at the HERA electron–proton collider, there still remain uncertainties in interpreting available data on charmed-particle production in hadron–hadron and lepton–hadron collisions. These uncertainties concern the details of the quark structure of hadrons—first of all, the structure of the proton. One of the problems is that of the intrinsic charm of the proton [1]—that is, the question of whether the proton wave function features a sizable (about 1%) nonperturbative admixture of charmed quarks having a hard "valence" distribution with respect to the longitudinal momentum. At the HERA collider, charm-production processes were explored at low values of the Bjorken variable x, in which case a dominant contribution comes from the mechanism of photon–gluon fusion. However, the low-x region corresponds to spatial distances much greater than the proton dimension; therefore, investigation of this kinematical region furnishes information about the structure of QCD vacuum rather than about the internal structure of the proton. In order to obtain deeper insight into the proton structure proper, it is necessary to study the charmed structure function for the proton at high values of the variable x. Unfortunately, the geometry of the ZEUS and H1 experiments gives no way to explore efficiently charm production in the forward direction at comparatively low momentum transfers, where the cross section for ep scattering is maximal. Possibly, the planned severalfold increase in the HERA luminosity will allow accumulation of sufficient statistics at moderate momentum transfers for experimentally investigating charm production in the high-x region. At present, however, the problem in question has not yet received adequate study.

A theoretical consideration of the intrinsic-charm problem is based on the following simple arguments. The proton wave function can be expanded in color-singlet eigenstates of the free Hamiltonian, such as $|uud\rangle$, $|uudg\rangle$, and $|uudq\bar{q}\rangle$. Within a comparatively short time, the proton may feature Fock states of arbitrarily intricate character, including charmed-quark pairs. In the proton rest frame, the lifetime of such fluctuations, τ, is on the order of the nuclear time of about R_h, where R_h is the hadron dimension. Charmed quarks are heavy objects, and the lifetime of a fluctuation involving heavy quarks is much less than that of a fluctuation consisting of light partons exclusively. Therefore, the admixture of heavy-quark pairs in the proton wave function must be small—specifically, their fraction is expected to be about $(m_q/m_Q)^2 \sim 10^{-2}$ with respect to the level of light partons. Since the c-quark mass is large, their momentum distribution proves to be much harder than that of light sea partons [1, 2]. The presence

[1)]Deutsches Elektronen-Synchrotron (DESY), Notkestrasse 85, D-22603 Hamburg, Germany.
[*]e-mail: golubkov@npi.msu.su

of fluctuations involving heavy quarks is a natural consequence of field theory. However, one makes here the important assumption that quantum fluctuations of the hadron wave function that involve charmed quarks are controlled by the self-interaction of the color field, and this implies that the structure of the Fock states of a hadron can be analyzed without considering hard interactions.

In assessing the level of the charmed-quark admixture in the proton, it is usually assumed that data on μp and hadron–hadron collisions in [3] and [4, 5], respectively, where the observed yields of charmed particles deviate from the predictions of the models of photon–gluon and parton–parton fusion, suggest the presence of intrinsic charm. However, the actual experimental situation is quite uncertain. The pioneering theoretical studies on the subject [1] were motivated by data obtained at ISR [4] by studying the yield of charmed particles—in those experiments, the charm yield was very high, an order of magnitude higher than that which is expected in the model of parton–parton fusion. A critical comparison of experimental data obtained at ISR with data of experiments that employed a fixed target can be found in the review article of Tavernier [6]. More recent experiments, which were, however, performed at lower energies, were not in so dramatic a contradiction with theoretical expectations (see, for example, [7]). An attempt at reconciling the ISR data with the predictions of the model of parton–parton fusion was made in [8] on the basis of the charm-excitation model, where it is assumed that a proton features a 0.5% admixture of charmed quarks, with the result that there arises hard charmed-quark scattering. It was shown in [8] that, owing to a large value of the hard-scattering cross section (which is, strictly speaking, divergent) and its strong dependence on the reaction energy, the ISR data can be described within the charm-excitation model. At the same time, this model does not make a sizable contribution to the charm yield at lower energies.

By merely varying the parameters of the string hadronization model within reasonable limits [9, 10], more recent experimental data on the longitudinal distributions of charmed quarks and on the asymmetry of their production can be reproduced to a fairly high precision without resort to the intrinsic-charm contribution.

The interpretation of data on the production of J/ψ particles is also contradictory. The NA3 experiment [5], which studied pion–nucleus collisions at an energy of 280 GeV, produced quite compelling pieces of evidence that there is an additional mechanism of the production of hard J/ψ particles. This additional contribution at a level of 20% of the total cross section for J/ψ production is faithfully reproduced within the modified intrinsic-charm model [2], but the assumption that there exists so large a contribution does not seem realistic. In [11, 12], it was found that intrinsic charm may explain an excess of the yield of fast correlated J/ψ pairs over theoretical expectations and their anomalous polarization that seems to have been observed by the NA3 experiment in inclusive J/ψ production. At the same time, the predictions of the intrinsic-charm model are in a glaring contradiction with data on the production of J/ψ particles in proton–nucleus collisions at an energy of 800 GeV [13] (see [14]).

It should be emphasized that the presence of a 1% charmed-quark admixture in the proton leads to the total cross section for charm production in nucleon–nucleon collisions at a level of a few hundred microbarns, but this is at odds with the bulk of experimental data on open-charm production in hadron–hadron collisions.

In theoretically analyzing hadronic data, it should be borne in mind that the main contribution to charm production in hadron–hadron collisions comes from the gluon–gluon fusion $gg \to c\bar{c}$. At the same time, direct experimental measurements of the gluon distribution in the proton are impossible. In order to extract gluon distributions from data, use is made either of charm-production calculations based on the aforementioned mechanisms of gluon–gluon or photon–gluon fusion, which contribute predominantly to the region of low values of the Feynman variable x_F, or of rather sophisticated methods relying on the assumption that gluons make a dominant contribution to the evolution of quark distributions. In view of this, the extraction of an additional mechanism of charm production in hadron–hadron collisions at a level of 0.5–1% cannot be highly reliable.

As a matter of fact, only the data obtained by European Muon Collaboration (EMC) by studying the charmed structure function for the proton in $\mu^+ p$ collisions at a muon energy of 280 GeV provide a firm basis for correctly verifying the presence of intrinsic charm in the proton. Early studies devoted to analyzing the EMC results employed old parametrizations of the gluon distribution in the proton, which are harder. In particular, the first EMC analysis was based on the scaling gluon distribution $G(x) \sim (1 - x)^5$. For the intrinsic-charm admixture in the proton, this yielded a value of about 0.3%, but the uncertainty was quite large. Currently used parametrizations of gluon distributions are softer, as a rule, and they naturally result in a greater intrinsic-charm contribution to the EMC data [2, 15, 16]. Specifically, the intrinsic-charm contribution as extracted from a thorough analysis of the EMC data varies from 0.3% [3, 17] to about 0.9% [2, 16]. At the same time,

the analysis of Harris *et al.* [16], who performed the most comprehensive calculation of the contribution from photon–gluon fusion, revealed that, at moderate energy transfers, the intrinsic-charm contribution vanishes within the experimental errors.

Since the photon features a hadronic structure [18–20], it is natural to expect that the total cross section for charm production in leptoproduction processes includes the contribution from the interaction of partons belonging to the hadronic component of a virtual photon with the partons of the proton. By taking into account the contribution of the hard scattering of the c quarks from a virtual J/ψ meson within the vector-dominance model, Berezhnoy and Likhoded [21] were able to describe, to a high precision, ZEUS data on D^* production at high transverse momenta. Although such processes are of the second order in the strong-interaction coupling constant α_s, they can contribute sizably owing to the divergence of the cross section for parton–parton scattering at small angles. Therefore, it is natural to expect that the hadronic component of the photon makes a sizable contribution to the charmed structure function measured by the EMC in the region $Q^2 \geq 40\ \mathrm{GeV}^2$, where there are indications of a discrepancy between experimental data and predictions of the model of boson–gluon fusion.

In the present study, we have calculated the contribution of the hadronic component of the photon and the contribution of the standard mechanism of photon–gluon fusion to the charmed structure function measured by the EMC. On the basis of our calculations, we conclude that the hypothesis of the intrinsic-charm admixture in the proton is not needed in interpreting the EMC results.

2. FUNDAMENTALS OF THE MODEL USED

2.1. Charm in the Hadronic Component of the Photon

The hadron structure function $F_2(x, Q^2)$ is a measurable physical quantity in studying deep-inelastic processes that involve hadrons. The charmed structure function $F_2^c(x, Q^2)$ is related to the cross section for charm production in leptoproduction processes, $d\sigma(lp \to c)$, by the equation

$$d\sigma(lp \to c) = \frac{2\pi\alpha^2}{xQ^4}\left[1 + (1-y)^2\right] F_2^c(x, Q^2)\,dx\,dQ^2. \tag{1}$$

In the approximation of equivalent photons [22], the charm-leptoproduction cross section can be expressed in terms of the cross section for γp interaction, $\sigma(\gamma p \to c)$, and the flux of equivalent photons, $n_\gamma(x, Q^2)$, as

$$\begin{aligned} d\sigma(lp \to c) &= dn_\gamma(x, Q^2)\sigma(\gamma p \to c) \\ dn_\gamma(x, Q^2) &= \frac{\alpha}{2\pi}\left[1 + (1-y)^2\right]\frac{dx}{x}\frac{dQ^2}{Q^2}; \end{aligned} \tag{2}$$

that is, the charmed structure function is related to the charm-photoproduction cross section by the equation

$$F_2^c(x, Q^2) = \frac{Q^2}{4\pi^2\alpha}\sigma(\gamma p \to c). \tag{3}$$

The hadronic structure of the photon can also be described in terms of the photon structure function $F_2^\gamma(x, Q^2)$, which depends on the Bjorken variable x and on the momentum transfer squared Q^2 [18]. Usually, the structure function $F_2^\gamma(x, Q^2)$ is broken down into two components, a perturbative pointlike one (so-called anomalous structure function) and a nonperturbative one (hadron structure function). This decomposition of $F_2^\gamma(x, Q^2)$ into a perturbative and a nonperturbative component is valid not only within the naive quark-parton model but also in the leading and next-to-leading orders of perturbative QCD [18, 19]. The perturbative component is due to the direct $\gamma \to q\bar{q}$ interaction and can be definitively calculated within perturbation theory. Within the quark-parton model, the contribution of this component is proportional to $\ln Q^2$ and is dominant for $Q^2 \to \infty$. The nonperturbative component $F_2^\gamma(x, Q^2)$ is completely analogous to the conventional hadron structure function. Within the naive quark-parton model, this component is independent of Q^2. The QCD evolution of F_2^γ differs from the evolution of the hadron structure function only in the presence of the perturbative component in the case of F_2^γ, with the evolution being described by the nonhomogeneous Dokshitzer–Gribov–Lipatov–Altarelli–Parisi equations. In order to calculate the QCD evolution of the nonperturbative component, it is necessary, in just the same way as in the case of hadrons, to specify initial conditions at some value of the momentum transfer squared Q_0^2. As a rule, it is assumed, in specifying the initial parton distributions in the photon at a momentum-transfer-squared value of $Q_0^2 \approx 1\ \mathrm{GeV}^2$, that the hadronic component $F_2^\gamma(x, Q_0^2)$ can be obtained on the basis of the vector-meson-dominance model, which postulates the $\gamma \to \rho^0$ transition in order to describe photon–hadron interaction. In this case, the parton distributions in the ρ^0 meson are taken to be identical to those that are known from experiments for pions. In order to describe experimental data better, the simple vector-meson-dominance model was extended in a natural way by including in it the light isoscalar

vector mesons ω and ϕ. Usually, the heavier mesons of the J/ψ family are not included because of their large mass, and the charm content in the photon is described on the basis of light-parton evolution and the presence of the $\gamma \to c\bar{c}$ perturbative term [20, 23]. As was shown in [20], however, charm must not be considered as a conventional light quark in the region $Q^2 \leq 50$ GeV^2, so that the evolution equations must be solved there only for three light quarks. This is because, in the threshold region $Q^2 \sim 4m_c^2$, charm production must be described by the Bethe–Heitler process $\gamma\gamma \to c\bar{c}$ and, in the case of lepton–hadron scattering, by the photon–gluon fusion $\gamma g \to c\bar{c}$, which is the analog of the Bethe–Heitler process. On the other hand, it was deduced in [24] from a comparison of the predictions of the QCD evolution of F_2^γ with experimental data that, even for light-quark evolution, the perturbative region in the case of a photon begins at $Q_0^2 \approx 5$ GeV^2 rather than at $Q_0^2 \approx 1$ GeV^2, as is usually assumed. In the present study, we therefore rely on the generalized vector-meson-dominance model that also takes into account nonperturbative transitions of a photon into J/ψ mesons (these transitions become possible above the threshold for J/ψ production).

Within the generalized vector-meson-dominance model, it is convenient to represent the wave function for the hadronic component of the photon as

$$|\gamma_{\text{had}}\rangle = \sum_V \sqrt{\frac{4\pi\alpha}{f_V^2}}|V\rangle + |\gamma_{\text{pert}}^c\rangle + \sum_q |\gamma_{\text{pert}}\rangle, \quad (4)$$

where the terms $|\gamma_{\text{pert}}\rangle$ and $|\gamma_{\text{pert}}^c\rangle$ take into account the perturbative contributions of the processes $\gamma \to q\bar{q}$ and $\gamma \to c\bar{c}$, respectively, while the vector mesons $V = \rho, \omega, \phi, J/\psi$ are responsible for the nonperturbative contribution to the hadronic component of the photon. The constants that characterize the vector-meson contributions are [23]

$$f_\rho^2/4\pi \approx 2.20, \quad f_\omega^2/4\pi \approx 23.6, \quad (5)$$
$$f_\phi^2/4\pi \approx 18.4, \quad f_\psi^2/4\pi \approx 11.5.$$

In the presence of a partonic structure in the photon, the interactions of its hadronic component with hadrons can be described as the interaction of partons from the photon with the projectile particle, as is done in dealing with the interactions of conventional hadrons. Within the parton model, the cross section for any process is the sum of the weighted cross sections for elementary processes, the relevant weights being determined by the distributions of partons involved in these elementary processes. In the presence of charmed quarks in the proton and at moderate momentum transfers, lepton scattering on a charmed quark of the proton, $lc \to lc$, is the leading process in the strong-interaction coupling constant. The process of photon–gluon fusion, $\gamma g \to c\bar{c}$, is of the next order in α_s, but its contribution is dominant since gluons carry nearly half the proton momentum. Thus, three processes contribute to charm photoproduction. These are the absorption of a pointlike photon by a c quark of the proton, photon–gluon fusion, and the scattering of the c quarks of a virtual photon on the light partons of the proton and the scattering of the light partons of the photon on the c quarks of the proton. In principle, the states of the vector mesons in (4) can interfere with one another. But such an interference has not yet been observed for virtual photons; as will be seen in what follows, the possible presence of this effect is immaterial in the present study.

The total charm-production cross section can then be represented in the form

$$\sigma(\gamma p) = \sigma^{\text{IC}} + \sigma^{\text{PGF}} + \sigma^\psi + \sigma^c + \sigma^q, \quad (6)$$

where the cross section σ^{IC} is determined by the absorption of a pointlike virtual photon by a c quark of the proton (the cross section for this process is proportional to the level of the intrinsic-charm admixture in the proton, $N_{\text{IC}} \leq 10^{-2}$), while the cross section σ^{PGF} is that for the photon–gluon fusion $\gamma g \to c\bar{c}$ and is calculable quite reliably.

The second pair of terms in (6) is caused by the scattering of the c quarks of the photon on the partons of the proton, while σ^q is determined by the scattering of the light partons of the photon on a c quark or on a $\bar{c}$ antiquark of the proton. The light partons of the photon can be associated both with the nonperturbative component (light vector mesons ρ, ω, ϕ) and with the perturbative component ($|\gamma_{\text{pert}}\rangle$). Within perturbative QCD, the cross sections σ^ψ, σ^c, and σ^q diverge in proportion to $1/p_T^4$ as the transverse momentum tends to zero. Therefore, their contribution can be significant. These terms depend on the minimum momentum transfer, $\hat{t}_{\text{min}}$, that must be introduced in order to obtain a finite total cross section. The cutoff momentum $\hat{t}_{\text{min}}$ cannot be calculated within perturbative QCD and is a parameter of the problem in our case. Below, we will discuss this point in greater detail.

The term σ^c is determined by the contribution from the scattering of a perturbative c quark from the photon on the partons of the proton. By perturbative c quarks, we mean those c quarks of the photon that either stem from the anomalous part of the hadronic component of the photon or emerge in the process of the QCD evolution of original light partons. Therefore, the distribution of these c quarks is obtained within perturbation theory [20, 25]; as

was indicated above, this contribution is contained within the region $Q^2 \geq 50$ GeV^2. By parametrizing the distribution of perturbative c quarks as in [26],[2)] where it was constructed on the basis of data reported in [20], we have verified that the contribution of the perturbative term σ^c is negligible in the kinematical region $Q^2 \leq 80$ GeV^2.

The term σ^q is proportional to the level of the intrinsic-charm admixture in the proton (N_{IC}). In general, this term must be retained since it is on the same order of magnitude as the term σ^{IC}, which describes the absorption of a pointlike photon by a charmed quark of the proton. However, we actually try to set here an upper bound on the level of the intrinsic-charm admixture in the proton. If one adds the additional term σ^q, the sought value of the parameter N_{IC} will naturally become smaller, provided that all of the remaining contributions remain unchanged. The contribution of photon–gluon fusion, σ^{PGF}, is fixed upon choosing the distribution of gluons. Therefore, there only remains the question of whether the J/ψ-meson contribution σ^{ψ} may change, but this contribution is approximately two orders of magnitude less than the contribution of light vector mesons, which is proportional to the small parameter N_{IC} (intrinsic-charm level). Therefore, the cutoff momentum $\hat{t}_{\min}$ will undergo virtually no change upon discarding the term σ^q, whence it follows that the J/ψ-meson contribution will also remain unchanged.

On the other hand, the structure functions for light vector mesons are required for calculating their contribution. However, there are no experimental data on the structure functions for light vector resonances; theoretical models that rely on any sound basis and which could produce them are not yet available either. In the existing parametrizations, it is merely postulated that the structure functions for vector resonances are identical to those for the pions, but this is rather strong an assumption since meson lifetimes are short on nuclear scales. Therefore, the parametrizations of their structure functions are not very reliable. Therefore, the inclusion of the light-vector-meson contribution increases the uncertainty of the calculations. In view of this, we will not take into account the term σ^q, thereby overestimating the level N_{IC} of the intrinsic-charm admixture in the proton. As will be seen, this overestimation does not change the main conclusion of the present study.

Charm production also receives a contribution from the parton–parton fusion processes $gg \to c\bar{c}$ and $q\bar{q} \to c\bar{c}$, which are analogous to the corresponding charm-production processes in hadron–hadron collisions. However, these processes have finite total cross sections, and their contribution to the charm yield is negligible against the contribution of photon–gluon fusion. Therefore, they can also be disregarded.

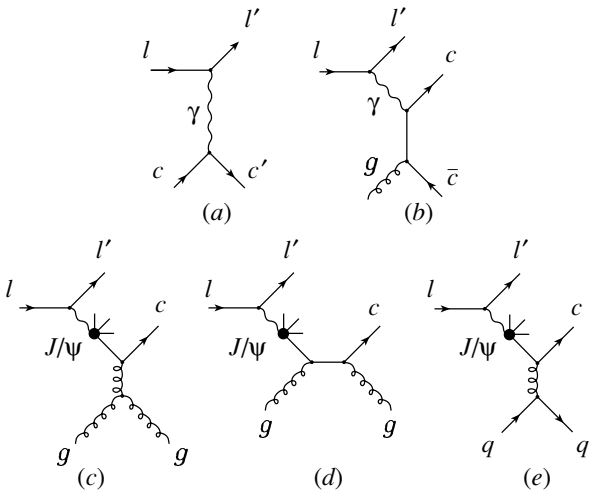

Fig. 1. Processes contributing to the structure function for charm leptoproduction: (*a*) lepton scattering on a c quark (radiative corrections to the diagram are not shown), (*b*) photon–gluon fusion, and (*c, d, e*) scattering of a c quark from the photon on a gluon and on a quark from the proton.

As a result, there remain only the terms σ^{IC}, σ^{PGF}, and σ^{ψ} in expression (6), and it is the contribution of these terms to the charmed structure function that will be the subject of the ensuing calculations. Diagrams for the processes that are taken into account in the present study are shown in Fig. 1.

2.2. Distributions of c Quarks in a Virtual J/ψ Meson

In order to find the nonperturbative distributions of c quarks and $\bar{c}$ antiquarks in a virtual J/ψ meson, one can apply the approach developed in [2]. This approach, which is based on the statistical model proposed in [28] and on the studies reported in [1], permits using noncovariant perturbation theory to take into account the heavy-quark masses for determining the probability of the formation of a Fock state featuring charmed quarks. The fact that we can make use of noncovariant perturbation theory for deriving the required distributions is of crucial importance for our purposes. A Feynman diagram is the sum of all relevant time-ordered diagrams of noncovariant perturbation theory. The contribution of diagrams of noncovariant perturbation theory that are not ordered in time is in proportion to inverse powers of the hadron momentum P_h. Within the

[2)]Technically, we employed the relevant subroutine from the PYTHIA 6.1 package [27].

parton model, an analysis is therefore performed in the so-called infinite-momentum frame, where the hadron momentum is much greater than all of the relevant mass parameters. At high energies of colliding particles, the hadron momentum is sufficiently high for ensuring the applicability of noncovariant perturbation theory. Only in this case can a virtual configuration of those Fock states where the hadron involved fluctuates be frozen over the interaction time. If we consider processes caused by the transition of a photon into a hadron (vector meson), the lifetime of a virtual hadron configuration (given Fock state) is $\Delta t \sim 1/\Delta E \approx 2P_h/(M^2 - m^2)$ (where P_h is the momentum of the hadron, m is its mass, and M is the mass of the fluctuation being considered) and can be long at high energies even at large values of the fluctuation mass M. It should be emphasized that we use the parton approach down to rather low momentum transfers ($Q^2 \approx 1.5$ GeV^2). There is no rigorous theoretical validation of the parton pattern of interactions at such low momentum transfers. However, the entire body of available experimental data, especially data from the HERA collider, unambiguously indicate that this approach is justified.

As matter of fact, expression (6) implies that the different terms in (4) do not interfere. This in turn admits a probabilistic interpretation of the expansion in (4); that is, one can assume that, throughout the interaction time, the photon occurs in one of the states that enter into the expansion in (4). In this case, the partons of the photon carry the entire momentum of the photon (more precisely, of its hadronic fluctuation). Owing to a sharp cutoff in the transverse momenta of the partons, it is sufficient to consider only the longitudinal phase space. We consider a hadron (the hadronic component of the photon in our case) as a statistical system consisting of m partons carrying together the quantum numbers of the original hadron and its momentum. Following the ideas of the parton model, we assume the independent formation of each parton of relative momentum ξ and its production in accordance with the probability density $\rho(\xi)$. Within noncovariant perturbation theory, the probability of finding an n-parton final state can then be represented in the form [2]

$$dW^{(n)} \sim \frac{1}{(E_{\text{fin}} - E_h)^2}\delta^{(3)}(\mathbf{P}_{\text{fin}} - \mathbf{P}_h)\prod_{i=1}^{n}\rho_i(\xi_i)\frac{d\xi_i}{\xi_i}, \tag{7}$$

where n is the total number of partons in the fluctuation being considered; $\mathbf{P}_h$ and E_h are the hadron momentum and energy, respectively; and $\mathbf{P}_{\text{fin}}$ and E_{fin} are the total momentum and the total energy of the parton fluctuation. The delta function in (7) ensures conservation of the total 3-momentum. The function $\rho_i(\xi_i)$ describes the probability of the formation of the ith parton without taking into account the conservation of the total 3-momentum of the system and of its quantum numbers. For the argument of the function that represents the parton distribution in a virtual J/ψ meson, we use the light-cone variable $\xi_i \equiv \xi_i^+ = (\varepsilon + p_L)/(E + P)$, where ε and p_L are, respectively, the energy and the longitudinal momentum of the parton and E and P are the energy and the longitudinal momentum of the J/ψ meson.

Since the lifetime of a fluctuation featuring a pair of charmed quarks is much shorter than the lifetime of a fluctuation consisting of only light quarks, the total quark–gluon cascade does not have time to develop fully. As a result, the fluctuation formed involves virtually no light partons, so that the charmed-quark pair carries nearly the entire momentum of the original virtual J/ψ meson. It follows that the probability of observing a Fock state that contains a $c\bar{c}$ pair can be represented in the form [2]

$$dW^{c\bar{c}} = \frac{\xi_c^2\xi_{\bar{c}}^2\rho_c(\xi_c)\rho_{\bar{c}}(\xi_{\bar{c}})}{(\xi_c + \xi_{\bar{c}})^2}\delta(1 - \xi_c - \xi_{\bar{c}})\frac{d\xi_c}{\xi_c}\frac{d\xi_{\bar{c}}}{\xi_{\bar{c}}}. \tag{8}$$

In the J/ψ meson, the charmed quarks are valence ones. On the basis of Regge phenomenology, one can therefore expect that, at low values of the relative momentum, their probability densities $\rho(\xi)$ are parametrized as

$$\rho_c(\xi) = \rho_{\bar{c}}(\xi) = \xi^\alpha, \tag{9}$$

where $\alpha \approx 0.5$, as in conventional hadrons. The inclusive momentum distribution of a charmed quark in the photon then has the form

$$c^\gamma(\xi) = \xi^\beta(1 - \xi)^\beta/B(\beta + 1, \beta + 1), \tag{10}$$

where $\beta = \alpha + 1$ and $B(u, v)$ is the Euler beta function; the distributions of charmed quarks are normalized to unity—that is, $\int_0^1 d\xi c^\gamma(\xi) = 1$. If, for α, one chooses the above value of $\alpha = 0.5$, then $\beta = 1.5$. This is the value that is used in the ensuing calculations. The value obtained for β is somewhat less than that which was used, for example, in [21] in describing the charmed-meson spectra measured in the ZEUS experiment. In our case, however, the shape of the c-quark distribution in the photon does not play a significant role, since the main contribution from parton scattering to the structure function is determined by the total scattering cross section, which involves the parton distribution in the integrand [see expression (15) below]. Further, the momentum-transfer region of the EMC experiment (and this is the region of our prime interest), $Q^2 \leq 80$ GeV^2, lies almost completely in the domain where a perturbative treatment of charmed-quark formation and evolution is illegitimate [20]. Instead of considering the evolution

of the c-quark distributions in the virtual J/ψ meson, we will therefore employ the scaling expressions (10) for these distributions.

2.3. Charmed Structure Function in Leptoproduction

Apart from a common factor, the structure function is merely the sum of the cross sections for the relevant processes. Therefore, it can also be represented as the sum of the contributions of the above three processes [see Eq. (6)]; that is,

$$F_2^c(x,Q^2) = F_2^{\mathrm{IC}}(x,Q^2) + F_2^{\mathrm{PGF}}(x,Q^2) + F_2^{\psi}(x,Q^2). \quad (11)$$

Within the parton model, the intrinsic-charm structure function F_2^{IC} is expressed in terms of the charmed-quark distribution in the proton, $c^p(x,Q^2)$, as

$$F_2^{\mathrm{IC}}(x,Q^2) = 2N_{\mathrm{IC}}e_c^2 x c^p(x,Q^2), \quad (12)$$

where $xc^p(x,Q^2)$ is normalized to unity; $e_c = \dfrac{2}{3}$ is the electric charge of a c quark; and N_{IC} is, as before, the level of the charmed-quark admixture in the proton.

The structure function F_2^{PGF} for the process of photon–gluon fusion has the form [29]

$$F_2^{\mathrm{PGF}}(x,Q^2) = \int\limits_{\sqrt{1+4\lambda}x}^{1} \frac{d\xi}{\xi} G(\xi,Q^2) f_2\left(\frac{x}{\xi},Q^2\right), \quad (13)$$

where $\lambda = m_c^2/Q^2$ and

$$f_2(z,Q^2) = \frac{\alpha_s(\hat{s})}{\pi} e_c^2 \pi z \times \left\{ V_c\left[-\frac{1}{2} + 2z(1-z)(2-\lambda)\right] + [1 - 2z(1-z) + 4\lambda z(1-3z) - 8\lambda^2 z^2] \ln\frac{1+V_c}{1-V_c}\right\}. \quad (14)$$

Here, $\hat{s} = Q^2(1-z)/z$ and $V_c(\hat{s}) = \sqrt{1-4m_c^2/\hat{s}}$ is the c-quark velocity in the (γg) c.m. frame.

The contribution of a virtual J/ψ meson to the charmed structure function, F_2^{ψ}, is determined by expression (3), while the cross section for the process $J/\psi p \to c$ within the parton model is given by

$$\sigma^{\psi} = 2\frac{4\pi\alpha}{f_{\psi}^2} \sum_i \int d\xi_i d\xi_c q^p(\xi_i) c^{\psi}(\xi_c) \hat{\sigma}_i(\hat{s}). \quad (15)$$

The factor of 2 takes into account the scattering of both c quarks and $\bar{c}$ antiquarks. The index i is used to label all of the proton partons on which a c quark of the photon may be scattered. The functions $q^p(\xi_i)$ and $c^{\psi}(\xi_c)$ describe the momentum distributions of, respectively, the ith light parton (a quark or a gluon) in the proton and a c quark in the virtual J/ψ meson. The cross section for c-quark scattering on a proton parton depends on $\hat{s}$, $\hat{\sigma}_i(\hat{s})$, where $\hat{s}$ is the square of the parton energy in the reference frame comoving with the center of mass of the scattered partons. As is well known, the parton model is not covariant in the presence of nonperturbative effects—for example, those that are associated with the quark masses. In performing integration in (15), it is therefore necessary to choose a specific reference frame. In our case, the photon–proton c.m. frame is the most convenient reference frame. If use is made of the line-cone variables, the quantity $\hat{s}$ is expressed in terms of the invariant variables x and Q^2 as $\hat{s} = m_c^2 + \xi_c\xi_i Q^2/x$.

The formulas that describe the cross sections $\hat{\sigma}_i$ for the c-quark-scattering processes $cg \to cg$ and $cq \to cq$ in the lowest order in α_s can be found in [8, 30]. For the sake of completeness, the expressions for heavy-quark-scattering cross sections are given in the Appendix, along with the expressions describing the cross sections for $c\bar{c}$-pair production in s-channel processes. For the minimum momentum transfer, a purely kinematical consideration yields $\hat{t}_{\min} = 0$. Since the cross sections for scattering processes diverge at the lower limit of integration with respect to the momentum transfer squared $\hat{t}$, the problem of the cutoff momentum transfer $\hat{t}_{\min}$ is the first problem to be solved. At low momentum transfers, perturbative QCD ceases to be valid because of the growth of the coupling constant α_s; therefore, the cutoff momentum transfer cannot be determined theoretically either. Different $|\hat{t}_{\min}|$ options, varying, as a rule, between $m_c^2/4$ and m_{cT}^2, where m_{cT} is the transverse mass of the c quark, can be found in the literature for processes involving charmed quarks. We will consider the quantity $\hat{t}_{\min}$ as an unknown parameter that is determined from experimental data. We will employ the same cutoff-momentum-transfer value $|\hat{t}_{\min}|$ in the argument of the strong-interaction coupling constant $[\alpha_s(|\hat{t}_{\min}|)]$ as well, since the main contribution to the total cross section comes from the region around $\hat{t} \sim \hat{t}_{\min}$.

Since we consider the case where the process $\gamma p \to c\bar{c} + X$ is accompanied by a high momentum transfer, the fusion of one of the c quarks with the proton residue is improbable. Owing to quantum-number conservation, the reaction final state must therefore involve at least three particles, a proton and two D mesons. It follows that, for the scattering of

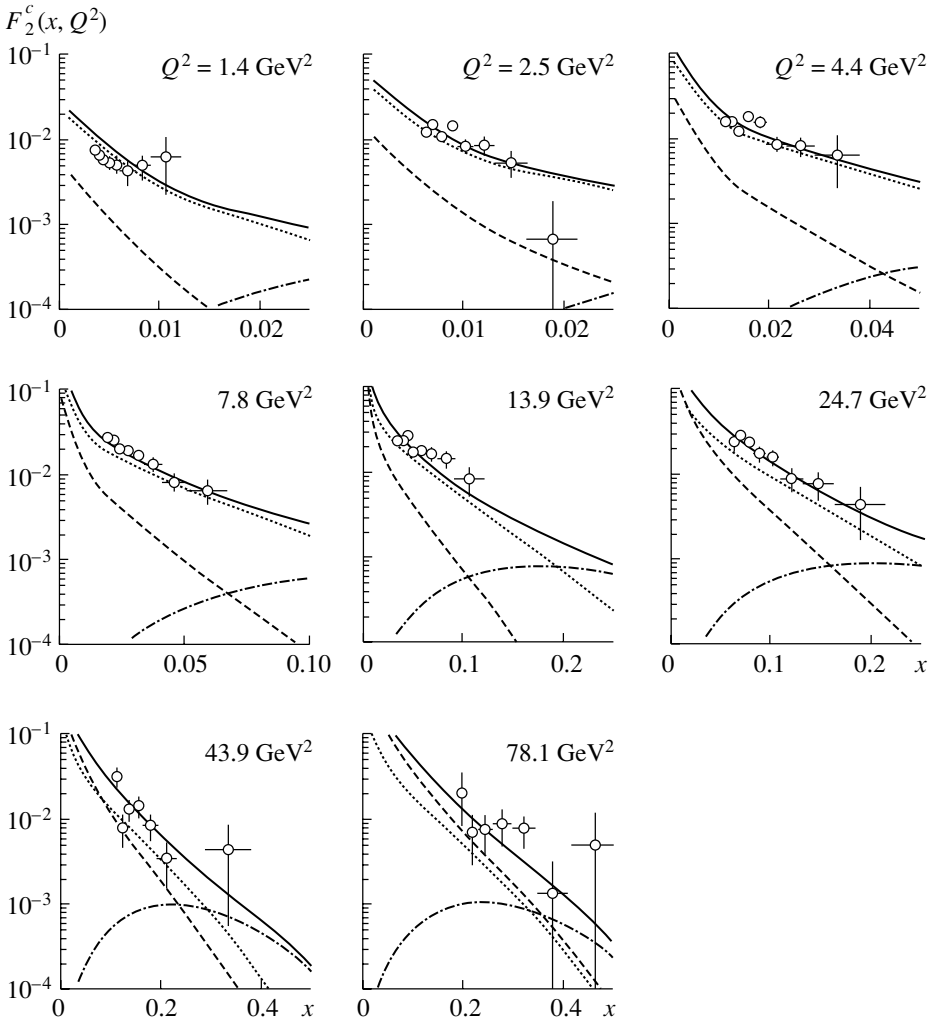

Fig. 2. Our results (curves) along with EMC experimental data [3] (points): (solid curve) sum of all contributions, (dashed curve) contribution of a c quark from the photon, (dotted curve) contribution of photon–gluon fusion, and (dash-dotted curve) contribution of pointlike-photon scattering on a c quark from the proton (intrinsic charm). The MRS(G) parametrization was used to describe the distribution of gluons in the proton. The curves are presented for the free-parameter values of $\hat{t}_{\min} = -3.01$ GeV^2 and $N_{\rm IC} = 0.20\%$ and for the c-quark mass of $m_c = 1.51$ GeV.

photon partons on proton partons, the general kinematical constraint assumes the form

$$\frac{(1-x)}{x}Q^2 + m_p^2 \geq (2m_D + m_p)^2, \qquad (16)$$

where m_D and m_p are, respectively, the D-meson and the proton mass.

Additional kinematical constraints on the threshold energies $\sqrt{\hat{s}_{\rm thr}}$ for elementary scattering processes in the presence of a cutoff $\hat{t}_{\min}$ in the momentum transfer squared are quoted in [8, 30]. We also present these constraints in the Appendix.

The required limits of integration in (15) can easily be obtained by analyzing the kinematics of parton scattering. Considering that $\hat{t}_{\min}$ differs from zero, we find that the limits on the relative momentum of a parton in the proton and a c quark in the J/ψ meson are the following:

$$x[1 + \frac{(\sqrt{\hat{s}_{\rm thr}} + m_c)^2}{Q^2}] \leq \xi_i \leq 1, \qquad (17)$$

$$\frac{x(\hat{s}_{\rm thr} - m_c^2)}{\xi_i Q^2} \leq \xi_c \leq 1.$$

3. RESULTS AND DISCUSSION

In our fitting procedure, we employed the dimuon data obtained by the EMC for charm-production cross sections $\sigma(\gamma p)$ and rescaled into charmed structure functions by the method described in [2]. In comparing the results of the calculations with the experimental data, we have taken into account corrections to the intrinsic-charm structure function $F_2^{\rm IC}$ both from higher orders of perturbative QCD and from the nonzero values of the c-quark and the proton

mass (see [2, 17, 31]). In calculating the contribution of photon–gluon fusion, the MRS(G) parametrization from the PDFLIB package [32] was used to describe the distribution of gluons in the proton. This parametrization was obtained by using the expression for α_s in the second order of perturbation theory and the value of $\Lambda_{\rm QCD} = 0.174$ GeV.

By fitting the EMC data, we have obtained the following parameter values (at $\chi^2/{\rm NDF} = 0.74$, which demonstrates that the quality of our fit is quite high):

$$N_{\rm IC} = (0.2 \pm 0.2)\%, \quad (18)$$
$$m_c = 1.51 \pm 0.03 \ \ {\rm GeV},$$
$$\hat{t}_{\rm min} = -3.0 \pm 0.3 \ \ {\rm GeV}^2.$$

The result quoted immediately above for the minimum momentum transfer squared in c-quark scattering on proton partons is approximately equal to the square of the transverse mass of the c quark, as might have been expected on the basis of general considerations. The above value of $m_c = 1.51 \pm 0.03$ GeV is in agreement with the value of $m_c = 1.50$ GeV, which was used in deriving the MRS(G) parametrization, thereby demonstrating the self-consistency of our approach. The resulting fit is given in Fig. 2 along with the data from [3]. It should be recalled that the estimate obtained here for the level $N_{\rm IC}$ of the intrinsic-charm admixture in the proton is exaggerated, since we have disregarded the contribution from the scattering of light partons of the virtual photon on the c quarks of the proton. In this connection, we note that the statistical uncertainty in $N_{\rm IC}$ is equal to the value of the parameter itself, whence it follows that the disregard of the term σ^q in expression (6) was justified.

It is worth mentioning that Odorico [8] performed calculations for the charm-excitation mechanism in hadron–hadron collisions; that is, he considered parton scattering on the charmed quarks of the proton (on intrinsic charm). The contribution to charm leptoproduction from the hadronic component of the photon is analogous to charm excitation in hadron interactions, which was considered in [8], where the level of the intrinsic-charm admixture in the proton was chosen to be 0.5% and where it was concluded that the charm-excitation mechanism ensures the required charm yield at ISR energies owing to a faster growth of the cross section with energy (this makes it possible to match ISR data with data from experiments with fixed targets at lower energies). In [8], the cutoff momentum transfer $\hat{t}_{\rm min}$ was taken to be $\hat{t}_{\rm min} = m_c^2/4 \approx 0.6$ GeV^2, which is much less than the value obtained here.

The results of the present study yield a much smaller intrinsic-charm admixture in the proton and a greater value of the cutoff momentum transfer $\hat{t}_{\rm min}$. Therefore, the contribution of parton scattering on the intrinsic charm to the charmed-particle yield in hadron–hadron collisions must be at least one order of magnitude lower than that which was obtained in [8] and is unable to explain the large charmed-particle yield obtained in experiments at the ISR. Thus, the discrepancy between the ISR data and data from experiments at lower energies has not been removed.

From the results obtained in the present study, it follows that, even if use is made of a soft gluon distribution, the EMC data can be described without resort to the hypothesis that the proton features a sizable intrinsic-charm admixture. The distinction between the data of the EMC experiment and the predictions based on the mechanism of photon–gluon fusion can be completely explained by the contribution of the hadronic component of the photon. In any case, the mechanism being considered reduces substantially the discrepancy between the predictions of the model of photon–gluon fusion and the data of the EMC experiment on the production of charmed particles and, accordingly, the required admixture of Fock states in the proton that involve charmed quarks.

On the other hand, we had to introduce a nonperturbative charmed component in the photon wave function. The reason that the photon does involve, in contrast to the proton, a sizable nonperturbative admixture of c quarks may be the following: as was indicated in [24], the nonperturbative regime in the photon begins at $Q^2 \approx 5.5$ GeV^2, but, for the proton, the DGLAP equations describe well the evolution of the structure function from $Q^2 \approx 1$–2 GeV^2. In view of this, there is no need for a sizable nonperturbative admixture of charmed states in the proton.

ACKNOWLEDGMENTS

We are grateful to DESY for hospitality and for providing good conditions for work.

APPENDIX

In the lowest order in α_s, the total cross sections for c-quark scattering [30] are given by (they are presented in the same form as in [8])

$$\frac{d\sigma(q\bar{q} \to c\bar{c})}{d\hat{t}} = \frac{4\pi}{9\hat{s}^2}\alpha_s^2(4m_c^2)$$
$$\times \frac{(m_c^2 - \hat{t})^2 + (m_c^2 - \hat{u})^2 + 2m_c^2\hat{s}}{\hat{s}^2};$$
$$\sigma(q\bar{q} \to c\bar{c}) = \frac{8\pi}{27\hat{s}}\alpha_s^2(4m_c^2)(\hat{s} + 2m_c^2)\sqrt{1 - \frac{4m_c^2}{\hat{s}}};$$
$$\hat{s}_{\rm thr} = 4m_c^2;$$
$$\frac{d\sigma(gg \to c\bar{c})}{d\hat{t}} = \frac{\pi}{16\hat{s}^2}\alpha_s^2(4m_c^2)$$

$$\times\left[\frac{12}{\hat{s}^2}(m_c^2-\hat{t})(m_c^2-\hat{u})\right.$$
$$+\frac{8}{3}\frac{(m_c^2-\hat{t})(m_c^2-\hat{u})-2m_c^2(m_c^2+\hat{t})}{(m_c^2-\hat{t})^2}$$
$$+\frac{8}{3}\frac{(m_c^2-\hat{t})(m_c^2-\hat{u})-2m_c^2(m_c^2+\hat{u})}{(m_c^2-\hat{u})^2}$$
$$-\frac{2m_c^2(\hat{s}-4m_c^2)}{3(m_c^2-\hat{t})(m_c^2-\hat{u})}$$
$$-6\frac{(m_c^2-\hat{t})(m_c^2-\hat{u})+m_c^2(\hat{u}-\hat{t})}{\hat{s}(m_c^2-\hat{t})}$$
$$\left.-6\frac{(m_c^2-\hat{t})(m_c^2-\hat{u})+m_c^2(\hat{t}-\hat{u})}{\hat{s}(m_c^2-\hat{u})}\right];$$

$$\sigma(gg\to c\bar{c})=\frac{\pi}{3\hat{s}}\alpha_s^2(4m_c^2)\left[-\frac{1}{4}\left(7+\frac{31m_c^2}{\hat{s}}\right)x\right.$$
$$\left.+\left(1+\frac{4m_c^2}{\hat{s}}+\frac{m_c^4}{\hat{s}^2}\right),\ln\frac{1+x}{1-x}\right],$$

where

$$x=\sqrt{1-\frac{4m_c^2}{\hat{s}}};\quad \hat{s}_{\rm thr}=4m_c^2;$$

$$\frac{d\sigma(qc\to qc)}{d\hat{t}}=\frac{4\pi}{9(\hat{s}-m_c^2)^2}\alpha_s^2(-\hat{t}_{\min})$$
$$\times\frac{(m_c^2-\hat{u})^2+(\hat{s}-m_c^2)^2+2m_c^2\hat{t}}{\hat{t}^2};$$
$$\sigma(qc\to qc)=\frac{4\pi}{9(\hat{s}-m_c^2)^2}\alpha_s^2(-\hat{t}_{\min})$$
$$\times\left[\left(1-\frac{2\hat{s}}{\hat{t}_{\min}}\right)\left(\frac{(\hat{s}-m_c^2)^2}{\hat{s}}+\hat{t}_{\min}\right)\right.$$
$$\left.-2\hat{s}\ln\frac{(\hat{s}-m_c^2)^2}{-\hat{t}_{\min}\hat{s}}\right],$$

where

$$\hat{t}_{\min}=0,\quad \hat{t}_{\max}=-(\hat{s}-m_c^2)^2/\hat{s},$$

$$\hat{s}_{\rm thr}=m_c^2-\frac{1}{2}\hat{t}_{\min}+\left(-m_c^2\hat{t}_{\min}+\frac{1}{4}\hat{t}_{\min}^2\right)^{1/2};$$

$$\frac{d\sigma(gc\to gc)}{d\hat{t}}=\frac{\pi}{16(\hat{s}-m_c^2)^2}\alpha_s^2(-\hat{t}_{\min})$$
$$\times\left[\frac{32(\hat{s}-m_c^2)(m_c^2-\hat{u})}{\hat{t}^2}\right.$$
$$+\frac{64}{9}\frac{(\hat{s}-m_c^2)(m_c^2-\hat{u})+2m_c^2(\hat{s}+m_c^2)}{(\hat{s}-m_c^2)^2}$$
$$+\frac{64}{9}\frac{(\hat{s}-m_c^2)(m_c^2-\hat{u})+2m_c^2(\hat{u}+m_c^2)}{(m_c^2-\hat{u})^2}$$
$$+\frac{16}{9}\frac{m_c^2(4m_c^2-\hat{t})}{(\hat{s}-m_c^2)(m_c^2-\hat{u})}$$
$$+16\frac{(\hat{s}-m_c^2)(m_c^2-\hat{u})+m_c^2(\hat{s}-\hat{u})}{\hat{t}(\hat{s}-m_c^2)}$$
$$\left.-16\frac{(\hat{s}-m_c^2)(m_c^2-\hat{u})-m_c^2(\hat{s}-\hat{u})}{\hat{t}(m_c^2-\hat{u})}\right];$$
$$\sigma(gc\to gc)=\frac{\pi}{(\hat{s}-m_c^2)^2}\alpha_s^2(-\hat{t}_{\min})$$
$$\times\left[\left(1+\frac{4}{9}\left(\frac{\hat{s}+m_c^2}{\hat{s}-m_c^2}\right)^2\right)(\hat{t}_{\min}-\hat{t}_{\max})\right.$$
$$+\frac{2}{9}\frac{\hat{t}_{\min}^2-\hat{t}_{\max}^2}{\hat{s}-m_c^2}+2(\hat{s}+m_c^2)\ln\frac{\hat{t}_{\min}}{\hat{t}_{\max}}$$
$$+\frac{4}{9}\frac{\hat{s}^2-6m_c^2\hat{s}+6m_c^4}{\hat{s}-m_c^2}\ln\frac{\hat{s}-m_c^2+\hat{t}_{\min}}{\hat{s}-m_c^2+\hat{t}_{\max}}$$
$$+2(\hat{s}-m_c^2)^2\left(\frac{1}{\hat{t}_{\max}}-\frac{1}{\hat{t}_{\min}}\right)$$
$$\left.+\frac{16}{9}m_c^4\left(\frac{1}{\hat{s}-m_c^2+\hat{t}_{\max}}-\frac{1}{\hat{s}-m_c^2+\hat{t}_{\min}}\right)\right];$$

where

$$\hat{t}_{\max}=-\max\left(\hat{s}-m_c^2+\hat{t}\min,(\hat{s}-m_c^2)/\hat{s}\right)$$
(in order to ensure fulfillment of the inequality
$$\hat{u}-m_c^2<\hat{t}_{\min}),$$

$$\hat{s}_{\rm thr}=\begin{cases}m_c^2-\frac{1}{2}\hat{t}_{\min}+\left(-m_c^2\hat{t}_{\min}+\frac{1}{4}\hat{t}_{\min}^2\right)^{1/2}, & -\hat{t}_{\min}<\frac{1}{2}m_c^2,\\ m_c^2-2\hat{t}_{\min}, & -\hat{t}_{\min}>\frac{1}{2}m_c^2.\end{cases}$$

REFERENCES

1. S. J. Brodsky, P. Hoyer, C. Peterson, and N. Sakai, Phys. Lett. B **93B**, 451 (1980); S. J. Brodsky and C. Peterson, Phys. Rev. D **23**, 2745 (1981).
2. Yu. A. Golubkov, Preprint No. 98-174 DESY (Hamburg, 1988); Yad. Fiz. **63**, 672 (2000) [Phys. At. Nucl.

63, 606 (2000)]; hep-ph/9811218.
3. European Muon Collab. (J. J. Aubert *et al.*), Phys. Lett. B **110B**, 73 (1982); Nucl. Phys. B **213**, 1, 31 (1983).
4. D. Drijard *et al.*, Phys. Lett. B **81B**, 250 (1979); **85B**, 452 (1979); K. L. Giboni *et al.*, Phys. Lett. B **85B**, 437 (1979); W. Lockman *et al.*, Phys. Lett. B **85B**, 443 (1979); A. Chilingarov *et al.*, Phys. Lett. B **83B**, 136 (1979).
5. J. Badier *et al.*, Phys. Lett. B **114B**, 457 (1982); **158**, 85 (1985); Z. Phys. C **20**, 101 (1983).
6. S. P. K. Tavernier, Rep. Prog. Phys. **50**, 1439 (1987).
7. S. Frixione *et al.*, Nucl. Phys. B **431**, 453 (1994).
8. R. Odorico, Nucl. Phys. B **209**, 77 (1982).
9. E. M. Aitala *et al.*, Phys. Lett. B **371**, 157 (1996); hep-ex/9601001.
10. E. M. Aitala *et al.*, Phys. Lett. B **462**, 225 (1999); hep-ex/9906034.
11. R. Vogt and S. J. Brodsky, Phys. Lett. B **349**, 569 (1995); R. Vogt, Nucl. Phys. B **446**, 149 (1995).
12. C. Biino *et al.*, Phys. Rev. Lett. **58**, 2523 (1987).
13. M. S. Kowitt *et al.*, Phys. Rev. Lett. **72**, 1318 (1994).
14. Yu. A. Golubkov, Preprint No. 96-30/437 INP MSU (Moscow, 1996); hep-ph/9609492.
15. Yu. A. Golubkov, Preprint No. 94-060 DESY (Hamburg, 1994).
16. B. W. Harris, J. Smith, and R. Vogt, Nucl. Phys. B **461**, 181 (1996).
17. E. Hoffmann and R. Moore, Z. Phys. C **20**, 71 (1983).
18. E. Witten, Nucl. Phys. B **120**, 189 (1977).
19. W. A. Bardeen and A. J. Buras, Phys. Rev. D **20**, 166 (1979); **21**, 2041 (1980).
20. M. Glück, K. Grassie, and E. Reya, Phys. Rev. D **30**, 1447 (1984).
21. A. V. Berezhnoy and A. K. Likhoded, hep-ph/0005200.
22. P. Kessler, Acta Phys. Austriaca **41**, 141 (1975); V. M. Budnev *et al.*, Phys. Rep. **15**, 181 (1975).
23. G. A. Schuler and T. Sjöstrand, Phys. Lett. B **300**, 169 (1993); Nucl. Phys. B **407**, 539 (1993).
24. J. H. Da Luz Vieira and J. K. Storrow, Z. Phys. C **51**, 241 (1991).
25. P. Aurenche, J.-P. Guillet, and M. Fontannaz, Z. Phys. C **64**, 621 (1994).
26. M. Drees and K. Grassie, Z. Phys. C **28**, 451 (1985).
27. T. Sjöstrand, Comput. Phys. Commun. **82**, 74 (1994); http://www.thep.lu.se/~torbjorn/Pythia.html
28. J. Kuti and V. F. Weisskopf, Phys. Rev. D **4**, 3418 (1971).
29. M. Glück and E. Reya, Phys. Lett. B **83B**, 98 (1979).
30. B. L. Combridge, Nucl. Phys. B **151**, 429 (1979).
31. R. Barbieri, J. Ellis, M. K. Gaillard, and G. G. Ross, Nucl. Phys. B **117**, 50 (1976).
32. H. Plothow-Besch, PDFLIB Version 7.09 (1997).

Translated by A. Isaakyan

Physics of Atomic Nuclei, Vol. 66, No. 2, 2003, pp. 334–337. From Yadernaya Fizika, Vol. 66, No. 2, 2003, pp. 359–362.

ELEMENTARY PARTICLES AND FIELDS
Theory

Analyticity and Quark–Gluon Structure of Hadron Total Cross Sections*

M. Majewski[1)] and V. A. Meshcheryakov

Joint Institute for Nuclear Research, Dubna, Moscow oblast, 141980 Russia

Received September 14, 2001; in final form, May 7, 2002

Abstract—The amplitudes of hadron–hadron forward elastic scattering at high energies are investigated on the basis of analyticity and crossing symmetry. A universal uniformizing variable for them is proposed, and the formulas for crossing-even and crossing-odd amplitudes are derived. The same parameters in these formulas determine the real and imaginary (total cross sections) parts of the amplitudes. The analysis of the parameters determined from experimental data clearly points to the quark–gluon structure of hadron total cross sections. The total cross sections for hyperon–proton scattering are predicted. They are consistent with experimental data and, in particular, with the new SELEX-collaboration measurement $\sigma_{\rm tot}(\Sigma^- p)$.

1. INTRODUCTION

The modern theory of strong interactions (QCD) involves a number of unsolved problems, for instance, the problem of whether glueballs exist or not. Among them, there is the problem of analytic properties of physical amplitudes. In [1], Ohme showed that, for gauge theories quantized on the basis of BRST algebra [2], the confinement conditions can be formulated so that physical amplitudes do possess the analytic properties and conditions of crossing symmetry established earlier [3]. In particular, the forward πp-scattering amplitude has two nucleon poles and two cuts corresponding to direct and cross processes. The problem of whether double dispersion relations are valid or not still remains open in gauge theories.

Below, Ohme's result is used to construct a model of the amplitude of scattering of a hadron A on a proton. This model allows one to determine the quark–gluon structure of hadron total cross sections on an experimental basis, avoiding controversial questions on the Pomeron multicomponent structure [4–6].

2. UNIVERSAL RIEMANN SURFACE OF THE FORWARD SCATTERING AMPLITUDE

The notion of a universal Riemann surface of the forward scattering amplitude for hadron–hadron processes at high energies arises when one introduces the well-known variable

$$\nu = \frac{s-u}{4M\mu},$$

where s, u are usual Mandelstam variables and M, μ are the masses of colliding particles. Thresholds of any elastic hadron–hadron process corresponding to the direct and cross reactions in the s plane transform into the points $\nu = \pm 1$. The thresholds of all inelastic processes (direct and crossed) lie on the cuts $(-\infty, -1]$, $[+1, +\infty)$. They make the Riemann surface of a scattering amplitude as a function of ν infinitely sheeted. This property of the Riemann surface can be modeled by a particular choice of the uniformizing variable, the same for all hadron–hadron processes,

$$w(\nu) = (1/\pi)\arcsin(\nu). \tag{1}$$

The Riemann surface of function $w(\nu)$ is just what we call the universal Riemann surface. It has three branch points: two of the square-root type at the points $\nu = \pm 1$ and one of the logarithmic type at infinity. The function $w(\nu)$ is suitable for taking account of the crossing symmetry of amplitudes of hadron–hadron scattering $F_\pm^A$. We choose the latter so that the equality

$$\mathrm{Im}F_\pm^A = \sigma_{\rm tot}^{\bar{A}p} \pm \sigma_{\rm tot}^{Ap} \tag{2}$$

will be valid on the upper edge of the right-hand cut of the ν plane; then, the condition of crossing symmetry is

$$F_\pm(\nu) = \pm F_\pm(-\nu). \tag{3}$$

In addition, the amplitudes obey the condition of reality

$$F_\pm^*(\nu) = -F_\pm(\nu^*). \tag{4}$$

In the w plane, a physical sheet of the ν plane is mapped into the strip $|\mathrm{Re}w| \le 1/2$, whose boundaries

*This article was submitted by the authors in English.

[1)]University of Lodz, Poland.

are images of cuts of the ν plane. We call it the physical strip in the w plane. Nonphysical sheets of the ν plane transform into strips $|\mathrm{Re}\,(w \pm n)| \le 1/2$ ($n = 1, 2, \dots$). This clearly demonstrates that the universal Riemann surface is infinitely sheeted.

Let $w = x + iy$. Then, owing to Eqs. (3) and (4), on the boundary of the physical strip, we find

$$F_\pm^*(1/2 + iy) = \mp F_\pm(-1/2 + iy). \qquad (5)$$

Let us expand the amplitudes $F_\pm(w)$ into Taylor series with the center at the point $w_0 = iy_0$. Their convergence radius is determined by the distance from the point w_0 to the nearest pole corresponding to the resonance on an unphysical sheet. The parameters of those expansions determine both the real and the imaginary parts of amplitudes $F_\pm(w)$. Below, we will use only the imaginary parts of amplitudes (the total cross sections) that can be represented by the following converging power series:

$$\mathrm{Im}F_+(1/2 + iy) = \sum_{n\ge1}\left(\frac{1}{2}\right)^{2n-2}\sigma_+^{(n)}(y), \qquad (6)$$

$$\sigma_+^{(n)}(y) = \frac{(-1)^{n+1}}{(2n-2)!}\frac{d^{2n-2}\sigma_+^{(1)}(y)}{dy^{2n-2}},$$

$$\sigma_+^{(1)}(y) = \sum_{m\ge1} a_m (y - y_0)^{m-1},$$

$$\mathrm{Im}F_-(1/2 + iy) = \sum_{n\ge1}\left(\frac{1}{2}\right)^{2n-1}\sigma_-^{(n)}(y),$$

$$\sigma_-^{(n)}(y) = \frac{(-1)^{n+1}}{(2n-2)!}\frac{d^{2n-2}\sigma_-^{(1)}(y)}{dy^{2n-2}},$$

$$\sigma_-^{(1)}(y) = \sum_{m\ge1} b_m (y - y_0)^{m-1}.$$

Expansions (6) satisfy Eq. (5). It is instructive to compare the argument of expansions (6) with commonly used expressions, for instance, $(s/s_0)^\alpha$, $s_0 = 1$ GeV^2 in [4, 6, 7] and $(p/20)^\alpha$ in [8] (hereafter, p is the momentum in the laboratory system). However, when one attempts to compare two different parametrizations of total cross sections in the region of $\sim$100 GeV/c, the function $\ln(p/p_0)$ arises naturally. Let us derive it from formula (6). From (1), it follows that $y = \ln(\nu + \sqrt{\nu^2 - 1})$. For $s \gg M^2$, we have $y \sim \ln(2p/\mu)$. In this case, the function $(y - y_0) \sim (1/\pi)\ln(p/p_0)$ is the argument of expansions (6). Here, the quantity p_0 has a clear mathematical meaning—it is the center of the expansion into the Taylor series, and at the same time, physically, it makes p dimensionless. We stress once more that formulas (6) are valid in the vicinity of point y_0, and they cannot be used to estimate the behavior of cross sections when $s \to \infty$; discussions on the Pomeron structure refer to the region where they are not applicable.

3. QUARK–GLUON STRUCTURE OF HADRON TOTAL CROSS SECTIONS

Formulas (6) were employed to analyze the experimental data on pp, $\bar{p}p$, $K^\pm p$, and $\pi^\pm p$ total cross sections [9]. The results are collected in the table. Twenty-four coefficients a_m, b_m are determined by 300 experimental points and describe the behavior of cross sections in the interval $p \in (10, 10^3)$ GeV/c. Values of y_0 correspond to $p = 100$ GeV/c, at which the correlations between parameters a_m, b_m are minimal. In the vicinity of y_0, these total cross sections have minima, and the real parts of amplitudes cross zero. Twelve coefficients b_m display the simple dependence

$$(b_m)_{pp} : (b_m)_{\pi p} : (b_m)_{Kp} : (b_m)_{np} = 5 : 1 : 2 : 4. \qquad (7)$$

The mean ratios are calculated from the table to be as follows:

$$\overline{\left(\frac{b_{pp}}{b_{\pi p}}\right)} = 5.37 \pm 0.22, \qquad \overline{\left(\frac{b_{Kp}}{b_{\pi p}}\right)} = 2.16 \pm 0.12,$$

$$\overline{\left(\frac{b_{np}}{b_{\pi p}}\right)} = 4.79 \pm 0.23.$$

They are in good agreement with ratios (7), except for the last one. It differs from (7) by three statistical errors as a result of large χ^2/n.d.f. for np scattering. Therefore, it is expedient to use it below only for qualitative estimations. Relations (7) are not new and are written in order to demonstrate that the analysis of coefficients a_m, b_m is important for determining quark and other degrees of freedom of hadrons. It is known [8] that relationships (7) are obtained from the consideration of annihilation components of amplitudes and are proportional to the number of dual diagrams of scattering of a hadron on a proton,

$$n_d(Ap) = 2N_{\bar{u}}^A + N_{\bar{d}}^A, \qquad (8)$$

where $N_{\bar{u}}^A$ and $N_{\bar{d}}^A$ are the numbers of antiquarks $\bar{u}, \bar{d}$ in hadron A.

It is of great interest but difficult to analyze the crossing-even part of the scattering amplitude. The additive quark model (AQM) [10] predicts the following ratios:

$$\sigma_{pp} : \sigma_{\pi p} : \sigma_{Kp} : \sigma_{np} = 3 : 2 : 2 : 3.$$

However, from our table, it is seen that only the coefficients a_1 and a_3 approximately follow that dependence. The difference $(a_1)_{pp} - (a_1)_{np} = 1.02 \pm 0.40$ can be considered compatible with zero, since it does

The values of the parameters a_m, b_m (all in mb), and y_0 in Eq. (6)

	pp	πp	Kp	np
a_1	84.51 ± 0.18	49.77 ± 0.09	41.03 ± 0.12	83.49 ± 0.36
a_2	-4.85 ± 0.36	1.92 ± 0.19	5.16 ± 0.25	-3.48 ± 0.62
a_3	15.97 ± 0.7	10.37 ± 0.34	7.37 ± 0.48	8.72 ± 1.48
b_1	8.52 ± 0.17	1.62 ± 0.07	3.51 ± 0.12	7.85 ± 0.26
b_2	-13.82 ± 0.79	-2.8 ± 0.17	-5.65 ± 0.51	-12.74 ± 1.24
b_3	15.33 ± 1.7	2.7 ± 1.8	5.04 ± 0.97	12.36 ± 2.97
y_0	1.71	2.31	1.91	1.71
χ^2/n.d.f.	112/109	82/73	48/38	96/50

not exceed three standard deviations, and the description of process np is not quite satisfactory. We will neglect the distinction between processes pp and np, though, for the coefficient a_3, this assumption is valid only due to χ^2/n.d.f. being large in magnitude. At the same time, the difference $(a_1)_{\pi p} - (a_1)_{Kp} = 8.74 \pm 0.15$ is significant and, together with other coefficients, determines 30% accuracy of the AQM. The values of coefficients a_2 from the table do not comport with the AQM predictions, and therefore, they are very important for choosing new models. Some attempts at refining the AQM are known [11, 12]. All of them suggest that the amplitude should be supplemented with terms bilinear in quark numbers of hadron A. In this case, the amplitude can be described satisfactorily under different assumptions on the form of bilinear terms. However, the clear physical justification of bilinear terms is rather difficult.

Below, we construct a new model by using the known idea of quarks being confined in a hadron by gluons. Then, it is natural to assume that the total cross section of scattering of hadron A on a proton contains a part that describes gluon–gluon interaction. With this in mind, we set

$$a_m = \alpha_m + \beta_m \cdot N_q^A + \gamma_m \cdot N_q^A \cdot N_{\rm ns}^A, \qquad (9)$$

where N_q^A is the total number of quarks, $N_{\rm ns}^A$ is the total number of nonstrange quarks in hadron A, and the numbers α_m do not depend on the quark content of hadron A [8]. The numbers α_m determine the fraction of the total cross section corresponding to the gluon–gluon interaction. It is just the gluon degree of freedom of hadrons A and p that is responsible for them. The assumption on a_m [Eq. (9)] corresponds to the hypothesis of Gershtein and Logunov [13]. They argue that the constant of the Froissart limit does not depend on the guark content of hadron A, but that it does depend on glueballs and is the same for all processes. The hypothesis has been verified by Prokoshkin [14] on the basis of similar experimental data as we use. In our model, one should attribute the Froissart behavior not to the variable y but to y_0. That justifies Eq. (9). The numbers $(a_m)_{pp}$, $(a_m)_{\pi p}$, $(a_m)_{Kp}$ from the table determine α_m, β_m, γ_m. Then, the predictive power of hypothesis (9) can be verified for the values of total cross sections of hyperon–proton interactions. In [15], results on the measurement of total cross sections of $\Sigma^- p$ and $\Xi^- p$ in the range of momenta (74.5, 136.9) GeV/c are presented. In this range, the total cross sections vary slightly, and to compare the predictions of the model given by formulas (1), (6), and (8), we take the momentum $p = 101$ GeV/c. In this case, the theoretical and experimental results are as follows:

$$\sigma_{\Xi^- p} = \frac{(29.25 \pm 0.5\,{\rm mb})_{\rm th}}{(29.12 \pm 0.22\,{\rm mb})_{\rm exp}},$$

$$\sigma_{\Sigma^- p} = \frac{(34.8 \pm 0.2\,{\rm mb})_{\rm th}}{(33.3 \pm 0.3\,{\rm mb})_{\rm exp}}.$$

Similar data [16] for Λp and $\Sigma^- p$ scattering at 20 GeV/c are

$$\sigma_{\Lambda p} = \frac{(33.3 \pm 0.5\,{\rm mb})_{\rm th}}{(34.7 \pm 3\,{\rm mb})_{\rm exp}},$$

$$\sigma_{\Sigma^- p} = \frac{(34.2 \pm 0.5\,{\rm mb})_{\rm th}}{(34 \pm 1\,{\rm mb})_{\rm exp}}.$$

Recently, the SELEX collaboration has published the data on $\Sigma^- p$ at $p = 609$ GeV/c [17]. The comparison with predictions of the model is

$$\sigma_{\Sigma^- p} = \frac{(35 \pm 7.5\,{\rm mb})_{\rm th}}{(37 \pm 0.7\,{\rm mb})_{\rm exp}}.$$

Although the obtained value of the total cross section is not as accurate as in [18], it should be considered satisfactory. In [4–6, 11, 18], devoted to the analysis of total cross sections, the errors of predicted values were not calculated, but they increase rapidly in the region of extrapolation.

4. CONCLUSION

A uniformizing variable for hadron–hadron forward scattering at high energies was proposed on the basis of analyzing the analytic properties of physical scattering amplitudes [1]. If one represents the scattering amplitudes as Taylor series in that variable and takes crossing symmetry into account, one can once more be convinced on an experimental basis that hadrons possess the quark–gluon structure. The total cross sections predicted for scattering of strange hadrons on a proton are in agreement with experiment in a wide energy range. The gluon–gluon part of the total cross sections at momenta $p = 100$ GeV/c amounts to about 10%.

REFERENCES

1. R. Ohme, Int. J. Mod. Phys. A **10**, 1995 (1995).
2. C. Becchi, A. Rouet, and R. Stora, Ann. Phys. (N.Y.) **98**, 287 (1976); I. V. Tyutin, Report No. 39, FIAN (Moscow, 1975).
3. N. N. Bogoliubov, B. V. Medvedev, and M. K. Polivanov, *Problems in Theory of Dispersion Relations* (Fizmatgiz, Moscow, 1958).
4. A. Donnachie and P. V. Landshoff, Phys. Lett. B **296**, 227 (1992).
5. H. J. Lipkin, Phys. Lett. B **335**, 500 (1994).
6. P. Gauron and B. Nicolescu, Preprint No. 00-02, LPNE (Paris, 2000).
7. Particle Data Group, Eur. Phys. J. C **3**, 205 (1998).
8. H. J. Lipkin, Phys. Rev. D **11**, 1827 (1975).
9. V. P. Gerdt, V. I. Inozemtsev, and V. A. Meshcheryakov, Lett. Nuovo Cimento **15**, 321 (1976).
10. E. M. Levin and L. L. Frankfurt, Pis'ma Zh. Éksp. Teor. Fiz. **2**, 105 (1965) [JETP Lett. **2**, 65 (1965)].
11. P. Joynson and B. Nicolescu, Nuovo Cimento A **37**, 97 (1977).
12. H. J. Lipkin, Nucl. Phys. B **78**, 1381 (1974).
13. S. S. Gershtein and A. A. Logunov, Yad. Fiz. **39**, 1514 (1984) [Sov. J. Nucl. Phys. **39**, 960 (1984)].
14. Y. D. Prokoshkin, Yad. Fiz. **40**, 1579 (1984) [Sov. J. Nucl. Phys. **40**, 1002 (1984)].
15. S. Gjesdal *et al.*, Phys. Lett. B **40B**, 152 (1972).
16. S. F. Biagis *et al.*, Nucl. Phys. B **186**, 1 (1981).
17. U. Dersch *et al.*, Nucl. Phys. B **579**, 277 (2000).
18. H. J. Lipkin, hep-ph/9911259.

Physics of Atomic Nuclei, Vol. 66, No. 2, 2003, pp. 338–354. From Yadernaya Fizika, Vol. 66, No. 2, 2003, pp. 363–380.

ELEMENTARY PARTICLES AND FIELDS
Theory

Nonperturbative Quark Dynamics in a Baryon*

Yu. A. Simonov

Jefferson Laboratory, Newport News, VA, USA
Institute of Theoretical and Experimental Physics, Bol'shaya Cheremushkinskaya ul. 25, Moscow, 117259 Russia

Received June 6, 2002

Abstract—The field-correlator method is used to calculate nonperturbative dynamics of quarks in a baryon. The general expression for the $3q$ Green's function is obtained using the Fock–Feynman–Schwinger (world-line) path-integral formalism, where all dynamics is contained in the $3q$ Wilson loop with spin-field insertions. Using the lowest cumulant contribution for the Wilson loop, one obtains a Y-shaped string potential vanishing at the string-junction position. Using the einbein formalism for the quark kinetic terms, one automatically obtains constituent quark masses, calculable through the string tension. The resulting effective action for $3q$ plus Y-shaped strings is quantized in the path-integral formalism to produce two versions of Hamiltonian: one is in the c.m. and the other is in the light-cone system. The hyperspherical formalism is used to calculate masses and wave functions. Simple estimates in the lowest approximation yield baryon masses in good agreement with experiment without fitting parameters.

1. INTRODUCTION

Baryons have been an object of an intensive theoretical study for a long time [1–11]. Both the perturbative dynamics and confinement interaction were considered decades ago [1–5] and a series of papers by Isgur and collaborators [7, 8] has clarified the structure of the baryon spectrum in good general agreement with experiment. In those works, dynamics was considered as QCD motivated and relativistic effects in kinematics have been accounted for. Recently, a more phenomenological approach based on the large-N_c expansion for baryons [12–15] was applied to baryon spectra [16, 17] and clearly demonstrated the most important operators forming the spectrum of 70-plet.

Summing up the information from the quark-based model, one has a picture of baryon spectra with a basically oscillator-type spectrum, modified by the presence of spin-dependent forces and other corrections. For example, the orbital excitation with $\Delta L = 1$ "costs" around 0.5 GeV, while the radial excitation (actually two types) amounts to around 0.8 GeV. Moreover, hyperfine splitting, which in experiment is large (for $\Delta - N$ system it is 0.3 GeV), is underestimated using perturbative forces with $\alpha_s \approx 0.4$, and spin–orbit splitting, typically small in experiment, needs some special cancellations in theory [18].

Moreover, some states cannot be well explained in the standard quark models. A good example is $N^*(1440)$, which is too low to be simply a radial excitation, and moreover its experimental electroproduction amplitudes [19] are in evident conflict with theory [20].

This example is probably not unique, and one can notice an interesting pattern in "radial" excitations of N, Δ, Λ, and Σ: in all cases, the three lowest states M_1, M_2, and M_3 have intervals $\Delta_1 \equiv M_2 - M_1 \sim 400$–$500$ MeV, $\Delta_2 \equiv M_3 - M_1 \sim 600$–$700$ MeV.

Namely, in

$N(939)$	$\Delta(1232)$	$\Lambda(1116)$	$\Sigma(1193)$
$N(1440)$	$\Delta(1600)$	$\Lambda(1600)$	$\Sigma(1660)$
$N(1710)$	$\Delta(1920)$	$\Lambda(1810)$	$\Sigma(1770)$
			$\Sigma(1880)$
$\Delta_1 = 500$	$\Delta_1 = 370$	$\Delta_1 = 480$	$\Delta_1 = 470$
$\Delta_2 = 770$	$\Delta_2 = 690$	$\Delta_2 = 700$	$\Delta_2 = 600$

one can see that Δ_2 corresponds to usual radial excitation, while the energy interval Δ_1 cannot be explained in a simple way in standard quark models.

One can say more about difficulties with the interpretation of the $\Lambda(1405)$ state, quantitative descriptions of ΔN transitions, etc. [19, 20].

In this situation, it sounds reasonable to apply new dynamical approaches that are directly connected to

*This article was submitted by the author in English.

the basic QCD Lagrangian and where all approximations can be checked both theoretically and numerically on the lattice.

The field correlator method (FCM) started in [21, 22] belongs here (for a review, see [23] and for more dynamical applications [24]). It is aimed at expressing all observables in terms of gauge-invariant field correlators. Its use is largely facilitated by recent observation on the lattice [25, 26] that the lowest bilocal correlator gives the dominant contribution to the quark–antiquark forces, while higher correlators contribute around 1%. The use of FCM for meson spectra [27, 28] has shown that gross features of spectra can be calculated through only string tension, while fine and hyperfine structure requires knowledge of other characteristics of bilocal correlator—the gluon correlation length [29], which is known from lattice data [30] and analytic calculations [31, 32].

In dynamical applications of the FCM to baryon spectra, two different schemes are currently used: the relativistic Hamiltonian method (RHM) and the method of Dirac orbitals. The first was suggested in [33, 34] and used for baryon Regge trajectories in [35, 36] and for magnetic moments in [37]. The second method was suggested in [38] and exploited to calculate baryon magnetic moments in [39].

Recently an important element was added to the RHM for baryons; namely, all spin-dependent forces between quarks have been calculated in the same Gaussian approximations [40]. To finalize the RHM for baryons, one still needs to construct the full baryonic Hamiltonian taking into account the energy of string motion, nonperturbative self-energy corrections [41], etc. The present paper is aimed at fulfilling this task. It contains the detailed derivation of the full baryonic Hamiltonian both in the c.m.s. and in the light-cone system of coordinates, simple estimates of spectra for spin-averaged masses, and a preparatory discussion of future explicit detailed calculations.

The paper is organized as follows. In Section 2, the $3q$ Green's function is written using the Fock–Feynman–Schwinger (FFS) representation [42]. In Section 3, the c.m. and relative coordinates are introduced and the einbein field $\mu(t)$ is introduced which will give rise to the quark constituent mass. In Section 4, the resulting effective action is quantized and the full c.m. Hamiltonian is explicitly written.

Section 5 is devoted to the derivation of the light-cone Hamiltonian, its physical interpretation, and correspondence to the partonic model.

In Section 6, the construction of the baryon wave function is discussed, as well as expansion of its coordinate part into a sum of hyperspherical harmonics and analytic estimates of spin-averaged spectra are given.

Spin-dependent forces are discussed in Section 7, and Section 8 is devoted to conclusions.

2. BARYON GREEN'S FUNCTION

One can define initial and final states of a baryon as a superposition of $3q$ states

$$\Psi_{\text{in,out}}(x^{(1)},x^{(2)},x^{(3)}) = \Gamma_{\text{in,out}} e_{a_1a_2a_3}\prod\psi^{a_i}_{\gamma_i}(x^{(i)},x^{(0)}), \tag{1}$$

where a_i are color indices, while γ_i contain both flavor and Dirac indices, and a sum over appropriate combinations of these last indices is assumed with Γ as coefficients. Moreover, $x^{(i)}$ and $x^{(0)}$ are coordinates of quarks and of the string junction, respectively.

The $3q$ Green's function can be written as

$$G_{3q}(x^{(i)}|y^{(k)}) = \left\langle \mathrm{tr}_Y \Gamma_{\text{out}} \prod_{i=1}^{3} S^{(i)}_{a_ib_i}(x^{(i)},y^{(i)})\Gamma_{\text{in}} \right\rangle, \tag{2}$$

where we have neglected the quark determinant and defined

$$\mathrm{tr}_Y = \frac{1}{6}\sum_{a_i,b_i} e_{a_1a_2a_3}e_{b_1b_2b_3} \tag{3}$$

and $S^{(i)}(x^{(i)},y^{(i)})$ is the quark Green's function in the external gluonic fields (vacuum and perturbative gluon exchanges). For the latter, one can use the exact FFS form [22, 24, 42]

$$S(x,y) = (m-\hat{D})\int_0^\infty ds (Dz)_{xy} e^{-K} W_z(x,y) \times \exp\left[g\int_0^s \sigma_{\mu\nu}F_{\mu\nu}(z(\tau))d\tau\right], \tag{4}$$

where W_z is the phase factor along the contour $C_z(x,y)$ starting at y and finishing at x, which goes along a trajectory which is integrated in $(Dz)_{xy}$, $K = m^2 s + (1/4)\int_0^s \dot{z}^2 d\tau$,

$$W_z(x,y) = P\exp\left(ig\int_y^x A_\mu dz_\mu\right), \tag{5}$$

and P is the ordering operator, while

$$\sigma_{\mu\nu}F_{\mu\nu} = \begin{pmatrix} \boldsymbol{\sigma}\cdot\mathbf{B} & \boldsymbol{\sigma}\cdot\mathbf{E} \\ \boldsymbol{\sigma}\cdot\mathbf{E} & \boldsymbol{\sigma}\cdot\mathbf{B}\end{pmatrix}. \tag{6}$$

Here, $\mathbf{E}$ and $\mathbf{B}$ are color-electric and color-magnetic fields, respectively. The average over gluon

fields, implied in (2) by angular brackets, is convenient to perform after the non-Abelian Stokes theorem is applied to the product of W_z.

Consider to this end, the gauge-invariant quantity

$$W_3(x,y) \equiv \mathrm{tr}_Y \prod_{i=1}^{3} W_{z_i}(x,y). \tag{7}$$

We can now write the non-Abelian Stokes theorem expressing A_μ in W_{z_i} (e.g., using a general contour gauge) through $F_{\mu\nu}(u,x^{(0)}) = \phi(x^{(0)},u)F_{\mu\nu}(u)\phi(u,x^{(0)})$, where $\phi(x,y)$ is a parallel transporter, and it is convenient to choose $x^{(0)}$ at the common point $x = x^{(1)} = x^{(2)} = x^{(3)}$.

Making final points also coincident, $y = y^{(1)} = y^{(2)} = y^{(3)}$, one can use the identity

$$\mathrm{tr}_Y \phi_{a_1b_1}(x,y)\phi_{a_2b_2}(x,y)\phi_{a_3b_3}(x,y) = 1 \tag{8}$$

and rewrite W_3 as (the simplest way to derive (9) and subsequent equations is to choose in the gauge invariant expressions (7), (9) the contour gauge, where $\phi_{ab} = \delta_{ab}$)

$$\langle\langle W_3(x,y)\rangle\rangle = \mathrm{tr}_Y \exp\sum_{n=0}^{\infty}\frac{(ig)^n}{n!} \times \int\limits_{\sum S_i} \langle\langle F(1)\dots F(n)\rangle\rangle ds(1)\dots ds(n), \tag{9}$$

where, in $F(i)$ and the surface elements $ds(i)$, the Lorentz indices and coordinates are omitted, and double angular brackets imply cumulants, as defined in [23]. Note that integration in (9) is over all three lobes S_i, made of contours $C_{z_i}(x,y)$ and the string-junction trajectory $z^{(Y)}(s)$, with $z^{(Y)}(0) = y$, $z^{(Y)}(1) = x$. The actual form of $z^{(Y)}(s)$ is defined by the minimal action principle and does not necessarily coincide with the trajectory of the center of mass of the $3q$ system.

For this case of a three-lobe loop as well as for several separate loops, one can use the following gauge-invariant averaging formula, where both field correlators are transported to one point x and a, b, and c are fundamental color indices:

$$\langle F(u,x)_{ab}F(v,x)_{cd}\rangle = \frac{\langle\mathrm{tr}(F(u,x)F(v,x))\rangle}{N_c^2-1}\left(\delta_{ad}\delta_{bc} - \frac{1}{N_c}\delta_{ab}\delta_{cd}\right). \tag{10}$$

Now, whenever $F(u,x)$ and $F(v,x)$ are on the same lobe, then indices b and c coincide and one obtains

$$\mathrm{tr}_Y\langle F(u,x)_{ab}F(v,x)_{bd}\rangle = \frac{\langle\mathrm{tr}(F(u,x)F(v,x))\rangle}{N_c}, \tag{11}$$

where (8) was used. For u and v on different lobes, one instead has

$$\mathrm{tr}_Y\langle F(u,x)_{ab}F(v,x)_{cd}\rangle = -\frac{\langle\mathrm{tr}(F(u,x)F(v,x))\rangle}{N_c(N_c-1)}. \tag{12}$$

As the last step in this chapter, one can include the quark spin operator $\sigma_{\mu\nu}F_{\mu\nu}$ in the cluster expansion (9), with the help of the relation

$$\left\langle F_{\mu\nu}(u,x)\exp\left[ig\int\limits_S F_{\lambda\sigma}(v,x)ds_{\lambda\sigma}(v)\right]\right\rangle = \frac{1}{ig}\frac{\delta}{\delta s_{\mu\nu}(v)}\left\langle\exp\left[ig\int\limits_S F_{\lambda\sigma}(v,x)ds_{\lambda\sigma}(v)\right]\right\rangle. \tag{13}$$

Exponentiating the operator $F_{\mu\nu}$, one arrives at the shift operator $\exp\left[\frac{1}{i}\left(s_{\mu\nu}\frac{\delta}{\delta s_{\mu\nu}(u)}\right)\right]$ and finally gets [cf. Eq. (4)]

$$\left\langle W_3\exp\left[g\sum_{i=1}^{3}\sigma_{\mu\nu}^{(i)}\int\limits_0^{S_i}F_{\mu\nu}(z^{(i)}(\tau^{(i)}))d\tau^{(i)}\right]\right\rangle \equiv \langle W_3\exp(g\sigma F)\rangle = \mathrm{tr}_Y\exp\left[\sum_{n=0}^{\infty}\frac{(ig)^n}{n!} \times \int\limits_{\sum S_i}\langle\langle F(1)\dots F(n)\rangle\rangle d\rho(1)\dots d\rho(n)\right], \tag{14}$$

where we have defined $d\rho(n) = \sum_{i=1}^{3} d\rho^{(i)}(n)$,

$$d\rho^{(i)}(n) = ds^{(i)}_{\mu_n\nu_n}(u^{(n)}) + \frac{1}{i}\sigma^{(i)}_{\mu_n\nu_n}d\tau^{(i)}(n). \tag{15}$$

Here, index $i = 1,2,3$ refers to three lobes S_i of the total surface, and it is understood that, whenever $F(i)$ under the cumulant sign $\langle\langle\dots\rangle\rangle$ is multiplied by $d\tau^{(i)}$, it is taken at the point $z^{(i)}(\tau_n^{(i)})$, lying on the quark trajectory $z^{(i)}(\tau)$ which forms the boundary of the lobe (i).

Inserting (4) and (14) into (2), one obtains

$$G_{3q}(x,y) = \mathrm{tr}_{\mathrm{L}}\left[\Gamma_{\mathrm{out}}\prod_{i=1}^{3}(m_i - \hat{D}^{(i)})_R \times \int\limits_0^{\infty} ds_i (Dz^{(i)})_{xy}e^{-K_i}\langle W_3\exp(g\sigma F)\rangle\Gamma_{\mathrm{in}}\right]. \tag{16}$$

Here, tr_{L} is the trace over Lorentz indices, and $(m_i - \hat{D}^{(i)})_R$ is the value of operator $(m_i - \hat{D}^{(i)})$

when acting on the path integral, which was found in [43] to be

$$(m_i - \hat{D}^{(i)})_R = m_i - i\hat{p}^{(i)}. \tag{17}$$

Here, $p^{(i)}$ is the operator of momentum of the quark i. Equations (16) and (14) give an exact and most general expression for the $3q$ Green's function, which is, however, intractable if all field correlators are retained there.

To simplify, we shall use the observation from lattice calculations [25, 26] that the lowest (Gaussian) correlator gives the dominant contribution (more than 95%) to the static $Q\bar{Q}$ quark potential. Assuming that the situation is similar for the $3Q$ case and also for light baryons, we now retain in (14) and (9) only the lowest cumulant $\langle\langle FF\rangle\rangle$ and express it in terms of scalar functions D and D_1 as in [21]:

$$\frac{g^2}{N_c}\langle \mathrm{tr}(F_{\mu\nu}(u,x)F_{\rho\lambda}(v,x))\rangle \tag{18}$$
$$= (\delta_{\mu\rho}\delta_{\nu\lambda} - \delta_{\mu\lambda}\delta_{\nu\rho})D(u-v)$$
$$+ \frac{1}{2}\left[\frac{\partial}{\partial u_\mu}(u-v)_\rho\delta_{\nu\lambda} + \text{perm.}\right]D_1(u-v).$$

Here, we have replaced parallel transporters $\phi(u,x)\phi(x,v)$ by the straight-line transporter $\phi(u,v)$, since, for the generic situation with $|u-v| \sim T_g$, $|u-x| \sim |v-x| \sim R$, $R \gg T_g$, the former and the latter are equal up to the terms $O((T_g/R)^2)$. Now, in view of (12) and (13), one can write in Gaussian approximation

$$\langle W_3 \exp(g\sigma F)\rangle = \exp\left[-\frac{g^2}{2N_c}\right. \tag{19}$$
$$\times \sum_{i=1}^{3}\int \langle \mathrm{tr}(F(u)F(v))\rangle d\rho^{(i)}(u)d\rho^{(i)}(v)$$
$$\left. + \frac{g^2}{N_c(N_c-1)}\sum_{i<j}\int \langle \mathrm{tr}(F(u)F(v))\rangle d\rho^{(i)}(u)d\rho^{(j)}(v)\right],$$

where $d\rho^{(i)}$ is defined in (15). Here, $\langle \mathrm{tr}FF\rangle$ can be expressed in terms of D and D_1, and one has a closed expression for the term $\langle W_3 \exp(g\sigma F)\rangle$, which acts as a dynamical kernel in the path integral (16).

Now, for large sizes of Wilson loop W_3, such that $R^{(i)} \gg T_g$, one can discard D_1 and retain D in (18), since only the latter ensures an area law (and, moreover, lattice data [30] show that $D_1 \ll D$). Then, the diagonal terms in the sum of the exponent in (19) can be written as (neglecting the spin-dependent part for the moment)

$$\langle W_3\rangle_{\mathrm{diag}} = \exp(-\sigma(S_1+S_2+S_3)), \tag{20}$$

where S_i is the area of the minimal surface between trajectory of quark (i) and trajectory of string junction (Y trajectory), and we have used the relation [21, 22]

$$\sigma = \frac{1}{2}\int d^2x D(x). \tag{21}$$

Let us turn now to nondiagonal terms in (19). Since $D(x)$ and $D_1(x)$ die exponentially fast for $x > T_g$ [30–32], only a region of width T_g around the Y trajectory contributes to these terms, which one can write as

$$V_{\mathrm{nondiag}}T = \sum_{i<j} V^{(ij)}_{\mathrm{nondiag}} = -\frac{g^2}{N_c(N_c-1)} \tag{22}$$
$$\times \sum_{i\neq j}\int \langle \mathrm{tr}(F_{\mu\nu}(u)F_{\rho\lambda}(v))\rangle ds^{(i)}_{\mu\nu}(u)ds^{(j)}_{\rho\lambda}(v).$$

Separating out time components, $u = (u_4, \mathbf{u})$ and $v = (v_4, \mathbf{v})$, one can write for the D contribution

$$V^{(D)}_{\mathrm{nondiag}} = \frac{1}{N_c-1}\sum_{i<j}\int D(u^{(i)}-v^{(j)})d(u^{(i)}_\parallel - v^{(j)}_\parallel)d\left(\frac{u^{(i)}_\perp + v^{(j)}_\perp}{2}\right)d(u^{(i)}_4 - v^{(j)}_4), \tag{23}$$

where we have introduced for $\mathbf{u}$ and $\mathbf{v}$ parallel and transverse components on the lobe S_i with respect to the lobe S_j.

Since $|u^{(i)}-v^{(j)}| = [(u^{(i)}_4 - v^{(j)}_4)^2 + (u^{(i)}_\parallel - v^{(j)}_\parallel)^2 + (u^{(i)}_\perp - v^{(j)}_\perp)^2]^{1/2}$ grows fast with $|u_\perp - v_\perp|$, one can estimate (20), (23) as

$$V^{(D)}_{\mathrm{nondiag}} \sim \sigma T_g, \quad V^{(D)}_{\mathrm{diag}} = \sigma(r^{(1)} + r^{(2)} + r^{(3)}), \tag{24}$$

where $\mathbf{r}^{(i)} = \mathbf{z}^{(i)} - \mathbf{z}^{(Y)}$, i.e., the difference of quark and string-junction coordinates at a given moment of time. Being always smaller than $V^{(D)}_{\mathrm{diag}}$ for large $r^{(i)}$, nevertheless, $V^{(D)}_{\mathrm{nondiag}}$ brings about an interesting effect for small $r^{(i)}$. Estimating integrals in (23) for small $r^{(i)}$, $r^{(i)} \lesssim T_g$, and using for $D(x)$ the Gaussian form, $D(x) = D(0)\exp(-x^2/(4T_g^2))$, one has

$$V_{\mathrm{conf}} = V_{\mathrm{diag}} + V_{\mathrm{nondiag}} = \frac{\sigma}{4\sqrt{\pi}T_g}\sum_{i<j}\left(\mathbf{r}^{(i)} - \mathbf{r}^{(j)}\right)^2. \tag{25}$$

It is clear that for a symmetric configuration $r^{(1)} = r^{(2)} = r^{(3)}$, one has $V_{\rm conf} = 0$. To study this cancellation further, let us take into account that, if the triangle made of quarks has all angles less than 120° (since the string junction is at the Torricelli point), then the string junction is inside this triangle. In this case, one can write

$$\sum_{i<j} (\mathbf{r}^{(i)} - \mathbf{r}^{(j)})^2 = 2((r^{(1)})^2 + (r^{(2)})^2 + (r^{(3)})^2) + r^{(1)}r^{(2)} + r^{(2)}r^{(3)} + r^{(1)}r^{(3)}; \quad (26)$$

i.e., $V_{\rm conf}$ vanishes quadratically in differences of quark distances from the string junction. In practice, this brings about a strong effective cancellation in $V_{\rm conf}$ for a $3q$ system with equal masses at approximately equal distances. Numerically and analytically, this fact was discovered first in [44] for a static $3Q$ potential. It was argued there that $V_{\rm nondiag}$ brings about a smaller slope of $V(3Q)$ at small to intermediate distances, as was indeed found on the lattice [45]. An assumption that a triangular $3q$ string configuration is responsible for the smaller slope, however, cannot explain it, since that configuration is impossible to construct in a gauge-invariant way [46]. Explicit expressions for $V^{(3)}$ in the general case are given in [46]. Here and in [46] a missing in [44] factor of $-1/2$ in front of $V_{\rm nondiag}$ is restored.

3. GAUSSIAN REPRESENTATION FOR THE EFFECTIVE ACTION OF QUARKS AND STRING

Consider now the exponent of the FFS representation for the $3q$ Green's function (16), (19) in the simplified case when (i) spin interaction is neglected and (ii) large distances $|\mathbf{R}_i| \gg T_g$ are taken into account.

In this situation, one can use the form (20) instead of (19) and write the exponential term in (16) as

$$G_{3q}(x,y) = {\rm tr}_{\rm L}\left[\Gamma_{\rm out}\prod(m_i - i\hat{p}_i)\int_0^\infty ds_i (Dz^{(i)})_{xy}\Gamma_{\rm in}\right] e^{-A}, \quad (27)$$

where A plays the role of effective action,

$$A = \sum_{i=1}^{3}(K_i + \sigma S_i). \quad (28)$$

Our purpose is finally to construct the effective Hamiltonian, considering A as an effective action for three quarks and the composite string with the string junction. To achieve this goal, one must (i) go over from the proper time s_i to real time integration in $4d$ Euclidean spacetime (later on to be transformed into Minkowskian time), and (ii) transform the Nambu–Goto form of the lobe area S_i [see below in (35)] into a quadratic form, as is necessarily done in string theory [since otherwise the path integral (27) is not properly defined]. Both operations are the same as in the $q\bar{q}$ case, considered in [34], and we shall follow closely that procedure.

The resulting Hamiltonian depends on the choice of the hypersurface, and for the $q\bar{q}$ system both the c.m. [34] and light-cone [47, 48] cases were considered.

Below, in the next chapter, the c.m. Hamiltonian will be derived, and to this end we choose the hyperplane intersecting all three quark trajectories and the Y trajectory at one common time t, to be considered in the interval $0 \le t \le T$, so that the quark coordinates are $z^{(i)} = (t, \mathbf{z}^{(i)})$, and the string junction coordinate is $z^{(Y)} = (t, \mathbf{z}^{(Y)})$.

Now, one can make a change of variables, introducing the einbein variable [34, 49] $\mu(t)$ for a given trajectory $z^{(i)}(\tau^{(i)})$, $0 \le \tau \le s$, and one defines

$$d\tau^{(i)} \equiv \frac{dz_4^{(i)}(\tau^{(i)})}{dz_4^{(i)}(\tau^{(i)})/d\tau^{(i)}} = \frac{dz_4^{(i)}(\tau^{(i)})}{2\mu_i(z_4^{(i)})}, \quad (29)$$

so that kinetic term K_i becomes

$$K_i = \int_0^T dt\left[\frac{m_i^2}{2\mu_i(t)} + \frac{\mu_i(t)}{2}(\dot{\mathbf{z}}^2(t) + 1)\right]. \quad (30)$$

The transition from the integral over $ds_i dz_4^{(i)}$ to the integral over $D\mu^{(i)}(t)$ is known to have a nonsingular Jacobian (see Appendix A of the second paper in [34] for more details and explanations),

$$D\mu^2(t) \sim \exp\left[-i\frac{\rm const}{\varepsilon}\int_0^T \sqrt{\mu^2(t)}dt\right] dsDz_4(t), \quad (31)$$

where $\varepsilon \sim 1/\Lambda$, and Λ is an ultraviolet cutoff parameter.

Hence, the integrals in (27) can be rewritten as

$$\prod_i ds_i D^4 z^{(i)} \to \prod D\mu_i D^3 z^{(i)}, \quad (32)$$

where the integration measure for $D\mu_i$ can be specified further to be [34] $D\mu(t) \sim \prod_{n=1}^{N} d\mu(t_n)/\mu^{3/2}(t_n)$. As a next step, one introduces the c.m. and relative coordinates

$$\dot{\mathbf{R}} = \frac{1}{\mu_+(t)}\sum_{i=1}^{3}\mu_i(t)\dot{\mathbf{z}}^{(i)}(t), \quad (33)$$

$$\boldsymbol{\xi} = \sqrt{\frac{3}{2}}\left(\frac{\mu_1\dot{\mathbf{z}}^{(1)} + \mu_2\dot{\mathbf{z}}^{(2)}}{2} - \mu_3\dot{\mathbf{z}}^{(3)}\right)\frac{1}{\mu_+},$$

$$\boldsymbol{\eta} = \frac{\mu_1\dot{\mathbf{z}}^{(1)} - \mu_2\dot{\mathbf{z}}^{(2)}}{\mu_+\sqrt{2}}.$$

Here, $\mu_+ = \sum_{i=1}^{3}\mu_i$.

From our discussion above, it is clear that the time t coincides with the fourth component of the c.m. coordinate, $t = R_4$, and the whole quark kinetic term in (28) is

$$\sum_{i=1}^{3} K_i = \int_0^T dt\left[\sum\left(\frac{m_i^2}{2\mu_i} + \frac{\mu_i}{2}\right)\right. \quad (34)$$
$$\left. + \frac{1}{2}\mu_+(t)\dot{\mathbf{R}}^2 + \frac{1}{2}\mu_\eta\dot{\boldsymbol{\eta}}^2 + \frac{1}{2}\mu_\xi\dot{\boldsymbol{\xi}}^2\right].$$

Here, μ_η and μ_ξ will be found below, (42). The area-law term in (28) can be written as follows:

$$\sum_{i=1}^{3}\sigma S_i \quad (35)$$
$$= \sigma\sum_{i=1}^{3}\int_0^T dt\int_0^1 d\beta_i\sqrt{(\dot{w}_\mu^{(i)})^2(w'^{(i)})^2 - (\dot{w}_\mu^{(i)}w_\mu'^{(i)})^2},$$

where $w_\mu^{(i)}(t,\beta)$ is the ith string position at time t and coordinate β along the string and the dot and prime signs have the meaning of time and β derivatives, respectively. In the spirit of our approach, one should take the world sheets of the strings corresponding to the minimal area of the sum of surfaces between quark trajectories and Y trajectory of the string junction. At this point, we make a simplifying approximation [33, 34] that strings at any moment t can be represented by pieces of straight lines. In this way, one disregards string excitations (hybrids) and mixing between these excitations and ground-state baryons. This can be done for ground states since the mass gap for string excitations is around 1 GeV [24].

For higher excited states, the mixing should be taken into account analogously to what was done in the meson sector [50].

Thus, one writes

$$w_\mu^{(i)}(t,\beta) = z_\mu^{(i)}(t)\beta + z_\mu^{(Y)}(t)(1-\beta), \quad (36)$$

and time derivatives of $w_\mu^{(i)}$ in (35) can be replaced using (36) by time derivatives of $z_\mu^{(i)}$ and $z_\mu^{(Y)}$. Since also the string junction position is expressed through the quark coordinates, the string does not possess dynamical degrees of freedom of its own (in this straight-line approximation). To recover the latter, one can use background perturbation theory and consider the states with $3q$ and additional valence gluon(s). The latter describes gluonic excitation of baryons and has its own dynamical degree of freedom. Note that this way of systematic description of string excitation is different from the ad hoc assumption that the string is described by Nambu–Goto action with all dynamical string degrees of freedom included,which does not follow from the QCD Lagrangian.

Consider now the string-junction trajectory. In line with the whole approach, one requires that, at any given moment, $z_\mu^{(Y)}(t)$ occupy the position which gives the minimal string energy; i.e., $z_\mu^{(Y)}(t)$ should coincide with the Torricelli point, giving the minimum of the sum of lengths of three strings:

$$L = \sum_{i=1}^{3}|\mathbf{z}^{(i)}(t) - \mathbf{z}^{(Y)}(t)|, \quad \frac{\partial L}{\partial z_k^{(Y)}(t)} = 0. \quad (37)$$

Therefore, $\mathbf{z}^{(Y)}(t)$ is not an independent dynamical degree of freedom and $\dot{\mathbf{z}}^{(Y)}$ is expressed in terms of $\dot{\mathbf{z}}^{(i)}$, $i = 1,2,3$.

Now, one can introduce (as is usual in string theory [51]) the auxiliary fields (einbein fields [49]) to replace the intractable square-root terms in (35) by quadratic expressions. In this way, one writes

$$S_i = \frac{1}{2\tilde{\nu}_i}[(\dot{w}^{(i)})^2 + (\sigma\tilde{\nu}_i)^2(r^{(i)})^2 \quad (38)$$
$$- 2\eta_i(\dot{w}_k^{(i)}r_k^{(i)}) + (\eta_i)^2(r^{(i)})^2].$$

Here, $\tilde{\nu}_i(t,\beta) \geq 0$ and $\eta_i(t,\beta)$ are two einbein fields [which are integrated out to yield back the form (35)], and $\mathbf{r}^{(i)} = \mathbf{z}^{(i)} - \mathbf{z}^{(Y)}$. As a result, one has for the $3q$ Green's function

$$G_{3q}(x,y) = \int DRD\xi D\eta\prod_{i=1}^{3}D\mu_i D\tilde{\nu}_i D\eta_i \mathrm{tr}(\Gamma_{\mathrm{out}}(m_i - i\hat{p}_i)\Gamma_{\mathrm{in}})e^{-A}. \quad (39)$$

4. QUANTIZATION OF THE STRINGS AND DERIVATION OF THE 3q-STRING HAMILTONIAN

The action (28) using (34), (36), and (38) can be written as

$$A=\int\limits_0^t dt\sum_{i=1}^3\left[\frac{m_i^2}{2\mu_i}+\frac{\mu_i\dot{\mathbf{z}}_i^2}{2}+\frac{\mu_i}{2}\right. \tag{40}$$
$$+\int\limits_0^1 d\beta_i\frac{\sigma^2r_i^2}{2\nu_i}+\frac{1}{2}\int\limits_0^1 d\beta_i\nu_i(\dot{\mathbf{r}}_i\beta_i+\dot{\mathbf{z}}^{(Y)})^2$$
$$\left.+\frac{1}{2}\int\limits_0^1 d\beta_i\nu_i\eta_i^2\mathbf{r}_i^2-\int\limits_0^1 d\beta_i\nu_i\eta_i\mathbf{r}_i(\dot{\mathbf{r}}_i\beta_i+\dot{\mathbf{z}}^{(Y)})\right],$$

where we have defined $\nu_i=1/\tilde{\nu}_i$ and $\mathbf{r}_i=\mathbf{z}^{(i)}-\mathbf{z}^{(Y)}$, $z_\mu^{(Y)}(t)=(t,\mathbf{z}^{(Y)})$.

As the next step, we introduce the c.m. coordinate $\mathbf{R}$ and Jacobi coordinates $\boldsymbol{\xi},\boldsymbol{\eta}$ as follows [36]:

$$\dot{z}_k^{(1)}=\dot{R}_k+\left(\frac{\mu\mu_3}{\mu_+(\mu_1+\mu_2)}\right)^{1/2}\dot{\xi}_k \tag{41}$$
$$-\left(\frac{\mu\mu_2}{\mu_1(\mu_1+\mu_2)}\right)^{1/2}\dot{\eta}_k,$$
$$\dot{z}_k^{(2)}=\dot{R}_k+\left(\frac{\mu\mu_3}{\mu_+(\mu_1+\mu_2)}\right)^{1/2}\dot{\xi}_k$$
$$+\left(\frac{\mu\mu_1}{\mu_2(\mu_1+\mu_2)}\right)^{1/2}\dot{\eta}_k,$$
$$\dot{z}_k^{(3)}=\dot{R}_k-\left(\frac{\mu(\mu_1+\mu_2)}{\mu_+\mu_3}\right)^{1/2}\dot{\xi}_k,$$

with the inverse expressions

$$\dot{R}_k=\frac{1}{\mu_+}\sum_{i=1}^3\mu_i\dot{z}_k^{(i)}, \tag{42}$$
$$\dot{\eta}_k=(\dot{z}_k^{(2)}-\dot{z}_k^{(1)})\left(\frac{\mu_1\mu_2}{\mu(\mu_1+\mu_2)}\right)^{1/2},$$
$$\dot{\xi}_k=\left(\frac{\mu_3}{\mu_+(\mu_1+\mu_2)\mu}\right)^{1/2}(\mu_1\dot{z}_k^{(1)}+\mu_2\dot{z}_k^{(2)}$$
$$-(\mu_1+\mu_2)\dot{z}_k^{(3)}).$$

In (41) and (42), the mass μ is arbitrary and drops out in the final expressions.

Using (41), one can rewrite the kinetic part of the action as follows:

$$\sum_{i=1}^3 K_i=\int\limits_0^T dt\Big[\sum_{i=1}^3\left(\frac{m_i^2}{2\mu_i}+\frac{\mu_i}{2}\right) \tag{43}$$
$$+\frac{1}{2}\mu_+\dot{\mathbf{R}}^2+\frac{1}{2}\mu(\dot{\boldsymbol{\eta}}^2+\dot{\boldsymbol{\xi}}^2)\Big].$$

The string part of the action can be transformed using (38) and integrating over η_i to the form

$$\exp\left(\sum_{i=1}^3\sigma S_i\right)=\exp\left\{-\int\limits_0^T dt\right. \tag{44}$$
$$\times\frac{1}{2}\sum_{i=1}^3\int d\beta_i\left[\nu_i\left((\dot{\mathbf{r}}^{(i)}\beta_i+\dot{\mathbf{z}}^{(Y)})^2\right.\right.$$
$$\left.\left.-[(\dot{\mathbf{r}}^{(i)}\beta+\dot{\mathbf{z}}^{(Y)})\mathbf{r}^{(i)}]^2\frac{1}{(\mathbf{r}^{(i)})^2}\right)+\frac{\sigma^2\mathbf{r}_i^2}{\nu_i}\right]\Big\}.$$

At this point, it is important to note that $\mathbf{z}^{(Y)}$ is not a dynamical variable, since it is defined by the minimum of the action.

Taking this minimum at a given moment, one arrives at the definition of $\mathbf{z}^{(Y)}(t)$ as a Torricelli point, which is to be expressed through the positions $\mathbf{z}^{(i)}(t)$:

$$\mathbf{z}^{(Y)}(t)=f(\mathbf{z}^{(1)}(t),\mathbf{z}^{(2)}(t),\mathbf{z}^{(3)}(t)), \tag{45}$$

where the function f is defined explicitly in [36]. Therefore $\dot{\mathbf{z}}^{(Y)}(t)$ is also expressed in terms of $\dot{\mathbf{z}}^{(i)}(t)$ or in terms of $\dot{\mathbf{R}}(t)$ and $\dot{\mathbf{r}}^{(i)}(t)$.

Below, a simplified procedure will be used in which one identifies $\mathbf{z}^{(Y)}$ with the c.m. coordinate $\mathbf{R}$, which is true on average for equal-mass quarks. Explicit formulas for the general case $\mathbf{z}^{(Y)}\neq\mathbf{R}$ are given in the Appendix. We are now in position to get the final coordinates $\boldsymbol{\eta}$, $\boldsymbol{\xi}$ or their linear combinations $\mathbf{r}^{(i)}\equiv\mathbf{z}^{(i)}-\mathbf{R}$ read from (41). To this end, we replace $\dot{\mathbf{z}}^{(Y)}$ by $\dot{\mathbf{R}}$ in (44) and integrate over $D\dot{\mathbf{R}}$ in both expressions (43) and (44) in the same way as was done in the second paper of [34] {Eqs. (37)–(49) in [34]}, with the result

$$\tilde{A}=\int\limits_0^T dt\frac{1}{2}\Big\{\sum_{i=1}^3\left(\frac{m_i^2}{\mu_i}+\mu_i\right) \tag{46}$$
$$+\mu(\dot{\boldsymbol{\eta}}^2+\dot{\boldsymbol{\xi}}^2)+\sum_{i=1}^3\int\limits_0^1 d\beta_i$$
$$\times\left[\nu_i(\beta_i)+\frac{\sigma^2(\mathbf{r}^{(i)})^2}{\nu_i}\right.$$
$$\left.+\nu_i\beta_i^2\left((\dot{\mathbf{r}}^{(i)})^2-\frac{(\dot{\mathbf{r}}^{(i)}\cdot\mathbf{r}^{(i)})^2}{(\mathbf{r}^{(i)})^2}\right)\right]\Big\}.$$

The last term on the right-hand side of (46) can be rewritten as $\nu_i\beta_i^2(\dot{\mathbf{r}}^{(i)}\times\dot{\mathbf{r}}^{(i)})^2/(\mathbf{r}^{(i)})^2$ and disappears when the partial angular momentum l_i vanishes.

In this case, (46) is simplified, and using in (46) $\dot{\mathbf{r}}^{(i)}$ instead of $\dot{\boldsymbol{\eta}}$ and $\dot{\boldsymbol{\xi}}$, one gets in a standard way the Hamiltonian

$$H_0 = \frac{1}{2}\sum_{i=1}^{3}\left[\frac{m_i^2}{\mu_i} + \mu_i + \frac{\mathbf{p}_i^2}{\mu_i} + \int_0^1 d\beta_i \left(\nu_i(\beta_i) + \frac{\sigma^2(\mathbf{r}^{(i)})^2}{\nu_i}\right)\right]. \quad (47)$$

One can now apply to (47) the minimization procedure to define μ_i and ν_i from the conditions

$$0 = \frac{\partial H_0}{\partial \mu_i} = \frac{\partial H_0}{\partial \nu_i}, \quad (48)$$

which yields

$$\mu_i = \sqrt{\mathbf{p}_i^2 + m_i^2}, \quad \nu_i = \sigma|\mathbf{r}_i|. \quad (49)$$

Note that, in this case ($l_i = 0$, $i = 1,2,3$), ν_i do not depend on β_i and they play the role of potential. Inserting (49) into (47), one obtains the form well known from the standard relativistic quark model (RQM) [1–9]

$$H_{\mathrm{RQM}} = \sum_{i=1}^{3}\left(\sqrt{\mathbf{p}_i^2 + m_i^2} + \sigma|\mathbf{r}^{(i)}|\right). \quad (50)$$

Note that (50) is valid under assumptions that (i) string junction $\mathbf{z}^{(Y)}$ coincides with the c.m.; (ii) $\sum_{i=1}^{3}\mathbf{p}_i = 0$; and (iii) all angular momenta of quarks $l_i, i = 1,2,3$, are zero, so that only the radial part of momentum $\mathbf{p}_i$ enters into (50). However, in the RQM, the form (50) is used without condition (3). As one will see in what follows, at nonzero l_i, the Hamiltonian H_0 will be modified, and for not large l_i, $l_i \le 4$, this modification can be taken into account as a string correction $\Delta H_{\mathrm{string}}$ similarly to the meson case in [27, 34].

We consider now the general case of $l_i > 0$. To this end, we separate transverse and longitudinal components for each $\mathbf{r}^{(i)}$ as follows (omitting index i for a moment):

$$\dot{\mathbf{r}}^2 = \frac{1}{\mathbf{r}^2}\{(\mathbf{r}\cdot\mathbf{r})^2 + (\dot{\mathbf{r}}\times\mathbf{r})^2\}, \quad (51)$$

and correspondingly define transverse and longitudinal momenta,

$$p_r^2 = \frac{(\mathbf{p}\cdot\mathbf{r})^2}{r^2} = \frac{(\mu\mathbf{r}\cdot\dot{\mathbf{r}})^2}{r^2}, \quad (52)$$

$$p_T^2 = \frac{(\mathbf{p}\times\mathbf{r})^2}{r^2} = \left(\mu + \int_0 d\beta\beta^2\nu(\beta)\right)^2\frac{(\dot{\mathbf{r}}\times\mathbf{r})^2}{r^2}. \quad (53)$$

One can now derive the Hamiltonian from (46) in the usual way,

$$H = \sum_{i=1}^{3}\left[\frac{m_i^2 + p_{r_i}^2}{2\mu_i} + \frac{\mu_i}{2} + \frac{\hat{l}_i^2/r_i^2}{2(\mu_i + \int_0^1 d\beta_i\beta_i^2\nu_i(\beta_i))} + \frac{\sigma^2}{2}\int_0^1\frac{d\beta_i}{\nu_i(\beta_i)}\mathbf{r}_i^2 + \frac{1}{2}\int_0^1\nu_i(\beta_i)d\beta_i\right]. \quad (54)$$

This is a general form for any values of l_i; the limit of $l_i \to 0$ is obtained in (50). Now, we shall derive the opposite limit $l_i \to \infty$. As in the meson case, one can argue that in this case $\mu_i \ll \nu_i$ and one can use the quasiclassical method and retain in (54) only the last three terms, expanding them around the stationary point at $r^{(i)} = r_0^{(i)}$, where

$$(r_0^{(i)})^2 = \left[\frac{\hat{l}_i^2}{2(\mu_i + \int_0^1 d\beta_i\beta_i^2\nu_i(\beta_i))\sigma^2\int_0^1 d\beta_i/\nu_i(\beta_i)}\right]^{1/2}. \quad (55)$$

Inserting (55) back into (54), one obtains the following quasiclassical energy of the ith string, $E = \sum_{i=1}^{3}E_i$:

$$E_i = \sigma\sqrt{\hat{l}_i^2}\left(\frac{\int_0^1 d\beta_i\nu_i^{-1}}{\int_0^1 d\beta_i\beta_i^2\nu_i}\right)^{1/2} + \frac{1}{2}\int_0^1\nu_i d\beta_i, \quad (56)$$

and from the stationary point of E_i, $\delta E_i/\delta\nu_i(\beta_i) = 0$, one has

$$\nu_i(\beta_i) = \sqrt{\frac{2}{\pi}}(1-\beta_i^2)^{-1/2}. \quad (57)$$

Inserting (57) into (56), one finally obtains the energy of rotating string

$$E_i^2 = 2\pi\sigma\sqrt{\hat{l}_i^2}, \quad \hat{l}_i^2 \equiv l_i(l_i+1). \quad (58)$$

This result shows that our general baryonic Hamiltonian indeed admits a simple rotating string limit at large l_i, as was in the case of mesonic Hamiltonian.

The difference from the mesonic case is, however, that, for the $3q$ system, one should be careful in proper exclusion of the c.m. motion and in quantizing angular momenta l_i, which should add up to a total angular momentum $\mathbf{L} = \sum_{i=1}^{3}\mathbf{l}_i$. To do this, one should go over from $\mathbf{r}^{(i)}$, $\mathbf{l}_i$ to the independent Jacobi coordinates and momenta $\boldsymbol{\xi}$, $\boldsymbol{\eta}$, $\mathbf{l}_\xi$, $\mathbf{l}_\eta$ which add up to $\mathbf{L}$ as $\mathbf{L} = \mathbf{l}_\xi + \mathbf{l}_\eta$.

To accomplish this task, one should express $r_k^{(i)} = z_k^{(i)} - z_k^{(Y)}$ using (41) and the Appendix through $\boldsymbol{\xi}$, $\boldsymbol{\eta}$, and $\mathbf{l}_i$ through $\mathbf{l}_\xi$, $\mathbf{l}_\eta$, and insert it into (54), which makes the whole expression rather complicated and not very tractable. Instead, we adopt here another strategy and consider the contribution of string rotation as a correction, similarly to the case of mesons [34], where this approach has proved to be successful up to $L = 4$ [27]. Therefore, we shall represent the Hamiltonian (54) as a sum of unperturbed term H_0 plus a string correction ΔH_{string}, which should work with accuracy better than 5% up to $l \approx 3$–4,

$$H = H_0 + \Delta H_{\text{string}}, \tag{59}$$

where we have defined

$$H_0 = \sum_{i=1}^{3}\left(\frac{m_i^2}{2\mu_i} + \frac{\mu_i}{2}\right) + \frac{\mathbf{p}_\xi^2 + \mathbf{p}_\eta^2}{2\mu} + V_{\text{conf}}(\mathbf{r}_1, \mathbf{r}_2, \mathbf{r}_3) \tag{60}$$

and

$$V_{\text{conf}} = \sigma \sum_{i=1}^{3} |\mathbf{z}^{(i)} - \mathbf{z}^{(Y)}| = \sigma \sum_{i=1}^{3} r_i. \tag{61}$$

The string correction ΔH_{string} is computed to be

$$\Delta H_{\text{string}} = -\sum_{i=1}^{3} \frac{\hat{l}_i^2 \sigma \langle r_i^{-1}\rangle}{2\langle \sigma r_i\rangle(\mu_i + \frac{1}{3}\langle \sigma r_i\rangle)}. \tag{62}$$

The total Hamiltonian for the bound $3q$ system in c.m. coordinates, taking into account only valence quarks, can now be written as follows:

$$H_{\text{tot}} = H_0 + \Delta H_{\text{string}} + \Delta H_{\text{Coul}} + \Delta H_{\text{self}} + \Delta H_{\text{spin}}, \tag{63}$$

where H_0 is given in (60); ΔH_{string} is given in (62); ΔH_{spin} is given in [40]; and ΔH_{Coul} is easily computed allowing for perturbative gluon exchanges in W_3, resulting in a standard expression

$$\Delta H_{\text{Coul}} = -\frac{2\alpha_s}{3} \sum_{i<j} \frac{1}{|\mathbf{z}^{(i)} - \mathbf{z}^{(j)}|}. \tag{64}$$

As to ΔH_{self}, it was found in [41] to originate from the $\langle \sigma F \sigma F\rangle$ correlator referring to the same quark line. It has the form {[41], Eq. (36)}

$$\Delta H_{\text{self}} = -\frac{2\sigma}{\pi} \sum_{i=1}^{3} \frac{\eta_i}{\mu_i}, \tag{65}$$

where $\eta_i = 1$ for light quarks.

5. THE LIGHT-CONE QUANTIZATION OF THE $3q$ SYSTEM: DERIVATION OF THE LIGHT-CONE HAMILTONIAN

The general expression of the $3q$ Green's function allows one to calculate the Hamiltonian corresponding to any prescribed hypersurface, with the evolution parameter T orthogonal to it, according to the equation (in Euclidean spacetime)

$$\frac{\partial G}{\partial T} = -HG. \tag{66}$$

In the previous section, the hypersurface was chosen to be $z_4^{(i)} = \text{const}$, and the corresponding c.m. Hamiltonian was written in (63). The obtained Hamiltonian is a $3q$ equivalent of the $q\bar{q}$ c.m. Hamiltonian found earlier in [34, 47, 48].

The light-cone version of the $q\bar{q}$ Hamiltonian was derived in [47] and solved numerically in [48].

In this section, we shall follow the same technique as in [47] to obtain the $3q$ Hamiltonian on the light cone. To this end, one should choose the hypersurface to be the plane with fixed values of $z_+^{(i)}$, where we use the following convention:

$$ab = a_\mu b_\mu = a_i b_i - a_0 b_0 = a_\perp b_\perp + a_+ b_- + a_- b_+ \tag{67}$$

and $a_\pm = (a_3 \pm a_0)/\sqrt{2}$.

The same decomposition of quark coordinate $z_\mu^{(i)}$ will be used as in (41), but for the light-cone (l.c.) coordinates (67). Again for simplicity, we shall identify R_μ and $z_\mu^{(Y)}$ so that

$$r_\mu^{(i)} = z_\mu^{(i)} - R_\mu = z_\mu^{(i)} - z_\mu^{(Y)}. \tag{68}$$

Some kinematical properties of the l.c. coordinates to be used below are

$$w_\mu^{(i)}(z_+, \beta_i) = z_\mu^{(i)}\beta_i + z_\mu^{(Y)}(1-\beta_i) = r_\mu^{(i)}\beta_i + z_\mu^{(Y)} \cong r_\mu^{(i)}\beta_i + R_\mu, \tag{69}$$

$$r_\mu^2 = r_\perp^2, \quad r_+ \equiv 0; \quad \frac{\partial w_\mu^{(i)}}{\partial \beta_i} = r_\mu^{(i)};$$

$$\dot{w}_\mu^2 = \dot{w}_\perp^2 + 2\dot{w}_-; \quad \dot{w}_\perp = \dot{r}_\perp \beta + \dot{R}.$$

Having this in mind, one can directly obtain the l.c. action from (40) (cf. [47] for the equivalent derivation of $q\bar{q}$ l.c. action),

$$A_{\text{l.c.}} = \int_0^T dz_+ \sum_{i=1}^{3} \left\{ \frac{m_i^2}{2\mu_i} + \frac{\mu_i}{2}((\dot{R}_\perp + \dot{r}_\perp^{(i)})^2 + 2(\dot{R}_- + \dot{r}_-^{(i)})) + \frac{1}{2}\int_0^1 d\beta_i \left[\frac{\sigma^2 (r_\perp^{(i)})^2}{\nu_i} \right. \right. \tag{70}$$

$$+\nu_i((\dot r_\perp^{(i)}\beta_i+\dot R_\perp)^2+2(\dot r_-^{(i)}\beta_i+\dot R_-))$$
$$+\nu_i\eta_i^2 r_\perp^{2(i)}-2\nu_i\eta_i((\dot r_\perp^{(i)}\beta_i+\dot R_\perp)r_\perp^{(i)}+r_-^{(i)})\Big]\Big\},$$

where $\dot r_\mu^{(i)}$ $(\mu=\perp,-)$ can be expressed in terms of $\dot\xi$ and $\dot\eta$ using the parametrization

$$\dot R_\mu=\sum_{i=1}^3 x_i\dot z_\mu^{(i)},\quad \sum_{i=1}^3 x_i=1,\quad x_i\ge 0, \tag{71}$$

$$\dot z_\mu^{(1)}-\dot R_\mu=\left(\frac{x_3}{x_1+x_2}\right)^{1/2}\dot\xi_\mu \tag{72}$$
$$-\left(\frac{x_2}{x_1(x_1+x_2)}\right)^{1/2}\dot\eta_\mu,$$
$$\dot z_\mu^{(2)}-\dot R_\mu=\left(\frac{x_3}{x_1+x_2}\right)^{1/2}\dot\xi_\mu$$
$$+\left(\frac{x_1}{x_2(x_1+x_2)}\right)^{1/2}\dot\eta_\mu,$$
$$\dot z_\mu^{(3)}-\dot R_\mu=-\left(\frac{x_1+x_2}{x_3}\right)^{1/2}\dot\xi_\mu.$$

One can rewrite (70) in the same form as in [47],

$$A_{\rm l.c.}=\frac{1}{2}\int_0^T dz_+\Big\{a_1\dot R_\perp^2+2a_1\dot R_- \tag{73}$$
$$+2a_{2\perp}\dot R_\perp+2a_{2-}-2c_{1\perp}\dot R_\perp$$
$$+\sum_{i=1}^3\Big[-2c_{2i}\dot r_\perp^{(i)}r_\perp^{(i)}+a_{3i}(\dot r_\perp^{(i)})^2-2c_{1i}r_-^{(i)}$$
$$+a_{4i}(r_\perp^{(i)})^2+\frac{m_i^2}{\mu_i}\Big]\Big\},$$

where we have defined

$$a_1=\sum_{i=1}^3\left(\mu_i+\int_0^1\nu_i(\beta)d\beta\right)=\sum_{i=1}^3 a_{1i}, \tag{74}$$
$$a_{2\perp}=\sum_{i=1}^3\left(\mu_i+\int_0^1\nu_i(\beta)\beta d\beta\right)\dot r_\perp^{(i)},$$
$$a_{2-}=\sum_{i=1}^3\left(\mu_i+\int_0^1\nu_i(\beta)\beta d\beta\right)\dot r_-^{(i)}=\sum_{i=1}^3 a_{2i}\dot r_-^{(i)},$$
$$c_{1\perp}=\sum_{i=1}^3\int_0^1 d\beta\nu_i(\beta)\eta_i r_\perp^{(i)}, \tag{75}$$
$$c_{1i}=\int_0^1\nu_i(\beta)\eta_i d\beta,\quad c_{2i}=\int_0^1 d\beta\nu_i(\beta)\beta\eta_i,$$
$$a_{3i}=\mu_i+\int_0^1\nu_i(\beta)\beta^2 d\beta,$$
$$a_{4i}=\int_0^1 d\beta\left(\nu_i\eta_i^2+\frac{\sigma^2}{\nu_i}\right).$$

We now require as in [47] that transverse velocity be diagonalized; i.e., we require the mixed term $a_{2\perp}$ to vanish. This gives conditions on coefficients x_i when $a_{2\perp}$ is expressed in terms of two independent velocities: $\dot\xi_\perp$ and $\dot\eta_\perp$.

This immediately yields expressions for x_i:

$$x_i=\frac{\mu_i+\int_0^1\nu_i(\beta)\beta d\beta}{\sum_{i=1}^3(\mu_i+\int_0^1\nu_i(\beta)\beta d\beta)}. \tag{76}$$

Now, one can integrate over $\prod_{i=1}^3 D\eta_i$ in the same way as was done for the $q\bar q$ system in [47] with the result

$$A'_{\rm l.c.}=\frac{1}{2}\int_0^T dz_+\Big\{a_1(\dot R_\perp^2+2\dot R_-) \tag{77}$$
$$+\sum_{i=1}^3\Big[\int_0^1 d\beta\frac{\sigma^2(r_\perp^{(i)})^2}{\nu_i}+\frac{m_i^2}{\mu_i}+a_{3i}(\dot r_\perp^{(i)})^2$$
$$-\frac{(r_-^{(i)}+r_\perp^{(i)}\dot R_\perp+\langle\beta\rangle_i\dot r_\perp^{(i)}r_\perp^{(i)})^2\int\nu_i d\beta}{(r_\perp^{(i)})^2}$$
$$-\frac{(r_\perp^{(i)}\dot r_\perp^{(i)})^2}{(r_\perp^{(i)})^2}\int_0^1 d\beta\nu_i(\beta)(\beta-\langle\beta\rangle_i)^2\Big]\Big\}.$$

Here, we have defined

$$\langle\beta\rangle_i=\int_0^1\nu_i(\beta)\beta d\beta\Big/\int_0^1\nu_i(\beta)d\beta. \tag{78}$$

Our next step is the integration over $D\dot R$, which is done in the same way as in [47], and choosing the system where the transverse total momentum vanishes, $\mathbf{P}_\perp=0$, one obtains

$$A_{\rm l.c}=\frac{1}{2}\int_0^T dz_+\sum_{i=1}^3\left\{\frac{m_i^2}{\mu_i}+\int_0^1 d\beta\frac{\sigma^2(r_\perp^{(i)})^2}{\nu_i}\right. \tag{79}$$

$$+ a_{3i}(\dot{r}_\perp^{(i)})^2 - \langle\nu_i^{(2)}\rangle\frac{(\dot{r}_\perp^{(i)}r_\perp^{(i)})^2}{(r_\perp^{(i)})^2}$$
$$- \frac{\langle\nu_i^{(0)}\rangle a_{1i}(r_-^{(i)} + \langle\beta\rangle_i\dot{r}_\perp^{(i)}r_\perp^{(i)})^2}{(r_\perp^{(i)})^2(a_{1i} - \langle\nu_i^{(0)}\rangle)}\Bigg\},$$

where we have defined

$$\langle\nu_i^{(k)}\rangle = \int_0^1 \nu_i(\beta)(\beta - \langle\beta\rangle_i)^k d\beta. \tag{80}$$

Integration over $D\dot{R}_-$ with $\exp(iP_\perp\int_0^T \dot{R}_- dz_+)$ (the exponent appearing in the standard way when going from Lagrangian to Hamiltonian representation) yields the important constraint $\delta(a_1 - P_+)$, i.e.,

$$a_1 = P_+, \tag{81}$$

and integration over DR_+ is trivial since $A_{\text{l.c.}}$ does not depend on R_+.

Before doing calculations for the l.c. Hamiltonian, one should go over to the Minkowskian action, which is achieved by replacements

$$\mu_i \to -i\mu_i^{(\text{M})}, \qquad \nu_i \to -i\nu_i^{(\text{M})}, \tag{82}$$
$$a_i \to -ia_i^{(\text{M})}, \qquad A \to -iA^{(\text{M})}.$$

Omitting the superscript "M" in what follows, one obtains for the Minkowskian action

$$A_{\text{l.c.}}^{(\text{M})} = \frac{1}{2}\int_0^T dz_+ \sum_{i=1}^3 \Bigg\{ -\frac{m_i^2}{\mu_i} + a_{3i}(\dot{r}_\perp^{(i)})^2 \tag{83}$$
$$- \int_0^1 \frac{\sigma^2 d\beta}{\nu_i}(r_\perp^{(i)})^2 - \langle\nu_i^{(2)}\rangle\frac{(\dot{r}_\perp^{(i)}r_\perp^{(i)})^2}{(r_\perp^{(i)})^2}$$
$$- \frac{\langle\nu_i^{(0)}\rangle a_{1i}(r_-^{(i)} + \langle\beta\rangle_i(\dot{r}_\perp^{(i)}r_\perp^{(i)}))^2}{(r_\perp^{(i)})^2(a_{1i} - \langle\nu_i^{(0)}\rangle)}\Bigg\}.$$

From (83), one can define in a direct way the l.c. Hamiltonian, writing

$$A_{\text{l.c.}}^{(\text{M})} = \int dz_+ L^{(\text{M})}, \quad H = \sum \mathbf{p}_\perp\cdot\dot{\mathbf{q}}_\perp - L^{(\text{M})}. \tag{84}$$

One cannot choose $\mathbf{q}_\perp^{(i)}$, strictly speaking, as a set of canonical momenta for coordinates $\mathbf{r}_\perp^{(i)}$, since the latter are not independent variables, subject according to (72) to a condition

$$\sum_{i=1}^3 x_i\dot{\mathbf{r}}_\perp^{(i)} = 0. \tag{85}$$

Instead, the pair of coordinates $\dot{\boldsymbol{\xi}}_\perp, \dot{\boldsymbol{\eta}}_\perp$ is independent, and one can define canonical momenta $\mathbf{p}_\perp^{(\xi)}$ and $\mathbf{p}_\perp^{(\eta)}$ as

$$\mathbf{p}_\perp^{(\xi)} = \frac{1}{i}\frac{\partial}{\partial\boldsymbol{\xi}_\perp}, \quad \mathbf{p}_\perp^{(\eta)} = \frac{1}{i}\frac{\partial}{\partial\boldsymbol{\eta}_\perp}. \tag{86}$$

We can nevertheless use $\mathbf{p}_\perp^{(i)} = \frac{1}{i}\frac{\partial}{\partial\mathbf{r}_\perp^{(i)}}$. Then,

$$\mathbf{p}_\perp^{(\xi)} = \sum_{i=1}^3 \mathbf{p}_\perp^{(i)}c_{i\xi}, \quad \mathbf{p}_\perp^{(\eta)} = \sum_{i=1}^3 \mathbf{p}_\perp^{(i)}c_{i\eta}, \tag{87}$$

where $c_{i\xi}$ and $c_{i\eta}$ are listed from (75):

$$c_{1\xi} = \left(\frac{x_3}{x_1+x_2}\right)^{1/2} = c_{2\xi}, \tag{88}$$
$$c_{3\xi} = -\left(\frac{x_1+x_2}{x_3}\right)^{1/2},$$
$$c_{1\eta} = -\left(\frac{x_2}{x_1(x_1+x_2)}\right)^{1/2},$$
$$c_{2\eta} = \left(\frac{x_1}{x_2(x_1+x_2)}\right)^{1/2}, \quad c_{3\eta} = 0.$$

We are now in the position to use (84) and calculate the l.c. Hamiltonian,

$$H = \sum_{i=1}^3 \Bigg\{ \frac{m_i^2}{2\mu_i} + \frac{1}{2}\int_0^1 \frac{\sigma^2 d\beta}{\nu_i} \tag{89}$$
$$+ \frac{(\mathbf{p}_\perp^{(i)})^2 - (\mathbf{p}_\perp^{(i)}\cdot\mathbf{r}_\perp^{(i)})^2/(\mathbf{r}_\perp^{(i)})^2}{2a_{3i}} + \frac{\langle\nu_i^{(0)}\rangle a_{1i}(r_-^{(i)})^2}{2(r_\perp^{(i)})^2\mu_i}$$
$$+ \frac{(p_\perp^{(i)}r_\perp^{(i)} + \frac{1}{\mu_i}\langle\nu_i^{(0)}\rangle a_{1i}r_-^{(i)})^2\mu_i^2}{2(r_\perp^{(i)})^2 a_{3i}a_{2i}^2(2\mu_i - a_{2i})^2}$$
$$\times\left[\mu_i a_{3i} + \frac{(a_{2i}-\mu_i)^2}{\mu_i}(a_{3i} - 2\mu_i)\right]\Bigg\},$$

where a_{ni} are defined in (74) and (75).

Momenta $\mathbf{p}_\perp^{(i)}$ are not linearly independent, and from (85), expressing $\dot{\mathbf{r}}_\perp^{(i)}$ through $\mathbf{p}_\perp^{(i)}$, one obtains the connection

$$\sum_{i=1}^3 \frac{x_i}{a_{3i}} \tag{90}$$
$$\times\left(\mathbf{p}^{(i)} - C\mathbf{r}^{(i)} + \mathbf{r}^{(i)}D\frac{\mathbf{p}^{(i)}\cdot\mathbf{r}^{(i)} - C(\mathbf{r}^{(i)})^2}{a_{3i} - (\mathbf{r}_\perp^{(i)})^2 D}\right) = 0,$$

where we have defined

$$C = -\frac{\langle\nu_i^{(0)}\rangle a_{1i}r_-^{(i)}\langle\beta\rangle_i}{(\mathbf{r}_\perp^{(i)})^2(a_{1i} - \langle\nu_i^{(0)}\rangle)}, \tag{91}$$

$$D = \frac{\langle \nu_i^{(2)} \rangle (a_{1i} - \langle \nu_i^{(0)} \rangle) + \langle \nu_i^{(0)} \rangle a_{1i} \langle \beta \rangle_i^2}{(\mathbf{r}_\perp^{(i)})^2 (a_{1i} - \langle \nu_i^{(0)} \rangle)}. \quad (92)$$

To understand the structure of the Hamiltonian (89) better, consider first the limit of heavy quarks $m_i \gg \sqrt{\sigma}$, in which case, as was shown in [47], the following inequality holds: $\mu_i \gg \nu_i$, $i = 1, 2, 3$. One has from (74) and (75) $a_{1i} = a_{2i} = a_{3i} = \mu_i$, and the Hamiltonian assumes the form

$$H_{\rm HQ} = \sum_{i=1}^{3} \left\{ \frac{m_i^2}{2\mu_i} + \frac{1}{2} \int_0^1 \frac{\sigma^2 d\beta}{\nu_i} \right. \quad (93)$$
$$+ \frac{(\mathbf{p}_\perp^{(i)})^2 - (\mathbf{p}_\perp^{(i)} \cdot \mathbf{r}_\perp^{(i)})^2 / (\mathbf{r}_\perp^{(i)})^2}{2\mu_i}$$
$$\left. + \frac{(r_-^{(i)})^2}{2(r_\perp^{(i)})^2} \int_0^1 \nu_i d\beta + \frac{(p_\perp^{(i)} r_\perp^{(i)} + \langle \nu_i^{(0)} \rangle r_-^{(i)})^2}{2(r_\perp^{(i)})^2 \mu_i} \right\}.$$

Introducing the dimensionless quantity $y_i \equiv \nu_i / P_+$ (which will be shown to be independent of β and small, $y_i \ll 1$), one has from (76) and (81)

$$x_i = \frac{1}{1 - Y} \left(\frac{\mu_i}{P_+} + \frac{1}{2} y_i \right), \quad (94)$$
$$\sum_{i=1}^{3} \left(\frac{\mu_i}{P_+} + y_i \right) = 1,$$

where $Y = (1/2) \sum y_i$.

This enables one to expand the mass term in (93) around stationary points in x_i, and retaining the first order term in y_i, one obtains

$$\sum_{i=1}^{3} \frac{m_i^2}{2\mu_i} = \frac{1}{2P_+} \left\{ M^2 (1 + 2Y) \right. \quad (95)$$
$$\left. + 2M \sum \left(x_i - \frac{m_i}{M} \right)^2 \frac{1}{2m_i} \right\},$$

where $M = \sum_{i=1}^{3} m_i$.

We now define, as in [47], the z component of momenta

$$M \left(x_i - \frac{m_i}{M} \right) \equiv p_z^{(i)}. \quad (96)$$

Retaining now in expansion of (93) only leading terms, one obtains $H_{\rm HQ} = \mathcal{M}^2 / (2P_+)$ with total mass operator

$$\mathcal{M}^2 = M^2 + 2M \sum_{i=1}^{3} \frac{(\mathbf{p}^{(i)})^2}{2m_i} + M^2 \sum_{i=1}^{3} \frac{y_i}{(r_\perp^{(i)})^2} \quad (97)$$
$$\times \left[(r_\perp^{(i)})^2 + \frac{(P_+ r_-^{(i)})^2}{M^2} + \frac{\sigma^2}{M^2} \left(\frac{(\mathbf{r}_\perp^{(i)})^2}{y_i} \right)^2 \right].$$

One can now define the stationary point of (97) with respect to y_i,

$$y_i^{(0)} = \frac{\sigma (\mathbf{r}_\perp^{(i)})^2}{M r^{(i)}}, \quad (r^{(i)})^2 = (\mathbf{r}_\perp^{(i)})^2 + r_z^{(i)}, \quad (98)$$
$$r_z^{(i)} \equiv \frac{P_+ r_-^{(i)}}{M}.$$

Inserting $y_i = y_i^{(0)}$ back into (97), one arrives at the familiar nonrelativistic expansion

$$\mathcal{M}^2 = M^2 + 2M \sum_{i=1}^{3} \left[\frac{(\mathbf{p}^{(i)})^2}{2m_i} + \sigma r^{(i)} \right]. \quad (99)$$

Connection between $\mathbf{p}^{(i)}$ is also simplified for $y_i \ll 1$, so that (90) goes over to a simple relation $\sum_{i=1}^{3} \mathbf{p}^{(i)} = 0$, as expected.

We now turn to the case of light quarks, where relations (76) and (81) hold with y_i nonzero, and observe that three strings contribute an amount $P_+^{\rm string} \equiv \sum_i \int_0^1 \nu_i(\beta) d\beta$ to the total momentum P_+, which can be significant and comparable to that of valence quarks, $\sum_{i=1}^{3} \mu_i$. The numerical value of $\langle y \rangle \approx 0.2$ obtained in [48] for a light meson suggests that a larger value can be obtained for $P_+^{\rm string} / P_+$, which can be comparable to the 55% of the energy–momentum sum rule observed in DIS experiment on nucleons. We suggest at this point following [48] that this 55% contribution is mostly due to the string contribution $P_+^{\rm string}$ from all Fock components of the nucleon, most importantly from the ground-state strings, and from hybrid baryon excitation, where the ratio $P_+^{\rm string} / P_+$ is even larger.

This point will be elaborated elsewhere [52].

Another topic connected to the l.c. Hamiltonian (89) is the whole range of dynamical calculations similar to those done for mesons in [48]. One can solve for the eigenfunctions of (89) and calculate the form factor and valence part of the structure function of the baryon for ground and excited states. To compute the full structure function, however, one needs higher Fock components and, first of all, the lowest hybrid excitations. Here one comes to the important problem of small x–Regge-type behavior and connection of t-channel Regge poles (including Pomeron) with s-channel summation over baryon resonances (primarily hybrid excitation), which is planned to be discussed in [52].

6. DISCUSSION OF THE c.m. WAVE-FUNCTION PROPERTIES

In this section, we consider possible strategies and first estimates in the determination of eigenvalues and eigenfunctions of the c.m. Hamiltonian (63). The latter is the sum of the spin-independent part [the first four terms on the right-hand side of (63)] and $\Delta H_{\rm spin}$, which is calculated in [40] and has a full relativistic Dirac $4\otimes 4\otimes 4$ structure.

At this point, one can apply two different approaches in treating $\Delta H_{\rm spin}$. In most of this section, we shall consider $\Delta H_{\rm spin}$ as a correction that should be taken into account in the first order of perturbation theory. This is especially consistent for the perturbative part of $\Delta H_{\rm spin}$, which is known for light quarks only to the order $O(\alpha_s)$. In the next section, we also consider another strategy, when $\Delta H_{\rm spin}$, and especially its hyperfine part, is treated in a full matrix form.

We start with the first approach and concentrate on the first term H_0 in (63), which is given in (60). This term was considered before in [36], and numerical solution of the Δ-type states is presented there, including the study of Regge trajectories.

Since H_0 does not depend on spin or isospin and color degrees of freedom are already integrated out, one should look for fully symmetric wave functions depending on spin variables σ, isospin variables τ, and coordinates $\boldsymbol{\xi}$, $\boldsymbol{\eta}$. Relativistic effects are taken into account in the kinematics, where einbein fields μ_i are introduced in (60), and the latter upon stationary point optimization in μ_i yield relativistic energies as in (50). However, it is more advantageous to solve (60), which has nonrelativistic form without square roots, and perform optimization in μ_i for the resulting total mass $M_0(\mu_i)$. The accuracy of this procedure for mesons was checked in [53] to be around or better than 5%. This type of procedure also simplifies calculation of all four corrections in (63), which contain μ_i explicitly.

Hence, one can follow the construction of the fully symmetric wave function as was done in [9, 36], which we slightly simplify and adopt the notation used before. Namely, Jacobi coordinates $\boldsymbol{\xi}, \boldsymbol{\eta}$ (41) are chosen to be symmetric (s) and antisymmetric (a) with respect to interchange of indices 1 and 2, and belong to the two-dimensional mixed representation of the permutation group S_3, denoted by ψ'' and ψ', while one-dimensional ones are ψ^s and ψ^a. The same holds true for isospin wave functions η'', η', η^s, and η^a and spin–isospin wave functions φ'', φ', φ^s, and φ^a, and, finally, the full coordinate–spin–isospin wave function which should be symmetric in interchange of all three indices is

$$\Psi(\mathbf{z}^{(i)},\sigma,\tau)=\psi^s\varphi^s+\psi^a\varphi^a+\psi''\varphi''+\psi'\varphi'. \quad (100)$$

An additional requirement is that $\varphi^{(i)}$ and $\psi^{(i)}$, $i=\ '',\ ',s,a$, must belong to given total angular momentum L,m_L and total spin S,m_S and isospin I,I_3.

Inclusion of $\Delta H_{\rm spin}$ helps to construct the wave function as the eigenfunction of total momentum J,m_J.

Since the construction of spin–isospin functions for three quarks is well known [1–9], we consider here only the coordinate part $\psi^{(i)}(\boldsymbol{\xi},\boldsymbol{\eta})$. As in [2–4, 9, 36], we shall use the hyperspherical formalism [54] that has proved to be very accurate for the $3q$ case; namely, the lowest hyperspherical function yields eigenvalues with 1% accuracy.

One can introduce hyperradius ρ in the following way (note the difference from the definition in [36], where the case of equal masses μ_i was considered):

$$\rho^2=\sum_{i=1}^{3}\frac{\mu_i(\mathbf{z}^{(i)}-\mathbf{R})^2}{\mu}=\boldsymbol{\xi}^2+\boldsymbol{\eta}^2. \quad (101)$$

The coordinate wave function $\psi(\boldsymbol{\xi},\boldsymbol{\eta})$ can be expanded in an infinite series of hyperspherical functions $u_K^\nu(\Omega)$ depending on angular variables Ω, with K being the grand angular momentum, $K=L,\ L+2,\ L+4,\ \ldots$, and ν being the set of all other quantum numbers (see [54] for a review),

$$\psi(\boldsymbol{\xi},\boldsymbol{\eta})=\frac{1}{\rho^2}\sum_{K,\nu}u_K^\nu(\Omega)\psi_K^\nu(\rho). \quad (102)$$

Writing (60) as

$$H_0=\sum_{i=1}^{3}\left(\frac{m_i^2}{2\mu_i}+\frac{\mu_i}{2}\right)+h_0, \quad (103)$$

one can reduce the equation $h_0\psi=E\psi$ to a system of equations

$$\frac{d^2\psi_K^\nu}{d\rho^2}+\frac{1}{\rho}\frac{d\psi_K^\nu}{d\rho}+\left[2\mu E-\frac{(K+2)^2}{\rho^2}\right]\psi_K^\nu = 2\mu\sum_{K',\nu'}U_{KK'}^{\nu\nu'}(\rho)\psi_{K'}^{\nu'}(\rho), \quad (104)$$

where one defined

$$U_{KK'}^{\nu\nu'}(\rho)=\int u_K^{\nu+}(\Omega)V_{\rm conf}(\boldsymbol{\xi},\boldsymbol{\eta})u_{K'}^{\nu'}(\Omega)d\Omega. \quad (105)$$

The confining potential $V_{\rm conf}$ was considered in [36] assuming a linear Y-type form. The analysis of matrix elements (105) is also given in [9, 54], and here we shall use only the simplest form, namely, the so-called hypercentral component, which for the equal-mass case ($\mu_i=\mu$) is

$$U_{00}^{00}(\rho)=1.118\sqrt{2}\sigma\rho=1.58\sigma\rho. \quad (106)$$

Baryon masses (in GeV) averaged over hyperfine spin splitting for $\sigma = 0.15\ \mathrm{GeV}^2$, $\alpha_s = 0.4$, $m_i = 0$

State	$M_{Kn} + \langle \Delta H_{\mathrm{self}} \rangle$	$\langle \Delta H_{\mathrm{Coul}} \rangle$	M^{tot}_{Kn}	$M^{\mathrm{tot}}(\mathrm{exp})$
$K = 0, n = 0$	1.36	−0.274	1.08	1.08
$K = 0, n = 1$	2.19	−0.274	1.91	?
$K = 0, n = 2$	2.9	−0.274	2.62	?
$K = L = 1, n = 0$	1.85	−0.217	1.63	1.6
$K = 2, n = 0$	2.23	−0.186	2.04	?

The lowest order equation (105) for $K = K' = 0$ was solved numerically in [2, 9]. Below, we shall demonstrate a simpler approach that allows one to obtain eigenvalues of this equation analytically with an accuracy of 1% for the lowest states. To this end, we take in (105) $K = K'$ (neglecting nondiagonal coupling) and, making the replacement $\psi^\nu_K(\rho) = \bar\psi^\nu_K(\rho)/\sqrt{\rho}$, reduce the equation to the form

$$-\frac{1}{2\mu}\frac{d^2\bar\psi^\nu_K(\rho)}{d\rho^2} + W_{KK}(\rho)\bar\psi^\nu_K(\rho) = E_{Kn}\bar\psi^\nu_K(\rho) \tag{107}$$

with

$$W_{KK}(\rho) = b\rho + \frac{d}{2\mu\rho^2}, \quad b = \sigma\sqrt{\frac{2}{3}}\frac{32}{5\pi}, \tag{108}$$
$$d = \left(K + \frac{3}{2}\right)\left(K + \frac{5}{2}\right).$$

The eigenvalue E_{Kn} can be found using the oscillator-well approximation near the minimum of $W_{KK}(\rho)$:

$$\left.\frac{dW_{KK}(\rho)}{d\rho}\right|_{\rho=\rho_0} = 0, \quad \rho_0 = \left(\frac{d}{\mu b}\right)^{1/3}, \tag{109}$$

which yields

$$E_{Kn} \cong W_{KK}(\rho_0) + \omega\left(n + \frac{1}{2}\right) \equiv \frac{\sigma^{2/3}}{\mu^{1/3}}c_n, \tag{110}$$

where, for $K = 0$,

$$W_{00}(\rho_0) = \frac{3}{2}\left(\frac{b^2 d}{\mu}\right)^{1/3}, \quad \omega = \frac{\sqrt{3d}}{\mu\rho_0^2}. \tag{111}$$

The spectrum ωn in (110) corresponds to the so-called "breathing modes," when a baryon is excited in its ρ-dependent mode only.

Finally, adding other terms in (60), one has for M_{Kn} the eigenvalue of H_0,

$$M_{Kn} = \frac{3}{2}\mu + E_{Kn}(\mu). \tag{112}$$

At this stage, one defines μ from the stationary point of (112), $\partial M_{Kn}/\partial\mu\,|_{\mu=\mu_0} = 0$, which yields

$$\mu_0 = \left(\frac{2}{9}c_n\right)^{3/4}\sqrt{\sigma}, \tag{113}$$

$$M_{Kn}(\mu_0) = \sqrt{\sigma}\cdot 6\left(\frac{2}{9}c_n\right)^{3/4}.$$

The total spin-averaged mass of the baryon corresponding to the Hamiltonian (63) is

$$M^{\mathrm{tot}}_{Kn} = M_{Kn}(\mu_0) + \langle \Delta H_{\mathrm{string}} \rangle + \langle \Delta H_{\mathrm{Coul}} \rangle + \langle \Delta H_{\mathrm{self}} \rangle. \tag{114}$$

For the lowest states with $L = 0, 1$, one can neglect $\langle \Delta H_{\mathrm{string}} \rangle$, while the other two terms are

$$\langle \Delta H_{\mathrm{self}} \rangle = -\frac{6\sigma}{\pi\mu_0}, \quad \langle \Delta H_{\mathrm{Coul}} \rangle = -\frac{\lambda b^{1/3}}{(2\mu_0)^{2/3}\rho_0}, \tag{115}$$

where $\langle \Delta H_{\mathrm{self}} \rangle$ is given in [41], while $\langle \Delta H_{\mathrm{Coul}} \rangle$ is given in [9, 37]. Here, the following notation is used:

$$\lambda = \alpha_s\frac{8}{3}\left(\frac{10\sqrt{3}\mu_0^2}{\pi^2\sigma}\right)^{1/3}. \tag{116}$$

Now, $M_{Kn}(\mu_0)$ is defined in (113) and one should choose the only input parameters (for light quarks, we set all $m_i = 0$) σ and α_s. The string tension σ is renormalized due to the presence of nondiagonal terms (23) and therefore is smaller than in the mesonic case (see [46] for a comparison with lattice data and more discussion). For a simple estimate below, we choose $\sigma = 0.15\ \mathrm{GeV}^2$ (the same value as in [8]) and take $\alpha_s = 0.4$, which is near its saturated value [55].

Results of calculations made according to Eqs. (112)–(115) are given in the table.

As is seen from the table, the calculated spin-averaged mass $(\frac{1}{2})(M_N + M_\Delta) = M^{\mathrm{tot}}_{00}$ agrees well with the experimental average, and the same is also true for the lowest negative-parity states with $K = L + 1$, which should be compared with the $1/2^-$ and $3/2^-$ states of N and Δ, respectively.

We also note that breathing modes ($n > 0$) have an excitation energy around 0.8 GeV, while orbital excitations $K = L = 1$ have an energy interval around 0.5 GeV.

7. PROBLEM OF SPIN-DEPENDENT FORCES

We now turn to the spin-dependent interaction. For the $3q$ case, the corresponding nonperturbative and perturbative terms are given in [40]. They have been derived only under the assumption of Gaussian dominance; i.e., only the contribution of the bilocal correlator (represented by scalar functions D and D_1) was retained in (9), Gaussian dominance being supported by recent lattice data [25, 26]. The resulting spin-dependent forces in general have the form of a product of two 4×4 matrices, one for each interacting quark, and this is the most general relativistic spin interaction.

The expansion in powers of inverse quark mass was not used in [40], and for light quarks the spin-dependent interaction is proportional to the terms $1/(\mu_i\mu_j)$ and higher inverse mass terms, where μ_i are the same as in (103) and (113) and have the meaning of constituent-quark masses, which grow with excitation. For the lowest states, $\mu_0 \cong 0.37$ GeV and grows fast with increasing K, L, and n.

Now, one could use two types of strategy to implement spin-dependent forces.

(i) Since all terms in (63) except the last one $\Delta H_{\rm spin}$ are diagonal in Dirac indices, one can calculate spin-independent wave functions and account for spin effects calculating matrix elements $\langle\Delta H_{\rm spin}\rangle_{KLn}$. This procedure is actually used by most authors, and one can mention two positive moments associated with it. First of all, in this procedure, one treats spin-dependent forces as a perturbation, and it should work at least for high enough excitation, when $\mu_i\mu_j$ in the denominator become large. Secondly, the perturbative spin-dependent forces are known for light quarks only to the lowest order in α_s, and therefore it is illegitimate to account for those terms in higher than first-order approximation.

However, doing so, one immediately comes to a serious contradiction. Namely, the theoretical estimates of perturbative hyperfine splitting for a reasonable value of $\alpha_s \approx 0.4$ yield values around 100 MeV instead of 300 MeV for the $\Delta-N$ case [9]. The phenomenological remedy used is to take $\alpha_s \sim 1$ and, smearing the hyperfine δ function, take the resulting potential to higher orders, which was criticized above.

To resolve this contradiction, it is suggested, first of all, to take into account the nonperturbative part of hyperfine interaction, which was derived in [40]. It is known to yield a large part of hyperfine splitting in light mesons [27, 28] and may also be large for baryons. Secondly, it is suggested in addition that another strategy discussed below be used.

(ii) In the case when spin forces are important, as was discussed in the hyperfine case, one should take into account that the same-type matrix element which creates hyperfine splitting also connects lower and higher components of the Dirac bispinor. Physically, this means excitation of negative-energy components of the quark wave function in baryons, which is also associated with the backward-in-time propagation of quarks.

Therefore, the strong hyperfine splitting also implies strong negative-energy-component excitation, and the solution to the total Hamiltonian (63) should be sought in the form

$$\Psi_B = \sum C_{ikl}^{\alpha\beta\gamma}\psi_\alpha^{(i)}\psi_\beta^{(k)}\psi_\gamma^{(l)},$$

where α, β, γ are Dirac bispinor indices and i, k, l refer to the excitation state of a given quark.

This strategy is equivalent to the full relativistic three-body Bethe–Salpeter equation, which was studied in the quasi-potential form in [56].

Another possible treatment of the same problem was recently initiated in [38, 39], where threefold Dirac equations were derived from the QCD Lagrangian for the baryon Green's function.

8. CONCLUSION

We have derived the $3q$ Hamiltonian both in the c.m. and in the l.c. coordinate systems. It was demonstrated that the c.m. Hamiltonian can be written conveniently as a sum of a main term H_0 and four corrections in (63), representing rotating string energy, Coulomb energy, nonperturbative self-energy correction, and spin interaction, respectively. The explicit form of all terms is given above, except for the last one, published recently in [40].

The spin-averaged energy levels have been calculated analytically, using the hyperspherical formalism yielding an accuracy of around 1% for energy levels in a linear confining potential. Results for the $\Delta-N$ system are in good agreement with experiment.The present paper is meant to be a starting point of a new treatment of baryons, where all types of forces are derived explicitly from first principles only under the assumption of Gaussian dominance. The spin-dependent forces derived for the first time in its totality in [40] constitute an essential part of this new approach.

ACKNOWLEDGMENTS

The author has benefited from a good working creative atmosphere in the Theory Group of the Jefferson Laboratory. It is a pleasure to thank all members of the Theory Group, all staff, and especially Franz Gross for their kind hospitality. Many useful discussions, remarks, and suggestions have been appreciated during talks and contacts with V. Burkert,

C. Carlson, R. Edwards, J. Goity, F. Gross, W. Melnitchouk, I. Musatov, A. Radyushkin, D. Richards, W. Roberts, C. Schat, R. Schiavilla, and J. Tjon. The partial support of the Russian Foundation for Basic Research (project nos. 00-02-17836 and 00-15-96736) and INTAS (grant nos. 00-110 and 00-366) is acknowledged. The author was supported by DOE contract DE-AC05-84ER40150, under which SURA operates the TJNAF.

APPENDIX

We start with the definition of the string-junction position $\mathbf{z}^{(Y)}$ which is obtained from the minimum condition of the sum

$$\sum_{i=1}^{3}|\mathbf{r}^{(i)}| = \sum_{i=1}^{3}|\mathbf{z}^{(i)} - \mathbf{z}^{(Y)}| \qquad (A.1)$$

and yields, after differentiating in $\mathbf{z}^{(Y)}$,

$$\sum_{i=1}^{3}\frac{\mathbf{r}^{(i)}}{|\mathbf{r}^{(i)}|} = \sum_{i=1}^{3}\mathbf{n}^{(i)} = 0. \qquad (A.2)$$

This implies that three unit vectors $\mathbf{n}^{(i)}$ are at 120° with respect to each other, being in one plane. Therefore, one can relate positions of quarks $\mathbf{z}^{(ij)} \equiv \mathbf{z}^{(i)} - \mathbf{z}^{(j)}$ to $\mathbf{r}^{(i)}$ as follows:

$$(\mathbf{z}^{(ij)})^2 = (\mathbf{r}^{(i)})^2 + (\mathbf{r}^{(j)})^2 + |\mathbf{r}^{(i)}||\mathbf{r}^{(j)}|, \qquad (A.3)$$
$$i \neq j = 1, 2, 3.$$

One can finally relate $\mathbf{r}^{(i)}$ to the Jacobi coordinates $\boldsymbol{\xi}$, $\boldsymbol{\eta}$ [Eq. (41)]:

$$\mathbf{r}^{(i)} = b_i\boldsymbol{\xi} + c_i\boldsymbol{\eta} + \boldsymbol{\delta}, \qquad (A.4)$$

where coefficients b_i and c_i are given in (41) and $\boldsymbol{\delta} = \mathbf{R} - \mathbf{z}^{(Y)}$ is found by solving (A.2) and (A.3). Equations (A.3) are algebraic and allow one to find the lengths $r_i \equiv |\mathbf{r}^{(i)}|$, $i = 1, 2, 3$, through the quark positions $|\mathbf{z}^{(ij)}|$; therefore, r_i will be assumed to be found explicitly. To find $\boldsymbol{\delta}$, we place three quarks on the plane x, y so that quarks 1 and 2 are on the x axis. Assuming the $3q$ triangle to have all angles less than 120°, one can compute both components δ_x, δ_y in terms of r_i. Thus, the position of the string junction $\mathbf{z}^{(Y)}(x_0, y_0)$ is found to be

$$y_0 = \frac{\sqrt{3}r_1r_2}{\sqrt{3r_2^2 + (2r_1 + r_2)^2}}, \qquad (A.5)$$
$$x_0 - x_1 = \frac{(2r_1 + r_2)r_1}{\sqrt{3r_2^2 + (2r_1 + r_2)^2}},$$

where $(x_1, 0)$ is the position of quark 1.

Similarly, one obtains for δ_x, δ_y

$$\delta_x = \frac{1}{3}\left[\left(\frac{r_2 + r_3}{2} - r_1\right)(2r_1 + r_2)\right. \qquad (A.6)$$
$$\left. + 3(r_2 - r_3)r_2\right]\frac{1}{\sqrt{3r_2^2 + (2r_1 + r_2)^2}}$$

$$\delta_y = \frac{r_3(r_1 + r_2) - 2r_1r_2}{\sqrt{3}\sqrt{3r_2^2 + (2r_1 + r_2)^2}}. \qquad (A.7)$$

One can see that, for the symmetric case $r_1 = r_2 = r_3$, the string junction and the c.m. positions coincide, $\delta_x = \delta_y = 0$.

Finally, we quote for the convenience of the reader the expression of the sum (A.1) through the quark positions only, taken from [36]:

$$\sum_{i=1}^{3}r_i = \frac{\sqrt{3}}{2}[(\mathbf{z}^{(12)})^2 + 3(\mathbf{z}^{(3)} - \mathbf{R})^2 \qquad (A.8)$$
$$+ 2\sqrt{3}|\mathbf{z}^{(12)} \times (\mathbf{z}^{(3)} - \mathbf{R})|]^{1/2}.$$

REFERENCES

1. A. De Rujula, H. Georgi, and S. L. Glashow, Phys. Rev. D **12**, 147 (1975).
2. P. Hasenfratz *et al.*, Phys. Lett. B **94B**, 401 (1980).
3. J. M. Richard, Phys. Lett. B **100B**, 515 (1980); **95**, 299 (1980).
4. A. B. Guimaraes, H. T. Coelho, and R. Chanda, Phys. Rev. D **24**, 1343 (1981).
5. J. Carlson, J. Kogut, and V. R. Pandharipande, Phys. Rev. D **27**, 233 (1983).
6. J. M. Richard and P. Taxil, Phys. Lett. B **128B**, 453 (1983); Ann. Phys. (N.Y.) **150**, 267 (1983).
7. S. Godfrey and N. Isgur, Phys. Rev. D **32**, 189 (1985).
8. S. Capstick and N. Isgur, Phys. Rev. D **34**, 2809 (1986).
9. A. M. Badalian, Phys. Lett. B **199**, 267 (1987); A. M. Badalian and D. I. Kitoroage, Yad. Fiz. **47**, 1343 (1988) [Sov. J. Nucl. Phys. **47**, 855 (1988)].
10. B. O. Kerbikov, M. I. Polikarpov, and L. V. Shevchenko, Nucl. Phys. B **331**, 19 (1990).
11. J. Kuti, hep-lat/9811021; Nucl. Phys. B (Proc. Suppl.) **73**, 72 (1999).
12. S. Coleman, *1/N in Aspects of Symmetry* (Cambridge Univ. Press, Cambridge, 1985).
13. E. Witten, Nucl. Phys. B **160**, 57 (1979).
14. R. Dashen and A. V. Manohar, Phys. Lett. B **315**, 425 (1993); **315**, 438 (1993); A. V. Manohar, in *Probing the Standard Model of Particle Interactions,* Ed. by F. David and R. Gupta (Elsevier, Amsterdam, 2001).
15. C. D. Carone, H. Georgi, and S. Osofsky, Phys. Lett. B **322**, 227 (1994); C. D. Carone, H. Georgi, L. Kaplan, and D. Morin, Phys. Rev. D **50**, 5793 (1994); C. E. Carlson and C. D. Carone, Phys. Lett. B **441**, 367 (1998).

16. J. L. Goity, Phys. Lett. B **414**, 140 (1997).
17. C. L. Schat, J. L. Goity, and N. N. Scoccola, Phys. Rev. Lett. **88**, 102002 (2002); C. L. Schat, hep-ph/0204044.
18. N. Isgur, Phys. Rev. D **62**, 014025 (2000); hep-ph/9910272; *Overview Talk at Workshop on N* Physics, Jefferson Laboratory, 2000,* nucl-th/0007008.
19. CLAS Collab. (V. Burkert *et al.*), Nucl. Phys. A **684**, 16 (2001).
20. V. Burkert, hep-ph/0106143.
21. H. G. Dosch, Phys. Lett. B **190**, 177 (1987); H. G. Dosch and Yu. A. Simonov, Phys. Lett. B **205**, 339 (1988).
22. Yu. A. Simonov, Nucl. Phys. B **307**, 512 (1988).
23. A. Di Giacomo, H. G. Dosch, V. I. Shevchenko, and Yu. A. Simonov, Phys. Rep. (in press); hep-ph/0007223.
24. Yu. A. Simonov, in *QCD Perturbative or Nonperturbative* (Interscience, Singapore, 2000); hep-ph/9911237.
25. G. Bali, Phys. Rev. D **62**, 114503 (2000); hep-lat/0006022; S. Deldar, Phys. Rev. D **62**, 034509 (2000); hep-lat/9911008.
26. Yu. A. Simonov, Pis'ma Zh. Éksp. Teor. Fiz. **71**, 187 (2000) [JETP Lett. **71**, 127 (2000)]; V. I. Shevchenko and Yu. A. Simonov, Phys. Rev. Lett. **85**, 1811 (2000).
27. A. M. Badalian and B. L. G. Bakker, hep-ph/0202246.
28. A. M. Badalian, B. L. G. Bakker, and V. L. Morgunov, Yad. Fiz. **63**, 1722 (2000) [Phys. At. Nucl. **63**, 1635 (2000)].
29. D. Gromes, Phys. Lett. B **115B**, 482 (1982); V. Marquard and H. G. Dosch, Phys. Rev. D **35**, 2238 (1987); A. Krämer, H. G. Dosch, and R. A. Bertlmann, Phys. Lett. B **223**, 105 (1989).
30. M. Campostrini, A. Di Giacomo, and G. Mussardo, Z. Phys. C **25**, 173 (1984); A. Di Giacomo and H. Panagopoulos, Phys. Lett. B **285**, 133 (1992); M. D'Elia, A. Di Giacomo, and E. Meggiolaro, Phys. Lett. B **408**, 315 (1997); A. Di Giacomo, E. Meggiolaro, and H. Panagopoulos, Nucl. Phys. B **483**, 371 (1997).
31. M. Eidemueller, H. G. Dosch, and M. Jamin, Nucl. Phys. B (Proc. Suppl.) **86**, 421 (2000); hep-ph/9908318.
32. Yu. A. Simonov, Nucl. Phys. B **592**, 350 (2001).
33. Yu. A. Simonov, Phys. Lett. B **226**, 151 (1989).
34. A. Yu. Dubin, A. B. Kaidalov, and Yu. A. Simonov, Phys. Lett. B **323**, 41 (1994); Yad. Fiz. **56** (12), 213 (1993) [Phys. At. Nucl. **56**, 1745 (1993)].
35. Yu. A. Simonov, Phys. Lett. B **228**, 413 (1989).
36. M. Fabre de la Ripelle and Yu. A. Simonov, Ann. Phys. (N.Y.) **212**, 235 (1991).
37. B. O. Kerbikov and Yu. A. Simonov, Phys. Rev. D **62**, 093016 (2000); hep-ph/0001243.
38. Yu. A. Simonov, Yad. Fiz. **62**, 2087 (1999) [Phys. At. Nucl. **62**, 1932 (1999)]; hep-ph/9912383.
39. Yu. A. Simonov, J. A. Tjon, and J. Weda, Phys. Rev. D (in press); hep-ph/0111344.
40. Yu. A. Simonov, hep-ph/0203059; Phys. Rev. D (in press).
41. Yu. A. Simonov, Phys. Lett. B **515**, 137 (2001).
42. Yu. A. Simonov and J. A. Tjon, Ann. Phys. (N.Y.) **228**, 1 (1993); hep-ph/0201005; hep-ph/0205165.
43. Yu. A. Simonov, Z. Phys. C **53**, 419 (1992).
44. D. S. Kuzmenko and Yu. A. Simonov, Phys. Lett. B **494**, 81 (2000); Yad. Fiz. **64**, 1971 (2001) [Phys. At. Nucl. **64**, 1887 (2001)]; hep-ph/0010114.
45. G. S. Bali, Phys. Rep. **343**, 1 (2001); C. Alexandrou, Ph. de Forcrand, and A. Tsapalis, Nucl. Phys. B (Proc. Suppl.) **109**, 153 (2002); nucl-th/0111046; Phys. Rev. D **65**, 054503 (2002); hep-lat/0107006.
46. D. S. Kuzmenko and Yu. A. Simonov, hep-ph/0202277; D. S. Kuzmenko, hep-ph/0204250.
47. A. Yu. Dubin, A. B. Kaidalov, and Yu. A. Simonov, Yad. Fiz. **58**, 348 (1995) [Phys. At. Nucl. **58**, 300 (1995)].
48. V. L. Morgunov, V. I. Shevchenko, and Yu. A. Simonov, Yad. Fiz. **61**, 739 (1998) [Phys. At. Nucl. **61**, 664 (1998)]; Phys. Lett. B **416**, 433 (1998); hep-ph/9704282.
49. Yu. S. Kalashnikova and A. V. Nefediev, Yad. Fiz. **61**, 871 (1998) [Phys. At. Nucl. **61**, 785 (1998)]; L. Brink, P. Di Vecchia, and P. Howe, Nucl. Phys. B **118**, 76 (1977).
50. Yu. A. Simonov, Yad. Fiz. **64**, 1959 (2001) [Phys. At. Nucl. **64**, 1876 (2001)]; hep-ph/0110033.
51. A. M. Polyakov, *Gauge Fields and Strings* (Harwood Academic, Chur, 1987).
52. Yu. A. Simonov (in preparation).
53. V. L. Morgunov, A. V. Nefediev, and Yu. A. Simonov, Phys. Lett. B **464**, 265 (1999); hep-ph/9906318.
54. Yu. A. Simonov, Yad. Fiz. **3**, 630 (1966) [Sov. J. Nucl. Phys. **3**, 461 (1966)]; A. M. Badalian and Yu. A. Simonov, Yad. Fiz. **3**, 1032 (1966) [Sov. J. Nucl. Phys. **3**, 755 (1966)]; F. Calogero and Yu. A. Simonov, Phys. Rev. **183**, 869 (1969); A. M. Badalian *et al.*, Nuovo Cimento A **68**, 577 (1970); M. Fabre de la Ripelle, Ann. Phys. (N.Y.) **123**, 185 (1979).
55. A. M. Badalian and D. S. Kuzmenko, Phys. Rev. D **65**, 016004 (2002); hep-ph/0104097.
56. S. Huang and J. Tjon, Phys. Rev. C **49**, 1702 (1994); hep-ph/9308362; B. Metsch and U. Loering, in *Proceedings of the 9th International Symposium on Meson–Nucleon Physics and the Structure of Nucleon (MENU 2001), Washington, 2001,* hep-ph/0110415.

Physics of Atomic Nuclei, Vol. 66, No. 2, 2003, pp. 355–361. Translated from Yadernaya Fizika, Vol. 66, No. 2, 2003, pp. 381–387.

ELEMENTARY PARTICLES AND FIELDS
Theory

Production of the $f_0(980)$ Resonance in the Reaction $\pi^- p \to \pi^0\pi^0 n$

N. N. Achasov* **and G. N. Shestakov****

Institute of Mathematics, Siberian Division, Russian Academy of Sciences, pr. Akademika Koptyuga 4, Novosibirsk, 630090 Russia

Received September 5, 2001; in final form, January 14, 2002

Abstract—Predictions of the model that relies on purely one-pion exchange and which describes well GAMS data on the rearrangement of the S-wave mass spectrum of the $\pi^0\pi^0$ system in the region of the $f_0(980)$ resonance with increasing $-t$ in the reaction $\pi^- p \to \pi^0\pi^0 n$ are compared with detailed data that were recently obtained at the Brookhaven National Laboratory (BNL) for the m and t distributions of the number of events of the reaction $\pi^- p \to \pi^0\pi^0 n$. An analysis revealed that these BNL data disagree with the predictions of this model. This suggests that a different mechanism must be responsible for the phenomenon discovered experimentally. Most likely, this is the a_1-exchange mechanism. © *2003 MAIK "Nauka/Interperiodica".*

1. INTRODUCTION

Recent experiments that were devoted to studying the reaction $\pi^- p \to \pi^0\pi^0 n$ at high energies and which were performed by the GAMS Collaboration at the Institute for High Energy Physics (IHEP, Protvino) [1, 2] and by the E852 Collaboration at the Brookhaven National Laboratory (BNL) [3, 4] discovered an interesting phenomenon: with increasing $-t$, where t is the square of the 4-momentum transfer from π^- to the $\pi^0\pi^0$ system, the S-wave mass spectrum of the $\pi^0\pi^0$ system undergoes a rearrangement in the region of the $f_0(980)$ resonance. At low $-t$—that is, in the region where the reaction $\pi^- p \to \pi^0\pi^0 n$ is determined predominantly by the one-pion-exchange mechanism—the $f_0(980)$ resonance manifests itself in the S-wave mass spectrum of the $\pi^0\pi^0$ system as a dip caused by the destructive interference between the contribution of the $f_0(980)$ resonance and a large smooth background accompanying it, while, at high $-t$, the resonance produces a distinct peak [1–4].

The fact that both the GAMS and the BNL data are based on high statistics imposes quite stringent limitations on the phenomenological models constructed for explaining these data.

Historically, the first description [5] of the GAMS data on the production of the $f_0(980)$ resonance [1] relied on the model of purely one-pion exchange. Within this model, the authors of this description had to assume very specific t dependences of the amplitudes for individual contributions that determine the total amplitude of the S-wave process $\pi^{*+}(t)\pi^- \to \pi^0\pi^0$ [where $\pi^*(t)$ is the Reggeized pion]. With minor modifications, this method for describing the GAMS data was repeatedly reproduced in later publications [6, 7]. A radically new explanation of the GAMS results in question was proposed in [8], where the main role was attributed to the amplitude of the reaction $\pi^- p \to \pi^0\pi^0 n$ involving the t-channel exchange of the quantum numbers of the a_1 Regge pole. Briefly, the scenario considered in [8] is the following. In the region of low $-t$, the reaction $\pi^- p \to (\pi^0\pi^0)_S n$ [hereafter, $(\pi\pi)_S$ means that we consider a $\pi\pi$ system having zero orbital angular momentum] is dominated by the one-pion-exchange mechanism, with the result that the $f_0(980)$ resonance produced via this mechanism manifests itself as a dip. With increasing $-t$, the contribution of one-pion exchange decreases fast, and the main contribution to the reaction $\pi^- p \to (\pi^0\pi^0)_S n$ at high $-t$ comes from a_1 exchange [8]. The $f_0(980)$ resonance produced owing to a_1 exchange is observed as a peak in the two-pion mass spectrum. It is precisely the way in which the $f_0(980)$ resonance manifests itself in all known reactions where it is produced through channels other than that of elastic $\pi\pi$ interaction [8].

Although the descriptions of the GAMS data were satisfactory both in [5] and in [8], the two models being considered require additional experimental tests [8]. We note that the scenario considered in [8] can be disproved solely by experiments studying the reaction $\pi^- p \to (\pi^0\pi^0)_S n$ with polarized targets, because only on the basis of data of such experiments can one separate the mechanisms of π and a_1 exchange. As

*e-mail: achasov@math.nsc.ru
**e-mail: shestako@math.nsc.ru

to the model relying on the mechanism of purely one-pion exchange [5], its experimental verification may be straightforward owing to spectacular predictions of the model—for example, the prediction for the t distribution of events of the reaction $\pi^- p \to (\pi^0\pi^0)_S n$ in the range $0 < -t < 0.2$ GeV^2 at the $\pi^0\pi^0$ invariant mass satisfying the condition $m < 1$ GeV—and we partly touched upon this point in [8]. A comparison with the existing GAMS data cannot reveal all predictions hidden in the model proposed in [5]. However, recent detailed BNL data [4] on the m and t distributions of events of the reaction $\pi^- p \to (\pi^0\pi^0)_S n$ offer a unique possibility for subjecting the predictions of this model [5] to a comprehensive experimental test, and this is precisely the main objective of present study.

The ensuing exposition is organized as follows. In Section 2, we give a concise account of the original one-pion-exchange model constructed in [5] to describe the dip in the mass spectrum of the $(\pi^0\pi^0)_S$ system in the region of the $f_0(980)$ resonance at low $-t$ and the emergence of a $f_0(980)$ peak instead of the dip with increasing $-t$ in the reaction $\pi^- p \to (\pi^0\pi^0)_S n$. We also briefly consider all further versions of this model [6, 7, 9, 10]. We emphasize that the model does not respect the standard hypothesis that the t dependence factorizes in the amplitude of the S-wave process $\pi^*(t)\pi \to \pi\pi$—previously, this hypothesis was always widely used as a reliable tool for obtaining data on partial waves in $\pi\pi$ scattering (see, for example, [8, 11–16])—and indicate that the predictions of the model that are associated with the violation of this hypothesis can be subjected to a direct experimental test. In Section 3, we perform a detailed comparison of the model proposed in [5] with the BNL data [4]. In Section 4, we briefly formulate our main conclusions.

2. MODEL OF THE ONE-PION-EXCHANGE AMPLITUDE FOR THE PRODUCTION OF THE $(\pi^0\pi^0)_S$ SYSTEM IN THE REACTION $\pi^- p \to (\pi^0\pi^0)_S n$

In [5], the differential distribution of events of the reaction $\pi^- p \to (\pi^0\pi^0)_S n$ at a fixed momentum of the incident π^- meson was represented in the form

$$\frac{d^2N}{dmdt} = C\left|\frac{\sqrt{-t}}{m_\pi^2 - t}F(t)a_{\pi\pi}(m,t)\right|^2, \qquad (1)$$

where C is a normalization factor, $F(t)$ is the form factor associated with the $\pi^*(t)NN$ vertex, and $a_{\pi\pi}(m,t)$ is the amplitude of the S-wave process $\pi^*(t)\pi \to \pi\pi$ for the isospin of $I = 0$. The amplitude $a_{\pi\pi}(m,t)$ was constructed in [5] by using the K-matrix method. In order to describe the data in the range $0.7 < m < 1.2$ GeV, two bare resonances coupled to the $\pi\pi$ and $K\bar{K}$ channels were taken into account in the K matrix, along with some background contributions. From the general expression $\hat{A} = \hat{K}(t)(\hat{I} - i\hat{\rho}\hat{K})^{-1}$ for the amplitude ($\hat{A}$ and $\hat{K}$ are 2×2 matrices that describe transitions in the $\pi\pi$ and $K\bar{K}$ channels, $\hat{I}$ is the identity matrix, and $\hat{\rho}$ is the diagonal phase-space matrix), it follows that

$$a_{\pi\pi}(m,t) = \frac{K_{\pi\pi}(t) + i\rho_K[K_{\pi K}(t)K_{K\pi} - K_{\pi\pi}(t)K_{K\bar{K}}]}{1 - i\rho_\pi K_{\pi\pi} - i\rho_K K_{K\bar{K}} + \rho_\pi\rho_K[K_{\pi K}K_{K\pi} - K_{\pi\pi}K_{K\bar{K}}]}, \qquad (2)$$

where, according to [5], $\rho_\pi = (1 - 4m_\pi^2/m^2)^{1/2}$ and $\rho_K = (1 - 4m_K^2/m^2)^{1/2}$ ($\rho_K \to i|\rho_K|$ for $0 < m < 2m_K$); $K_{\pi b}(t = m_\pi^2) = K_{\pi b}$; for $t \to m_\pi^2$, the amplitude $a_{\pi\pi}(m,t)$ reduces to the standard $\pi\pi$ scattering amplitude; $K_{\pi K} = K_{K\pi}$; and $K_{K\bar{K}}(t) \equiv K_{K\bar{K}}$. The specific expression for the K-matrix elements has the form

$$K_{ab}(t) = \left[\frac{g_a(t)g_b}{M_1^2 - m^2} + \frac{G_a(t)G_b}{M_2^2 - m^2} + f_{ab}(t)\right] \times \left(1 - \frac{m_\pi^2}{2m^2}\right), \qquad (3)$$

where the subscripts $a = \pi, K$ and $b = \pi, K$ (or $\bar{K}$) form the condensed notation used in [5] for the $\pi\pi$ and $K\bar{K}$ channels; $f_{K\bar{K}} = 0$; and g_b and G_b are the coupling constants of the input resonances having the masses M_1 and M_D, respectively.[1)]

In order to make the analysis of the structure of expression (2) clearer, it is convenient to discard the

[1)] By using representation (2), one can easily show that the expression for $d^2N/dmdt$ normalized correctly at the pion pole differs from (1) by the factor $m\rho_\pi/(1\text{ GeV})$, which, in [5], was unjustifiably set to unity for all values of m (this is so only in the vicinity of the point $m = 1$ GeV). We also note that the authors of [5] deemed that, with the aid of the factor $(1 - m_\pi^2/(2m^2))$ in expression (3), they took into account the Adler zero in the $\pi\pi$-scattering amplitude. However, this function is not good since it has a pole at $m^2 = 0$. Further, it reduces to unity at $m_\pi = 0$. At the same time, the Adler concept emerged from the theory where pions are massless, and the success of chiral theory gives every reason to believe that the world of massless pions is close to the real world.

background contributions in (3), which are described by the functions $f_{ab}(t)$, and to neglect, in the parenthetical factor, the term $m_\pi^2/(2m^2)$, which is much less than unity at the m values being considered. With allowance for these simplifications, expression (2) assumes the form

$$a_{\pi\pi}(m,t) = \frac{g_\pi(t)[D_2(m)g_\pi + \Pi_{12}(m)G_\pi] + G_\pi(t)[D_1(m)G_\pi + \Pi_{12}(m)g_\pi]}{D_1(m)D_2(m) - \Pi_{12}^2(m)}, \quad (4)$$

where $D_1(m) = M_1^2 - m^2 - ig_\pi^2\rho_\pi - ig_K^2\rho_K$ and $D_2(m) = M_2^2 - m^2 - iG_\pi^2\rho_\pi - iG_K^2\rho_K$ are the inverse propagators of the bare resonances and $\Pi_{12}(m) = ig_\pi G_\pi\rho_\pi + ig_K G_K\rho_K$ is the amplitude that describes the transitions between these two resonances via real intermediate $\pi\pi$ and $K\bar{K}$ states. One can easily see that expression (4) represents the amplitude of the process $\pi^*(t)\pi \to \pi\pi$ for $L = I = 0$ due to the contributions of two mixed resonances coupled to the $\pi\pi$ and $K\bar{K}$ channels.

It is now clear that the experimentally observed rearrangement of the $(\pi^0\pi^0)_S$ mass spectrum with increasing $-t$ can be explained within the model being considered only if the destructive interference between the contributions of two resonances at $m \approx 1$ GeV in the region of low $-t$ gives way to constructive interference with increasing $-t$. In terms of expression (4), this means the change in the character of the interference between the terms proportional to $g_\pi(t)$ and $G_\pi(t)$. This is possible only if one of the residues of, say, $g_\pi(t)$, decreases in magnitude with increasing $-t$, vanishes at some $t = t_0$, and then changes sign. According to the analysis of the GAMS data that is given in [5], this must occur at $-t < 0.2$ GeV^2. It follows that, within this approach, the t dependence does not factorize in the amplitude $a_{\pi\pi}(m,t)$ at $m \approx 1$ GeV even at low $-t$. As was mentioned in the Introduction, the hypothesis that the t dependence factorizes in the partial-wave amplitudes of the process $\pi^*(t)\pi \to \pi\pi$ was widely used as a standard tool for extracting information about $\pi\pi$ scattering from $\pi N \to \pi\pi N$ reactions. The results obtained in this way were always in good agreement with the results of the Chew–Low extrapolation method [8, 11–16], which is more general. In our case, this hypothesis essentially consists in the assumption that the amplitude $a_{\pi\pi}(m,t)$ is proportional to the amplitude $a_{\pi\pi}(m, t = m_\pi^2)$ at low $-t$—that is, at $-t$ in the range between 0 and 0.15–0.2 GeV^2 [8, 11–16]. The proportionality factor is usually taken to be a form factor of the $\exp[b(t - m_\pi^2)]$ type. On the other hand, it follows from [5] that, for the model of the purely one-pion exchange to be consistent with the GAMS data, the hypothesis in question must be completely rejected.

In [5], the residues of $g_\pi(t)$, $G_\pi(t)$, $f_{\pi\pi}(t)$, and $f_{\pi K}(t)$ were parametrized as

$$g_\pi(t) = g_\pi + (1 - t/m_\pi^2)tg'_\pi/m_\pi^2, \quad (5)$$
$$G_\pi(t) = G_\pi + (1 - t/m_\pi^2)tG'_\pi/m_\pi^2,$$

$$f_{\pi\pi}(t) = (1 - t/m_\pi^2)tf'_{\pi\pi}/m_\pi^2, \quad (6)$$
$$f_{\pi K}(t) = f_{\pi K} + (1 - t/m_\pi^2)tf'_{\pi K}/m_\pi^2.$$

Three versions of a fit to the GAMS data [1] were presented in [5]; in the best one, $M_1 = 0.773$ GeV, $M_2 = 1.163$ GeV, $g_\pi = 0.848$ GeV, $g'_\pi = 0.0479$ GeV, $G_\pi = 0.848$ GeV, $G'_\pi = -0.0259$ GeV, $f'_{\pi\pi} = 0.0963$, $f_{\pi K} = 0.687$, and $f'_{\pi K} = 0.0818$. It follows from (5) that $g_\pi(t)$ vanishes at $t \approx -0.0728$ GeV^2.[2)] With increasing $-t$, the dip in the mass spectrum of the $(\pi^0\pi^0)_S$ system in the region of the $f_0(980)$ resonance will therefore gradually disappear, finally giving way to a resonance-type enhancement [5]. We emphasize that, owing to the destructive interference between various contributions, the on-shell amplitude $a_{\pi\pi}(m, t = m_\pi^2)$ (2) vanishes at $m = m_0 \approx 0.986$ GeV—that is, slightly below the $K\bar{K}$ threshold—the phase of the amplitude at this point taking the value of 180°, in agreement with experimental data from [12, 13]. Analyzing the model proposed in [5], we found that, with increasing $-t$, the amplitude in (2) still retains the property of vanishing, but this occurs at other values of $m < 2m_K$, which

[2)] In addition, the functions $g_\pi^2(t)$ and $G_\pi^2(t)$ increase by factors of about 22 000 and 6000, respectively, as $-t$ grows from 0 to 1 GeV^2. In order to compensate for this anomalous growth, the form factor $F(t) = [(\Lambda - m_\pi^2)/(\Lambda - t)]^4$ with $\Lambda = 0.1607$ GeV^2 was introduced by Anisovich *et al.* [5] in the one-pion-exchange amplitude of the reaction $\pi^- p \to (\pi^0\pi^0)_S n$ [see expression (1)]. However, this form factor, which decreases fast with increasing $-t$ and which was associated in [5] with the nucleon vertex (see also [6, 7, 10]), leads to unsolvable difficulties in other reactions [8]. For example, this form factor causes an anomalously fast decrease in the one-pion-exchange (OPE) contribution to the differential cross section for the charge-exchange reaction $np \to pn$. Since $d\sigma^{(\mathrm{OPE})}(np \to pn)/dt \sim |F(t)|^4$, the cross section decreases approximately in proportion to $\exp(56t)$ in the interval of $-t$ values from 0 to 0.2 GeV^2; this is commensurate only with the decrease in cross sections for diffractive processes on heavy nuclei.

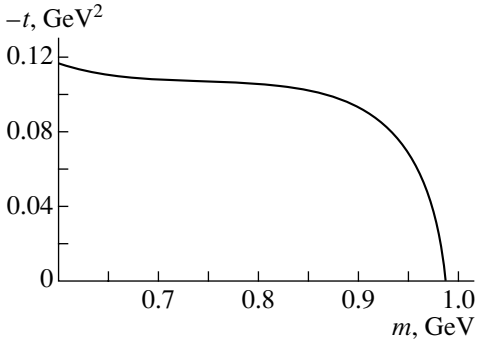

Fig. 1. Trajectory of the zero of the amplitude $a_{\pi\pi}(m,t)$ in the model proposed in [5].

depend on $-t$. Figure 1 displays the trajectory of the zero of the amplitude in (2) in the plane spanned by the variables m and $-t$. It is clear from the figure that, with increasing $-t$, the zero of the amplitude moves, at an ever greater rate, from the region around $m \approx 2m_K$ to the region of lower masses. By way of example, we indicate that, as $-t$ increases from 0.09 GeV^2 only by 0.026 GeV^2, the zero traverses a wide interval of m from 0.91 to 0.60 GeV.

Thus, we have found two spectacular predictions of the model constructed by Anisovich *et al.* [5]. First, the distribution dN/dt of events with respect to the square of 4-momentum transfer is predicted to have a dip in the region of low $-t$ at each fixed value of the mass of the $(\pi^0\pi^0)_S$ system in the region $m < 2m_K$ (more precisely in each narrow interval of the mass value). For example, the dip in dN/dt must occur at $-t \approx 0.1$ GeV^2 in each m interval from the range $0.6 < m < 0.91$ GeV; with increasing m from 0.91 to 0.986 GeV, the dip in dN/dt must move toward the point $t = 0$. Second, the cross section for the reaction $\pi^- p \to (\pi^0\pi^0)_S n$ at $0.6 < m < 0.9$ GeV is expected to be suppressed in the vicinity of the point $-t \approx 0.1$ GeV^2, because, in this region of variables, the one-pion-exchange amplitude is close to zero; for $m > 0.9$ GeV, the cross section must increase fast. Thus, the model being considered, which describes the GAMS data [1] on the rearrangement of the $(\pi^0\pi^0)_S$ mass spectrum in the region of the $f_0(980)$ resonance for $-t > 0.3$ GeV^2, can be unambiguously tested on the basis of its predictions for the distributions dN/dt and dN/dm of events for $0 < -t <$ 0.2–0.25 GeV^2 and 0.6 GeV$< m < 2m_K$. Of course, such tests require much more detailed data than those presented by the GAMS Collaboration [1]. We recall that the GAMS data [1] on the reaction $\pi^- p \to (\pi^0\pi^0)_S n$ include the distribution dN/dm of events for the m interval between 0.8 and 1.2 GeV for $0 < -t < 0.2$ GeV^2—that is, the distribution for the entire region of low $-t$—and five more distributions dN/dm in the m interval between 0.6 and 1.4 GeV for various $-t$ intervals from the range $0.3 < -t < 1$ GeV^2.

In the further versions of the model (see [6, 7, 9, 10]), the K-matrix analysis of the $IJ^{PC} = 00^{++}$ waves was extended to a wider region of invariant masses and a greater number of coupled channels. In [6], Anisovich and Sarantsev included, in the K matrix, four bare resonances coupled to the $\pi\pi$, $K\bar{K}$, $\eta\eta$, and 4π channels and analyzed the mass region up to 1.55 GeV. In [7, 9, 10], the authors included, in the K matrix, five bare resonances coupled to the $\pi\pi$, $K\bar{K}$, $\eta\eta$, $\eta\eta'$, and 4π channels and extended the m region over which they described data up to 1.9 GeV. Of course, the additional resonances from the mass range 1.2–1.9 GeV that were introduced in [6, 7, 9, 10] have an effect on the region $m < 1$ GeV. However, the main predictions of the two-resonance model in [5] at $m < 1$ GeV still remain valid, apart from some details. For example, the most significant feature of the parametrization proposed in [5] for the one-pion exchange amplitude—namely, the vanishing of the residue for the lightest bare resonance with increasing $-t$—occurs in all versions of the model. The mass of this resonance changed from one version of the model to another within the interval between 0.65 and 0.86 GeV. In the fit leading to the smallest value of χ^2, the zero of the residue for the lightest resonance occurs at $-t = 0.0728$ GeV^2 according to [5] (as was already mentioned), $-t = 0.117$ GeV^2 according to [6] (solution I), $-t = 0.0683$ GeV^2 according to [7] (solution I), and $-t = 0.038$ GeV^2 according to [9]. Unfortunately, the parameter values required for determining the position of the zero were not given in [10].

We note that, after the appearance of the analysis presented in [8] and aimed at providing a new description of the GAMS data [1], the contribution of a_1 exchange was also included in [9]. However, this contribution was taken into account there in a cosmetic manner: this did not induce any changes in the character of parametrization of the one-pion-exchange amplitude, while the amplitude itself retained its dominant role in the description of the effect found experimentally. Since the contribution of a_1 exchange at low $-t$ is in fact small, the predictions of the model from [9] for the region of low $-t$ and $m < 1$ GeV are by and large close to the predictions of the model proposed in [5], which have already been described qualitatively. This is clear from the curves for the distributions dN/dm and dN/dt in [9] (Figs. 3 and 5 in the article published in *Physics Letters* or Figs. 5 and 7 in the article published in *Physics of Atomic Nuclei*, these two pairs of figures being identical). It is interesting to note that, in the article quoted in [10], which was

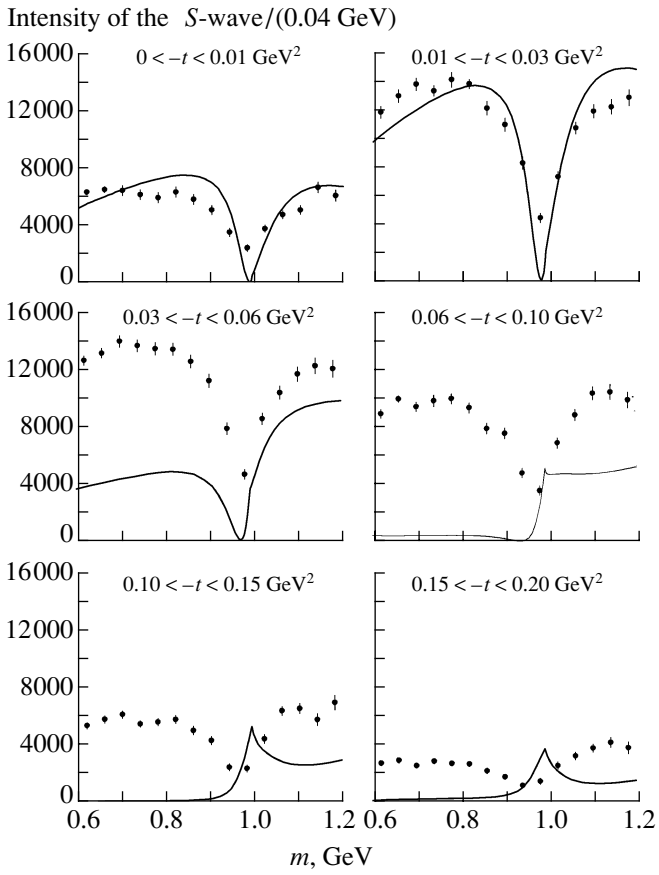

Fig. 2. Mass spectra of the $(\pi^0\pi^0)_S$ system from the reaction $\pi^-p \to (\pi^0\pi^0)_S n$ for six successive intervals of $-t$. Points represent BNL data from [4]. The curves were calculated on the basis of Eqs. (1)–(3), (5), and (6) by using the parameter values and the overall-normalization method indicated in the main body of the text.

published later than those in [9], the mechanism of a_1 exchange was disregarded, as earlier in [5–7].[3)]

We also note that the absence of data on the decay $a_1(1260) \to f_0(980)\pi$ cannot invalidate evidence obtained in [8] (see also [16]) that quantum numbers of the a_1 Regge pole are exchanged in the reaction $\pi^-p \to (\pi^0\pi^0)_S n$. The point is that this decay, which is a P-wave process, is strongly suppressed by the phase space; for this reason, it is difficult to separate it from the dominant background decay $a_1(1260) \to \rho\pi$. We emphasize once again that the contribution of a_1 exchange to the integrated cross section for the reaction $\pi^-p \to (\pi^0\pi^0)_S n$ is small—it does not exceed 5–10%. However, this small contribution is significant in the region of kinematical variables where one-pion exchange is small, describing the observed rearrangement of the $(\pi^0\pi^0)_S$ mass spectrum in the region of the $f_0(980)$ resonance [8].

[3)]It is worth noting that the comment following Eq. (8) in [5] and concerning the smooth term that effectively describes, among other things, the contribution of a_1 exchange to the $\pi N \to (\pi\pi)_S N$ amplitude with the quantum numbers of t-channel one-pion exchange from Eq. (5) or (6) in [5] may lead one astray. As a matter of fact, the amplitudes featuring the exchanges of π and a_1 Reggeons have different spin structures at high energies, their contributions to the cross section for the reaction involving unpolarized nucleons being noncoherent. Therefore, the exchange of a_1 was not included, even effectively, in the analyses given in [5–7, 10].

3. COMPARISON WITH BNL DATA

The E852 collaboration presented high-statistics data on the distribution dN/dm of events of the reaction $\pi^-p \to (\pi^0\pi^0)_S n$ in the m region from the $\pi\pi$ threshold to 2.2 GeV with step $\Delta m = 0.04$ GeV. These data cover nine successive intervals of $-t$ in the range $0 < -t < 0.4$ GeV^2 and one interval of $-t$ from 0.4 to 1.5 GeV^2 [4]. Figures 2 and 3 display those BNL data from [4] that we use here to test the predictions of the model proposed in [5]. We emphasize that we do not fit the data within this model [5]; we merely take the model with the same parameter values at which it provides a very good description of the GAMS data [1] and contrast its

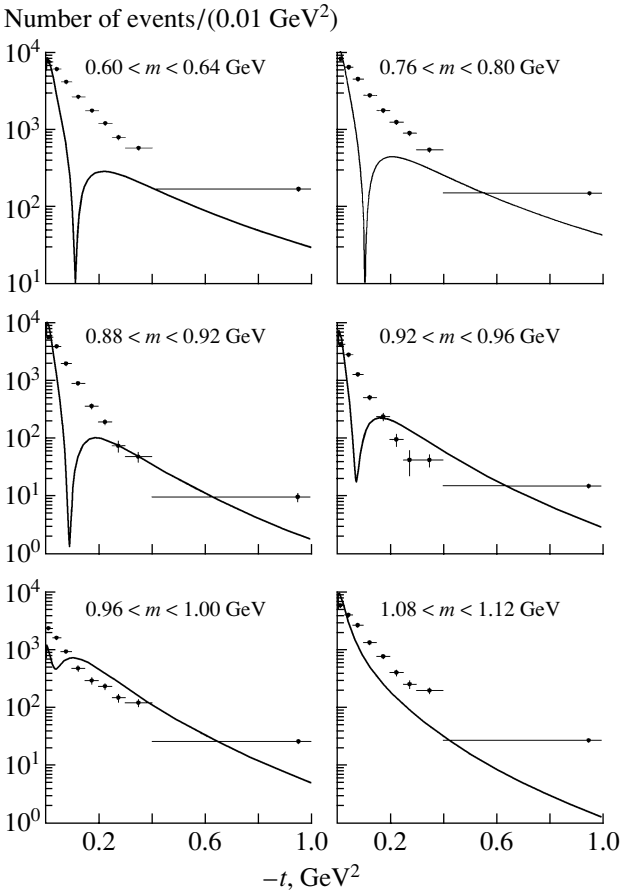

Fig. 3. Distribution of events of the reaction $\pi^- p \to (\pi^0\pi^0)_S n$ with respect to $-t$ for six intervals of the invariant mass m of the $(\pi^0\pi^0)_S$ system. Points represent BNL data from [4]. As in Fig. 14 from [4], the data for the intervals $0 < -t < 0.01$ GeV^2 and $0.01 < -t < 0.03$ GeV^2 are combined. The curves were calculated on the basis of Eqs. (1)–(3), (5), and (6) by using the parameter values and the overall-normalization method indicated in the main body of the text.

predictions against the BNL data [4] on the distributions dN/dm in all six narrow intervals of $-t$ from the range $0 < -t < 0.2$ GeV^2 and on the distributions dN/dt for six m intervals of width 0.04 GeV each that were chosen by way of example from the range $0.6 < m < 1.12$ GeV. There were no such detailed distributions in the GAMS data quoted in [1, 2]. The normalization factor C in (1) is the only parameter to be determined anew. We evaluate it by normalizing the theoretical distribution to the total number of events in the interval $0.6 < m < 1.2$ GeV for $0.01 < -t < 0.03$ GeV^2. Figure 2 displays the data on dN/dm for this region of the variables. We note that, of all $-t$ intervals of the same width, the interval $0.01 < -t < 0.03$ GeV^2 contains the maximum number of events for $0.6 < m < 1.2$ GeV. We deem that this choice of normalization is quite appropriate for performing an informative comparison of the experimental and theoretical distributions with respect to m and t.

It is clear from Fig. 2 that the experimental and theoretical distributions dN/dm are in satisfactory qualitative agreement in the intervals $0 < -t < 0.01$ GeV^2 and $0.01 < -t < 0.03$ GeV^2. With increasing $-t$, however, the behavior of the theoretical distributions dN/dm changes sharply, showing perfect conformity with the expectations described in Section 2 and disagreement with the data. In addition, it can be seen from Fig. 2 that, in the model proposed in [5], the dip in the region of the $f_0(980)$ resonance prematurely transforms with increasing $-t$ into a peak in the interval between 0.1 and 0.2 GeV^2. As to the experimental distributions dN/dm, they remain similar over the entire range of low $-t$ from 0 to 0.2 GeV^2 (see Fig. 2) and have a dip at the m value near the $K\bar{K}$ threshold. We emphasize once again that, in contrast to the detailed BNL data [4], shown in Fig. 2, the data of the GAMS Collaboration include only one "global" distribution dN/dm for the entire range $0 < -t < 0.2$ GeV^2, which contains about 90% of all events. It is precisely with this coarse distribution dN/dm (associated with a broad t interval) that satisfactory agreement was obtained in [5] by fitting the model of purely one-pion exchange.

Figure 3 shows the BNL data from [4] on t distributions. It can clearly be seen that, for $m < 1$ GeV, the dN/dt distributions feature no dips expected in the model proposed in [5]. That the t distributions for the reaction $\pi^- p \to \pi^0\pi^0 n$ behave smoothly in the region $m < 1$ GeV is also confirmed by KEK data reported in [17].

We emphasize that allowance for finite experimental resolutions in m and t in calculating theoretical curves cannot change the character of the predictions of the model constructed in [5] and does not improve its agreement with the BNL data.

4. CONCLUSION

The question of whether the rearrangement of the $(\pi^0\pi^0)_S$ mass spectrum in the region of the $f_0(980)$ resonance with increasing $-t$ in the reaction $\pi^- p \to (\pi^0\pi^0)_S n$ can be described in terms of only the amplitude involving the t-channel quantum numbers of the π Regge pole is quite reasonable and deserves a careful investigation. In this respect, the first attempt at answering this question in [5] was of paramount importance. In our opinion, it was to the credit of this attempt that it resulted in explicitly formulating the one-pion-exchange model capable of yielding spectacular predictions, which can easily be tested

experimentally. From the aforesaid, it is obvious that these predictions are in a glaring contradiction with detailed BNL data on the m and t distributions of events of the reaction $\pi^- p \to (\pi^0\pi^0)_S n$. In our opinion, however, the most important point is that the path outlined in [5] can be traced to the very end. Nevertheless, it is highly desirable that the GAMS Collaboration, which accumulated the highest statistics on the reaction $\pi^- p \to \pi^0\pi^0 n$ [1, 2], would also present data on the distributions dN/dm for narrow $-t$ intervals from the range $0 < -t < 0.2$ GeV^2 and on the distributions dN/dt for narrow m intervals in the region $m < 1$ GeV that are associated with the production of the S-wave $\pi^0\pi^0$ system.

In this connection, we also note that the conclusions drawn in [9, 18] from the analyses of GAMS data [1] on the basis of the model from [5] for the one-pion-exchange amplitude and its versions from [6, 7, 9, 10] are not justified.

ACKNOWLEDGMENTS

We are grateful to the E852 Collaboration for providing free access to detailed BNL data (http://dustbunny.physics.indiana.edu/piopio).

This work was supported in part by the Russian Foundation for Basic Research (RFBR), project no. 02-02-16061, and a joint grant (no. IR-97-232) from INTAS and RFBR.

REFERENCES

1. D. Alde *et al.*, Z. Phys. C **66**, 375 (1995).
2. Yu. D. Prokoshkin, A. A. Kondashov, and S. A. Sadovskiĭ, Dokl. Akad. Nauk **342**, 473 (1995).
3. B. B. Brabson, in *Proceedings of the 6th International Conference on Hadron Spectroscopy, HADRON'95, Manchester, UK, 1995*, Ed. by M. C. Birse, G. D. Lafferty, and J. A. McGovern (World Sci., Singapore, 1996), p. 494; A. R. Dzierba, Nucl. Phys. A **623**, 142c (1997).
4. J. Gunter, A. R. Dzierba, *et al.*, Phys. Rev. D **64**, 072003 (2001).
5. V. V. Anisovich *et al.*, Phys. Lett. B **355**, 363 (1995).
6. V. V. Anisovich and A. V. Sarantsev, Phys. Lett. B **382**, 429 (1996).
7. V. V. Anisovich, Yu. D. Prokoshkin, and A. V. Sarantsev, Phys. Lett. B **389**, 388 (1996).
8. N. N. Achasov and G. N. Shestakov, Phys. Rev. D **58**, 054011 (1998); hep-ph/9802286; Yad. Fiz. **62**, 548 (1999) [Phys. At. Nucl. **62**, 505 (1999)].
9. V. V. Anisovich, D. V. Bugg, and A. V. Sarantsev, Phys. Lett. B **437**, 209 (1998); Yad. Fiz. **62**, 1322 (1999) [Phys. At. Nucl. **62**, 1247 (1999)].
10. V. V. Anisovich *et al.*, Yad. Fiz. **63**, 1489 (2000) [Phys. At. Nucl. **63**, 1410 (2000)].
11. P. E. Schlein, Phys. Rev. Lett. **19**, 1052 (1967); E. Malamud and P. E. Schlein, Phys. Rev. Lett. **19**, 1056 (1967).
12. B. Hyams *et al.*, Nucl. Phys. B **64**, 134 (1973); **100**, 205 (1975).
13. P. Estabrooks and A. D. Martin, Nucl. Phys. B **79**, 301 (1974); **95**, 322 (1975).
14. W. Hoogland *et al.*, Nucl. Phys. B **69**, 266 (1974); **126**, 109 (1977).
15. M. Svec, Phys. Rev. D **53**, 2343 (1996).
16. R. Kamiński, L. Leśniak, and K. Rybicki, Z. Phys. C **74**, 79 (1997).
17. K. Takamatsu, Nucl. Phys. A **675**, 312c (2000).
18. V. V. Anisovich, V. A. Nikonov, and A. V. Sarantsev, hep-ph/0102338.

Translated by M. Kobrinsky

Physics of Atomic Nuclei, Vol. 66, No. 2, 2003, pp. 362–367. Translated from Yadernaya Fizika, Vol. 66, No. 2, 2003, pp. 388–394.

ELEMENTARY PARTICLES AND FIELDS
Theory

Fluctuations of Charged-Particle Multiplicities over Narrow Rapidity Intervals in $\pi^- A$ Collisions at 40 GeV/c

K. G. Akhobadze, T. S. Grigalashvili, E. Sh. Ioramashvili*, E. S. Mailian, M. I. Nikoladze, and L. V. Shalamberidze

Institute of Physics, Georgian Academy of Sciences, ul. Tamarishvili 6, GE-380077 Tbilisi, Republic of Georgia

Received August 1, 2001; in final form, January 9, 2002

Abstract—Maximum fluctuations of charged-particle multiplicities over narrow rapidity intervals are investigated for high-$P_\perp$ processes in $\pi^- A$ collisions (where $A =$ H, D, C, Cu, Pb) at 40 GeV/c. The observed fluctuations are studied by the method of factorial moments. The results show that the factorial moments $\langle F_i \rangle$ vary in proportion to a power of the rapidity gap δy. This suggests that there are dynamical fluctuations in the processes under study. The experimental data are compared with theoretical results obtained on the basis of the model of quark–gluon strings by using the FRITIOF-7.02 package.

1. INTRODUCTION

Multiparticle correlations in multiparticle-production processes induced by hadron–hadron and hadron–nucleus collisions attract much attention [1]. Interest in such phenomena is motivated both by searches for manifestations of the phase transition of hadron matter into a quark–gluon plasma and by the desire to study purely nuclear effects, which distinguish a hadron–nucleus collision from a superposition of nucleon–nucleon interactions [2–4].

Significant fluctuations in rapidity (or pseudorapidity) distributions have been observed in various high-energy experiments—for example, in those where nuclear photoemulsions are exposed to cosmic rays [5] and those that study hadron–hadron [6, 7] and nucleus–nucleus [8] collisions. The existence of such fluctuations can be explained within various models [9, 10].

In [9], it was proposed to study such fluctuations on the basis of an analysis of hadron multiplicities versus rapidity intervals. The dependence of hadron-multiplicity distributions on the rapidity interval can be characterized by factorial moments of order i that are defined as

$$\langle F_i \rangle = \frac{1}{\langle \bar{n}_m \rangle^i} \times \left\langle \frac{1}{M} \sum_{m=1}^{M} n_m (n_m - 1) \dots (n_m - i + 1) \right\rangle, \quad (1)$$

$$\langle \bar{n}_m \rangle = \left\langle \frac{1}{M} \sum_{m=1}^{M} n_m \right\rangle,$$

where the rapidity interval Δy is broken down into M intervals of dimension $\delta y = \Delta y / M$, n_m is the multiplicity in the mth interval ($m = 1, 2, \dots, M$), and the average is taken over all events.

The main results of the aforementioned studies can be summarized as follows:

(i) In the case of purely statistical fluctuations, the function $\langle F_i \rangle$ is expected to be saturated with increasing δy.

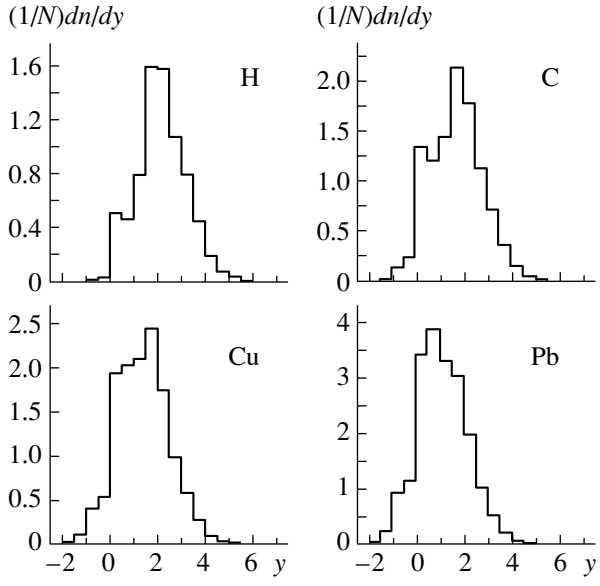

Fig. 1. Distributions in rapidity y for various nuclei.

*e-mail: etheri@iph.hepi.edu.ge

1063-7788/03/6602-0362$24.00

(ii) In the case of dynamical fluctuations, $\langle F_i \rangle$ is an exponential function of δy,

$$\langle F_i \rangle \sim (\Delta y/\delta y)^{f_i}, \quad f_i > 0. \qquad (2)$$

This dynamical effect is referred to as intermittency.

Of particular interest are fluctuations of the multiplicity of charged particles from hadron–nucleus collisions that produce hadrons of high transverse momenta (high-$P_\perp$ processes). Currently available experimental data on such processes at intermediate energies are scanty. Within QCD, the production of particles of high transverse momentum $P_\perp$ on nuclei may be due either to a deformation of the parton distribution in the nucleus involved (hard interaction) or to the rescattering of partons in nuclear matter. In either case, an outgoing particle acquires an additional transverse momentum, with the result that inclusive cross sections may become considerably larger.

It was found in [11] that, at intermediate energies, hard processes play a significant role in high-$P_\perp$ processes induced by $\pi^- A$ collisions. Observation of dynamical fluctuations of charged particles in such processes would provide an additional argument in favor of this conclusion.

In this article, we report on an investigation of fluctuations of charged-particle multiplicities over narrow rapidity intervals. Experimental data used in this investigation were obtained for high-$P_\perp$ processes in $\pi^- A$ collisions (where $A =$ H, D, C, Cu, Pb) at 40 GeV/c.

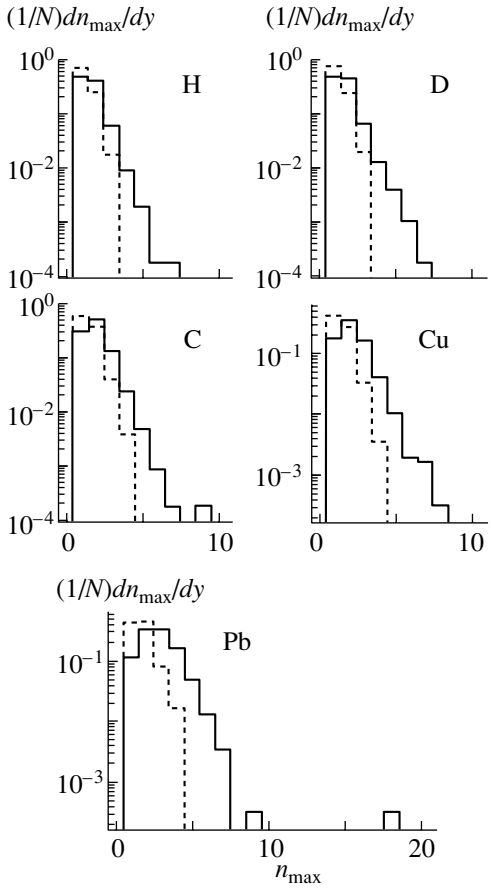

Fig. 2. Rapidity distributions of maximum fluctuations, $dn_{\max}/dy$, over the interval Δy ($\delta y = 0.1$) for various nuclei.

2. EXPERIMENTAL SETUP

A 5-m streamer chamber placed in a magnetic field of strength 15 kG is the hub of the RISC (Relativistic Ionization Streamer Chamber) apparatus used in our experiment. A beam of negatively charged particles produced in the internal target of the U-70 proton synchrotron installed at the Institute for High Energy Physics (IHEP, Protvino) was transported along the magnetooptical channel to a target arranged within the streamer chamber. The beam consisted of π^-, K^-, and $\bar{p}$ in the proportion of $\pi^- : K^- : \bar{p} = (98 : 1.7 : 0.3)\%$. Secondary charged particles of high transverse momenta were detected by a telescope consisting of three two-coordinate proportional chambers of width 1.0 m and height 0.5 m each. The proportional chambers were placed above the streamer chamber and covered the polar-angle range $12^\circ < \theta < 22^\circ$ in the laboratory frame for particles escaping from the target (this corresponds to the polar-angle range $85^\circ < \theta^* < 120^\circ$ in the reference frame comoving with the center of mass of the pion–nucleon system). The transverse-momentum cutoff was varied from 1.0 to 1.5 GeV/c. For targets, we used liquid hydrogen, deuterium, carbon, copper, and lead. A more detailed description of the experimental setup can be found in [12].

3. FLUCTUATIONS OF CHARGED-PARTICLE MULTIPLICITIES

Multiparticle correlations in maximum fluctuations of charged-particle multiplicities over narrow rapidity intervals were sought in the following way: for

Table 1. Experimental data

A	N_{int}	$\langle N_{\text{ch}} \rangle$
H	5427	6.3 ± 0.1
D	5496	6.8 ± 0.2
C	5003	9.9 ± 0.2
Cu	3478	14.3 ± 0.3
Pb	2393	19.4 ± 0.4

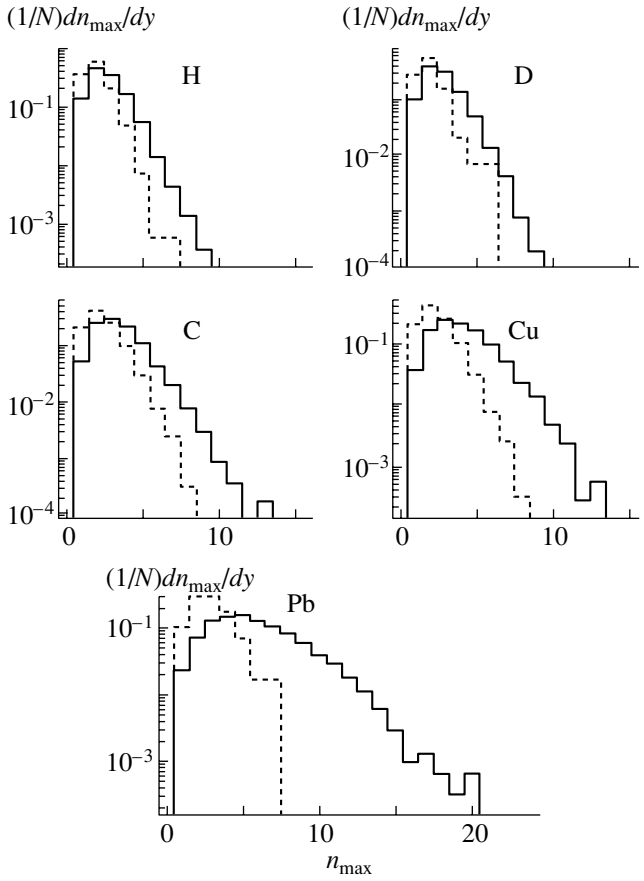

Fig. 3. As in Fig. 2, but for $\delta y = 0.5$.

each individual event, the distribution with respect to the rapidity

$$y = -0.5 \ln \frac{E + P_{||}}{E - P_{||}}, \qquad (3)$$

where E and $P_{||}$ are, respectively, the energy and the longitudinal momentum of a secondary particle, was scanned with a bin of fixed width δy in order to determine the maximum number $n_{\max}$ of particles that fall within this bin. The rapidity interval Δy was chosen in accordance with the actual rapidity distribution of secondaries. Such distributions, normalized to the total number of interactions, N_{int}, are shown in Fig. 1 for various nuclei. It is seen that, in all cases under study, $-2 < y < 7$.

Experimental data used in our study are compiled in Table 1.

The resulting distributions $dn_{\max}/dy$ of the maximum values of fluctuations, $n_{\max}$, over the interval Δy are shown in Fig. 2 (for $\delta y = 0.1$) and Fig. 3 (for $\delta y = 0.5$).

As can be seen from Figs. 2 and 3, large fluctuations of charged-particle multiplicities, $n_{\max} > 5$, over narrow rapidity intervals δy occur for both light and heavy nuclei. The question of whether these fluctuations are dynamical or statistical is considered in the next section.

It can also be seen from Figs. 2 and 3 that the central value of the distribution $dn_{\max}/dy$ increases with increasing mass number of the target nucleus. At the same time, the central value of the distribution $dn_{\max}/dy$ decreases as the interval δy becomes narrower.

The dashed curves in Figs. 2 and 3 represent theoretical predictions obtained on the basis of the model of quark–gluon strings by using the FRITIOF-7.02 package [13, 14]. It can be seen that, for $n_{\max} < 5$, the model predictions agree well with the experimental data, but that, in the region of large fluctuations, the model underestimates $dn_{\max}/dy$. The discrepancy between the predicted and experimental distributions for $n_{\max} > 5$ may stem from the fact that the FRITIOF-7.02 package does not include intranuclear rescatterings, which play a significant part in hA interactions at intermediate energies.

The existence of dynamical fluctuations of charged-particle multiplicities in high-$P_\perp$ processes induced by $\pi^- A$ collisions may be caused by hard interactions between the projectile and target nucleons.

Table 2. Slope parameters B_i and B_i^* for various factorial moments and nuclei

A	B_i	B_i^*	B_i^{**}	A	B_i	B_i^*	B_i^{**}
	$i=2$				$i=4$		
D	0.063 ± 0.006	0.09 ± 0.03		D	0.30 ± 0.02	0.3 ± 0.1	
C	0.058 ± 0.005	0.06 ± 0.02	0.026 ± 0.008	C	0.34 ± 0.02	0.35 ± 0.06	0.113 ± 0.041
Cu	0.065 ± 0.007	0.07 ± 0.02		Cu	0.24 ± 0.02	0.25 ± 0.07	
Pb	0060 ± 0.006	0.07 ± 0.02		Pb	0.17 ± 0.01	0.22 ± 0.05	
	$i=3$				$i=5$		
D	0.19 ± 0.02	0.24 ± 0.05		D	0.76 ± 0.03	0.8 ± 0.2	
C	0.18 ± 0.01	0.20 ± 0.05	0.067 ± 0.018	C	0.60 ± 0.03	0.63 ± 0.09	0.185 ± 0.153
Cu	0.16 ± 0.01	0.17 ± 0.06		Cu	0.22 ± 0.03	0.6 ± 0.1	
Pb	0.12 ± 0.01	0.14 ± 0.04		Pb	0.25 ± 0.02	0.27 ± 0.09	

However, large fluctuations may also result from intranuclear rescatterings.

In the present study, fluctuations of charged-particle multiplicities in events involving the production of neutral strange particles are explored individually. Investigations revealed that neutral strange particles originating from high-$P_\perp$ processes in $\pi^- A$ collisions are predominantly produced via hard interactions (this especially concerns K^0 mesons and $\bar{\Lambda}$ hyperons).

The rapidity distributions of the maximum fluctuations, $dn_{\max}/dy$, over the interval Δy in events involving the production of neutral strange particles are shown in Figs. 4 ($\delta y = 0.1$) and 5 ($\delta y = 0.5$). It can be seen that the fraction of large fluctuations in such events is smaller than that in ordinary high-$P_\perp$ processes (Figs. 2 and 3). This distinction can be explained by the fact that, in reactions leading to the production of neutral strange particles, intranuclear rescatterings, which give rise to large fluctuations, are suppressed.

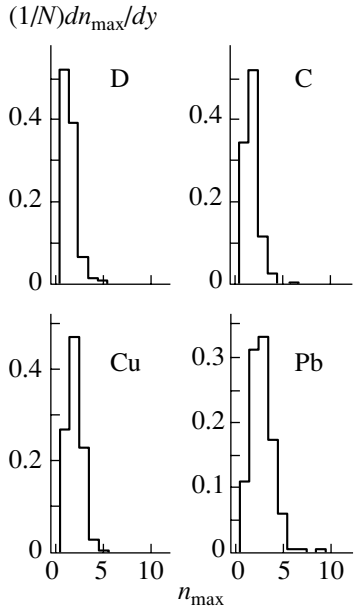

Fig. 4. Rapidity distributions of maximum fluctuations, $dn_{\max}/dy$, over the interval Δy ($\delta y = 0.1$) for the production of neutral strange particles on various nuclei.

4. ANALYSIS OF FLUCTUATIONS BY THE METHOD OF FACTORIAL MOMENTS

As was mentioned in the Introduction, the dynamical nature of the fluctuations in question can be established by the method of factorial moments.

The dependence of the logarithms of the factorial moments $\langle F_i \rangle$ ($i = 2, 3, 4, 5$) calculated by formula (1) on the variable $-\ln \delta y$ over the rapidity interval $-2 < y < 7$ is shown in Fig. 6 for all charged hadrons produced in high-$P_\perp$ processes induced by $\pi^- A$ collisions at 40 GeV/c. The analogous dependence for events involving the production of neutral strange particles is given in Fig. 7.

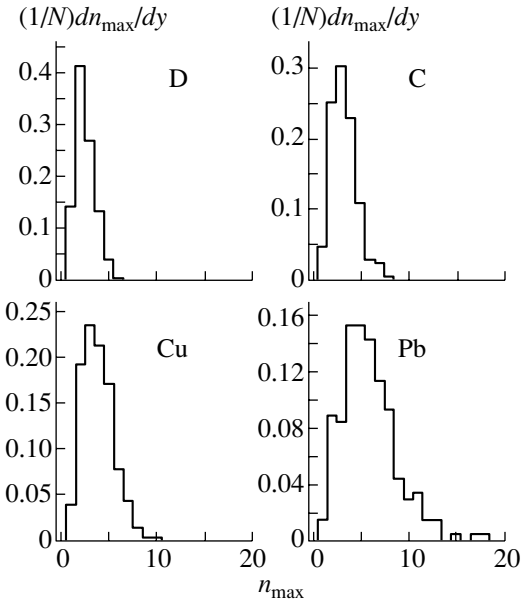

Fig. 5. As in Fig. 4, but for $\delta y = 0.5$.

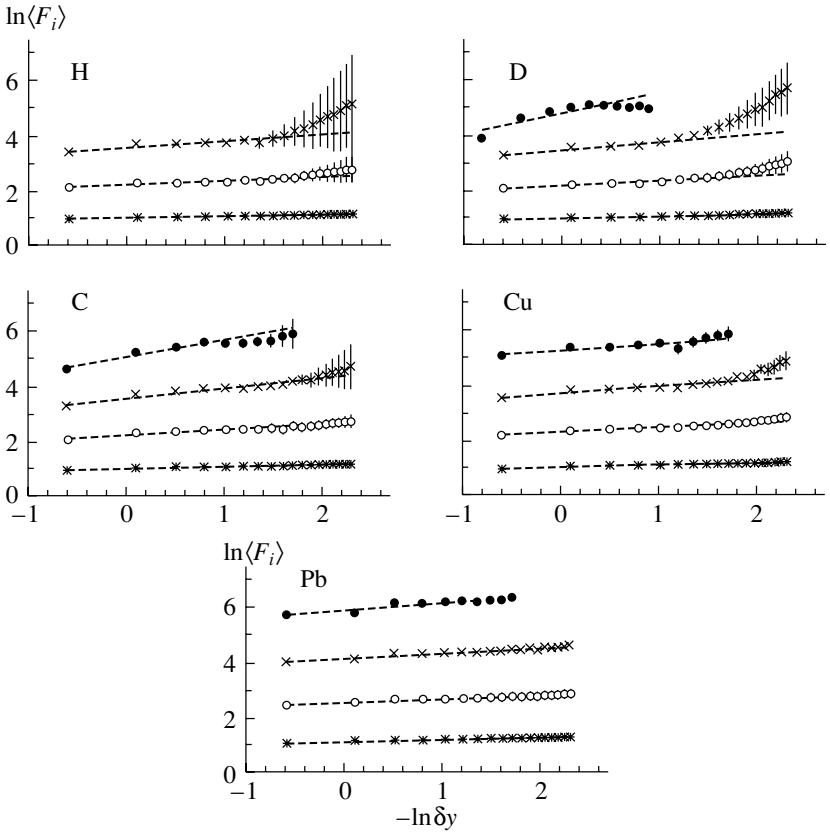

Fig. 6. Logarithms of the factorial moments $\langle F_i \rangle$ versus the variable $-\ln \delta y$ (over the interval $-2 < y < 7$).

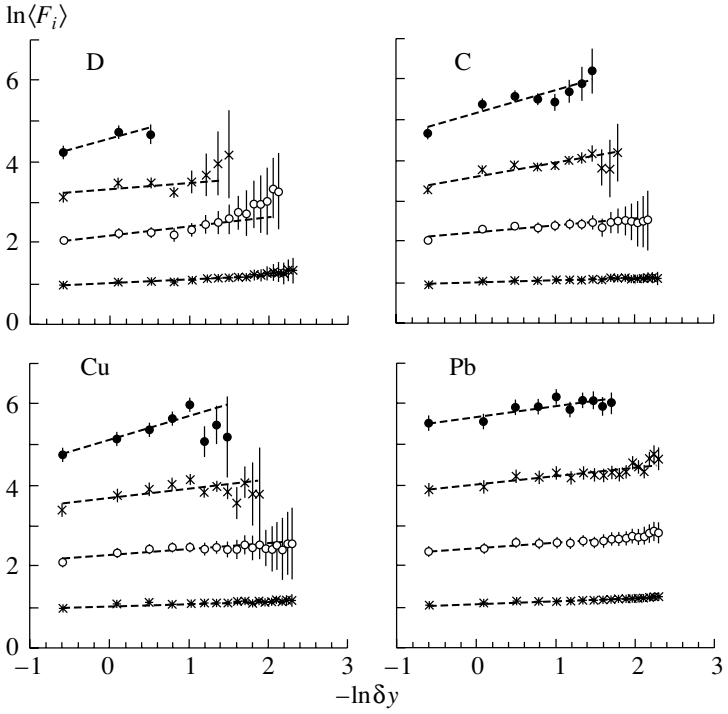

Fig. 7. As in Fig. 6, but for the production of neutral strange particles.

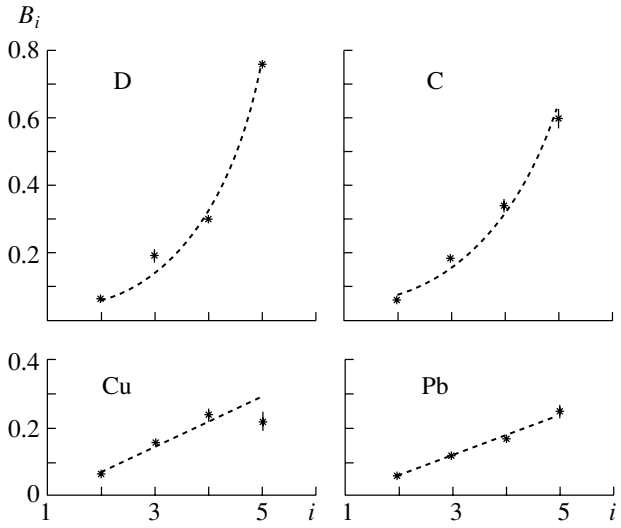

Fig. 8. Slope parameters B_i versus the order i of moments for various nuclei.

It can be seen from Figs. 6 and 7 that the functions F_i increase with decreasing δy. For the $i > 3$ factorial moments, this growth is more pronounced. In order to determine the slope parameter in (2), the experimental data were approximated by the linear function

$$\ln\langle F_i\rangle = A_i - B_i \ln M. \qquad (4)$$

The dependence of the slope parameters B_i on the order i of moments is shown in Fig. 8 for various target nuclei (D, C, Cu, and Pb). It can be seen that the slope parameter B_i increases with increasing i. The power-law dependence of $\langle F_i\rangle$ on δy provides evidence for the dynamical character of fluctuations in the processes under study.

The slope parameter B_i for all events and the slope parameter B_i^* for production of neutral strange particles are quoted in Table 2. Also given in this table for the sake of comparison are data for minimum-bias events (B_i^{**}) in π^-C interactions at 40 GeV/c [14].

It can be seen that B_i and B_i^* are both invariable within the errors, but that the parameter B_i^* exceeds B_i for all nuclei studied here. This trend may be attributed to the fact that neutral strange particles are produced for the most part in hard interactions, where the dynamical fluctuations are generated with a higher probability than in ordinary interactions. The data in Table 2 also show that the slope parameter B_i^{**} for minimum-bias events is substantially smaller than the parameters B_i^* and B_i. This is because the fraction of hard interactions is greater in high-$P_\perp$ processes than in ordinary minimum-bias processes.

Thus, the analysis of maximum fluctuations of charged-particle multiplicities in high-$P_\perp$ processes induced by π^-A collisions at 40 GeV/c reveals that $\langle F_i\rangle$ varies in proportion to a power of δy [see formula (4)]. This suggests a dynamical character of fluctuations in the processes under study.

5. CONCLUSION

Maximum fluctuations of charged particles produced in high-$P_\perp$ processes induced by π^-A collisions at 40 GeV/c have been obtained over narrow rapidity intervals δy. Our experimental data on fluctuations have been compared with theoretical predictions derived on the basis of the model of quark–gluon strings by using the FRITIOF-7.02 package, and the nature of fluctuations has been investigated by the method of scale factorial moments.

It has been found that large fluctuations of multiplicities, $n_{\max} > 5$, over narrow rapidity intervals δy (0.1 or 0.5) are observed for both light and heavy nuclei. The model of quark–gluon strings describes well experimental data for $n_{\max} < 5$, but it underestimates $dn_{\max}/dy$ in the region of large fluctuations. The analysis of maximum fluctuations for high-$P_\perp$ processes in π^-A collisions at 40 GeV/c has revealed that $\langle F_i\rangle$ varies in proportion to a power of δy [see formula (4)]. This suggests the presence of dynamical fluctuations.

ACKNOWLEDGMENTS

This study was supported in part by the Georgian Academy of Sciences (grant no. 2.13).

REFERENCES

1. V. S. Murzin and L. I. Sarycheva, *Physics of Hadronic Processes* (Énergoatomizdat, Moscow, 1986), Chap. 5.
2. R. C. Hwa, Phys. Lett. B **201**, 165 (1988).
3. M. Jacob, Nucl. Phys. A **498**, 1 (1989).
4. G. Giacomelli, Int. J. Mod. Phys. A **5**, 223 (1990).
5. T. H. Burnett *et al.*, Phys. Rev. Lett. **50**, 2062 (1983).
6. G. J. Alner *et al.*, Phys. Rep. **154**, 247 (1987).
7. M. Adamus *et al.*, Phys. Lett. B **185**, 200 (1987).
8. M. I. Adamovich *et al.*, Phys. Lett. B **201**, 397 (1988).
9. A. Bialas and R. Peschanski, Nucl. Phys. B **273**, 703 (1986).
10. J. V. Ajinenko *et al.*, Phys. Lett. B **222**, 306 (1989).
11. K. G. Akhobadze *et al.*, Yad. Fiz. **61**, 245 (1998) [Phys. At. Nucl. **61**, 196 (1998)].
12. A. K. Javrishvili *et al.*, Nucl. Instrum. Methods **177**, 381 (1980); A. V. Bannikov *et al.*, Prib. Tekh. Éksp., No. 2, 69 (1989).
13. B. Andersson *et al.*, Z. Phys. C **57**, 485 (1993).
14. B. Andersson *et al.*, Nucl. Phys. B **281**, 289 (1987).

Translated by R. Rogalyov

Physics of Atomic Nuclei, Vol. 66, No. 2, 2003, pp. 368–382. Translated from Yadernaya Fizika, Vol. 66, No. 2, 2003, pp. 395–409.

ELEMENTARY PARTICLES AND FIELDS
Theory

Theoretical Investigation of Tensor Analyzing Powers in Deuteron Fragmentation into Pions

A. Yu. Illarionov*, A. G. Litvinenko, and G. I. Lykasov*****

Joint Institute for Nuclear Research, Dubna, Moscow oblast, 141980 Russia

Received June 21, 2001; in final form, March 29, 2002

Abstract—A detailed analysis of the fragmentation of tensorially polarized deuterons into pions in the kinematical region forbidden for free nucleon–nucleon collisions is performed. Within the relativistic impulse approximation, the inclusive spectrum of product pions and the tensor analyzing power T_{20} are explored by using various forms of the deuteron wave function. The effect of the $\mathcal{P}$-wave component of the deuteron wave function on these observables is also investigated. It is shown that the invariant spectrum is more sensitive to the form of the $NN \to \pi X$ invariant amplitude than the tensor analyzing power T_{20}. The inclusion of nonnucleon degrees of freedom in the deuteron makes it possible to reproduce the pion spectrum over the entire kinematical region and improves the description of experimental data on T_{20}. According to present-day experimental data, T_{20} is positive and very small in magnitude, less than 0.2, which is at odds with the results of theoretical calculations disregarding nonnucleon degrees of freedom.

1. INTRODUCTION

The problem of nuclear structure at short internucleon distances ($r < 1$ fm), which correspond to high internal momenta ($k\,[\mathrm{GeV}/c] \approx 0.2/(r\,[\mathrm{fm}])$), has attracted the attention of theorists and experimentalists for more than two decades. A theoretical description of nucleon states at distances commensurate with nucleon dimensions is complicated at present by the absence of a unified theory of strong interactions. Within QCD, which is claimed to play the role of strong-interaction theory, the problem of the hadronization of quarks has yet to be solved. Perturbative QCD only describes the Q^2 evolution of quark distributions in hadrons and quark–hadron fragmentation functions, leaving aside the question of the form of distribution functions at low Q^2, where evolution equations are inapplicable. Existing nonperturbative models inspired by QCD make it possible to study quark distributions in hadrons at low and intermediate values of Q^2; however, a theoretical investigation of nuclear structure at short distances involves a number of difficulties. By way of example, we indicate that, because of the nonpointlike character of nucleons, not only is it unclear how one should describe their interaction, but also the very concept of nucleons as quasiparticles is questionable. An analogy with phenomena accompanying the rearrangement of the external electron shells of atoms upon the formation of molecules or solids suggests that nonnucleon degrees of freedom must manifest themselves here [1].

From the experimental point of view, difficulties in studying nuclear structure at short distances stem from a low probability of relevant configurations and, as a consequence, from small values of cross sections for corresponding processes. For example, the fact that data on deep-inelastic scattering, which is a traditional tool for studying the structure of particles and which is the most convenient for a theoretical interpretation among reactions used for this purpose, furnishes virtually no information about the high-momentum component in nuclei is partly due to small cross-section values. For deep-inelastic-scattering reactions, Bjorken variable values in the region $x_b > 1$ correspond to nonzero internal momenta. Currently available experimental data relevant to the problem in question are contradictory (the slopes of the spectra in [2] and [3] differ by nearly a factor of 2) and were obtained only for the region $x_b < 1.2$, which corresponds to internal momenta of $k \approx 0.2$ GeV/c (the relevant internal momentum, which is the relative momentum in the nucleon pair, can be estimated by the formula $k \approx m(x_b - 1)$, where m is the nucleon mass).

As is well known, cross sections for processes featuring a hadron probe are larger than similar cross sections for the case of a lepton probe. It was found that the momentum distribution of the deuteron nucleons that was extracted from data on

*e-mail: Alexei.Illarionov@jinr.ru
**e-mail: litvin@moonhe.jinr.ru
***e-mail: lykasov@nusun.jinr.ru

proton–deuteron reactions is in agreement with that from data on inelastic electron–deuteron scattering [4]. It can therefore be assumed that hadron and lepton probes furnish identical information about the structure of the deuteron. Hence, implementation of experimental programs at various facilities may provide comprehensive information about the internal structure of the deuteron. However, a relevant theoretical analysis is complicated by an intricate interaction mechanism. The fragmentation of a nucleus into hadrons in a kinematical region that is forbidden for free nucleon–nucleon scattering [1, 5]—these are so-called cumulative processes—exemplifies reactions for which a vast body of experimental data has been accumulated.

In this connection, the deuteron is of particular interest. First, this nucleus has received the most comprehensive study, both from the experimental and from the theoretical point of view. Second, it is easier to disentangle the reaction mechanisms for the deuteron since it is the simplest nucleus. Deuteron fragmentation into cumulative hadrons (often referred to as deuteron breakup), $dp \to p'X$, is among reactions involving a hadron probe that were used to investigate the deuteron core and which were studied more comprehensively. In order to single out nonzero values of internal momenta in this reaction, the secondary proton must be recorded with a momentum that ensures fulfillment of the following inequality for the light-front variable: $1 < x = 2(E' + p')/(E_d + P_d) \leq 2$, with E' (E_d) and p' (P_d) being, respectively, the energy and the momentum of the secondary proton (primary deuteron). Interest in this reaction was caused, first, by a large value of the cross section for the above internal momenta and, second, by the fact that secondary protons are rather easily identifiable in relevant experiments. In the impulse approximation, the inclusive spectrum of spectator protons in the deuteron-stripping reaction $dp \to p'X$ is proportional to the square of the deuteron wave function, which depends on the spectator momentum. As was shown in [6], the application of the impulse approximation in analyzing this reaction is quite legitimate at high x, $x > 1.7$, or at high spectator momenta, $p' > 0.4$ GeV/c. From experimental data on deuteron fragmentation into protons, one can therefore directly extract information about the high-momentum distribution of nucleons in the deuteron. It was shown in [6] that the deuteron wave function for the so-called Paris potential [7] provides a satisfactory description of the spectrum of protons in the deuteron-breakup reaction with respect to the Lorentz-invariant square of the internal momentum [5],

$$k^2 = \frac{m^2 + p_\perp^2}{4x(1-x)} - m^2,$$

where $p_\perp$ is the transverse momentum of the spectator proton. This relation between the proton momentum and the internal momentum arises in the so-called minimal-relativization scheme (see [5, 6]).

However, there appear difficulties in theoretically analyzing polarization observables. For example, only for $k < 0.25$ GeV/c can one describe, within the spectator mechanism, the tensor analyzing power T_{20} measured in the reaction $dp \to pX$. Moreover, a simultaneous description of data on the tensor analyzing power T_{20} and on the polarization-transfer factor $\varkappa$ proved to be impossible within the spectator mechanism if the deuteron was treated on the basis of the two-component model ($\mathcal{S}$ and $\mathcal{D}$ waves) [8]. The inclusion of additional product-hadron rescattering makes it possible to reproduce both the spectrum of protons and the analyzing power T_{20} up to internal momenta of $k \leq 0.65$ GeV/c by using only nucleon degrees of freedom [6]. However, the entire body of data on the deuteron-breakup reaction could not be described within the nucleon model.

It can be assumed that these discrepancies between theoretical and experimental results may be due largely to the decisive role of nonnucleon degrees of freedom in the formation of the deuteron structure at high internal momenta (greater than 0.20 GeV/c), which correspond to short internucleon distances (less than 1 fm). The inclusion of nonnucleon degrees of freedom, such as six-quark states [9] or $\Delta\Delta$, NN^*, and $NN\pi$ deuteron states, made it possible to describe the inclusive spectrum of protons for $x \geq 1.7$ [6]. However, a universal theoretical model that would be able to describe T_{20} and $\varkappa$ over the entire region of momenta of protons that are emitted into the forward hemisphere in the reaction $dp \to p'X$ has yet to be constructed.

In order to explore nonnucleon and quark states in nuclear structure, it seems natural to study, both experimentally and theoretically, polarization features of the cumulative production of hadrons that have different quark compositions. Such reactions are exemplified by relativistic-deuteron fragmentation into pions, $dp \to \pi X$, which was investigated at the Laboratory of High Energies at the Joint Institute for Nuclear Research (JINR, Dubna) [1, 10, 11]. In that case, a deuteron of momentum $P_d = 8.9$ GeV/c fragmented on target nuclei (hydrogen, carbon, beryllium) into pions at angles close to zero. The experiments involved measuring the spectra of outgoing pions [1] and the tensor analyzing power T_{20} [10, 11]. As a result, it was shown that the analyzing power T_{20} is virtually equal to zero in the precumulative region, $x < 1$, and is very small in the cumulative region, $x \geq 1$.

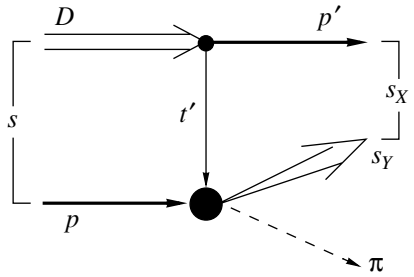

Fig. 1. Relativistic-impulse-approximation diagram for deuteron fragmentation into cumulative pions, $\vec{d}+p\to\pi+X$. Here, $s=(p+D)^2$ is the square of the total reaction energy; $t'=(D-p')^2$ is the invariant square of the momentum transfer; and s_X and s_Y are the squares of the effective masses of undetected composite particles X and Y, respectively.

It is well known that, in contrast to the deuteron-breakup reaction, the production of cumulative pions in the process $dp\to\pi(0^\circ)X$ proceeds predominantly through pion production on an intranuclear nucleon carrying a high internal momentum, and this corresponds to the impulse approximation or to the so-called direct mechanism [12, 13]. Rescattering and final-state interaction are much less intense here than in the deuteron-breakup reaction (see, for example, [14]) and can be disregarded for a first approximation. In turn, the impulse-approximation contribution is due to the high-momentum component of the deuteron wave function. Thus, the structure of the deuteron at short distances is studied directly here.

A rather high yield of high-momentum pions originating from pd and pA interactions in the kinematical region that is forbidden for free nucleon–nucleon scattering was described on the basis of the model of few-nucleon correlations [5, 15], the multiquark-bag model [9, 16], and the model of quark–gluon strings [17]. However, the polarization features of deuteron fragmentation into pions have not yet attracted the attention of theorists.

Before proceeding to consider contributions from nonnucleon degrees of freedom and from more complicated reaction mechanisms, it is necessary to take into account the predictions of the nucleon model in the leading order and for various schemes for the inclusion of relativistic effects in a bound system. It seems natural that only upon a consistent relativistic calculation of this leading contribution would it be reasonable to discuss the contribution of other (nonstandard) reaction mechanisms, and we focus here on performing precisely such a calculation.

Specifically, a Lorentz-invariant analysis of the tensor analyzing power T_{20} and of the inclusive spectrum of unpolarized pions from the reaction $\vec{d}p\to\pi X$ [18] is performed in the present study. The main problem addressed here is to describe this reaction within a consistent relativistic scheme on the basis of the nucleon model of the deuteron with various deuteron wave functions. For this purpose, fully covariant expressions for all observables are written within the Bethe–Salpeter formalism. This approach makes it possible to draw general conclusions on the amplitude of the process and to go over to various schemes for taking into account relativstic effects and to the nonrelativistic limit. In addition, we consider the question of how the results of our theoretical calculations are affected by theoretical uncertainties arising in the impulse approximation because of the need for using off-shell elementary amplitudes.

2. RELATIVISTIC IMPULSE APPROXIMATION

Let us consider an inclusive reaction of the form

$$\vec{d}+p\to\pi(0^\circ)+X, \tag{1}$$

where the incident polarized deuteron has an energy of a few GeV and where one final pion is detected in the direction of the projectile-deuteron momentum. Since the deuteron is a loosely bound system, this reaction can be considered, for a first approximation, as a process where one of the nucleons of the deuteron is knocked out from it upon undergoing a collision with a target nucleon, producing a pion, while the other nucleon continues moving at a nearly the same momentum as that before the collision event. If the reaction in question is indeed governed by this mechanism, its spectrum must not depend on the target mass number A; that is, the process is determined by the internal structure of the deuteron exclusively and can be represented by the diagram of the relativistic impulse approximation (see Fig. 1).

In this approximation, the amplitude $\mathcal{T}_{pd}^{\pi}$ for the reaction $\vec{d}p\to\pi X$ can be written in the Lorentz-invariant form [18–20]

$$\mathcal{T}_{pd}^{\pi}=\left(\bar{\mathcal{U}}_Y\Gamma_{NN}\right)_{\alpha\beta}\bar{u}_{\gamma}^{(\sigma_{p'})}(p') \tag{2}$$
$$\times\left(\frac{\hat{n}+m}{n^2-m^2}\right)_{\beta\delta}u_{\alpha}^{(\sigma_p)}(p)\left(\Gamma_\mu(D,q)\mathcal{C}\right)_{\delta\gamma}\xi_M^{\mu}(D),$$

where $(\bar{\mathcal{U}}_Y\Gamma_{NN})$ is the vertex for the $NN\to\pi Y$ elementary event; α, β, γ, and δ are Dirac indices (summation over dummy indices is implied here); μ is the Lorentz index; $\mathcal{C}=i\gamma_2\gamma_0$ is the charge-conjugation matrix; M is the polarization of the deuteron; and, finally, $\sigma_{p'}$ and σ_p stand for the nucleon-spin projections [21]. Further, we note that the deuteron vertex $(\Gamma_\mu(D,q)\mathcal{C})$ satisfies the Bethe–Salpeter equation and depends on two variables, the relative momentum $q=(n-p')/2$ and the total momentum $D=n+p'$

of the deuteron, its mass being denoted by M_d. The deuteron polarization vector $\xi^{\mu}_{M}(D)$ satisfies the conditions

$$\xi^{\mu M}(D)D_{\mu} = 0, \quad \xi^{\mu M}(D)\xi_{\mu M'}(D) = -\delta^{M}_{M'}; \quad (3)$$

$$\sum_{M} (\xi_{\mu M}(D))^{*}\, \xi_{\nu M}(D) = -g_{\mu\nu} + \frac{D_{\mu}D_{\nu}}{M_d^2}. \quad (4)$$

Since the spectrum depends only slightly on the target type, the vertices of the diagram factorize. It follows that, upon squaring the reaction amplitude (2), the corresponding inclusive spectrum of pions can be represented in the factorized form

$$\rho^{\pi}_{pd} = \varepsilon_{\pi}\frac{d\sigma}{d^3p_{\pi}} = \frac{1}{(2\pi)^3} \quad (5)$$

$$\times \int \frac{\sqrt{\lambda(p,n)}}{\sqrt{\lambda(p,D)}}\rho_{\mu\nu}(D)\left[\rho^{\pi}_{pN}\cdot\Phi^{\mu\nu}(D,q)\right]\frac{m^2d^3p'}{E'},$$

where $\lambda(p_1,p_2) \equiv (p_1p_2)^2 - m_1^2m_2^2 = \lambda(s_{12},m_1^2,m_2^2)/4$ is a kinematical factor, with s_{12} being defined as $s_{12} = (p_1+p_2)^2$; p and n are the 4-momenta of, respectively, the target proton and an intranuclear nucleon; and $\rho^{\pi}_{pN} \equiv \varepsilon_{\pi}d\sigma/d^3p_{\pi}$ is the Lorentz-invariant inclusive spectrum of pions produced in the interaction of a deuteron nucleon with a target proton. In general, this spectrum can be represented as a function of three variables, $\rho^{\pi}_{pN} = \rho(x_{\mathrm{F}},\pi_{\perp},s_{NN})$. Here, the Feynman variable x_{F} is defined as $x_{\mathrm{F}} = 2\pi_{||}/\sqrt{s_{NN}}$, where $\boldsymbol{\pi} = (\pi_{||},\boldsymbol{\pi}_{\perp})$ is the pion momentum in the c.m. frame of colliding nucleons and $s_{NN} = (p+N)^2$ is equal to the square of the total energy of these nucleons.

In expression (5), the quantity $\rho_{\mu\nu}(D)$ is the deuteron density matrix, which can be represented in the manifestly covariant form [22]

$$\rho_{\mu\nu}(D) = (\xi_{\mu M}(D))^{*}\xi_{\nu M}(D) \quad (6)$$

$$= \frac{1}{3}\left(-g_{\mu\nu} + \frac{D_{\mu}D_{\nu}}{M_d^2}\right) + \frac{1}{2}(W_{\lambda})_{\mu\nu}s_d^{\lambda}$$

$$- \left[\frac{1}{2}\left((W_{\lambda_1})_{\mu\rho}(W_{\lambda_2})^{\rho}_{\nu} + (W_{\lambda_2})_{\mu\rho}(W_{\lambda_1})^{\rho}_{\nu}\right)\right.$$

$$\left. + \frac{2}{3}\left(-g_{\lambda_1\lambda_2} + \frac{D_{\lambda_1}D_{\lambda_2}}{M_d^2}\right)\left(-g_{\mu\nu} + \frac{D_{\mu}D_{\nu}}{M_d^2}\right)\right]p_d^{\lambda_1\lambda_2},$$

where $(W_{\lambda})_{\mu\nu} = i\varepsilon_{\mu\nu\gamma\lambda}D^{\gamma}/M_d$ and s_d and p_d are the deuteron-spin vector and the deuteron-alignment tensor, respectively.

Further, the fully symmetric tensor $\Phi_{\mu\nu}(D,q)$ in Eq. (5) can be expanded in covariant quantities as

$$\Phi_{\mu\nu}(D,q) = \frac{1}{4}\mathrm{tr}\left[\bar{\Psi}_{\mu}\left(\frac{\hat{n}+m}{m}\right)^2\Psi_{\nu}\frac{\hat{p}'-m}{m}\right] \quad (7)$$

$$= -f_0(n^2)g_{\mu\nu} + f_1(n^2)\frac{q_{\mu}q_{\nu}}{m^2}.$$

In doing this, we have introduced the modified vertex $\Psi_{\mu}(D,q)$, which is related to the vertex $\Gamma_{\mu}(D,q)$ by the equation

$$\Psi_{\mu}(D,q) = \frac{\Gamma_{\mu}(D,q)}{m^2 - n^2 - i0} = \varphi_1(n^2)\gamma_{\mu} \quad (8)$$

$$+ \varphi_2(n^2)\frac{n_{\mu}}{m} + \frac{\hat{n}-m}{m}\left(\varphi_3(n^2)\gamma_{\mu} + \varphi_4(n^2)\frac{n_{\mu}}{m}\right).$$

The form factors $\varphi_i(n^2)$ are associated with two large deuteron-wave-function components U and W (corresponding to the ${}^3\mathcal{S}_1$ and ${}^3\mathcal{D}_1$ deuteron states) and two small components V_t and V_s (corresponding to the ${}^3\mathcal{P}_1$ and ${}^1\mathcal{P}_1$ states).

Substituting formula (8) into expression (7) and equating the structures at identical covariant quantities on the left- and the right-hand side of the resulting equation, we find that the invariant functions $f_{0,1}(n^2)$ can be explicitly written as

$$f_0(n^2) = \frac{M_d^2}{m^2}\left(\varphi_1 - \frac{m^2-n^2}{m^2}\varphi_3\right)\varphi_1 \quad (9)$$

$$- \left(\frac{m^2-n^2}{m^2}\right)^2(\varphi_1-\varphi_3)\,\varphi_3,$$

$$f_1(n^2) = -4\left\{\varphi_1 + \varphi_2 - \frac{m^2-n^2}{m^2}\right. \quad (10)$$

$$\left.\times\left(\frac{\varphi_2}{2} + \varphi_3 + \varphi_4\right)\right\}(\varphi_1+\varphi_2)$$

$$+ \frac{M_d^2}{m^2}\left(\varphi_2 - \frac{m^2-n^2}{m^2}\varphi_4\right)\varphi_2$$

$$- \left(\frac{m^2-n^2}{m^2}\right)^2(\varphi_2 + 2\varphi_3 + \varphi_4)\,\varphi_4.$$

The corresponding scalar functions $\varphi_i(n^2)$ in the deuteron vertex featuring one off-shell nucleon can be calculated in any reference frame. We note that, in our case, where one particle in on the mass shell, only four partial waves of the deuteron make nonzero contributions—namely, only the $U = {}^3\mathcal{S}_1^{++}$, $W = {}^3\mathcal{D}_1^{++}$, $V_s = {}^1\mathcal{P}_1^{-+}$, and $V_t = {}^3\mathcal{P}_1^{-+}$ partial waves are operative according to the ρ-spin classification [23].

In order to relate the functions $\varphi_i(n^2)$ to the nonrelativistic $\mathcal{S}$, $\mathcal{D}$, and $\mathcal{P}$ waves, it is convenient to recast them into the form

$$\mathcal{N}_d\varphi_1 = U - \frac{W}{\sqrt{2}} - \sqrt{\frac{3}{2}}\frac{m}{|\mathbf{q}|}V_t, \quad (11)$$

$$\mathcal{N}_d\varphi_2 = -\frac{m}{(E_{\mathbf{q}}+m)}U - \frac{m(2E_{\mathbf{q}}+m)}{|\mathbf{q}|^2} \quad (12)$$

$$\times \frac{W}{\sqrt{2}} + \sqrt{\frac{3}{2}}\frac{m}{|\mathbf{q}|}V_t,$$

$$\mathcal{N}_d\varphi_3 = -\sqrt{\frac{3}{2}}\frac{mE_{\mathbf{q}}}{|\mathbf{q}|(2E_{\mathbf{q}} - M_d)}V_t, \quad (13)$$

$$\mathcal{N}_d\varphi_4 = \frac{m^2}{M_d(E_{\mathbf{q}}+m)}U - \frac{m^2(E_{\mathbf{q}}+2m)}{M_d|\mathbf{q}|^2} \quad (14)$$

$$\times \frac{W}{\sqrt{2}} - \sqrt{3}\frac{m^2}{|\mathbf{q}|(2E_{\mathbf{q}} - M_d)}V_s,$$

where all functions are defined in the deuteron rest frame; all kinematical variables must be calculated precisely in this reference frame; and $E_{\mathbf{q}} = \sqrt{|\mathbf{q}|^2 + m^2}$. The normalization constant $\mathcal{N}_d^{-1} = \pi\sqrt{2/M_d}$ is chosen in accordance with the nonrelativistic normalization of the deuteron wave function:[1)]

$$\int_0^\infty |\mathbf{q}|^2 d|\mathbf{q}| \left[U^2(|\mathbf{q}|) + W^2(|\mathbf{q}|)\right] = 1. \quad (15)$$

Equations (11)–(14) define the invariant functions $f_{0,1}(|\mathbf{q}|)$ in terms of the partial waves of the deuteron as

$$f_0(|\mathbf{q}|) = \mathcal{N}_d^{-2}\frac{M_d^2}{m^2}\left[\left(U - \frac{W}{\sqrt{2}}\right)^2 \quad (16)\right.$$

$$\left. + \sqrt{6}\frac{|\mathbf{q}|}{m}\left(U - \frac{W}{\sqrt{2}}\right)V_t - \frac{3}{2}V_t^2\right],$$

$$\frac{2}{3}\frac{|\mathbf{q}|^2}{m^2}f_1(|\mathbf{q}|) = \mathcal{N}_d^{-2}\frac{M_d^2}{m^2}\left[2\sqrt{2}UW + W^2 \quad (17)\right.$$

$$+ V_t^2 - 2V_s^2 - \frac{4}{\sqrt{3}}\frac{|\mathbf{q}|}{m}\left(\left(U - \frac{W}{\sqrt{2}}\right)\frac{V_t}{\sqrt{2}}\right.$$

$$\left.\left. + (U + \sqrt{2}W)V_s\right)\right].$$

[1)]We note that the definition given by Gross [24] for the deuteron vertex $\widetilde{\Psi}_\mu(q)$ differs from our definition of the Bethe–Salpeter vertex $\Psi_\mu(q)$ (8). They are related as

$$\widetilde{\Psi}_\mu(q) = \Psi_\mu(-q).$$

Taking this into account and comparing Eqs. (11)–(14) with the corresponding Eqs. (46) from [24], one can see that the Gross wave functions $\widetilde{U}(q)$, $\widetilde{W}(q)$, $\widetilde{V}_s(q)$, and $\widetilde{V}_t(q)$, whose parametrizations will be used here below, are related to our functions by the equations

$$\widetilde{U}(q_0, |\mathbf{q}|) = U(-q_0, |\mathbf{q}|);$$
$$\widetilde{W}(q_0, |\mathbf{q}|) = W(-q_0, |\mathbf{q}|);$$
$$\widetilde{V}_s(q_0, |\mathbf{q}|) = -V_s(-q_0, |\mathbf{q}|);$$
$$\widetilde{V}_t(q_0, |\mathbf{q}|) = -V_t(-q_0, |\mathbf{p}|),$$

where $q_0 = M_d/2 - E_{\mathbf{q}}$.

Further, we use the explicit form (6) of the deuteron density matrix to obtain the identity

$$\Phi \equiv \rho_{\mu\nu}\Phi^{\mu\nu} = \Phi^{(u)} + \Phi_\lambda^{(v)}s_d^\lambda + \Phi_{\lambda_1\lambda_2}^{(t)}p_d^{\lambda_1\lambda_2}. \quad (18)$$

The superscripts (u, v, t) label functions corresponding to the cases of zero (unpolarized deuteron), vector, and tensor polarizations, respectively; that is,

$$\Phi^{(u)}(\mathbf{q}) = f_0 + \frac{1}{3}\frac{|\mathbf{q}|^2}{m^2}f_1, \quad (19)$$

$$\Phi_\lambda^{(v)}(\mathbf{q}) = 0, \quad (20)$$

$$\Phi_{\lambda_1\lambda_2}^{(t)}(\mathbf{q}) = \left[\frac{1}{3}\frac{|\mathbf{q}|^2}{m^2}\left(-g_{\lambda_1\lambda_2} + \frac{D_{\lambda_1}D_{\lambda_2}}{M_d^2}\right)\right. \quad (21)$$

$$\left. - \left(-g_{\lambda_1\mu} + \frac{D_{\lambda_1}D_\mu}{M_d^2}\right)\left(-g_{\lambda_2\nu} + \frac{D_{\lambda_2}D_\nu}{M_d^2}\right)\frac{q^\mu q^\nu}{m^2}\right]f_1.$$

The above formulas are applicable to calculating deuteron fragmentation into pions for any deuteron polarization. We now consider a specific case of tensor polarization, with the deuteron being aligned only along the p_d^{ZZ} component of the density matrix (6). In this case, the inclusive spectrum (5) of pions from the reaction $\vec{d}p \to \pi X$ can be represented in the form

$$\rho_{pd}^\pi\left(p_d^{ZZ}\right) = \rho_{pd}^\pi\left[1 + A_{ZZ}\cdot p_d^{ZZ}\right], \quad (22)$$

where ρ_{pd}^π is the inclusive spectrum of pions in the case of unpolarized deuterons and $A_{ZZ} \equiv \sqrt{2}T_{20}$ is the tensor analyzing power, $-\sqrt{2} \le T_{20} \le 1/\sqrt{2}$. In a compact form, we have

$$\rho_{pd}^\pi = \frac{1}{(2\pi)^3}\int \frac{\sqrt{\lambda(p,n)}}{\sqrt{\lambda(p,D)}}[\rho_{pN}^\pi \cdot \Phi^{(u)}(|\mathbf{q}|)]\frac{m^2 d^3q}{E_{\mathbf{q}}}; \quad (23)$$

$$\rho_{pd}^\pi \cdot A_{ZZ} = -\frac{1}{(2\pi)^3}\int \frac{\sqrt{\lambda(p,n)}}{\sqrt{\lambda(p,D)}}[\rho_{pN}^\pi \cdot \Phi^{(t)}(|\mathbf{q}|)] \quad (24)$$

$$\times \left(\frac{3\cos^2\vartheta_{\mathbf{q}} - 1}{2}\right)\frac{m^2 d^3q}{E_{\mathbf{q}}},$$

where the functions $\Phi^{(u)}(|\mathbf{q}|)$ and $\Phi^{(t)}(|\mathbf{q}|)$ are expressed in terms of deuteron partial waves as

$$\Phi^{(u)}(|\mathbf{q}|) = \mathcal{N}_d^{-2}\frac{M_d^2}{m^2}\left[U^2 + W^2 - V_t^2 - V_s^2 \quad (25)\right.$$

$$\left. + \frac{2}{\sqrt{3}}\frac{|\mathbf{q}|}{m}\left(\left(\sqrt{2}V_t - V_s\right)U - \left(V_t + \sqrt{2}V_s\right)W\right)\right],$$

$$\Phi^{(t)}(|\mathbf{q}|) = \mathcal{N}_d^{-2}\frac{M_d^2}{m^2}\left[2\sqrt{2}UW + W^2 + V_t^2 \quad (26)\right.$$

Minimum momenta of the deuteron nucleons involved in deuteron fragmentation into cumulative pions, $dp \to \pi X$, at $P_d = 8.9$ GeV/c and a pion emission angle of $\vartheta_\pi = 0°$, along with the expectation values of these momenta and their root-mean-square deviations

x_C	$\lvert\mathbf{q}\rvert_{\min}$, GeV/$c$	$\langle\mathbf{q}\rangle$, GeV/c	$\sqrt{\langle\delta\mathbf{q}^2\rangle}$, MeV/$c$	$\lvert\mathbf{k}\rvert_{\min}$, GeV/$c$	$\langle\mathbf{k}\rangle$, GeV/c	$\sqrt{\langle\delta\mathbf{k}^2\rangle}$, MeV/$c$
0–1	0.0	0.09	∼1.1	0.0	0.10	∼1.5
1.1	0.07	0.23	2.5	0.07	0.27	3.7
1.2	0.14	0.37	3.4	0.13	0.40	4.0
1.3	0.22	0.49	3.1	0.20	0.50	3.4
1.4	0.30	0.57	2.5	0.26	0.57	2.8
1.5	0.40	0.64	2.1	0.34	0.62	2.4
1.6	0.50	0.72	1.8	0.40	0.67	2.1
1.7	0.64	0.83	1.5	0.50	0.73	1.8
1.8	0.79	0.96	1.3	0.60	0.80	1.5
1.9	1.05	1.20	1.0	1.74	0.90	1.0

$$- 2V_s^2 - \frac{4}{\sqrt{3}}\frac{|\mathbf{q}|}{m}\left(\left(U - \frac{W}{\sqrt{2}}\right)\frac{V_t}{\sqrt{2}} + \left(U + \sqrt{2}W\right)V_s\right)\Bigg].$$

It is intuitively clear that, in the deuteron, which is a loosely bound nuclear system, nucleons occur predominantly in the states of angular momenta $L = 0, 2$, so that the probability of the $L = 1$ $V_{s,t}$ states in Eqs. (25) and (26) is much less than the probability of the U and W configurations. A similar conclusion follows from a numerical analysis of solutions to the Bethe–Salpeter equation in terms of ρ-spin amplitudes [25, 26]. Moreover, it can be shown that the U and W waves are in one-to-one correspondence with the nonrelativistic $\mathcal{S}$ and $\mathcal{D}$ waves of the deuteron. Thus, those terms in Eqs. (25) and (26) that involve only the U and W waves are identified as the main contributions to the respective observables and can be contrasted against their nonrelativistic counterparts. The remaining terms in the equations are proportional to the relative momentum $\mathbf{q}/m$ (the contribution of off-diagonal terms, $V_{s,t}^2$, is negligible) and can be referred to as relativistic corrections because of their relativistic origin.

In this approach, relativistic effects are of dynamical character [25, 26], involve (in addition to $\mathcal{S}$ and $\mathcal{D}$ waves) negative-energy components (that is, $\mathcal{P}$ waves), and do not reduce to a simple change of arguments (in contrast to what we have within the minimal-relativization scheme [5, 27–29]). The idea of the minimal-relativization scheme consists in constructing a relativistic quantum model by using a realistic nonrelativistic potential of nucleon–nucleon interaction as a starting point. This scheme was used quite successfully in describing differential cross sections for deuteron-breakup processes $A(d,p)X$ and is specified by

(i) the scale transformation from the momentum $\mathbf{q}$ to the light-front variables $\mathbf{k} = (\mathbf{k}_\perp, k_{||})$,

$$\mathbf{k}^2 = \frac{m^2 + \mathbf{k}_\perp^2}{4x(1-x)} - m^2, \qquad (27)$$

$$k_{||} = \sqrt{\frac{m^2 + \mathbf{k}_\perp^2}{x(1-x)}}\left(\frac{1}{2} - x\right),$$

where, in our case, $x = (E_\mathbf{q} + |\mathbf{q}|\cos\vartheta_\mathbf{q})/M_d = (\varepsilon' - p'_{||})/M_d$ and $|\mathbf{k}_\perp| = p'_\perp$;

(ii) a renormalization of the deuteron wave function such that this renormalization satisfies the requirement that the procedure of the change of arguments be unitary, which leads to a multiplication by a factor proportional to $1/(1-x)$.

As a result, the argument is shifted toward smaller values, so that the deuteron wave function decreases less fast. This effect of enhancement of the deuteron wave function is compensated by a kinematical factor proportional to $1/(1-x)$.

3. RESULTS AND DISCUSSION

Let us now proceed to discuss the results that are obtained by calculating the aforementioned observables—that is, the invariant spectrum $\rho_{pd}^\pi = \varepsilon_\pi d\sigma/d^3p_\pi$ (23) of pions and the tensor analyzing power T_{20} (24) for the fragmentation process $\vec{d}p \to$

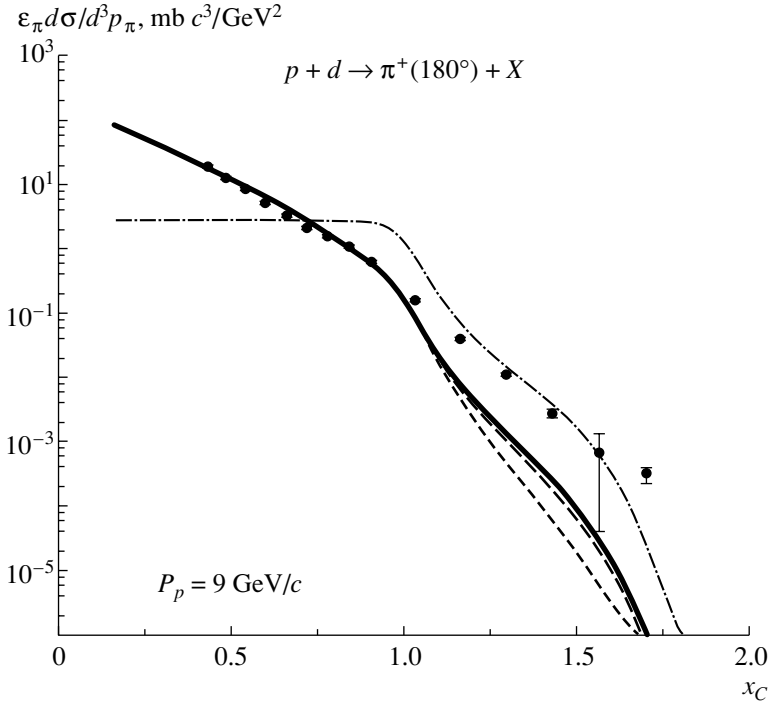

Fig. 2. Inclusive spectrum of pions according to calculations in the relativistic impulse approximation with various forms of the nonrelativistic deuteron wave function: (solid, long-dashed, and short-dashed curves) results obtained with the wave functions for the Reid ([35]), the Paris ([7]) and the Bonn ([36]) potential, respectively, and (dash-dotted curve) results obtained by evaluating the nonnormalized integral (23) under the assumption that the spectrum for the elementary process $NN \to \pi Y$ is independent of any Lorentz-invariant variables, $\rho^\pi_{NN} = 1$. Points represent experimental data borrowed from [1].

πX—and which are given in the figures below, along with available experimental data [1, 10, 11]. These results are presented versus the so-called cumulative scaling variable x_C (also referred to as the cumulative number [30]), which is defined as

$$x_C = 2\frac{(p\pi) - \mu^2/2}{(Dp) - M_d m - (D\pi)} \qquad (28)$$
$$= 2\frac{t - m^2}{(t - m^2) + (M_d + m)^2 - s_X} \leq 2$$

and which takes into account the fact that the primary-particle energy is finite. In the deuteron rest frame, $D = (M_d, \mathbf{0})$, the variable x_C has the form of the pion light-front variable $\alpha = (E_\pi - \pi\cos\vartheta_\pi)/M_d$ in the presence of a correction for the finiteness of interacting-particle masses:

$$x_C = 2\frac{EE_\pi - pp_\pi\cos\vartheta_\pi - \mu^2/2}{M_d(E - E_\pi - m)} \qquad (29)$$
$$\to 2\frac{E}{T_p}\frac{\alpha}{1 - E_\pi/T_p}.$$

The quantity x_C corresponds to the minimum mass (in nucleon-mass units) of the fragmenting-nucleus (deuteron) part involved in the process. Thus, a value of x_C in excess of unity corresponds to the production of a cumulative pion. As can be seen, this kinematical region corresponds to light-front-variable values of $x \geq 1$ (27) and to internal momenta of $k \geq 0$, as is demonstrated in the kinematical table.

The simplest reactions of deuteron fragmentation into hadrons are processes of forward or backward proton scattering. In particular, the deuteron-stripping reaction $d + A \to p(0°) + X$ (both for the case where the deuteron involved is polarized and for the case where it is unpolarized) is one of the reactions featuring a hadron probe that have been studied most intensively. The factors that motivated such a meticulous study are the following: (i) this reaction has a large cross section; (ii) in collinear geometry, the final-proton momentum is directly related to the argument of the deuteron wave function, provided that the reaction mechanism is dominated by one-nucleon exchange. This leads to a simple relationship between the inclusive spectrum in the reaction and polarization observables, on one hand, and the $\mathcal{S}$ and $\mathcal{D}$ waves of the deuteron wave function, on the other hand. By way of example, we indicate that, in the impulse approximation, the tensor analyzing power T_{20} for the stripping reaction $dp \to pX$ assumes the

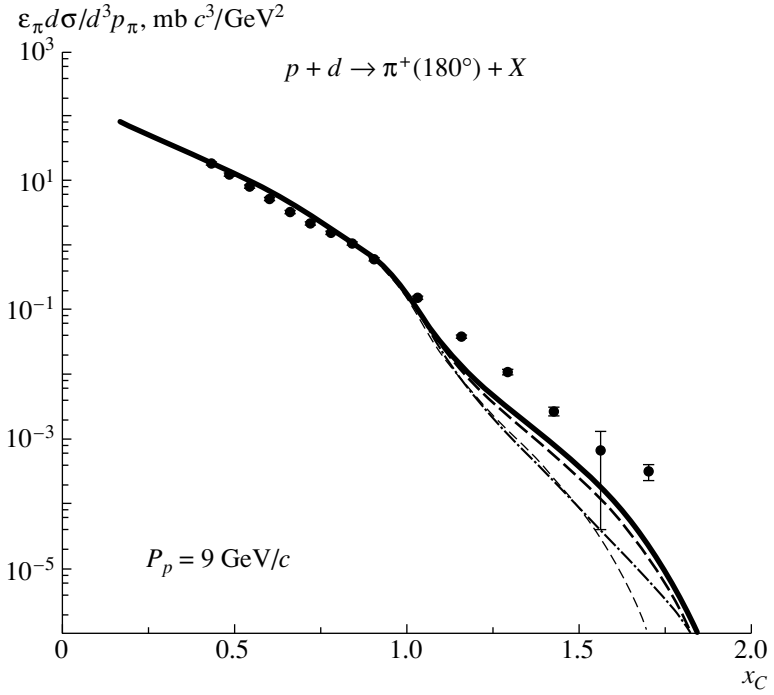

Fig. 3. Inclusive spectrum of pions according to calculations allowing for the contribution of $\mathcal{P}$ waves of the deuteron and employing the relativistic deuteron amplitudes of two forms, from [38] and from [24, 40], that involve different percentages of the $\mathcal{P}$-wave components, $P_V = \int_0^\infty |\mathbf{q}|^2 d|\mathbf{q}|[V_s^2(|\mathbf{q}|) + V_t^2(|\mathbf{q}|)]$: (solid curve) results obtained with the deuteron wave function from [38], where $P_V \simeq 0.2\%$, and (dashed and dash-dotted curves) results obtained with the Gross deuteron wave function [24, 40] for the cases where the limiting content of the small components in the deuteron is $P_V = 0.03$ and 1.46%, respectively. The thin dashed curve represents the results of the calculation with the nonrelativistic deuteron wave function for the Reid potential [35]. The displayed experimental data (points) were borrowed from [1].

simple form [31]

$$T_{20} = -\frac{1}{\sqrt{2}} \frac{2\sqrt{2}UW + W^2}{U^2 + W^2} \qquad (30)$$

and is independent of the amplitude for the subprocess $pn \to pX$. Thus, a direct experimental investigation of the momentum distribution in the deuteron seems quite feasible [31–34]. However, the impulse approximation both for the spectrum and for the analyzing power T_{20} is applicable only for internal momenta of $k \leq 0.2$ GeV/c [6]. At higher values of k, the contributions of nonpole diagrams—such as those describing nucleon or meson rescattering in the intermediate state and those corresponding to virtual-meson absorption by a nucleon—may become commensurate with the contribution of the pole diagram; therefore, they must be taken into account for observables to be described correctly. In view of this, it is hardly possible to extract nontrivial information about the structure of the deuteron at short internucleon distances.

In the case of deuteron fragmentation into cumulative pions, $d + p \to \pi(0°) + X$, rescattering mechanisms are kinematically suppressed [14]. It follows that, in studying this reaction theoretically, one can rely on the impulse approximation (see the diagrams in Fig. 1). We will now discuss the results of our calculations for the observables ρ_{pd}^{π} (23) and T_{20} (24).

The inclusive spectra of pions from the reaction $pd \to \pi X$ at $P_p = 9$ GeV/c were computed on the basis of the relativistic impulse approximation with the deuteron wave function of various forms [7, 35, 36]. In these calculations, the spectrum ρ_{NN}^{π} for the elementary event was parametrized in the form proposed in [37]. The results are presented in Figs. 2–4 for the pion emission angle of $\vartheta_\pi = 180°$. From these figures, it can be seen that the model used here produces results that are in excellent agreement with experimental data in the precumulative region $x_C < 1$, where the spectrum of pions is basically determined by the ratio of the reaction phase space to the normalization of the deuteron wave function (see table) and, hence, depends only slightly both on the choice of form of the deuteron wave function and on the structure of the vertex for the elementary process $NN \to \pi Y$. Figure 2 shows that, in the cumulative region, $x_C \geq 1$, ρ_{pd}^{π} exhibits a high sensitivity to the structure of this vertex and a low sensitivity to the form of the nonrelativistic deuteron wave function.

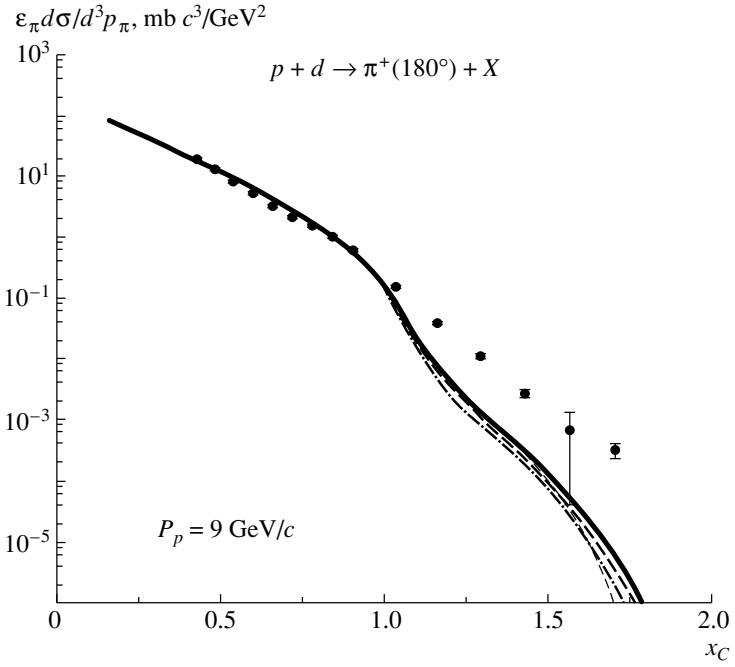

Fig. 4. Inclusive spectrum of pions according to calculations on the basis of the minimal-relativization scheme [5, 27–29] with the nonrelativistic deuteron wave function for (solid curve) the Reid potential [35], (dashed curve) the Paris potential [7], and (dash-dotted curve) the Bonn potential [36]. The thin dashed curve represents the results of the calculations with the nonrelativistic deuteron wave function for the Reid potential [35]. The displayed experimental data (points) were borrowed from [1].

The inclusion of the contribution of deuteron $\mathcal{P}$ waves (see Fig. 3) within the Bethe–Salpeter formalism [38] or within the Gross approximation [39, 40] improves insufficiently the description of the experimental situation. Figure 4 displays the results obtained for the spectrum of pions within the minimal-relativization scheme [5], which provides the best description of experimental data without going beyond the nucleon-model concepts for the deuteron.

Let us now proceed to discuss the results obtained by calculating, in the relativistic impulse approximation, the tensor analyzing power T_{20} for the reaction $\vec{d}p \to \pi X$ at $P_d = 8.9$ GeV/c for the pion emission angle of $\vartheta_\pi = 0°$. These results are displayed in Figs. 5–7, along with experimental data from [10, 11]. In the precumulative region, the analyzing power T_{20} is virtually equal to zero owing to the presence of the angular factor in (24), and this is confirmed by experimental data. Figure 5 shows that, in the cumulative region, $x_C \geq 1$, T_{20}, in contrast to the spectrum of pions, depends only slightly on the structure of the $NN \to \pi Y$ vertex, on one hand, and is highly sensitive to the form of the deuteron wave function, on the other hand. In other words, investigation of this polarization feature provides a direct means for extracting information about the structure of the deuteron.

As can be seen from Figs. 5–7, none of the forms used here for the deuteron wave function leads to an adequate description of the tensor analyzing power T_{20}. Naturally, this fact may be interpreted as a manifestation of a nontrivial structure in the deuteron.

The assumption that nonnucleon or quark degrees of freedom may exist in nuclei [6, 41–44] underlies an alternative approach to describing the structure of the deuteron at short internucleon distances. By way of example, we indicate that, according to [5], one can assume that intranuclear nucleons acquire high momenta owing to short-range few-nucleon correlations, and this makes it possible to find the form of the effective distribution of "nucleons" or color-singlet $3q$ clusters in a nucleus [9, 16]. On the other hand, the behavior of the high-momentum tail in the distribution of deuteron nucleons can be constructed on the basis of a correct Regge asymptotic behavior [15]; in [6, 15], this permitted extracting parameters of the distribution function from experimental data on the inclusive spectrum of protons originating from the deuteron-stripping reaction $dp \to pX$. According to [6, 15], one can therefore assume the renormalized form [20]

$$\widetilde{\Phi}^{(u)}(|\mathbf{k}|) = \mathcal{N}_d^{-1}\frac{M_d^2}{m^2} \tag{31}$$
$$\times \Big((1 - \alpha_{2(3q)})[U^2(|\mathbf{k}|) + W^2(|\mathbf{k}|)]$$

$$+\alpha_{2(3q)}\frac{8\pi x(1-x)}{E_{\mathbf{k}}}G_{2(3q)}(x,\mathbf{k}_\perp)\Big),$$

which is related to $\Phi^{(u)}(|\mathbf{q}|)$ (25) by the requirement that the transformation of variables be unitary:

$$\Phi^{(u)}(|\mathbf{q}|)=\frac{E_{\mathbf{k}}/E_{\mathbf{q}}}{2(1-x)}\widetilde{\Phi}^{(u)}(|\mathbf{k}|). \quad (32)$$

The parameter $\alpha_{2(3q)}$ is the probability that, in the deuteron, there exists a nonnucleon state of two bound color-singlet $3q$ clusters,

$$G_{2(3q)}(x,\mathbf{k}_\perp)=\frac{b^2}{2\pi} \quad (33)$$
$$\times\frac{\Gamma(A+B+2)}{\Gamma(A+1)\Gamma(B+1)}x^A(1-x)^B e^{-bk_\perp}.$$

Figure 8 shows the invariant spectrum ρ^π_{pd} of pions that was calculated with allowance for the nonnucleon component in the deuteron [see Eq. (31)] at $\alpha_{2(3q)}=0.02$ and 0.04 (dashed and dotted curves, respectively). From this figure, we can see that, at any value of the cumulative variable x_C, the results of our theoretical calculations are in excellent agreement with experimental data from [1].

A similar procedure for estimating the contribution of the nonnucleon component in the deuteron can be implemented for the tensor analyzing power T_{20}. We note that only the form of the distribution $\widetilde{\Phi}^{(u)}(|\mathbf{k}|)$ was constructed in [15], but this is not sufficient for evaluating T_{20}—the corresponding partial waves must be known for this. We will take into account the contribution of the nonnucleon component in the deuteron, assuming that it changes predominantly only the $\mathcal{S}$ and $\mathcal{D}$ waves in the deuteron. In doing this, we require that the square of the new wave function be equal to the square of the wave function in (31). We introduce the mixing parameter $\alpha=\pi a/4$ and, in accordance with [20], assume the renormalized form

$$\widetilde{U}(|\mathbf{k}|)=\sqrt{1-\alpha_{2(3q)}}U(|\mathbf{k}|)+\cos(\alpha)\Delta(|\mathbf{k}|); \quad (34)$$

$$\tilde{W}(|\mathbf{k}|)=\sqrt{1-\alpha_{2(3q)}}W(|\mathbf{k}|)+\sin(\alpha)\Delta(|\mathbf{k}|), \quad (35)$$

where the function $\Delta(|\mathbf{k}|)$ can be found from the equation

$$\widetilde{\Phi}^{(u)}(|\mathbf{k}|)=\mathcal{N}_d^{-1}\frac{M_d^2}{m^2}\left[\widetilde{U}^2(|\mathbf{k}|)+\tilde{W}^2(|\mathbf{k}|)\right]. \quad (36)$$

In Fig. 9, the solid, dashed, and dash-dotted curves ($\alpha_{2(3q)}=0.04, 0.03$) illustrate the contribution of this component to T_{20} under the assumption that it changes the $\mathcal{S}$ and $\mathcal{D}$ waves of the deuteron, with the mixing parameter being $a=0.0$ and 2.3. It can be seen the the inclusion of the nonnucleon component of the deuteron wave function in our consideration makes it possible to reproduce experimental data on T_{20} over the region $x_C>1.4$.

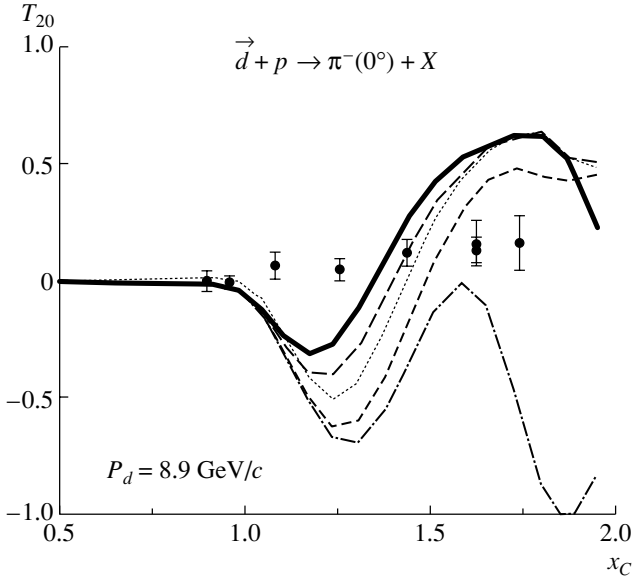

Fig. 5. Tensor analyzing power T_{20} calculated for deuterons within the relativistic impulse approximation by using various forms of the nonrelativistic deuteron wave function, along with experimental data from [10, 11] (points): (solid and dashed curves) results obtained with the deuteron wave function for the Reid ([35]) and the Paris ([7]) potential, respectively; (dash-dotted and short-dashed curves) results obtained with, respectively, the relativistic and the total deuteron wave function for the Bonn potential [36]; and (dotted curve) results obtained by evaluating expression (24) with the deuteron wave function for the Reid potential [35] without taking into account the internal structure of the elementary vertex, $\rho^\pi_{NN}=1$.

For incident deuterons of momentum $P_d=8.9$ GeV/c, the tensor analyzing power T_{20} as a function of the minimum nucleon momentum in the deuteron is shown in Fig. 10 for deuteron fragmentation into cumulative pions, $d(p,\pi)X$ [10, 11], and for deuteron fragmentation into protons, $d(p,p')X$ [45], the hadron emission angle being equal to zero in both cases.

4. PROSPECTS FOR STUDYING THE ANGULAR DEPENDENCE OF POLARIZATION OBSERVABLES

We have considered the fragmentation reaction $dp\to\pi X$ for the case where cumulative pions are emitted at zero angle. In recent years, the SFERA group at the Laboratory of High Energies at the Joint

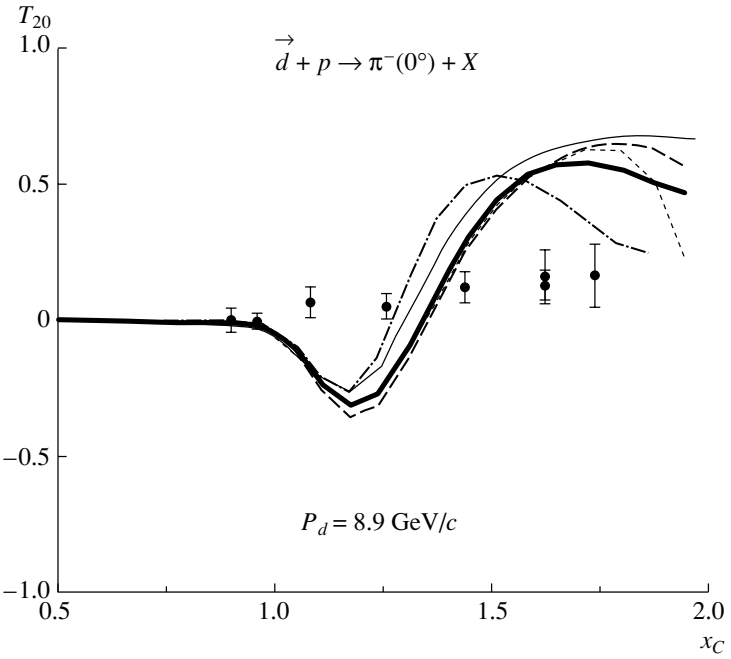

Fig. 6. Sensitivity of T_{20} to the contribution of deuteron $\mathcal{P}$ waves. The thin solid curve represents the results of the calculation with the Gross deuteron wave function from [24, 40] at $P_V = 0.44\%$. The rest of the notation is identical to that in Fig. 3. The displayed experimental data (points) were borrowed from [10, 11].

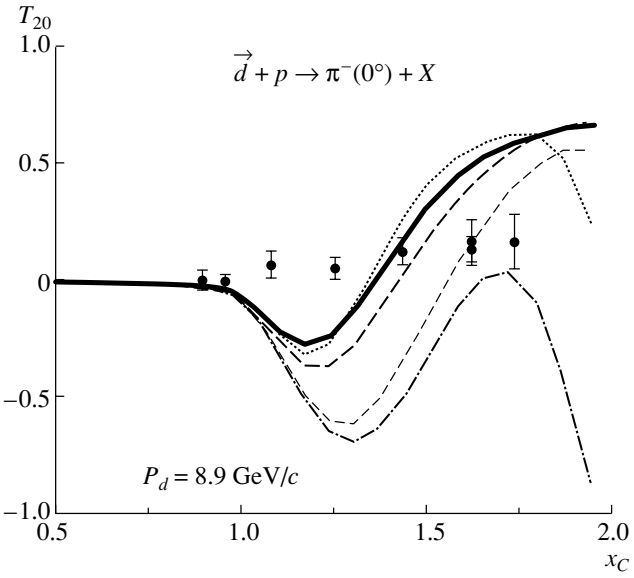

Fig. 7. Tensor analyzing power T_{20} as calculated within the minimal-relativization scheme [5, 27–29] by using (solid curve) the deuteron wave function for the Reid potential [35], (dashed curve) the deuteron wave function for the Paris potential [7], and (dashed curve) the relativistic and (thin dashed curve) the total deuteron wave function for the Bonn potential [36]. The dotted curve represents the results obtained with the Reid deuteron wave function [35]. The displayed experimental data (points) were borrowed from [10, 11].

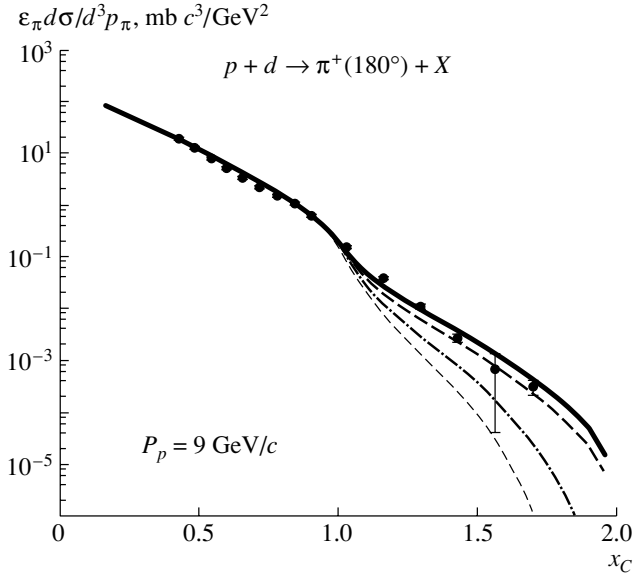

Fig. 8. Inclusive spectrum of pions according to calculations in the relativistic impulse approximation with allowance for the nonnucleon component in the deuteron [see Eq. (31)] at (solid curve) $\alpha_{2(3q)} = 4\%$ and (dashed curve) 2%. The thin dashed curve corresponds to the calculation with the nonrelativistic deuteron wave function for the Reid potential [35], while the dash-dotted curve represents the results of the calculation that employs the same deuteron wave function from [35], but which relies on the minimal-relativization scheme. The displayed experimental data (points) were borrowed from [1].

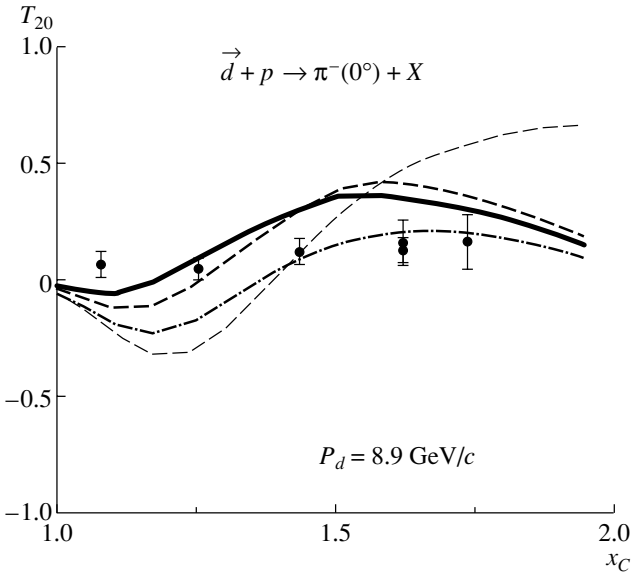

Fig. 9. Contribution of the nonnucleon component to T_{20} at various values of the mixing parameter a under the assumption that it changes only the $\mathcal{S}$ and $\mathcal{D}$ waves of the two nucleons in the deuteron [see Eqs. (34), (35)]: (solid curve) $a = 0.0$ ($\alpha_{2(3q)} = 4\%$), (dashed curve) $a = 0.0$ ($\alpha_{2(3q)} = 3\%$), and (dash-dotted curve) $a = 2.3$ ($\alpha_{2(3q)} = 3\%$). The thin dashed curve represents the results of the calculation that employed the deuteron wave function from [35], but which relied on the minimal-relativization scheme.

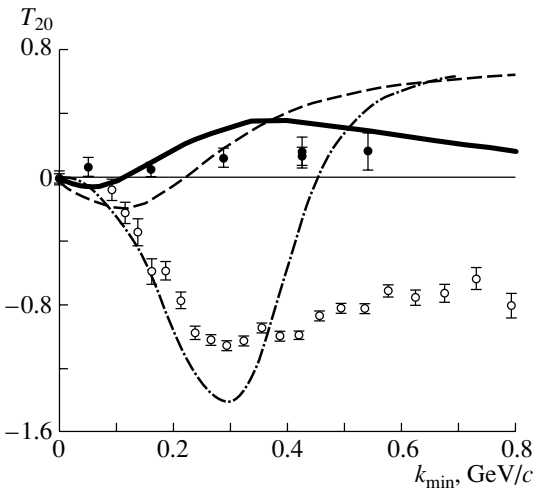

Fig. 10. Analyzing power T_{20} for deuteron fragmentation into cumulative pions, $d(p,\pi)X$ [10, 11], and into protons, $d(p,p')X$ [45], versus the minimum nucleon momentum in the deuteron at $P_d = 8.9$ GeV/c for zero hadron emission angle: (solid curve) T_{20} calculated for pions with allowance for the nonnucleon component ($\alpha_{2(3q)} = 4\%$) at zero mixing parameter ($a = 0.0$), (dashed curve) T_{20} calculated for pions with the deuteron wave function from [35] by using the minimal-relativization scheme, and (dash-dotted curve) T_{20} calculated for protons within the minimal-relativization scheme. The displayed experimental data were borrowed from [10, 11] for pions (closed circles) and from [45] for protons (open circles).

Institute for Nuclear Research (JINR, Dubna) investigated this reaction at nonzero pion emission angles [46]. For the case where deuterons of momentum $P_d = 8.9$ GeV/c fragmented into pions emitted at an angle of $\vartheta_\pi = 135$ mrad, the tensor analyzing power A_{YY}, which is linearly related to the polarization feature T_{20} at $\vartheta_\pi = 0$, $T_{20} = -\sqrt{2}A_{YY}$, was measured in those experiments over the cumulative-number range $x_C = 0.75$–1.6. It is also planned to measure A_{YY} at larger values of the angle ϑ_π—in particular, data on A_{YY} at $\vartheta_\pi = 178$ mrad are expected [47]. Since, in the process being discussed, the deuteron receives, from the proton, a momentum that is commensurate with the deuteron mass, investigation of the angular dependences of polarization observables would make it possible to deduce new information both about the structure of the deuteron at short internucleon distances and about the reaction mechanism. In Fig. 1, we present predictions for the tensor analyzing power A_{YY} that are obtained within the relativistic impulse approximation. In the case where the deuteron is aligned only with the p_d^{YY} component of the density matrix (6), the deuteron tensor analyzing power A_{YY} can be represented in the form [48]

$$\rho_{pd}^{\pi} A_{YY} = \frac{1}{(2\pi)^3} \int \frac{\sqrt{\lambda(p,n)}}{\sqrt{\lambda(p,D)}} [\rho_{pN}^{\pi} \cdot \Phi^{(t)}(|\mathbf{q}|)] \times \left(\frac{1 - 3\sin^2\vartheta_{\mathbf{q}} \sin^2\varphi_{\mathbf{q}}}{2} \right) \frac{m^2 d^3 q}{E_{\mathbf{q}}}, \quad (37)$$

which differs from expression (24) for A_{ZZ} only by the angular factor in the integrand. Concurrently, the domain of integration also changes of course.

The results for A_{YY} in the fragmentation reaction $dp \to \pi X$ at $P_d = 8.9$ GeV/c as a function of the pion emission angle ϑ_π that were obtained in the relativistic impulse approximation within the minimal-relativization scheme [5, 27–29] by using the deuteron wave function for the Reid potential [35] are displayed in Fig. 11, along with available experimental data from [46, 47]. From this figure, one can see that the relativistic impulse approximation is unable to reproduce the behavior of A_{YY}. It should be noted that, at nonzero pion emission angles, the contribution of higher, two-step, reaction mechanisms increases greatly [12]. However, estimation of nonpole diagrams shows that their contributions

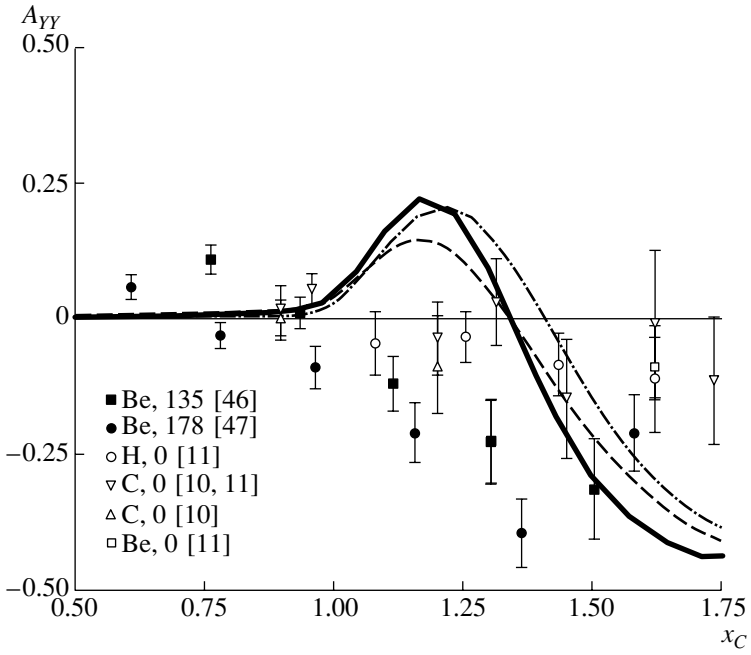

Fig. 11. Angular dependence of the tensor analyzing power A_{YY} for the fragmentation reaction $\vec{d}p \to \pi^- X$ at $P_d = 8.9$ GeV/c according to our calculations relying on the minimal-relativization scheme [5, 27–29] and employing the deuteron wave function for the Reid potential [35]. The solid, the dashed, and the dash-dotted curve correspond to the pion-emission-angle values of $\vartheta_\pi = 0$, 178, and 300 mrad, respectively. The displayed experimental data (points) were borrowed from [46, 47] ($\vartheta_\pi = 135$, 178 mrad) and [10, 11] ($\vartheta_\pi = 0$) and were obtained for different targets (beryllium, hydrogen, and carbon).

gradually die out as the process becomes more cumulative, so that the main contribution, at least to the momentum spectrum of pions, comes from the relativistic-impulse-approximation diagram, which, however, fails to describe available experimental data at large x_C within the nucleon model of the deuteron.

On the basis of the aforesaid, it can be concluded that the kinematical region that is the most favorable for studying the structure of the deuteron corresponds to large cumulative numbers (x_C) of product pions, while the region that is the most favorable for studying the reaction mechanism is that of large pion emission angles. Therefore, it is highly desirable to have data on the angular dependence of various polarization features at different values of the cumulative number x_C.

5. CONCLUSIONS

Here, we would like to summarize the conclusions drawn from the above analysis:

(i) In analyzing deuteron fragmentation into hadrons—in particular, into cumulative pions—it is incorrect to employ a nonrelativistic deuteron wave function. Relativistic effects are significant, especially in the kinematical region corresponding to short internucleon distances or high values of x. This conclusion follows from the behavior of the inclusive spectra of pions and, even more clearly, from the behavior of the tensor analyzing power T_{20} at high values of x_C.

(ii) At present, there is no consistent approach that would make it possible to take into account relativistic effects in the deuteron. It has been shown that the tensor analyzing power T_{20} for the reaction $dp \to \pi X$ in the kinematical region $x_C \geq 1$ displays a rather high sensitivity to the form of the relativistic wave function.

(iii) The inclusive spectrum of π mesons is highly sensitive to the choice of form of the $NN \to \pi X$ vertex, while the tensor analyzing power T_{20} is weakly sensitive to it. This may suggest the presence of some uncertainty in theoretical calculations that are associated with choosing the vertex appropriately.

(iv) New interesting experimental data on the analyzing power T_{20}, which indicate that it is approximately equal to zero in the region $x_C \geq 1$, cannot be understood within the standard nucleon model of the deuteron. The fact that, for the reaction of deuteron fragmentation into pions, a simultaneous satisfactory description of experimental data on the inclusive spectrum of pions from this reaction and the analyzing power T_{20} for it is impossible in the kinematical region that is forbidden for pion production on a free nucleon may give impetus to further studying, both theoretically and experimentally, polarization observables in similar processes.

(v) For the process of deuteron fragmentation into protons, the behavior of the tensor analyzing power T_{20} for $x_C \geq 1.7$ [6] cannot be reproduced within the standard nucleon model of the deuteron. At the same time, the behavior of T_{20} for deuteron fragmentation into pions cannot be described under similar assumptions over the entire cumulative region $x_C \geq 1$. The available experimental data on the inclusive spectrum of pions originating from the reaction under study can be described over the entire kinematical region (see Fig. 8) upon taking into account nonnucleon degrees of freedom in the deuteron within the model proposed in [15], the parameters of the model being fixed on the basis of a fit to experimental data on the inclusive spectra of protons from the deuteron-stripping reaction [6]. That the parameter values obtained in this way proved to be appropriate is not surprising since the same deuteron is the main subject of the analysis of the reactions $dp \to p'X$ and $dp \to \pi X$ within the relativistic impulse approximation. Therefore, investigation of the contribution from nonnucleon degrees of freedom in analyzing polarization observables in such processes may furnish new, independent information about the structure of the deuteron at short internucleon distances, and a comparison with experimental data may be a test of the modification used for the deuteron wave function. New interesting experimental data on the tensor analyzing power T_{20}, which indicate that it is positive and small in magnitude, less than 0.2, can be understood upon applying a rather simplified procedure for taking into account nonnucleon degrees of freedom in the region $x_C \geq 1.4$ (see Fig. 9). Of course, this procedure is quite rough, but it enables one to estimate qualitatively the contribution of the high-momentum component of the deuteron wave function to T_{20}. The inclusion of this component leads to a result that is consistent with the behavior of T_{20} for the deuteron-stripping reaction for $x_C > 1.7$.

ACKNOWLEDGMENTS

This work was supported in part by the Russian Foundation for Basic Research (project nos. 99-02-16528, 99-02-17463, and 99-02-17727).

REFERENCES

1. A. M. Baldin, Nucl. Phys. A **434**, 695 (1985).
2. BCDMS Collab., Preprint No. E1-93-133, JINR (Dubna, 1993).
3. CCFR Collab., Phys. Rev. D **61**, 052003 (2000).
4. V. Punjabi and Ch. F. Perdrisat, in *Proceedings of the 3rd International Symposium "Dubna Deuteron-95," Dubna, 1995,* Ed. by A. M. Baldin (Dubna, 1996), p. 304.
5. L. L. Frankfurt and M. I. Strikman, Phys. Rep. **76**, 215 (1981).
6. G. I. Lykasov, Fiz. Élem. Chastits At. Yadra **24**, 140 (1993) [Phys. Part. Nucl. **24**, 59 (1993)].
7. M. Lacombe *et al.*, Phys. Lett. B **101B**, 139 (1981).
8. B. Kuehn, Ch. F. Perdrisat, and E. A. Strokovsky, in *Proceedings of the 2nd International Symposium "Dubna Deuteron-93," Dubna, 1993,* Ed. by A. M. Baldin (Dubna, 1994), p. 31.
9. V. V. Burov, V. K. Luk'yanov, and A. I. Titov, Fiz. Élem. Chastits At. Yadra **15**, 1249 (1984) [Sov. J. Part. Nucl. **15**, 558 (1984)].
10. S. V. Afanasiev *et al.*, Nucl. Phys. A **625**, 817 (1997).
11. S. V. Afanasiev *et al.*, Phys. Lett. B **445**, 14 (1998); Preprint No. E2-98-319, JINR (Dubna, 1998).
12. N. S. Amelin and G. I. Lykasov, Yad. Fiz. **33**, 194 (1981) [Sov. J. Nucl. Phys. **33**, 100 (1981)].
13. P. Bosted *et al.*, Phys. Rev. Lett. **49**, 1380 (1982).
14. L. A. Kondratyuk and V. B. Kopeliovich, Pis'ma Zh. Éksp. Teor. Fiz. **21**, 88 (1975) [JETP Lett. **21**, 40 (1975)].
15. A. V. Efremov, A. B. Kaĭdalov, V. T. Kim, *et al.*, Yad. Fiz. **47**, 1364 (1988) [Sov. J. Nucl. Phys. **47**, 868 (1988)].
16. V. K. Luk'yanov and A. I. Titov, Fiz. Élem. Chastits At. Yadra **10**, 815 (1979) [Sov. J. Part. Nucl. **10**, 321 (1979)].
17. A. V. Efremov, A. B. Kaĭdalov, G. I. Lykasov, and N. V. Slavin, Yad. Fiz. **57**, 932 (1994) [Phys. At. Nucl. **57**, 874 (1994)].
18. A. Yu. Illarionov, A. G. Litvinenko, and G. I. Lykasov, Preprint No. P2-2001-104, OIYaI (Dubna, 2001); Eur. Phys. J. A **14**, 247 (2002).
19. A. Yu. Illarionov, A. G. Litvinenko, and G. I. Lykasov, in *Proceedings of the International Workshop "Relativistic Nuclear Physics: from Hundreds MeV to TeV," Stara Lesna, Slovak Republic, 2000* (JINR, Dubna, 2001).
20. A. Y. Illarionov, A. G. Litvinenko, and G. I. Lykasov, in *Proceedings of the 9th International Workshop on High-Energy Spin Physics "SPIN 01," Dubna, Russia, 2000,* Ed. by A. V. Efremov (JINR, Dubna, 2001), p. 102; hep-ph/0112215.
21. C. Itzykson and J. B. Zuber, *Quantum Field Theory* (McGraw-Hill, New York, 1980).
22. S. G. Bondarenko, V. V. Burov, M. Beyer, and S. M. Dorkin, nucl-th/9606035.
23. J. J. Kubis, Phys. Rev. D **6**, 547 (1972).
24. W. W. Buck and F. Gross, Phys. Rev. D **20**, 2361 (1979); Phys. Lett. B **63B**, 286 (1976).
25. L. P. Kaptari, A. Yu. Umnikov, F. C. Khanna, and B. Kampfer, Phys. Lett. B **351**, 400 (1995).
26. L. P. Kaptari, B. Kämpfer, S. M. Dorkin, and S. S. Semikh, Phys. Lett. B **404**, 8 (1997); nucl-th/9612027.
27. S. J. Brodsky *et al.*, Phys. Rev. D **8**, 4574 (1973).
28. J. B. Kogut and D. E. Soper, Phys. Rev. D **1**, 2901 (1970).
29. S. Weinberg, Phys. Rev. **150**, 1313 (1966).
30. V. S. Stavinskiĭ, Fiz. Élem. Chastits At. Yadra **10**, 949 (1979) [Sov. J. Part. Nucl. **10**, 373 (1979)].

31. V. G. Ableev *et al.*, Nucl. Phys. A **393**, 491 (1983); **411**, 541 (1983).
32. V. G. Ableev *et al.*, Pis'ma Zh. Éksp. Teor. Fiz. **37**, 196 (1983) [JETP Lett. **37**, 233 (1983)].
33. V. G. Ableev *et al.*, Pis'ma Zh. Éksp. Teor. Fiz. **47**, 233 (1988) [JETP Lett. **47**, 649 (1988)].
34. V. G. Ableev *et al.*, in *Proceedings of the 7th International Conference on Polarization Phenomena in Nuclear Physics, Paris, 1990,* Ed. by A. Boudard and Y. Terrien (Paris, 1990), p. 40F.
35. R. V. Reid, Ann. Phys. (N.Y.) **50**, 411 (1968).
36. R. Machleidt, K. Holinde, and Ch. Elster, Phys. Rep. **149**, 1 (1987).
37. V. S. Barashenkov and N. V. Slavin, Fiz. Élem. Chastits At. Yadra **15**, 997 (1984) [Sov. J. Part. Nucl. **15**, 446 (1984)].
38. A. Yu. Umnikov, Z. Phys. A **357**, 333 (1997).
39. F. Gross, J. W. van Orden, and K. Holinde, Phys. Rev. C **41**, R1909 (1990).
40. F. Gross, J. W. van Orden, and K. Holinde, Phys. Rev. C **45**, 2094 (1992).
41. L. Ya. Glozman, V. G. Neudatchin, and I. T. Obukhovsky, Phys. Rev. C **48**, 389 (1993).
42. A. P. Kobushkin, J. Phys. G **19**, 1993 (1993).
43. A. P. Kobushkin, Few-Body Systems, Suppl. **10**, 447 (1999).
44. E. R. Berger, F. Cano, M. Diehl, and B. Pire, Phys. Rev. Lett. **87**, 142302 (2001).
45. L. S. Azhgirei *et al.*, Phys. Lett. B **378**, 37 (1996).
46. S. Afanasiev *et al.*, in *Proceedings of the 13th International Symposium on High-Energy Spin Physics, Protvino, 1998,* Ed. by N. E. Tyurin, V. L. Solovianov, S. M. Troshin, and A. G. Ufimtsev (World Sci., Singapore, 1999), p. 400.
47. S. Afanasiev *et al.*, in *Proceedings of the 14th International Spin-Physics Symposium "SPIN 2000," Osaka, Japan, 2000,* Ed. by Kichiji Hatanaka, Takashi Nakano, Kenichi Imai, and Hiroyasu Ejiri, AIP Conf. Proc. **570**, 889 (2001).
48. A. Yu. Illarionov, A. G. Litvinenko, and G. I. Lykasov, Czech. J. Phys., Suppl. A **51**, A307 (2001); hep-ph/0012290.

Translated by A. Isaakyan

Physics of Atomic Nuclei, Vol. 66, No. 2, 2003, pp. 383–393. Translated from Yadernaya Fizika, Vol. 66, No. 2, 2003, pp. 410–420.

ELEMENTARY PARTICLES AND FIELDS
Theory

Analytic Calculation of Feynman Amplitudes

V. V. Andreev*

Gomel State University, Sovetskaya ul. 102, Gomel, 246699 Belarus

Received December 13, 2001; in final form, April 29, 2002

Abstract—A new method is proposed for calculating amplitudes of processes involving spin-1/2 fermions. The method is based on the use of the isotropic-vierbein vectors in Minkowski space and the basis spinors associated with them. The amplitudes for the electron–positron interaction processes $e^-e^+ \to f\bar{f}$ and $e^-e^+ \to W^-W^+$ and the amplitude for one of the possible diagrams for the process $e^+e^- \to e^+e^-e^+e^-e^+e^-$ are calculated in order to test and illustrate the potential of the method. © *2003 MAIK "Nauka/Interperiodica".*

1. INTRODUCTION

At present, a comparison of consequences from quantum-field theories with the results of experiments in high-energy physics requires a high-precision calculation of observables. A reduction of the square of the absolute value of the relevant matrix element to the trace of the products of γ matrices is a universally accepted method for calculating cross sections for reactions involving spin-1/2 fermions. In studying, however, multiparticle final states in reactions and polarization effects, there arose a need for new computational procedures, since the application of the standard method to those cases involves calculating traces for a rather large number of Dirac γ matrices.

An approach that is based on directly calculating matrix elements became an alternative to the standard method. The idea of calculating amplitudes has a rather long history. As early as 1949, Powell [1] proposed calculating a matrix element by using the explicit form of Dirac γ matrices and bispinors (a more comprehensive list of references to the studies dealing with this problem can be found in [2, 3]).

A great number of methods for calculating amplitudes of reactions involving spin-1/2 fermions have been developed up to the present time; therefore, it can be stated that, in high-energy physics, the method in question has become a standard means for deriving results. The set of methods used to calculate matrix elements can be broken down into two large classes. Methods involving a direct numerical calculation of the relevant Feynman diagram belong to the first class (see, for example, [4]).

The second class consists of methods where an analytic calculation of amplitudes is followed by a numerical computation of the reaction cross section. It should be noted that there are methods for calculating reaction cross sections without employing Feynman diagrams [5–7].

By convention, the group of analytic methods for calculating Feynman amplitudes can be divided into two subgroups. The first group includes methods that reduce the calculation of a matrix element to the evaluation of traces. This procedure forms a basis for many methods (see, for example, [2, 3, 8–16]). In this method, the matrix element reduces to a combination of scalar products and contractions with the Levi-Civita tensor.

The second subgroup consists of analytic methods that perform virtually no operations with traces of γ matrices. The method that was developed by the CALCUL group and which was used to calculate observables of reactions involving massless fermions [17–19] is the most widespread. Within this method, the matrix element being considered is reduced to spinor products, which in turn are calculated in terms of vector components with the aid of traces. Spinor products for two vectors are not much more complicated than scalar products. However, the reduction of a matrix element is not as simple as the calculation of traces. It requires employing the Chisholm spinor identities (see [18]) and expressing the contractions of γ matrices with the 4-momenta of particles and their polarization vectors in terms of bispinors. It should be emphasized that, although the latter renders the relevant calculations even more efficient in the case of massless fermions and bosons, additional mathematical constructions are necessary in the case of massive gauge bosons [18].

There are generalizations of this method to the case of massive Dirac particles both for a special

*e-mail: Andreev@gsu.unibel.by

choice of fermion polarization vectors [18, 20, 21] (in the following, such polarization states of fermions will be referred to as KS states) and for an arbitrary polarization vector [22, 23]. By using the Weyl representation for γ matrices, Hagiwara and Zeppenfeld [21] proposed an original algorithm of reduction to spinor products for massive chiral fermions. It should be noted that, for massless fermions, matrix elements can be reduced to products of the 4-momentum vectors and current constructions of the type $J^\mu \sim \overline{U}_\lambda(p)\gamma^\mu U_\lambda(k)$ [$U_\lambda(p)$ and $U_\lambda(k)$ are bispinors], which admit a component-by-component calculation in terms of the projections of the vectors p and k—this is the so-called E-vector formalism (see [24]).

For KS states, Ballestrero and Maina [25] proposed an iterative computational scheme that reduces the expression for the $\overline{U}_\lambda(p)QU_\nu(k)$ fermion line involving a matrix operator Q to a combination of the spinor products $\overline{U}_\lambda(p)U_\nu(k)$ and (or) $\overline{U}_\lambda(p)\gamma^\mu(g_V + g_A\gamma_5)U_\nu(k)$ by inserting, in the fermion line being considered, the total set of unphysical bispinor states (those for which $p^2 < 0$).

In the above methods, spinor products and current constructions were preliminarily calculated with the aid of traces and were then used as universal functions that are similar to the expression for the scalar product of 4-vectors in terms of their components.

It is rather difficult to assess the efficiency of one or another method for calculating a matrix element since it is the physical problem to be solved that dictates the application of a specific method. For example, computational methods employing traces are universal and do not require, in contrast to the spinor technique, additionally constructing contractions of particle polarization vectors. If, however, the number of particles in the final state is large, the number of terms in calculating relevant traces will strongly increase. Moreover, different spin configurations must be calculated separately.

The spinor technique is efficient in that the procedure for computing a matrix element in terms of the components of 4-vectors (or their scalar products) amounts to reducing the relevant amplitude to basic building blocks of corresponding Feynman diagrams—that is, to spinor products, which were preliminarily calculated. This reduces the number of terms and is convenient at the stage of direct numerical calculations. However, treatment of the simple process $e^+e^- \to W^+W^-$ involving polarized W bosons is more complicated within the spinor technique than within the procedure employing traces.

Other methods are disadvantageous in that they use a specific choice of polarization vectors and, accordingly, require additional calculations if it is necessary to calculate different polarization configurations of fermions.

Many analytic methods form a basis both for universal codes for calculating matrix elements and cross sections—such as CompHEP [26] (this package is intended for calculating matrix elements in terms of traces of γ matrices—see [27]), GRACE [28], and FeynCalc [29]—and for special codes developed to deal with processes of the types $e^+e^- \to 4f, 6f, f\bar{f} + n\gamma$. An extensive list of such codes can be found in [30, 31]. For reactions involving collinearly moving photons, Carimalo *et al.* [32] proposed a method that relies on approximately calculating matrix elements and which makes it possible to obtain compact expressions.

The objective of this article is to present a new method for calculating the amplitudes of processes involving both massive fermions of arbitrary polarization and massless fermions. This method is based on the use of basis vectors of an isotropic vierbein in Minkowski space and basis spinors that are associated with these vectors. The method does not employ either the explicit form of bispinors and Dirac γ matrices or the evaluation of traces. But as in methods that make use of traces, the matrix element being considered is reduced here to a combination of the scalar products of particle momenta and polarization vectors and the vectors of the isotropic vierbein. The method in question is efficient and is readily implemented in calculations owing to the simplicity of its algorithm featuring a small number of operations. In contrast to the spinor technique in the versions presented in [17–20], the proposed method does not invoke either the Chisholm spinor identities or representations of contractions of particle 4-momenta and polarization vectors with γ matrices in terms of bispinors.

Since the method in question is based on extensively using the basis spinors related to the isotropic-vierbein vectors, we will refer to this method in the following as the method of basis spinors.

The ensuing exposition is organized as follows. The isotropic vierbein and the complete set of massless spinors that is associated with it are defined in Section 2. Basic formulas of the proposed method are also given there. The coefficients in the expansion of bispinors for an arbitrary polarization vector in basis bispinors are considered in Section 3, and the expansion coefficients for fermions are presented there for the polarization states that are used most frequently. An account of the method of basis spinors and a concise comparison of the proposed computational scheme with spinor-technique methods and methods

employing traces are given in Section 4. In Section 5, the amplitudes for the reaction $e^+e^- \to f\bar{f}$ involving massive fermions f and for the process $e^+e^- \to W^+W^-$ involving polarized bosons are calculated to test the method of basis spinors; in addition, one of the possible diagrams for the reaction $e^+e^- \to e^+e^-e^+e^-e^+e^-$ (for the case of massless fermions) is calculated in the same section for purposes of illustration. Section 6 contains the conclusions and final comments.

2. ISOTROPIC VIERBEIN AND BASIS SPINORS

In Minkowski space, we introduce a quartet of orthonormalized vectors that satisfy the relations

$$l_0^\mu \cdot l_0^\nu - l_1^\mu \cdot l_1^\nu - l_2^\mu \cdot l_2^\nu - l_3^\mu \cdot l_3^\nu = g^{\mu\nu}, \quad (1)$$
$$(l_A)^\mu = \delta_A^\mu, \quad A, \mu, \nu = 0, 1, 2, 3,$$

where g is a metric tensor and δ is a Kronecker delta symbol. With the aid of (1), an arbitrary 4-vector p can be represented in the form

$$p = (pl_0) \cdot l_0 - (pl_1) \cdot l_1 - (pl_2) \cdot l_2 - (pl_3) \cdot l_3. \quad (2)$$

Using the vectors l_A, we determine lightlike vectors that form an isotropic vierbein in Minkowski space (for information about the isotropic vierbein, the interested reader is referred to [33]):

$$b_\rho = l_0 + \rho l_3, \quad n_\lambda = l_1 + i\lambda l_2, \quad \rho, \lambda = \pm 1. \quad (3)$$

From relations (1)–(3), it follows that

$$(b_\rho b_{-\lambda}) = 2\delta_{\lambda,\rho}, \quad (n_\lambda n_{-\rho}) = -2\delta_{\lambda,\rho}, \quad (4)$$
$$(b_\rho n_\lambda) = 0,$$

$$\frac{1}{2}\sum_{\lambda=-1}^{1} [b_\lambda^\mu \cdot b_{-\lambda}^\nu - n_\lambda^\mu \cdot n_{-\lambda}^\nu] = g^{\mu\nu}. \quad (5)$$

Therefore, the matrix γ^μ and, accordingly, its contraction $\hat{p} = \gamma^\mu p_\mu$ with an arbitrary 4-vector p_μ can be written as

$$\gamma^\mu = \frac{1}{2}\sum_{\lambda=-1}^{1} [\hat{b}_{-\lambda} b_\lambda^\mu - \hat{n}_{-\lambda} n_\lambda^\mu], \quad (6)$$

$$\hat{p} = \frac{1}{2}\sum_{\lambda=-1}^{1} [(b_{-\lambda}p)\hat{b}_\lambda - (n_{-\lambda}p)\hat{n}_\lambda]. \quad (7)$$

With the aid of the isotropic vierbein (3), we define the basis spinors $U_\lambda(b_{-1})$ and $U_\lambda(b_1)$ as

$$U_\lambda(b_{-1})\overline{U}_\lambda(b_{-1}) = \omega_\lambda \hat{b}_{-1}, \quad (8)$$

$$U_\lambda(b_1) \equiv \frac{\hat{b}_1}{2} U_{-\lambda}(b_{-1}), \quad (9)$$

$$\omega_\lambda U_\lambda(b_{\pm 1}) = U_\lambda(b_{\pm 1}), \quad (10)$$

where $\omega_\lambda \equiv 1/2(1 + \lambda\gamma_5)$.

Constructing the raising and lowering operators for spin via the relation

$$\frac{\lambda}{2}\hat{n}_\lambda U_{-\nu}(b_{-1}) = \delta_{\lambda,\nu} U_\lambda(b_{-1}), \quad (11)$$

we fix the phase of the basis spinor $U_\lambda(b_{-1})$ and the phase of the spinor $U_\lambda(b_1)$.

From the properties of the lightlike vectors (3) and the algebra of γ matrices, we obtain

$$\frac{\hat{b}_{-1}}{2} U_{-\lambda}(b_1) = U_\lambda(b_{-1}), \quad (12)$$

$$\frac{\lambda}{2}\hat{n}_\lambda U_\nu(b_1) = -\delta_{\lambda,\nu} U_{-\lambda}(b_1). \quad (13)$$

The completeness condition

$$\frac{1}{2}\sum_{\lambda,A=-1}^{1} U_\lambda(b_A)\overline{U}_{-\lambda}(b_{-A}) = I, \quad (14)$$

which can be derived from relations (8)–(10), is an important property of the basis spinors (8) and (9). Thus, an arbitrary bispinor can be expanded in the basis spinors $U_\lambda(b_A)$.

Since the phases of basis spinors are fixed, the result of applying the γ matrices to these spinors can be found with the aid of relations (6) and (11)–(13); that is,

$$\gamma^\mu U_\lambda(b_{-1}) = b_{-1}^\mu U_{-\lambda}(b_1) + \lambda n_\lambda^\mu U_{-\lambda}(b_{-1}), \quad (15)$$

$$\gamma^\mu U_\lambda(b_1) = b_1^\mu U_{-\lambda}(b_{-1}) + \lambda n_{-\lambda}^\mu U_{-\lambda}(b_1). \quad (16)$$

Relations (15) and (16) can be recast into the general form

$$\gamma^\mu U_\lambda(b_A) = b_A^\mu U_{-\lambda}(b_{-A}) + \lambda n_{-A\lambda}^\mu U_{-\lambda}(b_A). \quad (17)$$

The basis spinors possess yet another important property: their spinor products have a simple form and are similar to scalar products of the isotropic-vierbein vectors; that is,

$$\overline{U}_\lambda(b_C)U_\rho(b_A) = 2\delta_{\lambda,-\rho}\delta_{C,-A}, \quad (18)$$
$$C, A = \pm 1, \quad \lambda, \rho = \pm 1.$$

Relations (17) and (18), together with the equality

$$\omega_\lambda U_\rho(b_A) = \delta_{\lambda,\rho} U_\rho(b_A), \quad (19)$$

form a basis of the proposed method (method of basis spinors), whose algorithm will be described below.

3. EXPANSION OF BISPINORS IN BASIS SPINORS

Evaluation of the coefficients in the expansion of an arbitrary bispinor in the basis spinors (8) and (9) is an important ingredient of the method. The possibility of obtaining these coefficients is based on the fact that an arbitrary bispinor of a fermion can be determined in terms of the basis spinor $U_\rho(b_{-1})$ [or $U_\rho(b_1)$] with the aid of projection operators.

First, we will find the expansion coefficients for massless bispinors. An arbitrary bispinor $U_\lambda(p)$ characterized by a 4-momentum p [$p^2 = 0, (pb_{-1}) \neq 0$] and a helicity λ is defined in terms of a basis spinor as (see, for example, [18])

$$U_\lambda(p) = \frac{\hat{p}}{\sqrt{2(pb_{-1})}} U_{-\lambda}(b_{-1}). \tag{20}$$

From the completeness condition (14), it follows that the coefficient in the expansion in the basis spinors are spinor products of the type

$$D_{\lambda,\rho}(A;p) \equiv \frac{1}{2}\overline{U}_\lambda(b_A)U_\rho(p). \tag{21}$$

With the aid of (17)–(21), we obtain

$$D_{\lambda,\rho}(A;p) = \frac{\delta_{\lambda,-\rho}}{\sqrt{2}} \times \left[\delta_{A,-1}\sqrt{(pb_{-1})} + \delta_{A,1}\frac{\lambda(pn_\lambda)}{\sqrt{(pb_{-1})}}\right]. \tag{22}$$

If $p = \text{const} \cdot b_{-1}$, the expansion takes the simplest form, because, in this case, we have

$$U_\lambda(p) = \sqrt{\text{const}} \cdot U_\lambda(b_{-1}). \tag{23}$$

As in the case where use is made of the spinor technique, it is convenient, for numerical calculations, to rewrite coefficient (22) in terms of the components of the 4-vector $p = (p^0, p^x, p^y, p^z)$ as

$$D_{\lambda,\rho}(A;p) = \frac{\delta_{\lambda,-\rho}}{\sqrt{2}} \times \left[\delta_{A,-1}\sqrt{p^+} - \delta_{A,1}\lambda\exp(i\lambda\varphi_p)\sqrt{p^-}\right], \tag{24}$$

where

$$p^\pm = p^0 \pm p^z,$$
$$p^x + i\lambda p^y = \sqrt{(p^x)^2 + (p^y)^2}\exp(i\lambda\varphi_p).$$

The expansion for the antifermion $V_\lambda(p)$ is derived from the relation

$$V_\lambda(p) = U_{-\lambda}(p). \tag{25}$$

Let us now proceed to consider massive Dirac particles. The bispinors of massive fermions and antifermions having arbitrary polarization vectors can be defined with the aid of the basis spinor via the relations (see, for example, the Appendix in [20])

$$U_\lambda(p,s_p) = \frac{\tau_u^\lambda(p,s_p)}{\sqrt{b_{-1}(p+m_p s_p)}} U_{-\lambda}(b_{-1}), \tag{26}$$

$$V_\lambda(p,s_p) = \frac{\tau_v^\lambda(p,s_p)}{\sqrt{b_{-1}(p+m_p s_p)}} U_\lambda(b_{-1}), \tag{27}$$

where the projection operators $\tau_u^\lambda(p,s_p)$ and $\tau_v^\lambda(p,s_p)$ are given by

$$\tau_u^\lambda(p,s_p) = \frac{1}{2}(\hat{p}+m_p)(1+\lambda\gamma_5\hat{s}_p), \tag{28}$$

$$\tau_v^\lambda(p,s_p) = \frac{1}{2}(\hat{p}-m_p)(1+\lambda\gamma_5\hat{s}_p). \tag{29}$$

It can easily be shown that

$$\begin{aligned}
\hat{p}U_\lambda(p,s_p) &= m_p U_\lambda(p,s_p), \\
\hat{p}V_\lambda(p,s_p) &= -m_p V_\lambda(p,s_p), \\
\gamma_5\hat{s}_p U_\lambda(p,s_p) &= \lambda U_\lambda(p,s_p), \\
\gamma_5\hat{s}_p V_\lambda(p,s_p) &= \lambda V_\lambda(p,s_p);
\end{aligned} \tag{30}$$

that is, the bispinors $U_\lambda(p,s_p)$ and $V_\lambda(p,s_p)$ satisfy the Dirac equation and the spin conditions for a massive fermion and a massive antifermion. It can easily be proven that the bispinors in (26) and (27) are related by the equations

$$\begin{aligned}
V_\lambda(p,s_p) &= -\lambda\gamma_5 U_{-\lambda}(p,s_p), \\
\overline{V}_\lambda(p,s_p) &= \overline{U}_{-\lambda}(p,s_p)\lambda\gamma_5.
\end{aligned} \tag{31}$$

Upon calculations on the basis of (26) and (27), we find that the expansion coefficients for a massive fermion having a momentum p, an arbitrary polarization vector s_p, and a mass m_p can be written in the form of scalar products of the vierbein vectors and physical vectors:

$$\begin{aligned}
D_{\lambda,\rho}(A;p,s_p) &= \frac{1}{\sqrt{2(b_{-1}\xi_1^p)}} \\
&\times \left[\delta_{A,-1}\left\{\delta_{\lambda,-\rho}(b_{-1}\xi_1^p) - \frac{\rho\delta_{\lambda,\rho}}{2m_p}((b_{-1}\xi_1^p)(n_{-\rho}\xi_2^p)\right.\right. \\
&\left. + (n_{-\rho}\xi_1^p)(b_{-1}\xi_2^p))\right\} + \delta_{A,1}\left\{-\rho\delta_{\lambda,-\rho}(n_{-\rho}\xi_1^p)\right. \\
&\left.\left. + \frac{\delta_{\lambda,\rho}}{2m_p}((b_{-1}\xi_1^p)(b_1\xi_2^p) - (n_{-\rho}\xi_1^p)(n_\rho\xi_2^p))\right\}\right],
\end{aligned} \tag{32}$$

$$\xi_1^p = p + m_p s_p, \qquad \xi_2^p = p - m_p s_p. \tag{33}$$

Let us find the expansion coefficients for the KS helicity and polarization states of fermions. Such polarization states are most frequently used in calculating reactions induced by elementary-particle interactions.

The polarization vector for KS states is defined as [18, 23, 25]

$$s_p = \frac{p}{m_p} - m_p \frac{b_{-1}}{(pb_{-1})}. \quad (34)$$

In this case, the relation between the massive fermion and a basis bispinor has the simplest form [18, 25]

$$U_\lambda(p, KS) = \frac{\hat{p} + m_p}{\sqrt{2(pb_{-1})}} U_{-\lambda}(b_{-1}), \quad (35)$$

and the expansion coefficients have a compact form in terms of scalar products:

$$D_{\lambda,\rho}(A; p, KS) = \frac{1}{\sqrt{2}} \left\{ \delta_{\lambda,-\rho} \left[\delta_{A,-1} \sqrt{(pb_{-1})} \right.\right. \quad (36)$$
$$\left.\left. + \delta_{A,1} \frac{\lambda (pn_\lambda)}{\sqrt{(pb_{-1})}} \right] + \delta_{\lambda,\rho} \delta_{A,1} \frac{m_p}{\sqrt{(pb_{-1})}} \right\}.$$

Taking the polarization vector in the form

$$s_p = \frac{(pl_0)p - m_p^2 l_0}{m_p \sqrt{(pl_0)^2 - m_p^2}}, \quad (37)$$

we obtain helicity fermion states.

For helicity states, the expressions for the expansion coefficients in terms of the scalar products of physical vectors and the isotropic-vierbein vectors are more cumbersome than those for KS states. But if we consider this expression in terms of the components of the momentum $p = (p^0, |\mathbf{p}| \sin\theta_p \sin\varphi_p, |\mathbf{p}| \sin\theta_p \cos\varphi_p, |\mathbf{p}| \cos\theta_p)$, the coefficients will also assume the compact form

$$D_{\lambda,\rho}(A; p, \mathrm{Hel}) = \frac{1}{\sqrt{2}} \left[\sqrt{p^0 + |\mathbf{p}|} \left(\delta_{A,-1} \cos\frac{\theta_p}{2} \right.\right. \quad (38)$$
$$\left. + \delta_{A,1} \rho \exp(-i\rho\varphi_p) \sin\frac{\theta_p}{2} \right) \delta_{\lambda,-\rho} + \sqrt{p^0 - |\mathbf{p}|}$$
$$\left. \times \left(\delta_{A,1} \cos\frac{\theta_p}{2} + \delta_{A,-1} \rho \exp(-i\rho\varphi_p) \sin\frac{\theta_p}{2} \right) \delta_{\lambda,\rho} \right].$$

The absence of a denominator as in the massless case is a distinct feature of the expansion for helicity fermion states. It can easily be proven that, at $m_p = 0$, relation (38) reduces to (24).

An analysis of the expansion coefficients for massive and massless spin-1/2 fermions reveals that, for massless fermions, not only does there occur a natural decrease in terms proportional to the fermion mass, but also the expansion coefficients $D_{\lambda,\rho}$ become diagonal in the spin indices λ and ρ, the latter circumstance simplifying the calculation of relevant matrix elements.

The expansion coefficients for the antifermion described by the bispinors in (27) can easily be obtained with the aid of expression (31).

4. METHOD OF BASIS SPINORS

The amplitude for a Feynman diagram can be represented in the form

$$M_{\lambda_p,\lambda_k}(p, s_p; k, s_k) = \overline{U}_{\lambda_p}(p, s_p) Q U_{\lambda_k}(k, s_k). \quad (39)$$

Expression (39) corresponds to a disconnected fermion line involving a matrix operator Q that is a combination of γ matrices and (or) their contractions with 4-vectors.

In the method based on the use of traces, relation (39) is recast into the form

$$M_{\lambda_p,\lambda_k}(p, s_p; k, s_k) = \mathrm{tr}(U_{\lambda_k}(k, s_k) \overline{U}_{\lambda_p}(p, s_p) Q). \quad (40)$$

The main problem in this approach is to obtain an explicit form of the transition operators $U_{\lambda_k}(k, s_k)\overline{U}_{\lambda_p}(p, s_p)$. It is the solution to this problem that forms a basis of the methods for calculating matrix elements via traces. In our case, we can also derive, for various spin configurations of fermions, an expression for the matrix describing the transition from one bispinor to another using expressions (26) and (27); that is,

$$U_\lambda(k, s_k)\overline{U}_\lambda(p, s_p) \quad (41)$$
$$= \frac{\tau^u_\lambda(k, s_k)\omega_{-\lambda}\hat{b}_{-1}\tau^u_\lambda(p, s_p)}{4\sqrt{b_{-1}(p + m_p s_p)}\sqrt{b_{-1}(k + m_k s_k)}},$$

$$U_{-\lambda}(k, s_k)\overline{U}_\lambda(p, s_p) \quad (42)$$
$$= \frac{\lambda\tau^u_{-\lambda}(k, s_k)\hat{n}_\lambda\omega_\lambda\hat{b}_{-1}\tau^u_\lambda(p, s_p)}{8\sqrt{b_{-1}(p + m_p s_p)}\sqrt{b_{-1}(k + m_k s_k)}}.$$

Thus, we see that, in order to rewrite expression (39) in terms of scalar products and contractions with the Levi-Civita tensor, it is thus necessary to evaluate the relations

$$M_{\lambda,\lambda}(p, s_p; k, s_k) \quad (43)$$
$$= \frac{tr(\tau^u_\lambda(k, s_k)\omega_{-\lambda}\hat{b}_{-1}\tau^u_\lambda(p, s_p)Q)}{4\sqrt{b_{-1}(p + m_p s_p)}\sqrt{b_{-1}(k + m_k s_k)}},$$

$$M_{\lambda,-\lambda}(p, s_p; k, s_k) \quad (44)$$
$$= \frac{\lambda tr(\tau^u_{-\lambda}(k, s_k)\hat{n}_\lambda\omega_\lambda\hat{b}_{-1}\tau^u_\lambda(p, s_p)Q)}{8\sqrt{b_{-1}(p + m_p s_p)}\sqrt{b_{-1}(k + m_k s_k)}}.$$

That, with increasing number of γ matrices in the operator Q, the number of terms that arise in calculating the traces in (43) and (44) increases considerably is the main drawback of this method. For this reason, it was proposed in [27] to use KS polarization states in order to reduce the number of terms in the transition operator $U_{\lambda_k}(k, s_k)\overline{U}_{\lambda_p}(p, s_p)$ [see (35)] and, accordingly, in expressions (43) and (44). It can be

seen from (43) and (44) that each spin configuration of fermions must be computed separately, which also complicates the calculations.

Here, a method is proposed for evaluating expressions of the type in (39) without recourse to the above scheme—that is, a method that does not involve calculating traces of the types in (43) and (44). This procedure can be realized by using the properties of the basis spinors (8) and (9). Therefore, this method is referred to as the method of basis spinors.

The basic point of the method is as follows. With the aid of the completeness condition (14), we expand the bispinors in (39). The resulting matrix element takes the form

$$M_{\lambda_p,\lambda_k}(p,s_p;k,s_k) \tag{45}$$
$$= \sum_{\sigma,\rho=-1}^{1}\sum_{A,C=-1}^{1} D^{\dagger}_{\lambda_p,\sigma}(C;p,s_p)\Gamma^{-C,A}_{-\sigma,\rho}(Q) \times D_{-\rho,\lambda_k}(-A;k,s_k),$$

where the coefficients $D_{\rho,\lambda}$ are the coefficients in the expansion of bispinors and the quantity Γ is given by

$$\Gamma^{C,A}_{\sigma,\rho}(Q) \equiv \overline{U}_{\sigma}(b_C)QU_{\rho}(b_A). \tag{46}$$

Thus, we can see that, within the method of basis spinors, the problem of evaluating expressions of the type in (39) in terms of scalar products is broken down into two problems: (i) that of calculating the expansion coefficients and (ii) that of calculating the quantity $\Gamma^{C,A}_{\sigma,\rho}(Q)$ with subsequent summation.

The first part of the problem was solved in the preceding section. Obviously, such calculations are performed only once; further, the expansion coefficients are used as known functions.

With the aid of relations (17)–(19), we can easily determine the result of applying the matrix operator Q to the basis spinor in (46) and, accordingly, calculate the quantity $\Gamma(Q)$ in terms of the scalar products of the vectors appearing in Q and the isotropic-vierbein vectors. The ensuing summation procedure is substantially simplified owing to the Kronecker delta symbols that arise both in calculating the expansion coefficients and in calculating the quantity in (46). By way of example, we indicate that, if the operator Q contains an odd number of γ matrices, we obviously have $\Gamma^{C,A}_{\sigma,\rho}(Q) = \delta_{\sigma,\rho}\Gamma^{C,A}_{\rho,\rho}(Q)$.

But if Q involves uncontracted Lorentz indices, the final result will take the form of an appropriate tensor constructed from the isotropic-vierbein vectors.

We first illustrate the application of this method by calculating the current construction for massless fermions, in which case we have

$$M_{\lambda_p,\lambda_k}(p,k) = J^{\mu}_{\lambda_p,\lambda_k}(p,k) \equiv \overline{U}_{\lambda_p}(p)\gamma^{\mu}U_{\lambda_k}(k). \tag{47}$$

With the aid of the completeness condition (14) for the basis spinors, expression (47) can be reduced to the form

$$J^{\mu}_{\lambda_p,\lambda_k}(p,k) = \sum_{\sigma,\rho=-1}^{1}\sum_{A,C=-1}^{1} D^{\dagger}_{\lambda_p,\sigma}(C;p) \times \{\overline{U}_{-\sigma}(b_{-C})\gamma^{\mu}U_{\rho}(b_A)\}D_{-\rho,\lambda_k}(-A;k). \tag{48}$$

By using relations (17) and (18), we obtain

$$\Gamma^{-C,A}_{-\sigma,\rho}(\gamma^{\mu}) = 2\delta_{\sigma,-\rho}(\delta_{C,-A}b^{\mu}_A + \rho n^{\mu}_{-A\rho}\delta_{C,A}). \tag{49}$$

Thus, expression (47) can be recast into the form

$$J^{\mu}_{\lambda_p,\lambda_k}(p,k) \tag{50}$$
$$= 2\sum_{A,\sigma=-1}^{1}(b^{\mu}_A[D^{\dagger}_{\lambda_p,\sigma}(-A;p)D_{\sigma,\lambda_k}(-A;k)] - \sigma n^{\mu}_{A\sigma}[D^{\dagger}_{\lambda_p,\sigma}(A;p)D_{\sigma,\lambda_k}(-A;k)])$$
$$= 2\sum_{\sigma=-1}^{1}(b^{\mu}_{-1}[D^{\dagger}_{\lambda_p,\sigma}(1;p)D_{\sigma,\lambda_k}(1;k)] + b^{\mu}_1[D^{\dagger}_{\lambda_p,\sigma}(-1;p)D_{\sigma,\lambda_k}(-1;k)] - \sigma n^{\mu}_{-\sigma}[D^{\dagger}_{\lambda_p,\sigma}(-1;p)D_{\sigma,\lambda_k}(1;k)] - \sigma n^{\mu}_{\sigma}[D^{\dagger}_{\lambda_p,\sigma}(1;p)D_{\sigma,\lambda_k}(-1;k)]).$$

Substituting the expansion coefficients (22) and performing summation, we derive an expression in terms of scalar products of the physical vectors p and k and the isotropic-vierbein vectors:

$$J^{\mu}_{\lambda_p,\lambda_k}(p,k) = \delta_{\lambda_p,\lambda_k}\left([\sqrt{(pb_{-1})(kb_{-1})}]b^{\mu}_1 \right. \tag{51}$$
$$+\left[\frac{(pn_{\lambda_p})(kn_{-\lambda_p})}{\sqrt{(pb_{-1})(kb_{-1})}}\right]b^{\mu}_{-1} - \left[(pn_{\lambda_p})\sqrt{\frac{(kb_{-1})}{(pb_{-1})}}\right]n^{\mu}_{-\lambda_p}$$
$$\left. - \left[(kn_{-\lambda_p})\sqrt{\frac{(pb_{-1})}{(kb_{-1})}}\right]n^{\mu}_{\lambda_p}\right).$$

The corresponding calculation for massive fermions proceeds along similar lines and leads to the emergence of additional terms in front of the isotropic-vierbein vectors.

It should be noted that an increase in the number of γ matrices in the operator Q does not lead to an avalanche-like increase in the number of terms, in contrast to what occurs within methods employing traces. In the present approach, the matrix element can be obtained for arbitrary spin configurations of fermions.

We will now perform a concise comparison of the method of basis spinors and the spinor technique

applied in [18] by considering the example of massless fermions. For this, we reproduce some details of the spinor technique with small modifications. Instead of the vectors $k_0 = (1,1,0,0)$ and $k_1 = (0,0,1,0)$ used in [18], we take the vectors b_{-1} and n_λ, respectively.

The spinor technique involves the following mathematical transformations:

(i) An arbitrary massless spinor $U_\lambda(p)$ is defined in terms of the basis spinors by relation (20).

(ii) Use is made of the Chisholm identities

$$\gamma^\mu\{\overline{U}_\lambda(p)\gamma_\mu U_\lambda(k)\} = 2[U_\lambda(k)\overline{U}_\lambda(p) + U_{-\lambda}(p)\overline{U}_{-\lambda}(k)]. \quad (52)$$

(iii) The contraction of $\hat{p}$ satisfying the condition $p^2 = 0$ with the polarization vectors of a massless vector boson, $\varepsilon^\mu_\lambda(k)$, is expressed in terms of the bispinors as

$$\hat{p} = \sum_\lambda U_\lambda(p)\overline{U}_\lambda(p), \quad (53)$$

$$\varepsilon^\mu_\lambda(k) \sim \overline{U}_\lambda(q)\gamma^\mu U_\lambda(k). \quad (54)$$

The amplitude for the reaction involving massless fermions then reduces to a combination of spinor products of the type

$$s_\lambda(p,k) \equiv \overline{U}_\lambda(p)U_{-\lambda}(k) = -s_\lambda(k,p). \quad (55)$$

By virtue of (6)–(8), the spinor products (55) reduce to evaluating a trace [18]:

$$s_\lambda(p,k) = \frac{\lambda}{4}\frac{\mathrm{tr}(\omega_{-\lambda}\hat{b}_{-1}\hat{p}\hat{k}\hat{n}_\lambda)}{\sqrt{(b_{-1}p)}\sqrt{(b_{-1}k)}} \quad (56)$$

$$= \frac{\lambda[(pb_{-1})(kn_\lambda) - (kb_{-1})(pn_\lambda)] - i\epsilon(b_{-1},n_\lambda,p,k)}{2\sqrt{(b_{-1}p)(b_{-1}k)}}.$$

By using in (56) the properties of the isotropic vierbein, one can obtain the expression [23]

$$s_\lambda(p,k) = \frac{\lambda[(pb_{-1})(kn_\lambda) - (kb_{-1})(pn_\lambda)]}{\sqrt{(b_{-1}p)(b_{-1}k)}}. \quad (57)$$

A comparative analysis of the algorithms for reducing (calculating) matrix elements shows that the spinor technique and the method of basis spinors differ significantly. The method of basis spinors does not employ either the Chisholm identities (52) or additional constructions of the type in (53) or in (54), nor does it require a special procedure for constructing the polarization vectors of massive gauge bosons (see, for example, [18]), since all 4-vectors are treated in the same way within this method. In addition, it should be noted that, if the vector p or k coincides in (52) with b_1 or b_{-1}, one must use the spinor Chisholm identities with care, since they take a modified form (see [34]).

The method of basis spinors can be supplemented with a construction of the polarization vectors for massless and massive bosons in the isotropic-vierbein basis (for the case of photons, the interested reader is referred to [33]). The final expressions for (47) will then involve only the scalar products of the 4-momentum vectors for the process and the isotropic-vierbein vectors.

For a specific reaction, there is always the possibility for constructing the isotropic-vierbein basis (3) in terms of physical vectors. This procedure makes it possible to obtain an expression for the matrix element of a Feynman diagrams in terms of the scalar products involving only vectors characterizing the reaction being considered and their contractions with the Levi-Civita tensor. Thus, we can obtain a manifestly Lorentz-invariant matrix element. Additionally, an appropriate construction of the basis can lead to a significant reduction of the number of terms.

5. EXAMPLES

In order to illustrate and test the method of basis spinors, we will consider a number of examples. We restrict our consideration to reactions induced by electron–positron interactions, since there are numerous examples of analytic calculations of matrix elements for these reactions. For the sake of simplification and clarity, we assume that the initial fermions are massless.

By way of example, we will calculate the amplitude for the process

$$e^-(p_1,\lambda_1) + e^+(p_2,\lambda_2) \to W^-(k_1) + W^+(k_2). \quad (58)$$

This amplitude can be represented in the form

$$M_{e^+e^-\to W^+W^-} = M_{\gamma Z} + M_\nu, \quad (59)$$

$$M_{\gamma Z} = \frac{4\pi\alpha}{P^2}\left[\overline{V}_{\lambda_2}(p_2)\gamma_\mu U_{\lambda_1}(p_1) - \frac{P^2}{(P^2 - m_Z^2)2\sin^2\theta_\mathrm{W}} \times \overline{V}_{\lambda_2}(p_2)\gamma_\mu(g_V^e - g_A^e\gamma_5)U_{\lambda_1}(p_1)\right] \times \Gamma^{\mu\alpha\beta}(P,k_1,k_2)\varepsilon_\alpha(k_1)\varepsilon_\beta(k_2), \quad (60)$$

$$M_\nu = \frac{\pi\alpha}{2Q^2\sin^2\theta_\mathrm{W}} \times \overline{V}_{\lambda_2}(p_2)\hat{\varepsilon}(k_2)(1-\gamma_5)\hat{Q}\hat{\varepsilon}(k_1)(1-\gamma_5)U_{\lambda_1}(p_1), \quad (61)$$

where g_A^e and g_V^e are, respectively, the axial and the vector coupling constant of the electron and the element of the three-boson vertex within the Standard Model is given by

$$\Gamma^{\mu\alpha\beta}(P,k_1,k_2) = g^{\alpha\beta}(k_1-k_2)^\mu + 2(P^\alpha g^{\mu\beta} - P^\beta g^{\mu\alpha}). \quad (62)$$

In expression (59), we have also used the following notation: α is the fine-structure constant, θ_W is the Weinberg–Salam angle, and $P = p_1 + p_2$ and $Q = p_1 - k_1$ are momenta.

Let us consider reaction (58) in the e^+e^- c.m. frame. The isotropic-vierbein vectors (3) can then be expressed in terms of the physical vectors p_1, p_2, and k_1 as

$$b_1 = \frac{\sqrt{2}p_1}{\sqrt{(p_1p_2)}}, \quad b_{-1} = \frac{\sqrt{2}p_2}{\sqrt{(p_1p_2)}}, \quad (63)$$

$$n_\lambda = \frac{b_{-1}(k_1b_1) + b_1(k_1b_{-1}) - 2k_1 + i\lambda[b_1,b_{-1},k_1]}{2\sqrt{(b_{-1}k_1)(b_1k_1)}},$$

$$[p,r,k]^\mu = \epsilon^{\alpha\beta\rho\mu}p_\alpha r_\beta k_\rho.$$

By using the method of basis spinors, we can easily find, in this case, that

$$\overline{V}_{\lambda_2}(p_2)\gamma^\mu U_{\lambda_1}(p_1) = \lambda_1\delta_{-\lambda_2,\lambda_1}\sqrt{2(p_1p_2)}n^\mu_{\lambda_1}. \quad (64)$$

For the matrix elements corresponding to processes involving the exchange of a photon and a Z^0 boson, the expression in terms of the scalar products of the physical and isotropic-vierbein vectors is then immediately obtained in the form

$$M_{\gamma Z} = 4\pi\alpha\frac{\lambda_1\delta_{-\lambda_2,\lambda_1}}{\sqrt{2(p_1p_2)}}\left(1-\chi(P^2)\frac{g_e^{-\lambda_1}}{2\sin^2\theta_\mathrm{W}}\right) \quad (65)$$

$$\times (n_{\lambda_1})_\mu\Gamma^{\mu\alpha\beta}(P,k_1,k_2)\varepsilon_\alpha(k_1)\varepsilon_\beta(k_2)$$

$$= 4\pi\alpha\frac{\lambda_1\delta_{-\lambda_2,\lambda_1}}{\sqrt{2(p_1p_2)}}\left(1-\chi(P^2)\frac{g_e^{-\lambda_1}}{2\sin^2\theta_\mathrm{W}}\right)$$

$$\times [(\varepsilon(k_1)\varepsilon(k_2))((k_1-k_2)n_{\lambda_1})$$

$$+ 2((P\varepsilon(k_1))(\varepsilon(k_2)n_{\lambda_1}) - (P\varepsilon(k_2))(\varepsilon(k_1)n_{\lambda_1}))],$$

where $\chi(P^2) = P^2/(P^2-m_Z^2)$ and $g_e^\lambda = (g_V^e + \lambda g_A^e)$. It should be noted that the corresponding calculation on the basis of the spinor technique proposed by the CALCUL group requires a much greater amount of effort.

It is somewhat more difficult to calculate the neutrino-exchange diagram, but, even in this case, the use of relations (17)–(19) yields

$$M_\nu = \frac{\pi\alpha\sqrt{2(p_1p_2)}(-1+\lambda_1)}{\sin^2\theta_\mathrm{W}(m_W^2 - 2(k_1p_1))} \quad (66)$$

$$\times \left[\{(n_{-\lambda_1}k_1)(\varepsilon(k_1)b_1) - (b_1k_1)(\varepsilon(k_1)n_{-\lambda_1})\}\right.$$

$$\times (b_{-1}\varepsilon(k_2)) + \left\{(\varepsilon(k_1)n_{-\lambda_1})(k_1n_{\lambda_{-1}})\right.$$

$$\left.\left. + \left(\sqrt{2(p_1p_2)} - (b_{-1}k_1)\right)(\varepsilon(k_1)b_1)\right\}\right.$$

$$\left.\times (\varepsilon(k_2)n_{-\lambda_1})\right]\delta_{-\lambda_2,\lambda_1}.$$

In order to derive a manifestly Lorentz-invariant expression for amplitude (59) in terms of the scalar products of the vectors characterizing the process in (58) and their contractions with the Levi-Civita tensor, it is necessary to substitute the isotropic-vierbein vectors (63) into relations (65) and (66).

Considering that, in the c.m. frame, the components of the vectors characterizing the reaction being considered are given by (here, we take into account the kinematics of the process)

$$p_1 = \frac{\sqrt{s}}{2}(1,0,0,1), \quad p_2 = \frac{\sqrt{s}}{2}(1,0,0,-1), \quad (67)$$

$$k_1 = \frac{\sqrt{s}}{2}(1,\beta_W\sin\theta,0,\beta_W\cos\theta),$$

$$k_2 = \frac{\sqrt{s}}{2}(1,-\beta_W\sin\theta,0,-\beta_W\cos\theta),$$

$$\varepsilon_T^\mu(k_1) = \frac{1}{\sqrt{2}}(0,\cos\theta,\nu_1 i,-\sin\theta),$$

$$\varepsilon_T^\mu(k_2) = \frac{1}{\sqrt{2}}(0,\cos\theta,-\nu_2 i,-\sin\theta),$$

$$\varepsilon_L^\mu(k_1) = \gamma_W(\beta_W,\sin\theta,0,\cos\theta),$$

$$\varepsilon_L^\mu(k_2) = \gamma_W(\beta_W,-\sin\theta,0,-\cos\theta),$$

where $s = (p_1+p_2)^2$; $\beta_W = \sqrt{1-4m_W^2/s}$; $\gamma_W = \sqrt{s}/(2m_W)$; $\nu_1,\nu_2 = \pm 1$; and θ is the W^--boson scattering angle in the c.m. frame, and performing some simple transformations, we find for the longitudinally polarized W bosons ($\varepsilon(k_{1,2}) \equiv \varepsilon_L(k_{1,2})$) that

$$M_{\gamma Z}^{LL} = 4\pi\alpha\lambda_1\delta_{-\lambda_2,\lambda_1} \quad (68)$$

$$\times\left(1-\chi(s)\frac{g_e^{-\lambda_1}}{2\sin^2\theta_\mathrm{w}}\right)\beta_W(2\gamma_W^2+1)\sin\theta,$$

$$M_\nu^{LL} = \frac{2\pi\alpha\delta_{-\lambda_2,\lambda_1}}{\beta_W\sin^2\theta_\mathrm{W}}(1-\lambda_1)$$

$$\times\left(\gamma_W^2 - \frac{1}{\gamma_W^2(1+\beta_W^2-2\beta_W\cos\theta)}\right)\sin\theta.$$

Apart from a phase factor, expressions (68) coincide with the matrix elements calculated for this process in [35].

For yet another example, we consider the process

$$e^-(p_1,\lambda_1)+e^+(p_2,\lambda_2)\to f(k_1,\nu_1)+\bar f(k_2,\nu_2) \quad (f\neq e), \tag{69}$$

where $f(k,\nu)$ is a massive fermion having a momentum k and a spin projection ν.

The amplitude for this process can be represented in the form

$$M_{e^+e^-\to f\bar f}(\lambda_1,\lambda_2;\nu_1,\nu_2) = (4\pi\alpha/s)[M_\gamma(\lambda_1,\lambda_2;\nu_1,\nu_2)+M_{Z^0}(\lambda_1,\lambda_2;\nu_1,\nu_2)], \tag{70}$$

where

$$M_\gamma(\lambda_1,\lambda_2;\nu_1,\nu_2) = Q_f\overline{V}_{\lambda_2}(p_2)\gamma_\mu U_{\lambda_1}(p_1)\overline{U}_{\nu_1}(k_1)\gamma^\mu V_{\nu_2}(k_2), \tag{71}$$

$$M_{Z^0}(\lambda_1,\lambda_2;\nu_1,\nu_2) = R_Z(g^{\mu\nu}-P^\mu P^\nu/m_Z^2) \times \overline{V}_{\lambda_2}(p_2)\gamma_\nu(g_V^e-g_A^e\gamma_5)U_{\lambda_1}(p_1)\overline{U}_{\nu_1}(k_1) \times\gamma_\mu(g_V^f-g_A^f\gamma_5)V_{\nu_2}(k_2) \tag{72}$$

with $R_Z=(G_{\rm F}m_Z^2 s)/(2\sqrt{2}\pi\alpha(s-m_Z^2))$. The quantities g_V^f and g_A^f are the fermionic coupling constants, $G_{\rm F}$ is the Fermi constant, and Q_f is the charge of the fermion f in e units. We will now calculate the amplitude of process (69) for KS polarization states of final fermions in the c.m. frame.

By using relation (64) and the expansion coefficients (36) for the KS polarization states, it can easily be found within the method of basis spinors that the expressions for the relevant amplitudes in terms of scalar products and in terms of the vector components can be represented, respectively, as

$$M^{KS}_{e^+e^-\to f\bar f}(\lambda_1,\lambda_2;\nu_1,\nu_2) = \frac{-8\pi\alpha}{s} \times\frac{\sqrt{s}\delta_{\lambda_1,-\lambda_2}}{\sqrt{(b_{-1}k_1)(b_1k_2)}}[\delta_{\lambda_1,\nu_1}(b_{-1}k_1)(\lambda_2Q_f - R_Z g_e^{-\lambda_1}g_f^{-\nu_1})((n_{\nu_2}k_2)\delta_{\nu_1,-\nu_2}+m_f\nu_2\delta_{\nu_1,\nu_2}) + \nu_2(b_{-1}k_2)(\nu_1\delta_{\nu_1,-\nu_2}\delta_{-\lambda_1,\nu_1}(n_{\nu_1}k_1)(-Q_f\lambda_2 + R_Z g_e^{-\lambda_1}g_f^{-\nu_1}) + m_f(Q_f\lambda_2 - R_Z g_e^{-\lambda_1}g_f^{\nu_1}))] \tag{73}$$

and as

$$M^{KS}_{e^+e^-\to f\bar f}(\lambda_1,\lambda_2;\nu_1,\nu_2) = \frac{4\pi\alpha\delta_{\lambda_1,-\lambda_2}}{\sqrt{1-\beta_f^2\cos^2\theta}} \times\Bigg[\delta_{\nu_1,-\nu_2}\beta_f(\lambda_1Q_f+R_Z g_e^{-\lambda_1}g_f^{-\nu_1})\sin\theta \times\{\delta_{\lambda_1,\nu_1}(1+\beta_f\cos\theta)-\delta_{-\lambda_1,\nu_1}(1-\beta_f\cos\theta)\} + \delta_{\nu_1,\nu_2}\delta_{\nu_1,\lambda_1}\nu_1\frac{2m_f}{\sqrt{s}}\{2Q_f\lambda_1 + R_Z g_e^{-\lambda_1}[g_f^{-\nu_1}(1 + \beta_f\cos\theta)+g_f^{\nu_1}(1-\beta_f\cos\theta)]\}\Bigg]. \tag{74}$$

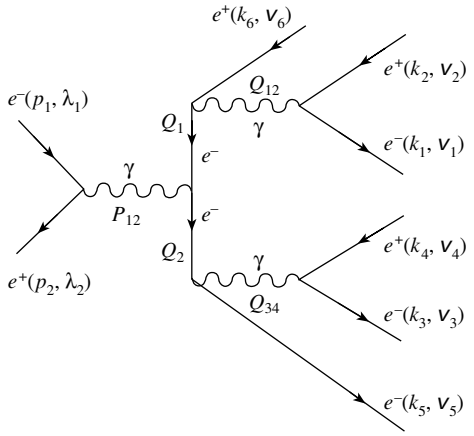

One of the possible diagrams for the reaction $e^+e^-\to e^+e^-e^+e^-e^+e^-$.

The differential cross section obtained by performing standard calculations for unpolarized fermions coincides with known expressions (see, for example, [33, 36]). Apart from a phase factor, the matrix element (74) coincides with the matrix element calculated in [16] for the limit of zero fermion masses.

It should be noted that the delta symbols in expressions (73) and (74) appear in the course of the calculation by the method that we use (and are not introduced in an ad hoc manner). Therefore, an analytic expression for the matrix elements is obtained within this method for all polarization states of fermions. Owing to this circumstance, the proposed method compares favorably with those that employ traces, since, in the latter, the polarization states of Dirac particles must be calculated individually for each configuration. In addition, it is worth mentioning that, within the method of basis spinors, it is convenient to use the left- and the right-handed coupling constant ($g_f^{\pm1}\equiv g_V^f\pm g_A^f$), because they factorize in calculating the quantity in (46) with spinors corresponding to massless fermions.

In order to avoid creating the impression that the proposed method is applicable only to trivial binary processes, we consider, by way of illustration, the calculation of one of the possible diagrams (see figure) for the process $e^+e^-\to e^+e^-e^+e^-e^+e^-$ involving massless fermions. It is obvious that, in contrast to the case of binary reactions, it is next to impossible to compare this calculation with analogous ones. Using the notation in (47) and disregarding the masses of electrons in the propagators, we can represent the matrix element for the Feynman diagram in the figure as

$$M_{e^+e^-\to e^+e^-e^+e^-e^+e^-} \tag{75}$$

$$= \frac{e^6}{P_{12}^2 Q_{12}^2 Q_{34}^2 Q_1^2 Q_2^2} J^{\beta}_{-\lambda_2,\lambda_1}(p_2,p_1) J^{\rho}_{\nu_1,-\nu_2}(k_1,k_2)$$
$$\times J^{\sigma}_{\nu_3,-\nu_4}(k_3,k_4)\overline{U}_{\nu_5}(k_5)\gamma_\sigma \hat{Q}_2\gamma_\beta\hat{Q}_1\gamma_\rho V_{\nu_6}(k_6),$$

where the following notation is used for the 4-vectors involved:

$$Q_1 = -(k_1+k_2+k_6), Q_2 = k_3+k_4+k_5, \quad (76)$$
$$Q_{34} = k_3+k_4, Q_{12} = k_1+k_2, P_{12} = p_1+p_2.$$

Within the method of basis spinors, the matrix element (75) can be reduced to the form

$$M_{e^+e^-\to e^+e^-e^+e^-e^+e^-} \quad (77)$$
$$= \frac{\delta_{\nu_1,-\nu_2}\delta_{\nu_3,-\nu_4}\delta_{\nu_5,-\nu_6}\delta_{\lambda_1,-\lambda_2}}{\sqrt{(k_5b_{-1})(k_6b_{-1})}} \frac{\sqrt{s}\lambda_1 e^6}{P_{12}^2 Q_{12}^2 Q_{34}^2 Q_1^2 Q_2^2}$$
$$\times (\delta_{\lambda_1,-\nu_5}[(Q_1b_1)((k_6b_{-1})(j_2n_{-\nu_5})$$
$$- (j_2b_{-1})(k_6n_{-\nu_5})) + (Q_1n_{-\nu_5})((j_2n_{\nu_5})$$
$$\times (k_6n_{-\nu_5}) - (k_6b_{-1})(j_2b_1))][(Q_2b_{-1})((k_5n_{\nu_5})$$
$$\times (j_3n_{-\nu_5}) - (k_5b_{-1})(j_3b_1))(Q_2n_{-\nu_5})((k_5b_{-1})$$
$$\times (j_3n_{\nu_5}) - (j_3b_{-1})(k_5n_{\nu_5}))] - \delta_{\lambda_1,\nu_5}[(k_6n_{-\nu_5})$$
$$\times ((j_2b_{-1})(Q_1n_{\nu_5}) - (Q_1b_{-1})(j_2n_{\nu_5}))$$
$$+ (k_6b_{-1})((j_2b_1)(Q_1b_{-1}) - (Q_1n_{\nu_5})(j_2n_{-\nu_5}))]$$
$$\times [(Q_2b_1)((k_5b_{-1})(j_3n_{\nu_5}) - (j_3b_{-1})(k_5n_{\nu_5}))$$
$$+ (Q_2n_{\nu_5})((j_3n_{-\nu_5})(k_5n_{\nu_5}) - (k_5b_{-1})(j_3b_1))]),$$

which is quite compact for such reactions and which involves the following conventions for the fermion currents:

$$j_2^\mu \equiv J^\mu_{\nu_1,-\nu_2}(k_1,k_2), \quad j_3^\mu \equiv J^\mu_{\nu_3,-\nu_4}(k_3,k_4). \quad (78)$$

The scalar products of the vectors j_2 and j_3 with the isotropic-vierbein vectors can easily be found with the aid of (51).

6. CONCLUSION

From the methodological (but not from the computational) point of view, the present method for calculating matrix elements is similar to the method proposed in [21, 25] for KS helicity and fermion states. In contrast to the latter, the former has a simpler algorithm, does not employ explicit expressions for γ matrices, and can be used for vectors having an arbitrary polarization.

The calculation of a matrix element within the method of basis spinors is simplified owing to the introduction of a complete set of massless basis spinors—as a result, some of the calculations become trivial. The calculation of the coefficients in the expansion of physical bispinors in basis bispinors is the main cumbersome operation. The proposed method combines advantages of methods exploiting traces and computational methods based on the spinor technique. In the present method, one can compute, in just the same way as in spinor-technique methods (see, for example, [18, 25]), blocks of Feynman diagrams (current constructions, spinor products, and even more involved structures) and employ them in subsequent calculations. As in methods relying on trace calculations, there is no need here either for a mandatory additional procedure of constructing boson polarization vectors, or for the transformations of the contraction of Dirac matrices with 4-momenta into bispinors, or for quite an involved procedure of reduction to spinor products.

The proposed method can easily be realized in systems for analytic calculations, such as Mathematica, Maple, and Reduce. For example, all of the present calculations have been performed with the aid of a code in the Mathematica system for analytic calculations. It should be noted that, with an ordinary computer (Pentium III), the analytic expression in terms of scalar products that is calculated with the preliminarily determined matrix element for the diagram describing a binary reaction is obtained within a time of less than 0.1 s.

In conclusion, it is worth emphasizing that the objective of this article was to present a new method for analytically calculating matrix elements for reactions featuring massless and massive fermions. In view of this, I would not like to focus on assessing the efficiency of one method versus another, especially as efficiency criteria may be different. In addition, a particular method may prove to be more straightforward or more involved, depending on the physical problem to which it is applied.

REFERENCES

1. J. L. Powell, Phys. Rev. **75**, 32 (1949).
2. M. V. Galynskiĭ and S. M. Sikach, Fiz. Élem. Chastits At. Yadra **29**, 1133 (1998) [Phys. Part. Nucl. **29**, 469 (1998)].
3. A. L. Bondarev, hep-ph/9710398.
4. G. R. Farrar and F. Neri, Phys. Lett. B **130B**, 109 (1983).
5. F. A. Berends and W. T. Giele, Nucl. Phys. B **294**, 700 (1987).
6. F. Caravaglios and M. Moretti, Phys. Lett. B **358**, 332 (1995).
7. A. Kanaki and C. G. Papadopoulos, Comput. Phys. Commun. **132**, 306 (2000).
8. E. Bellomo, Nuovo Cimento **21**, 730 (1961).
9. A. A. Bogush and F. I. Fedorov, Vestsi Akad. Navuk BSSR, Ser. Fiz.-Mat. Navuk, No. 2, 26 (1962).
10. A. A. Bogush, Vestsi Akad. Navuk BSSR, Ser. Fiz.-Mat. Navuk, No. 2, 29 (1964).
11. J. D Bjorken and M. C. Chen, Phys. Rev. **154**, 1335 (1967).
12. H. W. Fearing and R. R. Sillbar, Phys. Rev. D **6**, 471 (1972).

13. F. I. Fedorov, Izv. Vyssh. Uchebn. Zaved., Fiz., No. 2, 32 (1980).
14. M. Caffo and E. Remiddi, Helv. Phys. Acta **55**, 339 (1982).
15. M. I. Krivoruchenko, Yad. Fiz. **47**, 1823 (1988) [Sov. J. Nucl. Phys. **47**, 1153 (1988)].
16. R. Vega and J. Wudka, Phys. Rev. D **53**, 5286 (1996); **56**, 6037 (1997) (Erratum).
17. F. A. Berendz, P. H. Daverveldt, and R. Kleiss, Nucl. Phys. B **253**, 141 (1985).
18. R. Kleiss and W. J. Stirling, Nucl. Phys. B **262**, 235 (1985).
19. Zhan Xu, Da-Hua Zhang, and Lee Chang, Nucl. Phys. B **291**, 392 (1987).
20. R. Kleiss, Z. Phys. C **33**, 433 (1987).
21. K. Hagiwara and D. Zeppenfeld, Nucl. Phys. B **274**, 1 (1986).
22. A. Gongora and R. G. Stuart, Z. Phys. C **42**, 617 (1989).
23. V. V. Andreev, Phys. Rev. D **62**, 014029 (2000).
24. E. N. Argyres and C. G. Papadopoulos, Phys. Lett. B **263**, 298 (1991).
25. A. Ballestrero and E. Maina, Phys. Lett. B **350**, 225 (1995).
26. A. E. Pukhov *et al.*, Preprint No. 98-41/542, INP MSU (Moscow, 1998); hep-ph/9908288.
27. P. S. Cherzor, V. A. Ilyin, and A. E. Pukhov, hep-ph/0101265.
28. KEK Report 92-19, (Febr. 1993).
29. R. Mertig, M. Böhm, and A. Denner, Comput. Phys. Commun. **64**, 345 (1991).
30. T. Stelzer and W. F. Long, Comput. Phys. Commun. **81**, 357 (1994).
31. R. Harlander and M. Steinhauser, Prog. Part. Nucl. Phys. **43**, 167 (1999); hep-ph/9812357.
32. C. Carimalo, A. Schiller, and V. G. Serbo, hep-ph/0112256.
33. V. I. Borodulin, R. N. Rogalyov, and S. R. Slabospitsky, Preprint No. 95-90, IHEP (Protvino, 1995); hep-ph/9507456.
34. S. Jadach, B. F. L. Ward, and Z. Was, Phys. Lett. B **449**, 97 (1999).
35. K. Hagiwara, R. D. Peccei, and D. Zeppenfeld, Nucl. Phys. B **282**, 253 (1987).
36. S. M. Bilen'kiĭ, *Introduction to Feynman Diagrams and Physics of Electroweak Interaction* (Énergoatomizdat, Moscow, 1990).

Translated by A. Isaakyan

Physics of Atomic Nuclei, Vol. 66, No. 2, 2003, pp. 394–397. Translated from Yadernaya Fizika, Vol. 66, No. 2, 2003, pp. 421–424.

XXXI International Conference on the Physics of Charged-Particle Interaction with Crystals (Institute of Nuclear Physics, Moscow State University, Moscow, May 28–30, 2001)

Spectral–Angular Distributions of Radiation from Relativistic Electrons in a Thin Layer of Matter

S. P. Fomin[1)*], N. F. Shul'ga[1),2)], and S. N. Shul'ga[1)]

Received January 25, 2002

Abstract—Expressions for the spectral–angular density of bremsstrahlung from a relativistic electron in a thin layer of matter are obtained. The effect that the multiple scattering of electrons by medium atoms exerts on the spectral–angular features of radiation in a thin amorphous target is studied. It is shown that, if the root-mean-square angle of multiple scattering is much larger than the characteristic angle of relativistic-electron radiation, there occurs the bremsstrahlung-suppression effect, which is similar to the Landau–Pomeranchuk–Migdal effect. © *2003 MAIK "Nauka/Interperiodica"*.

1. The multiple scattering of high-energy electrons in a medium can have a considerable effect on bremsstrahlung. The case where the radiation coherence length is much greater than the target thickness is of particular interest. In [1–3], it was shown that the bremsstrahlung-suppression effect, which is similar to the Landau–Pomeranchuk–Migdal effect, can arise in this case. Experimentally, this effect was studied at the SLAC accelerator [4, 5], the spectral properties of bremsstrahlung in the low-frequency region being explored there.

Here, we consider the spectral–angular properties of bremsstrahlung from high-energy electrons in a thin layer of matter. Particular attention is given to the conditions under which the bremsstrahlung-suppression effect is more pronounced in the angular than in the spectral distribution. It is shown that, if the root-mean-square angle of multiple scattering is much larger than the characteristic angle of relativistic-electron radiation, $\theta \sim \gamma^{-1}$ (θ is the angle between the wave-propagation and the electron-velocity vectors, and γ is the electron Lorentz factor), the angular distribution of electron radiation within the region around the angle $\theta \sim \gamma^{-1}$ with respect to the projectile-beam direction is virtually independent of the target thickness, with its maximum being at an angle of $\theta_m \approx \gamma^{-1}$.

2. Within classical electrodynamics (see [6, 7]), the spectral–angular density of radiation from an electron moving along the trajectory $\mathbf{r}(t)$ is given by

$$\frac{d^2E}{d\omega do} = \frac{e^2}{4\pi^2}[\mathbf{k}\times\mathbf{I}]^2, \tag{1}$$

where

$$\mathbf{I} = \int\limits_{-\infty}^{\infty} \dot{\mathbf{r}}(t) e^{i(\omega t - \mathbf{k}\cdot\mathbf{r}(t))} dt, \tag{2}$$

and $\mathbf{k}$ and ω are, respectively, the wave vector and the frequency of the emitted wave (we use the system of units where the speed of light in a vacuum is taken to be unity).

In a thin layer of matter, characteristic values of the relativistic-electron-scattering angle ϑ_e are much smaller than unity. If, concurrently, the radiation coherence length is much greater than the target thickness T,

$$l_c \approx \frac{2\gamma^2}{\omega}\frac{1}{1+\gamma^2\theta^2+\gamma^2\vartheta_e^2} \gg T, \tag{3}$$

then the quantity $\mathbf{I}$ can be represented in the form (see [7])

$$\mathbf{I} \approx \frac{i}{\omega}\left(\frac{\mathbf{v}'}{1-\mathbf{n}\cdot\mathbf{v}'} - \frac{\mathbf{v}}{1-\mathbf{n}\cdot\mathbf{v}}\right), \tag{4}$$

where $\mathbf{v}$ and $\mathbf{v}'$ are the electron velocities before and after scattering, respectively, and $\mathbf{n} = \mathbf{k}/\omega$. In this case, the spectral–angular density of radiation from an electron depends only on the particle-scattering angle in matter. Substituting (4) into (1), we find that, at small values of the scattering and radiation angles,

$$\frac{d^2E}{d\omega do} = \frac{e^2\gamma^2}{\pi^2}\left\{\frac{1+\alpha^2+\alpha^2\beta^2+2\alpha\beta\cos\varphi}{1+\alpha^2+\beta^2-2\alpha\beta\cos\varphi}\right. \tag{5}$$

[1)]Kharkov Institute for Physics and Technology, Akademicheskaya ul. 1, Kharkov, 310108 Ukraine.
[2)]Belgorod State University, Studencheskaya ul. 12, Belgorod, 308007 Russia.
[*]e-mail: sfomin@kipt.kharkov.ua

$$\times \frac{1}{(1+\alpha^2)^2} - \frac{1}{(1+\alpha^2+\beta^2-2\alpha\beta\cos\varphi)^2}\Bigg\},$$

where $\alpha = \gamma\theta$, θ and φ being, respectively, the polar and the azimuthal angle of radiation, and $\beta = \gamma\vartheta_e$, ϑ_e being the electron-scattering angle. The angles θ and ϑ_e are reckoned from the direction of the initial electron velocity $\mathbf{v}$, while φ is the angle between the vectors $\mathbf{k}_\perp$ and $\mathbf{v}'_\perp$ in the plane orthogonal to $\mathbf{v}$.

Expression (5) must be averaged over the angles of particle scattering within the target. Given the angular distribution of scattered particles, $f(\vartheta_e)$, we can determine the averaged spectral–angular density of radiation according to the formula

$$\left\langle \frac{d^2E}{d\omega do} \right\rangle = \int d^2\vartheta_e f(\vartheta_e) \frac{d^2E}{d\omega do}, \qquad (6)$$

which is valid for any type of target, provided that its thickness is much smaller than the bremsstrahlung coherence length. The specific features of the scatterer would affect only the form of the distribution function $f(\vartheta_e)$.

For an amorphous target, the scattering-angle distribution of particles is described by the Bethe–Molière function (see [8, 9]),

$$f_{\mathrm{BM}}(\vartheta_e) = \frac{1}{2\pi}\int_0^\infty \eta d\eta J_0(\eta\vartheta_e) \qquad (7)$$

$$\times \exp\left\{-nT\int \chi d\chi \sigma(\chi)[1-J_0(\eta\chi)]\right\},$$

where n is the medium-atom density and $\sigma(\chi)$ is the differential cross section for electron scattering by a single medium atom at a small angle χ.

The distribution function (7) is independent of φ; therefore, integration with respect to φ in expression (6) can be performed in a general form. The result is

$$\left\langle \frac{d^2E}{d\omega do} \right\rangle = \int_0^\infty \vartheta_e d\vartheta_e f_{\mathrm{BM}}(\vartheta_e)\Phi(\theta,\vartheta_e), \qquad (8)$$

$$\Phi(\theta,\vartheta_e) = \frac{e^2\gamma^2}{\pi^2}\left\{\frac{2+\beta^2}{(1+\alpha^2)q^{1/2}}\right. \qquad (9)$$

$$\left. - \frac{1+\alpha^2+\beta^2}{q^{3/2}} - \frac{1}{(1+\beta^2)^2}\right\},$$

where $q = (1+\alpha^2+\beta^2)^2 - 4\alpha^2\beta^2$.

For the case of a screened atomic potential, Bethe derived a somewhat simplified expression for the distribution function (see [9]); that is,

$$f_{\mathrm{B}}(\vartheta_e) = \sum_{n=0}^\infty f_n(\vartheta_e)\frac{1}{B^n}, \qquad (10)$$

$$f_n(\vartheta_e) = \frac{1}{2\overline{\vartheta^2}}\int_0^\infty u du J_0\left(u\frac{\vartheta_e}{\chi_c B^{1/2}}\right) \qquad (11)$$

$$\times e^{-u^2/4}\frac{1}{n!}\left(\frac{u^2}{4B}\ln\frac{u^2}{4}\right)^n,$$

where $\overline{\vartheta^2} = \chi_c^2 B$ is the mean-square value of the multiple-scattering angle, $\chi_c^2 = 4\pi nTZ^2e^4/(pv)^2$, and B is obtained from the relation

$$B - \ln B = \ln\frac{\chi_c^2}{\chi_1^2} + 1 - 2C. \qquad (12)$$

Here, $Z|e|$ is the medium-atom charge; p is particle momentum; $\chi_1 = 1/pR$, R being the radius of atomic-potential screening; and $C = 0.577...$ is the Euler constant.

Expression (8), involving the distribution function (10), describes the spectral–angular distribution of bremsstrahlung from relativistic electrons in a thin amorphous-medium layer.

3. We will now focus on some special features of the spectral–angular distributions of radiation from a relativistic electron in a thin amorphous-medium layer. First, we consider the angular distribution of radiation from an electron in the $(\mathbf{v},\mathbf{v}')$ plane. Rewriting (5) in terms of the Cartesian coordinates (x,y,z), with the z axis being directed along $\mathbf{v}$ and the y axis being orthogonal to the $(\mathbf{v},\mathbf{v}')$ plane, we find that the distribution of radiation in the $(\mathbf{v},\mathbf{v}')$ plane is

$$\frac{d^2E}{d\omega do} = \frac{e^2\gamma^2}{\pi^2}\left[\frac{\alpha_x}{1+\alpha_x^2} - \frac{\alpha_x-\beta}{1+(\alpha_x-\beta)^2}\right]^2, \qquad (13)$$

where $\alpha_x = \alpha\cos\varphi$.

Let us examine the asymptotic behavior of this expression at small and large scattering angles.

For small scattering angle ($\beta \ll 1$), we have

$$\frac{d^2E}{d\omega do} = \frac{e^2\gamma^2}{\pi^2}\beta^2\frac{(1-\alpha_x^2)^2}{(1+\alpha_x^2)^4}. \qquad (14)$$

This expression shows that, for $\beta \ll 1$, the angular distribution of radiation peaks at $\alpha_x = 0$ and that the spectral–angular density of radiation from an electron vanishes at $\alpha_x = \pm 1$. In the case being considered, the bulk of the radiation spectral density is concentrated within the angular region $\theta_x \le \gamma^{-1}$, where $\theta_x = \theta\cos\varphi$.

For large values of the scattering angle ($\beta \gg 1$), the angular distribution (13) of radiation has maxima at $\alpha_x \approx 1$ and $\alpha_x \approx \beta - 1$ and vanishes at $\alpha_x \approx -1/\beta$ and $\alpha_x \approx \beta + 1/\beta$. Expression (13) also shows that the angular density of radiation decreases fast in the angular intervals corresponding to the regions $\alpha_x \le -1$ and $\alpha_x \ge \beta + 1$. In the region $1 \le \alpha_x \le \beta$, the

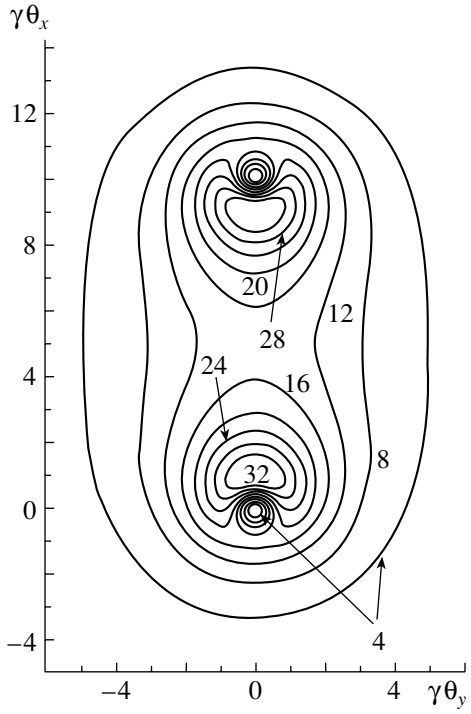

Fig. 1. Angular distribution of radiation from an electron in the xy plane, which is orthogonal to the direction of initial electron velocity at $\beta = 10$. The figures on the curves correspond to the values of the angular-distribution density (5) in units of $10^{-2}e^2\gamma^2/\pi^2$.

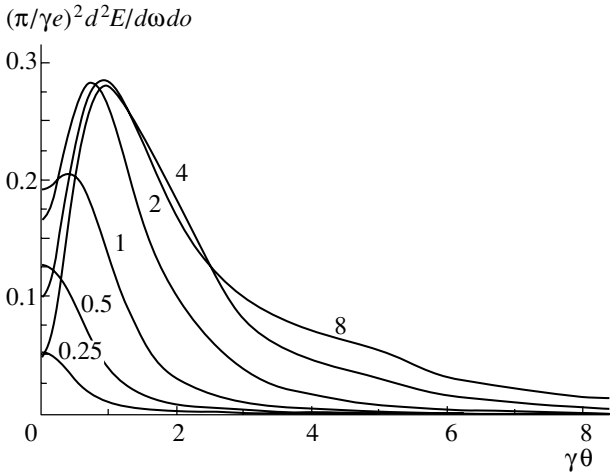

Fig. 2. Spectral–angular density of electron radiation as a function of the polar angle θ with respect to the direction of initial electron velocity. Figures on the curves correspond to the values of the parameter $\sqrt{\overline{\beta^2}}$.

angular density of radiation takes commensurate values over a rather broad interval of scattering angles. By way of example, we indicate that, for $\beta = 10$, the angular density of radiation has a minimum at $\alpha_x = \beta/2$, where the radiation intensity is about half its value at the maxima. This means that, at $\beta \gg 1$, the bulk of the spectral density of radiation from an electron is concentrated within the angular range $0 \leqslant \vartheta_x \leqslant \vartheta_e$.

For $\beta \gg 1$, it follows from (5) that, in directions close to that of the initial particle-motion velocity $\mathbf{v}$, the angular density of radiation can be represented as

$$\frac{d^2E}{d\omega do} \approx \frac{e^2\gamma^2}{\pi^2}\frac{\alpha^2}{(1+\alpha^2)^2} \quad (\alpha \ll \beta). \qquad (15)$$

In this case, the angular density of radiation is independent of the scattering angle.

These results are illustrated in Fig. 1, which displays, for $\beta = 10$, isolines of the angular density of radiation from an electron in the xy plane.

We now consider the multiple-scattering effect on the angular distribution of bremsstrahlung. For small scattering-angle values such that the condition $\overline{\beta^2} = \gamma^2\overline{\vartheta_e^2} \ll 1$ is satisfied, the function $\Phi(\theta, \vartheta_e)$ in (8) can be expanded in β. In the first order of this expansion, the spectral–angular density of radiation is given by the expression

$$\left\langle \frac{d^2E}{d\omega do} \right\rangle = \frac{2e^2\gamma^2}{\pi^2}\overline{\beta^2}\frac{1+\alpha^4}{(1+\alpha^2)^4}, \qquad (16)$$

which coincides with the corresponding result for the spectral–angular density of radiation in Bethe–Heitler theory, according to which the radiation intensity grows linearly with increasing target thickness {see, for example, expression (5.9) in [10]}.

The inequality $\overline{\beta^2} \ll 1$ is a condition under which the dipole approximation is valid in describing radiation from a particle in a medium [7]. As the target thickness is increased, the condition $\overline{\beta^2} \ll 1$ is violated (since $\overline{\beta^2} \sim T$); therefore, effects associated with a nondipole character of radiation must be taken into account. For arbitrary values of $\overline{\beta^2}$, averaging in (8) can be performed only on the basis of numerical methods.

The spectral–angular density of radiation as a function of its polar angle θ is given in Fig. 2 for various values of the parameter $\sqrt{\overline{\beta^2}}$. The displayed curves show that, for $\overline{\beta^2} < 1$, the angular distribution of radiation has a maximum in the direction of the initial particle velocity and decreases fast with increasing θ [see Eq. (16)]. At $\overline{\beta^2} \sim 1$, the maximum in the angular distribution of radiation is shifted into the region of angles around $\theta \sim \gamma^{-1}$. Concurrently, the growth of radiation intensity with increasing target thickness becomes slower than a linear one, which is typical of Bethe–Heitler theory. For $\overline{\beta^2} > 1$, the maximum in the angular distribution of radiation occurs in

the angular region around $\theta \sim \gamma^{-1}$, with the radiation intensity at this maximum being virtually independent of $\overline{\beta^2}$ (that is, of the target thickness). However, the angular distribution broadens with increasing target thickness. For $\overline{\beta^2} > 1$, the radiation intensity in the angular region $\theta \ll \gamma^{-1}$ decreases fast with increasing $\overline{\beta^2}$. For $\overline{\beta^2} \gg 1$, the distribution of radiation in the angular region $\theta \ll \sqrt{\overline{\beta^2}}$ is given by (15). Within this region of radiation angles, the angular distribution is of a universal form; that is, it is independent of the form of scattering-angle distribution of particles.

Thus, we see that, for $\overline{\beta^2} \gg 1$, bremsstrahlung is suppressed in the angular region $\theta \ll \sqrt{\overline{\vartheta_e^2}}$ in relation to the corresponding result in Bethe–Heitler theory. This bremsstrahlung-suppression effect is similar to the effect of suppression of the spectral density of bremsstrahlung in a thin layer of matter (see [2, 3]). For the spectral density of radiation as a function of the target thickness, however, there occurs a transition from a linear to a logarithmic target-thickness dependence of the radiation intensity, while, for the spectral–angular distribution of radiation, a linear growth of the radiation intensity with the target thickness at small $\overline{\beta^2}$ gives way to a constant value at large $\overline{\beta^2}$. This means that the bremsstrahlung-suppression effect is more pronounced in the spectral–angular distribution of radiation than in its spectral density.

ACKNOWLEDGMENTS

The work was supported in part by the Russian Foundation for Basic Research (project no. 00-02-16337).

REFERENCES

1. F. F. Ternovskiĭ, Zh. Éksp. Teor. Fiz. **39**, 171 (1960) [Sov. Phys. JETP **12**, 123 (1960)]; Zh. Éksp. Teor. Fiz. **39**, 471 (1960) [Sov. Phys. JETP **12**, 331 (1960)].
2. N. F. Shul'ga and S. P. Fomin, Pis'ma Zh. Éksp. Teor. Fiz. **27**, 126 (1978) [JETP Lett. **27**, 117 (1978)].
3. N. F. Shul'ga and S. P. Fomin, Zh. Éksp. Teor. Fiz. **113**, 58 (1998) [JETP **86**, 32 (1998)].
4. P. L. Anthony *et al.*, Phys. Rev. D **56**, 1373 (1997).
5. S. Klein, Rev. Mod. Phys. **71**, 1501 (1999).
6. J. D. Jackson, *Classical Electrodynamics* (Wiley, New York, 1962; Mir, Moscow, 1965).
7. A. I. Akhiezer and N. F. Shul'ga, *High-Energy Electrodynamics in Matter* (Nauka, Moscow, 1993).
8. G. Molière, Z. Naturforsch. A **3**, 78 (1948).
9. H. Bethe, Phys. Rev. **89**, 1256 (1953).
10. V. A. Bazylev and N. K. Zhivago, *Radiation from Fast Particles in Matter and External Fields* (Nauka, Moscow, 1987).

Translated by O. Chernavskaya

Physics of Atomic Nuclei, Vol. 66, No. 2, 2003, pp. 398–401. Translated from Yadernaya Fizika, Vol. 66, No. 2, 2003, pp. 425–428.

XXXI International Conference on the Physics of Charged-Particle Interaction with Crystals (Institute of Nuclear Physics, Moscow State University, Moscow, May 28–30, 2001)

Transition Radiation from Relativistic Charged Particles Interacting with Atomic Strings in a Crystal

N. F. Shul'ga[1] and V. V. Syshchenko[2]

Received January 25, 2002

Abstract—The problem of transition radiation generated by relativistic particles incident on atomic strings in a crystal at a small angle is considered. Conditions are obtained under which the problem of transition radiation reduces to that of radiation generated by a collision with a filament-like target. It is shown that the angular distribution of transition radiation is symmetric with respect to the atomic-string axis.

1. INTRODUCTION

Transition radiation is known to be generated by a charged particle traversing the interface between two media (see [1–4] and references therein). For a relativistic particle, radiation of this type is concentrated in the region of small angles with respect to the direction of particle motion. At such angles, radiation is generated over a long segment along the particle-velocity direction, the length of this segment being referred to as the radiation coherence length [2, 5, 6]. If, within such a segment, the particle being considered traverses a few interfaces between different media, the interference between the waves generated by the particle upon traversing each interface is of importance. It was shown in [7] that, in the limit of long-wave transition radiation, both longitudinal and transverse dimensions of the domain where transition radiation is generated may be macroscopic. If, concurrently, the transverse dimensions of the target used satisfy the condition $L_\perp \leq \gamma\lambda$ (where λ is the wavelength of the radiation and γ is the particle Lorentz factor), transition radiation depends strongly both on these transverse dimensions and on the shape of the target.

In this study, we consider the problem of transition radiation from relativistic particles incident on an atomic string in a crystal at a small angle ψ with respect to the string axis (see Fig. 1). We study this radiation at high frequencies, in which case the dielectric permittivity can be represented in the form

$$\varepsilon_\omega = 1 - \omega_p^2/\omega^2, \quad \omega \gg \omega_p, \tag{1}$$

where $\omega_p^2 = 4\pi e^2 n_e(\mathbf{r})/m$ is the plasma frequency, m is the electron mass, and $n_e(\mathbf{r})$ is the density of electrons in the target. Under such conditions, transition radiation is associated with the nonuniformity of the electron density in the atomic string. The problem under consideration is similar to the problem of the effect that the target boundaries exert on transition radiation, since electrons in the atomic string are concentrated near the string axis. We find conditions under which transition radiation is unaffected by the nonuniformity of the electron distribution along the string axis and determine the angular distribution of transition radiation for this case. We also study transition radiation generated by particle interaction with a set of atomic strings whose axes form a periodic or a chaotic structure in the transverse plane. (We use the system of units where the speed of light is equal to unity.)

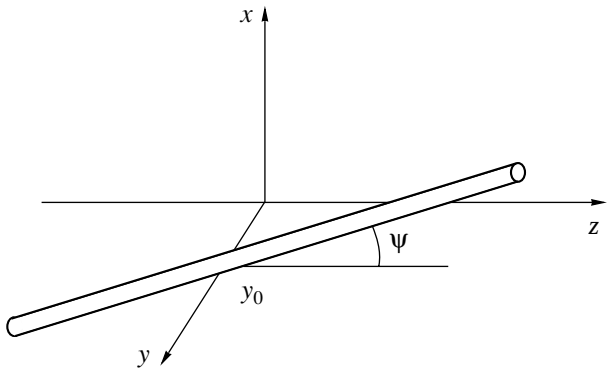

Fig. 1. Disposition of an atomic string (cylinder) and the trajectory of a particle incident on it (z axis) in the transition-radiation problem being considered.

[1]Kharkov Institute for Physics and Technology, Akademicheskaya ul. 1, Kharkov, 61108 Ukraine; e-mail: shulga@kipt.kharkov.ua.

[2]Belgorod State University, Studencheskaya ul. 12, Belgorod, 308007 Russia.

2. TRANSITION RADIATION IN A COLLISION OF A PARTICLE WITH AN ISOLATED ATOMIC STRING

The spectral–angular distribution of transition radiation in a heterogeneous medium whose dielectric permittivity is given by (1) has the form

$$\frac{dE}{d\omega do} = \frac{1}{4\pi^2}|\mathbf{k}\times\mathbf{I}|^2, \tag{2}$$

where

$$\mathbf{I} \approx \frac{1}{4\pi\omega}\int d^3r e^{i\mathbf{k}\cdot\mathbf{r}}\omega_p^2(\mathbf{r})\mathbf{E}_\omega(\mathbf{r}), \tag{3}$$

$\mathbf{k}$ is the wave vector of the emitted wave, and $\mathbf{E}_\omega(\mathbf{r})$ is the Fourier transform of the particle field with respect to time. In perturbation theory in the deviation of the dielectric permittivity from unity, the first-order expression for the quantity $\mathbf{E}_\omega(\mathbf{r})$ appearing in (3) has the form

$$\mathbf{E}_\omega^{(0)}(\mathbf{r}) = \int \frac{d^3k}{\pi} ie\frac{\mathbf{k}-\omega\mathbf{v}}{\omega^2-\mathbf{k}^2}\delta(\omega-\mathbf{k}\cdot\mathbf{v})e^{i\mathbf{k}\cdot\mathbf{r}}. \tag{4}$$

This quantity is the Fourier transform of the unperturbed Coulomb field of a particle moving at a constant velocity $\mathbf{v}$. Substituting (4) and (3) into (2), we obtain the angular distribution of transition radiation in the form

$$\frac{dE}{d\omega do} = \frac{e^6}{m^2}\left|\frac{\mathbf{k}}{\omega}\times\mathbf{J}_k\right|^2, \tag{5}$$

where

$$\mathbf{J}_k = \int \frac{d^3q}{2\pi^2} n_q \frac{\mathbf{k}-\mathbf{q}-\omega\mathbf{v}}{\omega^2-(\mathbf{k}-\mathbf{q})^2}\delta(\omega-(\mathbf{k}-\mathbf{q})\cdot\mathbf{v}) \tag{6}$$

and n_q is the Fourier transform of the electron density in the medium,

$$n_q = \int d^3r n_e(\mathbf{r})e^{-i\mathbf{q}\cdot\mathbf{r}}. \tag{7}$$

Let us consider the case where the coherence length is much greater than the length of the atomic string along the particle trajectory,

$$l_{\mathrm{coh}} \sim \frac{2\gamma^2}{\omega}\frac{1}{1+\gamma^2\theta^2} \gg \frac{2R}{\psi}, \tag{8}$$

where R is the radius of atomic-potential screening and θ is the angle between the wave vector of the emitted wave and the particle velocity (it is assumed that the particles are incident on the string at a small angle ψ with respect to the string axis). In this case, the atomic string can be considered as a homogeneous and infinitely thin dielectric filament; therefore, the spatial distribution of electrons can be represented in the form of a delta function:

$$n_e(\mathbf{r}) = n_e\delta(x-z\psi)\delta(y-y_0). \tag{9}$$

Here, n_e is the electron density per unit length of the string; the z axis is parallel to the particle velocity; and y_0 is the distance between the particle trajectory and the string axis (see Fig. 1). The Fourier transform of this distribution has the form

$$n_q = 2\pi n_e e^{-iq_y y_0}\delta(q_x\psi + q_z). \tag{10}$$

The spectral–angular distribution (5) must be averaged over all allowed values of the impact parameter y_0; that is,

$$\left\langle\frac{dE}{d\omega do}\right\rangle = \frac{1}{a_y}\int\limits_{-\infty}^{\infty} dy_0 \frac{dE(y_0)}{d\omega do}, \tag{11}$$

where a_y is the spacing between neighboring strings in the crystal along the y axis.

For the averaged distribution, we obtain

$$\left\langle\frac{dE}{d\omega do}\right\rangle = \frac{e^6 n_e^2\gamma}{a_y m^2\omega\psi^2}F(\theta,\varphi), \tag{12}$$

where $F(\theta,\varphi)$ is a function that describes the distribution of radiation with respect to the polar (θ) and the azimuthal (φ) emission angle [the polar angle was defined in (8)],

$$F(\theta,\varphi) = \frac{1+2\left(\gamma\theta\cos\varphi - \dfrac{1+\gamma^2\theta^2}{2\gamma\psi}\right)^2}{\left[1+\left(\gamma\theta\cos\varphi - \dfrac{1+\gamma^2\theta^2}{2\gamma\psi}\right)^2\right]^{3/2}}, \tag{13}$$

where φ is the angle between the x axis and the projection of the wave vector onto the xy plane; it is assumed that $\theta \ll 1$.

We will now focus on some special features of the angular distribution (12) of transition radiation intensity. First of all, we note that the distribution in (12) is symmetric with respect to the atomic-string axis ($\theta = \psi$, $\varphi = 0$). In order to demonstrate this explicitly, we go over from polar to Cartesian coordinates in (13) ($\theta_x = \theta\cos\varphi$, $\theta_y = \theta\sin\varphi$) and perform the transformation according to the formulas $\theta'_x = \psi - \theta_x$ and $\theta'_y = \theta_y$. For the function $F(\theta'_x,\theta'_y)$, this yields

$$F(\theta'_x,\theta'_y) = \frac{1+\dfrac{1}{2\gamma^2\psi^2}(1+\gamma^2(\theta'^2+\psi^2))^2}{\left[1+\dfrac{1}{4\gamma^2\psi^2}(1+\gamma^2(\theta'^2+\psi^2))^2\right]^{3/2}}. \tag{14}$$

Since this function depends only on the polar angle $\theta' = \sqrt{\theta'^2_x+\theta'^2_y}$, the distribution of radiation in (12) is symmetric with respect to the atomic-string axis.

Formula (13) indicates that the minimum of the radiation intensity is somewhat shifted from the value

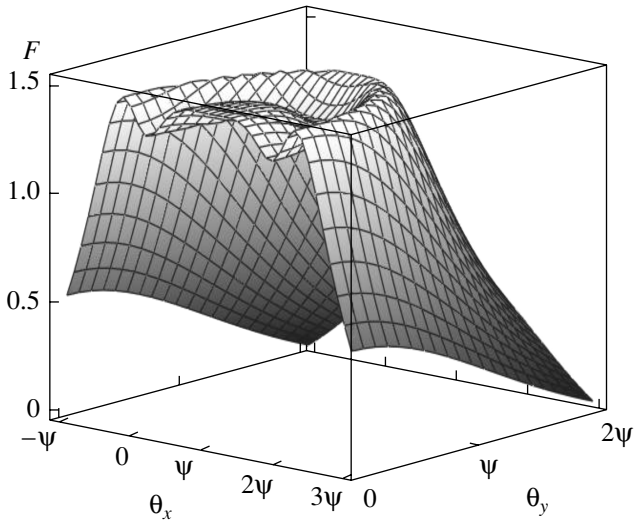

Fig. 2. Graph of the function $F(\theta, \varphi)$ that determines the angular distribution of transition radiation from a relativistic particle incident on a filament-like target for $\gamma = 2000$ and $\psi = 10^{-3}$; the values of $\theta_x = \theta\cos\varphi$ and $\theta_y = \theta\sin\varphi$ are plotted along the axes in the horizontal plane.

of $\theta = 0$, which corresponds to the direction of particle motion (see Fig. 2).

It should be noted that, in the vicinity of the symmetry axis of the distribution of radiation ($\theta = \psi$, $\varphi = 0$), the radiation intensity does not have a deep minimum, which often occurs there in transition-radiation problems; instead, it approaches a plateau that lies rather high.

3. TRANSITION RADIATION IN A COLLISION WITH A FEW ATOMIC STRINGS

We now proceed to consider special features of transition radiation generated in a collision of a particle with a few atomic strings.

If the atomic-string axes are disposed at random in the transverse plane (this corresponds to the chaotic motion of a particle in the periodic field of atomic strings in a crystal [8]), the interference between waves that are emitted in particle interaction with different atomic strings can be neglected. The total radiation will then be given by the sum of the contributions that arise from particle interactions with different atomic strings. Since the angular distribution of radiation is symmetric with respect to the axis of an atomic string, the resulting intensity of the radiation from a particle executing chaotic motion is proportional to the number of strings involved in the interaction with the particle, so that the form of the angular distribution of radiation will remain unchanged [that given by formula (12)].

But in the case where a particle executes a regular motion in a crystal, the effect of interference must be taken into account. By way of example, we indicate that, for a particle sequentially scattered by N ($N \gg 1$) parallel strings at the same impact-parameter value y_0, expression (12) reduces to the corresponding result of the theory of transition radiation (or resonance radiation, according to the terminology used by Ter-Mikaelyan) for relativistic electrons in a crystal {see formula (28.160) in [2]}; that is,

$$\left\langle \frac{dE}{d\omega do} \right\rangle = \frac{e^6 n_e^2 \gamma}{a_y m^2 \omega \psi^2} F(\theta, \varphi) \qquad (15)$$
$$\times N \frac{2\pi}{b} \sum_{n=-\infty}^{\infty} \delta\left(\frac{\omega}{2\gamma^2}(1 + \gamma^2\theta^2) - \frac{2\pi}{b} n \right),$$

where b is the spacing between atomic strings along the z axis. The presence of a delta function in formula (15) implies that the frequency of radiation at a given angle θ is given by

$$\omega_n = \frac{2\gamma^2}{1 + \gamma^2\theta_n^2} \frac{2\pi}{b} n. \qquad (16)$$

Thus, the disposition of atomic strings in a crystal in the transverse plane and the character of particle motion have a pronounced effect on transition radiation.

4. COMPARISON WITH PARAMETRIC (RESONANCE) RADIATION

In the case of a three-dimensional periodic medium (for example, a crystal), the integral with respect to $\mathbf{q}$ in (6) can be replaced by a sum over a discrete set of reciprocal-lattice vectors $\mathbf{g}$. In this case, the substitution of expression (6) into (5) leads to the required result for the angular distribution of parametric radiation in a periodic three-dimensional medium {see formula (28.160) in [2]}, provided that the dielectric permittivity is taken in the form (1). The transition from the integral with respect to $\mathbf{q}$ in (6) to a sum over $\mathbf{g}$ suggests the emergence of a relation between the frequency and the emission angle. This relation arises in the case of particle motion along a straight line in a crystal and is due to the interference between waves generated by a particle interacting with atoms that occupy the sites in a periodic crystal lattice.

Formula (12) describes the angular distribution of radiation in the case of particle interaction with an isolated atomic string. In contrast to the corresponding result of the theory of parametric radiation, this formula features no relation between the frequency and the emission angle.

As was mentioned above, formula (12) is appropriate for describing the radiation from an electron moving in the field of many atomic strings if particle interactions with different strings do not interfere with one another. This type of situation is realized under the conditions of dynamical chaos accompanying particle motion in the periodic field of atomic strings in a crystal (see [8]).

Formula (12) can also be derived from the corresponding result of the theory of parametric x-ray radiation if, in this result, one considers a particle moving at a small angle with respect to a crystallographic axis (axis z') and assumes that atomic strings parallel to this axis are widely spaced in the transverse direction. For this purpose, the lattice constants $a_{x'}$ and $a_{y'}$ along the x' and y' axes orthogonal to the crystallographic axis z' must be made to tend to infinity in the Ter-Mikaelyan formula {formula (28.160) in [2]}. In this limit, summation over the components $q_{x'}$ and $q_{y'}$ in the Ter-Mikaelyan formula can then be replaced by relevant integration. If the condition in (8) is satisfied, the main contribution to the angular density of radiation then comes from the component $g_{z'} = 0$, this corresponding to the approximation of a continuous electron-density distribution along the string axis (z' axis). It should be noted that the present analysis of the features of parametric x-ray radiation from a relativistic electron in a crystal is analogous to the analysis performed in Chapter 4 of [6] for coherent radiation generated by fast electrons in a crystal via various mechanisms.

ACKNOWLEDGMENTS

This work was supported in part by the International Association for the Promotion of Cooperation with Scientists from the Independent States of the Former Soviet Union (grant no. INTAS-97-30392), the Russian Foundation for Basic Research (project no. 00-02-16337), and the Ministry for Higher Education of the Russian Federation (grant no. 97-0-143-5).

REFERENCES

1. V. L. Ginzburg and V. N. Tsytovich, *Transition Radiation and Transition Scattering* (Nauka, Moscow, 1984).
2. M. L. Ter-Mikaelian, *High-Energy Electromagnetic Processes in Condensed Media* (Akad. Nauk Arm. SSR, Yerevan, 1969; Wiley, New York, 1972).
3. G. M. Garibyan and Yan Shi, *X-Ray Transition Radiation* (Akad. Nauk Arm. SSR, Yerevan, 1983).
4. P. Rullhusen, X. Artru, and P. Dhez, *Novel Radiation Sourses Using Relativistic Electrons* (World Sci., Singapore, 1998).
5. B. M. Bolotovsky, Tr. Fiz. Inst. Akad. Nauk SSSR **140**, 95 (1982).
6. A. I. Akhiezer and N. F. Shul'ga, *High-Energy Electrodynamics in Matter* (Nauka, Moscow, 1993).
7. N. F. Shul'ga and S. N. Dobrovol'skiĭ, Zh. Éksp. Teor. Fiz. **117**, 668 (2000) [JETP **90**, 579 (2000)].
8. A. I. Akhiezer, V. I. Truten', and N. F. Shul'ga, Phys. Rep. **203**, 289 (1991).

Translated by R. Rogalyov

Physics of Atomic Nuclei, Vol. 66, No. 2, 2003, pp. 402–408. Translated from Yadernaya Fizika, Vol. 66, No. 2, 2003, pp. 429–434.

XXXI International Conference on the Physics of Charged-Particle Interaction with Crystals (Institute of Nuclear Physics, Moscow State University, Moscow, May 28–30, 2001)

Numerical Analysis of the Intensity of Parametric X-Ray Radiation under the Conditions of Strong Multiple Scattering

I. J. Dubovskaj and O. M. Lugovskaj*

Institute for Nuclear Problems, Belarussian State University, Minsk, Belarus

Received February 25, 2002; in final form, April 23, 2002

Abstract—The properties of parametric x-ray radiation generated in a crystal are investigated in detail on the basis of a numerical simulation, strong multiple scattering being taken into account in this investigation. The contributions of various generation mechanisms to the total intensity of this radiation are explored. The results of numerical calculations are compared with experimental data obtained by measuring the integrated intensity of parametric x-ray radiation as a function of charged-particle energy. It is shown that theoretical results are in good agreement with experimental data. © *2003 MAIK "Nauka/Interperiodica".*

1. INTRODUCTION

The effect of multiple scattering on parametric x-ray radiation in a crystal target and the contribution of bremsstrahlung to the total intensity of this radiation at the diffraction maximum were taken phenomenologically into account in [1–4]. However, only in the case of weak multiple scattering—that is, in the case where the crystal-layer thickness along the direction of charged-particle motion satisfies the condition $L_0 \ll L_{\mathrm{Br}}$, where $L_{\mathrm{Br}} = \sqrt{4c/\omega\overline{\theta_s^2}}$ is the bremsstrahlung coherence length, $\overline{\theta_s^2}$ is the mean square of the multiple-scattering angle per unit of the distance that a charged particle travels in matter, and ω is the frequency of the emitted photon—do results obtained on the basis of this theory agree well with experimental data. In this case, multiple scattering only results in that the intensity of generated x-ray radiation develops a moderately small correction caused by the bremsstrahlung radiation mechanism and in that there appears the effect of multiple scattering in the phase of parametric x-ray radiation. In the opposite case of $L_0 > L_{\mathrm{Br}}$, multiple scattering changes significantly the parameters of parametric x-ray radiation itself. In the majority of relevant experiments (for example, in those reported in [5, 6]), the condition under which multiple scattering is weak was not satisfied; in order to interpret these experiments, it is therefore necessary to take rigorously into account multiple scattering and the contribution of various generation mechanisms to the total intensity.

A theoretical approach that may be used in quantitatively analyzing the effect that the multiple scattering of a charged particle exerts on the properties of parametric x-ray radiation was formulated as far back as some twenty years ago [1]. In the two-wave approximation, a theory of the multiple-scattering effect on the properties of parametric x-ray radiation was given in [7], where the kinetic equation for the distribution of particles with respect to coordinates and velocities was solved in constructing this theory. In the case of intense multiple scattering ($L_0 \geq L_{\mathrm{Br}}$), the expressions obtained in [7] for the spectral–angular distribution are very involved for exploring them analytically (they feature double integrals of quickly oscillating functions); therefore, it is desirable to perform a computer-based numerical analysis of the properties of the radiation in question.

In the present study, we give a detailed quantitative analysis of the properties of x-ray radiation generated in a crystal, taking consistently into account multiple scattering. In addition, we compare the results of our numerical calculations with experimental data reported in [5, 6].

2. CONTRIBUTION OF VARIOUS RADIATION MECHANISMS TO THE FORMATION OF DIFFRACTION MAXIMA

For radiation generated by the propagation of relativistic charged particles through a crystal layer, the expressions for the spectral–angular distributions of the intensity for the case where two-wave diffraction is realized and where no account is taken of the multiple scattering of charged particles on crystal atoms

*e-mail: olug@inp.minsk.by

1063-7788/03/6602-0402$24.00

are given in [8]. The contribution of one term in the expression for the spectral–angular intensity of the radiation or another ("vacuum" radiation formed as a particle traverses the crystal–vacuum interface or "volume" radiation associated with emission within the target) may change significantly in response to variations in diffraction geometry, the energy of the charged particles involved, and the crystal-layer thickness.

In an optically thick target, $L_0 \gg l_{\rm opt} = c/\omega|n-1|$ ($l_{\rm opt}$ is the optical thickness, and n is the medium refractive index), the main contribution to the intensity comes from volume radiation if the charged-particle energy satisfies the condition $E_p \geq E_{\rm thr}$ ($E_{\rm thr} = mc^2/\sqrt{|\chi_0'|}$ is the threshold energy of parametric x-ray radiation [3, 4], and χ_0' is the real part of the Fourier transform of the crystal susceptibility). An analysis reveals that, in the case where the crystal-layer thickness exceeds the transition-radiation coherence length $l = 2c/\omega(\gamma^{-2} + \omega_{\rm L}^2/\omega^2)$ ($\omega_{\rm L}$ is the Langmuir frequency, and γ is the particle Lorentz factor), but where it remains less than the radiation-absorption depth in the target, $l < L_0 \leq L_{\rm abs}$, the spectral–angular distribution develops, in addition to a peak due to fulfillment of the Vavilov–Cherenkov condition, a peak corresponding to angles and frequencies at which the factor $R_{\rm L(B)}$, which determines the efficiency of photon diffraction in Laue's or Bragg's geometry [7], is maximal. In [7], radiation associated with this peak was dubbed diffraction transition radiation. For a lateral diffraction maximum in Laue's geometry, this region of angles (θ, φ) and frequencies (ω) is determined by the equation

$$\chi_0'(\beta_1 - 1) + \alpha_{\rm B}(\theta, \varphi, \omega) = 0, \qquad (1)$$

where $\alpha_{\rm B} = (2\mathbf{k}\cdot\boldsymbol{\tau} + \tau^2)/k^2$ is a parameter that characterizes the deviation from exact fulfillment of Bragg's condition (here, $\mathbf{k}$ is the wave vector of the emitted photon and $\boldsymbol{\tau}$ is the reciprocal-lattice vector of crystal planes, $|\boldsymbol{\tau}| = 2\pi/d$, with d being the interplane spacing) and $\beta_1 = \gamma_0/\gamma_1$ [$\gamma_0 = \mathbf{n}_\gamma \cdot \mathbf{N}$ with $\mathbf{n}_\gamma = \mathbf{k}/|\mathbf{k}|$ and $\gamma_1 = \mathbf{n}_{\gamma\tau}\cdot\mathbf{N}$ with $\mathbf{n}_{\gamma\tau} = (\mathbf{k}+\boldsymbol{\tau})/|\mathbf{k}+\boldsymbol{\tau}|$, $\mathbf{N}$ being the unit vector that is orthogonal to the entrance surface of the crystal layer and which is directed toward the interior of the crystal].

An analysis of the expression for the spectral–angular distribution of radiation at a lateral diffraction maximum reveals [8] that, in the region of angles and frequencies satisfying the condition in (1), the spectral–angular distribution of diffraction transition radiation either (for $l \ll L_0 < L_{\rm abs}$) quickly oscillates or (in the case of $L_0 \gg L_{\rm abs}$) appears to be a uniform background under the spectral–angular peak for which the Cherenkov condition is satisfied. In either case, however, the intensity of parametric x-ray radiation exceeds the intensity of diffraction transition radiation.

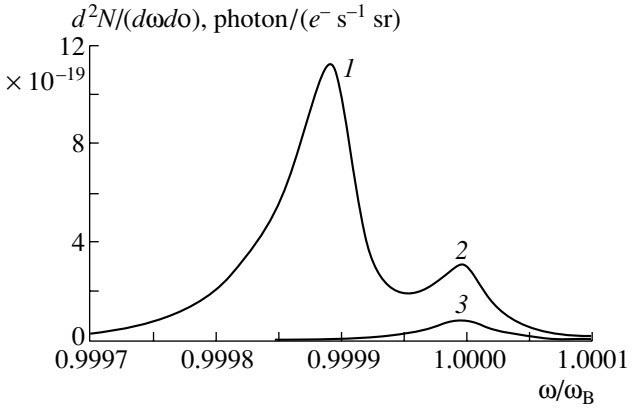

Fig. 1. Peaks of diffraction transition radiation and superlight bremsstrahlung radiation in the spectral–angular distribution of radiation. The curve that exhibits the maxima denoted by *1* and *2* was computed for a crystal layer of thickness $L_0 = 10 l_{\rm opt}$, the peaks being due to (*1*) superlight bremsstrahlung radiation and (*2*) diffraction transition radiation. The curve having the maximum denoted by *3* represents our results for a layer of thickness $L_0 = l_{\rm opt}$, the maximum corresponding to diffraction transition radiation.

In a thin crystal layer ($L_0 < l$), it is necessary to take into account, in addition to radiation in the medium, radiation due to the electromagnetic field generated by a charged particle moving in a vacuum prior to entering the layer. An analysis shows that the main contribution to the intensity of the diffraction maximum may come either from the term that represents diffraction transition radiation or from the term that represents resonance radiation, which was first considered by Ter-Mikaelyan in [9].

The multiple scattering of charged particles on medium atoms leads to the emergence of yet another type of radiation, bremsstrahlung, which, in a crystal target, also undergoes diffraction on a chosen system of planes. As the energy of charged particles is decreased or the layer thickness is increased, the relative bremsstrahlung contribution to the diffraction maximum becomes greater, which leads to a gradual change in the spectral–angular and the angular distribution of the radiation. In just the same way as in the case of the generation of parametric x-ray radiation, it can be shown that, in the two-wave approximation, diffraction in the first dispersion branch ($\mu = 1$) results in that the medium refractive index becomes greater than unity in some region of bremsstrahlung angles and frequencies. In [7], bremsstrahlung whose photons propagate in a crystal at a phase velocity less than the velocity of charged particles generating them

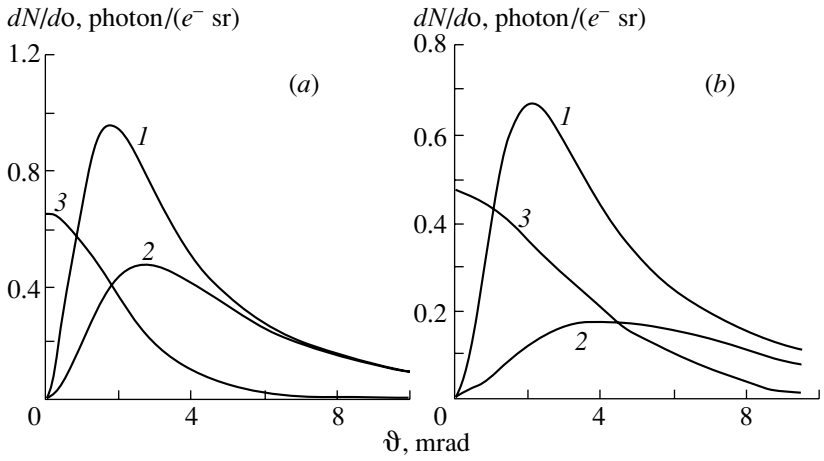

Fig. 2. Sections of the angular distributions for parametric x-ray radiation and bremsstrahlung radiation at an azimuthal angle of $\varphi = 0$ rad. The energy of the charged-particle beam was taken to be either (*a*) 900 or (*b*) 400 MeV. Curves *1* and *2* represent the results obtained for parametric x-ray radiation without and with allowance for multiple scattering, respectively, while curve *3* corresponds to bremsstrahlung radiation.

was dubbed superlight bremsstrahlung. In the same article, bremsstrahlung in the second dispersion branch ($\mu = 2$) and bremsstrahlung in the first branch for angles θ and frequencies ω such that the refractive index is less than unity, $n_{1s} < 1$, were called diffraction bremsstrahlung. Diffraction bremsstrahlung is emitted at the same angles and at the same frequencies as the diffraction transition radiation. In contrast to radiation generated by a particle moving along a straight line at a constant speed, bremsstrahlung (both of superlight and of diffraction species) has, however, a maximum in the angular distribution at $\vartheta = 0$ (that is, strictly along the direction toward the diffraction maximum).

If the particle energy satisfies the condition $E_p < E_{\mathrm{thr}}$, diffraction bremsstrahlung and diffraction transition radiation appear to be dominant radiation mechanisms for the target thickness taking values in the range $l < L_0 < l_{\mathrm{opt}}$. In the case where the crystal-layer thickness L_0 is much larger than the depth of radiation absorption in the crystal, there is no peak due to diffraction transition radiation, since this radiation is formed only as a charged particle traverses the first boundary of the layer and since, in the case of $L_0 \gg L_{\mathrm{abs}}$, it is completely absorbed in the medium. In the limit $L_{\mathrm{abs}} \ll L_0 \leq L_{\mathrm{Br}}$, the peak specified by Eq. (1) is therefore due exclusively to diffraction bremsstrahlung.

For symmetric geometry of Laue diffraction, Fig. 1 displays the spectra of radiation generated by a 200-MeV electron beam in a silicon crystal [(220) reflection and $2\theta_{\mathrm{B}} = 19°$, where θ_{B} is the angle between the particle-velocity vector $\mathbf{v}$ and the planes corresponding to the vector $\boldsymbol{\tau}$]. The threshold energy of charged particles was $E_{\mathrm{thr}} = 321$ MeV. The spectra were calculated at a polar angle of $\vartheta = 0$ for two values of the crystal-layer thickness. For the layer of thickness $L_0 = 10 l_{\mathrm{opt}} = 7.97 \times 10^{-3}$ cm (the thicker one), the maximum in the spectrum (*1*) is attained at the frequency that satisfies the Cherenkov condition at $\mu = 1$, which means that we are dealing here with superlight bremsstrahlung. The maximum labeled with *2* corresponds to fulfillment of the condition in (1) and is due to diffraction bremsstrahlung (the first dispersion branch is responsible for this maximum as well).

In the crystal layer of thickness about $l_{\mathrm{opt}} = 7.97 \times 10^{-4}$ cm (the thinner one), the intensity of diffraction bremsstrahlung at the maximum is one-third as great as that in the thick layer, but this peak becomes dominant because the peak corresponding to superlight bremsstrahlung disappears. A smaller value of the intensity at the diffraction-bremsstrahlung peak in the layer of thickness l_{opt} than in the layer of thickness $10 l_{\mathrm{opt}}$ is explained as follows: since the bremsstrahlung coherence length is $L_{\mathrm{Br}} = 2.7 \times 10^{-3}$ cm here, we have $L_0 = l_{\mathrm{opt}} < L_{\mathrm{Br}}$ for the thin layer and $L_0 = 10 l_{\mathrm{opt}} > L_{\mathrm{Br}}$ for the thick layer, so that the conditions of weak and strong multiple scattering hold in the first and the second case, respectively.

In the situation where the target thickness exceeds the bremsstrahlung coherence length, $L_0 > L_{\mathrm{Br}}$, and where the charged-particle energy is lower than the threshold energy of parametric x-ray radiation, $E_p < E_{\mathrm{thr}}$, the bremsstrahlung contribution to the intensity of the diffraction maximum may appear to be on the same order of magnitude as the intensity of parametric x-ray radiation or even exceed it. For a silicon

Table 1. Parameters of the experiment reported in [5] for various energy values

E_p, MeV	ϑ_{ph}, mrad	$\vartheta_{\mathrm{ph}}^{\mathrm{MP}}$, mrad	$L_{\mathrm{Br}} \times 10^3$, cm	$R = \dfrac{I_{\mathrm{PXR}}}{I_{\mathrm{BR}}}$
900	1.69	2.9	12.2	3.9
700	1.75	3.1	9.45	2.5
600	1.81	3.3	8.10	2.1
500	1.89	3.7	6.75	1.5
450	1.96	4.0	6.08	1.4
400	2.04	4.3	5.40	1.2
350	2.16	4.5	4.73	0.91
300	2.33	4.8	4.05	0.77

Table 2. Parameters of the experiment reported in [6] for various energy values

E_p, MeV	ϑ_{ph}, mrad	$\vartheta_{\mathrm{ph}}^{\mathrm{MP}}$, mrad	$L_{\mathrm{Br}} \times 10^3$, cm	$R = \dfrac{I_{\mathrm{PXR}}}{I_{\mathrm{BR}}}$
1100	2.21	2.65	17.3	6.7
900	2.24	2.87	14.2	5.3
700	2.28	3.24	11.0	4.3
500	2.39	4.02	7.87	2.3
400	2.51	4.76	6.30	1.4
300	2.75	6.04	4.72	0.69
200	3.35	8.74	3.15	0.23

crystal of thickness 0.01 cm, the angular distributions of parametric x-ray radiation and bremsstrahlung are displayed in Fig. 2 at the electron-beam energies of (*a*) 900 and (*b*) 400 MeV ($\gamma_0 = \gamma_1 = \cos 9.5^\circ$) for the (220) reflection; here, parametric x-ray radiation is π-polarized, while bremsstrahlung is of a mixed polarization. The distributions labeled with *1* were obtained by integrating the spectral–angular distribution [8] with respect to the frequency around the point ω_{B} ($\omega_{\mathrm{B}} = \pi c/d \sin\theta_{\mathrm{B}}$) over the range $\Delta\omega/\omega_{\mathrm{B}} = 10^{-3}$. In this case, a dominant contribution to the radiation intensity comes from terms that are proportional to $[\omega - \mathbf{k}_{1\tau\pi} \cdot \mathbf{v}]^{-1}$, the contribution of the remaining terms not exceeding a few percent. The distributions labeled with *2* are those of parametric x-ray radiation treated with allowance for multiple scattering—that is, they were obtained without including terms that are responsible for bremsstrahlung. The distributions labeled with *3* are the angular distributions of bremsstrahlung due to multiple scattering. The situation of strong multiple scattering is realized at either value of the charged-particle energy—specifically, $L_{\mathrm{Br}} = 5.4 \times 10^{-3}$ cm at 400 MeV and $L_{\mathrm{Br}} = 1.22 \times 10^{-2}$ cm at 900 MeV, whence it follows that $L_{\mathrm{Br}} \ll L_0$ in both cases.

Even at the energy value of 900 MeV, the angular intensity of bremsstrahlung at the maximum (for $\vartheta = 0$) exceeds the angular intensity of parametric x-ray radiation at the maximum (for an angle of $\vartheta = \vartheta_{\mathrm{ph}} = \sqrt{\gamma^{-2} - \chi_0'}$). This leads to a substantial change in the character of the angular distribution of parametric x-ray radiation—the intensity no longer shows a dip at an angle of $\vartheta = 0$. Thus, allowance for bremsstrahlung emitted owing to the multiple scattering of charged particles leads to significant changes both in the spectral–angular and in the integrated features of parametric x-ray radiation.

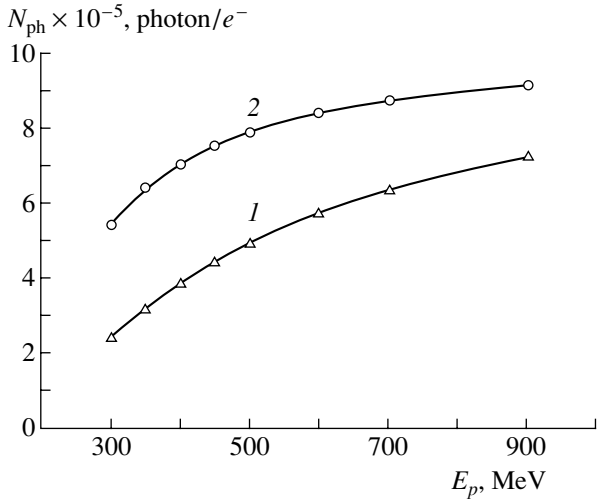

Fig. 3. Energy dependence of the quantum yield: (*1*) results for parametric x-ray radiation and (*2*) total intensity.

3. ANALYSIS OF THE RESULTS OF AN EXPERIMENTAL OBSERVATION OF PARAMETRIC X-RAY RADIATION WITH ALLOWANCE FOR THE MULTIPLE-SCATTERING EFFECT AND THE CONTRIBUTION OF VARIOUS SCATTERING MECHANISMS

For the first time, the goal of experimentally studying the multiple-scattering effect on the properties of parametric x-ray radiation was pursued by Afanasenko *et al.* [5], who measured the angular distributions and quantum yields of radiation generated by 300- to 900-MeV electron beams incident on diamond and silicon crystals having various thicknesses and various orientations and who obtained the experimental dependence of the quantum yield of radiation on the electron-beam energy. Instead of a dependence of the form $\ln E_p$ above the threshold value E_{thr} and a sharp drop in proportion to E_p^4 below E_{thr}, those authors observed a significant increase in the radiation yield at energies in the region 400–600 MeV. They attributed this to the effect of strong multiple scattering. A comparison of these experimental data with estimates obtained on the basis of formulas from [3, 4, 7], where multiple scattering was taken phenomenologically into account, revealed only qualitative agreement.

In Table 1, we quote main parameters that characterize the experimental situation at various values of the electron-beam energy; here, $\vartheta_{\text{ph}}^{\text{MS}}$ is the effective angle of the emission of parametric x-ray radiation with allowance for multiple scattering—this angle is defined as that at which the angular distribution of parametric x-ray radiation attains a maximum. The experiment was performed with a silicon crystal of thickness $L = 1.3$ mm for the (220) reflection ($\gamma_0 = \gamma_1 = \cos 9.5°$), the angular size of the detector used being 9.5×10^{-3} rad.

From the data in Table 1, it follows that, for all values of the electron-beam energy, $L_0 > L_{\text{Br}}$, which means that the case of strong multiple scattering is realized there. In this situation, the threshold energy E_{thr} for parametric x-ray radiation is 321 MeV; because of strong multiple scattering, however, the total threshold energy changes, reaching the value of $E_{\text{thr}}^{\text{MS}} = 1175$ MeV. This means that, even at the electron-beam energy of 900 MeV, the intensity of parametric x-ray radiation decreases because of multiple scattering.

The ratio of the integrated intensity of parametric x-ray radiation to the integrated intensity of bremsstrahlung is given in the last column of Table 1. It can be seen that, at energies in the region $E_p < 400$ MeV, the intensity of bremsstrahlung becomes commensurate with the intensity of parametric x-ray radiation and even begins to exceed it.

The quantum yield of parametric x-ray radiation proper and the quantum yield of the total radiation (parametric x-ray radiation plus superlight bremsstrahlung plus diffraction bremsstrahlung plus diffraction transition radiation) versus the charged-particle energy are displayed in Fig. 3 (curves *1* and *2*, respectively) according to the calculations based on rigorous formulas that take into account the contributions of various radiation mechanisms and the interference between them.

The experimental curve shows an increase in the intensity over the energy range 400–600 MeV, while the numerical calculations predict a smooth decrease in the intensity of the quantum yield with decreasing E_p (Fig. 3, curve *2*). The quantum yield at $E_p = 900$ MeV exceeds that at $E_p = 300$ MeV by a factor of 1.65, whereas the calculation by the Feranchuk–Ivashin formula (where multiple scattering is taken phenomenologically into account) [3] predicts a change by a factor of 2.3 (see Fig. 1 in [5]). Thus, our calculations did not exhibit an increase in the quantum yield at energies in the range 400–600 MeV; therefore, this effect is due to some other factors, which were also indicated in [5].

The results obtained by measuring the quantum yield of x-ray radiation as a function of the electron-beam energy in the range 200–1100 MeV were presented in [6].

The main parameters that characterize the experimental situation there are given in Table 2 (these parameters are analogous to those in Table 1). In that situation, the threshold energy for parametric x-ray radiation was $E_{\text{thr}} = 236$ MeV ($E_{\text{thr}}^{\text{MS}} = 730$ MeV). For all values of the electron-beam energy there, $L_0 =$

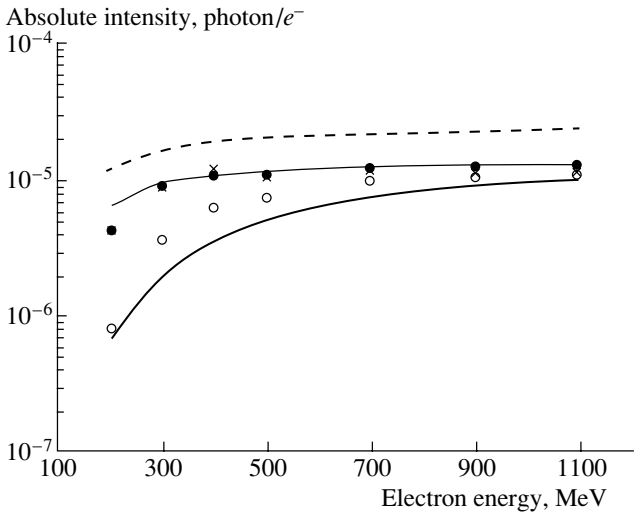

Fig. 4. Absolute radiation yield as a function of electron-beam energy: (thick solid curve) results obtained within the Feranchuk–Ivashin model [3], (dashed curve) results produced by the ideal model (without allowance for multiple scattering and absorption), (thin solid curve) results given by integration of the spectral–angular distribution with respect to the frequency (over the range $\Delta\omega/\omega_B = 10^{-3}$) and the angles without allowance for multiple scattering [8], (open circles) contribution of parametric x-ray radiation (and diffraction transition radiation) alone (without bremsstrahlung), (closed circles) results of the calculation by complete formulas allowing for multiple scattering (integration with respect to the frequency over the range $\triangle\omega/\omega_B = 10^{-3}$), and (crosses) experimental values from [6].

$L/\cos\theta_B > L_{abs}$ and $L_0 > L_{Br}$. This is the region of a strong multiple-scattering effect, and it is necessary to take everywhere into account the bremsstrahlung contribution to the total intensity of the radiation. The inclusion of bremsstrahlung is of crucial importance for $E_p < 700$ MeV (this radiation contributes here as much as about 20%), its contribution becoming dominant for $E_p < 400$ MeV. It should be noted that the contribution to the intensity from radiation generated in the non-Cherenkov dispersion branch, as well as from radiation formed over the vacuum segment of the trajectory and its interference with the radiation in the medium, does not exceed 5.5% in the geometric configuration being considered.

Experimental results obtained in [6] by measuring the quantum yield of radiation are given in Fig. 4, along with the absolute radiation yield calculated on the basis of various models of multiple scattering. The dashed curve represents results obtained within the ideal model, while the thick solid curve corresponds to the Feranchuck–Ivashin model, which takes into account multiple scattering in a phenomenological coherent way and absorption. The thin solid curve was computed by integrating the spectral–angular distribution with respect to the frequency (over the range $\Delta\omega/\omega_B = 10^{-3}$) and with respect to the angles. Closed circles represent the results of the calculations that employed exact formulas (integration with respect to the frequency covered the range $\Delta\omega/\omega_B = 10^{-3}$) allowing for radiation in both dispersion branches, radiation in a vacuum before the crystal used, and interference terms, as well as bremsstrahlung, while open circles correspond to taking into account only parametric x-ray radiation (and diffraction transition radiation), but not bremsstrahlung. The experimental values of the quantum yield (crosses) fall between the values obtained on the basis of the ideal and the "noncoherent" model and are virtually independent of energy in the range 400–1100 MeV, remaining approximately equal to 10^{-5} photon/e^-, decreasing somewhat at an energy of 350 MeV, and showing more than a twofold drop at an energy of 200 MeV.

As can be seen from Fig. 4, the results of the calculations in which multiple scattering is rigorously taken into account on the basis of complete formulas (closed circles) are in excellent agreement with experimental data. Indeed, multiple scattering changes significantly the properties of parametric x-ray radiation, reducing its intensity (curve formed by open circles); however, bremsstrahlung that arises owing to multiple scattering compensates for this decrease, with the result that the quantum yield of radiation exhibits a smooth dependence on the charged-particle energy without a manifest threshold behavior.

4. CONCLUSION

In interpreting experimental data on x-ray radiation generated by charged particles in crystals, use has so far been made either of a theory where a calculation of parametric x-ray radiation involves taking phenomenologically into account multiple scattering [2–4]; or of asymptotic formulas obtained in the approximation of weak multiple scattering [7]; or of the approach where multiple scattering is included in the analysis via averaging, over multiple-scattering angles, the expression found for the angular distribution of parametric x-ray radiation within the kinematical theory of diffraction [10].

All these approaches are unable to provide an adequate quantitative description of the radiation intensity in the case of strong multiple scattering. In order to obtain such a description, it is necessary to perform calculations on the basis of taking rigorously into account the multiple-scattering effect on the mechanism of the emission of parametric x rays, bremsstrahlung arising as the result of multiple scattering, and the interference of bremsstrahlung and

parametric x-ray radiation. A comparison of experimental data and the results of our theoretical calculations gives every reason to state that this approach to taking into account multiple scattering in radiation generated by charged particles ensures very good agreement between theoretical and experimental results.

REFERENCES

1. V. G. Baryshevsky, *Channeling, Radiation, and Reactions in Crystals at High Energies* (Belorus. Univ., Minsk, 1982).
2. V. G. Baryshevsky and I. D. Feranchuk, Phys. Lett. A **57A**, 183 (1976).
3. I. D. Feranchuk and A. V. Ivashin, J. Phys. (Paris) **46**, 1981 (1985).
4. V. G. Baryshevsky, I. D. Feranchuk, A. O. Grubich, and A. V. Ivashin, Nucl. Instrum. Methods Phys. Res. A **249**, 306 (1986).
5. V. P. Afanasenko, V. G. Baryshevsky, A. S. Lobko, *et al.*, Nucl. Instrum. Methods Phys. Res. A **334**, 631 (1993).
6. S. Asano, I. Endo, M. Harada, *et al.*, Phys. Rev. Lett. **70**, 3247 (1993).
7. V. G. Baryshevskiĭ, A. O. Grubich, and Le Tien Hai, Zh. Éksp. Teor. Fiz. **94** (5), 51 (1988) [Sov. Phys. JETP **67**, 895 (1988)].
8. V. G. Baryshevsky, Nucl. Instrum. Methods Phys. Res. B **122**, 13 (1997).
9. M. L. Ter-Mikaelian, *High Energy Electromagnetic Processes in Condensed Media* (Akad. Nauk Arm. SSR, Yerevan, 1969; Wiley, New York, 1972).
10. H. Nitta, Nucl. Instrum. Methods Phys. Res. B **115**, 401 (1996).

Translated by A. Isaakyan

Physics of Atomic Nuclei, Vol. 66, No. 2, 2003, pp. 409–415. Translated from Yadernaya Fizika, Vol. 66, No. 2, 2003, pp. 435–441.

XXXI International Conference on the Physics of Charged-Particle Interaction with Crystals (Institute of Nuclear Physics, Moscow State University, Moscow, May 28–30, 2001)

On Parametric X-ray Radiation

V. G. Baryshevsky* **and O. M. Lugovskaj**

Institute for Nuclear Problems, Belarussian State University, Minsk, Belarus

Received January 25, 2002; in final form, June 24, 2002

Abstract—The spectral–angular and angular distributions of parametric x-ray radiation generated in the vicinity of the maximum at small angles to the direction of charged-particle motion are studied under the conditions of Laue and Bragg diffraction geometries. Detector parameters at which the dynamical maxima of parametric x-ray radiation can be observed against the background of transition radiation are indicated. The spectral–angular and angular distributions of parametric x-ray radiation are analyzed for the case of backward geometry. The results of the present theoretical calculations are found to be in good agreement with experimental data. © *2003 MAIK "Nauka/Interperiodica"*.

1. INTRODUCTION

It was first shown in [1] that, if the conditions of dynamical diffraction are met for radiation generated by charged particles, an abrupt change in the refractive index of a medium for x rays leads to a substantial change in the spectral properties of this radiation. In particular, the refractive index can become greater than unity; therefore, the Vavilov–Cherenkov condition can be satisfied, which results in the generation of radiation. This mechanism of radiation was first predicted theoretically in the early 1970s [2, 3] (see also [4, 5]), and the radiation itself was dubbed parametric x-ray radiation. After parametric x-ray radiation had been observed experimentally [6, 7], there appeared many theoretical and experimental studies devoted to the subject (see, for example, [8–13] and [14–20], respectively). The results of some experiments agree well with the kinematical theory of parametric x-ray radiation [14–16], while the results of the others require a further theoretical interpretation [17–19]. Despite a large number of publications dealing with parametric x-ray radiation, the applicability range of dynamical theory and its consistency with available experimental data have not yet received adequate study. Moreover, the need for the dynamic approach is still the subject of lively discussions.

The main distinction between the kinematical and the dynamical approach is that, for example, in the case of two-wave diffraction, dynamical theory predicts, in addition to radiation emitted at large angles to the direction of the charged-particle velocity and described within both approaches, parametric x rays emitted at small angles to this direction [9]. The latter component has not yet been observed. The recent experiment reported in [20] did not yield a positive result in this respect either.

Thus, there are two problems to be solved: first, there are a number of experiments devoted to measuring parametric x-ray radiation in Bragg diffraction geometry that have yet to be interpreted theoretically; second, all attempts at experimentally observing parametric x-ray radiation at small angles to the direction of charged-particle motion have so far been futile. It is precisely the problems that are considered in the present article.

2. ANALYSIS OF THE INTENSITY OF PARAMETRIC X-RAY RADIATION AT SMALL ANGLES TO THE DIRECTION OF CHARGED-PARTICLE MOTION

General expressions for the spectral–angular distributions of parametric x-ray radiation at the maximum in the region of small angles to the charged-particle velocity were obtained in [9]. According to [9], the cases of Laue and Bragg diffraction must be distinguished in studying forward radiation. For the case of Laue diffraction geometry, the expression for the differential number of photons having the polarization vector $\mathbf{e}_s$ ($s = \sigma, \pi$) that are emitted in the directions determined by the wave vector $\mathbf{k}$ has the form

$$\frac{d^2N_s}{d\omega do} = \frac{e^2Q^2\omega}{4\pi^2\hbar c^3}(\mathbf{e}_s\cdot\mathbf{v})^2\left|\sum_{\mu=1,2}\xi^0_{\mu s}\exp\left(i\frac{\omega}{c\gamma_0}\varepsilon_{\mu s}L\right)\right. \quad (1)$$

*e-mail: bar@inp.minsk.by

1063-7788/03/6602-0409$24.00

$$\times \left[\frac{1}{\omega - \mathbf{k}\cdot\mathbf{v}} - \frac{1}{\omega - \mathbf{k}_{\mu s}\cdot\mathbf{v}}\right]$$
$$\times \left[\exp\left(\frac{i(\omega - \mathbf{k}_{\mu s}\cdot\mathbf{v})}{c}L_0\right) - 1\right]\Bigg|^2.$$

The analogous expression for the case of Bragg diffraction geometry is

$$\frac{d^2N_s}{d\omega do} = \frac{e^2Q^2\omega}{4\pi^2\hbar c^3}(\mathbf{e}_s\cdot\mathbf{v})^2 \qquad (2)$$
$$\times \left|\sum_{\mu=1,2}\gamma^0_{\mu s}\exp\left(i\frac{\omega}{c\gamma_0}\varepsilon_{\mu s}L\right)\right.$$
$$\times \left[\frac{1}{\omega - \mathbf{k}\cdot\mathbf{v}} - \frac{1}{\omega - \mathbf{k}_{\mu s}\cdot\mathbf{v}}\right]$$
$$\times \left[\exp\left(\frac{i(\omega - \mathbf{k}_{\mu s}\cdot\mathbf{v})}{c}L_0\right) - 1\right]\Bigg|^2.$$

In these expressions,

$$\xi^0_{1(2)s} = \frac{2\varepsilon_{2(1)s} - \chi_0}{2(\varepsilon_{2(1)s} - \varepsilon_{1(2)s})}; \quad \gamma^0_{1(2)s} = \frac{2\varepsilon_{2(1)s} - \chi_0}{(2\varepsilon_{2(1)s} - \chi_0) - (2\varepsilon_{1(2)s} - \chi_0)\exp\left(i\frac{\omega}{c\gamma_0}(\varepsilon_{2(1)s} - \varepsilon_{1(2)s})L\right)};$$

$\mathbf{e}_\sigma \parallel [\mathbf{k}\times\boldsymbol{\tau}]$, where $\boldsymbol{\tau}$ is reciprocal-lattice vector of crystallographic planes ($|\boldsymbol{\tau}| = 2\pi/d$, with d being the intraplanar spacing) and $\mathbf{e}_\pi \parallel [\mathbf{k}\times\mathbf{e}_\sigma]$ are the radiation-polarization vectors; $\mathbf{v}$ is the charged-particle-velocity vector; Q is the particle charge; ω is the radiation frequency; $\mathbf{k}_{\mu s} = \mathbf{k} + (\omega/c\gamma_0)\varepsilon_{\mu s}\mathbf{N}$, $\mathbf{N}$ being the unit vector that is orthogonal to the entrance surface of the plate and which is directed toward the interior of the crystal; L is the crystal plate thickness; $L_0 = L/\gamma_0$, where $\gamma_0 = \mathbf{n}_\gamma\cdot\mathbf{N}$ and $\mathbf{n}_\gamma = \mathbf{k}/k$, is the crystal thickness along the direction of charged-particle motion; and

$$\varepsilon_{\mu s} = \frac{1}{4}\left\{-\alpha_{\mathrm{B}}\beta_1 + \chi_0(\beta_1 + 1)\right. \qquad (3)$$
$$\left. \pm \sqrt{[-\alpha_{\mathrm{B}}\beta_1 + \chi_0(\beta_1 - 1)]^2 + 4\beta_1\chi^s_\tau\chi^s_{-\tau}}\right\}.$$

Here, the plus and minus signs in front of the square root correspond to $\mu = 1$ and $\mu = 2$, respectively; χ_0, χ^s_τ, and $\chi^s_{-\tau}$ are the Fourier components of the complex-valued polarizabilities of the crystal used;

$$\alpha_{\mathrm{B}} = \frac{2\mathbf{k}\cdot\boldsymbol{\tau} + \tau^2}{k^2} \qquad (4)$$

is a parameter that specifies the deviation from exact fulfillment of Bragg's condition; and $\beta_1 = \gamma_0/\gamma_1$, where $\gamma_1 = \mathbf{n}_{\gamma\tau}\cdot\mathbf{N}$ with $\mathbf{n}_{\gamma\tau} = (\mathbf{k} + \boldsymbol{\tau})/|\mathbf{k} + \boldsymbol{\tau}|$.

Let us compare formulas (1) and (2) with the known formula describing the transition radiation of x rays in an amorphous medium (see, for example, [8]) and having the form

$$\frac{d^2N_s}{d\omega do} = \frac{e^2Q^2\omega}{4\pi^2\hbar c^3}(\mathbf{e}_s\cdot\mathbf{v})^2 \qquad (5)$$
$$\times \left|\exp\left(i\frac{\chi_0\omega}{2c\gamma_0}L\right)\left[\frac{1}{\omega - \mathbf{k}\cdot\mathbf{v}} - \frac{1}{\omega - \mathbf{k}_a\cdot\mathbf{v}}\right]\right.$$
$$\times \left[\exp\left(\frac{i(\omega - \mathbf{k}_a\cdot\mathbf{v})}{c}L_0\right) - 1\right]\Bigg|^2,$$

where $\mathbf{k}_a = \mathbf{k} + (\omega\chi_0/2c\gamma_0)\mathbf{N}$ is the photon wave vector in the amorphous medium being considered.

Obviously, the formulas describing parametric x-ray radiation and transition radiation are similar in form, but the difference is that, in an amorphous medium, as well as in a crystal where the Bragg condition is strongly violated, only one wave, with wave vector $\mathbf{k}_a$, can propagate, while, in the case of parametric x-ray radiation, coherent superposition of a few waves propagates through a crystal owing to diffraction (see above).

If, however, the frequencies and angles in formulas (1) and (2) for parametric x-ray radiation emitted at small angles to the direction of charged-particle motion do not satisfy the conditions of diffraction (that is, the absolute value of the parameter characterizing the deviation from the exact Bragg condition, $|\alpha_{\mathrm{B}}|$, becomes much greater than $|\chi'_0|$, where χ'_0 is the real part of χ_0), then these formulas reduce to formula (5) for transition radiation, because, in this case, $\varepsilon_{1s} \to \chi_0/2$, $\xi^0_{1s} \to 1$, and $\xi^0_{2s} \to 0$ (or $\varepsilon_{2s} \to \chi_0/2$, $\xi^0_{2s} \to 1$, and $\xi^0_{1s} \to 0$, depending on whether $\alpha_{\mathrm{B}} \gg |\chi'_0|$ or $\alpha_B \ll -|\chi'_0|$). Concurrently, the expressions for the spectral–angular intensity of parametric x-ray radiation emitted at large angles tend to zero, because the conditions of diffraction are not satisfied.

Laue Diffraction

First and foremost, we note that $\chi'_0 < 0$, and it follows from the Vavilov–Cherenkov condition that the real part of the refractive index becomes greater than unity only for one dispersion root $\varepsilon_{\mu s}$ ($\mu = 1$ in this case). As a result, the difference $(\omega - \mathbf{k}_{1s}\cdot\mathbf{v})$ may vanish, and that term in (1) which involves this

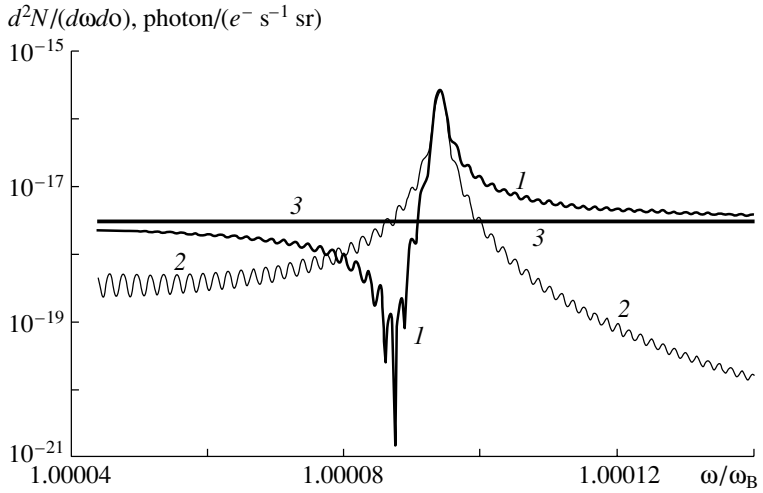

Fig. 1. Spectral–angular distribution of radiation generated by a single electron that traversed a crystal plate: (*1*) results of the calculation by formula (1) with allowance for all terms, (*2*) results of the calculation by formula (1) in the approximation where only the term proportional to $1/(\omega - \mathbf{k}_{1s} \cdot \mathbf{v})$ is taken into account, and (*3*) transition radiation contribution calculated by formula (5).

difference in the denominator begins to increase in proportion to L. At the same time, that term in (1) which involves the analogous difference $(\omega - \mathbf{k}_{2s} \cdot \mathbf{v})$ in the denominator will never increase in proportion to L, since this difference cannot vanish in principle. It follows that the term involving the difference $(\omega - \mathbf{k}_{1s} \cdot \mathbf{v})$ makes a dominant contribution to the radiation intensity if the crystal thickness along the direction of particle motion satisfies the condition $L/\gamma_0 \gg l_0$ ($l_0 = \lambda\gamma^2$ is the coherent radiation length in a vacuum, λ is the radiation wavelength, and γ is the charged-particle Lorentz factor). In the case of $L/\gamma_0 \sim l_0$, it is necessary to take into account all terms in (1) in performing integration with respect to frequencies. In order to observe dynamical maxima in the forward-radiation peak, the parameters of the experiment must be selected in such a way that the contribution of the quasi-Cherenkov radiation mode to the intensity would be noticeable against the background of the non-Cherenkov component.

By way of example, the spectral–angular distributions of 10-keV radiation at an angle of 2.4 mrad in a crystal of thickness $L = 0.1$ cm are shown in Fig. 1 for the case of the (111) diffraction plane and symmetric reflection. All the calculations in this study were performed for the electron-beam energy of $E =$ 855 MeV; the spectral–angular distributions and the sections corresponding to angular distribution were computed for an azimuthal angle of $\varphi = \pi/2$, which corresponds to the σ polarization of parametric x-ray radiation.

Bragg Diffraction

In the case of Bragg diffraction, physical phenomena occurring in a crystal differ significantly from those caused by Laue diffraction, because the conditions for the amplitudes at the crystal–vacuum interface are different. The distinction between the physical mechanisms of diffraction in different parts of the diffraction-maximum region is a typical feature of Bragg reflection. By way of example, we indicate that, in some region of the maximum, the wave vectors in the lattice become complex-valued. By analogy with wave vectors in absorbing crystals, this must cause an exponential decrease in the intensities of the relevant waves as they penetrate into the crystals. The corresponding region of the maximum is referred to as the region of total reflection.

The spectral–angular (at an angle of $\vartheta =$ 2.4 mrad) and angular distributions of 20-keV radiation for $\gamma_0 = 0.1636$ and $\gamma_1 = 0.0337$ are shown in Figs. 2 and 3, respectively, in a silicon crystal of thickness $L = 0.01$ cm for the (111) diffraction plane. As can be seen from Fig. 2, the $\mu = 1$ branch features a distinct maximum. The angular distributions were obtained by integrating expressions (2) and (5) over the range $\Delta\omega = 10^{-4}\omega_B$ [$\omega_B = \pi c/(d \sin\theta_B)$, where θ_B is the angle between the particle-velocity vector $\mathbf{v}$ and the planes corresponding to the reciprocal-lattice vector $\boldsymbol{\tau}$]. For polar angles $\vartheta > 1.5$ mrad, the radiation intensity obtained by integrating expressions (2) exceeds that which corresponds to integration of (5). It is precisely this excess of radiation in a crystal under dynamical-diffraction conditions over radiation emitted from a plate in the case where the diffraction conditions are not satisfied that can be used to reveal dynamical maxima of parametric x-ray radiation in experiments aimed at measuring angular distributions.

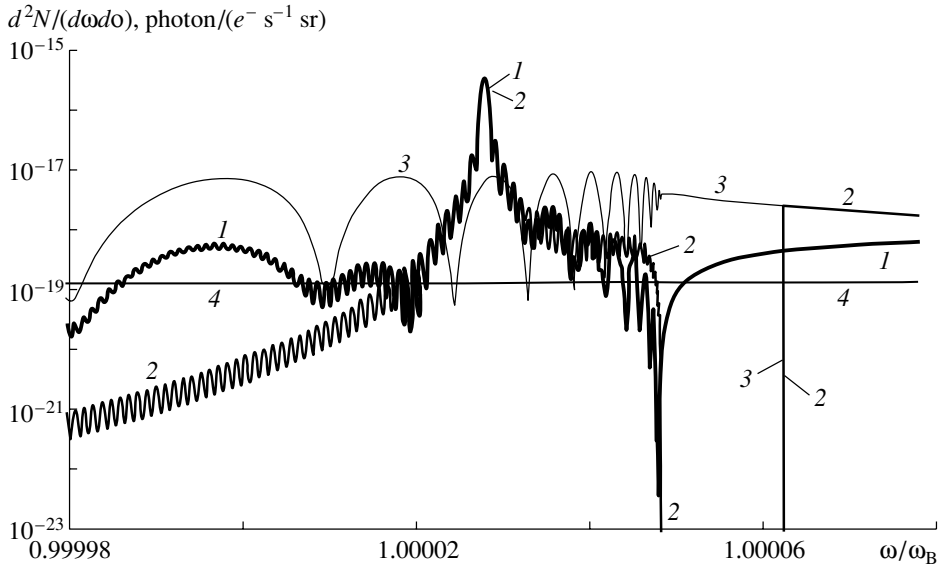

Fig. 2. Spectral–angular distribution of radiation: (*1*) results of the calculation by formula (2) with allowance for all the terms, (*2*) results of the calculation by formula (2) for $\mu = 1$ without retaining the terms proportional to $1/(\omega - \mathbf{k}\cdot\mathbf{v})$, (*3*) results for $\mu = 2$ that were obtained in the same way as in those labeled with *2*, and (*4*) transition-radiation contribution calculated by formula (5).

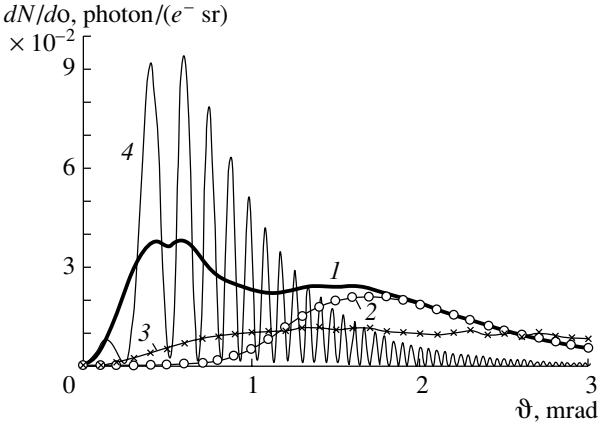

Fig. 3. Angular distributions of radiation that were obtained by means of (*1*) integration of (2) with allowance for all terms, (*2*) integration of (2) for $\mu = 1$ without retaining the terms proportional to $1/(\omega - \mathbf{k}\cdot\mathbf{v})$, (*3*) integration of (2) for $\mu = 2$ in the same approximation as that used to obtain results labeled with *2*, and (*4*) integration of (5).

3. RADIATION TO THE LATERAL DIFFRACTION MAXIMUM IN BRAGG DIFFRACTION GEOMETRY

For radiation that is generated by a charged particle traversing a crystal plate and which is characterized by the polarization vector $\mathbf{e}_{\tau s}$, it was shown in [9] that, in the case of Bragg diffraction, the spectral–angular distribution of the intensity in the region of the maximum occurring at the angle $2\theta_B$ to the direction of its motion is given by

$$\frac{d^2N_s}{d\omega do} = \frac{e^2Q^2\omega}{4\pi^2\hbar c^3}(\mathbf{e}_{\tau s}\cdot\mathbf{v})^2 \times \left|\sum_{\mu=1,2}\gamma^\tau_{\mu s}\left[\frac{1}{\omega - \mathbf{k}_\tau\cdot\mathbf{v}} - \frac{1}{\omega - \mathbf{k}_{\mu\tau s}\cdot\mathbf{v}}\right] \times \left[\exp\left(\frac{i(\omega - \mathbf{k}_{\mu\tau s}\cdot\mathbf{v})}{c}L_0\right) - 1\right]\right|^2, \quad (6)$$

where

$$\gamma^\tau_{1(2)s} = \frac{-\beta_1 C_s\chi_\tau}{(2\varepsilon_{2(1)s} - \chi_0) - (2\varepsilon_{1(2)s} - \chi_0)\exp\left(i\frac{\omega}{c\gamma_0}(\varepsilon_{2(1)s} - \varepsilon_{1(2)s})L\right)},$$

$$\mathbf{k}_\tau = \mathbf{k} + \boldsymbol{\tau}; \quad \mathbf{k}_{\mu\tau s} = \mathbf{k}_\tau + \frac{\omega}{c\gamma_0}\varepsilon_{\mu s}\mathbf{N}; \quad C_s = \mathbf{e}_s\cdot\mathbf{e}_{\tau s}.$$

Expression (6) comprises the terms describing radiation that arises as the charged particle traverses the crystal–vacuum interface, radiation generated within the crystal plate, and their interference. It was shown above that, in the case of Bragg diffraction, the wave vectors in the lattice become complex-

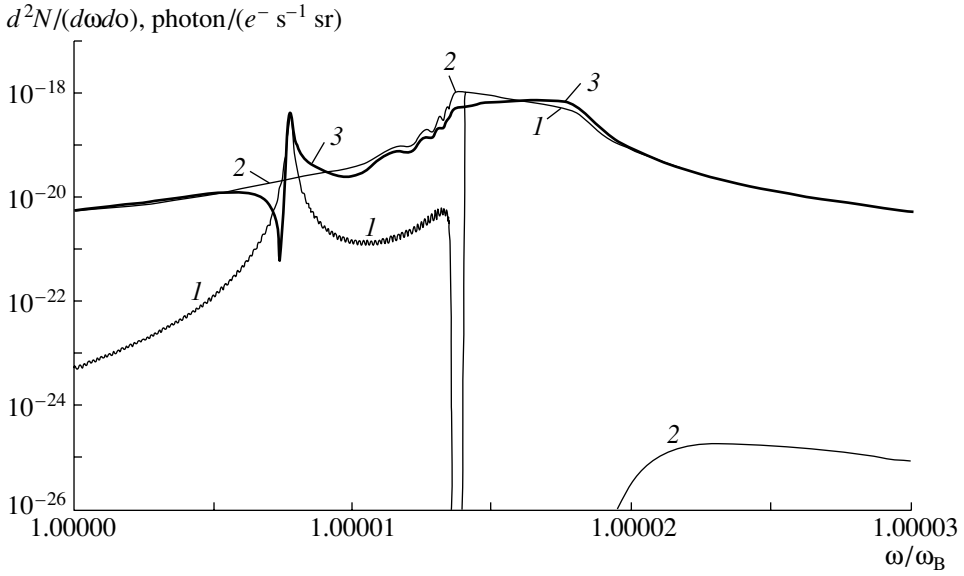

Fig. 4. Spectral–angular distribution of radiation calculated by formula (6): (*1*) results for $\mu = 1$, (*2*) results for $\mu = 2$, and (*3*) total radiation.

valued in a certain region of the maximum, so that the effect of total reflection is realized for the relevant waves. In addition to the peak at the angles and frequencies corresponding to fulfillment of the Vavilov–Cherenkov condition, the spectral–angular distribution of parametric x-ray radiation exhibits a peak associated with the existence of the total-reflection region.

Under the conditions of backward reflection, experiments were performed in [19] to study x-ray radiation generated by charged particles in Bragg diffraction geometry. The angular dependence of the radiation yield was measured there as a function of the crystal-rotation angle ψ with respect to the direction of charged-particle motion. We have performed calculations for the case where a silicon crystal plate 525 μm thick is irradiated with an electron beam of energy 855 MeV.

Figure 4 displays the spectral–angular distributions for the (555) reflection of the components forming total radiation—that is, radiation corresponding to various excitation points in the dispersion curves ($\mu = 1,\ 2$). For a crystal-rotation angle of $\psi = 0.3$ mrad, a narrow maximum in the radiation spectrum at a frequency of $\omega \approx 1.0000075\omega_B$ corresponds to the term proportional to $(\omega - \mathbf{k}_{1\tau\sigma} \cdot \mathbf{v})^{-1}$ if the calculation is based on expression (6); that is, this narrow maximum is associated with the first dispersion branch ($\mu = 1$). A broad maximum in the range $(1.0000125–1.00001875)\omega_B$ is due to both dispersion branches. With increasing crystal-rotation angle ψ (the corresponding polar angle of radiation is 2ψ), the spectral–angular intensity of the narrow maximum grows and, at an angle of about $\vartheta_{ph} = \sqrt{\gamma^{-2} - \chi_0'}$, begins to exceed the intensity of the maximum associated with the region of the total reflection of x-ray radiation from crystallographic planes.

An experiment in this geometry and with these parameters of the crystal and of the electron beam was performed at the Institute of Nuclear Physics at Gutenberg University.[1)] We have calculated the angular distributions of radiation for the (111), (333), and (444) reflections by integrating expression (6) with respect to the frequency over the range corresponding to the actual energy resolution of the detector used there. A comparison of our theoretical results with the experimental angular distributions courteously placed at our disposal by Prof. H. Backe and his colleagues showed fairly good agreement. For instance, the theoretical values of the angular intensity for the (111), (333) and (444) reflections are, respectively, 10%, 18%, and 21% lower than the experimental ones at a crystal-rotation angle of $\psi = 0.3$ mrad, at which the angular distribution of the radiation attains a maximum. The theoretical and experimental curves behave similarly, and the intensity values nearly coincide at angles of about ϑ_{ph}. At angles smaller than approximately 0.3 mrad, there is a distinction that grows with increasing energy of emitted photons. This effect can possibly be explained by the influence of multiple scattering—specifically,

[1)] Institut für Kernphysik, Johannes-Gutenberg-Universität, Mainz (Germany).

by the additional contribution to the intensity from bremsstrahlung generated at small angles.

The relative contribution of bremsstrahlung increases considerably with decreasing charged-particle energy. Experimental results obtained by studying parametric x-ray radiation in a similar geometry at an electron-beam energy that is an order of magnitude lower ($E = 86.9$ MeV) are presented in [19]. Our calculations for this experiment have shown that the result obtained for the intensity of the angular distribution at the maximum by integrating expression (6) with respect to the frequency over the range $\Delta\omega = 10^{-2}\omega_B$ is approximately equal to half the experimental value. However, it is necessary to take into account the contribution of bremsstrahlung to the total intensity, since bremsstrahlung becomes sizable at such electron-beam energies [8]. Thus, it can be stated that the results obtained theoretically for the angular intensity of radiation are in fairly good agreement with the available experimental data.

4. CONCLUSION

The spectral–angular distributions of radiation at the maximum along the direction of the charged-particle velocity have been studied on the basis of general Eqs. (1) and (2). The results demonstrate that, in the radiation spectra, there are distinct maxima corresponding to angles and frequencies at which the Vavilov–Cherenkov condition is satisfied. In comparing the angular distributions of radiation in a crystal under the conditions of diffraction and in an amorphous plate (or in a crystal where the diffraction conditions are strongly violated) for a narrow spectral range of width about $10^{-4}\omega_B$, one can see that, from a certain angle, the radiation intensity under the diffraction conditions exceeds the intensity of bremsstrahlung. For the case of Bragg diffraction, the type of measurement geometry for forward radiation can be chosen in such a way that the angular distribution obtained under the diffraction conditions for a narrow spectral range of radiation ($\Delta\omega/\omega_B \sim 10^{-4}$) would differ considerably from the distributions of radiation for which there are strong deviations from the diffraction conditions. It should be recalled that expressions (1) and (2) were derived without taking into account the multiple scattering of charged particles on the atoms of a crystal-plate material, but such multiple-scattering processes modify considerably the properties of parametric x-ray radiation: they change the spectral–angular and angular distributions (reduce the intensity and broaden spectral and angular peaks); concurrently, the intensity of bremsstrahlung associated with multiple scattering increases, with bremsstrahlung photons being emitted nearly into the same region of angles and frequencies as the photons of parametric x-ray radiation. In order to reduce the multiple-scattering effect, one can use light crystals—for example, LiF or LiH. The possibility of employing heavy-particle beams (that is, beams of protons or nuclei), as well as radiation from a beam of positrons moving in the mode of plane channeling, is a still more efficient method. In this case, multiple scattering can be neglected, so that expressions (1) and (2) can be used for spectral–angular distributions in planning relevant experiments.

The above comparison of our theoretical results, calculated by formula (6), with the experimental distributions of parametric x-ray radiation in backward geometry has revealed that these theoretical and experimental distributions are in good agreement. Therefore, it can be stated that, in the case of Bragg diffraction, only by applying dynamical theory to describing the radiation process can one adequately estimate the intensity of total radiation generated by charged particles in a crystal into the lateral diffraction maximum. It should be noted that all attempts at interpreting experiments of the kind in question within approximate theories (such as kinematical theory, description of radiation at the maximum at large angles as diffraction of transition radiation, or disregard of the interference between radiation corresponding to the different dispersion branches [11, 12]) failed to reproduce experimental data.

REFERENCES

1. V. G. Baryshevskiĭ, Dokl. Akad. Nauk BSSR **15**, 306 (1971).
2. V. G. Baryshevskiĭ and I. D. Feranchuk, Zh. Éksp. Teor. Fiz. **61**, 944 (1971) [Sov. Phys. JETP **34**, 502 (1972)].
3. V. G. Baryshevskiĭ and I. D. Feranchuk, Dokl. Akad. Nauk BSSR **18**, 499 (1974).
4. G. M. Garibyan and Yan Shi, Zh. Éksp. Teor. Fiz. **61**, 930 (1971) [Sov. Phys. JETP **34**, 495 (1972)].
5. G. M. Garibyan and Yan Shi, Zh. Éksp. Teor. Fiz. **63**, 1198 (1972) [Sov. Phys. JETP **36**, 631 (1973)].
6. Yu. N. Adishchev, V. G. Baryshevskiĭ, S. A. Vorob'ev, *et al.*, Pis'ma Zh. Éksp. Teor. Fiz. **41**, 259 (1985) [JETP Lett. **41**, 361 (1985)].
7. A. N. Didenko, B. N. Kalinin, S. Pak, *et al.*, Phys. Lett. A **110A**, 177 (1985).
8. V. G. Baryshevskiĭ, A. O. Grubich, and Le Tien Hai, Zh. Éksp. Teor. Fiz. **94** (5), 51 (1988) [Sov. Phys. JETP **67**, 895 (1988)].
9. V. G. Baryshevsky, Nucl. Instrum. Methods Phys. Res. B **122**, 13 (1997).
10. H. Nitta, Phys. Lett. A **158**, 270 (1991); Phys. Rev. B **45**, 7621 (1992); Nucl. Instrum. Methods Phys. Res. B **115**, 401 (1996).

11. A. Caticha, Phys. Rev. A **40**, 4322 (1989); Phys. Rev. B **45**, 9541 (1992).
12. V. P. Voronov, N. V. Kamyshanchenko, N. N. Nasonov, and V. A. Nasonova, Yad. Fiz. **63**, 2101 (2000) [Phys. At. Nucl. **63**, 2008 (2000)].
13. X. Artru and P. Rullhusen, Nucl. Instrum. Methods Phys. Res. B **145**, 1 (1998).
14. V. P. Afanasenko, V. G. Baryshevsky, A. S. Lobko, *et al.*, Nucl. Instrum. Methods Phys. Res. A **334**, 631 (1993).
15. S. Asano, I. Endo, M. Harada, *et al.*, Phys. Rev. Lett. **70**, 3247 (1993).
16. R. F. Fiorito *et al.*, Nucl. Instrum. Methods Phys. Res. B **79**, 758 (1993).
17. R. F. Fiorito *et al.*, Phys. Rev. E **51**, R2759 (1995).
18. I. Endo, M. Harada, H. Nitta, *et al.*, Phys. Rev. E **51**, 6305 (1995).
19. J. Freudenberger *et al.*, in *Abstracts of the International Workshop on Radiation Physics with Relativistic Electrons, Tabarz, Germany, 1998,* p. 24.
20. I. E. Vnukov, B. N. Kalinin, G. A. Naumenko, *et al.*, in *Proceedings of the XXIX Conference on the Physics of Charged-Particle Interaction with Crystals, Moscow, 1999,* p. 54.

Translated by E. Kozlovskiĭ

Physics of Atomic Nuclei, Vol. 66, No. 2, 2003, pp. 416–419. Translated from Yadernaya Fizika, Vol. 66, No. 2, 2003, pp. 442–445.

XXXI International Conference on the Physics of Charged-Particle Interaction with Crystals (Institute of Nuclear Physics, Moscow State University, Moscow, May 28–30, 2001)

Approximation of Hartree–Fock Atomic Form Factors within the Shell Model

F. P. Korshunov and A. P. Lazar

Institute of Solid State and Semiconductor Physics, National Academy of Sciences of Belarus, ul. P. Brovki 17, Minsk, 220072 Belarus

Received January 25, 2002; in final form, April 16, 2002

Abstract—On the basis of the shell model for the electron distribution in an atom, analytic expressions and approximations are constructed for relativistic Hartree–Fock atomic form factors. The proposed approach ensures a precision that is two to three times higher than that of approximations based on existing models. This approach makes it possible to obtain simple expressions for a screening function of the Thomas–Fermi type. © *2003 MAIK "Nauka/Interperiodica"*.

1. INTRODUCTION

The energies of lines of x-ray radiation accompanying the motion of relativistic electrons through a perfect single crystal is determined, to a precision of about 0.5%, by the form of the continuous potential and by the amplitude of thermal vibrations of atoms. The experimental accuracy in measuring the line positions is comparable with the theoretical accuracy; however, it is achieved via a complicated data treatment in the planar case. By way of example, we indicate that, for certain experimental geometries (plane–axis transition), it is necessary to take into account, in addition to other factors, the discrete structure of the channeling plane [1].

A basic idea that simplifies significantly a theoretical analysis of the channeling effect is to replace the true potential field of the crystal being considered by the sum of the potentials of individual atoms that is averaged along the axis or over the relevant plane. In doing this, it is sometimes necessary to take into account the type of chemical bonding of the atoms [2]; moreover, the accuracy of the approximation being discussed depends on the accuracy of simulating the actual potential of an individual atom. An atomic potential is often constructed in terms of various models for relativistic atomic form factors calculated in the Hartree–Fock approximation [3]. In this study, we obtain analytic approximations for the form factors on the basis of the shell model for the electron distribution and present coefficients in these approximations for the C, Si, and Ge atoms. We discuss the accuracy of the approximation used and consider the question of whether this description of the atom potential is adequate.

2. THEORETICAL ANALYSIS

One of the standard methods for calculating the energy of lines of radiation emitted by particles that traverse crystals in the channeling mode is based on the multichannel representation of the Schrödinger equation for the transverse motion of a particle [4]. In this formalism, the continuous potential of an axis or a plane is expanded in the Fourier series in basic reciprocal-lattice vectors, whereupon the problem of solving the equation reduces to diagonalizing the matrix that arises in the Fourier representation. The Fourier components of the continuous potential are proportional to the electron-scattering form factors $f_{\mathrm{el}}(q)$, which in turn are related to the atomic potential by the equation

$$f_{\mathrm{el}}(q) = \frac{2me}{\hbar^2}\int_0^\infty r^2 V(r)\frac{\sin(qr)}{qr}dr, \qquad (1)$$

where $V(r)$ is the atomic potential, q is the change in the wave vector of the scattered electron, and m is the electron mass [5]. Since calculations on the basis of the Hartree–Fock model describe wave functions more precisely than the potential, the continuous potential is often determined in practice with the aid of atomic form factors (x-ray scattering factors) $f_{\mathrm{X}}(q)$, which are in fact the Fourier transforms of the spatial atomic-electron density $\rho(r)$; that is,

$$f_{\mathrm{X}}(q) = 4\pi\int_0^\infty r^2\rho(r)\frac{\sin(qr)}{qr}dr. \qquad (2)$$

The functional relation between the quantities f_{el} and f_{X} is determined by Poisson's equation and is given

1063-7788/03/6602-0416$24.00

by

$$f_{\rm el}(q) = \frac{2}{a_0\, q^2}[Z - f_{\rm X}(q)], \qquad (3)$$

where a_0 is the Bohr radius and Z is the charge number of the atom.

Doyle and Turner [3] presented the values of the atomic form factors calculated in the Hartree–Fock approximation for $Z = 2$–92 atoms and approximated them by the nine-parameter expression

$$f_{\rm X}^{\rm DT}(s) = \sum_{i=1}^{4} a_i \exp(-b_i s^2) + c, \qquad (4)$$

where $s = q/4\pi$ ($0 < s < 2$ Å^{-1}) and a_i, b_i, and c are adjustable parameters. The s interval bounded from above by the value of 2 Å^{-1} is acceptable for analyzing experiments studying x-ray diffraction, where the reflection intensity decreases fast with increasing order, but it is insufficient for reconstructing the electron-density distribution in a crystal. This is manifested most clearly for axial channeling, in which case large reciprocal-lattice vectors are required in relevant expansions [6] because of a slow convergence of the series for the potential and for the eigenfunctions of the Hamiltonian. For values of $s > 2$ Å^{-1} (shorter distances from an atom), the approximation in question is therefore usually modified by increasing the number of terms.

As a rule, attempts at extending the wave-vector interval in this way run into difficulties. This is because the Gaussian regression of the atomic form factors is unstable to an increase in the number of approximation parameters. Additional coefficients degenerate, or the contributions of new terms prove to be negligible. In practice, one has to restrict the number of adjustable parameters by fixing those of them that are insignificant at large s [6, 7]. Alternatively, one can construct a fit with the same number of parameters, but with a lower accuracy [8].

An analysis revealed that the above procedure failed because of an inappropriate choice of approximating function rather than because of the bounded number of points at which the calculations were performed. If, in (4), one goes from momentum to coordinate space (first discarding the constant term, which does not have physical significance) and obtains the spatial electron density in an atom in the form

$$\rho^{\rm DT}(r) = \frac{Z}{\pi^{3/2}} \sum_i a_i \gamma_i^3 \exp(-(\gamma_i\, r)^2), \qquad (5)$$

where $\gamma_i = 2\pi b_i^{-1/2}$, it immediately becomes obvious that the asymptotic behavior of expression (5) at long distances is inappropriate: the distribution decreases overly fast with increasing r.

It is of interest to compare expressions (4) and (5) with their counterparts that are obtained in the Molière approximation, which is often used in radiation physics, even though its accuracy is low because of averaging over all Z values. In this case, the Thomas–Fermi screening function has the form [9]

$$\varphi(x) = \sum_{i=1}^{3} \alpha_i \exp(-\beta_i x), \qquad (6)$$

where $x = r/a$, a being the screening radius; $\alpha_i = \{0.1, 0.55, 0.35\}$; and $\beta_i = \{1.2, 0.6, 0.3\}$. Going over to the expression for the atomic potential, we then arrive at

$$\rho^{\rm M}(r) = \frac{Z}{4\pi r} \sum_i \alpha_i (\beta_i/a)^2 \exp(-\beta_i r/a), \qquad (7)$$

$$f_{\rm X}^{\rm M}(q) = Z \sum_i \frac{\alpha_i}{1 + (qa/\beta_i)^2}, \qquad (8)$$

where $\rho^{\rm M}(r)$ and $f_{\rm X}^{\rm M}(q)$ are the atomic-electron densities in coordinate and momentum space, respectively. In contrast to (5), expression (7) has an inappropriate asymptotic behavior for $r \to 0$, rather than for long distances. It can easily be seen that expression (8) is the expansion of (4) to the first-order terms inclusive; however, attempts at taking into account higher order corrections would lead to unsatisfactory results for $\rho(r)$, which would then have singularities both at large and at small r.

3. CHOICE OF MODEL

The above analysis has shown that, in choosing the type of regression for the atomic form factors, it is necessary to employ expressions that ensure a correct asymptotic behavior of the spatial electron density. The choice of approximation is essentially a physical rather than a mathematical problem. Models that provide a realistic pattern of the charge distribution in an atom are of interest in this connection.

Within the shell model, the atomic-electron density can be expressed in terms of the sum of monomial Slater orbitals featuring optimized exponents; that is,

$$\rho(r) = \frac{1}{4\pi} \sum_i \frac{c_i}{(2n_i)!} (2\zeta_i)^{2n_i+1} r^{2n_i-2} \exp(-2\zeta_i r), \qquad (9)$$

$$\zeta_i = Z_i/n_i a_0,$$

where n_i is the principal quantum number, c_i is the population factor for the ith shell, and Z_i is a dimensionless parameter that has the meaning of the

Coefficients in the approximation of the atomic form factors f_X for the C, Si, and Ge atoms

		K	L		M		N		σ, %
C	1.97133	3.11664	0.91203					0.0277	
	Z_i	5.85665	3.39163	2.14034					
Si	c_i	2.03252	5.38233	2.45530	2.88762	1.24223			0.0056
	Z_i	14.06573	10.32495	7.99497	4.98222	3.17091			
Ge	c_i	1.84349	8.16582		14.11045	4.05275	2.79390	1.03359	0.0087
	Z_i	38.10050	28.30468		17.55801	10.09968	8.09865	4.94393	

effective charge of the nucleus for electrons of the ith shell [10]. This expression was obtained in the self-consistent-field approximation and under the assumption that the charge distribution in the atom is spherically symmetric. Many other electron-density distributions can be found in the literature [9], but we choose (9) because it leads to the required asymptotic behavior and has a direct analog in the nonrelativistic theory of the hydrogen-like atom. The latter makes it possible to clarify the physical meaning of all of the parameters involved and, as a consequence, to specify their initial values in implementing the fit procedure.

Upon performing necessary transformations, we arrive at the expression for the atomic form factors corresponding to the spatial distribution of electrons that was preset above. The result is

$$f_X(q) = \sum_i f_X^{(i)}(q), \tag{10}$$

where

$$f_X^{(i)}(q) = \frac{c_i}{2n_i(1+(q/2\zeta_i)^2)^{2n_i}} \times \sum_{k=0}^{n_i-1}(-1)^k \binom{2n_i}{2k+1} \left(\frac{q}{2\zeta_i}\right)^{2k}, \tag{11}$$

$$\binom{n}{k} = \frac{n!}{k!(n-k)!}. \tag{12}$$

Summation in (10) covers the shells entering into the electron configuration of the atom being considered and follows the order of filling: K, L, M, etc. It is clear from (9) that we do not distinguish between electrons belonging to the same shell. As the shell is filled, a term of the same type is included in the sum, whereby the accuracy of the approximation is considerably improved.

The explicit expressions for the form factors corresponding to the K and L shells are

$$f_X^{(K)}(q) = \frac{c_K}{(1+(q/2\zeta_K)^2)^2}, \tag{13}$$

$$f_X^{(L)}(q) = c_L \frac{1-(q/2\zeta_L)^2}{(1+(q/2\zeta_L)^2)^4}. \tag{14}$$

Comparing these expressions with their counterparts in the Doyle–Turner and in the Molière approximation [expressions (4) and (8), respectively], we can see that all of them are equivalent in the small-q limit. Distinctions appear with increasing wave vector. The form factors calculated with the approximate expression (4) prove to be underestimated, while those that are computed with the approximate expression (8) are overestimated.

4. RESULTS OF THE CALCULATION AND DISCUSSION

The coefficients in the approximation of f_X for the C, Si, and Ge atoms are quoted in the table. In the fitting procedure, use was made of expressions (10)–(12) over the wave-vector range $0 < s < 6$ Å^{-1}. We would like to indicate from the outset that the proposed model ensured a high accuracy: the root-mean-square deviation was $\sigma = 0.0277$, 0.0056, and 0.0087% for C, Si, and Ge, respectively. The corresponding values obtained in [3] with the nine-parameter approximation in the interval $0 < s < 2$ Å^{-1} are 0.0244, 0.0167, and 0.0305%. In [7], the use of 13 parameters for the carbon atom resulted in $\sigma = 0.0344\%$, while there were only six parameters in our procedure, which yielded $\sigma = 0.0277\%$. Actually, the accuracy of approximation is restricted either by the accuracy of the representation of input data or by an insufficient number of points (27 per element) at which the calculation was performed. The latter plays a dominant role for large-Z atoms, in which case it is necessary to take into account a large number of electrons.

The second special feature is associated with the increase in the number of coefficients in the approximation with increasing charge number of the atom ($Z = 6$ for carbon versus 12 for germanium). The problem of whether a two-exponential (for $Z \leq 18$)

or a three-exponential ($Z > 18$) description of the screening function for the potential is adequate was discussed in [9], and it was concluded there that averaged potentials are unable to ensure a high precision of calculations for arbitrary atoms. In the model considered here, the number of terms in the screening function is not fixed, but it is determined by the number of shells entering into the electron configuration of the atom. Moreover, the table shows that, for a shell featuring a large number of electrons, an additional term is required to achieve the highest accuracy of the fit.

In conclusion, we would like to emphasize that screening functions of the Thomas–Fermi type that are obtained from (10)–(12) have a rather simple analytic form. In contrast to what we have for the Molière potential or in similar approximations (see, for example, [9]), the preexponential weight factor is a polynomial rather than a constant. By way of example, we indicate that, for the helium atom ($Z = 2$), this is a polynomial of first degree. For the atoms of the next period, the degree of the polynomial increases. We did not compare the results of our calculations with experimental data, but these results favor such a representation of the screening function.

ACKNOWLEDGMENTS

This work was supported by the Belarussian Foundation for Basic Research (project no. F00-122).

REFERENCES

1. A. P. Lazar', Poverkhnost, Nos. 5–6, 46 (1999).
2. J. O. Kephart, B. L. Berman, R. H. Pantell, *et al.*, Phys. Rev. B **44**, 1992 (1991).
3. P. A. Doyle and P. S. Turner, Acta Crystallogr. A **24**, 390 (1968).
4. J. U. Andersen, S. K. Andersen, and W. M. Augustyniak, K. Dan. Vidensk. Selsk. Mat. Fys. Medd. **39**, No. 10 (1977).
5. L. D. Landau and E. M. Lifshitz, *Course of Theoretical Physics,* Vol. 3: *Quantum Mechanics: Non-Relativistic Theory* (Nauka, Moscow, 1989, 4th ed.; Pergamon, Oxford, 1977, 3rd ed.).
6. R. K. Klein, J. O. Kephart, R. H. Pantell, *et al.*, Phys. Rev. B **31**, 68 (1985).
7. S. A. Mikheev and A. V. Tulupov, Kristallografiya **36**, 555 (1991) [Sov. Phys. Crystallogr. **36**, 303 (1991)].
8. J. U. Andersen, E. Bonderup, *et al.*, Nucl. Instrum. Methods **194**, 209 (1982).
9. G. V. Dudkov, Usp. Fiz. Nauk **165**, 919 (1995) [Phys. Usp. **38**, 877 (1995)].
10. V. H. Kumar and A. P. Pathak, Phys. Status Solidi B **177**, 269 (1993).

Translated by M. Kobrinsky

Physics of Atomic Nuclei, Vol. 66, No. 2, 2003, pp. 420–422. Translated from Yadernaya Fizika, Vol. 66, No. 2, 2003, pp. 446–448.

XXXI International Conference on the Physics of Charged-Particle Interaction with Crystals (Institute of Nuclear Physics, Moscow State University, Moscow, May 28–30, 2001)

Parametric X-Ray Radiation Generated by 5.7-MeV Electrons in a Pyrolytic-Graphite Crystal

Yu. N. Adishev, V. N. Zabaev*, V. V. Kaplin, S. V. Razin, S. R. Uglov, S. I. Kuznetsov, and Yu. P. Kunashenko

Institute of Nuclear Physics, Tomsk Polytechnic University, pr. Lenina 2a, Tomsk, 634050 Russia

Received January 25, 2002

Abstract—Parametric x-ray radiation is observed in a mosaic pyrolytic-graphite crystal irradiated with a 5.7-MeV electron beam. The first-order (002) reflection of parametric x-ray radiation is detected in Bragg geometry. In the measured spectra, there is a peak at about 8 keV. The detector used is arranged at an angle of $\Theta_D = 2\Theta_B = 27°$ with respect to the electron beam, where Θ_B is the Bragg angle. The target thickness is 0.3 mm. The spectra of parametric x-ray radiation are measured at various angles of target orientation with respect to the axis of the incident-electron beam. © *2003 MAIK "Nauka/Interperiodica".*

Parametric x-ray radiation is emitted by relativistic electrons in crystals at the Bragg angle Θ_B with respect to crystallographic planes owing to diffraction of the pseudophotons of the field generated by these electrons [1]. Special features of parametric x-ray radiation such as a high intensity, pencil-like character of its angular distribution, and a very high degree of monochromatism are reasons behind keen interest in studying this radiation in recent years [2–6]. This article reports on a continuation of the experiment described in [6] and devoted to investigating parametric x-ray radiation generated by 5.7-MeV electrons in a pyrolytic-graphite crystal. The measured radiation spectrum is quasimonochromatic. Its maximum occurring at about 8 keV corresponds to the first order (002) reflection of parametric x-ray radiation.

In this experiment, the equipment used was upgraded in order to suppress the background and to isolate parametric x-ray radiation more correctly. We reduced the target thickness from 1.0 to 0.3 mm, improved the detector energy resolution, diminished the air-layer thickness on the path of detected photons to the detector, and realized the possibility of normalizing the absolute values of measured quantities to the current of electrons traversing the crystal.

The geometry of the measurement is similar to that in [6]. The layout of the experiment is shown in Fig. 1. An electron beam accelerated to an energy of 5.7 ± 0.02 MeV and extracted from the MI-5 microtron installed at the Institute of Nuclear Physics (Tomsk Polytechnic University) was focused and collimated by a transportation system (*1*, *2*) to obtain an angular spread of 0.02° and a diameter of 0.8 mm. After a parallel shift (*3*), the electron beam entered a scattering chamber (*7*). The basic parameters of the accelerator were the following: the accelerated-electron current at the target in a pulse was about 50 μA, the current-pulse duration was 0.5 μs, the pulse-repetition frequency was 25 Hz, and the energy spread was $\Delta E/E = 10^{-3}$. A highly sensitive magneto-inductive sensor (MIS) (*4*) and a special amplifier (*12*) with an amplification factor of 20 000 were developed for detecting and monitoring the beam current. This enabled us to normalize measured quantities and obtain their absolute values. For the target, we used a mosaic pyrolytic-graphite crystal (*5*) of dimensions $10 \times 20 \times 0.3$ mm^3 fixed in the goniometer head (*6*) at the center of the scattering chamber (*7*). The mosaic structure of the crystal was about 0.4 mrad. The electron beam hit the target surface at an angle Θ_0. Throughout the experiment, this angle could be varied by rotating the crystal. The experiment was performed under the conditions of Bragg geometry; the photons of parametric x-ray radiation were emitted from the crystal through the same surface and were incident on a detector (*10*) arranged at an angle of $\Theta_D = 2\Theta_B = 27°$ with respect to the electron-beam axis.

For a detector, we used the XR-100-CdTe Amptek x-ray spectrometer of energy resolution about 1 keV and diameter 2 mm. The spectrometer was calibrated by using the K-series γ lines ($E_{\gamma 1} = 13.94$ keV, $E_{\gamma 2} = 17.75$ keV, etc.) of the ^{241}Am radioactive isotope. To take correctly into account the effect of high-frequency stray currents from the microtron

*e-mail: zabaev@npi.tpu.ru

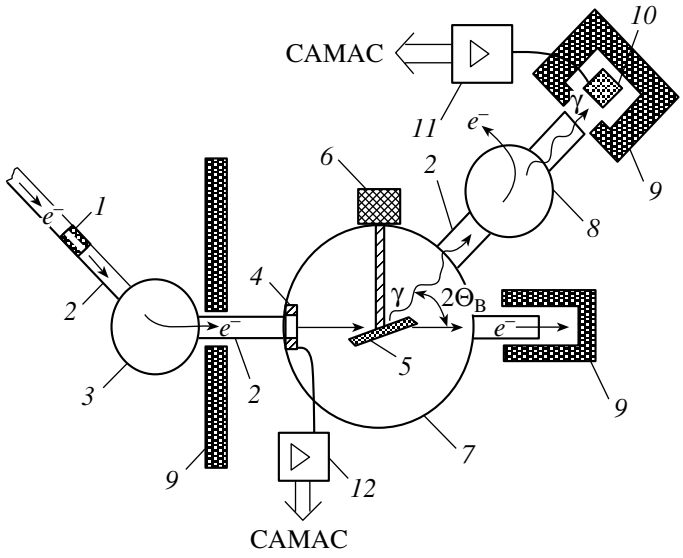

Fig. 1. Layout of the experiment: (*1*) collimator, (*2*) vacuum guide, (*3*) deflecting magnet, (*4*) MIS, (*5*) crystal target, (*6*) goniometer, (*7*) scattering chamber, (*8*) purifying magnet for removing background electrons from the beam of parametric x-ray radiation, (*9*) shield, (*10*) semiconductor detector for x rays, (*11*) detector-signal preamplifier, and (*12*) MIS preamplifier.

modulator on the detector-pulse amplitude, we measured the spectrum of characteristic x-ray radiation from a thin amorphous copper target ($E_\gamma \approx 8$ keV line). In the process of measurements, the contribution from events associated with the overlap of detector pulses was eliminated by maintaining the accelerated-electron current from the microtron at a level for which, on average, one event was detected per five beam spills onto the target (five events per second). The target–detector spacing was 90 cm. The angular acceptance of the detector, $\Delta\Theta_D$, was about 2 mrad. Thus, the measurements were performed under conditions of a strong collimation of the radiation with $\Delta\Theta_D \ll \Delta\Theta_\gamma = 5\gamma^{-1}$, where $\Delta\Theta_\gamma$ is the angular width of the reflection of parametric x-ray radiation and γ is the Lorentz factor. At an energy of 5.7 MeV, $\Delta\Theta_\gamma \approx 450$ mrad. A purifying magnet (*8*) arranged in between the target and the detector removed the charged component from the detected x-ray beam.

Figure 2 shows the spectra of x-ray intensity that were measured for a symmetric position of the crystal with respect to the detector and the electron-beam direction $\Theta_0 = \Theta_B = 13.5°$, as well as for the case of

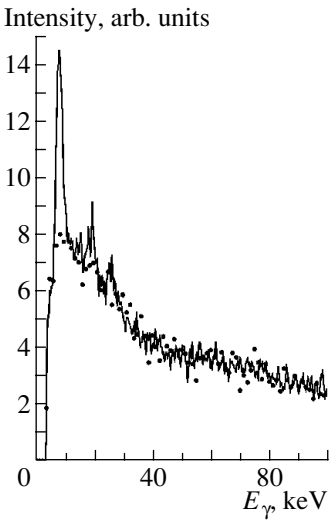

Fig. 2. X-ray-intensity spectrum: (curve) spectrum for $\Theta_0 = \Theta_B$ and (points) spectrum for $\Theta_0 = \Theta_B + 7°$ (background).

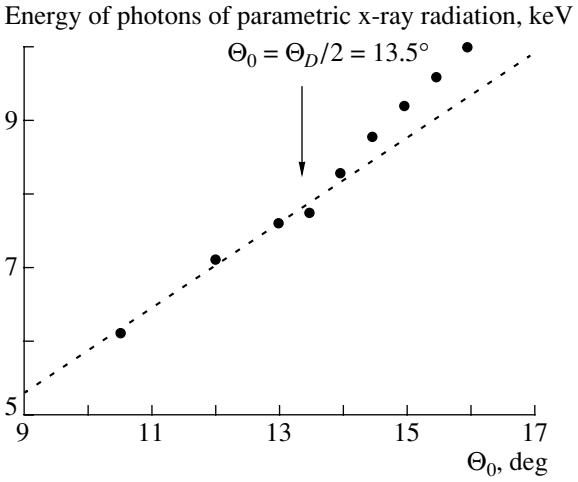

Fig. 3. Position of the first peak in the spectrum as a function of the target-rotation angle.

a disoriented crystal with $\Theta_0 = \Theta_B + 7°$ (background spectrum). The primary instrumental spectra of intensity that were measured by an ADC-712 1024-channel analog–digital converter were grouped and averaged with a step equal to the detector energy resolution. The detection threshold depended on the noise level and amounted to 4 keV. During the experiment, the spectra were measured at various values of the crystal-rotation angle in the range $\Theta_0 = 9.5°–18.5°$. On average, statistics corresponding to one measured spectrum comprised about 12 000 events. The results were normalized to unity of the electron current incident on the crystal. The presence of a peak in the energy range $E_\gamma = 7–12$ keV for those cases where the angle of electron incidence on the target was close to the Bragg value of $\Theta_B = 13.5°$ was the most spectacular feature of the measured spectrum. With increasing angle, the peaks in the spectra were shifted toward higher energies.

Figure 3 shows the position of the first peak in the spectrum as a function of the angle of electron incidence on the crystal surface. Points represent experimental data. The calculations were performed by the formula that determines the position of the first peak associated with parametric x-ray radiation [1]; that is,

$$E_\gamma = \frac{2\pi\hbar c \sin\Theta_0}{d(1 - \cos\Theta_D + 1/(2\gamma^2))},$$

where d is the interplanar spacing in the pyrolytic-graphite crystal.

The disposition of the peaks and the dynamics of their shift toward the harder region of the spectrum with increasing angle Θ_0 are in satisfactory agreement, within the energy and angular errors of the measurements, with the results of the calculations. The deviation of the experimental data from the results of the calculation for $\Theta_0 > 13.5°$ can be explained by the contribution from other radiation mechanisms, such as the diffraction of bremsstrahlung and transition radiation and coherent bremsstrahlung. The discrepancy between the theory and experiment will be explored in detail at the next stage of this investigation.

The data reported here refine the results presented in [6] and form a methodological basis for a future program intended for studying the spectra of parametric x-ray radiation in pyrolytic graphite and silicon more comprehensively.

ACKNOWLEDGMENTS

This work was supported by the Russian Foundation for Basic Research (project no. 02-00-17647).

REFERENCES

1. M. L. Ter-Mikaelian, *High-Energy Electromagnetic Processes in Condensed Media* (Wiley, New York, 1972; Akad. Nauk Arm. SSR, Yerevan, 1969).
2. S. A. Vorob'ev, B. N. Kalinin, S. Pak, and A. P. Potylitsyn, Pis'ma Zh. Éksp. Teor. Fiz. **41**, 3 (1985) [JETP Lett. **41**, 1 (1985)].
3. K. Yu. Amosov, M. Yu. Andreyashkin, V. A. Verzilov, *et al.*, Pis'ma Zh. Éksp. Teor. Fiz. **60**, 506 (1994) [JETP Lett. **60**, 518 (1994)].
4. J. Freudenberger, V. B. Gavrikov, M. Galemann, *et al.*, Phys. Rev. Lett. **74** (13), 2487 (1995).
5. A. P. Potylitsyn, Izv. Vyssh. Uchebn. Zaved., Fiz., No. 4, 26 (1998).
6. V. V. Kaplin, M. Moran, Yu. Pivovarov, *et al.*, Nucl. Instrum. Methods Phys. Res. B **122**, 625 (1997).

Translated by V. Bukhanov